sciendo

POLISH MARITIME RESEARCH 2 (102) 2019 Vol. 26; pp. 15-21
10.2478/pomr-2019-0021

POLISH DGPS SYSTEM: 1995–2017 – STUDY OF POSITIONING ACCURACY

Cezary Specht
Leszek Smolarek
Jan Pawelski
Mariusz Specht
Paweł Dąbrowski
Gdynia Maritime University, Poland

ABSTRACT

This paper is the fourth in a series of publications presenting the process of installation, testing and long-term assessment of the navigational parameters of the Polish DGPS system. This series of publications intends to present – to the general public – the accomplishments of teams of Polish scientists who have been working for years to make the DGPS the main positioning system used in the Polish sea areas. A considerable part of the materials presented in this paper has never been published.
The article presents changes in the position accuracy of the Polish DGPS system over 20 years. Both dynamic tests performed on vessels as well as static measurements campaigns were analysed. The publication contains selected results achieved in its installation and testing in 1995–1997 supplemented with the results of studies conducted in the years: 2006, 2010, 2014, 2017. During this period the position accuracy increased from 2–8 m (1996) to approx. 1–2 m (2010) due to three reasons: turning – off the Selective Availability (2000), technical modernization of reference stations (2010) and continuous – over many years – reducing GPS signal-in-space pseudorange errors, which results in increased position accuracy in all GPS augmentation systems.

Keywords: Polish DGPS system, positioning accuracy, position accuracy measures

INTRODUCTION

To make oneself aware of the importance of the DGPS system implementation in the Polish sea areas in the 1990s, one has to make an assessment of the condition of maritime radio navigation systems available on the Polish coast during the period in question.

The beginnings of radio navigation in Poland date back to the 1950s, when a network of circular (non-directional) radiobeacons was set up on the Polish coast to cover the Polish Exclusive Economic Zone (EEZ). The deployment of the beacons was supposed to enable positioning (conducting at least two radio direction findings) at any place within it. A complex process of computation and placing the results on a map was considerably improved after installation (1970) of the OA chain of the Decca-Navigator system on the Swedish coast [14]. It became the main system of positioning for civil (Mark series receivers) and military ships (Russian Pirs receivers) until the early 1990s when first Transit receivers appeared.

The systems of radio navigation operating on the Polish coast, which are of particular interest included: the AD-2 phase-location system – developed in the 1970s in the Bay of Gdańsk and intended for tankers entering the Gdansk north port [21] and Syledis – intended for maritime pilotage and hydrography in the Szczecin-Świnoujscie harbour complex [9].

Launching the DGPS system on the Polish coast in 1995–1997was of fundamental importance for navigation in the South Baltic Sea. The DGPS system is a positioning solution supporting the GPS in navigation. Like other supporting systems: EGNOS or GNSS geodetic networks [16], it has a particular feature which involves the emission signals of service reliability, which is of particular importance in every type of navigation.

Unlike the GPS, which is used in open sea (oceanic) navigation, the DGPS is used mainly in navigation when approaching ports – on coastal maritime highways [2]. The system is also used in precision hydrographic measurements, both in sea [7] and inland waters [13].

It is noteworthy that positioning accuracy can be improved by modernisation of existing positioning systems, launching new ones and developing reserve ones [8]. Alternatively, this can be achieved with a range of other solutions. The most frequently applied solutions include: Kalman filter [23], data fusion from various sensors [24] or using satellite network and multi-constellation solutions [15]. Other methods that cannot be ignored include: comparative ones [11], advanced methods employing adjustment computations in coastal navigation, positioning algorithms alternative to existing ones [12] or, increasingly popular, employing neural networks. However, despite being highly advanced, these numerical methods will never replace a modern radio navigation positioning system, such as DGPS.

CONCEPT STUDY OF THE POLISH DGPS SYSTEM IN 1995–1997

Unlike other positioning solutions of a local range in the South Baltic Sea, the DGPS was a national system covering the entire Polish coast. During the initial stage of its implementation in 1995–1997 a number of studies were conducted to determine the accuracy of position, range and availability of the system. The implementation work was carried out in two directions: an assessment of the actual range of operation as well as positioning accuracy and availability. It is beyond doubt that the Institute of Navigation and Hydrography of the Polish Naval Academy was the leader in the implementation process. The team led by prof. Kopacz, together with another led by prof. Oszczak of the Academy of Agriculture and Technology in Olsztyn as well as with the Maritime Office in Gdynia, conducted the core accuracy measurements of the Rozewie reference station (RS) and determined the range of operation of both stations. Stationary studies enabling to assess the accuracy and range of operation were conducted between April 1995 and May 1996. Tab. 1 shows all of the measurement campaigns completed at the time.

In terms of the area the tests covered virtually the entire Polish coastal area. The positioning accuracy in the stationary measurements was assessed by examining both Polish stations and those whose range of operation covered the Polish EEZ (Hammerodde, Hoburg, Wustrow). The core accuracy measurements were conducted on the coast, whereas the area of operation of both stations was measured inland using a mobile measurement station (a car with a Leica MX9212 receiver).

Fig. 1. Location of measurements conducted in the seaside areas. Acc. these authors' study based on [10]

Tab. 1. A list of the stationary tests and measurements conducted in the seaside areas as part of the calibration and start-up process of the DGPS on the Polish coast [10]

No.	Measurement contractor	Date of measurements	Place of measurements	Tested DGPS reference stations
1.	Polish Naval Academy	13–14.04.1995	Braniewo, Elbląg, Frombork, Jarosławiec, Kołobrzeg, Słupsk	Hammerodde, Hoburg, Rozewie, Wustrow
2.	Polish Naval Academy	23–26.05.1995	Gdynia	Hammerodde, Hoburg, Rozewie
3.	Polish Naval Academy	26–27.05.1995	Pomerania coast	Hoburg, Rozewie
4.	Polish Naval Academy	03–09.02.1996	Dziwnów, Gdynia	Dziwnów, Rozewie
5.	Academy of Agriculture and Technology in Olsztyn	18–19.08.1995 27–28.08.1995 20–21.08.1995 14.10.1995	Dziwnów, Hel, Jarosławiec, Jastarnia, Łeba, Rozewie, Świnoujście, Władysławowo	Dziwnów, Hammerodde, Hoburg, Rozewie, Wustrow
6.	Maritime Academy in Szczecin	22–28.05.1996	Szczecin Lagoon	Dziwnów, Hammerodde, Wustrow
7.	Maritime Office in Gdynia	12–13.06.1995	Hel, Jastarnia, Łeba, Władysławowo, Żarnowiec	Rozewie

MEASUREMENTS OF POSITIONING ACCURACY IN 1995–1997

Positioning accuracy is the most frequently quoted criterion of a navigation system evaluation, which is commonly regarded as a measure of its quality. However, other features of operation are often disregarded, which makes this approach superficial. Before presenting the individual quality features of a system, let us analyze briefly the position accuracy measures whose understanding helps to interpret correctly these values. The term positioning accuracy is understood as the extent of conformity of statistics (distribution) of measured (determined) position coordinates either with the real values or those taken as real. It is noteworthy that accuracy of a position is measured as its error which can be assessed in reference to any dimension of a space or planes – horizontal error, vertical error.

The study involved conducting a range of measurement campaigns in 1995–1997 to determine the positioning accuracy. The most representative (lasting many days without a break) stationary studies included measurements with the use of two receivers: Leica MX9212+MX51R and Magnavox MX200+MX50R. The receivers were put at the Rozewie reference station (Leica MX9212+MX51R) and at the Gdynia Polish Naval Academy monitoring station (Magnavox MX200+MX50R). The below presented graphs show the measurement results. The measurement sessions being part of static studies included 1000 to 500000 measurements (Polish Naval Academy, on 03–09.02.1996) of position coordinates as well as a number of other parameters.

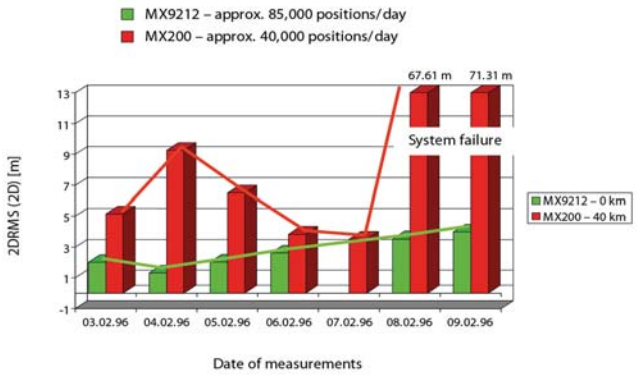

Fig. 2. Position error (determined every 24 h) for two DGPS receivers operating in parallel. Corrections were obtained from the DGPS station in Rozewie [10]

In Fig. 3 a typical position distribution around the mean value is shown for the Polish DGPS reference stations at Rozewie and Dziwnów. The DGPS system had a considerable effect on the possibility of obtaining highly accurate position coordinates in the Polish sea areas. For comparison, Fig. 3 (on the right) shows a position distribution of the Decca Navigator system determined during a campaign conducted in Jarosławiec in 1995.

The accuracy of the DGPS system was tested periodically in successive years of the system operation. The experience gained during the measurement campaign of 1994–1996 provided the basis for a strategy which involved regular

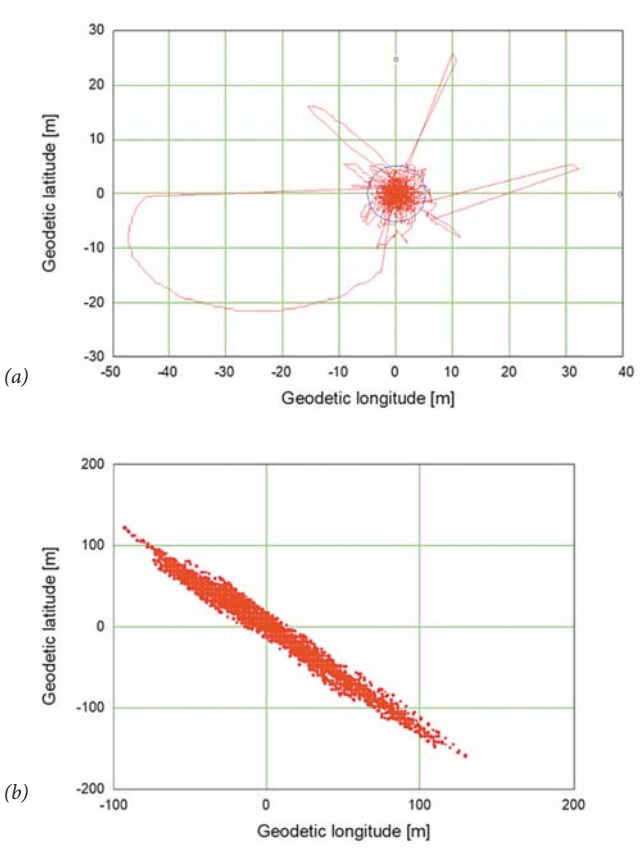

Fig. 3. A position distribution around the mean value for the DGPS system; (a) – Rozewie DGPS reference station, measurement on 03.02.1996, number of measurements approx. 50 000; [10] and the Decca Navigator system in 1995 (b) – acc. these authors' study

testing of the Polish DGPS system in measurement campaigns of 1–2 million measurements [5]. The results of campaigns in the years 2006, 2009 and 2014 show that the DGPS-PL system increased its positioning accuracy year after year (Fig. 4).

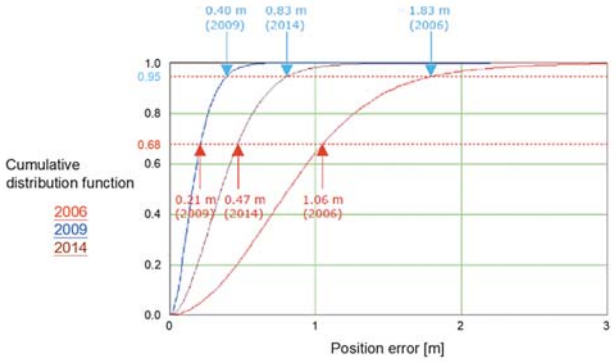

Fig. 4. The cumulative distribution functions of the 2D position errors for the DGPS-PL system (Rozewie) determined in 2006, 2009, 2014 based on 1–2 million measurements per campaign

Consideration of the causes of the increased accuracy of the Polish DGPS system shows that the most important of them includes: turn-off the Selective Availability (SA) in the GPS, change of the emission of RTCM messages from No. 1 to message No. 9–3 [22] which considerably increases the availability of highly accurate position [19] as well as technical

modernisation of both Polish stations, in the same way as it has been done in many other countries [6]. It is noteworthy that the positioning accuracy of the GPS is also improving [18], which also results in improved positioning accuracy of all the supporting systems, including DGPS.

DYNAMIC MEASUREMENTS OF THE DGPS SYSTEM

The first sea trials of the DGPS system in Poland were conducted in the Bay of Gdańsk in 1993 [3], where the telemetric connection in the very high frequency (VHF) range was used instead of the DGPS reference station in the low-/medium-frequency (LF/MF) bands [4]. Studies have shown that accuracies of several metres can be achieved, clearly indicating that the idea of transmission of differential corrections for the GPS system can be applied in marine navigation. Dynamic measurements were a very important part of the DGPS implementation project carried out in 1994–1996. Dynamic measurements were the most difficult part of the project from the technical point of view and in regard to the involved resources. Measurements in motion were conducted three times during the project by the teams coming from four universities (Polish Naval Academy, Academy of Agriculture and Technology in Olsztyn, Maritime Academy in Gdynia, Maritime Academy in Szczecin) and the Maritime Office in Gdynia [10]:

- the team of Polish Naval Academy (leader) – during a voyage of the ORP Wodnik on: 03–09.02.1996;
- the team of Polish Naval Academy (leader) – a voyage of the hydrographic cutter on: 16.10.1996;
- the team of Maritime Academy in Szczecin (leader) – dynamic measurements: July 1996.

The main measurements of the Polish DGPS system in the Bay of Gdańsk and in the middle of the Polish Baltic coast were conducted (on 03–09.02.1996) by the measurement team of the Institute of Navigation and Hydrography at the Polish Naval Academy, with the assistance of a team of the Academy of Agriculture and Technology in Olsztyn. The following DGPS receivers were used in the measurements:

- Leica MX9212+MX51R – measurement receiver;
- Magnavox MX200+MX50R – monitoring receiver;
- Magnavox MX300+MX51R – measurement receiver;
- Ashtech MDXII – reference receiver.

The dynamic measurements included eight trials (circulation and a figure of eight). The figure below shows an example of a full trial consisting of a circulation and figures of eight in the Bay of Gdańsk on 03.02.1996 at: 09:57–10:30 (Fig. 5, left). When the results were worked out it turned out that the positions of the reference receiver (Ashtech) and the measurement receiver (MX9212+MX51R) recorded at the same time (as shown by the receivers) are shifted relative to each other by a time constant.

An analysis showed that the geodetic receiver presented time on the GPS scale, whereas the measurement receiver operated according to the UTC scale. After adjusting the

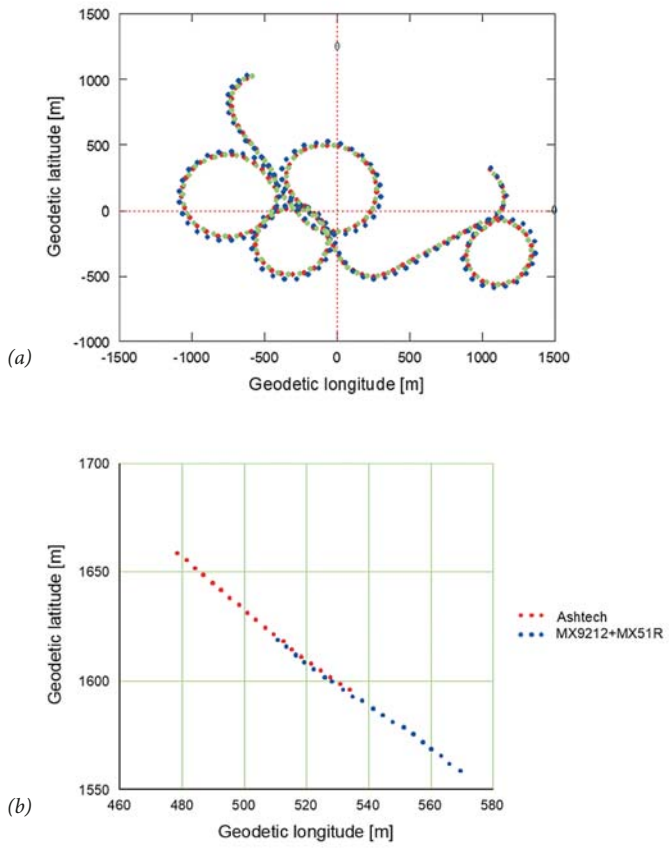

Fig. 5. The trajectories obtained from Ashtech and DGPS receivers in the dynamic trials (a) and indications of the receiver position without taking into consideration the synchronisation of the UTC and GPS times (b) [10]

time shift, the error of the DGPS position error (Rozewie RS), represented by the shift between the indications of the Ashtech (standard) receiver and MX9212+MX51R, was between 1 and 4 m (Fig. 6), showing that the system calibration (coordinates of the reference station antennas) was done properly.

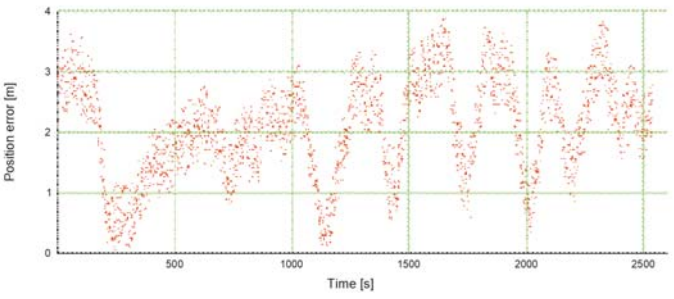

Fig. 6. Position error in function of time of dynamic measurements of the DGPS system on 03.02.1996 [10]

This project also involved examination of the accuracy and range of operation of the Dziwnów DGPS RS by the team from the Maritime Academy in Szczecin [1]. The results were very similar to those presented in the study carried out at the Polish Naval Academy.

In 2017, dynamic measurements were conducted again; their aim was to verify the accuracy of the DGPS system and

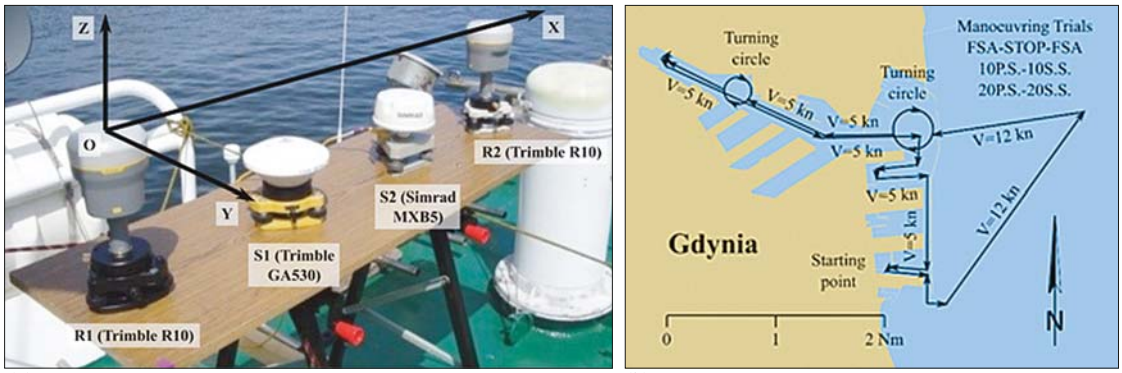

(a) *(b)*

Fig. 7. Position of antennas and receivers during dynamic measurements of the DGPS system in 2017 (a) and the ship's route (b)

a comparative assessment of the results relative to the EGNOS system. The measurements were conducted at the roadstead of the Port of Gdynia. The results of these measurements will be published in another paper, but it is noteworthy that the positioning methodology of a DGPS antenna was changed compared to the 1996 study because it was placed between two RTK receivers which used the GNSS geodetic networks (Fig. 7, a), whose expected accuracy in stationary measurements was 1–2 cm (2DRMS) [20]. On the other hand, in dynamic measurements (conducted at 20 Hz frequency), the estimated accuracy was approx. 1–2 cm [17].

The following statistics of positioning accuracy were obtained in the dynamic measurements of 2017.

Tab. 2. Position accuracy statistics of the DGPS system in the dynamic measurements of 2017

Values of DGPS parameters	Statistics
Number of fixes	11697
Average	0.614 m
Standard deviation	0.404 m
Coefficient of variation	65.7928%
Minimum	0.008 m
Maximum	8.621 m
Range	8.613 m

CONCLUSIONS

The Polish DGPS system was examined and thoroughly tested during the start-up phase. An assessment of the positioning accuracy made in stationary and dynamic measurements was one of key elements of such tests and examinations. The stationary measurements conducted in 1994–1996 showed that the accuracy positioning ensured by the Polish systems ranged from 2 to 8 m (2DRMS). It was also noted that an error increase could be caused by a low signal-to-noise ratio (SNR) which may result from insufficient power beamed by the reference station or from high industrial or inter-channel interference. Due to Selective Availability in the GPS (before 2000), in the 1990s it was proposed that the data transmission speed in the DGPS-PL stations should be increased to 200 bauds and that the emission of RTCM 9–3 messages should be started as soon as possible. In fact, the transmission speed has never been changed, and the RTCM 9–3 messages were not broadcasted until 2010.

Regular tests of the Polish DGPS system accuracy were conducted in 2006, 2009, 2014 and 2017. They showed a steady increase in position accuracy. Currently, the position accuracy of the Polish DGPS system is 1–2 m (2DRMS). The increase is basically due to three reasons: turning-off the Selective Availability (2000), technical modernization of reference stations (2010) and continuous – over many years – reducing GPS signal-in-space (SIS) pseudorange errors, which results in increased position accuracy of all GPS augmentation systems.

REFERENCES

1. Banachowicz A., Bober R., Wolski A., Banachowicz G.: *Statistical Research into GPS and DGPS Measurements in West Pomerania in the years 1996–2004,* Reports on Geodesy, No. 2, 2005, pp. 331–335.

2. Beškovnik B.: *Possibilities for Motorways of the Sea Development in the Eastern Part of the Adriatic Sea.* Polish Maritime Research, Vol. 20(1),2013, pp. 87–93.

3. Cydejko J., Wawruch R.: *Examination of Operating Parameters of the Local Differential GPS System in Static Conditions* (in Polish). Gdynia Maritime Academy Publishing House, Gdynia 1993.

4. Cydejko J., Wawruch R.: *Preliminary Assessment of the DGPS System for Determining the Position and Manoeuvring Parameters of the Ship During Maritime Trials* (in Polish). Proceedings of the 9th International Scientific and Technical Conference on the *„Role of Navigation to Protect the Human Activity in Sea",* Gdynia, 1994, pp. 21–33.

5. Dziewicki M., Specht C.: *Position Accuracy Evaluation of the Modernized Polish DGPS.* Polish Maritime Research, Vol. 16(4), 2009, pp. 57–61.

6. Ferguson K., Albright M., Remondi B.W., Cleveland A., Parsons M.: *NDGPS Reference Station and Integrity Monitor*

Architecture Modernization. Proceedings of the 60th Annual Meeting of the Institute of Navigation, Dayton, 2004, pp. 729–740.

7. Grządziel A., Felski A., Wąż M.: *Experience with the Use of a Rigidly-Mounted Side-Scan Sonar in a Harbour Basin Bottom Investigation.* Ocean Engineering, Vol. 109, 2015, pp. 439–443.

8. Kelner J.M., Ziółkowski C., Nowosielski L., Wnuk M.: *Reserve Navigation System for Ships Based on Coastal Radio Beacons.* Proceedings of the 2016 IEEE/ION Position, Location and Navigation Symposium (PLANS), Savannah, 2016.

9. Kopacz Z., Mor aś W., Pawłowski P. et al.: *Modernization of the SYLEDIS Radio-Navigation System in the Pomeranian Bay* (in Polish). Research project under the code name „SYLEDIS-3", 2001.

10. Kopacz Z., Specht C. et al.: *Radio-navigation Service in the Polish Sea Areas* (in Polish). Research project report, Polish Naval Academy, Gdynia 1996.

11. Naus K., Wąż M.: *Precision in Determining Ship Position Using the Method of Comparing an Omnidirectional Map to a Visual Shoreline Image.* Journal of Navigation, Vol. 69(2), 2016, pp. 391–413.

12. Oszczak B.: *New Algorithm for GNSS Positioning Using System of Linear Equations.* Proceedings of the 26th International Technical Meeting of the Satellite Division of the Institute of Navigation (ION GNSS+ 2013), Nashville, 2013, pp. 3560–3563.

13. Popielarczyk D.: *RTK Water Level Determination in Precise Inland Bathymetric Measurements.* Proceedings of the 25th International Technical Meeting of the Satellite Division of the Institute of Navigation (ION GNSS 2012), Nashville, 2012, pp. 1158–1163.

14. Proc J. (2014): *Hyperbolic Radio-navigation Systems* (in Polish). http://www.jproc.ca/hyperbolic/index.html, Accessed on 30 April 2018.

15. Przestrzelski P., Bakuła M., Galas R.: *The Integrated Use of GPS/GLONASS Observations in Network Code Differential Positioning.* GPS Solutions, Vol. 21(2), 2017, pp. 627–638.

16. Sitnik E., Oszczak B., Specht C.: *Availability Characteristics Determination of FKP and VRS Techniques of ASG-EUPOS System.* Proceedings of the 14th International Multidisciplinary Scientific GeoConference & EXPO SGEM2014, Albena, 2014, pp. 97–104.

17. Specht C., Koc W., Smolarek L., Grządziela A., Szmagliński J., Specht M.: *Diagnostics of the Tram Track Shape with the Use of the Global Positioning Satellite Systems (GPS/GLONASS) Measurements with a 20 Hz Frequency Rate.* Journal of Vibroengineering, Vol. 16(6), 2014, pp. 3076–3085.

18. Specht C., Mania M., Skóra M., Specht M.: *Accuracy of the GPS Positioning System in the Context of Increasing the Number of Satellites in the Constellation.* Polish Maritime Research, Vol. 22(2), 2015, pp. 9–14.

19. Specht C., Rudnicki J.: *A Method for the Assessing of Reliability Characteristics Relevant to an Assumed Position-Fixing Accuracy in Navigational Positioning Systems.* Polish Maritime Research, Vol. 23(3), 2016, pp. 20–27.

20. Specht C., Specht M., Dąbrowski P.: *Comparative Analysis of Active Geodetic Networks in Poland.* Proceedings of the 17th International Multidisciplinary Scientific GeoConference & EXPO SGEM2017, Albena, 2017, pp. 163–176.

21. Specht C., Weintrit A., Specht M.: *A History of Maritime Radio-Navigation Positioning Systems Used in Poland.* Journal of Navigation, Vol. 69(3), 2016, pp. 468–480.

22. Ward N.: *Future of IALA DGNSS.* Proceedings of the 2006 National Technical Meeting of the Institute of Navigation, Monterey, 2006, pp. 184–187.

23. Xinchun Z., Ximin C., Dongkun Y.: *Application of Modified Kalman Filtering Restraining Outliers Based on Orthogonality of Innovation to Track Tester.* Proceedings of the 2016 IEEE International Conference on Mechatronics and Automation (ICMA), Harbin, 2016, pp. 171–175.

24. Yang C., Mohammadi A., Chen Q.-W.: *Multi-Sensor Fusion with Interaction Multiple Model and Chi-Square Test Tolerant Filter.* Sensors, Vol. 16(11), 2016, pp. 1835.

CONTACT WITH THE AUTHORS

Cezary Specht
e-mail: c.specht@wn.am.gdynia.pl

Leszek Smolarek
e-mail: leszsmol@am.gdynia.pl

Jan Pawelski
e-mail: j.pawelski@wn.am.gdynia.pl

Mariusz Specht
e-mail: m.specht@wn.am.gdynia.pl

Paweł Dąbrowski
e-mail: p.dabrowski@wn.am.gdynia.pl

Gdynia Maritime University
81–87 Morska Str., 81–225 Gdynia
Poland

sciendo

POLISH MARITIME RESEARCH 2 (102) 2019 Vol. 26; pp. 22-25
10.2478/pomr-2019-0022

DAMAGE AND FRACTURE ANALYSIS OF BOLTED JOINTS OF COMPOSITE MATERIALS BASED ON PERIDYNAMIC THEORY

Na-Na Yang
Tian-You Zhao
Ji-Guang Gu
Zhi-Peng Chen
Harbin Engineering University, China

ABSTRACT

It is clear that the advantages of fibre glass-reinforced plastics surpass those of steel, but the failure analysis of composite structures is much more complex than that of isotropic materials as composite materials may fail in a variety of ways. In order to simulate the damage and fracture of bolted joints of fibre reinforced composite, the bond-based peridynamic method suitable for elastic, brittle and anisotropic characteristics of composite material is used. The peridynamic model for composite laminate is validated by the finite element method. Then a peridynamic program of composite damage is applied to calculating the damage of bolted joint structure and the damage propagation process and failure mode of the structure is obtained.

Keywords: Peridynamic theory, composite material, damage and fracture, joints

INTRODUCTION

Composite materials have been widely used in modern engineering due to their high ratios of strength and stiffness to weight. It is clear that the advantages of fibre glass-reinforced plastics surpass those of steel, but the failure analysis of composite structures is much more complex than that of isotropic materials as composite laminates may fail in a variety of ways. At present, there are many theoretical and numerical methods to simulate the damage and fracture of composites, the most widely used of which is the classic theory of continuum mechanics. However, it can be rather challenging to solve this way the discontinuity problems such as structural damage, crack propagation, delamination and penetration. The motion equations in classic continuum mechanics are in the form of partial differential equations, that involve the spatial displacement derivatives, but these derivatives are undefined when the displacement are discontinuous. It is difficult to simulate the process of crack generation and propagation, even though with the aid of dynamic grid or adaptive grid technology. Researchers put forward the cohesive elements [1] and Extended Finite Element Method(XFEM) [2] to introduce the additional function reflecting the discontinuity in the finite element method, but there is still a great challenge for complex damage of composite.

In 2000, Silling proposed a non-local particle method, named Peridynamics(PD) [3], shown in Fig. 1, which combines the advantages of molecular dynamics, mesh-less method and finite element method [4]. In PD theory, the solution domain is discretized into a finite number of material points, the interaction between different material points is used to describe the non-local interaction between particles and the state of a material point is influenced by the number of points located in a region of defined radius. The main difference between the PD and classic continuum mechanics is the using of integral equations instead of derivatives of the displacement components, therefore such approach is especially suitable to predict the damage and fracture process of composite materials. Moreover, in the PD theory internal forces are expressed through non-local interactions between pairs of material points within

a continuous body and damage is a part of the constitutive model. This feature allows to model damage initiation and propagation at multiple region with arbitrary paths inside the material without resorting to special crack growth criteria.

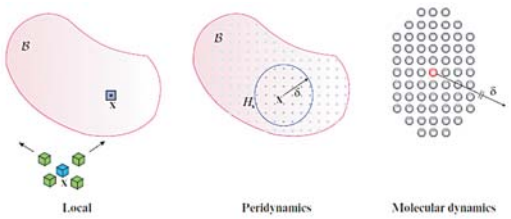

Fig. 1. Local and non-local continuum models [5]

PERIDYNAMIC THEORY OF COMPOSITE LAMINATES

The fibre reinforced composite plate of structure shown in Fig. 2 is analyzed in this paper. Laminated plate is a structure composed of a certain number of lamina according to the corresponding rules. The so-called fibre orientation in composite structure is the angle between a fibre and x coordinate axis and each lamina has its own properties and thickness. For the orthotropic lamina there are four independent material constants, namely: the elastic modulus in longitudinal direction E_{11}, elastic modulus in transverse direction E_{22}, in-plane shear modulus G_{12}, and in-plane Poisson's ratio ν_{12}.

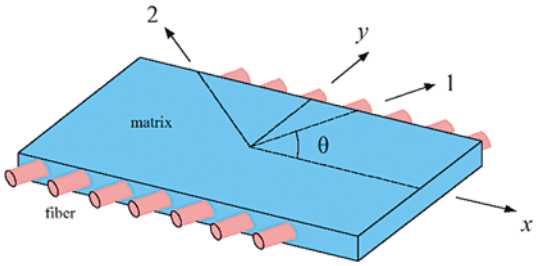

Fig. 2. A lamina and its material coordinate system

Composite materials have the characteristics of inhomogeneity and anisotropy compared with isotropic materials, therefore different kinds of bonds are usually needed to describe them. For the bond-based peridynamic model of fibre reinforced composite laminates, fibre bonds, matrix bonds, interlayer bonds and shear bonds are defined to describe the in-plane, interlayer and shear characteristics [6], that is to say there are matrix bonds between the material points in each ply, the fibre bonds exist only between the material points along the direction of layer angle, the interlayer bonds exist only in the material points in the vertical direction of the adjacent layer, while the shear bonds exist in the other direction of the adjacent layer. The model diagram is shown in Fig. 3. Each bond constant can be obtained by equating the strain energy density expressed by peridynamics and the classic continuum mechanics for a composite under simple loading.

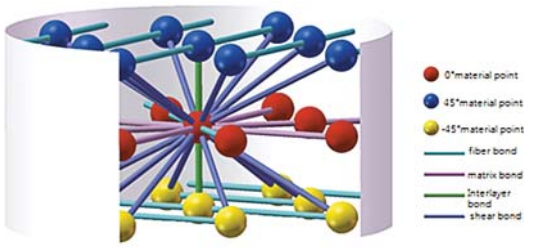

Fig. 3. Bond-based peridynamic model of fibre reinforced composites[6]

For the lamina, the thickness is usually far smaller dimension than that in other direction, therefore it can be approximately assumed that $\sigma_3 = 0$, $\tau_{23} = \tau_{13} = 0$. For orthotropic materials in plane stress state the stress-strain relationship can be expressed as:

$$\begin{Bmatrix} \sigma_{11} \\ \sigma_{22} \\ \tau_{12} \end{Bmatrix} = \begin{bmatrix} Q_{11} & Q_{12} & 0 \\ Q_{12} & Q_{22} & 0 \\ 0 & 0 & Q_{66} \end{bmatrix} \begin{Bmatrix} \varepsilon_{11} \\ \varepsilon_{22} \\ \gamma_{12} \end{Bmatrix} \Rightarrow \boldsymbol{\sigma} = \mathbf{D}\boldsymbol{\varepsilon} \tag{1}$$

where **D** is the stiffness matrix of the material, each component of which is represented as: $Q_{11} = E_{11}/(1 - \nu_{12}\nu_{21})$, $Q_{66} = G_{12}$, $Q_{22} = E_{22}/(1 - \nu_{12}\nu_{21})$, $Q_{12} = \nu_{21}E_{22}/(1 - \nu_{12}\nu_{21})$.When the layer angle between the principal direction of the fibre and X-axis is θ, the stress- strain relationship of the lamina is as follows:

$$\begin{Bmatrix} \sigma_x \\ \sigma_y \\ \tau_{xy} \end{Bmatrix} = \begin{bmatrix} \bar{Q}_{11} & \bar{Q}_{12} & \bar{Q}_{16} \\ \bar{Q}_{12} & \bar{Q}_{22} & \bar{Q}_{26} \\ \bar{Q}_{16} & \bar{Q}_{26} & \bar{Q}_{66} \end{bmatrix} \begin{Bmatrix} \varepsilon_x \\ \varepsilon_y \\ \gamma_{xy} \end{Bmatrix} = \bar{\mathbf{Q}} \begin{Bmatrix} \varepsilon_x \\ \varepsilon_y \\ \gamma_{xy} \end{Bmatrix} \tag{2}$$

where $\bar{\mathbf{Q}}$ is the reduced stiffness matrix of the material.

In the classic continuum mechanics, the strain energy density W^{CM} at any point of two-dimensional composite lamina can be expressed as:

$$W^{CM} = \frac{1}{2}\boldsymbol{\sigma}^T\boldsymbol{\varepsilon} = \frac{1}{2}\sigma_{11}\varepsilon_{11} + \frac{1}{2}\sigma_{22}\varepsilon_{22} + \frac{1}{2}\sigma_{12}\gamma_{12} \tag{3}$$

or

$$W^{CM} = \frac{1}{2}(Q_{11}\varepsilon_{11}^2 + 2Q_{12}\varepsilon_{22}\varepsilon_{11} + Q_{66}\gamma_{12}^2 + Q_{22}\varepsilon_{22}^2) \tag{4}$$

In the PD theory the strain energy density at arbitrary material point can be obtained by integrating the micro-potential energy of the material points in the defined horizon. The strain energy density of the material point k can be expressed as:

$$W^{PD} = \frac{1}{2}\sum_{j=1}^{N} w_{(j)(k)}V_{(j)} + \frac{1}{2}\int_H w dH \tag{5}$$

where N indicates the number of fibre bonds in the horizon of the material point k, and the potential energy can be expressed according to the PD theory as:

$$w = \frac{1}{2}c(\phi)s^2(\phi)\xi \tag{6}$$

It is worth noting that the stretch of bonds between material point k and j, $s(\phi)$,is expressed in the polar coordinate system,

as shown in Fig. 4. The bond constant $c(\phi)$ in the PD theory can be expressed as:

$$c(\phi) = \begin{cases} c_F + c_A & \phi = \theta \\ c_A & \phi \neq \theta \end{cases} \tag{7}$$

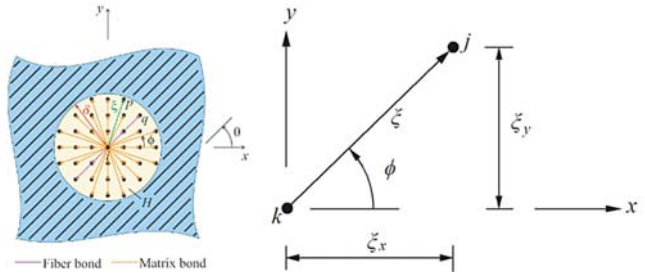

Fig. 4. Stretch of material points k in PD model of lamina[7]

Therefore, W^{PD} can be expressed by substituting Eqs. (6)~(7) into (5):

$$W^{PD} = \frac{1}{2}\sum_{j=1}^{N}\frac{c_F s_{jk}^2 \xi_{jk}}{2} V_{(j)} + \frac{1}{2}\int_H \frac{c_A s^2 \xi}{2} dH \tag{8}$$

Putting $W^{PD} = W^{CM}$, the bond constants of fibre and matrix under action of shear, axial tension and other loads can be expressed as:

$$c_F = \frac{2E_{11}(E_{11} - E_{22})}{(E_{11} - \frac{1}{9}E_{22})(\sum_{j=1}^{N}\xi_{jk}V_{(j)})} \tag{9}$$

$$c_A = \frac{8E_{11}E_{22}}{(E_{11} - \frac{1}{9}E_{22})\pi t \delta^3} \tag{10}$$

It is assumed that the relative displacement occurs between a material point *a* and other material points in the horizon within the laminate, as shown in Fig. 5, the strain energy density at the material point *a* can be expressed by the sum of the strain energy density of interlayer bond and shear bond.

$$W^{PD} = \hat{W}^{PD} + \tilde{W}^{PD} = \frac{1}{2}\sum_{j=d,e}\frac{c_N s_{ja}^2 \xi_{ja}}{2} V_j + \frac{1}{2}\int_H \frac{c_S \varphi^2}{2} dH \tag{11}$$

where the shear angle φ can be obtained by averaging the shear angle φ_{ad} between the material point *a*, *d* and the shear angle φ_{bc} between the material point *b* and *c*, as shown in Fig. 6.

$$\varphi = \frac{\varphi_{da} + \varphi_{bc}}{2} \tag{12}$$

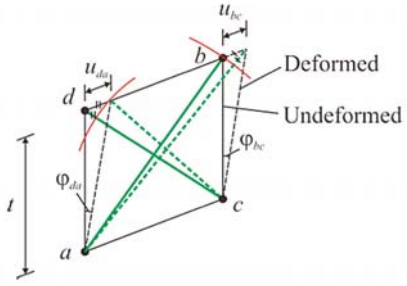

Fig. 5. Definition of shear angle [7]

As shown in Fig. 6, the interlayer bond and shear bond can be obtained by equating the strain energy density expressed by the PD theory and the continuum mechanics. It is worth noting that the strain energy density due to the deformation is related to the matrix material parameters which are independent of the fibre material parameters.

$$c_N = \frac{E_m}{t\overline{V}}, \qquad c_S = \frac{2G_m}{\pi t}\frac{1}{\delta^2 + t^2\ln(t^2/(\delta^2 + t^2))} \tag{13}$$

where, $\overline{V}$ is the volume of the material point *d* and *e*, $\overline{V} = V_d = V_e$. *t* is the interlayer thickness, E_m and G_m are the elastic modulus and the shear modulus of matrix material, respectively. For the material points near the free surface, the surface correction is required because the material points are there not entirely embedded within its horizon.

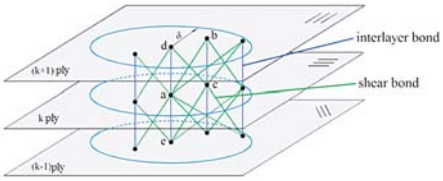

Fig. 6. The interlayer and shear bond of the laminates [7]

The damage can be determined by using the strength of macroscopic materials [8]: the critical stretch of the fibre and matrix bond are: $s_{ft} = X_T/E_{11}(s \geq 0)$ and $s_{mt} = Y_T/E_{22}(s \geq 0)$, respectively. The critical compression of the fibre and matrix bond are: $s_{fc} = X_C/E_{11}(s < 0)$ and $s_{mc} = s_{fc} = X_C/E_{11}(s < 0)$, respectively. The relationship between stretch and pair-wise response function is shown in Fig. 7.

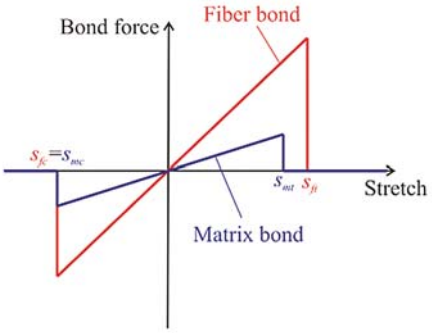

Fig. 7. Force-stretch relation for fibre and matrix bonds [8]

Oterkus and Madenci [5] proposed that the critical parameters of interlayer bond and shear bond based on the theory of fracture mechanics can be expressed as:

$$s_N = \sqrt{\frac{2G_{IC}}{tE_m}}, \varphi_S = \sqrt{\frac{G_{IIC}}{tG_m}} \tag{14}$$

where G_{IC} and G_{IIC} are the mode-I and mode-II of critical energy release rate of the matrix material, respectively. It is worth noting that the interlayer bonds show only stretch failure of delamination as this is the main failure mode of laminates.

The relationship between the relative deformation and the force density function of the material points is shown in Fig. 8.

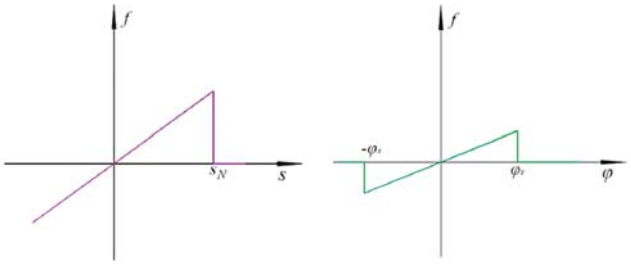

(a) interlayer bond *(b) shear bond*

Fig. 8. The relationship between stretch of interlayer bond, shear angle and pair-wise response function

VALIDATION STUDY

In this section, a set of peridynamic calculation programs for composite structures is compiled based on the FORTRAN (2013) language and the Visual Studio (2012) environment and then used to simulate behaviour of two examples. Their results are compared with the simulation results obtained from the finite element software ABAQUS for checking validity of the composite PD models.

LAMINA WITH CIRCULAR HOLE

The finite element method and PD one are used to calculate the composite lamina with circular hole under axial tensile load. The particulars of the lamina shown in Fig. 9 are as follows: the thickness of 0.165 mm, the ply direction of 0° and the axial tensile load of 159.96MPa. The material parameters are shown in Tab. 1. In the PD model there are 250 material points in the length direction, 75 material points in the width direction and the horizon radius is $\delta = 3\Delta x$. The displacement components in x- and y-directions calculated by using the finite element method and PD one are shown in Fig. 10. The horizontal and vertical displacements along the central axis are shown in Fig. 11. The results obtained from the finite element method and PD one are in a good agreement.

Tab. 1. The material parameters of the lamina

Elastic modulus in longitudinal direction	E_{11} = 259.96 GPa
Elastic modulus in transverse direction	E_{22} = 8.96 GPa
In-plane shear modulus	G_{11} = 3.05 GPa
In-plane Poisson ratio	ν_{12} = 1/3
Density	ρ = 1800 kg/m^3

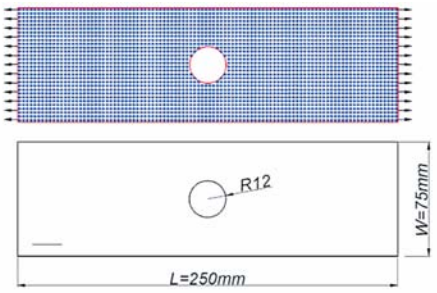

Fig. 9. PD model of the lamina with central circular hole

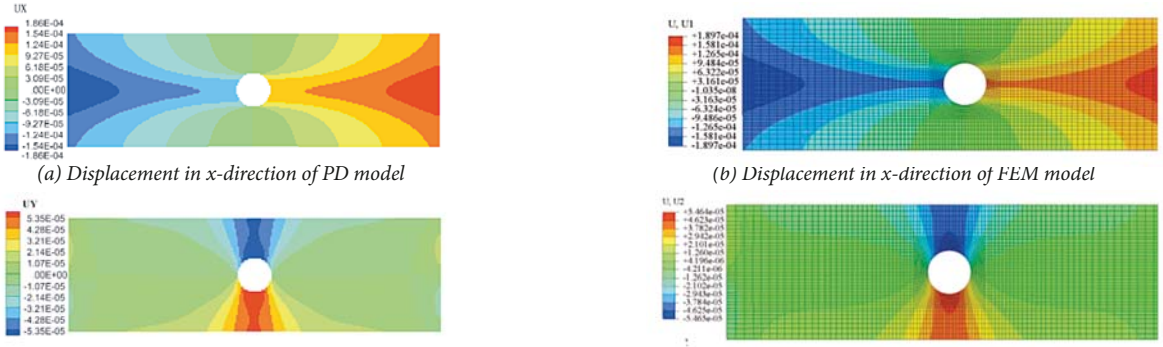

(a) Displacement in x-direction of PD model *(b) Displacement in x-direction of FEM model*

(c) Displacement in y-direction of PD model *(d) Displacement in y-direction of FEM model*

Fig. 10. Calculation results of displacements in PD and FEM models

(a) Horizontal displacement along longitudinal / symmetry axis *(b) Vertical displacement along transverse / symmetry axis*

Fig. 11. Displacements along the symmetry axes in case of PD and FEM models

In the bond-based peridynamic models the stress results cannot be directly obtained. Therefore, in this paper the least square method is introduced to get the stress results from PD calculation process. The accuracy of the stress obtained from this method is significantly higher than that from the direct difference method. It is suitable for finding the solution of uniform discrete mesh-less space deviation. It is assumed that the displacement function at a material point is as follows:

$$\begin{cases} u(x,y) = a_0 + a_1 x + a_2 y \\ v(x,y) = b_0 + b_1 x + b_2 y \end{cases} \tag{15}$$

where a_0, a_1, a_2 and b_0, b_1, b_2 are polynomial coefficients to be fitted. The displacement matrix, location of material point k and other material points in the horizon are expressed in the form of matrix equation:

$$\begin{bmatrix} 1 & x_k & y_k \\ 1 & x_1 & y_2 \\ \cdots & \cdots & \cdots \\ 1 & x_{n-1} & y_{n-1} \\ 1 & x_n & y_n \end{bmatrix} \begin{bmatrix} a_0 \\ a_1 \\ a_2 \end{bmatrix} = \begin{bmatrix} u_k \\ u_1 \\ \cdots \\ u_{n-1} \\ u_n \end{bmatrix} \quad \Rightarrow \quad \mathbf{Xa} = \mathbf{u} \quad \forall \left| \mathbf{x}_n - \mathbf{x}_k \right| \le \delta \tag{16}$$

The least squares method can be used to solve the undetermined coefficient matrix.

$$\mathbf{a} = \begin{bmatrix} a_0 \\ a_1 \\ a_2 \end{bmatrix} = \left(\mathbf{X}^T \mathbf{X} \right)^{-1} \mathbf{X}^T \mathbf{u} \tag{17}$$

The displacement $v(x, y)$ can be obtained by the same way as well. The strain components at material points are given as follows:

$$\begin{aligned} \varepsilon_x &= \partial u / \partial x = a_1 \\ \varepsilon_y &= \partial v / \partial y = b_2 \\ \gamma_{xy} &= \partial u / \partial y + \partial v / \partial x = a_2 + b_1 \end{aligned} \tag{18}$$

The stress-strain relationship at the state of plane stress can be obtained by the equation (2). By comparing the stress results calculated with the use of PD and FEM methods, shown in Fig. 12, it is found that the two results are in good agreement.

LAMINA WITH PREFABRICATED CRACKS

The damage and fracture modes of laminas with central prefabricated cracks were analyzed and the effects of the central pre-crack angles on forms of in-plane damage and crack propagation were investigated. The lamina in question is 150 mm long, 50 mm wide and 0.165 mm thick, the central pre-crack length is 12 mm and the angle between x axis is set to be, successively: –60°, –45°, –30°, 0°, 30°, 45°, 60° and 90°. The assumed calculation model is shown in Fig. 13, the material point spacing in PD model Δx = 0.625 mm, the horizon radius $\delta = 3\Delta x$, the critical elongation of the resin bond is 0.0135, and the critical elongation of the fibre bond is 0.027. Simultaneously there is assumed: the tensile load speed v = 8 m/s in the plate width direction, the calculation time step equal to 2×10^{-8}s and the total number of steps reaching 5000.

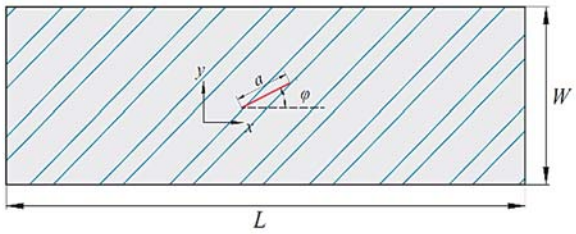

Fig. 13. The lamina with pre-crack under 45° angle

The results given below in Fig. 14 show that the damage mode of the lamina with pre-crack in its centre is mainly based on the tensile damage of the matrix, the direction of damage and crack propagation is always along the fibre

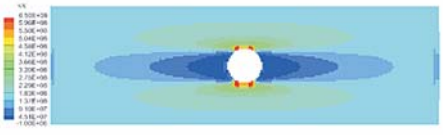

(a) Stress component in x-direction of PD model

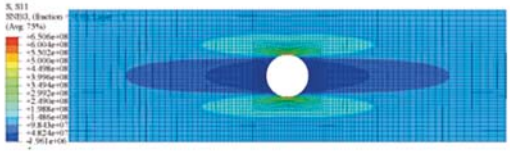

(b) Stress component in x-direction of FEM model

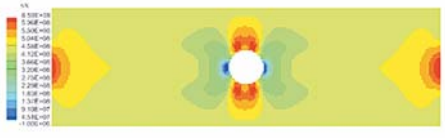

(c) Stress component in y-direction of PD model

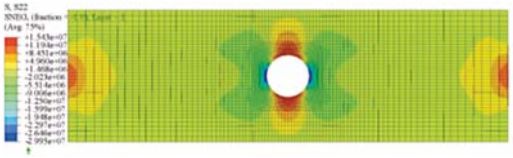

(d) Stress component in y-direction of FEM model

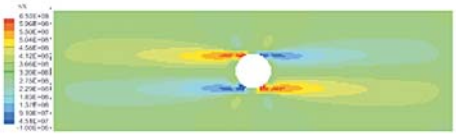

(e) Stress component in x-y plane of PD model

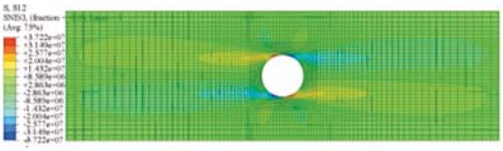

(f) Stress component in x-y plane of FEM model

Fig. 12. Stress components in the lamina with central circular hole

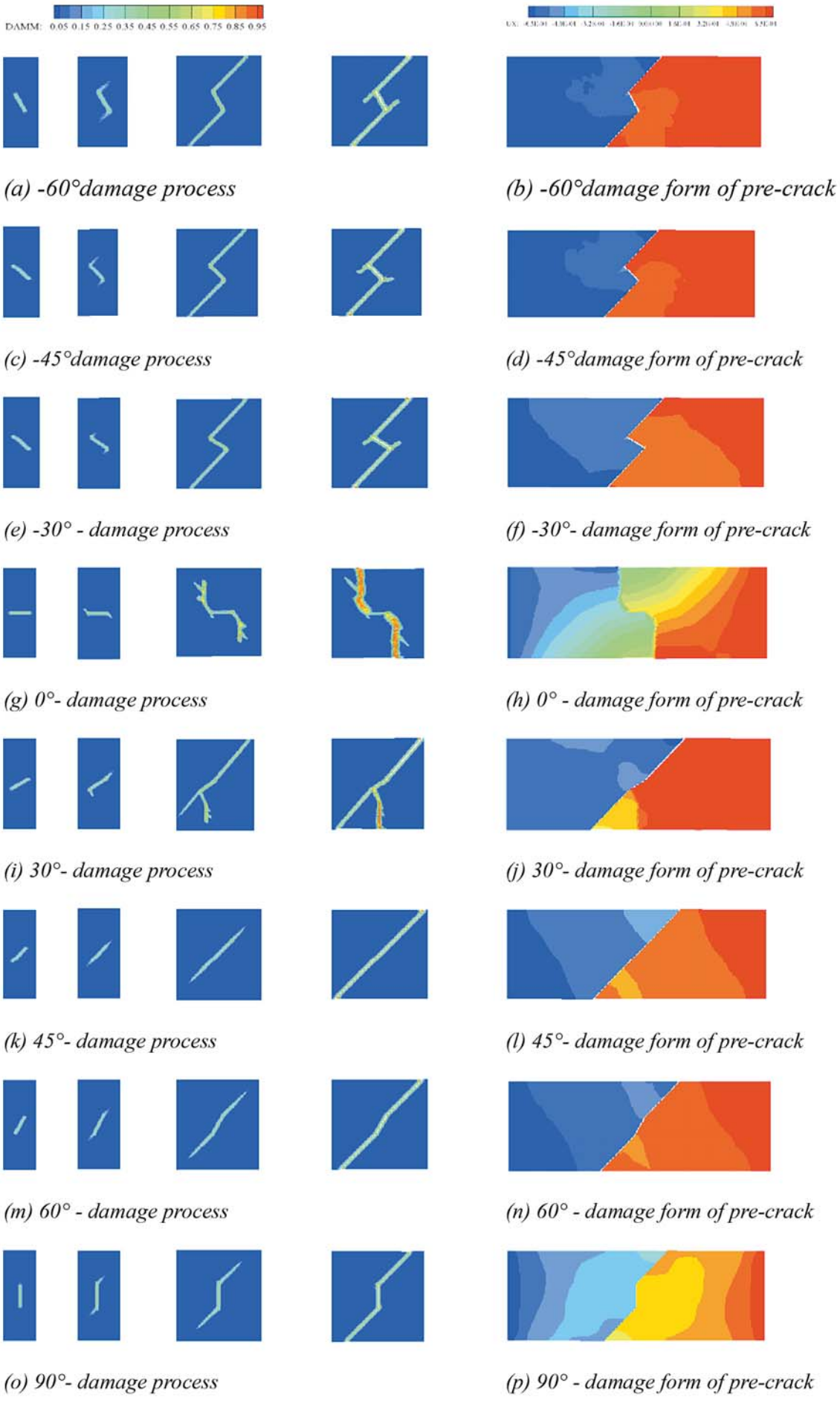

Fig. 14. Pre-crack damage and crack propagation for different pre-crack angles

direction and the damage starts from the tip of the initial pre-crack and progresses to the two sides. The lamina with 0° – pre-crack is not damaged along the fibre layer, and the fibres still bear the load while the matrix damage extends to the edge of the plate, the lamina is not broken even if the loading process reaches 5000 time-steps.

The tension load-time step curves for eight kinds of lamina are shown in Fig. 15: in the first 2000 steps the laminas are in the elastic phase, and their curves coincide. After the 2000 steps, the curves begin to be gradually different until their maxima are reached. Cracks continue to develop gradually; and after 3400 steps the matrix damage starts to proceed step by step. The damage gradually spreads and eventually leads to fracture, the load-carrying capacity of lamina is decreasing. Generally, the higher the coincidence between the pre-crack and the ply angle, the less the loss of general load-carrying capacity.

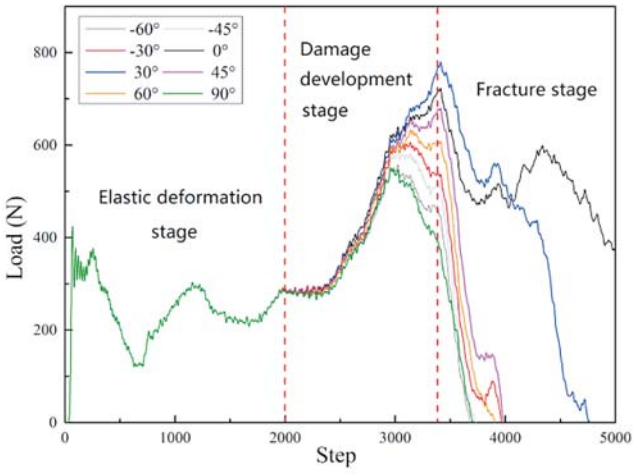

Fig. 15. Tension load-time step curves for laminas with pre-cracks at different angles

DAMAGE ANALYSIS OF COMPOSITE MATERIAL STRUCTURE WITH BOLT CONNECTION

The damage and failure modes of bolted joints under axial load are analyzed by means of the peridynamic method. The model is simplified by omitting the elastic-plastic deformation of bolts. The correction method of displacement is used when the material points in the laminate enter the model of bolted joints at any time [8]; its schematic diagram is shown in Fig. 16.

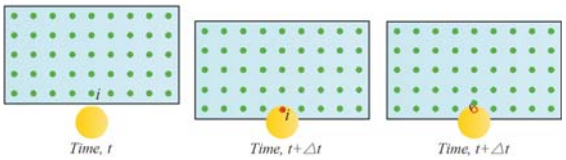

Fig. 16. Schematic diagram of material point relocation

The particulars of composite laminates with bolted joints are: length L = 90 mm, width W = 50 mm, bolt diameter ϕ = 12 mm, thickness of laminate plate t = 8 mm, the lay-up configuration is [45/0/-45/90/0], the material properties are the same as given in the Tab. 1 above. The PD model of the laminate is generated by 180 material points in length direction and 100 material points in width direction; it means that Δx = 0.5 mm. The simplified diagram of the bolted joint is shown in Fig. 17.

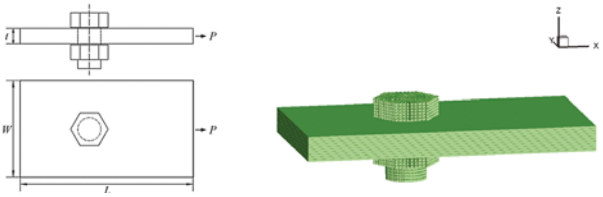

(a) Bolt connection structure

(b) Discrete model of bolt connection structure

Fig. 17. Simplified bolt connection structure

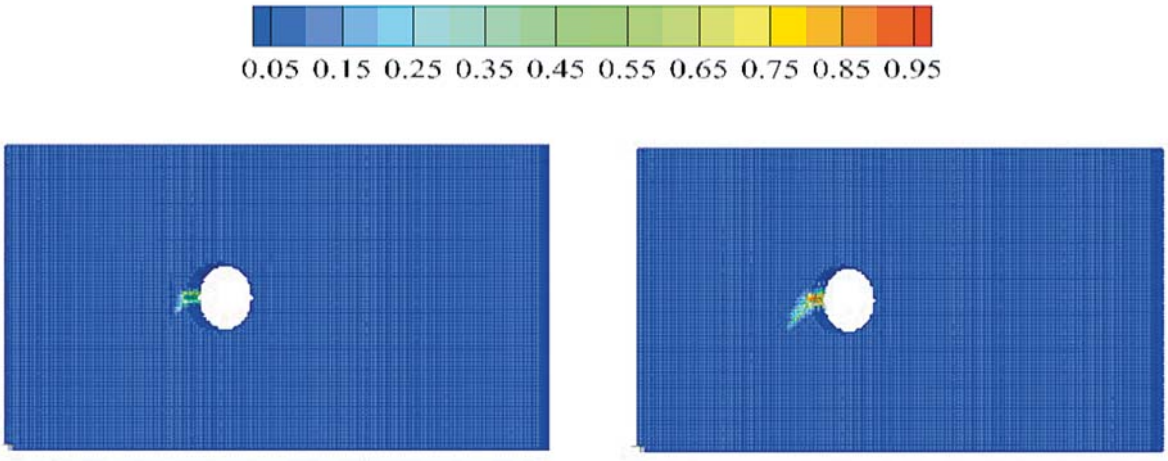

(a) Matrix damage at 1200th time-step

(b) Matrix damage at 1600th time-step

Fig. 18. Results of PD simulation of the bolted joint damage forms and displacements |→

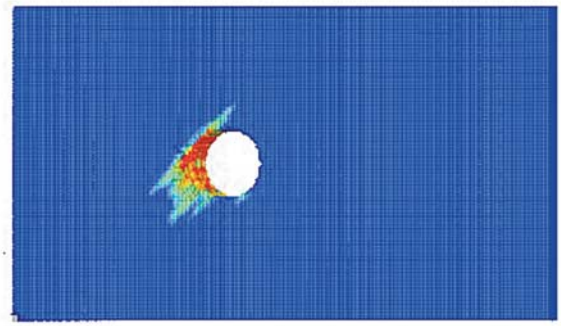

(c) Matrix damage at 4800th time-step

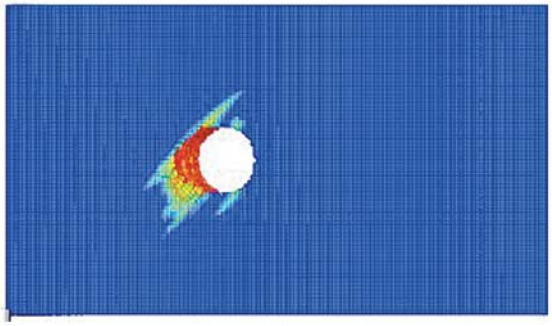

(d) Matrix damage at 6000th time-step

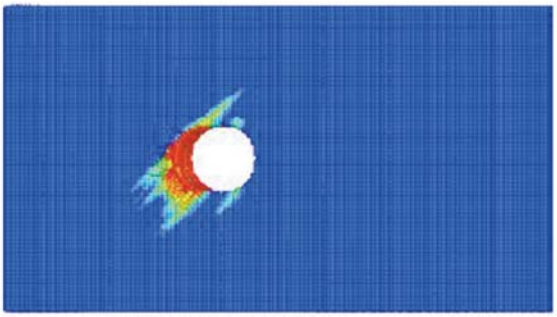

(e) Matrix damage at 12000th time-step

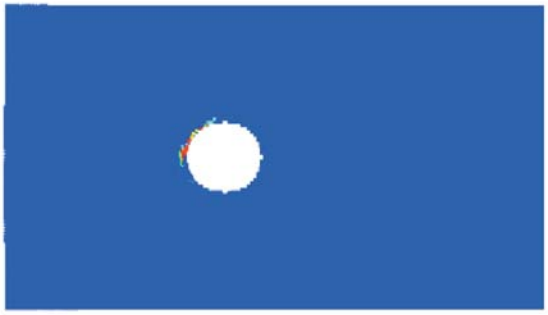

(f) Fibre compression damage at 6000th time-step

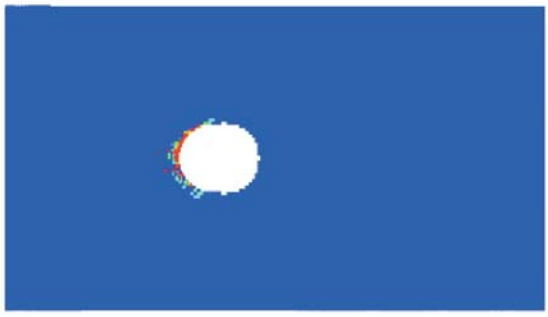

(g) Fibre compression damage at 12000th time-step

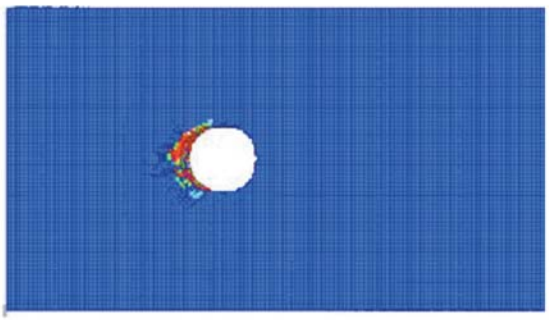

(h) Fibre compression damage at 15000th time-step

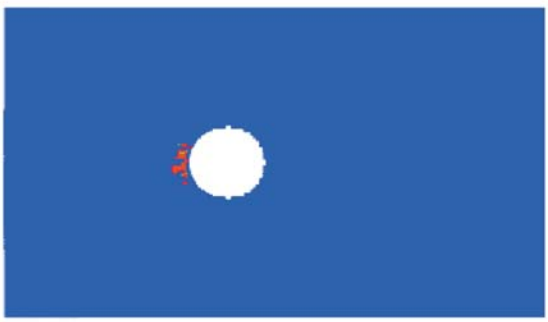

(i) Delamination at 6000th time-step

(j) Delamination at 12000th time-step

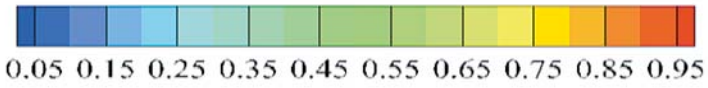

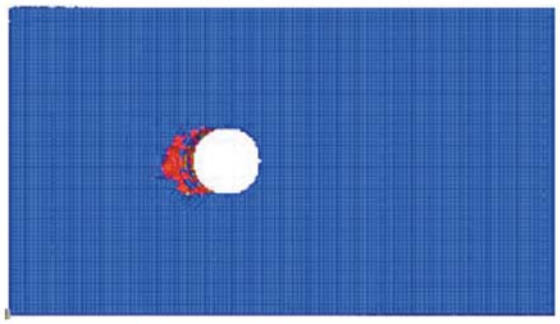

(k) Delamination at 15000th time-step

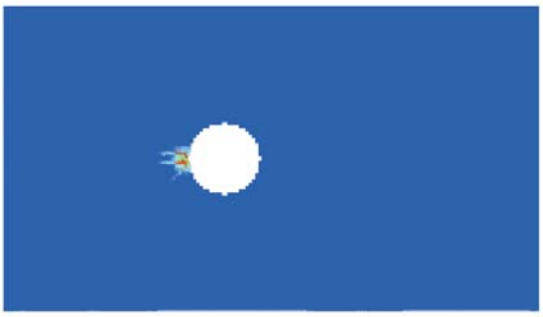

(l) Sheare damage at 16000th time-step

(m) Sheare damage at 4000th time-step

(n) Sheare damage at 6000th time-step

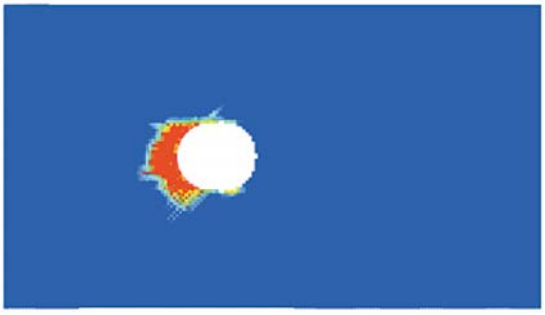

(o) Sheare damage at 12000th time-step

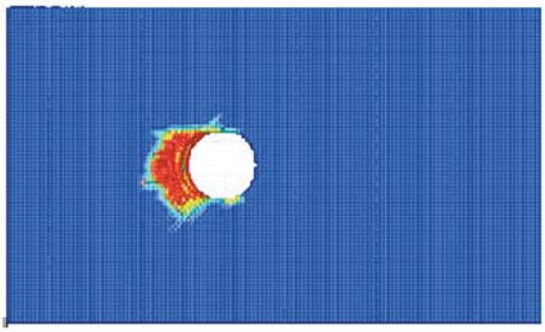

(p) Sheare damage at 15000th time-step

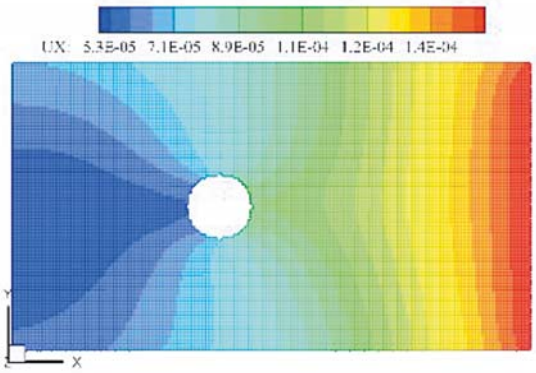

(q) Displacement Ux at 800th time-step

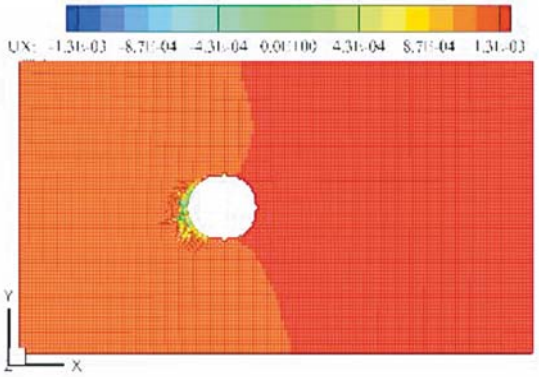

(r) Displacement Ux at 15000th time-step

Fig. 18. Results of PD simulation of the bolted joint damage forms and displacements

The progressive damage results are shown in Fig. 18. Initially, the matrix compression damage occurred around the bolt hole, then, as the load increases, the compression damage is gradually extended to the contact surface of bolt hole. The damage of the matrix is also accompanied by the compression damage of fibres, delamination and shear damage. The damage region is concentrated around the contact zone of the bolt and its hole.

The curve of the extrusion force in function of time – step number for the region of the bolt hole is shown in the Fig. 19. With the increase of the boundary displacement the structure is damaged and its load-carrying capacity decreases. When the load is further increased the bolt hole is crushed, a large damage occurs and the resisting force falls to zero. The force-time step curve correctly reflects the load-carrying characteristics of the composite bolted joints. At the same time, the PD simulation of the bolt connection structure reveals the process of damage occurrence and its expansion without resorting to special crack-growth criteria.

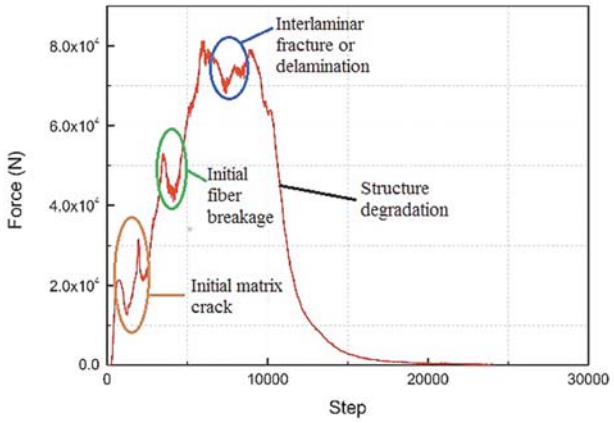

Fig. 19. The force-time step curve for the region of the bolt hole

CONCLUSION

In order to simulate the damage and fracture of fibre reinforced composite laminates and joints, the bond-based peridynamic method suitable for elastic, brittle and anisotropic characteristics of composite material, is used. The bond-based PD model of composites is validated by means of the finite element method and used for analyzing the damage and fracture process of the bolted joints of composite materials under axial load. The mechanism and process of damage occurrence and its expansion revealed that the PD method has a great advantage over the traditional method in the simulation and analysis of damage and fracture. This way it is possible to solve easily the fracture initiation and propagation without resorting to special crack-growth criteria.

ACKNOWLEDGEMENT

The authors would like to acknowledge the support of the National Natural Science Foundation of China (Grant No. 51879048)

REFERENCES

1. Dugdale DS.: *Yielding of Steel Sheets Containing Slits.* Journal of the Mechanics & Physics of Solids, 1960, 8(2): pp. 100–104.
2. Dolbow J., Belytschko T.: *Numerical Integration of the Galerkin Weak Form in Mesh-free Methods*. Computational Mechanics, 1999, 23(3): pp. 219–230.
3. Silling S.A.: *Reformulation of Elasticity Theory for Discontinuities and Long-range Forces*. Journal of the Mechanics & Physics of Solids, 2000, 48(1): pp. 175–209.
4. Dan Huang, Qin Zhang: *Peridynamic Theory and Its Application*. Advance In Mechanics, 2010, 40(4): pp. 448-459.
5. Madenci E, Oterkus E.: *Peridynamic Theory and Its Applications*. Springer, New York, 2014.
6. Hu Y., Madenci E., Phan N.: *Peridynamic Modeling of Defects in Composites*. 56thAIAA/ASCE/AHS/ASC Structures, Structural Dynamics, and Materials Conference, American Institute of Aeronautics and Astronautics Inc., 2015.
7. Oterkus E., Madenci E.: *Peridynamic Analysis of Fibre-reinforced Composite Materials*. Journal of Mechanics of Materials & Structures, 2012, 7(1): pp. 45–84.
8. Y.L. Hu, Yin Yu, Hai Wang: *Peridymics for damage analysis method of composite laminates*. Chinese Journal of Theoretical and Applied Mechanics, 2013, 45(4): pp. 624–628.

CONTACT WITH THE AUTHORS

Na-Na Yang
e-mail: nanayang1980@hotmail.com

Tian-You Zhao
e-mail: 894517736@qq.com

Ji-Guang Gu
e-mail: gujiguang@hrbeu.edu.cn

Zhi-Peng Chen
e-mail: henzhipeng2012@163.com

Harbin Engineering University
Nangang, Heilongjiang Province
150001 Harbin
China

sciendo

POLISH MARITIME RESEARCH 2 (102) 2019 Vol. 26; pp. 33-46
10.2478/pomr-2019-0023

NEW DESIGNS OF CENTRIFUGAL MAGNETIC FLUID SEALS FOR ROTATING SHAFTS IN MARINE TECHNOLOGY

Leszek Matuszewski
Gdansk University of Technology, Poland

ABSTRACT

The centrifugal magnetic fluid seals have important advantage over the conventional centrifugal seals. They maintain very good sealing capacity at static, medium and high speeds of shaft rotation, with the increased seal lifetime, and minimum torque and static friction. These seals are particularly useful in cases when the angular shaft velocity varies and sometimes decreases to nearly or exactly zero, such as in flywheel applications, ship propeller main shafts, etc. Unique properties of the magnetic fluid give rare opportunities for application in marine design, where perfect sealing together with reliable lubrication are required.
The paper presents a typical design and operation principle of a centrifugal magnetic fluid shaft seal, along with new design solutions. Not only in ocean technology and underwater robotics. Some cases of application of centrifugal magnetic fluid seals in modern sealing technology are included.

Keywords: magnetic fluids, ferrofluids, lubricants, magnetic seals, static seals, rotational seals

INTRODUCTION

At present, magnetic fluid seals are the most important industrial application of magnetic fluid (Ferro fluid) technology. The sealing technique making use of magnetic fluids offers good solutions to many difficult sealing problems in modern machinery and processing equipment, especially in gas and vacuum applications for high-speed rotating shafts [1–2]. Centrifugal magnetic fluid seals belong to a special type of seals and are used in a wide range of rotational shaft speeds, e.g. in rotary pumps, compressors, generators, and in flywheel applications [10–15]. In medicine, shaft seals for rotary blood pumps with low friction requirements are critical for micro leakage and long-lasting usage. Magnetic fluid seals seem perspective for these applications with their zero leakage, no wear, and constant density and viscosity properties [1–4]. A magnetic fluid sealing system can work together with magnetic bearings in one hybrid device being a common seal and bearing kit. Non-contact bearings are expected to give a long life without wear either [3–9].

Many researchers have attempted to apply magnetic bearings and fluid sealing to centrifugal blood pumps [24–26]. However, a totally passive magnetic bearing is not possible and thus at least one degree of freedom must be compensated by an active magnetic bearing. Then, the magnetic bearings need actuators with displacement sensors for stable operation, which increases the system complexity and consumed power. In addition, the bearing stiffness in the radial and axial directions is low for actual use in rotary blood pumps [27]. For small devices, the compromise is an axial diamond settle, which allows replacement of actuators and sensors.

Recently, magnetic fluid seals have been investigated for rotary pumps of various body fluids e.g. blood, lymph, etc., as another promising application for the shaft seal. Magnetic fluid seals were developed in the 1960s in devices controlling the rocket fuel flow, and their use has been extended to various other applications [28, 49–54]. These seals work without rubbing contact of the rotating shaft surface, and hence, there is no wear. Magnetic fluid bridges are covering a gap around the shaft and perfectly block the leakage, while still allowing the shaft to

rotate with relatively small viscous frictional loss [43–46]. In addition, the seal does not require as high-precision matching as mechanical seals. Therefore, developing a clinically proven magnetic fluid seal is extremely valuable for rotary lymph and blood pumps. Mitamura et al. [6, 31–43] developed a magnetic fluid seal with a shield mechanism. The objective of installing the shield is to minimize contact between the sealed liquid and the magnetic fluid seal. The gap between the shield and the shaft was set to 50 μm, which is the same as that between the pole piece and the shaft. The authors installed the seal system in an axial-flow pump and investigated its performance. However, the effect of contact with body liquids upon the performance of the magnetic fluid seals was not investigated. Further investigations of the seal performance during acceleration tests [47–52] have proved that the radial clearance between the pole piece and the shaft can be up to 400 μm, i.e. is much larger than the conventional setting (50 μm).

The conventional centrifugal seals employ the centrifugal forces generated at high rotary speeds to retain the sealing fluid. They work satisfactorily at high shaft speeds, while at lower speeds the sealing fluid is not kept in place and in the static condition the seal does not support any pressure at all. Other difficulties associated with conventional centrifugal seals include problems related to fluid leakage, limited lifetime due to the wear of elastomer seal, high torque, and high static friction, which result from the use of elastomeric auxiliary seals [56–59].

A centrifugal magnetic fluid seal is a completely hermetic shaft seal at static, low- and high-speed modes, with the increased seal lifetime, and the minimum torque and static friction. Patented applications are indicated in the article with their particular numbers and listed in Bibliography.

PRINCIPLE OF OPERATION

A schematic of the centrifugal magnetic fluid seal (CMFS) is shown in Fig. 1. The magnetic flux loops, which are drawn as dotted lines, are created by: a permanent magnet, a pair of magnet covers with several concentric projections and grooves, a pair of annular rings, a sleeve, and the magnetic fluid injected into the gap. The covers protecting the magnet, the annular rings, and the sleeve are made of ferromagnetic materials.

The magnetic fluid entrapped in the gap carries the force generated by the pressure difference across the seal by means of magnetic attraction at a low shaft rotating speed or at rest, and by the centrifugal force at a higher rotating speed. The CMFS can operate without any contact between rotating and fixed parts even under large rotating vibration, because the gap ΔR in this seal can be kept very large. In addition, the CMFS differs from ordinary centrifugal seals in that it can store the sealing fluid in the gap even when the shaft is at rest.

The sealing pressure pm generated by the magnetic attraction on each stage can be expressed by the following equation:

$$p_m = \frac{2\,\mu_o\ M * H * w}{\delta} \tag{1}$$

where:

μ_o – magnetic permeability of vacuum,
M – intensity of magnetization,
H – magnetic field intensity,
w – width of one stage,
δ – sealing gap.

The sealing pressure p_c caused by the centrifugal force due to one stage can be expressed as:

$$p_c = r * \omega^2 \rho * w \tag{2}$$

where:

r – radial coordinate,
ω – rotating speed,
ρ – density of magnetic fluid.

The ratio between pressures p_c and p_m is:

$$\eta = \frac{p_C}{p_m} = \frac{r * \omega^2 * \rho * \delta}{2\,\mu_0 * M * H} \tag{3}$$

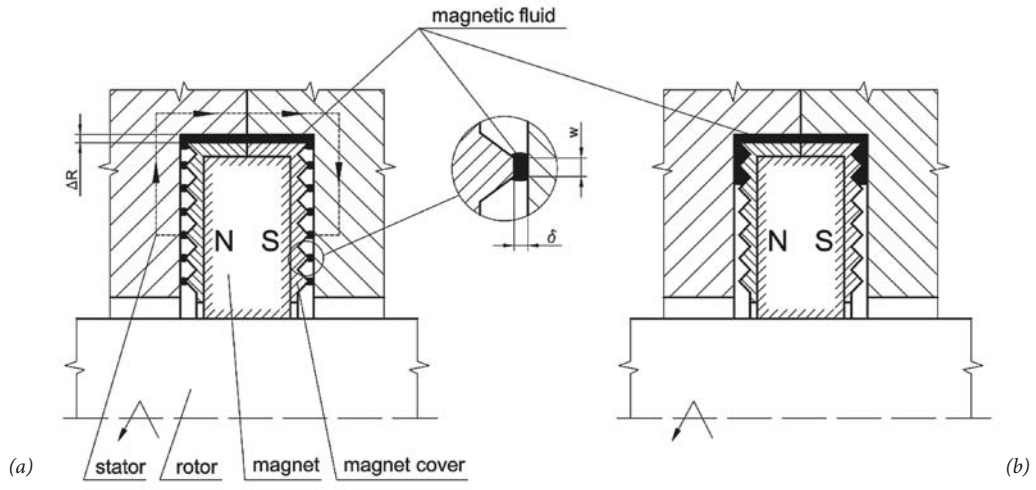

Fig. 1. Operation principle of centrifugal magnetic fluid seal (C.M.F.S.)
(a) position of magnetic fluid at low rotating speed, (b) position of magnetic fluid at high rotating speed

Thus, when the rotating speed ω is low, η will be less than unity and the sealing pressure will be governed by magnetic attraction. Conversely, when the rotating speed ω is high, η will be greater than unity and the sealing pressure will be generated by the centrifugal force. This phenomenon is illustrated in Fig. 2 [11].

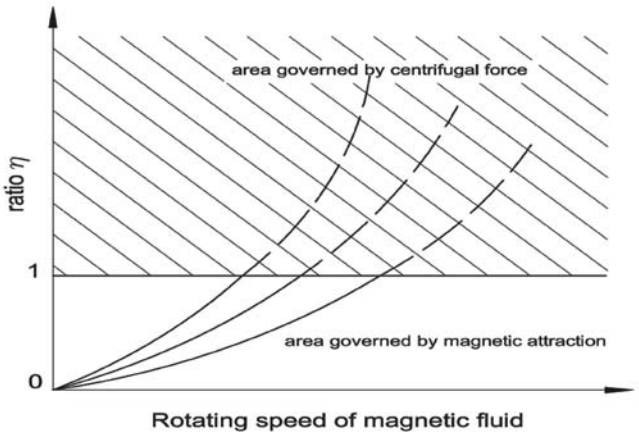

Fig. 2. Relation between the effect of magnetic attraction and centrifugal force in centrifugal magnetic fluid seal

BASIC DESIGNS OF CENTRIFUGAL MAGNETIC FLUID SEALS

Fig. 3 present the design of the centrifugal magnetic fluid seal with disc of rectangular cross-section and stationary magnetic system [16]. The seal consists of: axially polarized permanent magnets 5, two inner pole pieces 6, elements of housing 3, 4 with outer pole pieces in form of flanges 3a, 4a, and magnetic fluid 7. The pole pieces 3a, 4a have projections made on their inner cylindrical surfaces situated near shaft 1, while the pole pieces 6 have projections made on their side surfaces situated near the face of disc 2 mounted on shaft 1. The permanent magnets 5 and the inner pole pieces 6 are placed in the elements of housing 3, 4.

At rest or at low rotary shaft speed (Fig. 3a), the magnetic fluid 7 is kept in the axial sealing gaps δ_a between the projections of inner pole pieces 6 and the face of disc 2, thus forming the sealing barriers. At high rotary shaft speed (Fig. 3b), the magnetic fluid 7 is moved from the stages toward the outer extending perimeter of the cavity formed between disc 2 and the elements of housing 3, 4, thus creating the sealing barrier.

Fig. 4 shows the centrifugal magnetic fluid seal for a rotating shaft with rotary magnetic system [17]. The seal consists of: elements of housing 2, 3, flanged sleeve 4, axially polarized permanent magnets 5, multi-edged pole pieces 6, and magnetic fluid 7. The flanged sleeve 4 is mounted on shaft 1. The permanent magnets 5 with pole pieces 6 adhere with the same N poles to two side surfaces of flange 4a. The magnets 5 and the pole pieces 6 are fastened to the outer cylindrical surfaces of sleeve 4. The multi-edged pole pieces 6 have sealing projections made on their outer side surfaces. Similar sealing projections are also made on outer cylindrical surfaces of the flanged sleeve 4, at its both ends. At rest or at low rotary speed of shaft 1 (Fig. 4a), the magnetic forces keep the magnetic fluid 7 in the axial gaps δ_a between the sealing projections of pole pieces 6 and the side surfaces of recesses in elements of housing 2, 3, as well as in the radial gaps δ_r between sealing projections of flanged sleeve 4 and inner cylindrical surfaces of elements of housing 2, 3, thus creating the sealing barriers. At high rotary speed of shaft 1 (Fig. 4b), the action of the centrifugal force, which is greater at that moment than the magnetic attraction force, moves the magnetic fluid 7 from the axial gaps δ_a to the circumferential gaps δ_o situated around the outer cylindrical surfaces of pole pieces 6. This ferrofluid, together with the magnetic fluid 7 in the radial gaps δ_r, forms a layer being the sealing barrier for the working medium.

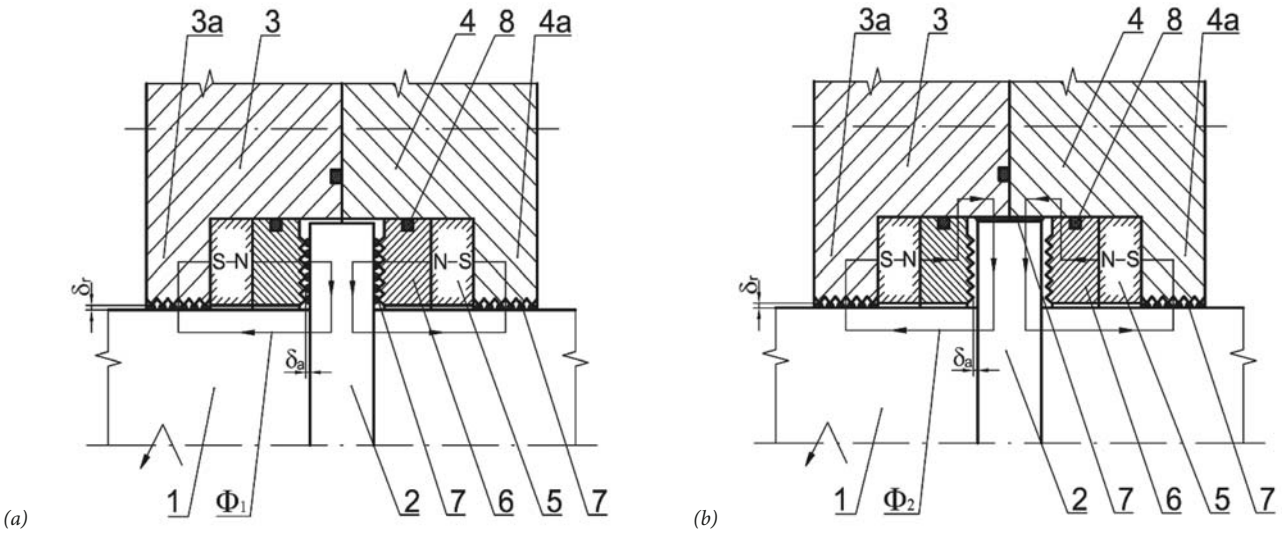

Fig. 3. Centrifugal magnetic fluid seal with disc of rectangular cross-section and stationary magnetic system (a) at low rotating shaft speed, (b) at high rotating shaft speed: 1 – shaft, 2 – disc, 3, 4 – elements of housing, 3a, 4a – outer pole pieces, 5 – permanent magnet, 6 – inner pole piece, 7 – magnetic fluid, 8 – "O"– ring seal, δ_a – axial sealing gap, δ_r – radial sealing gap, Φ_1, Φ_2 – closed magnetic circuits

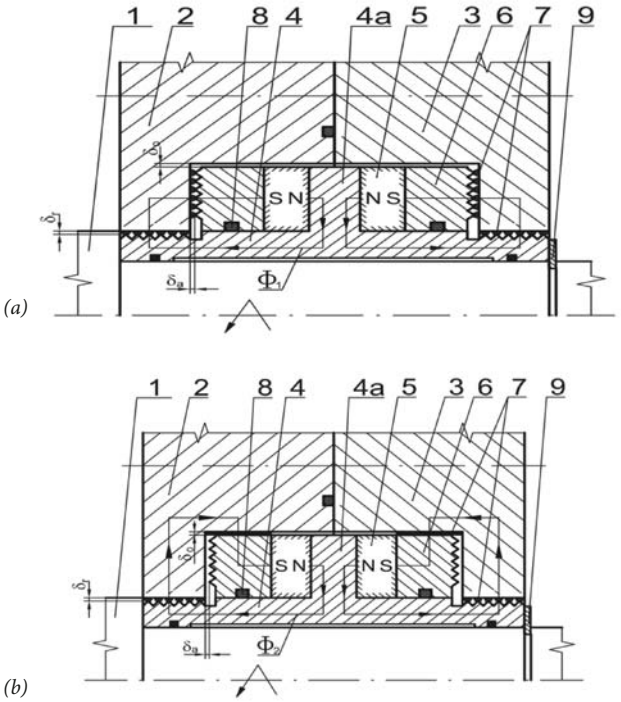

Fig. 4. Centrifugal magnetic fluid seal for rotating shaft with rotary magnetic system (a) at low rotating shaft speed, (b) at high rotating shaft speed: 1 – shaft, 2, 3 – elements of housing, 4 – flanged sleeve, 4a – flange, 5 – permanent magnet, 6 – pole piece, 7 – magnetic fluid, 8 – "O"– ring seal, 9 – snap ring, δ_a – axial sealing gap, δ_r – radial sealing gap, δ_o – circumferential sealing gap, Φ_1, Φ_2-closed magnetic circuits

Fig. 5 shows the design of the centrifugal magnetic fluid seal with disc of vee-shaped cross section and stationary magnetic system [18]. The seal consists of: axially polarized permanent magnet 4, two pole pieces 5, and magnetic fluid 6. The permanent magnet 4 and the pole pieces 5 are mounted in the recess of housing 2. The disc 3 with conical side surfaces is mounted on shaft 1. Projections of triangular cross-section are made on the conical side surfaces of pole pieces 5. At rest or at low rotational speed of shaft 1 (Fig. 5a), the strong magnetic field keeps the magnetic fluid 6 in the sealing gaps δ_a between the projections of pole pieces 5 and disc 3, thus providing hermetic sealing. In this case the permanent magnet 4, the pole pieces 5, and the disc 3 form a closed magnetic circuit Φ. At high rotational speed of shaft 1 (Fig. 5b), the action of the centrifugal force, which is greater at that moment than the magnetic attraction force, moves the magnetic fluid 6 from the sealing stages towards the outer perimeter of disc 3. In this case the magnetic fluid 6 fills a small passageway between the top of disc 3 and the magnet 4, thus forming a seal which operates in the centrifugal sealing mode.

Fig. 6 shows the centrifugal magnetic fluid seal with disc of vee-shaped cross-section and rotating magnetic system [19]. The seal consists of: rotating shaft 1, multi-edged pole pieces 3, axially polarized permanent magnet 4, rings 5 of trapezoidal cross-sections, magnetic fluid 6, cover 9, and non-magnetic ring 10. The rings 5 are mounted in the recess of housing 2, while the multi-edged pole pieces 3, having the form of sleeves with flanges 3a of conical outer surfaces, are mounted on shaft 1 equipped with flange 1a. The inclination angle of the conical surfaces in pole pieces 3 is the same as that in rings 5. Sealing projections are made on conical surfaces of flanges 3a of pole pieces 3. The permanent magnet 4, with the non-magnetic ring 10 fastened onto it, is mounted on flange 1a of shaft 1, between pole pieces 3. The flanges 3a of pole pieces 3, together with permanent magnet 4 and ring 10, are mounted with some clearance between rings 5. At rest or at low rotary speed of shaft 1 (Fig. 6a), the magnetic forces keep the magnetic fluid 6 in the gaps δ between the sealing projections of pole pieces 3 and the conical surfaces of rings 5, thus creating the sealing barriers. At high rotary speed of shaft 1 (Fig. 6b), the magnetic fluid 6 is moved to the gap between the inner cylindrical surface of the housing recess and the outer moving part of the sealing, thus creating the liquid barrier for the sealed medium.

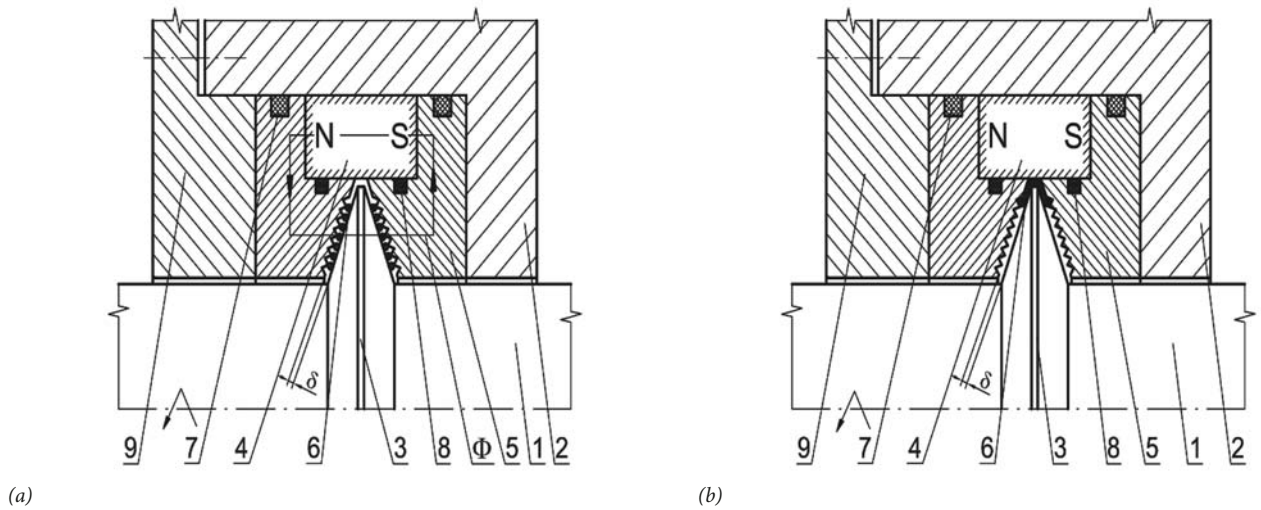

Fig. 5. Centrifugal magnetic fluid seal with disc of vee-shaped cross-section and stationary magnetic system (a) at low rotating shaft speed, (b) at high rotating shaft speed: 1 – shaft, 2 – housing, 3 – disc of vee-shaped cross-section, 4 – permanent magnet, 5 – pole piece, 6 – magnetic fluid, 7, 8 – "O" – ring seals, 9 – cover, δ – sealing gap, Φ – closed magnetic circuit

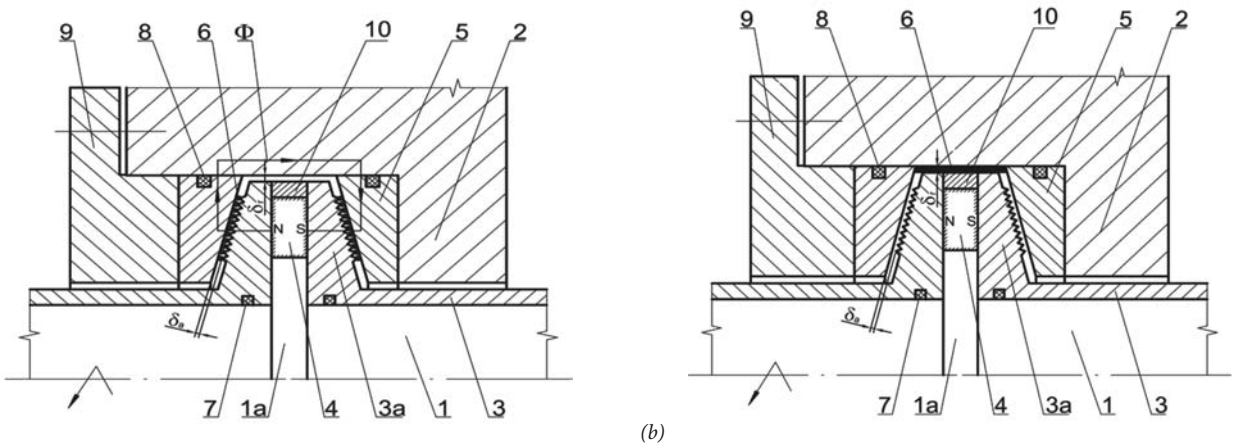

Fig. 6. Centrifugal magnetic fluid seal with disc of vee-shaped cross-section and rotary magnetic system (a) at low rotating shaft speed, (b) at high rotating shaft speed: 1 – rotating shaft, 1a – flange of shaft, 2 – housing, 3 – pole piece, 3a – flange, 4 – permanent magnet, 5 – ring of trapezoidal cross-section, 6 – magnetic fluid, 7, 8 – "O" – rings seals, 9 – cover, 10 – non-magnetic ring, δ_a – axial sealing gap, δ_r – radial sealing gap, Φ – closed magnetic circuit

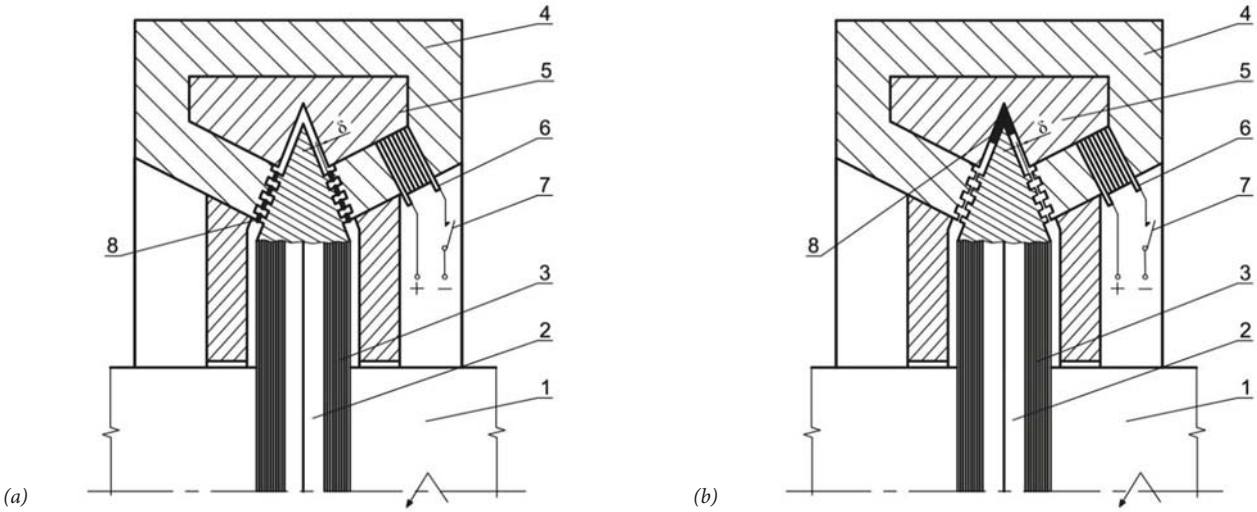

Fig. 7. Vee-shaped magnetic/centrifugal fluid seal (a) at low rotating shaft speed, (b) at high rotating shaft speed: 1 – shaft, 2 – disc of vee-shaped cross-section, 3 – projection, 4 – magnetic core, 5 – housing, 6 – electromagnetic coil, 7 – switch, 8 – magnetic fluid, δ – sealing gap

Fig. 7 presents the design of the vee-shaped magnetic/centrifugal fluid seal [20]. The seal comprises the rotating shaft 1, which is journaled within and supported by the housing 5. The circular disc 2 having an outer, peripheral vee-shaped cross-section is mounted on shaft 1. The housing 5 has a complementary vee-shaped cross-section part within which the vee-shaped disc 2 rides. Radially extending projections of rectangular cross-section are formed on disc 2 and on the magnetic core 4 of the horseshoe-shaped cross-section. The magnetic field can be generated by a permanent magnet or an electromagnet. If the permanent magnet is employed, then it would be inserted as part of the horseshoe-shaped core 4. If the electromagnet is used, it would employ an electromagnetic coil 6 energized from a DC source, via the selectively operable on-off switch 7. At rest or at low rotating shaft speed (Fig. 7a), the magnetic fluid 8 is kept in the gaps δ between the projections on disc 2 and on the horseshoe-shaped core 4, thus forming the multi-stage magnetic fluid seal. At high rotating shaft speed, the centrifugal force acting on the ferrofluid 8 is greater than the magnetic forces keeping the ferrofluid 8 between the projections and moves the fluid into the vee-shaped part, as shown in Fig. 7b. In this case the seal operates in the centrifugal sealing mode.

Fig. 8 shows the design of the centrifugal magnetic fluid seal with stationary vane and rotating magnetic system [21]. The seal consists of the fluid cavity composed of the rotatable magnetic structure assembly 3-6 and the stationary holder 7, 8 with vane 9. The vane 9 with blade 10 and projections 11 of rectangular cross-section located on its side surfaces completes the magnetic circuit Φ. At rest or low rotating shaft speed (Fig. 8a), the strong magnetic field gradients keep the ferrofluid 13 in the gaps δ under each sealing stage, thus providing the necessary differential pressure capability. At high rotating shaft speed (Fig. 8b), the centrifugal force is greater than the magnetic attraction forces in the multistage seal and moves the ferrofluid 13 from the sealing gaps δ to the top cavity blade passageway, thus forming the ferrofluid barrier around the blade 10.

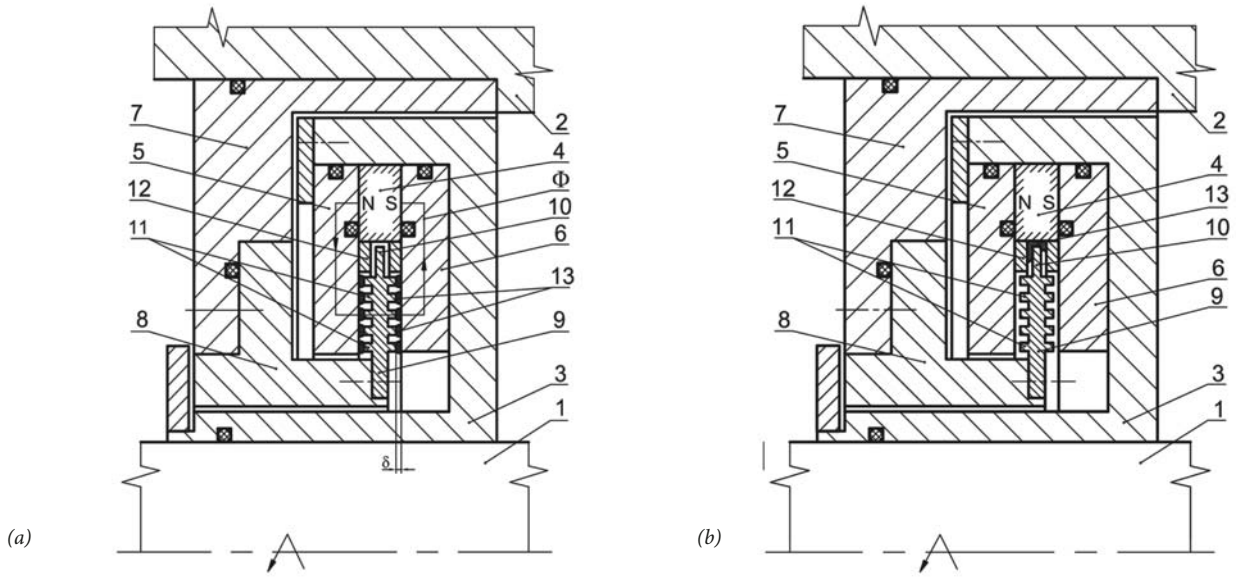

Fig. 8. Ferrofluid centrifugal seal with stationary vane and rotating magnetic system (a) at low rotating shaft speed, (b) at high rotating shaft speed: 1 – shaft, 2 – housing, 3 – movable holder, 4 – permanent magnet, 5, 6 –pole pieces, 7, 8 – elements of stationary holder, 9 – vane, 10 – blade, 11 – projections, 12 – spacing ring, 13 – ferrofluid, δ – sealing gap, Φ – closed magnetic circuit

SELECTED NEW DESIGNS OF CENTRIFUGAL MAGNETIC FLUID SEALS

Fig. 9 shows the centrifugal seal with magnetic fluid and stationary magnetic system [22]. The seal consists of: flanged sleeve 4 mounted on shaft 1, multi-edged pole pieces 5 and 6, axially polarized permanent magnets 7, non-magnetic sleeves 9, and magnetic fluid 8. The pole pieces 5, having the angle-bar cross-sections, are placed in recesses made in elements of housing 2, 3, on both sides of flange 4a of sleeve 4. In turn, the pole pieces 6, of rectangular cross-sections, are mounted in the recesses of pole pieces 5. The pole pieces 6 are separated from pole pieces 5 by permanent magnets 7 and non-magnetic sleeves 9. The pole pieces 5 have sealing projections on inner cylindrical surfaces of their flanges and on front surfaces of their arms, while the pole pieces 6 have sealing projections on their inner cylindrical surfaces. At rest or at low rotary speed of shaft 1 (Fig. 9a), the magnetic fluid 8 fills the axial gaps δ_a between the sealing projections situated on front surfaces of pole pieces 5 and side surfaces of flange 4a of sleeve 4, and the radial gaps δ_r between the sealing projections on inner cylindrical surfaces of pole pieces 5, 6 and the outer cylindrical surfaces of flanged sleeve 4, thus creating the sealing barriers. At high rotary speed of shaft 1 (Fig. 9b), the magnetic fluid 8 is moved from the axial gaps δ_a to the gap created in elements of housing 2, 3 around the flange 4a of sleeve 4, along its perimeter, thus forming a liquid ring being an additional sealing barrier for the working medium.

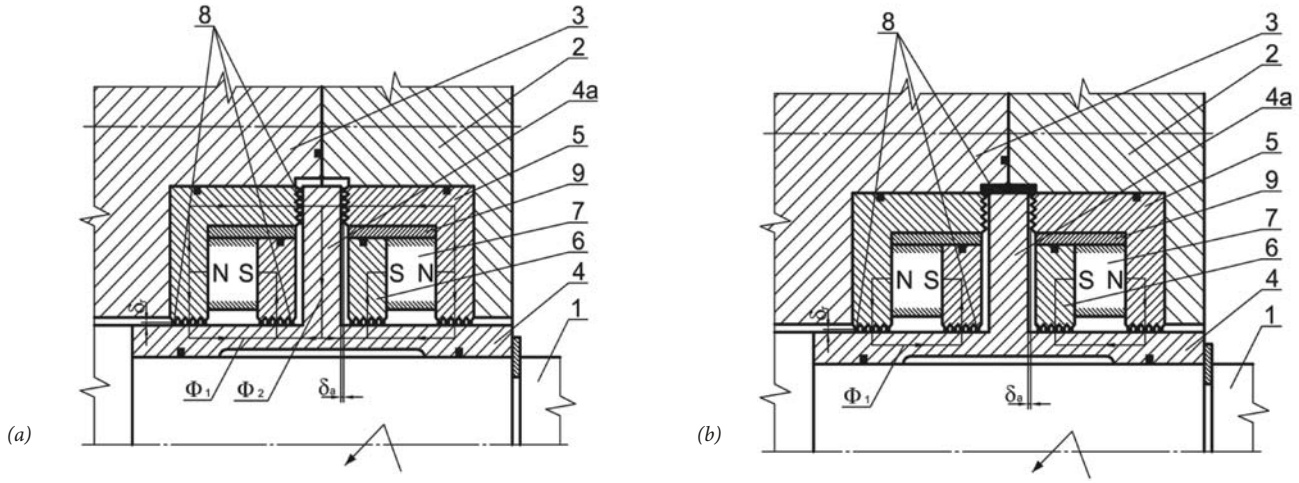

Fig. 9. Centrifugal seal with magnetic fluid and stationary magnetic system (a) position of magnetic fluid at low rotating speed, (b) position of magnetic fluid at high rotating speed; 1 – shaft, 2, 3 – elements of housing, 4 – flanged sleeve, 4a – flange, 5, 6 – multi-edged pole pieces, 7 – permanent magnet, 8 – magnetic fluid, 9 – non-magnetic sleeve, δ_a – axial sealing gap, δ_r – radial sealing gap, Φ_1, Φ_2–closed magnetic circuits

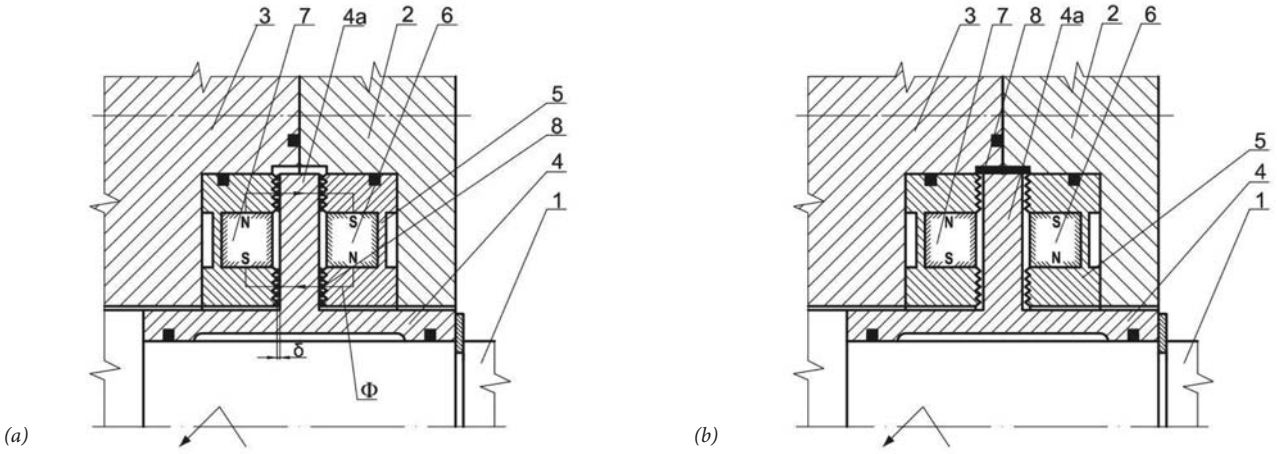

Fig. 10. Centrifugal seal with magnetic fluid (a) position of magnetic fluid at low rotating speed, (b) position of magnetic fluid at high rotating speed 1 – shaft, 2, 3 – elements of housing, 4 – flanged sleeve, 4a – flange, 5 – multi-edged pole piece, 6, 7 – permanent magnets polarized radially, 8 – magnetic fluid, δ – sealing gap, Φ – closed magnetic circuit

Another design of the centrifugal seal with magnetic fluid and stationary magnetic system is shown in Fig. 10 [23]. This seal consists of: flanged sleeve 4 mounted on shaft 1, multi-edged pole pieces 5, permanent magnets 6, 7, and magnetic fluid 8. The pole pieces 5, having the angle-bar cross-sections, are placed in recesses made in elements of housing 2, 3, on both sides of flange 4a of sleeve 4. In turn, the radially polarized permanent magnets 6, 7 are mounted in the recesses of pole pieces 5. The magnet 6 is polarized in the N-S pole arrangement, while the magnet 7 – in the S-N arrangement with respect to shaft 1. The pole pieces 5 have sealing projections on their front surfaces directed towards the side surfaces of flange 4a of sleeve 4. At rest or at low rotary speed of shaft 1 (Fig. 10a), the magnetic fluid 8 fills the axial gaps δ between the sealing projections of pole pieces 5 and the side surfaces of flange 4a of sleeve 4, thus creating the sealing barriers. At high rotary speed of shaft 1 (Fig. 10b), the magnetic fluid 8 is moved from the axial gaps δ to the gap created in the elements of housing 2, 3 around the flange 4a, along its perimeter, thus forming a liquid ring being in this case the sealing barrier for the working medium.

Fig. 11 shows the centrifugal seal with magnetic liquid for high-speed shaft with movable magnetic system [24]. The seal consists of: flanged sleeve 3 mounted on shaft 1, axially polarized cylindrical permanent magnets 4, multi-edged pole pieces 5, magnetic fluid 6, and cover 7. The multi-edged pole pieces 5 of rectangular cross-section, with sealing projections situated on their outer side surfaces, are mounted in sockets made on the side surfaces of flange 3a of sleeve 3. The cylindrical permanent magnets 4 are placed in holes evenly distributed around the perimeter in the necking of flange 3a of sleeve 3, situated between pole pieces 5. The flange 3a of sleeve 3 with magnets 4 and pole pieces 5 is mounted, with some clearance, in the recess of housing 2 covered with cover 7. At rest or at low rotary speed of shaft 1 (Fig. 11a), the magnetic fluid 6 is kept in the axial gaps δ_a between the sealing projections of pole pieces 5 and the side surfaces of the recess in housing 2 and cover 7, thus creating the sealing barriers. At high rotary speed of shaft 1 (Fig. 11b), the magnetic fluid 6 is moved from the axial gaps δ_a to the radial gap δ_r situated around flange 3a of sleeve 3, along its perimeter, thus forming a liquid ring being in this case the sealing barrier for the working medium.

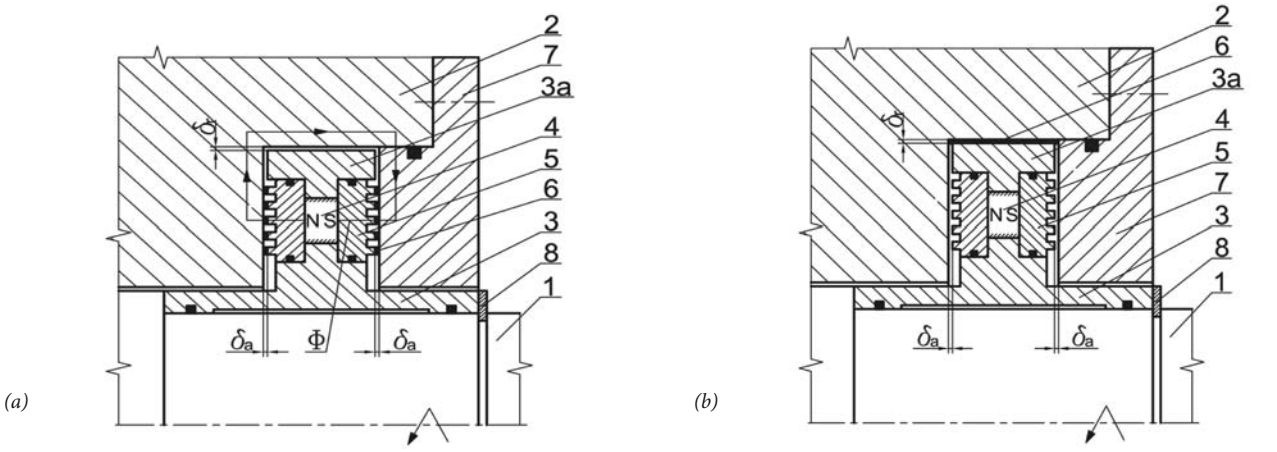

Fig. 11. Centrifugal seal with magnetic fluid for high-speed shaft and movable magnetic system (a) position of magnetic fluid at low rotating speed, (b) position of magnetic fluid at high rotating speed 1 – shaft, 2 – housing, 3 – flanged sleeve, 3a – flange, 4 – cylindrical permanent magnet, 5 – multi-edged pole piece, 6 – magnetic fluid, 7 – cover, 8 – snap ring, δ_a – axial sealing gap, δ_r – radial sealing gap, Φ – closed magnetic circuit

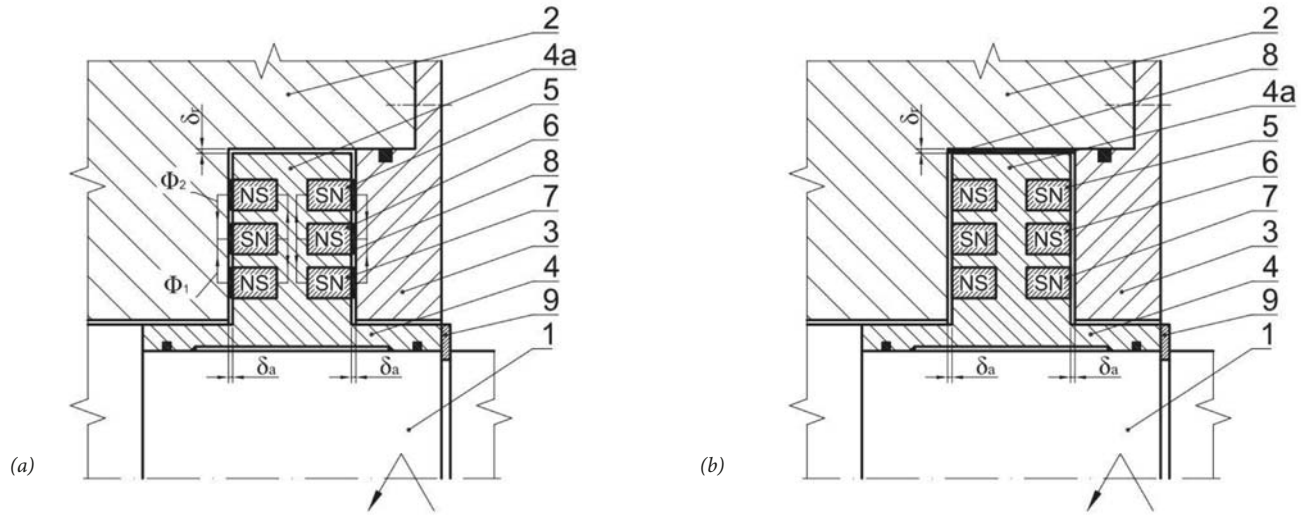

Fig. 12. Centrifugal seal with magnetic fluid for rotating shaft and movable magnetic system (a) position of magnetic fluid at low rotating speed, (b) position of magnetic fluid at high rotating speed 1 – shaft, 2 – housing, 3 – cover, 4 – flanged sleeve, 4a – flange, 5, 6, 7 – annular permanent magnets, 8 – magnetic fluid, 9 – snap ring, δ_a – axial sealing gap, δ_r – radial sealing gap, Φ_1, Φ_2 – closed magnetic circuits

Another design of the centrifugal seal with magnetic fluid for rotating shaft and movable magnetic system is shown in Fig. 12 [25]. This seal consists of: flanged sleeve 4, axially polarized annular permanent magnets 5, 6, 7, magnetic fluid 8, and cover 3. The flange 4a of sleeve 4 mounted on shaft 1 is placed with some clearance in the recess of housing 2 covered with cover 3. The annular permanent magnets 5, 6, 7 are placed in sockets symmetrically distributed on side surfaces of flange 4a of sleeve 4. The poles of these magnets are arranged in turns, N-S-N, with respect to the side surfaces of flange 4a. At rest or at low rotary speed of shaft 1 (Fig. 12a), the magnetic fluid 8 is kept in the axial gaps δa between the end surfaces of permanent magnets 5, 6, 7, being the N or S poles, and the corresponding side surfaces of the recess in housing 2 and cover 3, thus creating the sealing barriers. At high rotary speed of shaft 1 (Fig. 12b), the magnetic fluid 8 is moved from the axial gaps δa to the radial gap δr situated between flange 4a of sleeve 4, along its perimeter, and the inner cylindrical surface of the recess in housing 2, thus forming a liquid ring being in this case the sealing barrier for the working medium.

SELECTED APPLICATIONS OF CENTRIFUGAL MAGNETIC FLUID SEALS IN MODERN SEALING TECHNOLOGY

Fig. 13 shows an example of application of the compact, centrifugal seal with magnetic fluid for rolling bearing [26]. The seal consists of: the outer pole piece 7, of L-shaped cross-section, mounted in housing 2, the inner pole piece 6, also of L-shaped cross-section, placed by overlapping in the outer pole piece 7, and the axially polarized annular permanent magnet 5 placed in the non-magnetic sleeve 4 mounted on shaft 1. At rest

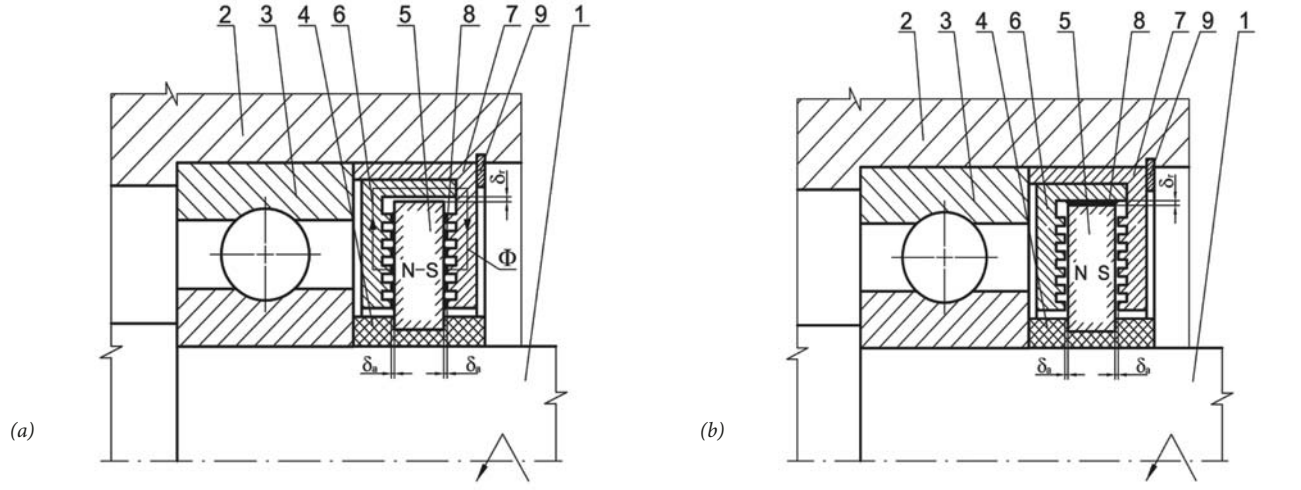

Fig. 13. Compact centrifugal seal with magnetic fluid for rolling bearing (a) position of magnetic fluid at low rotating speed, (b) position of magnetic fluid at high rotating speed 1 – shaft, 2 – housing, 3 – rolling bearing, 4 – sleeve, 5 – annular permanent magnet, 6 – inner pole piece, 7 – outer pole piece, 8 – magnetic fluid, δ_a – axial sealing gap, δ_r – radial sealing gap, Φ – closed magnetic circuit

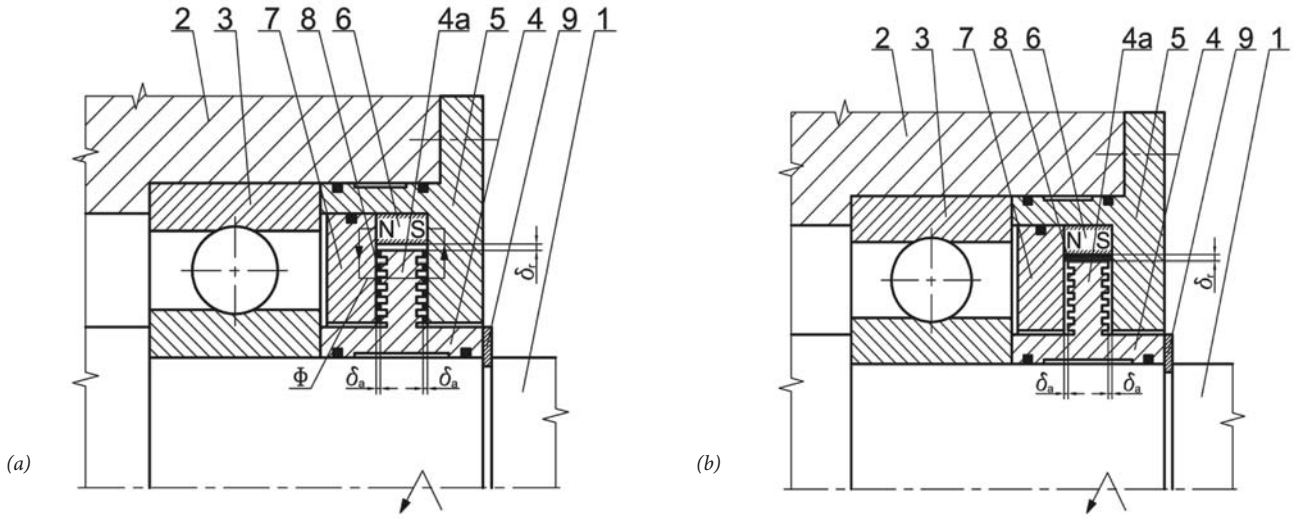

Fig. 14. Hybrid protective seal with magnetic fluid for rolling bearing (a) position of magnetic fluid at low rotating speed, (b) position of magnetic fluid at high rotating speed 1 – shaft, 2 – housing, 3 – rolling bearing, 4 – flanged sleeve, 4a – flange, 5 – cover, 6 – permanent magnet, 7 – pole piece, 8 – magnetic fluid, 9 – snap ring, δ_a – axial sealing gap, δ_r – radial sealing gap, Φ – closed magnetic circuit

or at low rotary speed of shaft 1 (Fig. 13a), the magnetic fluid 8 fills the axial gaps δ_a between the sealing projections on side surfaces of the arms of pole pieces 6, 7 and the side surfaces of permanent magnet 5, thus creating the sealing barriers. At high rotary speed of shaft 1 (Fig. 13b), the magnetic fluid 8 is moved to the radial gap δ_r situated between the permanent magnet 5 and the inner pole piece 6, thus forming the layer of liquid being in this case the sealing barrier for the working medium.

Fig. 14 shows the hybrid protective seal with magnetic fluid for rolling bearing [27]. The seal consists of: flanged sleeve 4, cover 5, axially polarized permanent magnet 6, pole piece 7 of rectangular cross-section, and magnetic fluid 8. The flanged sleeve 4 mounted on shaft 1 adheres to the inner ring of rolling bearing 3 and has flange 4a directed towards housing 2. Sealing projections are made on side surfaces of flange 4a of sleeve 4. The permanent magnet 6 and the pole piece 7 are mounted in recesses made in cover 5, while the flange 4a of sleeve 4 is mounted with some clearance, in the chamber created by cover 5, permanent magnet 6, and pole piece 7. At rest or at low rotary speed of shaft 1 (Fig. 14a), the magnetic forces keep the magnetic fluid 8 in the axial gaps δ_a between the sealing projections on flange 4a of sleeve 4 and the side surfaces of pole piece 7 and cover 5, thus creating the sealing barriers. At high rotary speed of shaft 1 (Fig. 14b), the magnetic fluid 8 is moved from the axial gaps δ_a to the radial gap δ_r around the flange 4a, along its perimeter, and forms a liquid ring being in this case the sealing barrier, which protects the rolling bearing 3 against penetration of impurities into it. Moreover, the axial-radial labyrinth seal created by the flanged sleeve 4 and cover 5 with magnet 6 and pole piece 7 acts as an additional sealing barrier.

Fig. 15 shows the double sealing system for shaft in vertical arrangement. The seal consists of the centrifugal seal with magnetic fluid, situated over the rolling bearing 3, and the outer axial labyrinth seal. The labyrinth seal consists of the stationary flanged sleeve 4 fixed to housing 2 and the movable

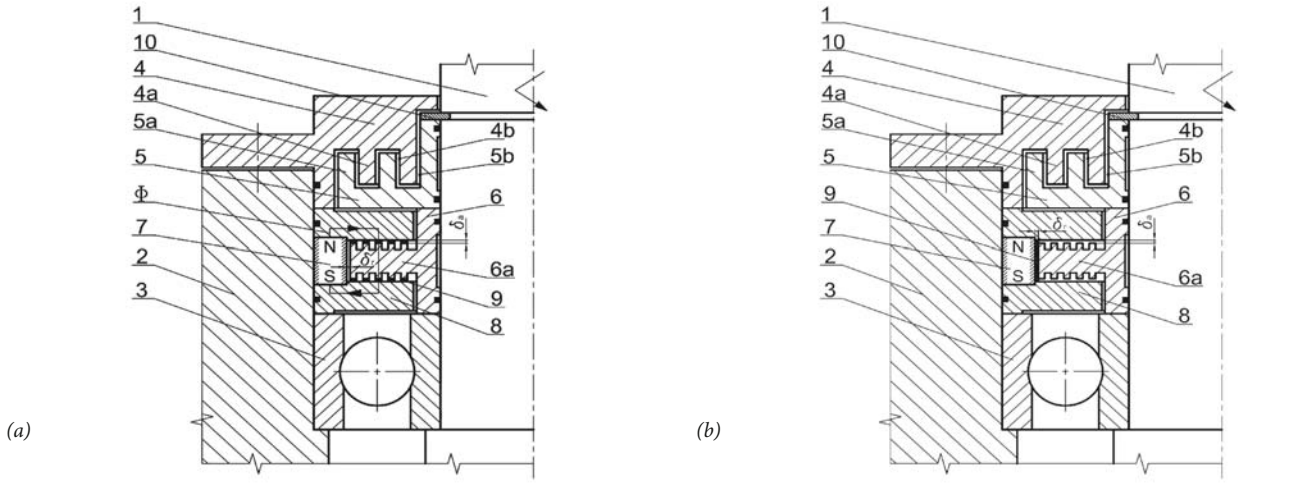

Fig. 15. Double sealing system for shaft in vertical arrangement (a) position of magnetic fluid at low rotating speed, (b) position of magnetic fluid at high rotating speed 1 – vertical shaft, 2 – housing, 3 – rolling bearing, 4 – stationary flanged sleeve, 4a – annular projection, 4b – annular cavity, 5 – movable flanged sleeve, 5a – annular projection, 5b – annular cavity, 6 – bushing, 6a – flange with sealing projections, 7 – permanent magnet, 8 – pole piece, 9 – magnetic fluid, 10 – snap ring, δ_a – axial sealing gap, δ_r – radial sealing gap, Φ – closed magnetic circuit

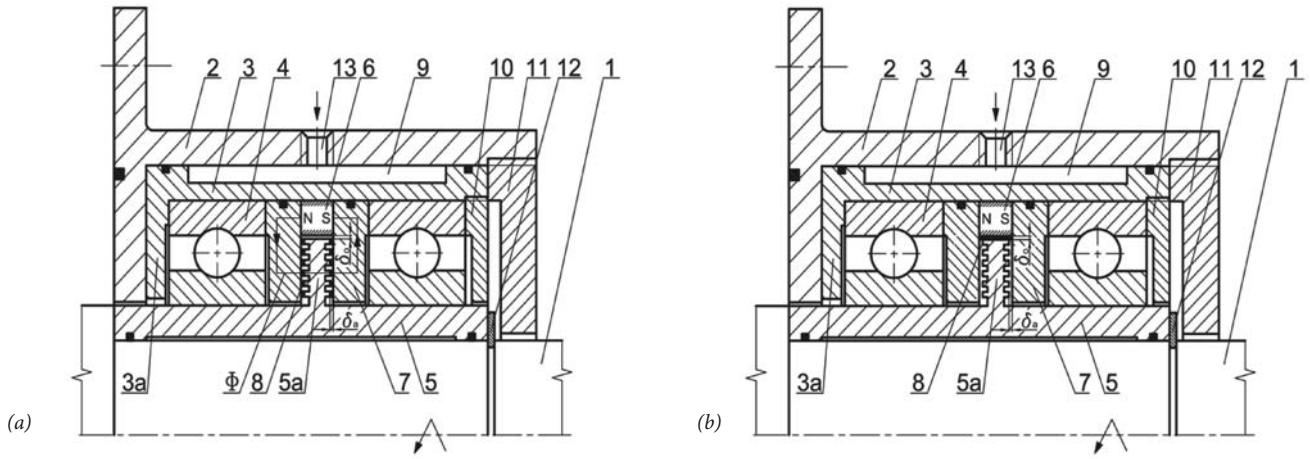

Fig. 16. Feedthrough of high-speed shaft with magnetic fluid centrifugal seal (a) position of magnetic fluid at low rotating speed, (b) position of magnetic fluid at high rotating speed 1 – shaft, 2 – housing, 3 – stationary flanged sleeve, 3a – flange, 4 – rolling bearing, 5 – movable flanged sleeve, 5a – flange with sealing projections, 6 – cylindrical permanent magnet, 7 – pole piece, 8 – magnetic fluid, 9 – cooling chamber, 10, 11 – setting nuts, 12 – snap ring, 13 – hole for cooling medium, δ_a – axial sealing gap, δ_o – circumferential sealing gap, Φ – closed magnetic circuit

flanged sleeve 5 with suitable recesses and projections mounted on shaft 1. The centrifugal seal consists of the bushing 6 with flange 6a directed towards housing 2 mounted on shaft 1, and two pole pieces 8 of rectangular cross-section separated by the axially polarized permanent magnet 7 mounted in housing 2. The flange 6a of bushing 6 has sealing projections on its side surfaces. At rest or at low rotary speed of shaft 1 (Fig. 15a), the magnetic forces keep the magnetic fluid 9 in the axial gaps δ_a between the sealing projections on flange 6a of sleeve 6 and the inner side surfaces of pole pieces 8, thus creating the sealing barriers. At high rotary speed of shaft 1 (Fig. 15b), the magnetic fluid 9 is moved from the axial gaps δ_a to the radial gap δ_r situated around the flange 6a, along its perimeter, thus forming a liquid ring being an additional sealing barrier which protects the rolling bearing 3 against penetration of impurities.

Fig. 16 presents the design of the feedthrough of high-speed shaft with centrifugal magnetic fluid seal, used in low-pressure and vacuum applications [28]. The feedthrough of shaft 1 consists of: housing 2, stationary flanged sleeve 3 with flange 3a, movable flanged sleeve 5 with flange 5a, rolling bearings 4, axially polarized permanent magnet 6, pole pieces 7, and magnetic fluid 8. The stationary flanged sleeve 3 with flange 3a directed towards shaft 1 is mounted in the housing 2, while the movable flanged sleeve 5 with flange 5a directed towards the housing 2 and equipped with sealing projections is mounted on the rotating shaft 1. The pole pieces 7 of rectangular cross-section, separated by the permanent magnet 6, are mounted in the chamber between the rolling bearings 4 fastened in sleeves 3, 5, while the flange 5a of sleeve 5a is mounted with some clearance between the side surfaces of pole pieces 7. The outer cylindrical surface of the stationary flanged sleeve 3 has a circumferential recess which, together with the inner cylindrical surface of housing 2, creates the cooling chamber 9. The hole 13 in housing 2 is used for delivering the cooling medium to chamber 9. At rest or at low rotary speed of shaft 1 (Fig. 16a),

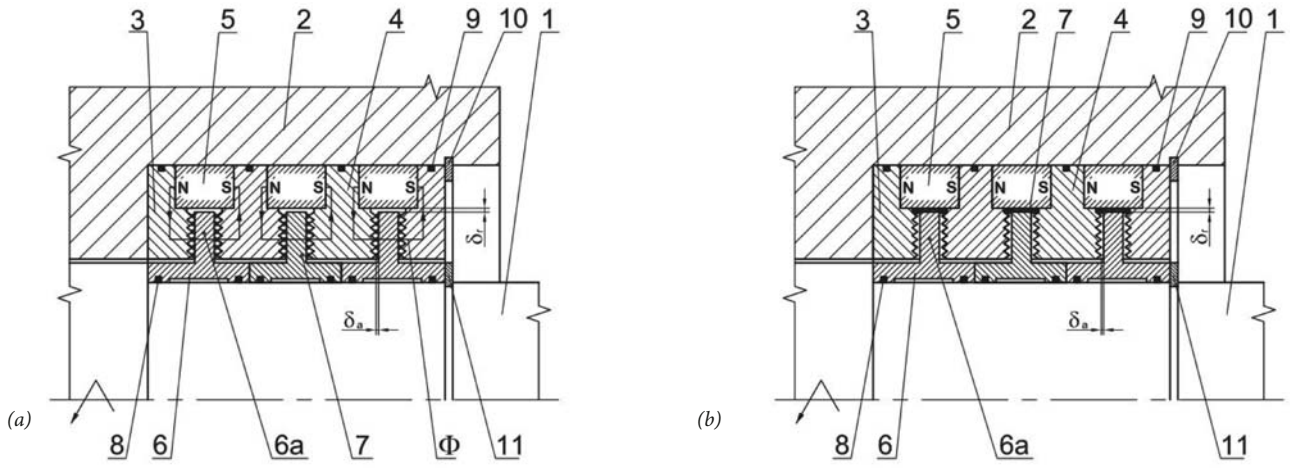

Fig. 17. Multi-staged ferromagnetic seal for rotating shaft (a) position of magnetic fluid at low rotating speed, (b) position of magnetic fluid at high rotating speed, 1 – shaft, 2 – housing, 3, 4 – multi-edged pole pieces, 5 – permanent magnet, 6 – flanged sleeve, 6a – flange, 7 – ferromagnetic fluid, 8, 9 – "O" – ring seals, 10, 11 – snap rings, δ_a – axial sealing gap, δ_r – radial sealing gap, Φ – closed magnetic circuit

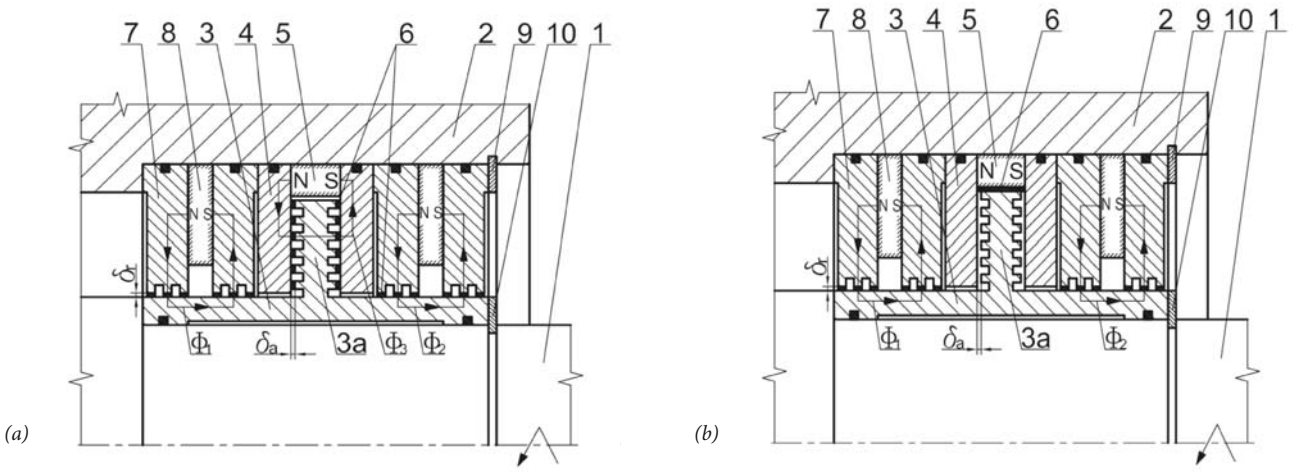

Fig. 18. Hybrid seal with magnetic fluid for high-speed shaft (a) position of magnetic fluid at low rotating speed, (b) position of magnetic fluid at high rotatingspeed, 1 – shaft, 2 – housing, 3 – flanged sleeve, 3a – flange with sealing projections, 4 – rectangular cross-section pole piece, 5, 8 – permanent magnets, 6 – magnetic fluid, 7 – multi-edged pole piece, 9, 10 – snap rings, δ_a – axial sealing gap, δ_r – radial sealing gap, Φ_1, Φ_2, Φ_3 – closed magnetic circuits

the magnetic fluid 8 fills the axial gaps δa between the sealing projections of flange 5a of movable sleeve 5 and the inner side surfaces of pole pieces 7, thus creating the sealing barriers. At high rotary speed of shaft 1 (Fig. 16b), the magnetic fluid 8 is moved to the circumferential gap δo between the cylindrical surface of flange 5a of movable sleeve 5 and the inner cylindrical surface of permanent magnet 6, thus forming a liquid ring being an additional sealing barrier for the working medium. Moreover, at high rotary speed of the shaft, the applied cooling system ensures maintaining the appropriate operating temperature of the seal, which increases its durability.

Fig. 17 presents the multi-staged ferromagnetic fluid seal for rotating shaft [29]. The seal consists of: multi-edged pole pieces 3 and 4, separated by axially polarized annual permanent magnets 5 and placed in the packing chamber in housing 2, and flanged sleeves 6 mounted on shaft 1. The side surfaces of pole pieces 3, 4 have sealing projections. The flanges 6a of sleeves 6 are placed, with some clearance, in the annular chambers created between pole pieces 3, 4 and permanent magnets 5. At rest or at low rotary speed of shaft 1 (Fig. 17a), the magnetic forces keep the ferromagnetic fluid 7 in the axial gaps δ_a between the sealing projections on pole pieces 3, 4 and the side surfaces of flanges 6a of sleeves 6, thus creating the sealing barriers. At high rotary speed of shaft 1 (Fig. 17b), the ferromagnetic fluid 7 is moved from the axial gaps δ_a to the radial gaps δ_r situated around flanges 6a of sleeves 6, along their perimeter, thus forming liquid rings being additional sealing barriers for the working medium.

Fig. 18 shows the hybrid seal with magnetic fluid which is especially applicable for high-speed shaft [30]. The seal consists of: flanged sleeve 3, axially polarized permanent magnets 5, 8, pole pieces 4 of rectangular cross-section, multi-edged pole pieces 7, and magnetic fluid 6. The flanged sleeve 3 is mounted on shaft 1 and has the flange 3a directed towards housing 2. Sealing projections are made on side surfaces of flange 3a of sleeve 3 and on inner cylindrical surfaces of multi-edged pole pieces 7. The flange 3a of sleeve 3 is mounted with some clearance in the chamber created between the rectangular cross-section pole pieces 4 separated by the permanent magnet 5 and fastened in housing 2. Moreover, pairs of multi-edged pole pieces 7 separated by permanent magnets 8 are mounted in housing 2, on both sides of rectangular cross-section pole pieces 4. When the shaft 1 is at rest or rotates with low speed (Fig. 18a), the magnetic fluid 6 is kept in the radial gaps δ_r of two outer magnetic fluid seals and in the axial gaps δ_a of the centrifugal seal, thus creating the sealing barriers. At high rotary speed of shaft 1 (Fig. 18b), the magnetic fluid 6 is moved from the axial gaps δ_a of the centrifugal seal to the annular gap situated between the outer perimeter of flange 3a of sleeve 3 and the permanent magnet 5, thus forming an additional sealing barrier for the working medium.

CONCLUDING REMARKS

The centrifugal magnetic fluid seals have important advantage over the conventional centrifugal seals, as they maintain very good sealing capacity at static, medium and high speeds of the shaft, with the increased seal lifetime, and minimum torque and static friction. These seals are particularly useful in cases when the angular shaft velocity varies and may decrease to nearly or exactly zero, such as in flywheel applications for instance.

Compared to the ordinary magnetic fluid seal, the centrifugal magnetic fluid seal (CMFS) has the following three distinguishing features:

1) at stationary conditions and at low shaft rotating speed, the force caused by the effect of magnetic attraction is used for sealing, while at higher speed, it is the centrifugal force which provides the effective sealing action;

2) the CMFS operates well even in the presence of large rotational vibration amplitudes;
3) the centrifugal magnetic fluid seals ensure completely hermetic sealing of the shaft at static, low- and high-speed modes, with the increased seal lifetime, and minimum torque and static friction.

REFERENCES

1. Y. Mitamura, S. Takahashi, S. Amari, E. Okamoto, S. Murabayashi, I. Nishimura, *A magnetic fluid seal for rotary blood pumps: effects of seal structure on long-term performance in liquid*, J Artif Organs 14 (2011) 23–30.

2. J. Lee, C. Ahn, J. Choi, J. Park, S. Song, K. Sun, *Development of magnetic bearing system for a new third-generation blood pump*, Artif Organs 35 (11) (2011) 1082–1094.

3. Huang W, Wang X. *Ferrofluids lubrication: a status report.* Lubric Sci 2016;28:3–26.

4. Wang Z, Hu Z, Huang W, Wang X. *Elastic support of magnetic fluids bearing.* J Phys Appl Phys 2017;50:435004.

5. Li D, Xu H, He X, Lan H. *Study on the magnetic fluid sealing for dry Roots pump*. J Magn Magn Mater 2005;289:419–22.

6. Y. Mitamura et al., "A hydrodynamically suspended, magnetically sealed mechanically noncontact axial flow blood pump: Design of a hydrodynamic bearing," Artif. Organs, 2007.

7. L. Matuszewski and Z. Szydło, "The application of magnetic fluids in sealing nodes designed for operation in difficult conditions and in machines used in sea environment," Polish Marit. Res., 2008.

8. T. Kanno, Y. Kouda, Y. Takeishi, T. Minagawa, and Y. Yamamoto, "Preparation of magnetic fluid having active-gas resistance and ultra-low vapor pressure for magnetic fluid vacuum seals," Tribol. Int., 1997.

9. T. Liu, Y. Cheng, and Z. Yang, "Design optimization of seal structure for sealing liquid by magnetic fluids," in Journal of Magnetism and Magnetic Materials, 2005.

10. Raj K., Stahl P., Bottenberg W.: *Magnetic fluid seals for special applications*, LE Transactions, vol.23, no 4, 1980.

11. Mizumoto M.,Imai M., Inoue H.: *Development of a centrifugal magnetic liquid seal for superconducting generators*, Proc. of the 9th Int. Conference on Fluid Sealing, Noordwijkerhout, Netherlands, 1981.

12. Wilcock D.F, Gay S.: *The role of magnetic fluid seal in modern machinery*, Lubrication Engineering, vol.40, no 6, 1984.

13. Ochoński W.: *Dynamic sealing with magnetic fluids*, Wear, vol. 130, no 1, 1989

14. Ochoński W.: *High technology of sealing solved by ferrofluids*, Industrial Lubrication and Tribology, vol. 45, no 4, 1993.

15. Ochoński W.: *New designs of magnetic fluid exclusion seals for rolling bearings*, Industrial Lubrication and Tribology, vol. 57, no 3, 2005.

16. Patent PL, Int.Cl. F16J15/43, no 202542, Centrifugal magnetic fluid shaft seal (in Polish).

17. Patent application PL, no P-420053 Centrifugal seal with magnetic fluid for high-speed shaft (in Polish).

18. Patent PL, Int.Cl. F16J15/453, no 174460, Ferromagnetic fluid centrifugal seal (in Polish).

19. Patent PL, Int.Cl.F16J15/53, no 202306, Centrifugal magnetic fluid seal for high -speed shaft (in Polish).

20. Patent USA, Int.Cl. F16J15/42, no 4455026, Vee-shaped magnetic/centrifugal seal and method of operation.

21. Patent USA, Int.Cl. F16J15/42, no 4200296, Ferrofluid centrifugal seal.

22. Patent PL, Int.Cl. F16J15/453, no 218345, Centrifugal seal with magnetic fluid (in Polish).

23. Patent PL, Int.Cl.F16J15/42, no 220279, Centrifugal seal with magnetic fluid (in Polish).

24. Patent application PL, no P-418800, Centrifugal seal with magnetic liquid for a high-speed shaft (in Polish).

25. Patent application PL, no P-423513, Centrifugal seal with magnetic fluid for rotating shaft (in Polish).

26. Patent PL, Int.Cl.F16J15-53, no 206282, Compact, centrifugal seal with magnetic fluid (in Polish).

27. Patent application PL, no P-419854, Hybrid protective seal with magnetic fluid for rotating bearing (in Polish).

28. Patent application PL, no P-418797, Feedthrough of high-speed shaft with centrifugal magnetic fluid seal (in Polish).

29. Patent PL, Int.Cl.F16J15/40, no 1`163174, Multistage ferromagnetic fluid seal (in Polish).

30. Patent application PL, no P-423713, Hybrid seal with magnetic fluid, especially for high-speed shaft (in Polish).

31. Y. Mitamura and C. A. Durst, "Miniature magnetic fluid seal working in liquid environments," *J. Magn. Magn. Mater.*, 2017.

32. M. Cong and H. Shi, "A study of magnetic fluid rotary seals for wafer handling robot," in 1*5th International Conference on Mechatronics and Machine Vision in Practice, M2VIP'08*, 2008.

33. D. Li, H. Xu, X. He, and H. Lan, "Theoretical and experimental study on the magnetic fluid seal of reciprocating shaft," in *Journal of Magnetism and Magnetic Materials*, 2005.

34. M. Szczech and W. Horak, "Tightness testing of rotary ferromagnetic fluid seal working in water environment," *Ind. Lubr. Tribol.*, 2015.

35. H. Urreta, G. Aguirre, P. Kuzhir, and L. N. Lopez de Lacalle, "Seals Based on Magnetic Fluids for High Precision Spindles of Machine Tools," *Int. J. Precis. Eng. Manuf.,* 2018.

36. Y. Mitamura, S. Arioka, D. Sakota, K. Sekine, and M. Azegami, "Application of a magnetic fluid seal to rotary blood pumps," *J. Phys. Condens.* Matter, 2008.

37. Y. Mitamura, T. Yano, W. Nakamura, and E. Okamoto, "A magnetic fluid seal for rotary blood pumps: Behaviors of magnetic fluids in a magnetic fluid sealwith a shield," *Magnetohydrodynamics*, 2013.

38. T. Dimond, R. D. Rockwell, P. N. Sheth, and P. E. Allaire, "A New Fluid Film Bearing Test Rig for Oil and Water Bearings," Proc. ASME Turbo Expo 2008 Power Land, Sea Air, 2008.

39. K. Sekine, Y. Mitamura, S. Murabayashi, I. Nishimura, R. Yozu, and D. W. Kim, "Development of a Magnetic Fluid Shaft Seal for an Axial-Flow Blood Pump," in *Artificial Organs*, 2003.

40. M. S. Krakov and I. V. Nikiforov, "Effect of diffusion of magnetic particles on the parameters of the magnetic fluid seal: A numerical simulation," *Magnetohydrodynamics*, 2014.

41. Y. Mitamura et al., "Sealing Performance of a Magnetic Fluid Seal for Rotary Blood Pumps," *Artif. Organs*, 2009.

42. S. Chen and D. Li, "Influence of particle size distribution of magnetic fluid on the resistance torque of magnetic fluid seal," *J. Magn*., 2017.

43. A. Radionov, A. Podoltsev, and A. Zahorulko, "Finite-element analysis of magnetic field and the flow of magnetic fluid in the core of magnetic-fluid seal for rotational shaft," in *Procedia Engineering,* 2012.

44. Y. Mizutani, H. Sawano, H. Yoshioka, and H. Shinno, "Magnetic fluid seal for linear motion system with gravity compensator," in *Procedia CIRP*, 2015.

45. M. S. Krakov and I. V. Nikiforov, "Regarding the influence of heating and the Soret effect on a magnetic fluid seal," *J. Magn. Magn. Mater.*, 2017.

46. Z. Meng, Z. Jibin, and H. Jianhui, "An analysis on the magnetic fluid seal capacity," *J. Magn. Magn. Mater.*, 2006.

47. J. Salwiński and W. Horak, "Measurement of Normal Force in Magnetorheological and Ferrofluid Lubricated Bearings," *Key Eng. Mater.*, 2011.

48. D. A. Bompos and P. G. Nikolakopoulos, "Experimental and Analytical Investigations of Dynamic Characteristics of Magnetorheological and Nanomagnetorheological Fluid Film Journal Bearing," *J. Vib. Acoust.*, 2016.

49. I. F. Santos, "On the future of controllable fluid film bearings," in *9th EDF/Pprime (LMS) Poitiers Workshop*, 2010.

50. S. E. Mushi, Z. Lin, and P. E. Allaire, "Design, construction, and modeling of a flexible rotor active magnetic bearing test rig," *IEEE/ASME Trans. Mechatronics*, 2012.

51. H. Montazeri, "Numerical analysis of hydrodynamic journal bearings lubricated with ferrofluid," *Proc. Inst. Mech. Eng. Part J J. Eng. Tribol.*, 2008.

52. D. A. Bompos and P. G. Nikolakopoulos, "Journal Bearing Stiffness and Damping Coefficients Using Nanomagnetorheological Fluids and Stability Analysis," *J. Tribol.*, 2014.

53. Z. Huang, J. Fang, X. Liu, and B. Han, "Loss Calculation and Thermal Analysis of Rotors Supported by Active Magnetic Bearings for High-Speed Permanent-Magnet Electrical Machines," *IEEE Trans. Ind. Electron.*, 2016.

54. M. L. Chan et al., "Design and characterization of MEMS micromotor supported on low friction liquid bearing," *Sensors Actuators, A Phys.*, 2012.

55. X. Song and H. G. Wood, "Application of CFX to Implantable Rotary Blood Pumps Suspended by Magnetic Bearings," in *International ANSYS Conference*, 2004.

56. D. A. Bompos and P. G. Nikolakopoulos, "CFD simulation of magnetorheological fluid journal bearings," *Simul. Model. Pract. Theory*, 2011.

57. S. Jahanmir et al., "Design of a small centrifugal blood pump with magnetic bearings," *Artif. Organs*, 2009.

58. W. Ochoński, "Sliding bearings lubricated with magnetic fluids," *Industrial Lubrication and Tribology*. 2007.

59. T. M. Lim, S. Cheng, and L. P. Chua, "Parameter estimation and actuator characteristics of hybrid magnetic bearings for axial flow blood pump applications," *Artificial Organs*. 2009.

CONTACT WITH THE AUTHOR

Leszek Matuszewski
e-mail: leszekma@pg.gda.pl

Gdansk University of Technology
Narutowicza 11/12
80–233 Gdansk
Poland

sciendo

POLISH MARITIME RESEARCH 2 (102) 2019 Vol. 26; pp. 47-54
10.2478/pomr-2019-0024

STRUCTURAL RELIABILITY ASSESSMENT OF CORRODED TANKER SHIP BASED ON EXPERIMENTALLY ESTIMATED ULTIMATE STRENGTH

Krzysztof Woloszyk[1]
Yordan Garbatov[2]
[1] Faculty of Ocean Engineering and Ship Technology, Gdansk University of Technology, Poland
[2] Centre for Marine Technology and Engineering (CENTEC), Instituto Superior Técnico, Universidade de Lisboa, Portugal

ABSTRACT

This work deals with the reliability assessment of a tanker ship hull structure subjected to a vertical bending moment and corrosion degradation. The progressive collapse and ultimate load carrying capacity are estimated based on experimentally tested scaled box-shaped-specimens. The translation of the strength estimate of the scaled specimen to the real tanker ship hull structure is performed based on the dimensional theory developing a step-wise linear stress-strain relationship. The load-carrying capacity is considered as a stochastic variable, and the uncertainties resulted from the scaled-specimen to the real-structure strength translation, and the subjected load of the real ship are also accounted for. A sensitivity analysis concerning the stochastic variables, included in the ultimate limit state function is performed. The partial safety factors, in the case of a scaled specimen and real structure, are also identified, and conclusions are derived.

Keywords: ship structures; reliability assessment; corrosion; ultimate strength; tanker ship

INTRODUCTION

Many studies have been dedicated to the ultimate strength of ship structures in the last decades. The study of the ultimate strength of ship structures was performed by Caldwell in 1965 [1], where a simplified direct formulation taking into account material yield and buckling was introduced. Alternatively, in 1977, the incremental-iterative approach was developed by Smith [2], considering the longitudinal elasto-plastic response of individual structural components.

Nowadays both improved, direct and progressive approaches are part of the IACS Common Structural Rules [3]. The progressive collapse method discretises the ship cross section into appropriate elements, usually stiffened plates (stiffener with attached plating) and rigid corners. The structural behaviour of each component is predicted in the form of a load-shortening curve. Next, the incremental procedure is introduced to obtain the moment-curvature response of the ship hull subjected to a combined horizontal and vertical bending.

The progressive collapse method has been widely employed to predict the load-carrying capacity of intact [4] and damaged [5] ship sections. However, it was discovered that non-uniform corrosion degradation is the factor that can significantly affect the load carrying capacity [6–8] mainly due to the cross-sectional area reduction and mechanical properties changes [9].

Paik et al. [10] investigated the influence of pitting corrosion on the ultimate strength using the finite element method. The reduction observed was significant, the smallest

cross-sectional area governs the ultimate strength of a plate under axial compressive load.

Saad-Eldeen et al. [11] tested experimentally three corroded box girders subjected to pure vertical bending and studied the initial and post-collapse plate deflections. As a conclusion, crossing specific slenderness ratio the initial shape governs the post-collapse shape. The analysis was furtherly developed into the ultimate strength assessment of the tanker ship with the use of the dimensional theory [12].

The influence of a random corrosion thickness distribution on the ultimate strength of rectangular steel plates was also investigated by Silva et al. [13]. Applying the Monte Carlo Simulation, the plate thickness distribution was generated considering the degree of degradation. Furtherly, they used to perform a reliability analysis [14].

The reduction of mechanical properties of corroded steel small-specimens was investigated by Garbatov et al. [9]. Tensile strength tests have been performed for various corrosion degradation levels. The observed reduction of mechanical properties (modulus of elasticity, yield stress, tensile strength and others) was significant. Garbatov et al. [15] also investigated numerically and experimentally the ultimate strength of stiffened plates with different corrosion degradation levels. The ultimate strength reduction was significant. The experimental results were furtherly compared with the Finite Element analysis by Woloszyk et al. [16].

To determine the uncertainty level in the ultimate strength assessment due to various governing parameters, reliability methods are employed. One of the first attempts to employ probability-based methods in the field of ship structural design was by Mansour [17, 18] and Mansour & Faulkner [19]. The first applications dealt with the safety of ship hulls subjected to a wave-induced bending load.

The methodologies for single structural components were developed too. An oil tanker hull girder was analysed by Saydam et al. [20] considering different speeds, headings and sea states. The reliability index was determined for the intact and six damaged hull cases, where the limit state function was based on the hull girder ultimate strength at a midship section.

Zayed et al. [21] performed a reliability analysis of ship hulls subjected to corrosion and maintenance, where ship loading uncertainties, random variables and inspection events were considered. The advanced uncertainty analysis was performed by Teixeira et al. [22], where the approach to assess the ultimate strength of plates considering the random initial distortions, material and geometrical properties and random corrosion degradation was presented.

The paper deals with the reliability assessment of corroded tanker ship subjected to a compressive load employing the result of tested scaled small box specimens. The target reliability function considers the ultimate hull girder capacity, which is derived based on the experimental and numerical estimates. A sensitivity analysis concerning the stochastic variables, included in the ultimate limit state function is also performed.

TIME-DEPENDENT ULTIMATE STRENGTH

Based on the experimental and numerical results [15,16] the ultimate time-dependent strength of stiffened plate is derived. The specimens analysed in [15] are taken from the box girder subjected to the incrementally increasing bending moment [23] with depth, length and breadth of 1,400 mm, 800 mm and 600 mm respectively. Using the dimensional theory, the box girder can represent the midship section of the single-skin hull tanker with a length, breadth and depth of 108 m, 16 m and 12 m respectively and specimens correspond to the stiffened plate of the deck.

The analysis of the similarity between the model and real structure concerning the ship hull ultimate capacity was conducted in [12], and more information about the dimensional theory may be found in [24,25]. The scaling factors are as follows:

– the linear dimensions:

$$\frac{x}{x'} = \frac{y}{y'} = \frac{z}{z'} = \frac{l}{l'} = C_l \tag{1}$$

– stresses:

$$\frac{\sigma_x}{\sigma_x'} = \frac{\sigma_y}{\sigma_y'} = \frac{\tau_{xy}}{\tau_{xy}'} = \frac{\sigma}{\sigma'} = C_\sigma \tag{2}$$

– strains:

$$\frac{\varepsilon_x}{\varepsilon_x'} = \frac{\varepsilon_y}{\varepsilon_y'} = \frac{\gamma_{xy}}{\gamma_{xy}'} = \frac{\varepsilon}{\varepsilon'} = C_\varepsilon \tag{3}$$

– displacements:

$$\frac{u}{u'} = \frac{v}{v'} = \frac{w}{w'} = C_u \tag{4}$$

where l, σ, ε and u are the dimesnsions of real structure and and l', σ', ε' and u' are for the model respectively. The thickness term need to be defined independently of the plane stress terms:

$$C_t = \frac{t}{t'} \tag{5}$$

The relations between the ship hull (real structure) and the model are as follows:

– length

$$C_l = \frac{L_{structure}}{L_{model}} = \frac{B_{structure}}{B_{model}} = \frac{D_{structure}}{D_{model}} = 20 \tag{6}$$

– thickness

$$C_t = \frac{t_{stucture}}{t_{model}} = 3 \quad (7)$$

– subjected force

$$C_p = \frac{P_{real}}{P_{model}} = 60 \quad (8)$$

– bending moment

$$C_m = \frac{M_{structure}}{M_{model}} = C_p C_l = 1{,}200 \quad (9)$$

resulting in the same stresses in the model and real structure:

$$\sigma_{structure} = \sigma_{model} \frac{C_m}{C_l^2 C_t} = \sigma_{model} \quad (10)$$

Based on that, the ultimate stress is the same for the model and real structure.

Since the thickness scale is 3 and it is assumed that the corrosion depth follows the same time dependency in real structure and specimen, the degree of degradation (DoD) of the tanker ship model is:

$$t_{corroded} = t'_{corroded} \quad (11)$$

$$t = t_{netto} + t_{corroded} \quad (12)$$

$$DoD = \frac{t_{corroded}}{t} = \frac{t_{corroded}}{C_t t'} = \frac{DoD'}{C_t} \quad (13)$$

Since the stress scale is 1, the DoD-dependent ultimate-strength of the tanker ship is defined as:

$$\sigma_U(DoD) = \sigma_U\left(\frac{DoD'}{C_t}\right) = \sigma_U\left(\frac{DoD'}{3}\right) \quad (14)$$

The degree of degradation of the tanker ship plate is a function of the time, which can be derived from the corrosion degradation model as presented in [26]. The corrosion depth versus time is shown in Figure 1, where the coating life is not considered.

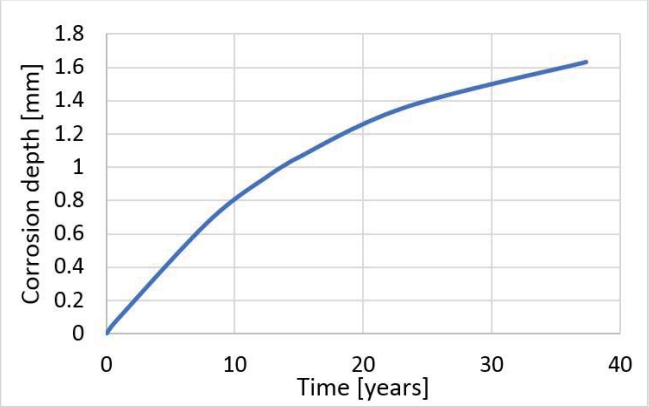

Fig. 1. Corrosion depth versus time

Based on that, the ultimate time-dependent strength of both model and tanker ship can be derived. The ultimate time-dependent strength of the tanker stiffened plate based on the experimental and numerical investigations is presented in Figure 2.

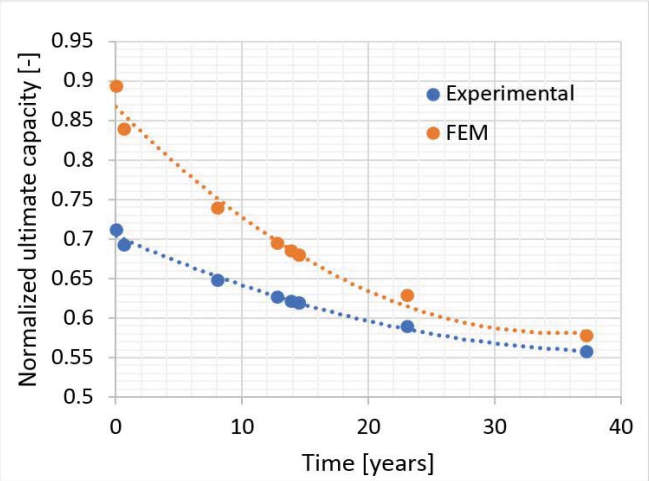

Fig. 2. Time-dependent ultimate strength, experimental and numerical results

For the current analysis, the assumption is made that the ultimate strength is equal to initial member collapse strength (the collapse of the weakest stiffened plate in the cross-section which initiates the progressive collapse). However, after the collapse of the first stiffened plate, the hull girder section still has some capacity [27] making the current assumption conservative one.

Bottom and deck of the analysed tanker ship are made from high tensile steel with a yield stress of 315 MPa, and the Young modulus is 206 GPa.

STRENGTH ASSESSMENT

Based on the dimensional theory, the section modulus at the deck and bottom of the tanker ship is estimated using small-scale box girder specimens as presented in [12]. The deck section modulus is $Z_d = 3.64\ m^3$ and the bottom section modulus is $Z_d = 3.32\ m^3$.

The still water and wave-induced bending moments are estimated from the Common Structural Rules [3] in hogging and sagging condition respectively as follows:

$$M_{sw,h} = 156{,}043\ kNm \tag{15}$$

$$M_{sw,s} = -121{,}714\ kNm \tag{16}$$

$$M_{wv,h} = 246{,}686\ kNm \tag{17}$$

$$M_{wv,s} = -259{,}537\ kNm \tag{18}$$

In the Common Structural Rules [3], the ultimate strength limit state is formulated as:

$$\gamma_{sw} M_{sw} + \gamma_{wv} M_{wv} \leq \frac{M_U}{\gamma_R} \tag{19}$$

where M_u is the hull girder ultimate bending capacity and γ_{sw}, γ_{wv}, γ_R are the partial safety factors.

The ultimate capacity is estimated based on the experimental or numerical results and dimensional theory as:

$$M_u = \left(\frac{\sigma_U}{\sigma_Y}\right)_{experimental/FEM} Z_{d/b} Re \tag{20}$$

where $(\sigma_U/\sigma_Y)_{experimental/FEM}$ is the normalized ultimate capacity based on the experimental or numerical results, $Z_{d/b}$ is the section modulus of deck or bottom and *Re* is the yield strength of material.

RELIABILITY ANALYSIS

To analyse the impact of the uncertainty in the ultimate strength assessment due to various governing parameters, the FORM [28] method is used here employing own algorithm.

The term formulated deterministically in Eqn (19) can be transformed into a limit state function:

$$g = \widetilde{x_U}\widetilde{M_U} - \widetilde{x_{sw}}\widetilde{M_{sw}} - \widetilde{x_w}\widetilde{x_s}\widetilde{M_{wv}} \tag{21}$$

where $\widetilde{M_U}, \widetilde{M_{sw}}, \widetilde{M_{wv}}$ are the bending moments described as random variables, $\widetilde{x_U}$ is the model uncertainty related to the ultimate strength, $\widetilde{x_{sw}}$ is the uncertainty in the model of predicting the still water bending moment, $\widetilde{x_w}$ is the uncertainty in the wave-induced bending moment due to the linear sea keeping analysis and $\widetilde{x_s}$ takes into account nonlinearities in the sagging loading condition.

The statistical descriptors of the uncertainty coefficients presented in Eqn (21) are assumed to follow the Normal distribution function [29,30]:

$$\widetilde{x_U} \sim N\{1.1; 0.1\} \tag{22}$$

$$\widetilde{x_{sw}} \sim N\{1.0; 0.1\} \tag{23}$$

$$\widetilde{x_w} \sim N\{1.0; 0.1\} \tag{24}$$

$$\widetilde{x_s} \sim N\{1.0; 0.1\} \tag{25}$$

The First Order Reliability Method, FORM [28] is used to estimate the reliability index of the ultimate limit state. Since the ultimate capacity depends on time – the reliability index isl also time-dependent.

The still water bending moment can be fitted to the Normal distribution as stipulated in [31] where the statistical descriptors are defined by regression equations based on about 2000 data points as a function of the length and the dead-weight ratio (W = DWT/Full Load). The estimated coefficients are shown in Table 1.

Tab. 1. Statistical descriptors of Still water bending moment [31]

	$\mathbf{a_o}$	$\mathbf{a_1}$	$\mathbf{a_2}$
$Mean(M_{sw,max})=a_o+a_1.W+a_2.L$	114.7	-105.6	-0.154
$StDev(M_{sw,max})=a_o+a_1.W+a_2.L$	17.4	-7	0.035

The mean value and standard deviation of still water bending moment are estimated as:

$$Mean(M_{sw}) = \frac{Mean(M_{sw,max})M_{sw,CSR}}{100} \tag{26}$$

$$StDev(M_{sw}) = \frac{StDev(M_{sw,max})M_{sw,CSR}}{100} \tag{27}$$

where the $M_{sw,CSR}$ are the still water bending moments calculated with the formulas provided in Common Structural Rules [3].

The dead-weight ratio of the analysed tanker ship is 0.82 in the full-load condition, 0.61 in the partial load condition and 0.41 in the ballast condition.

The still water bending moments for the analysed tanker ship under different loading conditions are shown in Table 2.

As can be noticed, the positive mean value indicates that the maximum bending moment is in a hogging loading condition and it has to be pointed out that the analysed ship is a single-hull oil tanker. Due to that, the hogging condition is furtherly analysed.

Tab. 2. Still water bending moments

Loading condition	$Mean(M_{sw})$	$StDev(M_{sw})$
Full-load	17,908	24,093
Partial	52,512	26,387
Ballast	85,468	28,572

The distribution of the extreme values of the wave-induced bending moment at a random point of time, over a specified time period can be represented as a Gumbel distribution as proposed by Guedes Soares et al. [32], considering that the wave-induced bending moment given by the Common Structural Rules [3] may be modelled as a Weibull distribution with a probability of exceedance of 10^{-8}.

The Gumbel distribution, for the extreme values of the vertical wave-induced bending moment, over the reference period T is derived based on the shape, h and scale, q factors of the Weibull distribution function as [32]:

$$\alpha_m = q(\ln(n))^h \tag{28}$$

$$\beta_m = \frac{q}{h}(\ln(n))^{\frac{1-h}{h}} \tag{29}$$

where α_m and β_m are the parameters of the Gumbel distribution, n is the mean number of load cycles, expected over the reference time period T_r for a given mean value period T_w. It is assumed that $T_w = 8$ *sec*. and T_w is equal to 1 year. The number of load cycles n is calculated as:

$$n = \frac{p_i \cdot T_r \cdot 365 \cdot 24 \cdot 3600}{T_w} \tag{30}$$

where p_i is the partial time in which the ship is in seagoning conditons.

The partial time factors and extreme values of the vertical wave-induced bending moment in hogging are shown in Table 3.

Tab. 3. Statistical descriptors wave-induced bending moment $\boldsymbol{M_{wv,h}}$

Loading condition	p_i[–]	$\alpha_m(M_{wv,h})$	$\beta_m(M_{wv,h})$
Full-load	0.4	341,542	9,246
Partial	0.1	303,302	9,378
Ballast	0.4	341,542	9,246
Harbour	0.1	–	–

The CoV of the ultimate capacity is based on the previous results [15,16] and is assumed as 0.0208 for the experimental one and 0.0363 for the FEM estimates. Additionally, due to the differences between experimental and FEM results the bias factor is introduced:

$$x_{FEM} = \frac{\sigma_{U,FEM}}{\sigma_{U,exp}} \tag{31}$$

The bias factor is modelled as a random variable following the Normal probability function, $\widetilde{x_{FEM}} \sim N\{0.893; 0.052\}$, since both experimentally and numerically obtained capacities are fitted to the Normal probability function. The x_{FEM} is assumed constant for different corrosion degradation levels and the mean value of the distribution is calculated as the mean of the fractions $\sigma_{U,FEM}/\sigma_{U,exp}$ for different time of exploitation. The standard deviation is calculated as the square root of the sum of squares of differences between the mean value and particular fractions. The limit state function for the ultimate capacity based on the FEM results is:

$$g = \widetilde{x_{FEM}}\widetilde{x_U}\widetilde{M_U} - \widetilde{x_{sw}}\widetilde{M_{sw}} - \widetilde{x_w}\widetilde{x_s}\widetilde{M_{wv}} \tag{32}$$

All random variables are considered here as non-correlated ones. When the reliability analysis is performed, the estimated reliability index needs to be compared with the target one. The target level is related to the failure cause and according to DnV [33] is equal to $\beta = 3.09$ ($P_f = 10^{-3}$) for the less serious and $\beta = 3.71$ ($P_f = 10^{-4}$) for serious consequences of failure. The targed reliability level is considered here as $\beta_{target} = 3.71$.

The required Beta index is based on the sum of probabilities of failure for different loading conditions:

$$\beta = -\Phi^{-1}(\Sigma P_{fi}) \tag{33}$$

RESULTS AND DISCUSSION

For the analysed tanker ship, a more severe loading is the hogging case, due to the contribution of the still water bending moment comparing to the sagging condition. The calculations performed for sagging condition showed that the probability of failure is significantly smaller compared to the hogging condition.

The reliability safety indices for different load cases and the total Beta index are shown in Table 4.

Tab. 4. Reliability safety indices for different load cases, experiment

Time (years)	Load Beta index [-]			Beta index [-]
	Full load	Ballast load	Partial load	
0.0	5.201	4.315	5.268	4.31
0.7	5.041	4.141	5.108	4.14
8.0	4.644	3.715	4.714	3.71
12.8	4.424	3.481	4.496	3.47

Time (years)	Load Beta index [-]			Beta index [-]
	Full load	Ballast load	Partial load	
13.9	4.377	3.431	4.449	3.42
14.5	4.353	3.406	4.425	3.40
23.1	4.042	3.077	4.115	3.06
37.3	3.682	2.700	3.756	2.68

The results of the reliability safety index versus time for the ultimate capacity based on the experimental results are presented in Figure 3.

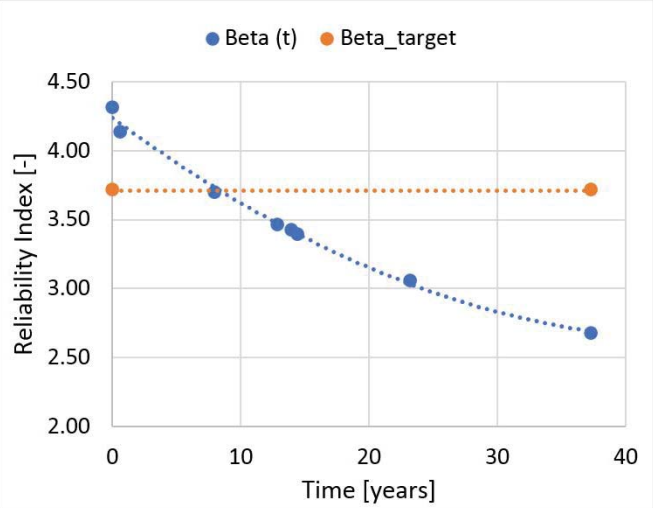

Fig. 3. Reliability safety index of analysed tanker ship, experimental results

As it can be noticed, after eight years of exploitation, without accounting for the coating life, the required reliability index is not satisfied. After this time, some maintenance action needs to be done. The most critical condition is the ballast one, and as it can be noticed, full and partial load conditions have almost no influence on the resulting reliability safety index.

Figure 4 shows the sensitivity analysis concerning the influence of different random variables. As it can be noticed, the most influencing variable is the model uncertainty of the ultimate capacity.

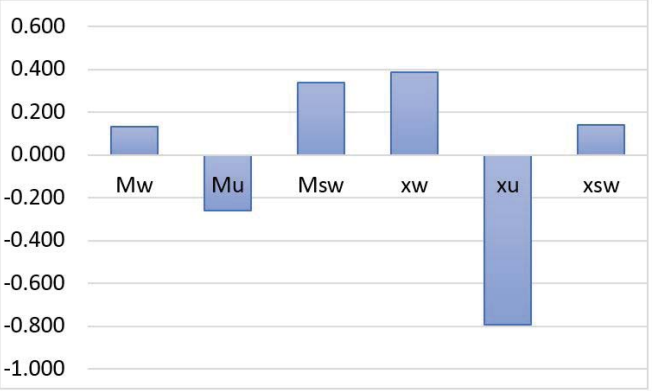

Fig. 4. Sensitivity analysis

The reliability safety indices obtained based on the FEM is shown in Table 5. Very similarly to the experimental results, the most critical condition which governs the resulting Beta index is the ballast one.

Tab. 5. Reliability safety indices for different load cases, FEM

Time (years)	Load Beta index [-]			Beta index [-]
	Full load	Ballast load	Partial load	
0.0	5.639	4.788	5.682	4.784
0.7	5.316	4.442	5.362	4.437
8.0	4.595	3.675	4.653	3.667
12.8	4.231	3.292	4.298	3.281
13.9	4.155	3.214	4.225	3.202
14.5	4.117	3.174	4.188	3.161
23.1	3.638	2.674	3.727	2.654
37.3	3.125	2.137	3.199	2.100

The results of the Beta index versus time for the ultimate capacity based on the FEM results are presented in Figure 5.

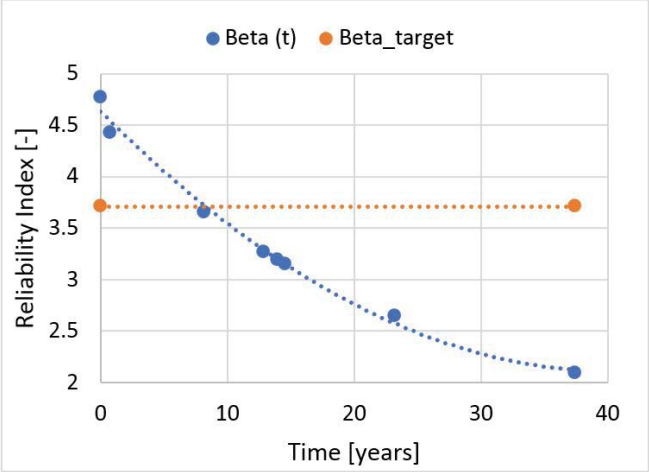

Fig. 5. Reliability safety index of analysed tanker ship, numerical results

The service time, where the Beta index crosses the target value is very similar to the results obtained based on the experiment, and it is about eight years.

Figure 6 shows the sensitivity analysis concerning reliability based on the FEM. Similarly, to the experimental data, the most influencing parameters are the model uncertainty of the ultimate capacity and FEM calculations.

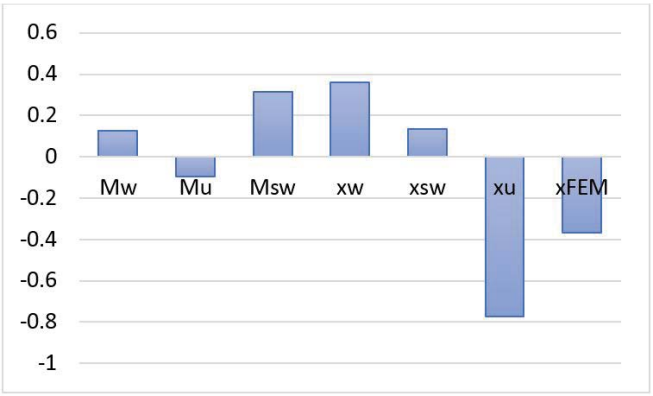

Fig. 6. Sensitivity analysis

The partial safety factors for the initial value of the plate thickness are presented in Table 6.

Tab. 6. Partial safety factors

Partial Safety Factors	FEM	Experiment
γ_{Mw}	1.10	1.09
γ_{Msw}	1.67	1.29
γ_{Mu}	0.97	0.98

CONCLUSIONS

The objective of this work was to perform a structural reliability assessment based on the experimentally and numerically estimated ultimate strength.

The results show that it is possible to estimate the ultimate strength of the ship cross section based on the experimental results and dimensional theory. Additional modelling uncertainties need to be taken into account for proper estimation of reliability safety index considering the FE model. The reliability safety index was calculated as a function of the time, and the assumed target reliability safety index was crossed after around eight years. The study revealed that the reliability analysis conducted in hogging condition, considering only the ballast load case for the present oil tanker, would give satisfying results.

The presented methodology is flexible and can be furtherly used in more complex systems.

REFERENCES

1. Caldwell J. Ultimate longitudinal strength. Trans RINA 1965.

2. Smith S. Influence of Local Compressive Failure on Ultimate Longitudinal Strength of a Ship's Hull. Proc Int Sym Pract Des Shipbuild 1977:73–9.

3. International Association of Classification Societies. Common Structural Rules (BC & OT). 2018.

4. Gordo JM, Guedes Soares C. Approximate method to evaluate the hull girder collapse strength. Mar Struct 1996;9:449–70.

5. Tekgoz M, Garbatov Y, Guedes Soares C. Strength assessment of an intact and damaged container ship subjected to asymmetrical bending loadings. Mar Struct 2018;58:172–98.

6. Melchers RE. Development of new applied models for steel corrosion in marine applications including shipping. Ships Offshore Struct 2008;3:135–44.

7. Guedes Soares C, Garbatov Y, Zayed A, Wang G. Corrosion wastage model for ship crude oil tanks. Corros Sci 2008;50:3095–106.

8. Bai Y, Jin W-L. Reassessment of Jacket Structure. Mar. Struct. Des., Elsevier; 2016, p. 875–89.

9. Garbatov Y, Guedes Soares C, Parunov J, Kodvanj J. Tensile strength assessment of corroded small scale specimens. Corros Sci 2014;85:296–303.

10. Paik JK, Lee JM, Ko J. Ultimate shear strength of plate elements with pit corrosion wastage. Thin-Walled Struct 2004;42:1161–76.

11. Saad-Eldeen S, Garbatov Y, Guedes Soares C. Analysis of plate deflections during ultimate strength experiments of corroded box girders. Thin-Walled Struct 2012;54:164–76.

12. Garbatov Y, Saad-Eldeen S, Guedes Soares C. Hull girder ultimate strength assessment based on experimental results and the dimensional theory. Eng Struct 2015;100:742–50.

13. Silva JE, Garbatov Y, Guedes Soares C. Ultimate strength assessment of rectangular steel plates subjected to a random localised corrosion degradation. Eng Struct 2013;52:295–305.

14. Silva JE, Garbatov Y, Guedes Soares C. Reliability assessment of a steel plate subjected to distributed and localized corrosion wastage. Eng Struct 2014;59:13–20.

15. Garbatov Y, Tekgoz M, Guedes Soares C. Experimental and numerical strength assessment of stiffened plates subjected to severe non-uniform corrosion degradation and compressive load. Ships Offshore Struct 2017;12:461–73.

16. Woloszyk K, Kahsin M, Garbatov Y. Numerical assessment of ultimate strength of severe corroded stiffened plates. Eng Struct 2018;168:346–54.

17. Mansour A. Methods of computing the probability of failure under extreme values of bending moment. J Sh Res 1972.

18. Mansour AE. Probabilistic design concepts in ship structural safety and reliability. Trans SNAME 1972;80:64–97.

19. Mansour AE, Faulkner D. On applying the statistical approach to extreme sea loads and ship hull strength. Trans RINA 1972;114:273–314.

20. Saydam D, Frangopol DM. Performance assessment of damaged ship hulls. Ocean Eng 2013;68:65–76.

21. Zayed A, Garbatov Y, Guedes Soares C. Reliability of ship hulls subjected to corrosion and maintenance. Struct Saf 2013;43:1–11.

22. Teixeira AP, Ivanov LD, Guedes Soares C. Assessment of characteristic values of the ultimate strength of corroded steel plates with initial imperfections. Eng Struct 2013;56:517–27.

23. Saad-Eldeen S, Garbatov Y, Guedes Soares C. Experimental assessment of the ultimate strength of a box girder subjected to severe corrosion. Mar Struct 2011;24:338–57.

24. Buckingham E. Dimensional analysis. Phys Rev 1914;4(345):12–23.

25. Harris HG, Sabnis GM. Structural modeling and experimental techniques. CRC Press; 1999.

26. Garbatov Y, Guedes Soares C, Wang G. Nonlinear Time Dependent Corrosion Wastage of Deck Plates of Ballast and Cargo Tanks of Tankers. J Offshore Mech Arct Eng 2006;129:48–55.

27. Yao T, Fujikubo M. Buckling and ultimate strength of ship and ship-like floating structures. 2016.

28. Hasofer AM, Lind NC. Exact and Invariant Second-Moment Code Format. J Eng Mech Div 1974;100:111–21.

29. Guedes Soares C, Teixeira A. Structural reliability of two bulk carrier designs. Mar Struct 2000;13:107–28.

30. Garbatov Y, Sisci F, Ventura M. Risk-based framework for ship and structural design accounting for maintenance planning. Ocean Eng 2018;166:12–25.

31. Guedes Soares C, Moan T. Statistical analysis of stillwater load effects in ship structures. Soc Nav Archit Mar Eng 1988;96.

32. Guedes Soares, C., Dogliani, M., Ostergaard, C., Parmentier G, & Pedersen PT. Reliability Based Ship Structural Design. Trans Soc Nav Archit Mar Eng 1996;104:359–89.

33. DnV. Structural Reliability Analysis of Marine Structures. Classif Notes No 306 1992.

CONTACT WITH THE AUTHORS

Krzysztof Woloszyk
e-mail: krzwolos@pg.edu.pl

Gdansk University of Technology
Faculty of Ocean Engineering and Ship Technology
Narutowicza 11/12, 80-233 Gdańsk
Poland

Yordan Garbatov
e-mail: yordan.garbatov@tecnico.ulisboa.pt

Centre for Marine Technology and Engineering (CENTEC)
Instituto Superior Técnico
Universidade de Lisboa
Avenida Rovisco Pais, 1049-001 Lisbon
Portugal

sciendo

POLISH MARITIME RESEARCH 2 (102) 2019 Vol. 26; pp. 55-67
10.2478/pomr-2019-0025

METHOD OF EMERGENCY COLLISION AVOIDANCE FOR UNMANNED SURFACE VEHICLE (USV) BASED ON MOTION ABILITY DATABASE

Lifei Song[1, 2]
Houjing Chen[1, 3]
Wenhao Xiong[2]
Zaopeng Dong[2]
Puxiu Mao[4]
Zuquan Xiang[2]
Kai Hu[3]

[1] Key Laboratory of High Performance Ship Technology (Wuhan University of Technology), Ministry of Education, Wuhan, China
[2] School of Transportation, Wuhan University of Technology, China
[3] China Ship Development and Design Center, Wuhan, China
[4] University of Southern California, Los Angeles, USA

ABSTRACT

The unmanned surface vehicles (USV) are required to perform a dynamic obstacle avoidance during fulfilling a task. This is essential for USV safety in case of an emergency and such action has been proved to be difficult. However, little research has been done in this area. This study proposes an emergency collision avoidance algorithm for unmanned surface vehicles (USVs) based on a motion ability database. The algorithm is aimed to address the inconsistency of the existing algorithm. It is proposed to avoid collision in emergency situations by sharp turning and treating the collision avoidance process as a part of the turning movement of USV. In addition, the rolling safety and effect of speed reduction during the collision avoidance process are considered. First, a USV motion ability database is established by numerical simulation. The database includes maximum rolling angle, velocity vector, position scalar, and steering time data during the turning process. In emergency collision avoidance planning, the expected steering angle is obtained based on the International Regulations for Preventing Collisions at Sea (COLREGs), and the solution space, with initial velocity and rudder angle taken as independent variables, is determined by combining the steering time and rolling angle data. On the basis of this solution space, the objective function is solved by the particle swarm optimization (PSO) algorithm, and the optimal initial velocity and rudder angle are obtained. The position data corresponding to this solution is the emergency collision avoidance trajectory. Then, the collision avoidance parameters were calculated based on the afore mentioned model of motion. With the use of MATLAB and Unity software, a semi-physical simulation platform was established to perform the avoidance simulation experiment under emergency situation. Results show the validity of the algorithm. Hence results of this research can be useful for performing intelligent collision avoidance operations of USV and other autonomous ships

Keywords: Unmanned surface vehicle; emergency collision avoidance; velocity obstacle method; motion ability

INTRODUCTION

An unmanned surface vehicle (USV) is a ship that navigates on water in an autonomous manner. Its autonomous collision avoidance capability is the basis for safe navigation and undertaking maritime tasks. Autonomous obstacle avoidance skill is the foundation for executing tasks and also the reflection of its intelligence [1, 2].

The International Maritime Organization (IMO) approved the International Regulations for Preventing Collisions at Sea (COLREGS) in 1972 [3]. The regulations specify certain rules of navigation for ships at risk of collision. During collision avoidance action USVs should follow the regulations and assume that the obstacles (obstacle boats in this article) comply with the regulations, which has become the consensus for research on intelligent collision avoidance [4].

On this premise, various algorithms have been proposed in many studies. The artificial potential field [8] is one of them. The path planned by this method is smooth and safe, but the method also falls into the local optimal solution. In most

studies the local optimal solution are avoided through manual interference and correction, but the effect is not good when multiple obstacles are present [9–10].

Evolutionary algorithms [5] include several methods which are all-population optimization algorithms taking individuals as optional paths. The optimization of the collision avoidance paths is carried out along with the evolution of the population. The above-mentioned population evolution methods generally establish the path model in two ways. As shown in Fig. 2, the first one is 2-D grid maps [6, 7] where the obstacle space and free space are determined by coordinates, and the other one consists in establishing a path model according to the individual size of the population. The map of the path model can be further divided into that Cartesian coordinates-based and that polar coordinates-based.

Regardless of which of the above coordinate systems is used, each alternative path is represented as an individual in the population. The length and smoothness of the path polyline is used as a measure of the fitness function during the population optimization. The alternative paths are evolved by internal operators such as selection, crossover and mutation.

However, the population evolution methods have three disadvantages. First, the methods require a large amount of data and lead to a high computation cost; furthermore, the evolutionary process of individuals lacks regularity when they are represented by paths, which makes it difficult to find problems when unreasonable number of iterations occur. Second, in the case of dynamic collision avoidance, the continuous motion of obstacles makes the environmental information varying in time, but as any change is not considered in these methods a low intelligence in collision avoidance actions is produced. Third, the motion of multiple obstacles is represented simply by the change in 2D grid coordinates, hence the comprehensive impact of obstacles on collision avoidance process cannot be included, which leads to unsatisfactory results in emergency dynamic avoidance situation.

The velocity obstacle (VO) approach was first introduced in the robotics field [11]. The VO method forms a cone-shaped space on the obstacle, and ensures that the USV never collides with the obstacle if it remains outside the space. Extensive research on the velocity obstacle approach has been conducted in collision avoidance planning for unmanned surface vehicles [12–14]. The fast computing capability of the algorithm ensures a quick reaction of robots. However, for a USV which moves at a high speed, the avoidance effect against dynamic obstacles is difficult to ensure in complex circumstances. Thus, it is mainly used under relatively safe conditions. Neural networks [15] have also been widely studied in collision avoidance issues. An algorithm which uses a neural network exhibits fast convergence and good adaptability, but it considers all inference processes as numerical calculations, thereby leading to poor generalization and falling into local optima, especially under the condition of dynamic collision avoidance of multiple obstacles, where the feasible space is narrow and the environment changes in real time, and a relatively high accuracy and real-time performance in collision avoidance process is required. Therefore, the application of this method is limited in practical maritime navigation.

Moreover, existing research focuses mainly on situations in which the movements of obstacles do not pose an extreme threat to the USV. Therefore, when the obstacles do not follow the COLREGS and lead to an urgent situation, the afore mentioned algorithms may fail.

In emergency case of collision avoidance, the above mentioned algorithms are rarely used mainly due to the following reasons [16–17]:

(1) The collision avoidance strategy is non-continuous. In the case of dynamic collision avoidance, the continuous motion of obstacles makes the environmental information varying in time, but as any change is not considered in these methods, a low intelligence in collision avoidance actions is produced. The existing collision-avoidance algorithms, such as the VO algorithm, adjust only the motion based on the information at current time, that leads to a lack of prediction about the movement of both the USV and the obstacles, thereby also to an incoherence of the algorithm in obstacle avoidance problems and making the USV to move along a zigzag trajectory. In addition, the course of a USV must be sharply adjusted in an emergency situation, which may lead to a lack of a solution complying with the principle of the VO algorithm.

(2) The relationship between velocity and position is nonlinear. Fig. 1 shows the relationship between instantaneous velocity and position. The green arrow in the figure stands for the velocity vector and the blue arrow for the actual position vector. In non-emergency collision avoidance situation, as shown in Fig. 1(a) and given by Eq. (1), position and velocity have a linear relationship. The above mentioned algorithms estimate mainly the collision risk based on the following relationship:

$$\boldsymbol{p}(t) = \boldsymbol{p}(t-1) + \boldsymbol{v}(t) \tag{1}$$

where, $\boldsymbol{p}(t)$ is the position vector at time t, $\boldsymbol{v}(t)$ is the velocity vector at time t.
In the case of large-range steering, as shown in Fig. 1(b), the course of the USV significantly changes during one cycle, and the relationship between position and velocity is nonlinear. Consequently, the position is difficult to approximate by using the velocity vector.

(3) The effect of ship heeling on its safety is not considered. The current research generally does not consider the heel of USV. However, in an emergency situation the large turn of the USV produces a large heel angle that may cause the USV to capsize.

(4) The influence of speed reduction is not considered. The speed may be reduced when the USV sharply turns to avoid collision, and the speed reduction extent varies with the initial speed and rudder angle. If speed reduction is not considered during collision avoidance action, collision may occur during actual execution of the action in a result

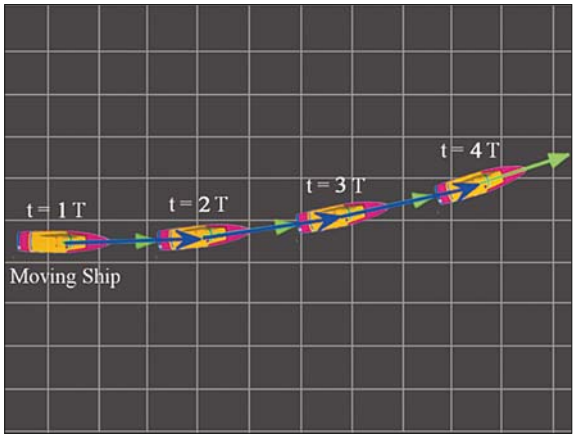

(a) Rarely changing course

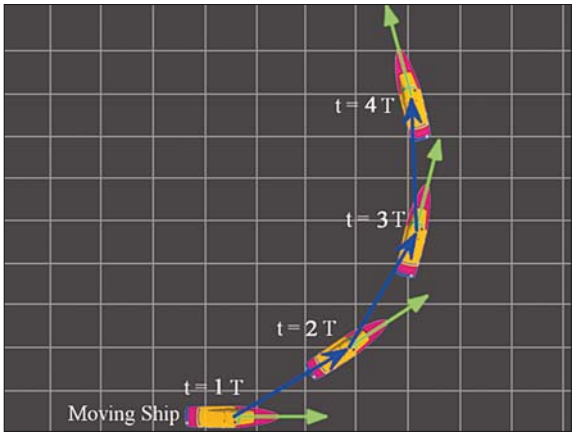

(b) Significantly changing course

Fig. 1. Relationship between position and velocity of a ship

of the decrease of speed, otherwise the USV engine must be forced to speed up for safety [18–20].

In view of the preceding deficiencies, the collision avoidance movement of USVs should have the following characteristics in an emergency situation:

(1) Priority should be given to adjusting the course. Course adjustment has a better effect than speed adjustment, and a change in course is easier to be recognized by other ships enabling them to adjust their motions, accordingly [21].

(2) Given the speed reduction and heeling problem, collision avoidance planning should be established based on the dynamics of USVs to ensure that the planned trajectory can be tracked easily.

(3) Avoidance operations should be continuous. Frequent adjustments delay avoidance action in emergency situations. Therefore, correct collision avoidance planning should be conducted at the beginning and implemented thereafter.

According to the above presented analysis, in urgent situations, the optimal collision avoidance operation should include consistent steering the rudder to a certain angle to alter the direction of the USV to avoid obstacles. Meanwhile, the speed and heading are continuously fine tuned. This obstacle avoidance process can be simplified as a part of the turning motion. This paper proposes an algorithm based on the motion ability database of USVs for collision avoidance in emergency situations.

The paper is organized as follows. In Section 1, the motion ability database of the USV was established by simulation. In Section 2, the positional relationship model between USV and obstacles was established and the classification of the collision risk carried out. In Section 3, the collision avoidance strategy and solution method are defined. In Section 4, simulations of trajectory prediction and obstacle avoidance are carried out, and their results are analyzed in detail to verify the effectiveness of the algorithm. In Section 5, the recapitulation of the study is offered.

ESTABLISHING AN USV POWER DATABASE

ANALYSIS OF USV MOTION CHARACTERISTICS

A dynamic model is established for USVs by using the separate model structure (MMG, Ship Manoeuvring Mathematical Model Group), and the state equation is solved by means of the fourth-order Runge–Kutta method. The rotary motion of a USV is analyzed in terms of rigid body mechanics. USVs use propeller propulsion, and propeller speed and rudder angle are the dynamic control parameters. The basic parameters of USVs are shown in Tab. 1.

Tab. 1. Basic parameters of unmanned boats

Term	Symbol	Unit	Value
Design length of waterline	L	m	8.2
Design width of waterline	B	m	2.3
Average draught	d	m	0.71
Drainage volume	∇	m^3	5.54
Displacement	Δ	t	5.69
Initial velocity	V_0	m/s	5
Safe heel angle		Deg	30

The trajectory of the vessel under different rudder angles at the same initial speed of 5 m/s is shown in Fig. 2. In all cases the start points and simulation time periods of 50 sec are the same. The trajectories indicate that the larger the rudder angle the smaller the turning diameter. When the rudder angle reaches 35°, the constant turning diameter is 24 m, which is approximately three times greater than the length of the boat, which indicates a good turning performance to avoid obstacles. When the rudder angle is small, e.g. 5°, the constant turning diameter is more than 200 m, which shows an insufficient manoeuvrability.

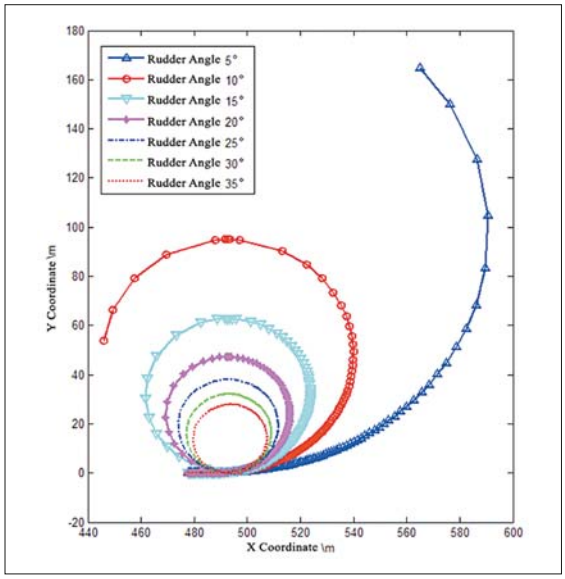

Fig. 2. USV motion track within 50 sec steering period at initial speed of 5 m/s

Fig. 3 shows the heeling angle curves for the boat at different rudder angles at the initial speed of 5 m/s. The heel angle tends to be stable at approximately 15 sec, its value is stable and relatively small due to the low speed of 5 m/s. However, prior to this condition, the maximum heel angle value is large and the rolling curves oscillate 1–2 times because of the rapidly increasing hydrodynamic force during the steering process and the quick occurrence of the camber moment. The simulation shows that a high-speed rotation produces much larger heel angle than that at a low speed, and the maximum heel angle is much larger than the steady heel angle, which is consistent with the theoretical analysis. Sailing at a high speed, USVs are often steered at a large rudder angle to avoid collision, which may cause the vehicles to roll over or overturn.

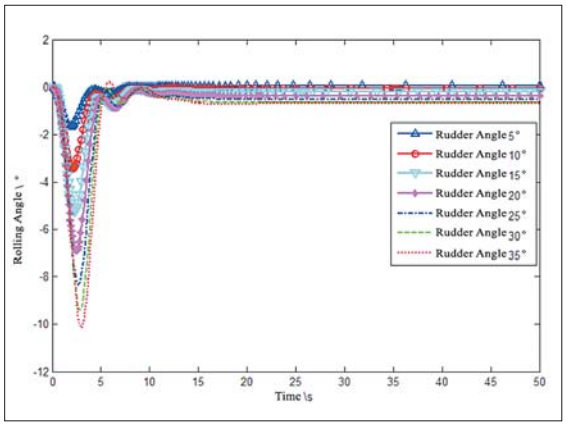

Fig. 3. USV rolling angle curves for different rudder angles at the initial speed of 5 m/s

Fig. 4 shows the speed drop curve during the rotation of the boat. The steering inevitably causes a drop in speed. When turning at a large rudder angle, the speed drop can reach 40% of the initial speed because the drift angle gradually increases with the steering angle thereby resulting in an increase in resistance against forward motion. Meanwhile, the thrust of the propeller is also consumed by the forward direction component of the centrifugal force and the rotational process changes the working conditions of the propeller, resulting in the decline of the rotational speed and efficiency and significant decrease of the forward speed.

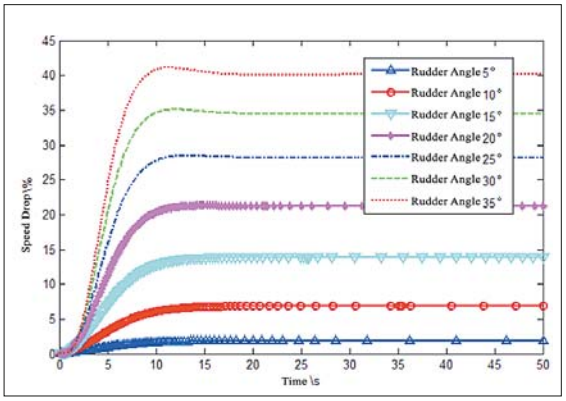

Fig. 4. USV rolling angle curves for different rudder angles at the initial speed of 5 m/s

The main data of the simulation at different rudder angles and the initial speed of 5 m/s are listed in Tab. 2. At this speed, when the rudder angle is below 10°, the heel and speed drop are also small. If the speed must be maintained while steering, the rotational speed of the main engine should be increased slightly. The larger the rudder angle, the larger the drift angle, speed drop, and heel angle and the greater the impact on the USV collision avoidance trajectory.

Tab. 2. Main data of USV rotary motion

Initial velocity (m/s)	Rudder angle (degree)	Constant speed (m/s)	Constant rotation diameter (m)	Downhill ? (percentage)	Maximum roll angle (degree)	Constant drift angle (degree)
5	5	4.8201	195.3463	1.86%	–1.6763	1.9890
5	10	4.5744	94.0141	6.86%	–3.4655	4.1122
5	15	4.2336	61.9975	13.8%	–5.2480	6.2078
5	20	3.8712	46.7099	21.18%	–6.9001	8.2072
5	25	3.5287	37.8469	28.16%	–8.3118	10.0946
5	30	3.2191	32.0803	34.46%	–9.4037	11.8738
5	35	2.9425	28.0322	40.09%	–10.1358	13.5533

ESTABLISHING A STEERING HEEL ANGLE DATABASE FOR HEEL SAFETY

Given that the emergency obstacle avoidance movement of the USV occurs in the early stage of the rotary motion, the probability of encountering the maximum roll angle is high. The rotary motion of an USV is numerically simulated within the initial speed range from 0 to 18 m/s and rudder angle range

from 5° to 35°. The scatter data of maximum heeling angle, initial speed, and rudder angle are obtained, and then fitted by means of a polynomial expressed as follows:

$$\begin{aligned}\phi_{\max}(V_x, \delta_y) = &-3.054 + 0.7447V_x + 0.6606\delta_y \\ &- 0.04852V_x^2 - 0.1532V\delta_y - 0.02769\delta_y^2 \\ &+ 0.001591V_x^3 - 0.00398V_x^2\delta_y + 0.002558V_x\delta_y^2 \\ &+ 0.003651\delta_y^3 \end{aligned} \quad (2)$$

where, $\phi_{\max}()$ represents the function of maximum roll angle. V_x – the initial speed and δ_y – the rudder angle.

The precision parameters of the polynomial fitting are as follows: the sum of square errors is 6.831, the complex correlation coefficient (R-square) is 0.9997, the adjusted R-square is 0.9996, and the root mean square error (RMSE) is 0.359. The square error and RMSE are small, and the complex correlation coefficient and the adjusted R-square are near 1, indicating a high fitting accuracy.

The polynomial surface is shown in Fig. 5. The larger the initial speed and rudder angle, the larger the maximum heel angle of the USV. When the maximum heeling angle exceeds the safe heeling angle of the USV, the risk of collision non-avoidance is great. The curve formed by the intersection of the surface and the 30° heeling plane represents the boundary between safe heel zone and danger one.

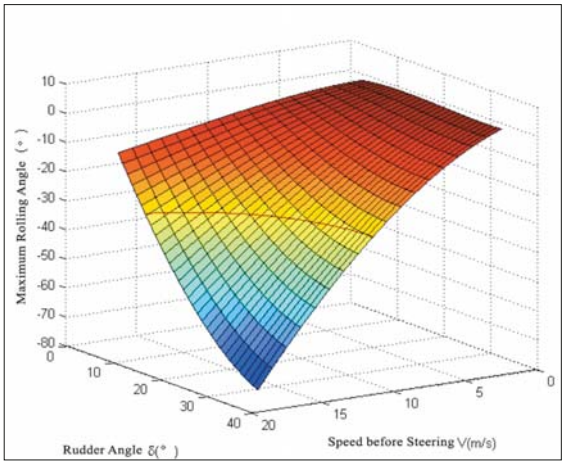

Fig. 5. Three-dimensional diagram of maximum roll angle obtained from simulation of USV turning motion

ESTABLISHING A ROTARY MOTION VELOCITY VECTOR DATABASE AND A POSITION VECTOR DATABASE

According to the numerical calculation results, the data points of the velocity vector and the position scalar in the 10 collision avoidance cycles after the start of steering, are extracted. The radar information for the boat is updated every 5 seconds, so the collision avoidance cycle is set to last 5 sec. Then, the relationships between the data and the initial velocity and between the data and the rudder angle of the USV, are established, respectively. The velocity vector is used to determine the collision avoidance direction, while the position scalar is used to determine the prediction of safety against collision.

The velocity vector database is expressed by the following equation:

$$\boldsymbol{V} = \boldsymbol{\Gamma}([\boldsymbol{U}, \boldsymbol{\delta}]) \quad (3)$$

where $\boldsymbol{\Gamma} = [\Gamma_0, \ldots, \Gamma_t, \ldots, \Gamma_{10}]^T$ is a mapping function that indicates the correspondence between the velocity vector and the initial speed and rudder angle:

$$\boldsymbol{V} = [\boldsymbol{V}_0, \ldots, \boldsymbol{V}_t, \ldots, \boldsymbol{V}_{10}]^T,$$

$$[\boldsymbol{U}, \boldsymbol{\delta}] = [(\boldsymbol{U}, \boldsymbol{\delta})|_0, \ldots (\boldsymbol{U}, \boldsymbol{\delta})|_t, \ldots (\boldsymbol{U}, \boldsymbol{\delta})|_{10}]^T$$

$$\boldsymbol{V}_t = \begin{bmatrix} \vec{V}_{0,0,t} & \cdots & \vec{V}_{0,7,t} \\ \vdots & \vec{V}_{i,j,t} & \vdots \\ \vec{V}_{19,0,t} & \cdots & \vec{V}_{19,7,t} \end{bmatrix}$$

where $t = 0,1\ldots, 9, 10$; $i = 0,1\ldots,16, 17$, stand for the index of different speeds. $j = 0,1\ldots,6, 7$,– the index of different rudder angles.

$$(\boldsymbol{U}, \boldsymbol{\delta})|_t = \begin{bmatrix} (V_0, \delta_0) & \cdots & (V_0, \delta_7) \\ \vdots & (V_i, \delta_j) & \vdots \\ (V_{19}, \delta_0) & \cdots & (V_{19}, \delta_7) \end{bmatrix}$$

For example, $V_{i,j,t}$ represents the speed vector at the *t-th* turning cycle at the *i-th* initial speed and the *j-th* rudder angle (V_i, δ_j).

In collision avoidance situation, the direction of the USV must be judged through the direction information from the velocity database. During the turning motion simulation, the time required to change the speed direction by 30°, 60°, 90°, 120°, 150°, and 180° is recorded for different initial speeds and different rudder angles of the USV, For ships with a poor turning performance a denser heading angle division can be used.

The scatter data are fitted to a polynomial for easy recall. The mathematical relationship between the time required for the six steering angles, the rudder angle and the speed before steering, is expressed as follows:

$$\begin{aligned} t_\psi(V_x, \delta_y) = &\, p_{00} + p_{01}\delta_y + p_{20}V_x^2 \\ &+ p_{11}V_x\delta_y + p_{02}\delta_y^2 + p_{30}V_x^3 \\ &+ p_{21}V_x^2\delta_y + p_{12}V_x\delta_y^2 + p_{03}\delta_y^3 \\ &+ p_{40}V_x^4 + p_{31}V_x^3\delta_y + p_{22}V_x^2\delta_y^2 \\ &+ p_{13}V_x\delta_y^3 + p_{50}V_x^5 + p_{41}V_x^4\delta_y \\ &+ p_{32}V_x^3\delta_y^2 + p_{23}V_x^2\delta_y^3 \end{aligned} \quad (4)$$

where $t_\psi()$ indicates the function of the time required for different steering angles; the coefficients of each surface polynomial are shown in Tab. 3.

Tab. 3. Polynomial coefficients corresponding to target steering angle ψ

ψ (deg)	30	60	90	120	150	180
p_{00}	105.3	191.4	294.7	394	493.8	596.2
p_{10}	–33.13	–58.44	–90.96	–121	–153	–187.2
p_{01}	–8.534	–15.61	–26.02	–35.07	–43.73	–52.36
p_{20}	4.8	8.28	12.97	16.93	21.55	26.54
p_{11}	1.931	3.419	5.796	7.908	9.953	12.06
p_{02}	0.3046	0.5453	0.9616	1.289	1.587	1.874
p_{30}	–0.3653	–0.6183	–0.98	–1.243	–1.582	–1.957
p_{21}	–0.1695	–0.297	–0.4958	–0.6818	–0.8769	–1.072
p_{12}	–0.05546	–0.09564	–0.1756	–0.2381	–0.2928	–0.3476
p_{03}	–0.003715	–0.006529	–0.01199	–0.01596	–0.01939	–0.02263
p_{40}	0.01423	0.02372	0.03827	0.04693	0.05943	0.07373
p_{31}	0.006567	0.0114	0.01854	0.02551	0.03355	0.04147
p_{22}	0.003233	0.005554	0.01014	0.01393	0.01746	0.0208
p_{13}	0.000578	0.0009671	0.001895	0.002541	0.00303	0.003534
p_{50}	–0.000223	–0.000368	–0.0006045	–0.0007168	–0.0009	–0.00112
p_{41}	–9.93E–05	–0.0001686	–0.0002719	–0.0003698	–0.00049	–0.00061
p_{32}	–5.31E–05	–9.32E–05	–0.0001605	–0.0002248	–0.0003	–0.00036
p_{23}	–2.30E–05	–3.78E–05	–7.63E–05	–0.0001029	–0.00012	–0.00014

The polynomial surfaces are shown in Fig. 6. The six surfaces indicate the time required for changing the heading angle by 30°, 60°, 90°, 120°, 150°, and 180° after the start of USV steering, respectively. As the steering angle increases, the required time increases approximately in the same way. In addition, the time required to turn by the same angle at a high speed and large rudder angle is much longer than that at a low speed or small rudder angle.

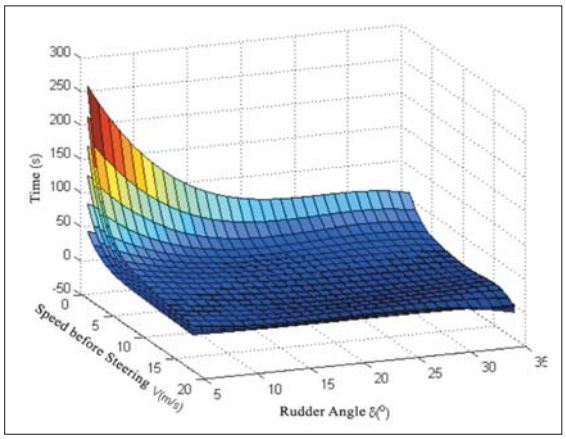

Fig. 6. Three-dimensional surface map of the time required to change the heading angle by 30°, 60°, 90°, 120°, 150°and 180°, successively

The position database is expressed as follows:

$$\boldsymbol{P} = \boldsymbol{\Lambda}\,([\boldsymbol{U}, \boldsymbol{\delta}]) \tag{5}$$

where $\boldsymbol{\Lambda} = [\Lambda_0,\ldots, \Lambda_t,\ldots, \Lambda_{10}]^T$ is a mapping function that indicates the correspondence between the position, the initial speed and rudder angle.

$$\boldsymbol{P} = [\boldsymbol{P}_0,\ldots, \boldsymbol{P}_t,\ldots, \boldsymbol{P}_{10}]^T,$$

$$\boldsymbol{P}_t = \begin{bmatrix} P_{0,0,t} & \cdots & P_{0,7,t} \\ \vdots & P_{i,j,t} & \vdots \\ P_{19,0,t} & \cdots & P_{19,7,t} \end{bmatrix}$$

In the above given formula, the meanings of the indices *i*, *j*, and *t*, and ($[\boldsymbol{U}, \boldsymbol{\delta}]$) are the same as those in the speed variable database. For instance,indicates the position coordinates of the USV at the *t-th* cycle when the rudder angle *j* is used for the initial speed *i*.

ESTABLISHING A COLLISION AVOIDANCE MODEL TO DETERMINE WHETHER COLLISION AVOIDANCE IS NECESSARY

JUDGMENT OF URGENCY OF USV

A low capability of error detection in the estimation and prediction of trajectories of obstacles may cause serious problems in accuracy, thereby damaging the judgment of USV and affecting the effectiveness of collision avoidance.

Considering the radar observation error to improve the prediction accuracy of the obstacle position, the prediction period $T_p(k)$ is introduced in accordance with [22] to reasonably increase the data sampling period and improve the accuracy of error elimination. Moreover, the bidirectional adaptive filtering algorithm based on polynomial fitting and particle swarm optimization [22] is used to eliminate the observed errors in ordinate and abscissa coordinates, and the trajectory of obstacle is predicted by using the autoregressive model. The value of $T_p(k)$ is given by Eq. (6):

$$T_p(k) = \left\lfloor \frac{R_w}{10 \max(\boldsymbol{v}_k)} \right\rfloor T \tag{6}$$

where R_w is the radius of the radar observation scope and T is the observation period of the radar. v_k is the relative velocity between the USV and the k-th obstacle, set for various periods, in particular, $v_k = \{v_{k,1}, v_{k,1} \ldots v_{k,n}\}$. The symbol $\lfloor x \rfloor$ indicates that the real x is rounded down. Eq. (6) shows that $T_p(k)$ is a positive integer multiple of T, and the value of T_p differs with different obstacles. $T_p(k)$ is introduced for reasonable increasing the data sampling period and improving the accuracy of error elimination.

As shown in Fig. 7, a USV with shape $\mathcal{A}$ and a moving ship with shape $\mathcal{B}$, which have velocity vectors $\mathbf{v_R}$ and $\mathbf{v_0}$, respectively, are used. The safe zone of the US is given as $\mathcal{C}$. The domain of the moving ship is $\mathcal{D}$, which is used to represent the area of an obstacle that should be avoided. The blue points in the Fig. 7 represent the obstacle position collected in the previous multiple sampling period, T. Based on the sampling coordinates and the error elimination algorithm taken from the literature, the predicted positions of the obstacle at the moment $1T_p$ and $2T_p$ are shown as **ON** and **ONN**, respectively, and the corresponding ship domains are marked $\mathcal{DN}$ and $\mathcal{DNN}$. Given the uncertainty of prediction, the domains of the $\mathcal{DN}$ and $\mathcal{DNN}$ zones are expanded. For the USV at the position P, the predicted positions in the next two T_ps are marked PN and PNN in the figure, and the corresponding safety zones are denoted by $\mathcal{CN}$ and $\mathcal{CNN}$, respectively. Given that the USV has a minimum observation error in itself, the prediction is relatively accurate and in consequence the safe zone is not expanded.

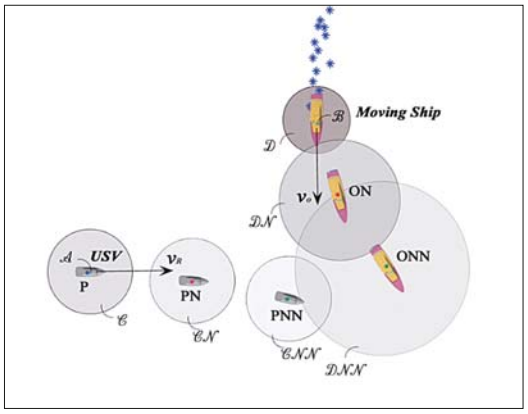

Fig. 7. Position relationship between USV and obstacle in three consecutive moments

Tab. 4. Different states of emergency situation

Symbol	Status	Description	Expected status
λ_1	$\{\mathcal{A} \cap \mathcal{B} \neq \varnothing\}$	Collision, failure to avoid collision	
λ_2	$\{\mathcal{CN} \cap \mathcal{D} \neq \varnothing\}$	Critical, must avoid collision immediately	
λ_3	$\{\mathcal{CN} \cap \mathcal{DN} \neq \varnothing\}$	Critical, must avoid collision immediately	
λ_4	$\{\mathcal{C} \cap \mathcal{DNN} \neq \varnothing\}$	Critical, must avoid collision immediately	
λ_5	$\{\mathcal{CNN} \cap \mathcal{D} \neq \varnothing\}$	Judgment is kept, collision is not avoided	Expected to enter state 2
λ_6	$\{\mathcal{CNN} \cap \mathcal{DN} \neq \varnothing\}$	Judgment is kept, collision is not avoided	Expected to enter state 3
λ_7	$\{\mathcal{C} \cap \mathcal{DNN} \neq \varnothing\}$	Judgment is kept, collision is not avoided	Expected to enter state 4
λ_8	$\{\mathcal{CN} \cap \mathcal{DNN} \neq \varnothing\}$	Judgment is kept, collision is not avoided	Expected to enter other tensions
λ_9	$\{\mathcal{CNN} \cap \mathcal{DNN} \neq \varnothing\}$	Judgment is kept, collision is not avoided	Expected to enter other tensions

In a state of emergency which can be expressed as λ_0, a strategy of collision avoidance must be introduced:

$$\lambda_0 : \lambda_2 \cup \lambda_3 \cup \lambda_4 \cup \lambda_5 \cup \lambda_6 \cup \lambda_7 \cup \lambda_8 \cup \lambda_9$$

In a state of non-emergency marked λ_{10}, the VO algorithm can be used for collision avoidance.

$$\lambda_0 : \overline{\lambda}_2 \cap \overline{\lambda}_1$$

The degree of danger at each state and the level of corresponding collision avoidance strategy are as follows:

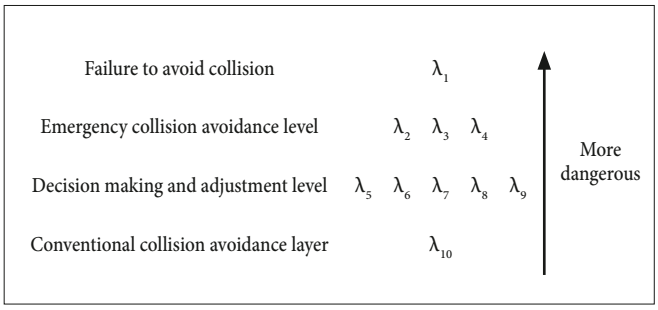

Fig. 8. Three cycles of criticality of USV and obstacle positional relation

1. **When multiple situations occur at the same time, the situation with a higher level of danger is chosen.**

With the movement of the USV and obstacle, the situation may change or the USV may be lifted from the urgent situation. After the emergency situation is lifted, the USV returns to a non-emergency state or sails directly to the sub-target point in an obstacle-free situation.

2. Cancellation of emergency situation

The cancellation of the emergency situation is not an inverse process relative to entering it. Otherwise the USVs will constantly enter and exit the emergency situation. To make sure that the cancellation of emergency situation is trustworthy, the judgment method is used as follows:

$$\lambda_{11}: \{(RO \geq d_2) \frown (TCP < 0)\} \quad (7)$$

In Eq. (7), d_2 indicates the arena of the obstacle boat, The TCPA indicates the time to the closest point of approach: a bigger TCPA indicates a safer situation while a negative TCPA indicates that the USV is kept away from the obstacle boat.

$$TCPA = |RO| \cos(|\gamma|)/|\Delta v|$$

where: $\gamma = \angle(RO, \Delta v)$which is the angle that the line α performs rotation to the line b through the minor arc, so it can be either positive or negative depending on whether the rotation is made in anticlockwise direction or clockwise direction. RO is a vector connecting the coordinates of the USV and the obstacle, Δv is the relative speed between the USV and obstacle ship.Eq. (7) expresses that the USV is outside the boat's area and the two ships are moving away from each other at the moment. The USV is temporarily safe, so the emergency situation could be cancelled.

After the cancellation of emergency situation, the USV returns to a non-emergency state, or sails directly to the sub-target point in an obstacle-free situation.

3. Emergency collision avoidance

In a more urgent situation, the above given VO algorithm may not function. Consequently, the decision-making process and adjustment layer are activated. In such case the USV is not allowed to adjust the course frequently because doing so may lead to misjudgement of the obstacle ship. On the one hand, the USV should work out an emergency avoidance strategy; on the other hand, its speed should be adjusted according to the strategy to be prepared for making a large angle change to avoid collision. To prepare a collision avoidance strategy, the following work is required:

(1) Determining the steering angle of the collision avoidance target, $\bar{\gamma}$ Setting the desired steering angle of the USV to $\bar{\gamma}$:

$$\bar{\gamma} = 30 \left\lceil \frac{\gamma}{30} \right\rceil \quad (8)$$

In this equation: $\lceil\ \rceil$ indicates rounding-up procedure, γ is the collision avoidance steering angle stipulated by International Regulations for Preventing Collisions at Sea (COLREGS), which may be taken as $\gamma+$ or $\gamma-$ where $\gamma+$ is the angle required to turn to the direction required by COLREGS, and $\gamma-$ is the angle in the opposite direction, as shown in Fig. 9. According to the time to the closest point of approach (TCPA), when the USV turns to γ, the USV does not collide with the obstacle. In the planning process, priority is given to $\gamma+$ considering the turning target and $\gamma-$ the candidate target when $\gamma+$ does not work.

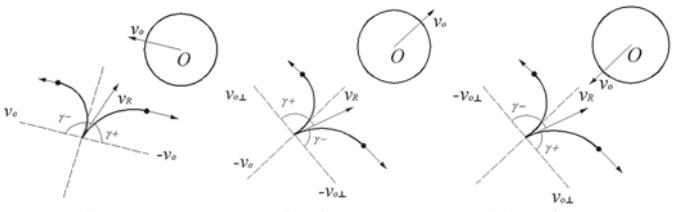

(a) Cross situation *(b) Chasing situation* *(c) Confrontation situation*

Fig. 9. Steering requirements for large rudder angle collision avoidance

$\boldsymbol{v}_{o\perp}$ is $\boldsymbol{v}_o$ rotated by 90° counterclockwise. $-\boldsymbol{v}_{o\perp}$ is $\boldsymbol{v}_o$ rotated by 90° in the opposite direction relative to $\boldsymbol{v}_{o\perp}$

According to Eq. (8), the angle values (30°, 60°, 90°, 120°, 150°, and 180°) can be selected as the steering targets. On the one hand, a sufficient margin for turning time is guaranteed; on the other hand, the data can be fitted by a polynomial previously obtained from the velocity vector database, this way the amount of data to be processed can be reduced. For ships that are difficult to manoeuvre, a more detailed range of angle values is required.

(2) Selecting the time function $t_{\bar{\gamma}}(V_x, \delta_y)$ required to obtain the angle $\bar{\gamma}$

According to the velocity vector database of the USV the polynomial function $t_{\bar{\gamma}}(V_x, \delta_y)$ acc. Eq. (4) is selected. This can be used to calculate the time required for the USV to make an emergency turn by $\bar{\gamma}$ angle at different initial values of the velocity V_x and rudder angle δ_y.

(3) Determining the constraints

Two requirements should be met by the USV to avoid obstacles safely in an emergency situation. First, the time of steering to safety angle should be less than the collision time. Second, the maximum heeling angle of the USV should be kept within the safe range. According to the two conditions, the feasible solution space for collision avoidance can be expressed in the form of the set Q:

$$Q: (V_m, \delta_n) = \{V_m \in V_i, \delta_n \in \delta_j \mid t_{\bar{\gamma}}(V_m, \delta_n) < TCPA, \phi_{\max}(V_m, \delta_n) < \phi_o\} \quad (9)$$

where ϕ_o is the maximum heeling angle in the state of safety, which is set to be 30° in this study. For example, when $\bar{\gamma} = 120°$, the dark area on the left side of Fig. 10 denotes the initial velocities and rudder angles that cannot meet the safe steering time, and the dark area on the right side denotes the initial velocities and rudder angles that cannot meet the maximum heeling angle within the safe range. The intermediate domain represents the set of feasible solutions which satisfy the initial velocity (V_m) and rudder angle (δ_n) conditions.

(4) Solving optimal collision avoidance speed and rudder angle in feasible solution space

The objective function of the collision avoidance strategy is:

$$\{V_{\bar{i}}, \delta_{\bar{j}} \mid \min f(V_{\bar{i}}, \delta_{\bar{j}}) = w_1 \mid V_{\bar{i}} - v_R \mid + w_2 \delta_{\bar{j}}\}, \quad (10)$$

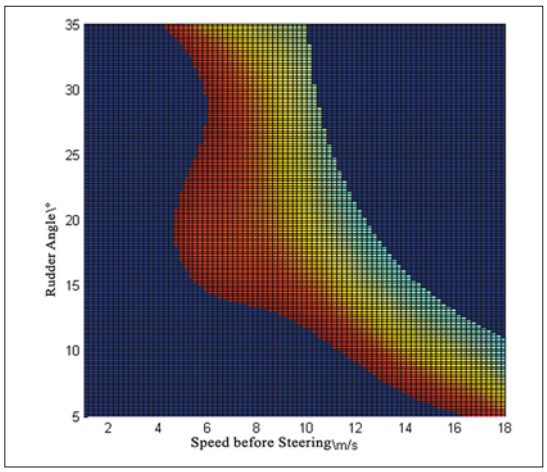

Fig. 10. Feasible solution determined by roll and turn time

meanwhile $(V_{\bar{i}}, \delta_{\bar{j}})$ Q,
where w_1 and w_2 are adjustable weights.

$$w_1 = \begin{cases} 1.2 & if\ v_0' > v_R \\ 0.8 & if\ v_0' \le v_R \end{cases},\ w_2 = 1$$

Eq. (10) shows that the solution with the smallest adjustment loss is selected from the feasible solution space Q, and thus, the USV can avoid collisions by changing its current motion as little as possible. For practical collision avoidance, in this study the two weighting values are set to prioritize change in rudder angle rather than that in speed. Moreover, when necessary, a deceleration is preferred over acceleration because speed increase requires the main engine to develop a higher rotational speed, which increases the power load of the USV, and to increase the speed is more difficult than to reduce it. Eq. (10) is solved by the particle swarm optimization.

(5) Obtaining an emergency collision avoidance track
Based on the mapping relations between the position coordinates of Eq. (5) and the initial velocity and rudder angle, the trajectory ($\boldsymbol{P}^*$) of the USV for emergency collision avoidance can be obtained by using the corresponding values of $(V_{\bar{i}}, \delta_{\bar{j}})$.

$$\boldsymbol{P}^* = [\boldsymbol{P}_{\bar{i},\bar{j},0}, \ldots, \boldsymbol{P}_{\bar{i},\bar{j},t}, \ldots, \boldsymbol{P}_{\bar{i},\bar{j},10}]^T$$

The collision avoidance process is shown in Fig. 11.

The USV path planning contains two parts, global path planning and local path planning. In global path planning, based on the electronic chart, the USV plans a global path which consists of a series of sub-goals for the USV to navigate as long as to arrive at the goal in the end. In the local path planning, the USV avoids all obstacles (boats) in the process of sailing from one sub-goal to the next. The collision avoidance process considered in this article belongs to the kind of local path planning. In each cycle, the USV calculates the process shown in the flowchart. At first, it checks the status λ_1, and, if TRUE is revealed it means that a crash happens and the collision avoidance process is failed. If λ_1 appears FALSE,

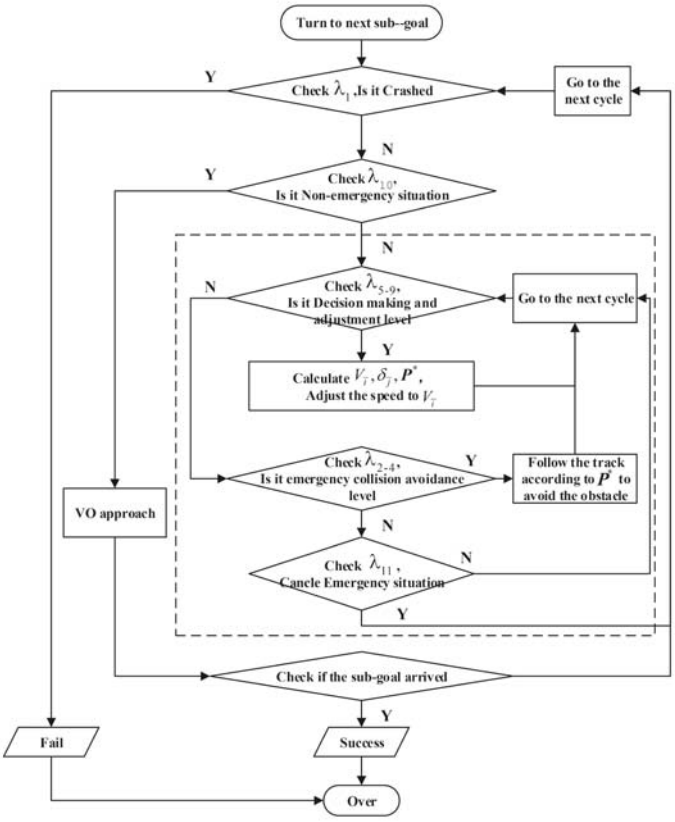

Fig. 11. Flowchart of collision avoidance process

the USV checks the status λ_{10} to make sure if it is in a non-emergency situation. TRUE means the USV is in a non-emergency situation, under this circumstance, to apply VO method is useful for the USV to avoid the obstacles. FALSE indicates that the USV is in an emergency situation. Under this condition, the expressions λ_2 through λ_9 are all checked to make sure which degree of danger is reached at each state and the level of corresponding collision avoidance strategy. In decision and adjustment making, $(V_{\bar{i}}, \delta_{\bar{j}})$ and the trajectory $\boldsymbol{P}^*$ of the USV is calculated for emergency collision avoidance, and then the operation goes to the next cycle. On the emergency collision avoidance level, the USV follows $\boldsymbol{P}^*$ to get away from the obstacle. If the status λ_{10} is correct, the emergency situation is cancelled. In the whole process, if a sub-goal arrived, the local path planning succeeds and the USV continues turning to the next sub-goal.

SIMULATION EXPERIMENT

To test the effect of the proposed method, we simulated the collision avoidance of a USV under a MATLAB environment. For better observation, we constructed a 3D view with the use of the Unity on the basis of MATLAB environment. The work was programmed in C# script where the calculation in MATLAB was linked to form a dynamic link library. The development platform is the Visual Studio. In all simulation models, the USV simulates real conditions, it is unaware of the following movement of obstacles and can only react based

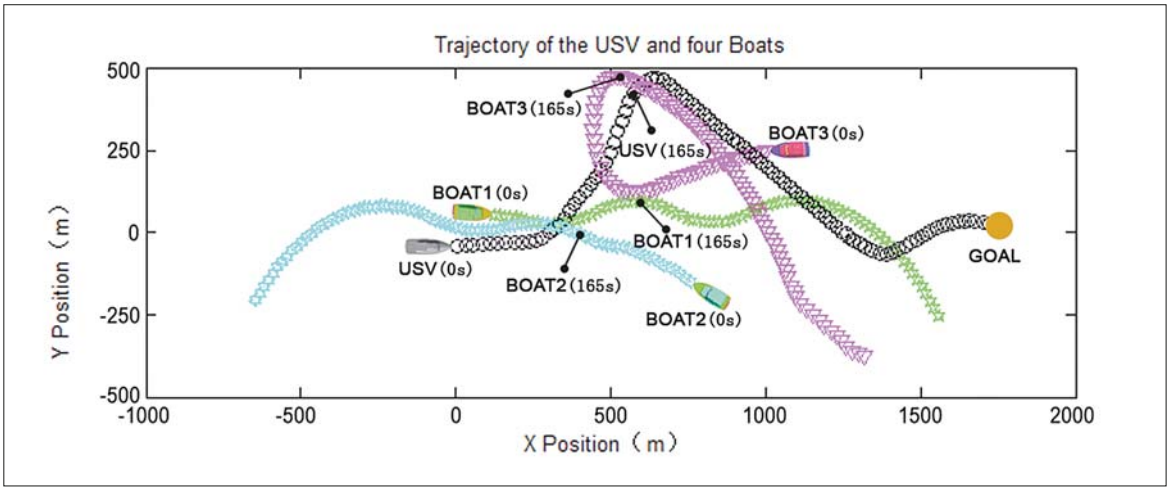

Fig. 12 Trajectories of the USV and three obstacle boats

on boats' current motion. The simulation cycle T is set to five seconds, which means that the movements of USV and obstacles are recorded every five seconds.

The USV represented by the black circle has an initial position of (0, -50) and an eastward velocity. The BOAT1 represented by the green pentacle is located at (80,50), and its velocity points to the east. The BOAT2 represented by the blue-green hexagon is located at (900,-200) and its velocity points to the northwest. The BOAT 3 represented by the magenta triangle is located at (1100,250), and its velocity points to the west. The obstacle ships move randomly. Fig. 12 shows the trajectories of the USV and the three ships. The movements of the obstacle ships cause interferences, but the USV could still safely avoid all the obstacles and successfully reach the end point.

In Fig. 12, the positions of the USV and the obstacles at 165 sec are shown, and Fig. 13 presents the moving relations between the ships at this moment. The magenta areas around BOAT3, marked from deep to light shade, represent the above mentioned D, DN, and DNN regions, respectively. The figure shows that at a particular moment, $\mathcal{C} \cap \mathcal{DNN} \neq \varnothing$, the BOAT3 is in λ_4 state. Thus, the USV should enter the execution layer and start emergency collision avoidance.

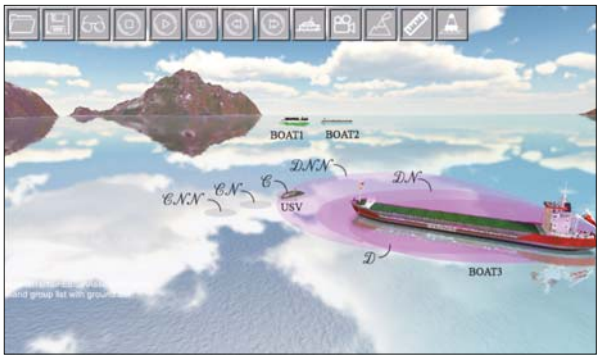

Fig. 13. Positional relationship between USV and obstacles at 165 sec

Fig. 14 shows the changes in encounter types when the USV meets the three obstacle ships. Throughout the process, BOAT2 maintains in a non-urgent situation, λ_{10}, with the USV, indicating that the VO algorithm is used for the USV to avoid BOAT2. BOAT1 and BOAT3 remain at λ_{10} state for a long time. During this period, the VO algorithm is also used by the USV. Subsequently, they enter an urgent situation, and the states change to λ_3 or even λ_2. This condition shows that the VO algorithm is no longer sufficient to guarantee the safety of the USV. Therefore, the USV starts using the emergency strategy to plan the trajectory and adjust the speed in the planning and adjustment layer ($\lambda_5 - \lambda_9$), and the steering has not yet been commenced. Thus, the emergency state is still under testing until it enters the execution layer ($\lambda_2 - \lambda_4$). At this time, the USV makes a large turn as planned to avoid collision. Consequently, the emergency state is quickly recovered, and then the USV briefly returns to the state λ_{10} but still uses the emergency collision strategy until it changes to state λ_{11}. After the emergency state is lifted, the USV jumps to the state λ_{10} and uses the VO algorithm for conventional collision avoidance planning.

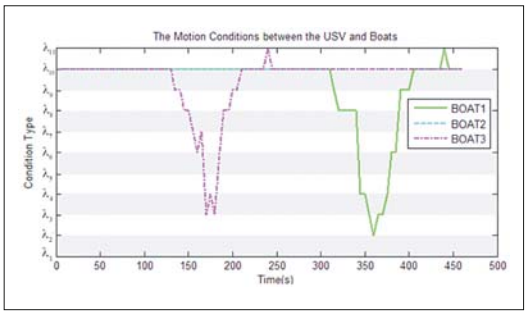

Fig. 14. The motion conditions between the USV and obstacle boats

Fig. 15 presents the curve of changing the heading angle and velocity of the USV during the collision avoidance process. The slanting direction and the speed are continuously and smoothly adjusted. In planning and adjusting layer, the speed of the USV is slowly adjusted and lowered in preparation for the execution layer that may appear later, indicating that the collision avoidance speed solved by the PSO algorithm is less than the current speed. When entering the executive level, the heading angle of the USV is quickly adjusted, indicating that a large steering to avoid collision is initiated. After the

emergency situation is lifted, the speed of the USV increases, and the VO algorithm is used to perform conventional collision avoidance process.

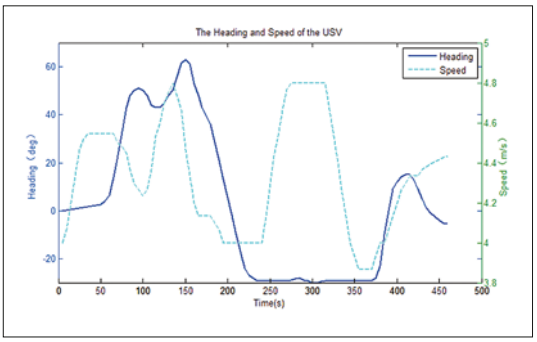

Fig. 15. The USV heading and speed in function of time

RECAPITULATION

This study proposes an emergency collision avoidance algorithm for USVs based on a motion ability database. The algorithm is aimed at addressing the inconsistency of the existing algorithm. It is proposed to avoid collision in emergency situations by sharp turning and treating the collision avoidance process as a part of the turning movement of USVs. In addition, the rolling safety and effect of speed reduction during the collision avoidance process are considered. Both the maximum heeling angle and the velocity vector are fitted into polynomials to perform quickly calculation when executing obstacle avoidance. After that, the time of steering to safety angle and the maximum heeling angle form two infeasible solution spaces, the obstacle avoidance problem turns to be an optimization problem in the feasible solution space. Moreover, the cancellation function of the emergency situation is proposed to avoid the USVs entering the emergency situation and exiting from it, over and over again. When a USV is in emergency collision avoidance process, the velocity vector and position vector are nonlinear. The existing algorithm is inconsistent or impossible to solve and does not consider the impact of speed drop on safety during heeling and steering. To address the problems, this study proposes a collision avoidance algorithm based on the USV motion ability database, which realizes emergency collision avoidance by sharp turning. First, a USV rotary motion simulation is conducted numerically and the motion ability database (with pre-steering initial velocity and steering rudder angle taken as independent variables) is obtained, including the heeling angle function for ensuring safety, which is used to determine the collision avoidance course. The velocity vector database and location database are used to determine the steering time function and collision avoidance trajectory. Second, a collision avoidance model is established for USVs and obstacles in emergency situations. By introducing the prediction period, the model is correlated with relative speed, which ensures the accuracy of emergency judgment. On the basis of the model, different emergency states are set and three layers of emergency avoidance process are formed, namely, the conventional collision avoidance layers using VO algorithm, the decision and adjustment layer for planning and speed adjustment, and the collision avoidance layer performing steering tasks. Third, the collision avoidance planning method in the decision and adjustment layer is determined. The expected steering angle is obtained by combining the COLREGS rule. The feasible solution space, with the initial velocity and rudder angle as the independent variables, is determined by combining the steering time and heel angle functions. On the basis of this solution space, the objective function is formed and solved by the PSO algorithm to obtain the optimal initial velocity and rudder angle. Then, the optimal trajectory can be obtained by referring to the corresponding position data. A simulation is conducted to confirm the validity of the proposed approach. The results of the simulation indicate that the proposed approach is valid and efficient.

ACKNOWLEDGMENT

This work is supported by the National Natural Science Foundation of China (Grant No. 51809203 and 51709214) and the Fundamental Research Funds for the Central Universities (WUT: 2019IVB011, 2017IVA008 and 2017IVA006).

REFERENCES

1. Campbell S., Naeem W., Irwin G.W.: *A review on improving the autonomy of unmanned surface vehicles through intelligent collision avoidance manoeuvre*. Annu. Rev. Control 2012, 36(23): pp. 267–283.

2. Simetti E., Turetta A., Casalino G.: *Towards the Use of a Team of USVs for Civilian Harbour Protection: the Problem of Intercepting Detected Menaces*, OCEANS 2010 IEEE – Sydney.

3. U.S.Dept. Homeland Security/U.S. Coast Guard; *Navigation rules*. Paradise Cay Publications, 2010.

4. Larson J., Bruch M., Halterman R., Rogers J., Webster R.: *Advances in Autonomous Obstacle Avoidance for Unmanned Surface Vehicles*. Space and Naval Warfare Systems Center, San Diego, CA., 2007.

5. Colito J.: *Autonomous mission planning and execution for unmanned surface vehicles in compliance with the marine rules of the road*, M.S. thesis, Dept. Aeronaut. Astronaut., Univ. Washington, Seattle, WA, US., 2007.

6. Choi, S., Yu, W.: *Any-angle path planning on non-uniform costmaps*. In: Proceedings of the IEEE International Conference on Robotics and Automation (ICRA), 2011: pp. 5615–5621.

7. Kim H., Park B., Myung H.: *Curvature path planning with high resolution graph for unmanned surface vehicle*. In: Proceedings of the Robot Intelligence Technology and Applications (RiTA), 2012: pp. 147–154.

8. Khatib, O.: *Real-time obstacle avoidance for manipulators and mobile robots*. Int. J. Robot. Res. 1986, 5: pp. 90–98.

9. Wang J., Wu X., Xu Z.: *Potential-based obstacle avoidance in formation control*. J. Control Theory Appl. 2008, 6: pp. 311–316.

10. Ge S., Cui Y.: *Dynamic motion planning for mobile robots using potential field method*. Auton. Robots 2007, 13: pp. 207–222.

11. Fiorini P., Shiller Z.: *Motion planning in dynamic environments using velocity obstalces*, Int. J. Robot, Res. 1998, 17(7): pp. 760–772.

12. Berg J., Lin M., and Manocha D.: *Reciprocal velocity obstacles for real-time multi-agent navigation*, Proc. IEEE Int. Conf. Robot. Autom., 2008: pp. 1928–1935.

13. Kluge B., 2004 Parssler: *Reflective navigation: Individual behaviors and group behaviors*, Proc. IEEE Int. Conf. Robot. Autom., 2004, 4: pp. 4172–4177.

14. Berg J., Patil S., Sewall J., Manocha D., and Lin M. C.: *Interactive navigation of multiple agents in crowded environments*, Proc. Symp. Interactive 3D Graphics Games, 2004, pp. 139–147.

15. Zhao Y.X., Li W., Shi P.: *A real-time collision avoidance learning system for Unmanned Surface Vessels*. Neurocomputing, 2016, 182: pp. 255–266.

16. Li W. F., Ma W. Y.: *Simulation on Vessel Intelligent Collision Avoidance Based on Artificial Fish Swarm Algorithm*. Polish Maritime Research, 2016, 23: pp. 138–143.

17. Lazarowska A.: *Swarm Intelligence Approach to Safe Ship Control*. Polish Maritime Research, 2015, 22(4): pp. 34–40

18. Soulignac M.: *Feasible and optimal path planning in strong current fields*. IEEE Trans. Robot. 2011, 27: pp. 89–98.

19. Isern G., Hernández, S. D., Fernández P. E., Cabrera G., Dominguez B., Prieto M. V.: *Path planning for underwater gliders using iterative optimisation*. In: Proceedings of the IEEE International Conference on Robotics and Automation (ICRA), 2011: pp. 1538–1543.

20. Yang Y., Wang S., Wu Z., Wang Y.: *Motion planning for multi-HUG formation in an environment with obstacles*. Ocean Engineering. 2011, 38: pp. 2262–2269.

21. Song L.F., Su Y.R., Dong Z.P.: *A two-level dynamic obstacle avoidance algorithm for unmanned surface vehicles*, Ocean Engineering, 2018, 170: pp. 351–360.

22. Song L.F., Chen Z., Xiang Z.Q.: *Error Mitigation Algorithm based on Bidirectional Fitting Method for Collision Avoidance of Unmanned Surface Vehicle*, Polish Maritime Research, 2018.

CONTACT WITH THE AUTHORS

Lifei Song
e-mail: songlifei@whut.edu.cn

Key Laboratory of High Performance Ship Technology
(Wuhan University of Technology)
Ministry of Education
Heping Avenue, 430063 Wuhan

School of Transportation
Wuhan University of Technology
Heping Avenue, 430063 Wuhan
China

Houjing Chen
e-mail: Hawking2006@sina.cn

Key Laboratory of High Performance Ship Technology
(Wuhan University of Technology)
Ministry of Education
Heping Avenue, 430063 Wuhan

China Ship Development and Design Center
Zhangzhidong Road, Wuhan
China

Wenhao Xiong
e-mail: 2569403518@qq.com

School of Transportation
Wuhan University of Technology
Heping Avenue, 430063 Wuhan
China

Zaopeng Dong
e-mail: dongzaopeng@whut.edu.cn

Key Laboratory of High Performance Ship Technology
(Wuhan University of Technology)
Ministry of Education
Heping Avenue, 430063 Wuhan

School of Transportation
Wuhan University of Technology
Heping Avenue, 430063 Wuhan
China

Puxiu Mao
e-mail: Puxiumao@usc.edu

University of Southern California
University Park Los Angeles
740–2311 Los Angeles
USA

Zuquan Xiang
e-mail: xiangzuquan@whut.edu.cn

Key Laboratory of High Performance Ship Technology
(Wuhan University of Technology)
Ministry of Education
Heping Avenue, 430063 Wuhan

School of Transportation
Wuhan University of Technology
Heping Avenue, 430063 Wuhan
China

sciendo

POLISH MARITIME RESEARCH 2 (102) 2019 Vol. 26; pp. 68-75
10.2478/pomr-2019-0026

PRE-FILTERED BACKSTEPPING CONTROL FOR UNDERACTUATED SHIP PATH FOLLOWING

Zhiquan Liu
Shanghai Maritime University, China

ABSTRACT

Robust path following control for underactuated surface ships is an important issue in marine control practice. This paper aims to improve the robustness of the close-loop system with model uncertainties and time-varying disturbances. A practical adaptive backstepping control scheme with a pre-filter is proposed to force a surface vessel to track the predefined path generated by the virtual ship. Based on the Lyapunov stability theorem, this algorithm can guarantee all error signals in the overall system to be uniformly ultimately bounded, and it can be implemented without exact knowledge of the nonlinear damping structure and environmental disturbances. The proposed pre-filter can smooth the commanded heading order and obtain a better performance of the waypoint-based navigation control system. Two simulation cases are drawn to illustrate the validity of the proposed control strategy.

Keywords: Underactuated ships; path following; backstepping; pre-filter

INTRODUCTION

During the past decades, the path following and tracking control for marine vehicles have caused much attention in marine control areas, especially in the area concerning the motion control of an underactuated marine vehicle (i.e. underactuated surface ship or underwater autonomous vehicle) [1, 2]. This paper focuses on the control of an underactuated surface ship. The term "underactuated ship" means that the vessel is equipped with rudder and thrusters for the heading angle and forward speed control, whereas the sway axis cannot be actuated directly, which is the main challenge.

Linear model-based control strategies may be easy to implement. Several authors have contributed ideas for surface vessel path following control with linear ship model, including model predictive control taking into account the roll motion constraint [3, 4], PID control [5], and disturbance observer based composite control [6, 7]. When a marine surface vessel is moving in the open sea, it cannot move exactly along the desired path due to the action of rough environmental disturbances, which make the ship dynamics nonlinear and burdened with uncertainties. Robust and adaptive schemes are always selected to sustain the system robustness. Alfi et al. [8] have designed a robust H-infinity controller for tracking control of a container ship. Sliding mode controllers are also selected to solve the robust tracking control problem for underactuated ships [9, 10]. Shin et al. [11] have proposed an adaptive path following control algorithm with the surface vessel dynamic model identified from several trials. In some studies, parameter identification and neural network can also be selected to cope with tracking model uncertainties [12, 13]. These robust and adaptive algorithms are always combined with the backstepping method when solving a tracking control problem of underactuated ship. Do and Pan [14] have designed an adaptive backstepping controller for the path following control of underactuated ship under deterministic disturbances. This control considered the known linear damping coefficients and unknown nonlinear damping coefficients. Moreover, the modified practical control method based on coordinate transformation has been developed [15]. Li et al. [16] have

developed the robust nonlinear backstepping path following control with feedback dominance, but it was designed with a reduced order model. Li et al. [17] have proposed a point to point navigation controller to make tracking errors converge to an invariant set. Furthermore, Sun et al. [18] have introduced a PI sliding mode backstepping path following controller with unknown plant parameters. However, the above two methods require that the nonlinear damping parameters are unknown constant vectors with known dimensions, which is a too restrictive condition. For the system nonlinear damping problem, Xu et al. [19] have designed a dynamical sliding mode adaptive tracking controller to handle uncertainties and unknown external disturbances, but it is unreasonable in practice that the two uncertain nonlinear parts are combined together to estimate.

In this paper, a pre-filtered adaptive controller is designed to deal with the path following problem of underactuated surface vessel by combining the backstepping technique. Unlike the controller developed by Li et al. [17], the here proposed control law does not require exact information on the structure and parameter vector dimensions of the uncertainty term, as the whole nonlinear hydrodynamic function and the upper bound of external disturbances are estimated individually. The pre-filtered technique can avoid larger outputs of actuators, and limits the control input of the actuation system in the vessel control system [20]. In this paper, a third order filter is used to relax the smooth trajectory assumption and thus enhance the robustness of the proposed controller, especially in point to point navigation control.

The organization of the paper is as follows. Section 2 gives the problem formulation and the system models. Section 3 formulates the systematic procedure of the proposed algorithm. The numerical simulation results are presented in Section 4 to expound the effectiveness of the tracking controller, and the conclusions are formulated in Section 5.

PROBLEM FORMULATION

Following the description by Zhang et al. [21], we consider the general kinematic and kinetic mathematical model of 3-DOF motion (surge, sway and yaw) of the underactuated ship as:

$$\begin{aligned}
\dot{x} &= u\cos(\psi) - v\sin(\psi)\\
\dot{y} &= u\sin(\psi) + v\cos(\psi)\\
\dot{\psi} &= r\\
\dot{u} &= f_u(\theta) + \frac{1}{m_{11}}\tau_u + \frac{1}{m_{11}}\tau_{wu}\\
\dot{v} &= f_v(\theta) + \frac{1}{m_{22}}\tau_{wv}\\
\dot{r} &= f_r(\theta) + \frac{1}{m_{33}}\tau_r + \frac{1}{m_{33}}\tau_{wr}
\end{aligned} \tag{1}$$

with

$$f_u(\theta) = \frac{m_{22}}{m_{11}}vr - \frac{d_{u1}}{m_{11}}u - \frac{d_{u2}}{m_{11}}|u|u - \frac{d_{u3}}{m_{11}}u^3$$

$$f_v(\theta) = -\frac{m_{11}}{m_{22}}ur - \frac{d_{v1}}{m_{22}}v - \frac{d_{v2}}{m_{22}}|v|v - \frac{d_{v3}}{m_{22}}v^3$$

$$f_r(\theta) = \frac{m_{11}-m_{22}}{m_{33}}uv - \frac{d_{r1}}{m_{33}}r - \frac{d_{r2}}{m_{33}}|r|r - \frac{d_{r3}}{m_{33}}r^3$$

where (x, y, ψ) are the ship's position coordinates and yaw angle expressed in the earth-fixed frame, and $\theta = (u, v, r)$ denotes the velocity vector with surge, sway and yaw components. $f_u(\theta), f_v(\theta)$ and $f_r(\theta)$ are the unknown nonlinear hydrodynamic functions, τ_u and τ_r denote the control force and moment, and $(\tau_{wu}, \tau_{wv}, \tau_{wr})$ are the external disturbances. The positive constants m_{11}, m_{22} and m_{33} are the ship inertia parameters which are assumed known. The unknown parameters $d_{ij}(i = u, v, r; j = 1, 2, 3)$ are considered as hydrodynamic damping terms.

Assumption 1.
The ocean environmental disturbances are bounded, i.e. $|\tau_{wu}| \le \tau_{wu\max}$, $|\tau_{wv}| \le \tau_{wv\max}$ and $|\tau_{wr}| \le \tau_{wr\max}$, where $\tau_{wu\max}$, $\tau_{wv\max}$ and $\tau_{wr\max}$ are unknown positive constants. We define new symbols $\tau_{mwu\max} = \tau_{wu\max}/m_{11}$, $\tau_{mwv\max} = \tau_{wv\max}/m_{22}$ and $\tau_{mwr\max} = \tau_{wr\max}/m_{33}$ which satisfy equations $|\tau_{wu}/m_{11}| \le \tau_{mwu\max}$, $|\tau_{wv}/m_{22}| \le \tau_{mwv\max}$ and $|\tau_{wr}/m_{33}| \le \tau_{mwr\max}$.

Assumption 2.
The states of the desired trajectory x_d, $\dot{x}_d$, $\ddot{x}_d$, y_d, $\dot{y}_d$, $\ddot{y}_d$, ψ_d, $\dot{\psi}_d$ and $\ddot{\psi}_d$ are all bounded, and the reference path is smooth.

Assumption 3.
The sway velocity v is passive bounded in the sense that $|v| \le v_{\max}$, following Li et al. [17].

Assumption 4.
The unknown environmental disturbances and uncertain hydrodynamic functions are slowly varying, i.e. $\dot{f}_i(\theta) = 0$ and $\dot{\tau}_{wi} = 0$, $i = u, v, r$.

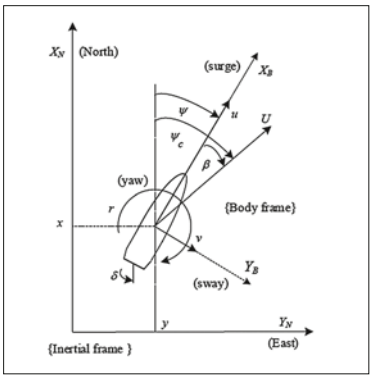

Fig. 1. General frame of path following control

In the overviewed literature, the dynamics of underactuated ship tracking control is addressed by two methods, i.e. as error dynamics in the inertial coordinate frame or the Serret-Frenet

frame. Here, the first framework is selected, see Fig. 1. For the tracking control, the following tracking error variables are defined:

$$x_e = x_d - x \qquad y_e = y_d - y$$
$$\psi_e = \psi_r - \psi \qquad z_e = \sqrt{x_e^2 + y_e^2} \tag{2}$$

where (x_d, y_d) is the desired point generated by the virtual ship, ψ_e is the heading error and $|\psi_e| < \pi/2$ is required in the following control law design, z_e is the position tracking error, and $\psi_r \in (-\pi, \pi)$ is the azimuth angle related to the desired virtual ship, defined as follows:

$$\psi_r = 0.5[1 - \mathrm{sgn}(x_e)]\,\mathrm{sgn}(y_e) \cdot \pi + \arctan\left(\frac{y_e}{x_e}\right) \tag{3}$$

where sgn(·) is the sign function. Considering $\psi_r = \psi_d$ when the position tracking error satisfies $z_e = 0$, $\psi_d = \arctan(\dot{y}_d/\dot{x}_d)$ is the desired yaw angle of the virtual ship.

CONTROL DESIGN

The control objective of this paper is to design a backstepping scheme for tracking control of an underactuated ship with Assumptions 1–3. In this section, the control design procedure is achieved in following steps.

SURGE CONTROL

In order to stabilize the position error, we define the Lyapunov function candidate (LFC):

$$V_1 = \frac{1}{2} z_e^2 \tag{4}$$

Its first derivative along the solutions of the system (1) is given as:

$$\dot{V}_1 = z_e \dot{z}_e = z_e(\dot{x}_d \cos\psi_r + \dot{y}_d \sin\psi_r) - z_e(v \sin\psi_e + u \cos\psi_e) \tag{5}$$

Remark 1. In order to derive (6), we should show the way of deriving $\dot{z}_e$. Obviously, we know that $z_e^2 = x_e^2 + y_e^2$ and $z_e \dot{z}_e = x_e \dot{x}_e + y_e \dot{y}_e$ according to the position error equation in (2). Based on (1) and (2), we derive the expression of $\dot{z}_e$ as follows:

$$\begin{aligned}
\dot{z}_e &= \frac{x_e}{z_e}\dot{x}_e + \frac{y_e}{z_e}\dot{y}_e \\
&= \cos\psi_r(\dot{x}_d - \dot{x}) + \sin\psi_r(\dot{y}_d - \dot{y}) \\
&= \cos\psi_r \dot{x}_d - \cos\psi_r(u\cos\psi - v\sin\psi) \\
&\quad + \sin\psi_r \dot{y}_d - \sin\psi_r(u\sin\psi + v\cos\psi) \\
&= \dot{x}_d \cos\psi_r - u(\cos\psi_r\cos\psi + \sin\psi_r\sin\psi) \\
&\quad + \dot{y}_d \sin\psi_r - v(\sin\psi_r\cos\psi - \cos\psi_r\sin\psi) \\
&= \dot{x}_d \cos\psi_r + \dot{y}_d \sin\psi_r - u\cos\psi_e - v\sin\psi_e
\end{aligned}$$

We define a virtual control signal α_u that makes $u_e = \alpha_u - u$. The virtual control is selected as

$$\alpha_u = \frac{\dot{x}_d \cos\psi_r + \dot{y}_d \sin\psi_r - v\sin\psi_e + k_{ze} z_e}{\cos\psi_e} \tag{6}$$

where $k_{ze} > 0$ is a designed parameter.

Substituting $u = \alpha_u - u_e$ and the virtual control equation (6) into (5), we get

$$\dot{V}_1 = -k_{ze} z_e^2 + z_e u_e \cos\psi_e \tag{7}$$

Rewriting the surge dynamics using the new variable yields

$$\dot{u}_e = \dot{\alpha}_u - \dot{u} = \dot{\alpha}_u - f_u(\theta) - \frac{1}{m_{11}}\tau_u - \frac{1}{m_{11}}\tau_{wu} \tag{8}$$

Then, we define a new Lyapunov function:

$$V_2 = V_1 + \frac{1}{2} u_e^2 \tag{9}$$

and its first derivative:

$$\begin{aligned}
\dot{V}_2 &= \dot{V}_1 + u_e \dot{u}_e = -k_{ze} z_e^2 + z_e u_e \cos\psi_e \\
&\quad + u_e\left[\dot{\alpha}_u - f_u(\theta) - \frac{1}{m_{11}}\tau_u - \frac{1}{m_{11}}\tau_{wu}\right]
\end{aligned} \tag{10}$$

In order to make (10) negative, we design the actual control law as follows:

$$\begin{aligned}
\tau_u &= m_{11} k_{ue} u_e + m_{11}[z_e \cos\psi_e + \\
&\quad \dot{\alpha}_u - \hat{f}_u(\theta) + \delta_u \hat{\tau}_{mwu\max} u_e]
\end{aligned} \tag{11}$$

where k_{ue} and δ_u are the designed positive constants, $\hat{f}_u(\theta)$ is the estimate of the nonlinear hydrodynamic function, and $\hat{\tau}_{wu\max}$ is the estimate of the upper bound of the external surge force. The corresponding update laws are chosen as follows:

$$\begin{aligned}
\dot{\hat{f}}_u(\theta) &= \Gamma_u[-u_e - a_u(\hat{f}_u(\theta) - \hat{f}_{u0}(\theta))] \\
\dot{\hat{\tau}}_{mwu\max} &= \gamma_u[\delta_u u_e^2 - a_{tu}(\hat{\tau}_{mwu\max} - \hat{\tau}_{mwu\max}(0))]
\end{aligned} \tag{12}$$

where Γ_u, γ_u, a_u and a_{tu} are the positive designed parameters, while $\hat{f}_{u0}(\theta)$ and $\hat{\tau}_{mwu\max}(0)$ are the initial values of the corresponding update state.

To stabilize the estimation errors, we consider the following LFC

$$V_3 = V_2 + \frac{1}{2\Gamma_u}\tilde{f}_u^2(\theta) + \frac{1}{2\gamma_u}\tilde{\tau}_{mwu\max}^2 \tag{13}$$

where $\tilde{f}_u(\theta) = \hat{f}_u(\theta) - f_u(\theta)$ is the estimation error of the surge nonlinear damping function, and $\tilde{\tau}_{mwu\max} = \hat{\tau}_{mwu\max} - \tau_{mwu\max}$ is the estimation error of the bound of the surge disturbance.

Differentiating both sides of (13) gives:

$$\dot{V}_3 = V_2 + \frac{1}{\Gamma_u}\tilde{f}_u(\theta)\dot{\hat{f}}_u(\theta) + \frac{1}{\gamma_u}\tilde{\tau}_{mwu\max}\dot{\hat{\tau}}_{mwu\max}$$
$$= k_{ze}z_e^2 - k_{ue}u_e^2 + u_e\tilde{f}_u(\theta) + \frac{1}{\Gamma_u}\tilde{f}_u(\theta)\dot{\hat{f}}_u(\theta)$$
$$-\delta_u\hat{\tau}_{mwu\max}u_e^2 - \frac{u_e}{m_{11}}\tau_{wu} + \frac{1}{\gamma_u}\tilde{\tau}_{mwu\max}\dot{\hat{\tau}}_{mwu\max}$$
$$\le -k_{ze}z_e^2 - a_u\tilde{f}_u(\theta)[\tilde{f}_u(\theta) + f_u(\theta) - \hat{f}_{u0}(\theta)]$$
$$-k_{ue}u_e^2 - \delta_u\hat{\tau}_{mwu\max}u_e^2 + |u_e|\tau_{mwu\max} + \tilde{\tau}_{mwu\max}\delta_u u_e^2$$
$$-\tilde{\tau}_{mwu\max}[a_{tu}(\tilde{\tau}_{mwu\max} + \tau_{mwu\max} - \hat{\tau}_{mwu\max}(0))]$$
$$\le -k_{ze}z_e^2 - k_{ue}u_e^2 - a_u\tilde{f}_u^2(\theta)$$
$$-a_u\tilde{f}_u(\theta)[f_u(\theta) - \hat{f}_{u0}(\theta)] - \delta_u\hat{\tau}_{mwu\max}u_e^2$$
$$+\delta_u\tau_{mwu\max}u_e^2 + \frac{1}{4\delta_u}\tau_{mwu\max} + \delta_u\tilde{\tau}_{mwu\max}u_e^2$$
$$-a_{tu}\tilde{\tau}_{mwu\max}^2 - a_{tu}[\tau_{mwu\max} - \hat{\tau}_{mwu\max}(0)]$$
$$\le -k_{ze}z_e^2 - k_{ue}u_e^2 - a_u\tilde{f}_u^2(\theta) - a_{tu}\tilde{\tau}_{mwu\max}^2 + \rho_u \quad (14)$$

where

$$\rho_u = \frac{1}{4\delta_u}\tau_{mwu\max} + \frac{1}{2}[|\tilde{f}_u(\theta)|^2 + |f_u(\theta) + \hat{f}_{u0}(\theta)|^2]$$
$$+\frac{1}{2}[|\tilde{\tau}_{mwu\max}|^2 + |\tau_{mwu\max} - \hat{\tau}_{mwu\max}(0)|^2]$$

is a positive constant.

Let $\lambda_u = \min\{2k_{ue}, 2k_{ze}, a_u\Gamma_u, a_{tu}\gamma_u\}$, then (14) can be rewritten as

$$\dot{V}_3 \le -\lambda_u V_3 + \rho_u \quad (15)$$

Therefore, all tracking errors listed in (13) are uniformly ultimately bounded (UUB).

YAW CONTROL

According to the error dynamics of yaw motion in (1) and (2), we define the following LFC:

$$V_4 = \frac{1}{2}\psi_e^2 \quad (16)$$

and its time derivative yields:

$$\dot{V}_4 = \psi_e\dot{\psi}_e = \psi_e(\dot{\psi}_r - r) \quad (17)$$

Similarly, in order to let $\dot{V}_4$ negative, we introduce a virtual control of yaw rate that satisfies $r_e = \alpha_r - r$. This control can be expressed as follows:

$$\alpha_r = k_{\psi e}\psi_e + \dot{\psi}_r \quad (18)$$

where $k_{\psi e}$ is the designed positive constant.

In order to stabilize the new error signal, we define LFC:

$$V_5 = V_4 + \frac{1}{2}r_e^2 \quad (19)$$

Differentiating both sides of (19) gives the derivative of that LFC:

$$\dot{V}_5 = \dot{V}_4 + r_e\dot{r}_e = -k_{\psi e}\psi_e^2 + r_e\psi_e$$
$$+r_e[\dot{\alpha}_r - f_r(\theta) - \frac{1}{m_{33}}\tau_r - \frac{1}{m_{33}}\tau_{wr}] \quad (20)$$

In order to stabilize the heading error and yaw velocity error, we choose the control law τ_r as follows:

$$\tau_r = m_{33}[k_{re}r_e + \dot{\alpha}_r + \psi_e - \hat{f}_r(\theta) + \delta_r\hat{\tau}_{mwr\max}r_e] \quad (21)$$

where k_{re} and δ_r are the designed positive constants, $\hat{f}_r(\theta)$ is the estimate of the nonlinear hydrodynamic term, and $\hat{\tau}_{wr\max}$ is the estimate of the upper bound of the yaw moment caused by waves. The corresponding update laws are chosen as follows:

$$\dot{\hat{f}}_r(\theta) = \Gamma_r[-r_e - a_r(\hat{f}_r(\theta) - \hat{f}_{r0}(\theta))]$$
$$\dot{\hat{\tau}}_{mwr\max} = \gamma_r[\delta_r r_e^2 - a_{tr}(\hat{\tau}_{mwr\max} - \hat{\tau}_{mwr\max}(0))] \quad (22)$$

where Γ_r, γ_r, a_r and a_{tr} are the positive designed parameters, while $\hat{f}_{r0}(\theta)$ and $\hat{\tau}_{wr\max}(0)$ are the initial values of the corresponding update state.

If we intend to stabilize the estimation errors, the following Lyapunov function is selected:

$$V_6 = V_5 + \frac{1}{2\Gamma_r}\tilde{f}_r^2(\theta) + \frac{1}{2\gamma_r}\tilde{\tau}_{mwr\max}^2 \quad (23)$$

Its derivative yields:

$$\dot{V}_6 = \dot{V}_5 + \frac{1}{\Gamma_r}\tilde{f}_r(\theta)\dot{\hat{f}}_r(\theta) + \frac{1}{\gamma_r}\tilde{\tau}_{mwr\max}\dot{\hat{\tau}}_{mwr\max}$$
$$= -k_{\psi e}\psi_e^2 - k_{re}r_e^2 + r_e\tilde{f}_r(\theta) + \frac{1}{\Gamma_r}\tilde{f}_r(\theta)\dot{\hat{f}}_r(\theta)$$
$$-\delta_r\hat{\tau}_{mwr\max}r_e^2 - \frac{r_e}{m_{33}}\tau_{wr} + \frac{1}{\gamma_r}\tilde{\tau}_{mwr\max}\dot{\hat{\tau}}_{mwr\max}$$
$$\le -k_{\psi e}\psi_e^2 - k_{re}r_e^2 - a_r\tilde{f}_r(\theta)[\tilde{f}_r(\theta) + f_r(\theta) - \hat{f}_{r0}(\theta)]$$
$$-\delta_r\hat{\tau}_{mwr\max}r_e^2 + |r_e|\tau_{mwr\max} + \tilde{\tau}_{mwr\max}\delta_r r_e^2$$
$$-\tilde{\tau}_{mwr\max}[a_{tr}(\tilde{\tau}_{mwr\max} + \tau_{mwr\max} - \hat{\tau}_{mwr\max}(0))]$$
$$\le -k_{\psi e}\psi_e^2 - k_{re}r_e^2 - a_r\tilde{f}_r^2(\theta)$$
$$-a_r\tilde{f}_r(\theta)[f_r(\theta) - \hat{f}_{r0}(\theta)] - \delta_r\hat{\tau}_{mwr\max}r_e^2$$
$$+\delta_r\tau_{mwr\max}r_e^2 + \frac{1}{4\delta_r}\tau_{mwr\max} + \delta_r\tilde{\tau}_{mwr\max}r_e^2$$
$$-a_{tr}\tilde{\tau}_{mwr\max}^2 - a_{tr}[\tau_{mwr\max} - \hat{\tau}_{mwr\max}(0)]$$
$$\le -\lambda_r V_6 + \rho_r \quad (24)$$

where: $\lambda_r = \min\{2k_{re}, 2k_{\psi e}, a_r, \Gamma_r, a_{tr}\gamma_r\}$, and

$$\rho_r = \frac{1}{4\delta_r}\tau_{mwr\max} + \frac{1}{2}[\left|\tilde{f}_r(\theta)\right|^2 + \left|f_r(\theta) - \hat{f}_{r0}(\theta)\right|^2] + \frac{1}{2}[\left|\tilde{\tau}_{mwr\max}\right|^2 + \left|\tau_{mwr\max} - \hat{\tau}_{mwr\max}(0)\right|^2]$$

is the positive constant. Then, all error signals listed in (23) are UUB.

PRE-FILTER

According to the formulas (18) and (21), the yaw control law needs the smooth first and second derivatives of the reference heading angle ψ_r. To avoid algebraic loop problems caused by the derivative modulus, and to obtain the derivative of the reference heading angle and heading rate easily, Zhang et al. [21] selected the discrete transformation method instead of the direct analytical method to get differential signals. Alternatively, a pre-filter is proposed in this paper to obtain smooth signals of ψ_r, $\dot{\psi}_r$ and $\ddot{\psi}_r$. Based on the commanded heading angle ψ_r^c calculated by the trajectory generator (3), the third order pre-filter [22] is modified as follows:

$$\dddot{\psi}_r + (2\xi + 1)\omega\ddot{\psi}_r + (2\xi + 1)\omega^2\dot{\psi}_r + \omega^3\psi_r = \omega^3\psi_r^c \quad (25)$$

where ξ is the damping, and ω is the frequency of this filter. The reference model also satisfies $\lim\psi_r(t) = \psi_r^c$ if ψ_r^c is constant. The values of filter parameters are chosen as $\xi = 1$ and $\omega = 10$.

SIMULATIONS

In this section, two simulation cases are analyzed to demonstrate the effectiveness of the proposed algorithm. The results of these simulations are compared with those obtained by Li et al. [17]. The vessel model in this paper is taken from Do et al. [22], while the external disturbance models are taken directly from Zhang et al. [21]. The initial values of the plant and controller are similar to those applied in Ref. [17], and are as follows:

$$[x(0), y(0), \psi(0), u(0), v(0), r(0)] = [-80, 20, 0, 0, 0, 0]$$

$$\hat{\tau}_{mwu\max}(0) = 0{,}7\,\tau_{mwu\max} \qquad \hat{\tau}_{mwr\max}(0) = 0{,}7\,\tau_{mwr\max}$$

$$\tau_{mwu\max} = 1 \qquad \tau_{mwr\max} = 1.5$$

$$\hat{f}_{u0}(\theta) = 0{,}7\,f_u(\theta) \qquad \hat{f}_{r0}(\theta) = 0{,}7\,f_r(\theta)$$

$$f_u(\theta) = -20 \qquad f_r(\theta) = 1$$

The parameters of the controller are defined as

$$k_{ze} = 0.1 \qquad k_{ue} = 0.5 \qquad k_{\psi e} = 0.5 \qquad k_{re} = 10$$

$$a_u = 0.002 \qquad a_r = 0.2 \qquad a_{tu} = 0.005 \qquad a_{tu} = 0.1$$

$$\Gamma_u = 0.003 \qquad \Gamma_r = 0.05$$

$$\gamma_u = \gamma_r = 1 \qquad \delta_u = \delta_r = 0.1$$

Case 1 is the curve path following. The sinusoidal reference trajectory has been taken from Do and Pan [14]. The obtained simulation results are displaced in Figs. 2–6. As shown in Fig. 2, the ship can track the reference path accurately and smoothly under the condition of time-varying disturbances and unknown dynamics. Fig. 3 compares the attitude errors and the position errors. It is observed that both methods make the tracking error quickly converge to an invariant set. However, the heading error performance is visibly improved by the proposed control law.

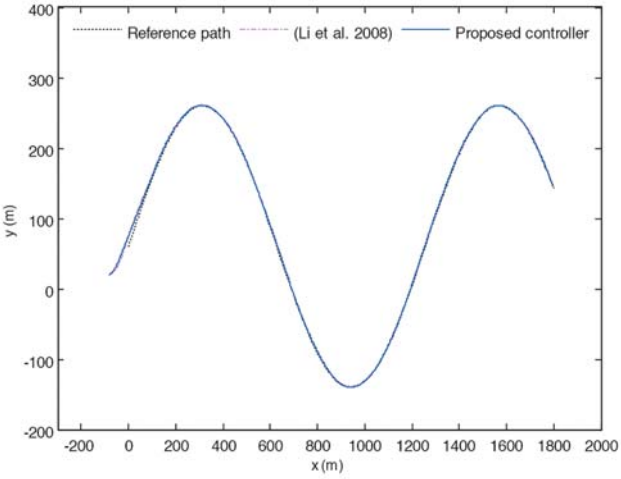

Fig. 2. Curve path tracking

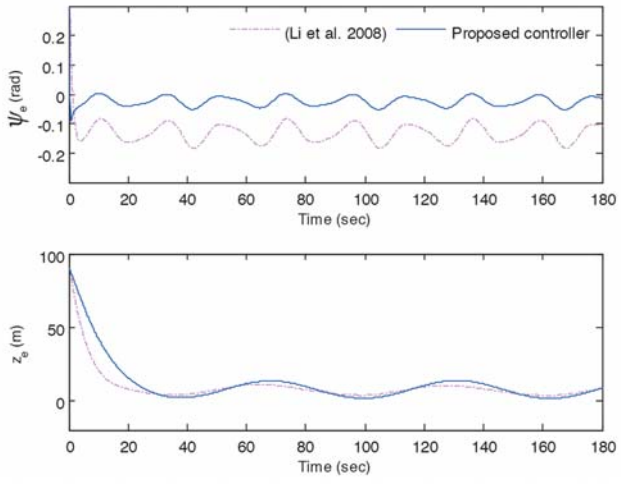

Fig. 3. Tracking errors – case 1

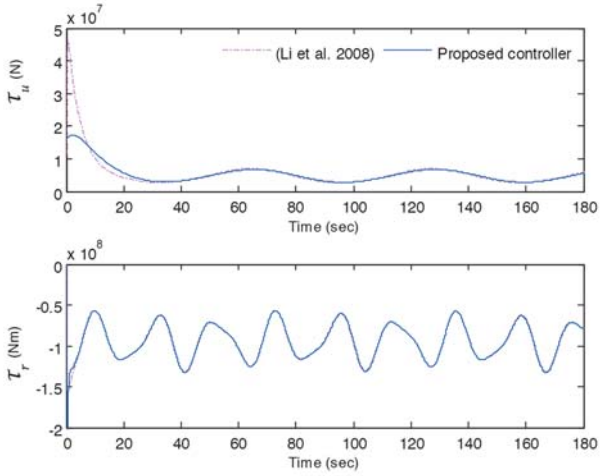

Fig. 4. Control inputs – case 1

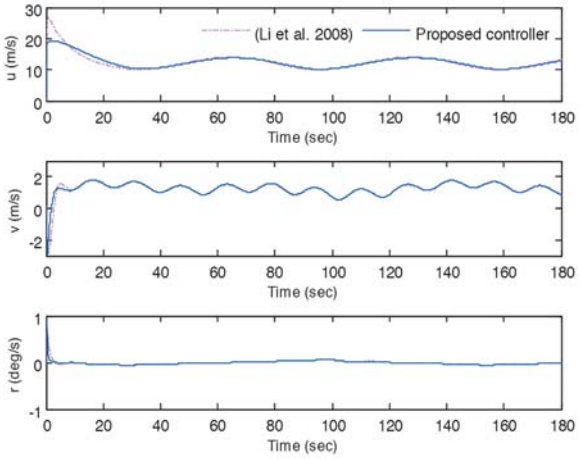

Fig. 5. Ship motion responses – case 1

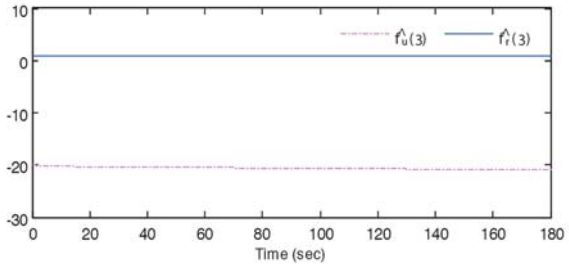

Fig. 6. Estimates of nonlinear hydrodynamic terms – case 1

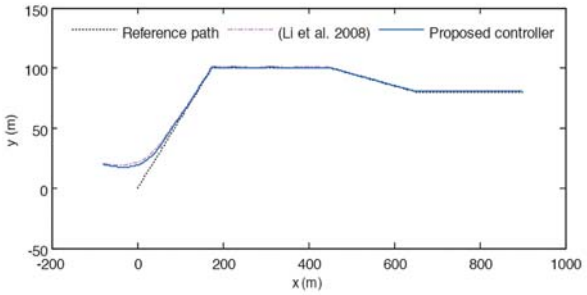

Fig. 7. Point to point navigation

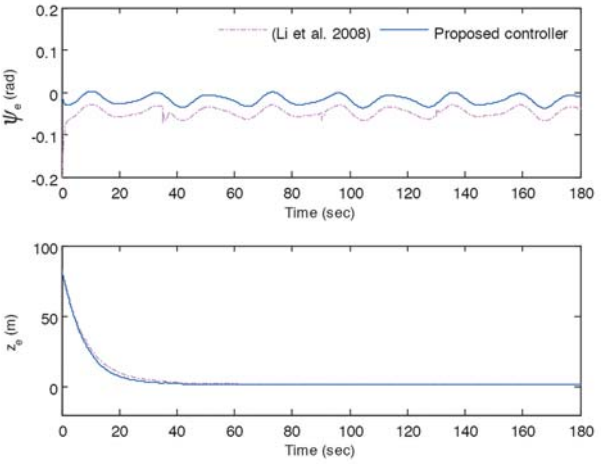

Fig. 8. Tracking errors – case 2

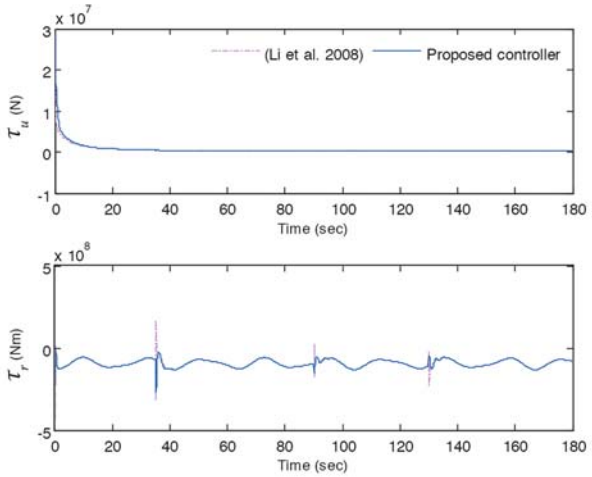

Fig. 9. Control inputs – case 2

Fig. 4 compares the control input surge forces and the yaw moments. It can be seen that the proposed algorithm can produce a much smoother surge control force, which decreases the power consumption by the propeller and the resultant energy cost. The ship motion responses are compared in Fig. 5, and the estimates of the nonlinear hydrodynamic force and moment, given in (12) and (22), are presented in Fig. 6.

Case 2 is the point-to-point navigation. Following the route analyzed by Do et al. [23], we assume that the vessel moves along the trajectory which consists of straight lines connecting the desired points: (0,0), (175,100), (450,100) and (650,80). Consequently, the reference trajectory is non-smooth. Figs. 7–11 present the simulation results. Fig. 7 shows that both control schemes force the underactuated vessel to track the predefined path closely. The position tracking errors converge to small nonzero values at similar rates, as shown in Fig. 8. The proposed controller can effectively reduce the heading error and let it converge to a smaller set.

The corresponding control inputs are detailed in Fig. 9. As can be seen, similar control forces and moments are generated by the two control laws. Their high magnitudes mainly result from the fact that the system with large-magnitude external disturbances is simulated. Several

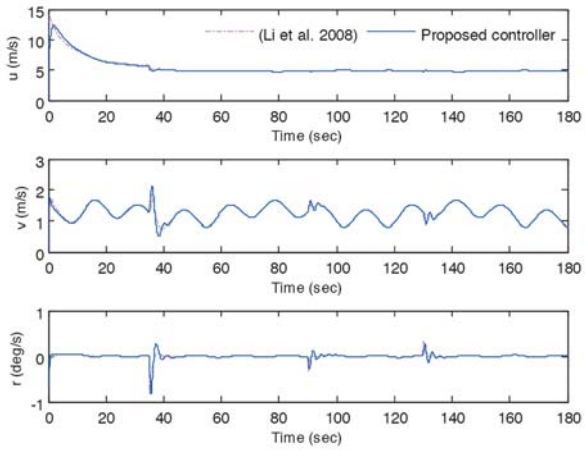

Fig. 10. Ship motion responses – case 2

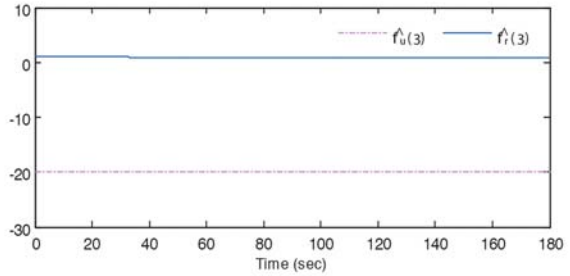

Fig. 11. Estimates of nonlinear hydrodynamic terms – case 2

picks observed in τ_r are due to the inflection points in the trajectory. Furthermore, compared to the controller in Li et al [17], the proposed controller can more effectively reject the chattering (picks) of the yaw moment when the vessel crosses the waypoint. These picks are mainly caused by the large inertia of the ship and the non-smooth reference heading. The corresponding ship motion responses in Case 2 are addressed in Fig. 10, and the corresponding estimates of the nonlinear hydrodynamic force and moment, given in (12) and (22), are presented in Fig. 11.

CONCLUSIONS

The paper presents a practical backstepping controller that is able to steer an underactuated surface vessel along a desired trajectory under the conditions of time-varying disturbances and uncertainties. Under the assumption that the sway dynamics is passive bounded, the adaptive technique is applied to estimate the nonlinear hydrodynamic term and the upper bound of the unknown external disturbances. This method does not require the knowledge about the non-modeled dynamics. In order to relax the assumption of smooth reference heading and trajectory, a pre-filter is applied to smooth the commanded heading signal and enhance the system robustness. By comparison with the scheme in Li et al. [17], the presented numerical simulations demonstrate the validity and effectiveness of the proposed controller.

REFERENCES

1. Liu T., Dong Z., Du H., Song L. Mao Y.: *Path following control of the underactuated USV on the improved line-of-sight guidance algorithm*. Polish Maritime Research, 2017, 24(1): 3–11.

2. Shojaei K., DolatshahiM.: *Line-of-sight target tracking control of underactuated autonomous underwater vehicles*. Ocean Engineering, 2017, 133: 244–252.

3. Liu C., Sun J., Zou Z.: *Integrated line of sight and model predictive control for path following and roll motion control using rudder*. Journal of Ship Research, 2015, 59(2): 99–112.

4. Zhang J., Sun T., Liu Z.: *Robust model predictive control for path following of underactuated surface vessels with roll constraints*. Ocean Engineering, 2017, 143: 125–132.

5. Moreira L., Fossen T.I., Soares C.G.: *Path following control system for a tanker ship model*. Ocean Engineering, 2007, 34(14): 2074–2085.

6. Hu C., Wang R., Yan F., Chen N.: *Robust composite nonlinear feedback path following control for underactuated surface vessels with desired heading amendment*. IEEE Transactions on Industrial Electronic, 2016, 63(10): 6386–6394.

7. Das S., Talole S.E.: *GESO based robust output tracking controller for marine vessels*. Ocean Engineering, 2016, 121: 156–165.

8. Alfi A., Shokrzadeh A., Asadi M.: *Reliability analysis of H-infinity control for a container ship in way-point tracking*. Applied Ocean Research, 2015, 52: 309–316.

9. Ashrafiuon H., Muske K.R., Mcninch L.C., Slotan R.A.: *Sliding mode tracking control of surface vessels*. IEEE Transactions on Industrial Electronics, 2008, 55(11): 4004–4012.

10. Yu R., Zhu Q., Xia G., Liu Z.: *Sliding mode tracking control of an underactuated surface vessel*. IET Control Theory and Applications, 2012, 6(3): 461–466.

11. Shin J., Kwak D., Lee Y.: *Adaptive path following control for an unmanned surface vessel using an identified dynamic model*. IEEE Transactions on Mechatronics, 2017, 22(3): 1143–1153.

12. Xu H., Soares C.G.: *Vector field path following for surface marine vessel and parameter identification based on LS-SVM*. Ocean Engineering, 2016, 113: 151–161.

13. Zhang G., Zhang X.: *Practical robust neural path following control for underactuated marine vessels with actuators uncertainties*. Asian Journal of Control, 2017, 19(1): 173–187.

14. Do K.D., Pan J.: *Global robust adaptive path following of underactuated ships*. Automatica, 2006, 42(10): 1713–1722.

15. Do K.D.: *Practical control of underactuated ships*. Ocean Engineering, 2010, 37(13): 1111–1119.

16. Li Z., Sun J., Oh S.: *Design, analysis and experimental validation of a robust nonlinear path following controller for marine surface vessels*. Automatica, 2009, 45(7): 1649–1658.

17. Li J., Lee P.M., Jun B.H., Kim Y.K.: *Point-to-point navigation of underactuated ships*. Automatica, 2008, 44(12): 3201–3205.

18. Sun Z., Zhang G., Yi B., Zhang W.: *Practical proportional integral sliding mode control for underactuated surface ship in the fields of marine practice*. Ocean Engineering, 2017, 142: 217–223.

19. Xu J., Wang M., Qiao L.: *Dynamical sliding mode control for trajectory tracking of underactuated unmanned underwater vehicles*. Ocean Engineering, 2015, 105: 54–63.

20. Peara L.P., Soares C.G.: *Pre-filtered sliding mode control for nonlinear ship steering associated with disturbances*. Ocean Engineering, 2012, 51(3): 49–62.

21. Zhang G., Zhang X., Zhang Y.: *Adaptive neural path-following control for underactuated ships in fields of marine practice*. Ocean Engineering, 2015, 104: 558–567.

22. Fossen T.I.: *Handbook of marine craft hydrodynamics and motion control*. Wiley, United Kingdom 2011.

23. Do K.D., Jiang Z.P., Pan J.: *Robust adaptive path following of underactuated ships*. Automatica, 2004, 40(6): 929–944.

CONTACT WITH THE AUTHORS

Zhiquan Liu
e-mail: liuzhiquan215@sina.com

Key Laboratory of Marine Technology
and Control Engineering
Ministry of Communications
Shanghai Maritime University
1550 Haigang AVE, 201306 Shanghai
China

sciendo

POLISH MARITIME RESEARCH 2 (102) 2019 Vol. 26; pp. 76-84
10.2478/pomr-2019-0027

NUMERICAL ANALYSIS OF AN IMPACT OF PLANNED LOCATION OF SEWAGE DISCHARGE ON NATURA 2000 AREAS – THE DEAD VISTULA REGION CASE STUDY

Piotr Zima
Gdańsk University of Technology, Faculty of Civil and Environment Engineering, Poland

ABSTRACT

This article presents results of an analysis of impact of a designed discharge of contaminated water into the Dead Vistula (Wisła Martwa) in the region of the Isthmus (Przesmyk) with the aim of determination of a possible effect of the pollution onto protected areas of Natura 2000 (bird habitats and sites, especially the Bird Paradise – Ptasi Raj) nature reserve. The analysis was conducted on the basis of the two-dimensional modelling of unsteady transport of non-degradable dissolved matter. To this end, a numerical model of a section of the Dead Vistula was worked out. Four scenarios of hydro-dynamical conditions (2 – for average weather conditions and 2 – for stormy weather conditions) were selected. To solving the equation of pollution migration the finite volumes method (MOS) was applied. Two localizations of contaminated water discharge outlet were considered, namely: the first from the side of Siennicki Bridge before the Isthmus and the other in the section of the Brave Vistula (Wisła Śmiała) downstream the Isthmus. The obtained results made it possible to assess positively the first localization of the designed discharge outlet. In the other case there is a fear that at unfavourable hydro-meteorological conditions a water pollution may happen over Natura 2000 protected areas.

Keywords: Numerical simulations, pollution migration, method of finite volumes, dispersion

INTRODUCTION

In Computer simulations of pollution migration in rivers are an important tool for aiding design projects in the scope of localization of sewage discharge outlets. They can be also used for analyzing dispersion of pollutants and their impact on receiving body waters and surrounding environment [20, 21]. This is especially important in the case of water areas close to protected regions for which a sewage discharge localization may form a threat of pollution. Unfavourable changes in water physical, chemical or bacteriological features may then occur due to introducing excessive amounts of inorganic and organic substances or water of an elevated temperature. Each of the factors (even in a small quantity) may unfavourably affects natural biocoenosis in water environment, that especially in protected regions may disturb homeostasis, i.e. a dynamic equilibrium in which the ecosystem remains [10]. The following anthropogenic pollutants of surface waters belong to the most frequently occurring [7]: pesticides, surface active substances, crude oil hydrocarbons, phenols, polychlorinated biphenyls and heavy metals (lead, copper, chrome, cadmium, mercury and zinc). Warm water (thermal pollution) is also a threat which may be especially dangerous for surface waters stagnant or slow running. Most of the anthropogenic water pollutants act toxically onto water organisms and some of them may be deposited in the ecosystem for a long time. For this reason it is important to correctly locate sewage discharge outlets and estimate their effect on a sewage receiving body. One of the methods to do it is to perform an analysis of such discharge by using computer simulation based on mathematical modelling.

Mathematical modelling of contamination spreading may be conducted in many ways [16]. The first phase of such

Fig. 1. Image of the Dead Vistula region with marked Natura 2000 protected areas and planned localization sites of contaminated water discharge outlets (based on: ortophotomap received from http://mapy.geoportal.gov.pl)

procedure is to work out a mathematical model of a considered object. Then, a mathematical model for description of factors affecting an analyzed process should be formed [19, 2]. In case of pollution migration it is necessary to combine into a functional whole at least two important elements: a water flow description model and pollution transport description model. The notion of "pollution" is related, in this case, to every factor which is discharge in an excessive amount to receiving body.

This paper presents an analysis of effects of designed sewage discharge to the Dead Vistula, performed with the use of numerical simulations. This case constitutes one of the concepts of localization of of the discharge and is an interesting issue due to dispersion conditions of the contaminated water. The analysis was focused on a site close to the marina and a specific pass in the Dead Vistula region, where water flow is very diversified spatially. Around the discharge site water flow direction depends on hydro-meteorological conditions. In the neighbourhood of the marina flow velocity ceases practically to zero forming dead zones of difficult exchange of water. Next, the water flows towards the pass in which due to the narrowing its velocity increases many times. Behind the pass there is a short section of the Brave Vistula with neighbouring terrain of Natura 2000 protected areas (bird habitats and sites, in particular, the nature reserve Ptasi Raj – Birds' Paradise) (Fig. 1). Close localization of the designed sewage discharge installations requires to perform an analysis of their effect on the protected areas.

The Dead Vistula is a part of the hydrographically complicated estuary which has been formed for the last centuries. (Fig. 1). The region is characteristic of mutual interaction of inland and sea waters. The Dead Vistula is connected to sea through two arms: the New Port canal and Brave Vistula. This fact significantly affects hydrodynamic conditions present in the Dead Vistula, in which water motion is determined first of all by sea states and blowing winds. An analysis of meteorological data recorded for the last 15 years showed that over the considered area the westerly winds of the mean speed of abt. 5 m/s dominate [22]. There were also observed winds of 15 and 25 m/s speed from this direction [8]. In this work the case of the easterly wind of 5 m/s speed was also taken into account, the significant case affecting the spread of contaminations in the area of potential sewage discharge localization sites.

MATHEMATICAL MODEL

In case of broad rivers the most frequently applied are flat two-dimensional models vertically averaged (in depth) in which a real flow area is represented by the two-dimensional flow in x-y plane [17, 15, 16]. The works associated with an analysis of contamination spreading require first of all to determine hydrodynamic conditions occurring in a receiving body. In rivers it can be achieved by determining velocity distribution as well as water depth (resulting from ordinates of bottom and water surface level). In this paper the results of simulation of hydrodynamic conditions in the considered area, carried out for a few extreme calculation scenarios, were taken into account acc. [22].The results were obtained from a simplified model by solving a modified Helmholtz equation [1], in which effect of wind generated stresses was taken into consideration. Four scenarios on hydro-meteorological conditions resulting from sea states

and wind speed were assumed. For the conditions, the calculations of spreading the contamination in the form of a dissolved, permanent, non-degradable matter were performed. Localization of two potential discharge outlets in the considered section of the Dead Vistula (Fig. 1) as well as their impact on the neighbouring Natura 2000 protected areas were analyzed. The localization sites were selected based on an analysis of economic conditions for a potential industrial plant situated on a free industrial development area in this region.

THE ASSUMED SOLUTION SPACE AND SPEED DISTRIBUTION

In compliance with the assumed scope of the work the results of calculation of velocity distribution presented in [22] were used for simulation of pollution transport. There was assumed a numerical model with taking into account bathymetry of the section of the Dead Vistula from the cross-section at Siennicki Bridge up to the cross-section at Sobieszewo (abt. 8,5 km long) together with 2,5 km section of the Brave Vistula up to its outlet to the Bay of Gdansk. By making use of the available data on the measurement calculation cross-sections (20 transverse cross-sections of the river bed) the numerical model of the river bed along the considered section of the Dead Vistula was generated (Fig. 2). The bathymetry between the measurement cross-sections was generated by linear interpolation.

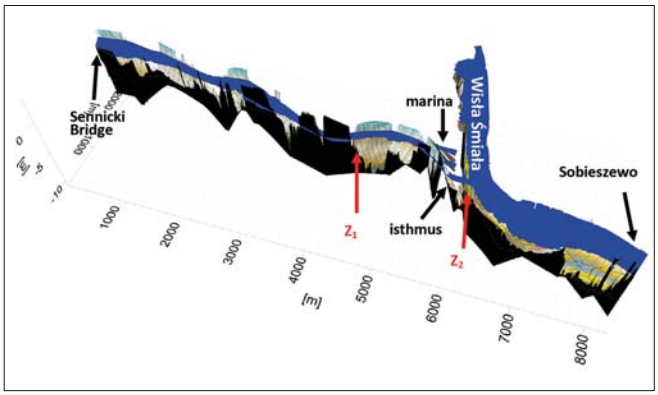

Fig. 2. Numerical model of the section of the Dead Vistula from Sobieszewo Bridge up to its outlet to the Bay of Gdansk together with the branch from the Watershed (Przełom) up to Siennicki Bridge (Z_1, Z_2 – planned sewage discharge localization sites)

In the publication [22] there were presented the results of hydrodynamic simulations for 4 hydro-meteorological conditions (for a given sea state, water level in the Dead Vistula as well as wind direction and speed – Tab. 1). The conditions (in the form of two-dimensional fields of water velocity and depth) were taken as input data to pollution transport model in order to determine their impact on water state in the receiver body and Natura 2000 protected areas. Two scenarios for the moderate conditions were assumed, namely: the easterly and westerly winds of 5 m/s speed and two scenarios for the extreme conditions – the westerly winds of 15 m/s and 25 m/s speed, respectively. The extreme conditions were assumed based on the available data from hydro-meteorological measurements and observations [8].

TRANSPORT EQUATION FOR DISSOLVED SUBSTANCE

Transport of indecomposable substance dissolved in two-dimensional space can be described by means of the following equation [3, 13, 14]:

$$\frac{\partial(hc)}{\partial t}+\frac{\partial(hu_x c)}{\partial x}+\frac{\partial(hu_y c)}{\partial y}=$$
$$\frac{1}{h}\frac{\partial}{\partial x}\left(hD_{xx}\frac{\partial c}{\partial x}+hD_{xy}\frac{\partial c}{\partial y}\right)+\frac{1}{h}\frac{\partial}{\partial y}\left(hD_{yx}\frac{\partial c}{\partial x}+hD_{yy}\frac{\partial c}{\partial y}\right) \quad (1)$$

where: t – time, x, y – spatial variables, h – depth, c – dissolved matter concentration, u_x, u_y – coordinates of the velocity vector **u**. The coordinates of the dispersion tensor **D** are defined as follows [5]:

$$D_{xx}=D_L n^2_x+D_T n^2_y$$
$$D_{xy}=D_{yx}=(D_L+D_T)\,n_x n_y \quad (2)$$
$$D_{yy}=D_L n^2_y+D_T n^2_x$$

where: n_x, n_y – the coordinates of the velocity field directional vector:

$$n_x=\frac{u_x}{|\mathbf{u}|},\ n_y=\frac{u_y}{|\mathbf{u}|}$$

The longitudinal coordinates D_L and transverse ones D_T of the dispersion tensor (2) are described by the Elder's formula [6]:

Tab. 1. Overall characteristics of the assumed variants of hydro-meteorological conditions applied to calculations of spreading the pollution over the analyzed section of the Dead Vistula

Variant	Sea state	Wind		Average flow speed and direction in the cross – section at:							
				Siennicki Bridge		Sobieszewo		Brave Vistual (outlet)		The Pass (Isthmus)	
	[m a.s.l]	[m/s]	[–]	[m/s]	[–]	[m/s]	[–]	[m/s]	[–]	[m/s]	[–]
1.	0.00	5	← E	0.04	←	0.02	←	0.05	↓	0.25	←
2.	0.00	5	→ W	0.06	→	0.03	→	0.05	↑	0.28	→
3.	0.70	15	→ W	0.36	→	0.32	→	0.62	↑	1.51	→
4.	1.25	25	→ W	0.57	←	0.53	→	2.96	↓	1.02	←

$$D_L = \alpha \cdot h \cdot v^* \quad 30 < \alpha < 3000$$
$$D_T = \beta \cdot h \cdot v^* \quad 0.15 < \beta < 0.30 \tag{3}$$

where: v^* – the so called dynamic velocity acc. Prandtl, α, β – constants. In this work $\alpha = 300$ and $\beta = 0.23$ was assumed. The values were confirmed by investigations carried out earlier in broad and shallow rivers [9].

Eq. (1) formally expresses the mass conservation law for non-degradable matter (described by the mass concentration c) added to water solution. Time change of the solution component concentration c results from mass flow due to advection, mass motion against carrier molecules (diffusion) as well as dispersion (which results from the averaging along one of the variables, depth in this case). The taking into account additional effects (e.g. biological or chemical) makes it necessary to expand Eq. (1) by terms describing a loss or increase of dissolved substance mass (e.g. reaction equations). This is frequent practice in case of biodegradable substances, which – if applied – accelerates drop in concentration of organic contaminations and limits their spatial range. The omitting of the terms (especially in case of lacking information on factors affecting reaction rate of self-cleaning processes) makes it possible to assess maximum range of contaminations resulting from their analyzed discharge. Such approach was selected for purposes of this work.

METHOD OF SOLVING

In a general case the solving of Eq. (1) is possible only by means of numerical methods [16]. In this work the method of finite volumes (MOS) was applied. To integrate Eq. (1) in the two-dimensional space (x, y) it is necessary to transform a continuous area to a discrete one by replacing it with computational cells [11]. The assumed computational area (Fig. 2) was divided into square elements (cells), where $\Delta x = \Delta y$ (Fig. 3). The approach results in that values of the concentration c in the cell centre points (their centres of gravity), (at node i, j) are unknown, whereas values of the velocity vector **u** are given in the mesh points located in the cell corners (but having half-step values between step i and j). Intermediate values between mesh nodes (necessary in determining values of flow rates through particular edges) were calculated by averaging neighbouring values. It deals both with values of the concentration c and velocity vector components u_x and u_y.

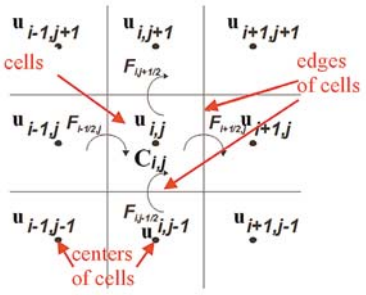

Fig. 3. Split of the computational area into two-dimensional cells and the assumed parameters of the models used for solving the equation of non-stationary transport of contaminations

The MOS applied to solving the equation of non-stationary transport of dissolved substance relates to physical laws of behaviour at the level of control volumes. It can be described by using the homogeneous hyperbolic equation as follows [11]:

$$\frac{\partial(hc)}{\partial t} + \frac{\partial(hF_x)}{\partial x} + \frac{\partial(hF_y)}{\partial y} = 0 \tag{4}$$

where: F_x, F_y – flow rates through computational cell edges, defined as follows:

$$F_x = u_x c - \frac{1}{h} D_{xx} \frac{\partial c}{\partial x} - \frac{1}{h} D_{xy} \frac{\partial c}{\partial y},$$
$$F_y = u_y c - \frac{1}{h} D_{yy} \frac{\partial c}{\partial y} - \frac{1}{h} D_{yx} \frac{\partial c}{\partial x} \tag{5}$$

To determine values of flow rates trough cell edges in the advection part of the Eq. (4) taken together with the flow rates defined by Eq. (5) the open scheme of Lax-Wendroff [12] was used. In the case of the dispersion equation the central differences schemes were employed. In the method of integration of Eq. (1) there was assumed that control area is equivalent to mesh cell. In the phase of hydro-dynamical calculations wind effect was taken into account in result of which velocity and depth distribution – an element of solution of Eq. (1) – was obtained.

Eq. (1) of pollution migration is a partial differential equation which describes distribution of their concentration over a given area in function of time. To solve the equation additional limiting conditions are to be fulfilled, namely: an initial condition and boundary conditions. In this case the initial condition is the contaminations concentration over the whole considered area in the beginning instance of simulation (for $t = 0$), i.e. c (x, y, $t = 0$) = c_0. In addition, two types of boundary conditions were assumed. At the impervious edge the Neumann's condition of the following form was used:

$$\frac{\partial c}{\partial n} = 0 \tag{6}$$

where Eq. (6) means that the normal flux of mass towards the area edge is equal to zero. In order to apply the condition it was necessary to modify the final version of difference analogue of Eq. (1). And, at the permeable edge the flux in the condition (6) was estimated on the basis of a result from the preceding step. In the discharge outlet Dirichlet condition was applied as follows:

$$c = const \tag{7}$$

The application of the condition consists in using Eq. 7 directly in the calculation node i, j.

To assure stability of the obtained solution the condition of Courant–Friedrichs–Lewy (CFL) had to be fulfilled [4, 18]:

$$\max\left(\frac{\Delta t^m}{\Delta x}\max_c |F_x'(c)|, \frac{\Delta t^m}{\Delta y}\max_c |F_y'(c)|\right) \le \frac{1}{8} \tag{8}$$

where: m – time level, Δt – time step, Δx, Δy – spatial steps (in x and y direction, respectively). At the determined spatial

mesh dimensions Δx and Δy, the integration step over the time Δt, fulfilling the condition (8), was calculated.

NUMERICAL SIMULATIONS

The simulation calculations were carried out for 4 variants described in [22], namely: for the easterly wind of 5 m/s speed (Variant 1), the westerly wind of 5 m/s speed (Variant 2) as well as the extreme conditions – the westerly wind of 15 m/s speed (Variant 3) and the westerly wind of 25 m/s speed (Variant 4). Two sewage discharge localizations based on possible technical conditions for discharging the contaminations into receiving body were selected, namely: a) at the branch of the Dead Vistula from the side of the New Port of Gdansk, Z_1, and b) at the branch of the Brave Vistula, Z_2.

Next, the simulations of pollution migration were performed with the use of the assumed model. The calculations were carried out based on the square mesh of the sides: $\Delta x = \Delta y = 5{,}0$ m. The obtained results are presented in Fig. 4 through Fig. 7. The simulations were conducted independently for every discharge outlet and every condition variant (8 computational scenarios). In view of a significant distance between the discharge outlets and a lack of their interaction the results are presented in common figures for each of the variants. In each of the figures the spreading of contaminations is presented against the background of the velocity field. To reach the aim defined in the title of this paper the discharge was assumed in the form of the indecomposable substance of the maximum concentration $c = 100\%$ at the discharge outlet, and $c = 0\%$ in the receiving body. The calculations were continued up to the moment of reaching stable distribution of concentration values. In the analyzed cases duration time of this process did not exceed 24h. After that time changes in the spatial distribution of concentration values were practically unnoticeable.

Fig. 4 presents the results of sewage discharge simulation in the conditions of the slight easterly wind of 5 m/s speed at a moderate sea state. The wind causes a water flow from the side of the Bay of Gdansk through the section of the Brave Vistula, an inflow from the side of Przegalina, a westward flow through the branch of the Dead Vistula and an outflow towards the Bay of Gdansk in the region of the New Port of Gdansk. The maximum flow velocity appeared at the Isthmus and was equal to around 0,25 m/s. In these conditions the contaminations discharged to the Dead Vistula in the assumed localizations Z_1 and Z_2 migrate along directions of the water flow caused by wind and sea states. The flux of contaminations migrates from the point Z_1 towards Siennicki Bridge. The range of impact of the discharge is observed along the river side section up to abt. 0.5 km from the discharge point. In the conditions there is no threat of reaching the protected areas by the contaminations discharged from the point Z_1. A greater potential threat may constitute the discharge from the point Z_2. However in these flow conditions water current makes that the contaminations flux is carried away toward the Isthmus. There is a lack of an observable breaking-through of the contaminations flux into the section of the Brave Vistula towards the protected areas.

The slight westerly wind blowing with 5 m/s speed at a moderate sea state results in an almost different flow circulation in the Dead Vistula (Fig. 5). In the cross-section at the Brave Vistula outlet there is visible an outflow of 0,05 m/s speed towards the Bay of Gdansk. In the region of Sobieszewo there is observed a water flow of abt. 0,03 m/s velocity coinciding with wind direction. From the side of Siennicki Bridge a water inflow with abt. 0,06 m/s velocity is observed. As a result, an eastward water flow of 0,28 m/s velocity can be observed in the branch of the Dead Vistula close to the Pass. In these conditions the spread of contaminations is quite different from that in Variant 1. The pollution discharged to the Dead Vistula waters in the point Z_1 migrate towards

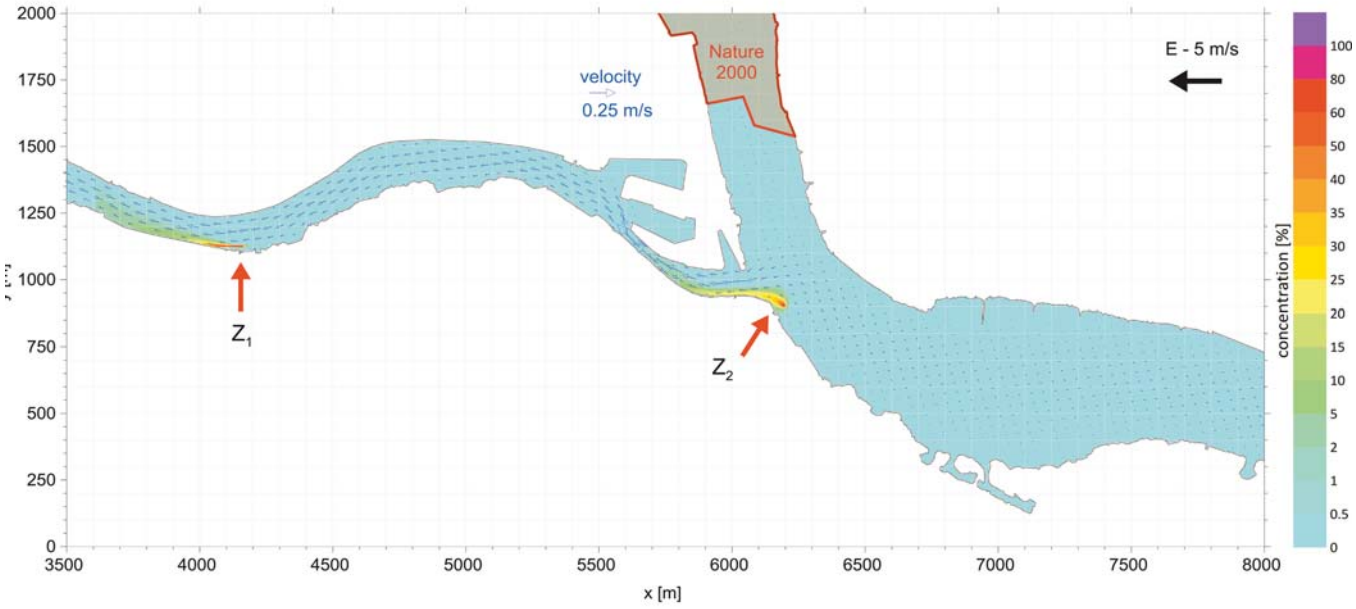

Fig. 4. Calculation results of spreading the pollution in the conditions of the easterly wind E – 5 m/s (Variant 1)

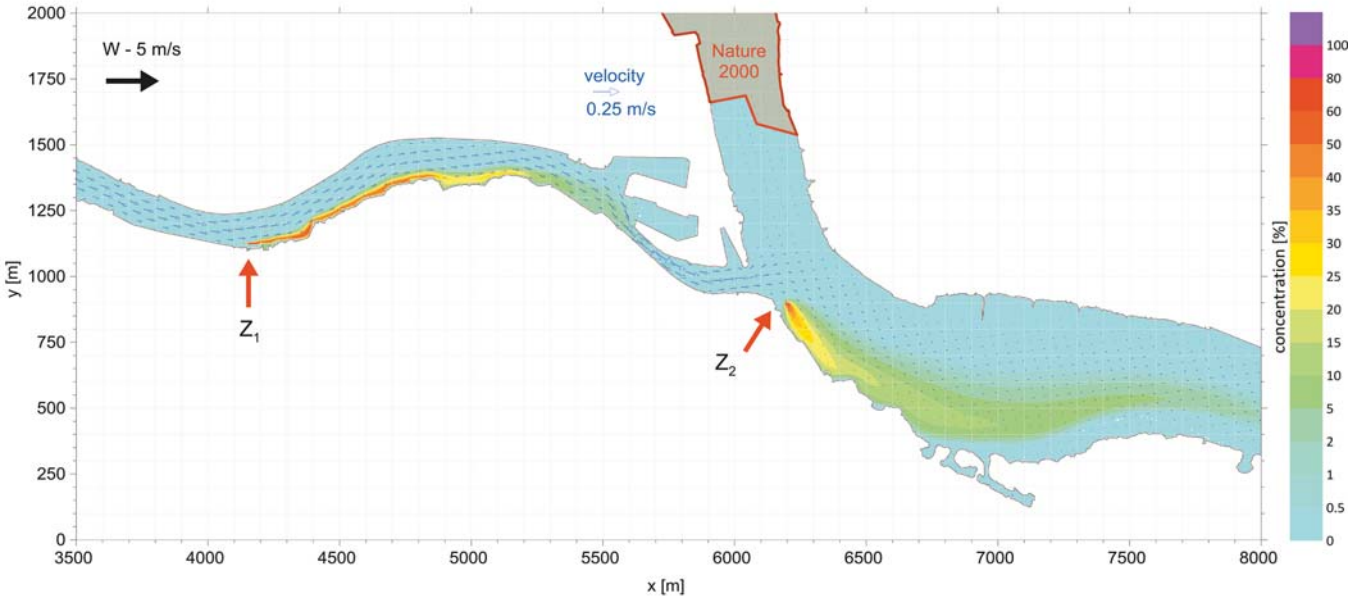

Fig. 5. Calculation results of spreading the pollution in the conditions of the westerly wind W – 5 m/s (Variant 2)

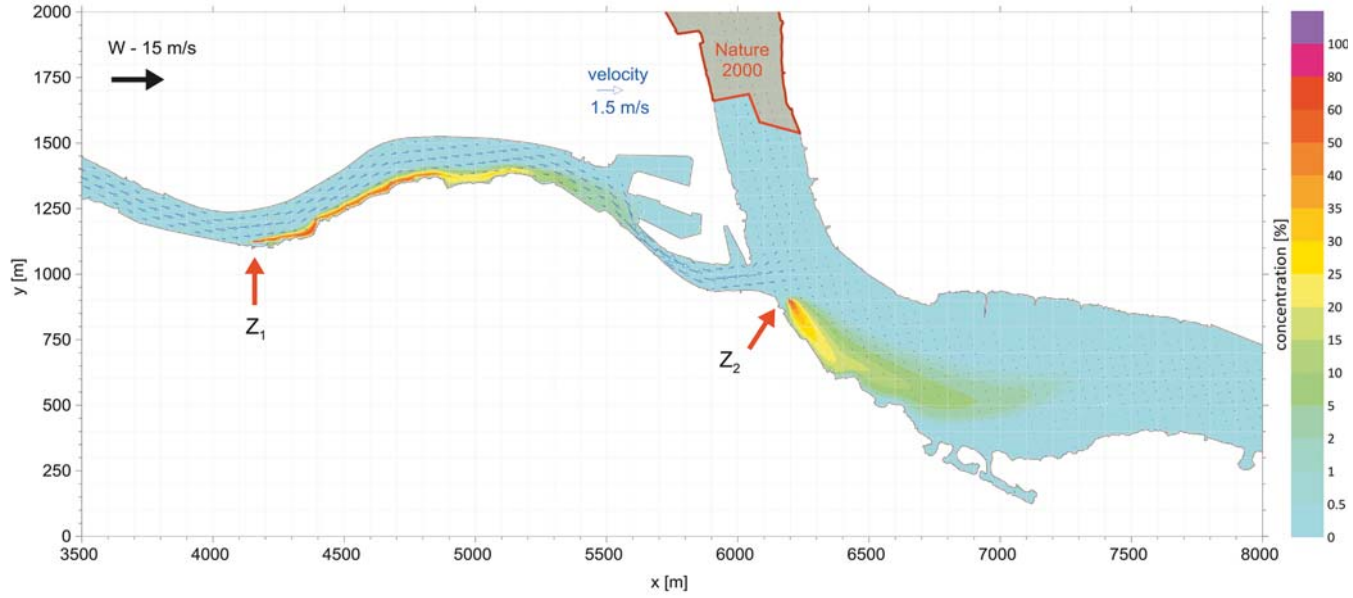

Fig. 6. Calculation results of spreading the pollution in the conditions of the westerly wind W – 15 m/s (Variant 3)

the Isthmus, and their range is observable along the river side section of abt. 2 km in length (practically up to the Isthmus itself). However no breaking – through of the contaminated water to the Brave Vistula and its migration towards Natura 2000 protected areas, occurs. In the case of the discharge from the point Z_2 the pollution migrate toward Sobieszewo along the 2.5 km river side section, i.e. in the opposite direction to the site of protected areas.

The successive two calculation variants were performed for the extreme hydro-meteorological conditions occurring in the region of the Dead Vistula. First, the simulations for the case of the westerly wind of 15 m/s speed were carried out, assuming an increase in the sea state by 0,7 m over the average (Fig. 6).

In the region of the Brave Vistula estuary the outflow of 0,6 m/s speed to the Bay of Gdansk then occurs. In the westerly branch of the Dead Vistula in the region of Siennicki Bridge an eastward flow (inflow) of abt. 0,3 ÷ 0,4 m/s speed occurs. In the easterly branch of the Dead Vistula in the region of Sobieszewo a faster eastward flow (outflow) of 0,3 m/s velocity can be observed. As a result, in the branch of the Dead Vistula a distinct eastward flow of the maximum velocity values of 1,5 m/s in the vicinity of the Isthmus appears. The bigger velocity makes that in waters of the Dead Vistula the pollution mixing processes proceed more intensive. In consequence, the range and concentration of the pollution changes. Also in this case, migration directions of contaminated water are

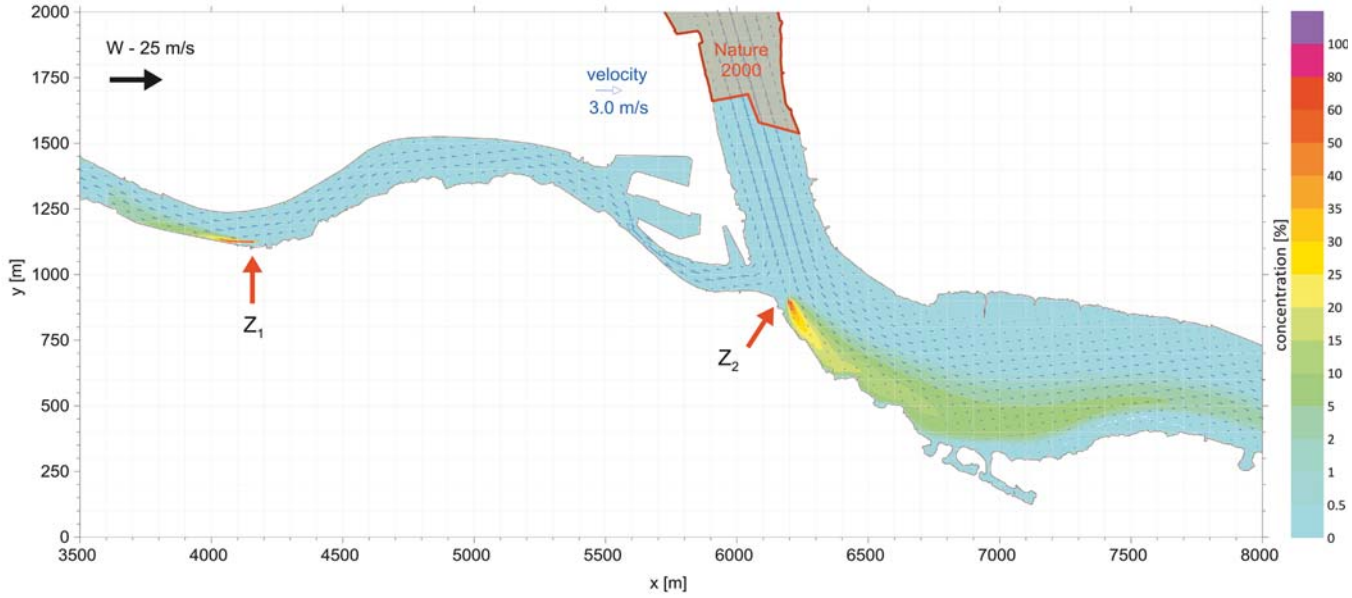

Fig. 7. Calculation results of spreading the pollution in the conditions of the westerly wind W – 25 m/s (Variant 4)

in line with those observed in the Dead Vistula branches. In this respect, directions of spreading the pollution are the same as in Variant 2. However the range of impact of the discharge in the point Z_1 reaches the section abt. 1 km long. In the case of the discharge in the point Z_2 its range is similar as that in Variant 2. There is a lack of noticeable breaking-through the flux of contaminated water towards the protected areas.

The last variant concerns the case of the westerly wind blowing with 25 m/s speed at the observed rise of sea state by 1,25 m [8] (Jasińska, 2002) over the average (Fig. 7). In such extreme conditions of the very high sea state and very fast westerly wind the flow conditions in estuaries change. Then in the region of the Brave Vistula an inflow of a very great velocity up to 3,0 m/s from the Gulf of Gdansk is observed. In the westerly branch of the Dead Vistula in the region of Siennicki Bridge a westward flow (outflow) of 0,5 – 0,6 m/s speed takes place. In the easterly branch of the Dead Vistula (in the region of Sobieszewo) a faster eastward flow (outflow) of abt. 0,5 m/s speed occurs. As a result, in the branch of the Dead Vistula a distinct westward flow with the maximum speed values of over 1,0 m/s can be observed in the vicinity of the Isthmus. The simulation of spreading the pollution from the designed discharge outlets is presented in Fig. 7. In view of the prevailing hydro-meteorological conditions their impact onto waters of the receiving body is slight and there is no potential circumstances to pollute the protected areas in question.

SUMMARY AND CONCLUSIONS

In the frame of this work there were performed computer simulations of migration process of pollution from two example localizations of industrial sewage discharge and their impact on the neighbouring Natura 2000 protected areas. The calculations were made for the section of the Dead Vistula between Sobieszewo and Siennicki Bridge together with the section of the Brave Vistula running to the Bay of Gdansk. Based on the available materials a numerical model of the considered river section was prepared. The model was supplemented with the data on water level position depending on hydro-meteorological conditions, presented in the work [8]. On the basis of the calculations given in [22]. 4 variants of hydrodynamic conditions were selected depending on wind direction and force and sea states (for the easterly wind E – 5 m/s, westerly wind W – 5 m/s as well as extreme conditions of the westerly winds: W – 15 m/s and W – 25 m/s). Next, the calculations of spreading the pollution from two selected sewage discharge localizations were performed for each of the assumed calculation variants. The results obtained from the computer simulations demonstrated that the planned sites of potential sewage discharge in the region of the Isthmus in the Dead Vistula could not cause migration of the contaminations into the Natura 2000 protected areas. A greater impact of the discharge can be observed for the moderate conditions (Variant 1 and 2). In the case of the stormy conditions the discharge range is more restrained due to intensification of their mixing processes in receiving body waters as well as the increased water flows. In the case of the discharge outlet Z_1 it may be deemed that no migration of the pollution towards the protected areas can happen.

However in the case of the discharge outlet Z_2 located in the branch of the Brave Vistula the conclusions are not so unambiguous. Though the simulations performed in 4 variants of hydro-meteorological conditions showed that a pollution of the Natura 2000 areas in the estuary section of the Brave Vistula could occur, but unfortunately it should not be considered impossible. If to assume that the water running through the Brave Vistula bed is directed towards the Gulf of Gdansk and is increased by the inflow from the Dead Vistula through the Isthmus, a water pollution from the discharge Z_2

will be possible to occur in the protected areas. However such case would be low probable because of hydro-meteorological conditions (a water outflow to the Gulf of Gdansk through the Brave Vistula and a simultaneous inflow from the Gulf in the region of the New Port of Gdansk) and also due to the fact that the section of the Dead Vistula from the side of Sobieszewo is separated from the Vistula Cutting (Przekop Wisły) by a closed lock. But, such scenario should be also taken into consideration as there is a connection through an open channel between the discharge region and protected areas. For this reason the localization of the discharge outlet in the point Z_1 is more favourable from the point of view of protection of Natura 2000 areas.

ACKNOWLEDGEMENT

This work is a part of the research project WaterPuck supported by the National Centre for Research and Development within the BIOSTRATEG III program No. BIOSTRATEG3/343927/3/NCBR/2017.

REFERENCES

1. Anderson J. D.: *Computational Fluid Dynamics. The Basics with Applications*, McGraw-Hill Inc., New York (1995), pp. 1–547.
2. Chapara S.C.: *Surface water-quality modeling*. MacGraw Hill Company, New York, (1994), pp. 1–884.
3. Crank J.: *The mathematics of diffusion*. Clarendon Press, Oxford, (1975), pp. 1–414.
4. Courant R., Friedrichs K. and Lewy H.: *On the partial difference equations of mathematical physics*, IBM Journal, (1967), pp. 215–234.
5. Czernuszenko W.: *Dispersion of pollutants in flowing surface water*. Encyclopedia of Fluid Mechanics, Surface and Groundwater flow phenomena. Houston, London, Paris: Gulf Publishing Company, 10 (1990), pp. 119–168.
6. Elder J.W.: *The dispersion of marked fluid in turbulent shear flow*. J Fluid Mech. 5, (1959), pp. 544–560.
7. Harrison R.M.: *Pollution: Causes, Effects and Control (5th ed.)*. Royal Society of Chemistry, Cambridge, (2013), pp. 1–558.
8. Jasińska E.: *Hydrology and hydrodynamics of the Dead Vistula and Vistula Cutting*, (in Polish), Wydawnictwo Instytutu Budownictwa Wodnego Polskiej Akademii Nauk, Gdańsk, (2002), pp. 1–133.
9. Kalinowska M., Rowiński P., Kubrak J., Mirosław-Świątek D.: *Scenarios of the spread of a waste heat discharge in a river – Vistula River case study*. Acta Geophys 60 (2012), pp. 214–231.
10. *Laws E.A.: Aquatic Pollution: An Introductory Text (4th ed.)*. Hoboken, NJ: John Wiley & Sons, (2017), pp. 1–760.
11. LeVeque R.J.: *Finite Volume Method for Hyperbolic Problems*. Cambridge University Press, New York, (2002), 1–578.
12. Potter D. E.: *Computational Physics*, John Wiley & Sons Ltd., Chichester (1980), pp.1–304.
13. Rutherford J.C.: *River Mixing*. Wiley, Chichester, (1994), pp. 1–362.
14. Sawicki J.M., Zima P.: *The Influence of Mixed Derivatives on The Mathematical Simulation of Pollutants Transfer*. 4th International Conference on Water Pollution, Slovenia, (1997), pp. 627–635.
15. Szydłowski M., Szpakowski W., Zima P.: *Numerical simulation of catastrophic flood: the case study of hypothetical failure of the Bielkowo hydro-power plant reservoir*, Acta Geophys 61 (2013), pp. 1229–1245.
16. Szymkiewicz R.: *Numerical Modeling in Open Channel Hydraulics*, Book Series: Water Science and Technology Library, vol. 83 (2010), pp. 1–419.
17. Tan W.Y.: *Shallow Water Hydrodynamics, Mathematical Theory and Numerical Solution for a Two-dimensional System of Shallow Water Equations*, Elsevier Oceanography Series, vol. 55 (1992), pp. 1–434.
18. Tannehill J.C., Anderson D.A. and Pletcher R.H.: *Computational Fluid Mechanics and Heat Transfer (2nd ed.),* Francis & Taylor, Philadelphia, (1997), pp.1–774.
19. Waite T.D.: Principles of Water Quality, Elsevier Academic Press, Orlando, (1984), pp. 1–287.
20. Wielgat P., Zima P.: *Analysis of the impact of the planned sewage discharge from the 'North' Power Plant on the Vistula water quality*, 16th International Multidisciplinary Scientific GeoConference SGEM 2016, Vienna, Book 3 vol. 3 (2016), pp. 19–26.
21. Zima P: *Mathematical Modeling of the Impact Range of Sewage Discharge on the Vistula Water Quality in the Region of Włocławek*. In: Kalinowska M, Mrokowska M, Rowiński P. (eds) Free Surface Flows and Transport Processes. GeoPlanet: Earth and Planetary Sciences. Springer, Cham, (2018) pp. 489–502.
22. Zima P.: *Modeling of the Two-Dimensional Flow Caused by Sea Conditions and Wind Stresses on the Example of Dead Vistula*. Pol. Marit. Res., vol. 97 (2018), pp. 166–171.

CONTACT WITH THE AUTHORS

Piotr Zima
e-mail: piotr.zima@pg.edu.pl

Gdańsk University of Technology
Faculty of Civil and Environment Engineering
Narutowicza 11/12
80–233 Gdańsk
Poland

sciendo

POLISH MARITIME RESEARCH 2 (102) 2019 Vol. 26; pp. 85-92
10.2478/pomr-2019-0028

ENERGY EFFICIENT SMALL INLAND PASSENGER SHUTTLE FERRY WITH HYBRID PROPULSION - CONCEPT DESIGN, CALCULATIONS AND MODEL TESTS

Magdalena Kunicka, Wojciech Litwin
Gdańsk University of Technology, Poland

ABSTRACT

In recent years, there has been a significant development in "green" and energy efficient propulsion systems, which fits into the general trend of environmentally friendly "green shipping".
The pursued goal is to construct a safe passenger ship that is low in energy demand and equipped with a highly energy efficient, emission-free propulsion system.
The paper presents main problems encountered by designers of a small, hybrid-powered ferry powered lithium batteries. The conducted research allowed to create a design of an energy efficient hull shape, which decreases the demand for energy. Completed remote control model tests resulted in a proposal of an energy efficient and safe propulsion system with good manoeuvring capabilities. Measurements completed on an existing ferry permitted completing energy balance and forming an energy management policy.
The paper contains the emission calculations computed for the existing ferry that are necessary for the environmental impact analysis.
The soon to be constructed, newly designed vessel will provide a valuable contribution to hybrid-propulsion, energy management and unmanned technologies research.

Keywords: ship hybrid propulsion, energy efficiency, green shipping, energy management
Abbreviations: BMS – Battery Management System
RACK – universal terminal with connecting rail for easy connecting electrical modules, usually ventilated and with integrated energy supply

INTRODUCTION

Recent years have witnessed a significant increase of interest in eco-friendly ship propulsion systems being part of the environmentally conscious green shipping trend. This is caused by a number of factors, including economic reasons, possibilities of employing modern and sophisticated technological solutions and operational level savings [1] [2][3][4]. Environmental protection regulations become increasingly restrictive with each passing year. An example of this is creating strictly defining acceptable levels of toxic substance emissions, especially regarding carbon dioxide, sulphur and nitrogen compounds, which are closely linked to fuel quality and consumption. In addition, the age and technical condition of used propulsion systems is being regulated [5][6]. At the same time, the accompanying issue of noise pollution is an increasing source of concern [7][8]. This directly results in a conclusion that in the near future, environmental concerns – mainly the awareness that certain environmental changes resulting from pollution cannot be reversed - might become of such high importance that the currently used propulsion systems will not be allowed to operate any longer. This especially applies to older units. These units may represent certain historical value force in some cases, and may be used to search for solutions which can serve as an alternative to classic and conventional ship propulsion

systems. One such option is a hybrid propulsion system that produces less emissions of harmful substances [9][10][1]. The hybrid solution also presents a definite, economic advantage since operating an electrically-powered vessel is significantly less expensive than a vessel powered by a combustion engine [10][11]. While searching for sources of clean energy, scientists have also been working on fuel cells, which have successfully been implemented in shipbuilding applications [12][13][14]. Unfortunately, this solution has not become widely popular due to technical difficulties, safety concerns and its high cost.

There exists a number of modern propulsion solutions which may be employed in a small passenger ferry. In each case, all of their specific advantages and disadvantages should be thoroughly considered, respectively.

The parallel hybrid system that was designed and used for the first time in submarine propulsion is over one hundred years old [9][15][16]. The type of system consists of a combustion engine and an electric motor which may also operate as a generator. Both sources of power are connected to a transmission shaft by controllable clutches. Such solutions are characterized by their high energy efficiency and are frequently used in various applications, including on inland waterways vessels that navigate diverse bodies of water at varied speeds. Such watercraft often use battery-powered electric motors to manoeuvre in the port, while they use locks or restricted speed in populated urban areas. When going through open waters, during which navigational speeds are higher and the demand for power rapidly increases, the internal combustion engine is activated. In addition, the electric motor may work in a generator mode, which makes it possible to charge the batteries. In exceptional situations, these two types of propulsion may work together and make their combined maximum power available. However, such a solution is not without its limits and shortcomings. The main one is usually its considerable size. Such a system may be employed with relative ease in the case of a conventional propulsion system where the engine room is located at the stern and the shaft transmits power to the propeller.

In a series-hybrid propulsion system, the propeller is driven by an electric motor [9]. The energy supplied to the motor usually comes from a number of sources. Among the most popular are battery packs, diesel powered generators, photovoltaic panels and fuel cells. In certain cases, while in port, the ship batteries are charged from the power grid – such a system is known as a plug-in hybrid. The fundamental advantage of a series hybrid system is the compact construction of its power transmission system which occupies very little hull space. In addition, if azimuth pod thrusters are used, which also provide steering control, then the propulsion system is located practically entirely outside the hull. The power supply system may be installed in a dispersed way inside the hull, allowing for optimum distribution of weight throughout the ship. One of the disadvantages is its low efficiency while operating in a diesel-electric mode due to the efficiency of the operating machines. Therefore, the choice of propulsion system and power supply sources is of key importance to watercraft's lasting operational capability, which should span many years. This of course also holds true for the solution described here. Various concepts of propulsion and power supply systems were considered, and the final choice was made on the basis of optimum environmental, economic and practical impact which would be obtained based on the authors' best knowledge.

Numerous problems which were encountered during the execution of the project were eventually successfully overcome. Some of them stemmed from strict regulations of ship classification societies which permit watercraft to operate. Their foremost priority is safety which quite often manifests itself as resistance to non-standard, untested in operational conditions and novel solutions which, though quite understandable and natural, may still constitute a source of frustration to designers.

The hybrid propulsion solution and the power supply system based on lithium batteries proposed by the authors continue to be viewed by the shipbuilding industry as rather novel in character. As is frequently the case, it is challenging to break through long-established habits and traditions of employing traditional solutions. They are based on fossil fuels which have proven their merit on countless occasions. Nevertheless, it seems that the system described in this paper is indeed optimum for the operating conditions mentioned below.

THE MOTŁAWA 2 FERRY – CONCEPTUAL DESIGN

The newly designed vessel is to replace the Motława Ferry currently operating in Gdańsk, which has been in service for over three decades and became quite worn out from both a technical and an aesthetic perspective (Fig. 1a). Its propulsion system and functional range are quite distant from modern standards. The new ferry conceptual design process had to take into account external limitations regarding dimensions resulting from the character of the waterbody and conducted work: hull length L=12.00 m; ship's breadth B=5.00 m; total draught T_{max}=1.30m. In addition, the capability to transport 36 passengers was required (Fig. 1b).

Fig. 1. The Motława Ferry; a) the ship in operation since 1987; b) visualization of the new ferry

SHIP POWER DEMANDS DISTRIBUTION TESTS – TOWING TANK TESTS

Experimental tests were carried out in the towing tank of the Gdańsk University of Technology's Faculty of Ocean Engineering and Ship Technology in calm water conditions. The tests were conducted using a 1:10 scale laminate model (Fig. 2). During the initial phase of testing, the model had no protruding parts (propulsive and skeg). However, in subsequent tests the model was equipped with miniature azimuth thrusters and a remote control. These tests demonstrated that the vessel would be difficult to manoeuvre. Initiating any type of manoeuvring resulted in the model entering into a practically uncontrollable rotation. This problem was solved by installing skegs (Fig. 2a), which made it possible to maintain a stable course while only slightly limiting manoeuvring capabilities. Unfortunately, the improvement in manoeuvring came with the increase of movement resistance which also meant a rise in the power demand stemming from the larger total underwater area of the hull.

The measured total resistance of the model was recalculated to the scale of the actual ferry using three-dimensional extrapolation based on the extended Froude method. The total resistance coefficient was assumed to be typically composed of:

- friction resistance coefficient depending on the Reynolds number,
- residual resistance coefficient (wave, splash and pressure) as a function of the Froude number,
- pressure resistance coefficient, that takes into account the k shape coefficient, which increases the level of friction resistance both of the ship and of the model in relation to the corresponding flat panels

The results of the initial calculations were completed using approximate parametric methods during the hull shape selection phase. The results of model tests are presented in the diagram below (Fig. 3a).

It is worth emphasizing the fact that the results of approximate calculations performed using parametric methods are close to the model tests of the hull without protruding elements (Fig. 3a). The hull modernization consisting of adding the skegs and models of moving azimuth thrusters resulted in nearly doubling its drag and, as a consequence, also doubled the demand for power. The significant difference between the results obtained using parametric methods and the results of model studies for the hull equipped with skegs and thrusters is typical since approximate parametric methods do not take into account the protruding hull parts. Nevertheless, the nearly twofold rise in power demand following the mounting of skegs and azimuth thrusters seems to be overestimated. According to the study's authors, it stems mostly from larger dimensions of the model azimuth thrusters than from the accepted scale (Fig. 3a).

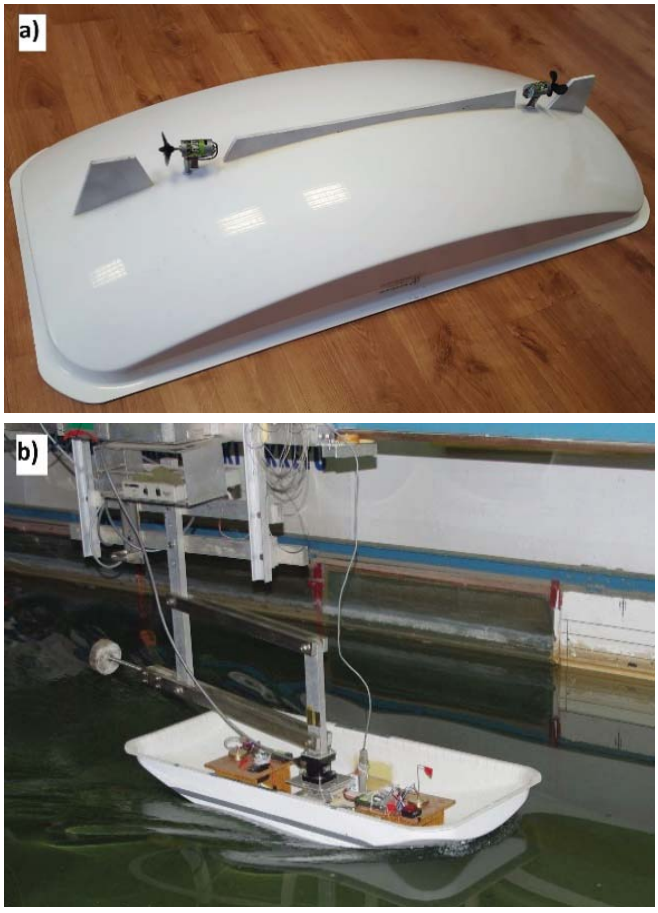

Fig. 2. The 1:10 scale ferry model; a) the final version with skegs and propulsion allowing for conducting remote control maneuvering tests using remote control; b) the model of the towing tank during tests, speed 10 km/h

Based on the towing power graph presented below, the propulsion power necessary for obtaining set speed may be approximately computed. Despite the fact that during actual operation the ferry speed does not exceed 6 km/h, due to navigational safety regulations the vessel has to be capable of operating at the speed of 12 km/h. In order to calculate the demand for electric motor power and estimate the capacity

of batteries, the following moderate and obtainable energy efficiency levels were accepted:

- propeller – 55%,
- motor and controller system based on laboratory conducted measurements of similar system – 95%.

Therefore, it follows that in order for the vessel to reach a speed above higher than the one requested by the regulations, the power of both azimuth thrusters should amount to about 33 kW (Fig.4b).

The impact of air resistance or the increasing hull drag resulting from algae and crustacean deposits might be estimated at this stage. However, bearing in mind that the vessel in question is to operate on a small, well-protected body of water and its hull will be carefully shielded against biofouling by a special paint or film, the impact of these factors was not considered.

It is also worth noticing that at low speeds the drag of the submerged hull part is very low, which indicates that the demand for power is minimal (Fig. 4b). For the speed of 6 km/h the power drawn by the propulsion system amounts to just 2.5 kW. Nevertheless, one should bear in mind that the presented results were obtained in conditions of steady-state and uniform motion. As such they do not take into account the considerable forces of inertia exerted by the twenty ton vessel. Especially during sudden emergency manoeuvres, such as collision avoidance, the helmsman may use the entire available power of propulsion.

Specific operating conditions and watercraft properties, such as low drag, short distance between the river banks, and considerable inertia of the twenty ton ship lead to a conclusion that the strategy of ferry operation should be considered through the perspective of minimizing energy consumption.

CONCEPT OF PROPULSION AND POWER SUPPLY SYSTEM

The body of water on which the Motława Ferry operates is located in the historic old city centre which is very crowded, especially during the tourist season. The character of its covered route is not typical for shuttle ferries and requires considerable manoeuvring skills from the helmsman. Even though the covered distance is quite short and amounts to only 100 meters or so, navigating it requires operating along a curved trajectory. In addition, the helmsman is forced to correct the course quite frequently in order to avoid collisions.

The proposed solution – a parallel hybrid propulsion system based on two azimuth thrusters (Fig. 4) – allows for obtaining the desired sound manoeuvring capability. In order to obtain high reliability of propulsion, each of the two azimuth thrusters powered by permanent magnet electric motors is equipped with its own battery pack. Due to safety requirements and the expected unsinkability, the ship is divided into watertight compartments. The bow thruster is powered by batteries installed in the bow compartment and the stern thruster draws power from the stern compartment battery pack (Fig. 4). The design reviewing classification society made a suggestion of employing a solution which would allow for switching the power supply between the bow and the stern. However, the design authors decided not to follow the suggestion, based on their conclusion that it would unnecessarily complicate the control system and make it harder for the crew to use, especially in emergency situations. The two main power supplying electrical installations do not overlap. Therefore, a breakdown in one of them will not result in malfunction of the second one and will allow the vessel to maintain its operational capability. The heart of the entire power supplying system is the main switchboard located in the central part of the ship, which is easily accessible from the crew room (Fig.4).

Due to safety concerns, the lithium batteries are placed inside sealed containers with mechanical ventilation of varying outputs as a function of the battery cell temperature.

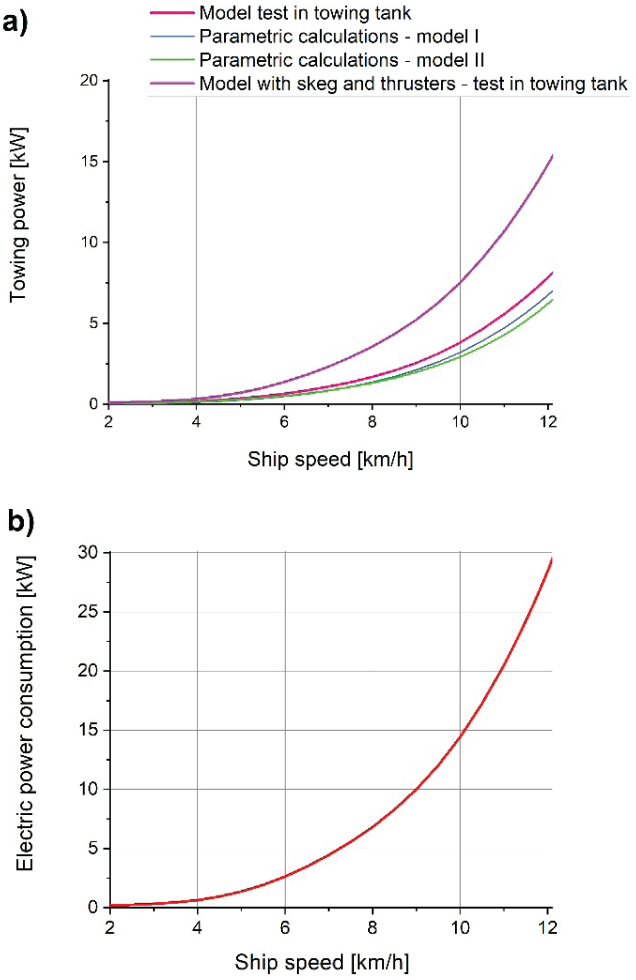

Fig. 3. The results of calculations and model tests; a) comparison of calculation results and measurements performance in the towing tank, b) electrical power consumption of ship's propulsion system as a function of speed

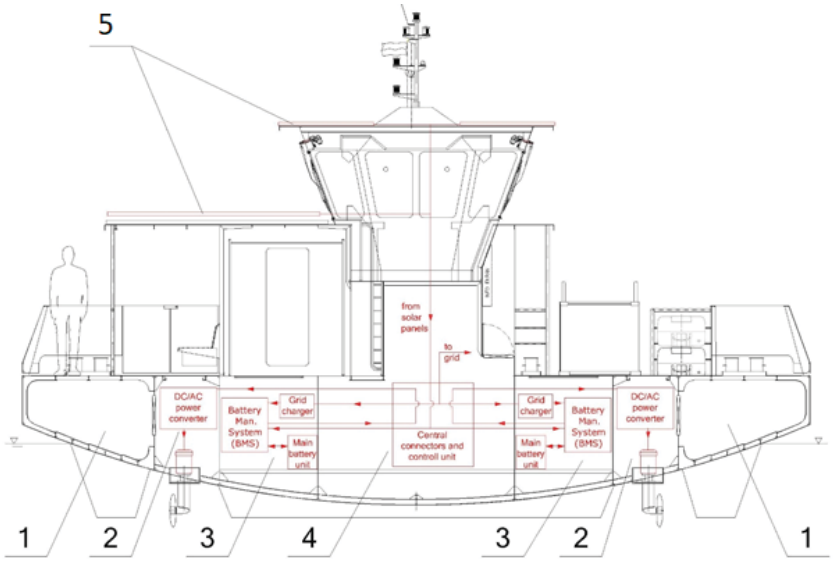

Fig. 4. Propulsion and power supply system schematic of the Motława II Ferry; 1 – collision bulkhead; 2 – propulsion compartment, 3 –battery compartment, 4 – crew room with main switchboard, 5 – solar panels

Lithium batteries grouped into water resistant modules of 86V rated voltage and 5kWh capacity were proposed for the power supply. Each of such modules consists of 78 LiFePO4 cells connected in a series-parallel circuit (configuration 26S3P). The modules are provided with a battery management system (BMS) which protects them from excessive discharging, overcharging and overheating. In addition, the system is equipped with a balancer responsible for charging evenly the series-connected cells.

The battery compartment will house typical RACK type cabinets inside which a given number of battery modules may be installed. Communication with the BMS will be conducted through a CAM rail. The control system allows for easy identification of a damaged or depleted battery module and allows for unproblematic replacement without a total shutdown of the entire power supply system, which is quite important from an operational perspective.

The selected battery capacity must provide a full day of continuous operation during the summer season. During navigation, the thrusters are powered from the batteries and photovoltaic panels. At night the ferry will be connected to the power grid and, due to the expected high durability of the batteries, will not be charged more than once in 24 hours. Similar watercraft are quite frequently equipped with an emergency source of electricity, either a diesel generator or an emergency battery, allowing the vessel to operate for at least 30 minutes. However, the classification society agreed, that the ferry is not necessary to be equipped with such an emergency power source. This decision was justified by the character of the navigated body of water - in particular its small size, as well as the fact that two independent propulsion and power supply systems are employed.

ENERGY BALANCE AND ENERGY MANAGEMENT

The power demand curve presented earlier is sufficient to show the energy balance of a typical ship. Consumption of electrical energy is of key importance on longer routes with the vessel travelling at a constant speed. The amount of energy required for manoeuvring, which takes only a fraction of the entire travel time, is estimated as a certain percentage of the total demand. However, in the case of the planned ferry, a different approach was necessary due to the ship's distinctive operating characteristics.

During the preliminary design phase the capacity of batteries had to be assessed, especially in the aspect of their mass. This data was required by the hull designers to determine the ship's draught and then the levels of resistance generated by the ferry hull. The parameters assumed during that stage are presented in Table 1.

Tab. 1. Initially assumed preliminary battery capacities and weights

	Power demand and capacity of main batteries	Number/ Amount	Mass	Unit
1	Daily operating time during peak summer season	12		h
2	Number of full cycles both ways in one hour	10		
3	Effective travel time both ways	4		minute
4	Average estimated power demand	12		kW
6	Hourly electric energy consumption	8		kWh
7	Daily electric energy consumption	96		kWh
8	Total battery capacity with 10% reserve	105,6		kWh
	Estimated specifications of the main battery pack			
1	Battery module 86.5V 5kWh	1	45	kg

	Power demand and capacity of main batteries	Number/ Amount	Mass	Unit
2	Number of modules	22	990	kg
3	Mass reserve (cables, protection etc.)		150	
	TOTAL:		**1185**	**kg**

The conducted model tests demonstrated that the resistance generated by such small watercraft travelling at low speeds is minor. However, the fact that about a third of the approximately 2 minute long river crossing time is spent accelerating or slowing down does create a problem. Speed distributions recorded using GPS during consecutive river crossings are very similar to each other but by no means identical. This of course stems from the fact that the vessel is controlled by a helmsman who, by manoeuvring, adjusts the speed and course to the conditions on the busy waterway. The recorded and then generalized navigational strategy employed by the helmsman was used for verifying the preliminary energy balance. The diagrams below present the speed profile of a 2 minute long river crossing and the approximate power demand based on the conducted model tests. (Fig. 5).

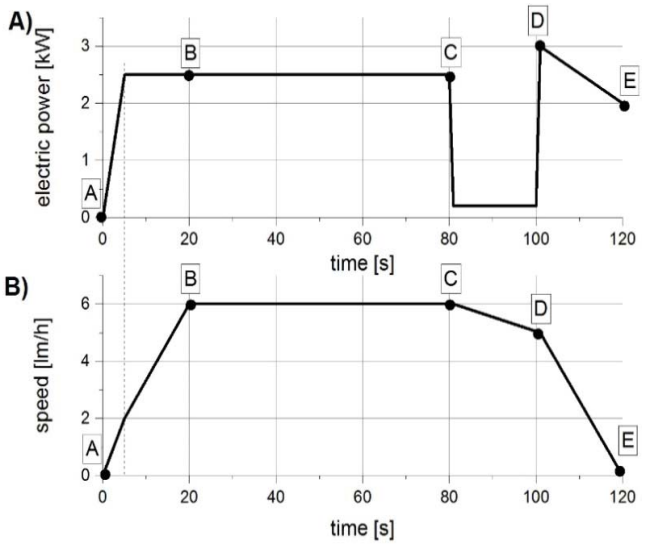

Fig. 5. Approximate power demand (A) and speed profile (B) during the 2 minute long Motława II crossing

The capital letters mark successive phases of navigation resulting from concrete steps taken by the helmsman. Following unmooring (A), the helmsman increases the engine speed and the ferry starts to gently accelerate. After approximately twenty seconds (B), the vessel reaches the speed of 6 km/h and covers most of the route at that constant pace. During that time the helmsman usually does not alter the engine speed. At a certain distance from the river bank, following approximately 180 seconds of travel, the helmsman reduces the engine speed and the ferry gradually loses velocity. In direct proximity of the berth (D), the helmsman activates the reverse gear of the propeller and the ferry starts to decisively slow down (with decrease power usage). The ferry stops and is moored at the berth (E). Successive river crossings demonstrated that time differences in performing the consecutive manoeuvres do not differ significantly. The approximate power distribution diagram (Fig. 5A) allows for initial verification of the energy balance presented in Table 1.

As the diagram indicates (fig. 3), the initially accepted average propulsion power is five times higher than the one stemming from the resistance curve and the specific character of navigation. It is worth adding that the consumption of power from the batteries may be even lower because, on sunny days, about one additional kilowatt of energy may be expected (minimum power of solar panels was set as 1 kWp). Performed calculations indicate that a single two-way ferry crossing requires approximately 0.14 kWh of electrical energy. Assuming 12 hours of daily operation in a season and ten crossings per hour, the energy demand amounts to approximately 17 kWh i.e. over six times less than initially assumed (Table 1).

If the battery capacity was limited to about 17 kWh, then, in the event of a necessary shipyard visit, the ferry travelling at a speed of 10 km/h would have the range of only 10 km. Therefore, in the opinion of the authors, the battery capacity may not be drastically reduced because of operating safety and battery life concerns, among other reasons.

Another challenging issue is the human factor. The authors are familiar with a case when an inexperienced helmsman in just four hours managed to deplete all the energy meant for a full day of operation. In view of that fact, a special training for the crew is planned. In addition, data on the power consumption of each crossing will be displayed on an information screen. The display will also indicate the crossing which consumed the least energy. This will allow for analysing and drawing conclusions as to the optimum strategy of operation.

In the opinion of the authors, the batteries should have the capacity of approximately 35 kWh. The one hundred percent energy reserve relative to the performed energy balance, should allow for ensuring a high level of energy safety even during the most intense, daily, summer season operations. It is worth adding that it is technically possible to increase the battery capacity by connecting additional modules of 5 kW capacity in RACK type cabinets installed in the battery compartments and that the maximum capacity may amount to 110 kWh (Fig. 5).

Utilizing electrical propulsion on the new vessel is of significant impact to the natural environment. As it has already been mentioned, the currently operating Motława Ferry is powered by a diesel engine of technological level dating back to the 1980s. The engine does not meet any current standards regarding emission levels. The graph below (fig. 6) illustrates its impact on the natural environment resulting from a year-long operation which on average consumes three tons of fuel.

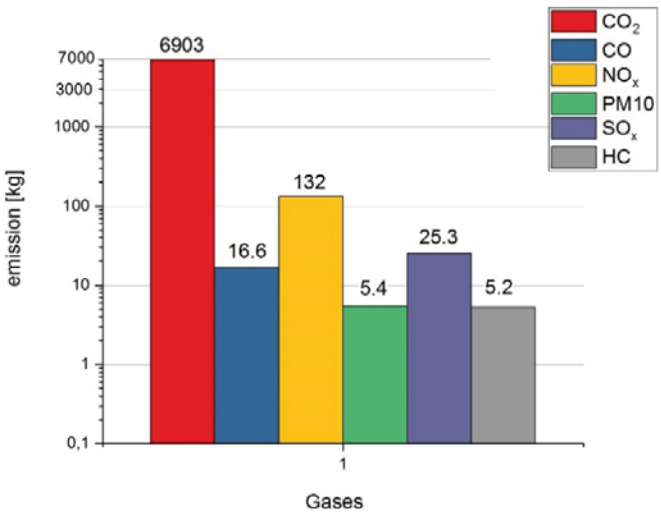

Fig. 6. Average annual engine exhaust gas emissions of the Motława Ferry. (Authors calculations)

Employing clean and quiet electrical propulsion is in line with the global trend of environmentally friendly transport i.e. green shipping. It is worth adding, that the new, increasingly strict regulations will likely lead to a complete elimination of conventionally powered watercraft from city centers, as is already the case with certain other types of vehicles.

SUMMARY AND CONCLUSIONS

Lithium batteries of considerable capacity placed in a single location constitute a significant hazard to the safety of passengers, crew and surrounding environment. In order to increase the safety level, the individual cells are enclosed in hermetic casings. The whole batteries are placed in watertight compartments. The BMS system described earlier guards, among others, against increase in cell temperature and in the event of its rise disconnects the pack from the circuit. Therefore, in the opinion of the authors, it can be stated with confidence that the system ensures a reasonably high level of safety.

Studies to be performed on the new ship will allow for assessing whether the energy balance was performed correctly. Nevertheless, the power supply system is designed in a way which allows for increasing the battery capacity if the need arises. The ferry will also be a valuable object of research which will no doubt provide very interesting data covering, among others, energy management - especially in the aspect of operating strategy's impact on energy consumption. Another future point of interest is complete automation of navigation leading to creation of an unmanned surface vessel.

Excessive weight and underestimated energy consumption of propulsion systems are among the most frequently encountered faults in watercraft design. One should bear in mind that in fact, one mistake stems from the other. The increased mass means greater resistance and therefore also a rise in energy demand.

REFERENCES

1. H.N. Psaraftis, Green Maritime Logistics: The Quest for Win-win Solutions, Transp. Res. Procedia. 14 (2016) 133–142. doi:10.1016/j.trpro.2016.05.049.

2. C. Sys, T. Vanelslander, M. Adriaenssens, I. Van Rillaer, International emission regulation in sea transport: Economic feasibility and impact, Transp. Res. Part D Transp. Environ. 45 (2014) 139–151. doi:10.1016/j.trd.2015.06.009.

3. J. Lister, R.T. Poulsen, S. Ponte, Orchestrating transnational environmental governance in maritime shipping, Glob. Environ. Chang. 34 (2015) 185–195. doi:10.1016/j.gloenvcha.2015.06.011.

4. W. Sihn, H. Pascher, K. Ott, S. Stein, A. Schumacher, G. Mascolo, A Green and Economic Future of Inland Waterway Shipping, Procedia CIRP. 29 (2015) 317–322. doi:10.1016/j.procir.2015.02.171.

5. P. Gilbert, P. Wilson, C. Walsh, P. Hodgson, The role of material efficiency to reduce CO2 emissions during ship manufacture: A life cycle approach, Mar. Policy. 75 (2016) 227–237. doi:10.1016/j.marpol.2016.04.003.

6. S.I. Salem A., TECHNO-ECONOMIC APPROACH TO SOLAR ENERGY SYSTEMS ONBOARD MARINE VEHICLES, Polish Marit. Res. 23 (2016) 64–71. doi:0.1515/pom r-2016 - 0033.

7. D. Borelli, T. Gaggero, E. Rizzuto, C. Schenone, Analysis of noise on board a ship during navigation and manoeuvres, Ocean Eng. 105 (2015) 256–269. doi:10.1016/j.oceaneng.2015.06.040.

8. A. Badino, D. Borelli, T. Gaggero, E. Rizzuto, C. Schenone, Airborne noise emissions from ships: Experimental characterization of the source and propagation over land, Appl. Acoust. 104 (2016) 158–171. doi:10.1016/j.apacoust.2015.11.005.

9. A.M. Bassam, A.B. Phillips, S.R. Turnock, P.A. Wilson, Development of a multi-scheme energy management strategy for a hybrid fuel cell driven passenger ship, Int. J. Hydrogen Energy. (2016) 1–13. doi:10.1016/j.ijhydene.2016.08.209.

10. L.K. Mitropoulos, P.D. Prevedouros, Life cycle emissions and cost model for urban light duty vehicles, Transp. Res. Part D Transp. Environ. 41 (2015) 147–159. doi:10.1016/j.trd.2015.09.024.

11. E.K. Dedes, D.A. Hudson, S.R. Turnock, Investigation of Diesel Hybrid systems for fuel oil reduction in slow

speed ocean going ships, Energy. 114 (2016) 444–456. doi:10.1016/j.energy.2016.07.121.

12. J.J. De-Troya, C. Álvarez, C. Fernández-Garrido, L. Carral, Analysing the possibilities of using fuel cells in ships, Int. J. Hydrogen Energy. 41 (2016) 2853–2866. doi:10.1016/j.ijhydene.2015.11.145.

13. Y.M.A. Welaya, M.M. El Gohary, N.R. Ammar, A comparison between fuel cells and other alternatives for marine electric power generation, Int. J. Nav. Archit. Ocean Eng. 3 (2011) 141–149. doi:10.3744/JNAOE.2011.3.2.141.

14. N.C. Shih, B.J. Weng, J.Y. Lee, Y.C. Hsiao, Development of a 20 kW generic hybrid fuel cell power system for small ships and underwater vehicles, Int. J. Hydrogen Energy. 39 (2014) 13894–13901. doi:10.1016/j.ijhydene.2014.01.113.

15. V. Alfonsin, A. Suarez, S. Urrejola, J. Miguez, A. Sanchez, Integration of several renewable energies for internal combustion engine substitution in a commercial sailboat, Int. J. Hydrogen Energy. 40 (2015) 6689–6701. doi:10.1016/j.ijhydene.2015.02.113.

16. J. Kowalski, W. Leśniewski, W. Litwin, Multi-source-supplied parallel hybrid propulsion of the inland passenger ship STA.H. Research work on energy efficiency of a hybrid propulsion system operating in the electric motor drive mode, Polish Marit. Res. 20 (2013) 20–27. doi:10.2478/pomr-2013-0031.

CONTACT WITH THE AUTHORS

Magdalena Kunicka
e-mail: magkunic@pg.edu.pl

Gdańsk University of Technology
Narutowicza 11/12, 80-233 Gdańsk
Poland

Wojciech Litwin
e-mail: wlitwin@pg.edu.pl

Gdańsk University of Technology
Narutowicza 11/12, 80-233 Gdańsk
Poland

sciendo

POLISH MARITIME RESEARCH 2 (102) 2019 Vol. 26; pp. 93-103
10.2478/pomr-2019-0029

INJURY PREDICTION MODELS FOR ONSHORE ROAD NETWORK DEVELOPMENT

Wojciech Kustra
Joanna Żukowska
Marcin Budzyński
Kazimierz Jamroz
Gdańsk University of Technology, Faculty od Civil and Environmental Engineering, Poland

ABSTRACT

Integrating different modes of transport (road, rail, air and water) is important for port cities. To accommodate this need, new transport hubs must be built such as airports or sea ports. If ports are to grow, they must be accessible, a feature which is best achieved by building new roads, including fast roads. Poland must develop a network of fast roads that will provide good access to ports. What is equally important is to upgrade the network of national roads to complement fast roads. A key criterion in this case is to ensure that the roads are efficient to minimise time lost for road users and safe.

With safety standards and safety management practices varying vastly across the EU, Directive 2008/96/EC of the European Parliament and of the Council was a way to ensure that countries follow procedures for assessing the impact of road projects on road safety and conduct road safety audits, road safety management and road safety inspections. The main goal of the research was to build mathematical models to combine road safety measures, i.e. injury density (DI) and accident density (DA), with road and traffic factors on longer sections, all based on risk analysis. The practical objective is to use these models to develop tools for assessing how new road projects will impact road safety.

Because previous research on models to help estimate injuries (I) or injury density (DI) on long sections was scarce, the authors addressed that problem in their work. The idea goes back to how Poland is introducing procedures for assessing the effects of infrastructure on safety and developing a method to estimate accident indicators to support economic analysis for new roads, a solution applied in JASPERS. Another reason for the research was Poland's insufficient and ineffective pool of road safety management tools in Poland. The paper presents analyses of several models which achieved satisfactory results. They are consistent with the work of other researchers and the outcomes of previous research conducted by the authors.

The authors built the models based on a segmentation of national roads into sections from 10 to 50 km, making sure that they feature consistent cross-sections and average daily traffic volumes. Models were built based on the method described by Jamroz (Jamroz, 2011). Using the available road traffic volume data, each section was assigned variables defining geometric and traffic features. Based on studies conducted on road sections, the variables were either averaged over the entire length of the section or calculated as a percentage of the variable occurring over the entire length: related to traffic volume, roadside environment or cross section

Keywords: Road safety, Polish national roads, density of injuries, log logistic and gamma distribution, risk management

INTRODUCTION

In Poland, the number of road traffic fatalities is among the highest in the European Union. In 2016, 3,026 road users died and 12,109 were seriously injured. Although national single carriageway roads account for less than 5% of the entire road network in Poland, in terms of risk they are the most dangerous. In the past three years 15 thousand accidents occurred on these roads, in which more than 20 thousand people were injured and nearly 2,600 died. The death toll is more than 27% of all fatalities in Poland, while the number of injured is 15% of the total. This indicates the need to develop methods to support a high standard of road infrastructure and its management because of the great potential to reduce the number of injuries and fatalities (The National Police Headquarters, 2015). Poland's big opportunity comes with the implementation of road infrastructure safety management principles adopted under Directive 2008/96/EC. In the document, Member States are recommended to use tried and tested road safety management tools with the Road Safety Impact Assessment as one of them (RIA).

When a new road is assessed for its impact on road safety, a strategic analysis is carried out looking at how different variants of the road will change the road safety across the public roads network. The purpose of the RIA is to determine the ranking of variants of the planned road and their impact on traffic safety across a network of interconnected roads in the road's catchment area. The results should be included in a multicriteria analysis (along with other technical, economic and environmental criteria) evaluating the variants of the analysed road.

When new roads are built, this may have a great impact on how the area will develop over the years to come. Therefore, a number of decisions are required at several stages before the optimal variant is selected. The RIA procedure can use the support of scientific methods which help to choose the best option for road safety. To that end, mathematical models combining the influence of selected factors with traffic safety measures are very helpful.

LITERATURE REVIEW

There is an extensive body of road safety research and a variety of analyses such as forecasting national trends (Broughton, 1991), the effects of the human factor on safety (Donmez et al., 2007, Deffenbacher et al., 2003) (Hewson, 2004, Zhang et al., 2006, Scott-Parker et al., 2012), the effects of junctions (Asgarzadeh et al., 2017, Xie et al., 2013, Peer and Rosenbloom, 2013), the effects of speed (Lee et al., 2006, Peer and Rosenbloom, 2013) and the effects of vehicles (Ryb et al., 2013). Since the early 1980s, a lot of the research focussed on building mathematical models of the relationship between traffic incidents and traffic volume and other roadside-related factors using generalised linear regression models.

The most frequently used model for estimating accidents is an equation which describes the expected accidents $E(Y_i)$ as a function of traffic Q, road length L, and a set of other factors referred to as risk factors x_i $(i=2, 2, 3……n)$. The effects of traffic volume on accidents described with the traffic volume function to the power of β_0 were first described by Hauer (Hauer, 1995). By applying this approach, a power-exponential model could be used to estimate the expected accidents on sections of road with Q, L parameters representing the risk exposure and the sum of variables $\beta_i x_i$ representing the likelihood of the severity of the consequences.

When discussing the relations between road, traffic, accidents and casualties over specific road sections, the effects are usually divided into road type and location: motorways, rural single carriageways, rural multiple carriageways, and urban single and multiple carriageways. The majority of research on road sections focussed on short sections, the length of which does not exceed 2 km. Longer sections, above 5 km, are covered rarely (Hakkert, 2011; Iyinam et al., 1997).

While the majority of researchers focus on estimating accidents and types of accidents (fatality, injury and serious injury accidents), there is very little work on the number of injuries or deaths (Ivan et al., 2006; Kiec, 2009; Yannis et al., 2014).

There are numerous independent variables affecting the extent and variability of individual road safety measures on road sections. Based on the available literature, approximately 50 independent variables related to traffic and road parameters were identified and then included in the design of models for estimating the measures. The authors studied the following variables, which were also analysed in previous works: length of section (AASHTO, 2010; Anastasopoulos et al., 2012c; Bared and Vogt, 1998; Ma et al., 2008a), road class (Abdel-Aty and Radwan, 2000a), traffic parameters (Anastasopoulos et al., 2012a; Council et al., 2000; Elvik, 2008; Fernandes and Neves, 2013a; Lao et al., 2011a; Lord and Park, 2012), type of area (built-up, rural) (Abdel-Aty and Radwan, 2000b; Fernandes and Neves, 2013b; Lao et al., 2011b), roadside environment (Hauer, 2007; Lee and Mannering, 2002; Martinelli et al., 2009, Jurewicz and Steinmetz, 2012), parameters of cross-section (Anastasopoulos et al., 2012a; Cafiso et al., 2010; Hauer, 2007; Lao et al., 2011; Ma et al., 2008, Ambros and Sedoník, 2016), intersection, interchange and driveway density (Anastasopoulos et al., 2012b; Bhatia et al., 2009; El-Basyouny and Sayed, 2009; Hauer, 2007).

OBJECTIVE OF THE WORK

The main objective was to build mathematical models to combine road safety measures, such as injury density (DI) and accident density (DA), with road and traffic factors over long sections based on risk analysis. The models help to assess selected parameters for their impact on road safety. They will also support the development of tools to help with the assessment of road projects and road safety and to rank the risks when conducting road safety inspections (RSI). With Poland's road safety far from sufficient and road infrastructure standards not meeting the criteria, it is critical to have the tools and improve the quality and effectiveness of road infrastructure safety management.

MODELLING METHODOLOGY

Road safety management includes two terms which are defined as follows: hazard – the possibility that a specific type of road accident may occur and cause specific consequences (financial consequences, injuries and fatalities) when sources of that hazard are present, and risk – the product of probability and consequences as a result of a specific road accident. (Jamroz, 2011; Technical Committee 18, 2004).

The research presented in this article is based on the relationship between a source of hazard and accident consequences such as costs, injuries and fatalities. This relationship is described by the societal risk formula (1).

The level of risk on road sections is given by the formula (Jamroz, 2011):

$$RS_O = E \cdot P \cdot C \quad (1)$$

where: RS_O – overall collective risk, E – exposure to risk, P – probability of a dangerous event, C – consequence of a dangerous event.

Test site. The analysis aiming to develop models for forecasting road accident consequences was conducted on national roads. The total length of the road network managed by the GDDKIA is 17.200 km (nearest 93% of all national roads). The research focused on two types of road:

- single carriageway – main (G) and fast traffic (GP) roads, express (S) roads – length of 15.200 km,
- dual carriageway – main and fast traffic roads (G, GP), express roads (S), motorways (A) – length of 2.100 km.

For the purpose of constructing social risk models for road safety analyses at the strategic level, sections of national roads were divided into 10 to 50 km lengths. The criteria for road section division included the usual features such as: road cross-section, class, traffic volume, intersections with other national or provincial roads, change in cross-section, road discontinuity, urban county boundaries (for G and GP roads).

In this article, the authors focus on accidents on single carriageways. Table 1 shows the characteristics of the study site. The road class (G, GP, S) determines, among other things, the design parameters such as design speed, vertical and horizontal curve radius, road accessibility, intersection type (e.g. the S class road is characterised by the lowest accessibility and presence of interchanges, while the G class road is characterised by the lowest geometric parameters and the highest road accessibility).

Tab. 1. Length [km] of sections on national roads

Symbol	N	μ	Min	max	σ	v
	[sections]	[km]	[km]	[km]	[km]	-
G	155	30.1	4.7	49.2	9.7	0.35
GP	375	27.5	1.9	55.5	10.1	0.38
S	11	14.9	2.7	28.4	8.3	0.54
Avg/sum	541	28.1	1.9	55.3	10.1	0.36

where: N – number of sections, μ – mean value, σ – standard deviation, v – variability rate.

As we know from analyses, the accident severity is very high on S class roads (single carriageways) which suggests that such roads should no longer be designed or built. (Jamroz and Kustra, 2011) (Table 2, fig 1).

Tab. 2. Numbers and density of accidents and victims on single carriageway roads

Road type	Length	Number of			Cost of accidents	Density of			
		Accidents	Injuries	Fatalities		Accidents	Injuries	Fatalities	Cost of accidents
T	L	A	I	F	AC	DA	DI	DF	DAC
	[km]	[accidents/ 3 years]	[injuries/ 3 years]	[fatalities/ 3 years]	PLN m/ 3 years	[accidents/ km/3 years]	[injuries/ km/3 years]	[fatalities/ km/3 years]	PLN m/ km/ 3 years
G	4615.3	5166	6913	849	2694.8	1.12	1.50	0.18	0.58
GP	10361.4	17305	24206	3251	9921.0	1.67	2.34	0.31	0.96
S	163.2	108	155	43	97.0	0.66	0.95	0.26	0.59

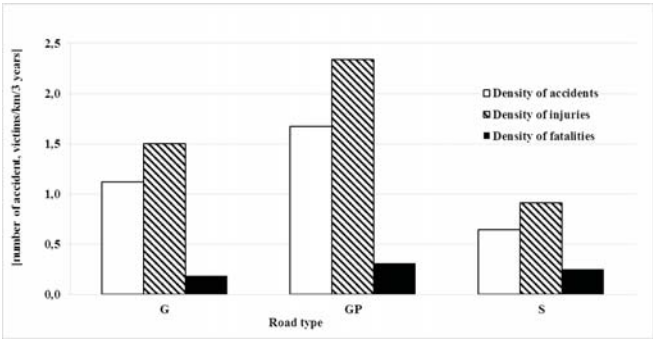

Fig. 1. Density of accidents, injuries and fatalities on Poland's national road network

RS_O^1 shows a model used for calculating overall collective risk (I) using individual risk models. The model is described with the formula:

$$RS_O^1 = E_L \cdot P_{DI} \quad (2)$$

where: P_{DI} - probability of a consequence, E_L - risk exposure.

RS_O^2 shows a three-component model used for calculating overall collective risk (I) using individual risk models. The model is described with the formula:

$$RS_O^2 = E_L \cdot P_{DA} \cdot C_{SVT} \quad (3)$$

where: E_L – exposure, P_{DA} – probability of risk occurrence, C_{SVT} – probability of occurrence of selected victim types.

The product of risk exposure obtained by converting formulas 2, 3 using the standardised road safety measures RS_N^{DI}, RS_N^{DA} is represented by the length of road (L), the probability of consequences of selected category in a unit

of time (*DI, DA*), and the level of selected victim types (C_I). This approach will help to build models for standardised measures only disregarding the length of the section. The models are described with the formulas:

$$RS_O^3 = E_L \cdot P_{DI} = E_L \cdot RS_N^{DI} = L \cdot DI \quad (4)$$

$$RS_O^4 = E_L \cdot P_{DA} \cdot C_{SVT} = E_L \cdot RS_N^{DA} \cdot C_I = L \cdot DA \cdot C_I \quad (5)$$

where:
L – section length, *DA* - density of accidents, *DI* – density of injuries, C_I – injury rate.

Explanatory variables. Using the available road traffic volume data from the GDDKIA road traffic database, each section was assigned variables defining geometric and traffic features. Based on studies conducted on long road sections (from 5 to 50 km), the variables were either averaged over the entire length of the section (*DIT, DITE, DIS, DD*) or calculated as a percentage of the variable occurring over the entire length: related to traffic volume (*AADT, PHV*), roadside environment or cross section (*PBA, PWS, PNS, PUS, PEL, PCL, PAL, PST, PPPC*). A set of variables, used in the process of constructing injury prediction models on single-carriageway roads, is presented in Table 3. Due to the lack of data related to selected geometrical features (land use, transit traffic, local traffic, road network maintenance, bendiness, waviness, journey speed, speed limits) the average RLA was used.

Tab. 3. List of independent variables on single carriageway roads

Symbol	Unit	μ	min	max	σ	ν
T	-	4.921	2.20	5.90	-	-
RLA	-	1.503	1.00	1.97	0.29	0.19
L	[km]	27.985	5.76	55.10	10.30	0.37
AADT	[P/24h*10^{-4}]	0.817	0.04	2.67	0.44	0.54
PHV	[%]	0.172	0.03	0.64	0.08	0.49
PBA	[%]	0.259	0.00	1.00	0.18	0.68
PWS	[%]	0.234	0.00	1.00	0.33	1.40
PNS	[%]	0.049	0.00	0.87	0.14	2.95
PUS	[%]	0.561	0.00	1.00	0.35	0.62
PEL	[%]	0.005	0.00	0.93	0.05	10.67
PCL	[%]	0.004	0.00	0.23	0.02	5.02
PAL	[%]	0.013	0.00	0.48	0.05	3.53
DIT	[numbers/km]	0.004	0.00	0.78	0.04	9.40
DITE	[numbers/km]	0.016	0.00	1.17	0.09	5.69
DIS_N	[numbers/km]	0.015	0.00	0.24	0.03	1.87
DIS_R	[numbers/km]	0.065	0.00	0.63	0.06	0.90
DIS_L	[numbers/km]	0.852	0.00	7.65	0.70	0.82
DIS	[numbers/km]	0.932	0.00	7.65	0.71	0.76
DD_P	[numbers/km]	2.303	0.00	20.17	1.95	0.85
DD_R	[numbers/km]	7.641	0.00	39.06	6.48	0.85
DD_F	[numbers/km]	5.332	0.00	44.51	4.30	0.81
PST	[%]	0.4	0.00	1.00	0.31	0.77
PP_{PC}	[%]	0.205	0.00	1.00	0.16	0.78

The symbols used in Table 5: *T* - class, cross section, *RLA* – location of road, L – length of section, *AADT* – annual average traffic volume, *PHV* – share of heavy vehicles, *PBA* – share of built-up sections, *PWS* – share of sections with paved houlder width ≥ 2m, *PNS* – share of sections with paved shoulder width < 2m, *PUS* – share of sections with unpaved shoulder, *PEL* – share of sections with emergency lane, *PCL* – share of sections with climbing lane, *PAL* – share of sections with additional lane for going straight ahead (additional), *DIT* – density of interchanges, *DITE* – density of interchange entries and exits, *DIS* - density of junctions with others roads (N – national, R – regional, L – local), *DD* – density of driveway – (P – public, R – private, F – forest), *PST* – share of sections with roadside trees, PP_{PC} – share of sections with pedestrian or bike paths, *DSC* - density of speed cameras.

ANALYSIS AND RESULTS

Following the literature review (Garber and Lei, 2001; Ivan et al., 2005; Ptak-Chmielewska, 2013; Rakha et al., 2010; Son et al., 2011; Wood, 2005; Ye et al., 2013a), and the previous research (Budzynski et al., 2011; Kustra et al., 2015), it was agreed to build the safety models based on generalised models of linear regression. Each model consists of three components: probability distributions of the dependent variable, linear predictor η_i, and nonlinear link function.

For the purposes of this work the Gamma (Negative binominal) and loglogistic distributions were used. The former one is the most common probabilistic distribution used by transport safety analysts for modelling accident or injury numbers (Geedipally et al., 2012a; Hauer, 2001, 1986; Lord, 2006; Lord and Geedipally, 2012; Lord and Park, 2008; Reurings et al., 2005; Schafer, 2006; Ye et al., 2013b) transportation safety analysts have used the empirical Bayes (EB. The density function takes the form:

$$RS_O^4 = E_L \cdot P_{DA} \cdot C_{SVT} = E_L \cdot RS_N^{DA} \cdot C_I = L \cdot DA \cdot C_I \quad (6)$$

However:

$$E(Y_i) = \mu_{it} \quad (7)$$

$$Var(Y_i) = \mu_{it} + \frac{{\mu_{it}}^2}{\phi} \quad (8)$$

where $Y_i = 0, 1, 2, 3 \ldots N$, Γ - gamma function, μ_{it} – mean value for the observation and time t, ϕ – overdispersion parameter.

The loglogistic distribution is used much less frequently in modelling accident and victim numbers. However, the authors (Li and Shang, 2014, Al-ghamdi, 2002) use it to estimate the number of accidents.

In this case, the density function takes the form:

$$P(Y_i = y_i) = f(y_i, \alpha, \gamma) = \frac{\left(\frac{\gamma}{\alpha}\right)\cdot\left(\frac{y_i}{\alpha}\right)^{\gamma-1}}{\left(1+\left(\frac{y_i}{\alpha}\right)^{\gamma}\right)^2} \quad (9)$$

However:

$$E(Y_i) = \mu_{it} = \ln(\alpha) \quad (10)$$

where γ – shape parameter, α – median of distribution.

The density of injuries (Table 4) was analysed using the probability density function. Figure 2 shows the fit between the data, the gamma distribution (shape = 2.362, scale = 3.272, Chi-Square test: 45.76, Log Likelihood: -273.429), and the loglogistic distribution (median = 0.596, shape = 0.394, Chi-Square test: 39.67, Log Likelihood: -279.73).

Tab. 4. Number of injuries on a single carriageway

Symbol	Injuries	Density of injuries				
	N	μ	min	max	σ	v
G	6913	0.513	0.044	1.784	0.319	0.62
GP	24206	0.819	0.038	3.366	0.518	0.63
S	155	0.325	0.030	0.851	0.276	0.85
Sum/avg.	31274	0.721	0.030	3.366	0.488	0.68

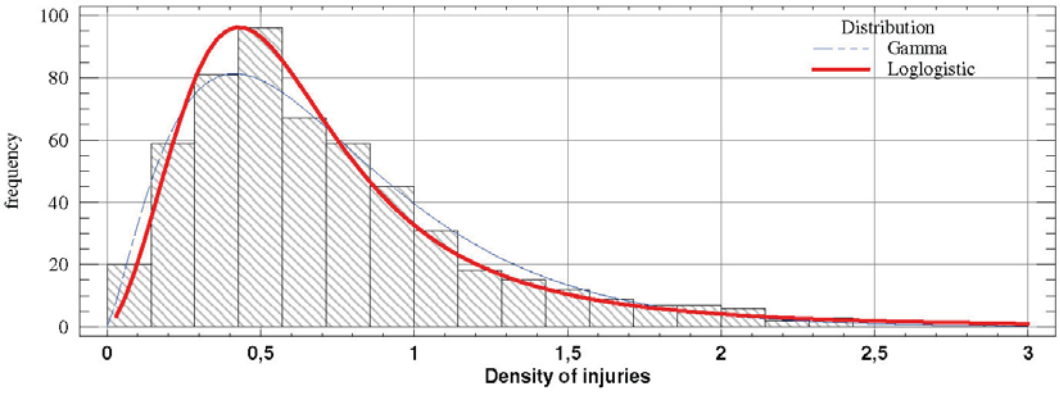

*Fig. 2 Probability density function – density of injuries (**DI**)*

In the case of the negative binominal, the logarithmic form of the copula function was used and the formula is:

$$\mu_i = E(Y_i) = \beta_0 \cdot X_{i1}^{\beta_{i1}} \cdot X_{i2}^{\beta_{i2}} \cdot exp^{(\eta_i)} \quad (11)$$

where: μ_i, – vale of expected dependent variable, η_i – linear predictor, x_{ik} – observed non-random independent variables, β_i, – equation coefficient.

Linear predictor η_i:

$$\eta_i = \varepsilon + \beta_1 x_{i1} + \beta_2 x_{i2} + \cdots + \beta_k x_{ik} = \varepsilon + \sum_{i=1}^{k} \beta_i x_{ik} \quad (12)$$

where: ε – unobservable variable representing a component of random error.

By transforming the risk models RS_N^{DI} (formula 4 and 5) and adopting the probability density function we obtain:

$$\mu_i = DI = \beta_0 \cdot T \cdot AADT^{\beta_1} \cdot exp(\eta_i) \quad (13)$$

$$\mu_i = DI = (DA + \beta_0 \cdot T \cdot DA^{\beta_1}\, exp(\eta_i) \quad (14)$$

$$\mu_i = DI = Y_{max} \cdot exp(-\beta_0 \cdot exp(-\eta_i)) \quad (15)$$

In the process of building models, the following variables were statistically significant: *AADT, PHV, DA, PBA, PWS, PAL, T, RLA*. The injury density models for long sections of single carriageways which offer the best approximation of actual data to observations are represented by the equations:

$$DI = \beta_0 \cdot T \cdot AADT^{\beta_1} \cdot \exp(\beta_3 \cdot PHV + \beta_4 \cdot PBA + \beta_5 \cdot PWS + \beta_6 \cdot PAL + \beta_7 \cdot T + \beta_8 \cdot RLA) \quad (16)$$

$$DI = (DA + \beta_0 \cdot T \cdot DA^{\beta_2} \exp(\beta_4 \cdot PBA + \beta_7 \cdot \mathrm{T} + \beta_9 \cdot \mathrm{AADT_1}) \quad (17)$$

$$DI = Y_{max} \cdot \exp(-\beta_0 \cdot \exp(-(\beta_3 \cdot PHV + \beta_4 \cdot PBA + \beta_6 \cdot PAL + \beta_7 \cdot T + \beta_8 \cdot RLA) \quad (18)$$

Table 5 presents the values of equation coefficients, while Table 6 gives the characteristics of statistical parameters.

Tab. 5. Values of equation coefficients

Equation	Variable										
	Y_{max}		*AADT*	*DA*	*PHV*	*PBA*	*PWS*	*PAL*	*T*	*RLA*	$AADT_1$
		β_0	B_1	B_2	B_3	B_4	B_5	B_6	B_7	B_8	B_9
16		0.164	0.963		-0.369	-0.185	-0.313	-0.890	-0.155	0.702	
17		0.452		1.324		-1.163			-0.238		-0.153
18	2.4	9.110	0.962		-0.557	-0.240		-0.992	0.086	0.637	

Tab. 6. Characteristics of statistical parameters

Equation	Parameters			
	R^2	R_{co}^2	SMSE	AIC
16	0.683	0.679	0.238	-628.572
17	0.958	0.957	0.093	-1056.370
18	0.635	0.630	0.251	-605.463

To test the models for their applicability to the entire range of road traffic volumes, a method proposed by Hauer was used (Hauer, 2004). Based on estimating cumulative residuals (CURE plot), the method helps to understand the extent of the AADT which the model can use to forecast injury density. In the case of models described with function 16 (figure 3a) and 18, the derived confidence limits were not exceeded across the entire traffic volume (± 2σ). However, in the case of the model described with function 17 (figure 3b) in the range of AADT 1400 – 4200, the upper limit + 2σ was exceeded, which suggests that the model should not be applied to this range of traffic volume.

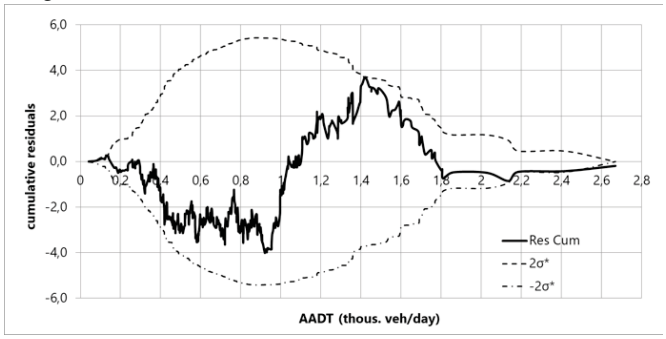

a)

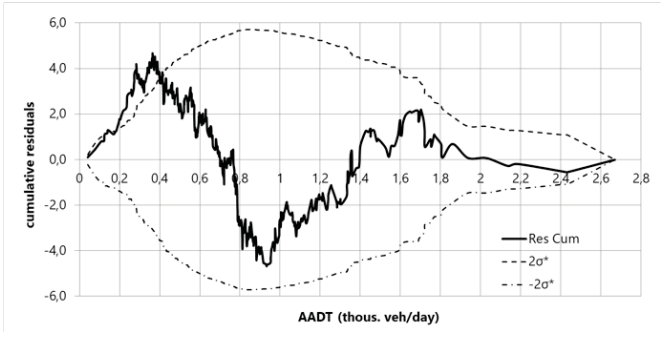

b)

Fig. 3. CURE plot for AADT for equation 16 (a) and 18 (b)

DISCUSSION

The effects of the selected independent variables on the models are consistent with the expectations arising from the physical interpretation of the role of these variables observed by other researchers. They are also consistent with the results of previous research conducted by the authors (AASHTO, 2010; Budzynski et al., 2013; Geedipally et al., 2012b).

All the models ensure a very good match between the actual data and those estimated from the model. The highest value of R_{co}^2 and the lowest value of AIC are found in model 17. It should be noted, however, that to estimate the density of injuries, the accident density variable (*DA*) must also be estimated. Its estimation carries an error that will cause error multiplication in model 17. The methodology for estimating this measure on single-carriageway national roads was presented by the author in his doctoral thesis (Kustra, 2016) and in the paper (Budzynski et al., 2015). An example of a function for estimating accident density can be described with the equation:

$$DA = \beta_0 \cdot T \cdot AADT^{\beta_1} \cdot \exp(\beta_2 \cdot PBA + \beta_3 \cdot PWS + \beta_3 \cdot PAL + \beta_4 \cdot DIS_N + \beta_5 \cdot DIS_R + \beta_6 \cdot T + \beta_7 \cdot RLA) \quad (19)$$

The corrected coefficient of the multi-dimensional correlation for equation 19 is 0.769. This means that the minimum R_{co}^2 value for equation 17 is 0.734, which indicates a very good match between the estimated and observed data.

The impact of all describing variables on the described variable was assessed using the arc elasticity index (*AE)*. Where the models of selected measures are concerned, the *AE* index determines the average percentage change of dependent variable *Y* when the independent variable x^i changes by one percent in the interval $t_1 - t_2$ (Abdel-Aty and Radwan, 2000c; Litman, 2010; Mannering et al., 1996; Vaziri, 2010).

When analysing the elasticity indicator of the independent variables' influence on a selected road safety measure (*DI*), the variables that proved to be statistically significant in the constructed models were the following (Figure 4):

– variables influencing an increase in the value of the measure: *AADT, DA, RLA, T,*
– variables influencing a decrease in the value of the measure: *PAL, PBA, PHV.*

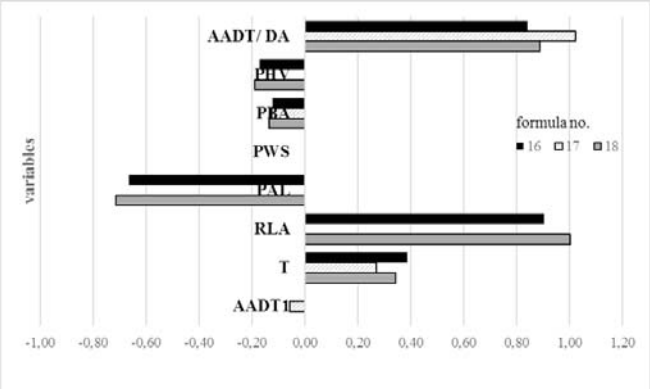

Fig. 4. Density of injuries – arc elasticity (equations 16–18)

Figure 5 shows a chart of the relations between *DI* on national roads and *AADT* for different classes of road, Figure 6 – a chart of the relations between *RLA* and *DI*, Figure 7 – between *PBA* and density of injuries (*DI*), and Figure 8 – between *PHV* and *DI*. Based on the results of the study, it is possible to determine the impact of those factors that have the greatest influence on the level of road traffic hazards.

Annual average traffic volume (AADT). The most commonly encountered models for estimating the predicted number of accidents are power-exponential models, the most important element of which is the risk exposure variable represented by AADT. An increase by 1% of this variable results in a 0.84-0.9% increase in the number of injured.

Location of road (RLA). The RLA variable has a significant impact on the risk on single carriageways. It contains factors which were not included in the model due to the lack of data (land use, transit traffic, maintenance of the road network, curvature, share of pedestrian traffic, etc.).

Share of built-up sections (PBA). An increase by 1% in built-up areas results in a decrease in casualties by 0.12-0.14%. The built-up areas are typically more accessible to a larger number of road users (number of exits, intersections, pedestrian crossings, etc.) with more traffic on side roads, all this resulting in the increased exposure (increase in accidents). On the other hand, the speed limits in these areas determine the accident severity.

Share of heavy vehicles (PHV). An increase by 1% in the share of heavy-duty vehicles results in a decrease in casualties ranging from 0.17 to 0.19%. Paradoxically, this situation is not favourable. The decline in injuries may result from an increase in the number of fatalities. The reason for this is the greater need for overtaking, which unfortunately results in an increase in the number of head-on accidents, having some of the highest rates of severity in relation to fatalities.

Technical grade and road cross-section type (T). The important role of this variable is confirmed in research by other authors who point to the significant impact of this feature on the number of road accidents and victims. The technical class and cross-section of the road have an impact on road parameters (curvature, waviness, design speed, road accessibility, etc.) and indirectly affect the speed of travel that affects the road safety level.

Share of sections with additional lane for going straight ahead (additional) (PAL). An increase in the share of sections with additional lanes allows for safe overtaking, among other things. Furthermore, on such sections there are traffic separation and limited accessibility lanes, which result in higher levels of road safety.

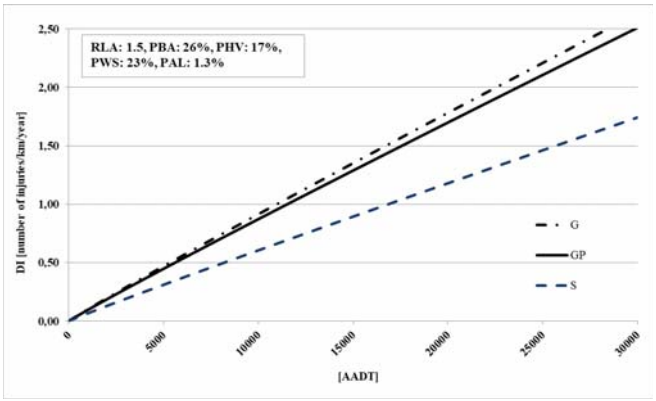

Fig. 5. Density of injuries – effects of traffic volume (AADT) - equation 16

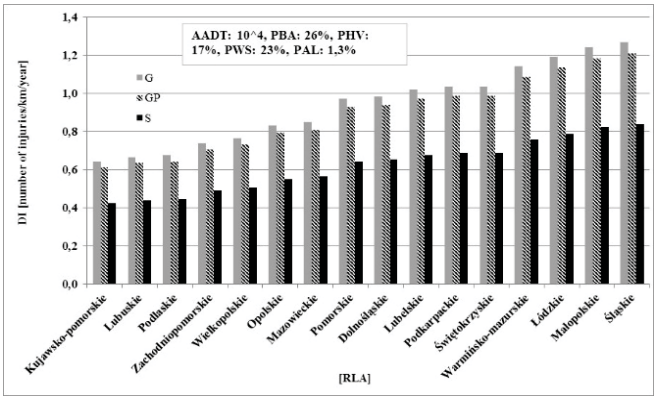

Fig. 6. Density of injuries – effects of location of road (RLA) - equation 16

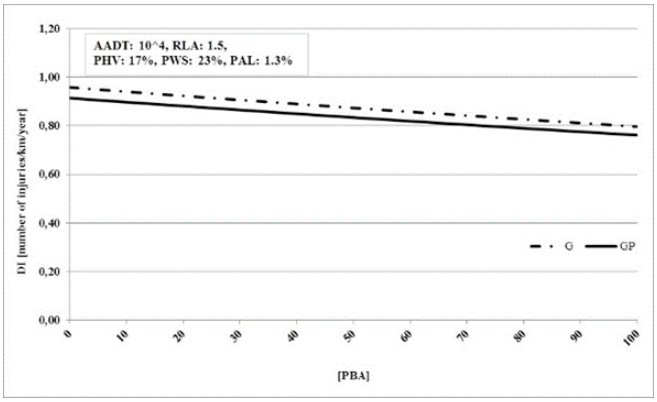

Fig. 7. Density of injuries – effects of share of built-up sections (PBA) – equation 16

** Class S roads cannot pass through built-up areas (PBA), so they do not appear on the chart.*

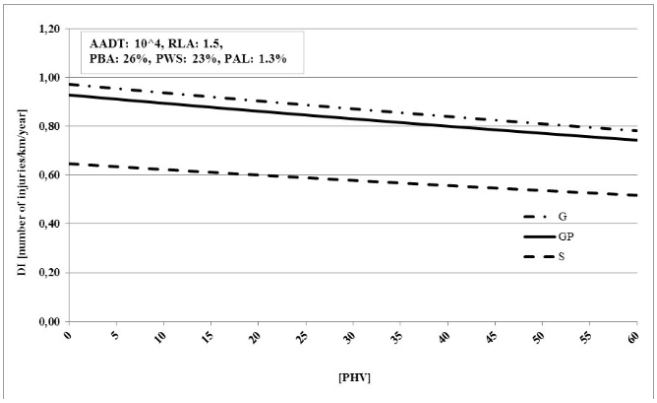

Fig. 8. Density of injuries – effects of share of heavy vehicles (PHV) – equation 16

CONCLUSIONS AND RECOMMENDATIONS

As well as explaining how mathematical models should be built, the article presents a model of injury density (DI), based on a number of road and traffic factors. The design of the model includes variables of traffic (AADT, PHV), location (PBA), cross-section (PWS, PNS, PUS, PEL, PCL, PAL), density of junctions and exits (DIT, DITE, DIS, DD), roadside (PST), pedestrian and cyclist facilities (PP), and automatic enforcement (DCS). The results are consistent with those reported by other researchers and help to fill the gap when it comes to research on long sections and modelling road safety measures for accident victims.

The main goal of the research has been achieved which was to estimate, based on risk analysis, the effects of selected road and traffic factors on the density of injuries (DI) on long sections. All the models offer a very good match between the data observed and those estimated from the model. This helps to achieve a practical objective which is to build tools for road safety management, primarily to understand how new infrastructure projects will impact road safety. The models can also be used as a component of the road safety analysis method in multi-criteria analyses and in software for estimating the number of accidents depending on traffic distribution within the road network.

The next stage of the work will be to build models for fatality and serious injury numbers and density which will help to estimate potential accident severity. The authors are planning to improve short section models (less than 5 km). While the literature on this is quite rich, the specificity of Poland's road network calls for dedicated models for a more effective operational risk management. This will support road safety inspections and ranking of road and roadside hazards.

A key element to the continued work will be the implementation of selected road safety management tools for regional roads whose safety standards are inferior to those of national roads and accident risks are higher.

FUNDING

The analyses were carried out and financed under a contract with the Gdansk University of Technology.

ACKNOWLEDGEMENTS

The authors wish to thank the National Police of Poland for the accident data and the General Directorate for National Roads and Motorways for the data from the Road Databank. The work and its outcomes build on earlier work aimed to develop methods for estimating accident indicators to support analyses of economic effectiveness of new roads and develop a method for assessing the effects of new road infrastructure projects on road safety.

REFERENCES

1. AASHTO, 2010. Highway Safety Manual. American Association of State Highway and Transportation Officials, Washington.

2. Abdel-Aty, M., Radwan, A.E., 2000a. Developing crash predictive models for a principal arterial, in: Traffic Safety on Two Continents. pp. 177–194.

3. Abdel-Aty, M., Radwan, A.E., 2000b. Modeling traffic accident occurrence and involvement. Accid. Anal. Prev. 32 5 , 633–42.

4. Abdel-Aty, M., Radwan, A.E., 2000c. Modeling traffic accident occurrence and involvement. Accid. Anal. Prev. 32 5 , 633–42.

5. Al-ghamdi, A.S., 2002. Using logistic regression to estimate the influence of accident factors on accident severity. Accid. Anal. Prev. 34, 729–741.

6. Ambros, J., Sedoník, J., 2016. A Feasibility Study for Developing a Transferable Accident Prediction Model for Czech Regions. Transp. Res. Procedia 14, 2054–2063. doi:10.1016/J.TRPRO.2016.05.103

7. Anastasopoulos, P.C., Mannering, F., Shankar, V.N., Haddock, J.E., 2012a. A study of factors affecting highway accident rates using the random-parameters tobit model. Accid. Anal. Prev. 45, 628–33. doi:10.1016/j.aap.2011.09.015

8. Anastasopoulos, P.C., Mannering, F., Shankar, V.N., Haddock, J.E., 2012b. A study of factors affecting highway accident rates using the random-parameters tobit model. Accid. Anal. Prev. 45, 628–33. doi:10.1016/j.aap.2011.09.015

9. Anastasopoulos, P.C., Shankar, V.N., Haddock, J.E., Mannering, F., 2012c. A multivariate tobit analysis of highway accident-injury-severity rates. Accid. Anal. Prev. 45, 110–9. doi:10.1016/j.aap.2011.11.006

10. Asgarzadeh, M., Verma, S., Mekary, R.A., Courtney, T.K., Christiani, D.C., 2017. The role of intersection and street design on severity of bicycle-motor vehicle crashes. Inj. Prev. 23 3 , 179–185. doi:10.1136/injuryprev-2016-042045

11. Bared, J.G., Vogt, A., 1998. Accident models for two-lane rural roads: segments and intersections. Federal Highway Administration.

12. Bhatia, R., Wier, M., Weintraub, J., Humphreys, E.H., Seto, E., 2009. An area-level model of vehicle-pedestrian injury collisions with implications for land use and transportation planning. Accid. Anal. Prev. doi:10.1016/j.aap.2008.10.001

13. Broughton, J., 1991. Forecasting road accident casualties in Great Britain. Accid. Anal. Prev. 23 5 , 353–362.

14. Budzynski, M., Jamroz, K., Kustra, W., Gaca, S., Michalski, L., 2011. Instructions for road safety auditors – Part One Assessing the effects of road infrastructure projects on road safety, Part Two Road safety audit – for the GDDKiA. Gdansk University of Technology, Krakow University of Technology, Gdansk.

15. Budzynski, M., Jamroz, K., Kustra, W., Zukowska, J., 2015. Modeling of traffic safety indicators on Polish national road network, in: Safety and Reliability of Complex Engineered Systems - Proceedings of the 25th European Safety and Reliability Conference, ESREL 2015. pp. 23–30.

16. Budzynski, M., Kustra, W., Jamroz, K., Gaca, S., Michalski, L., Guminska, L., 2013. Method for forecasting road safety indicators for the purposes of economic effectiveness analyses for projects on Poland's national roads – for the GDDKiA. Gdansk University of Technology, Krakow University of Technology, Gdansk.

17. Budzynski, M., Rys, D., Kustra, W., 2017. Selected Problems of Transport in Port Towns - Tri-City as an Example. Polish Marit. Res. 24 s1 , 16–24. doi:10.1515/pomr-2017-0016

18. Cafiso, S., Di Graziano, A., Di Silvestro, G., La Cava, G., Persaud, B., 2010. Development of comprehensive accident models for two-lane rural highways using exposure, geometry, consistency and context variables. Accid. Anal. Prev. 42 4 , 1072–9. doi:10.1016/j.aap.2009.12.015

19. Council, F.M., Harwood, D.W., Hauer, E., Hughes, W.E., Vogt, A., 2000. Prediction of the Expected Safety Performance of Rural Two-Lane Highways. Federal Highway Administration.

20. Deffenbacher, J.L., Lynch, R.S., Filetti, L.B., Dahlen, E.R., Oetting, E.R., 2003. Anger, aggression, risky behavior, and crash-related outcomes in three groups of drivers. Behav. Res. Ther. 41, 333–349. doi:10.1016/S0005-7967(02)00014-1

21. Donmez, B., Boyle, L.N., Lee, J.D., 2007. Safety implications of providing real-time feedback to distracted drivers. Accid. Anal. Prev. 39 3 , 581–590. doi:10.1016/J.AAP.2006.10.003

22. El-Basyouny, K., Sayed, T., 2009. Accident prediction models with random corridor parameters. Accid. Anal. Prev. 41 5 , 1118–23. doi:10.1016/j.aap.2009.06.025

23. Elvik, R., 2008. The predictive validity of empirical Bayes estimates of road safety. Accid. Anal. Prev. 40 6 , 1964–9. doi:10.1016/j.aap.2008.07.007

24. Fernandes, A., Neves, J., 2013a. An approach to accidents modeling based on compounds road environments. Accid. Anal. Prev. 53 2013 , 39–45. doi:10.1016/j.aap.2012.12.041

25. Fernandes, A., Neves, J., 2013b. An approach to accidents modeling based on compounds road environments. Accid. Anal. Prev. 53 2013 , 39–45. doi:10.1016/j.aap.2012.12.041

26. Garber, N.J., Lei, W., 2001. Stochastic Models Relating Crash Probabilities With Geometric And Corresponding Traffic Characteristics Data. University of Virginia, Charlottesville.

27. Geedipally, S.R., Lord, D., Dhavala, S.S., 2012a. The negative binomial-Lindley generalized linear model: characteristics and application using crash data. Accid. Anal. Prev. 45 2012 , 258–65. doi:10.1016/j.aap.2011.07.012

28. Geedipally, S.R., Lord, D., Dhavala, S.S., 2012b. The negative binomial-Lindley generalized linear model: characteristics and application using crash data. Accid. Anal. Prev. 45 2012 , 258–65. doi:10.1016/j.aap.2011.07.012

29. Hakkert, S., 2011. EuroRAP evaluation experience alongside other measures in Israel, in: EuroRAP Plenary, Policy Seminar and Training Course, Belgrade.

30. Hauer, E., 2007. Safety Models for Urban Four-lane Undivided Road Segments. Transp. Res. Rec. J. Transp. Res. Board 96–105 , 1–22.

31. Hauer, E., 2004. Statistical Road Safety Modeling. Transp. Res. Rec. J. Transp. Res. Board 1897 May , 81–87. doi:10.3141/1897-11

32. Hauer, E., 2001. Overdispersion in modelling accidents on road sections and in empirical bayes estimation. Accid. Anal. Prev. 33 6 , 799–808.

33. Hauer, E., 1995. On exposure and accident rate. Traffic Eng. Control 36, 134–138.

34. Hauer, E., 1986. On the estimation of the expected number of accidents. Accid. Anal. Prev. 18 1, 1–12. doi:10.1016/0001-4575(86)90031-X

35. Hewson, P., 2004. Deprived children or deprived neighbourhoods? A public health approach to the investigation of links between deprivation and injury risk with specific reference to child road safety in Devon County, UK. BMC Public Health 4, 15. doi:10.1186/1471-2458-4-15

36. Ivan, J.N., Garder, P.E., Deng, Z., Zhang, C., 2006. The effect of segment characteristics on the severity of head-on crashes on two-lane rural highways. University of Connecticut, University of Maine.

37. Ivan, J.N., Lord, D., Washington, S.P., 2005. Poisson, Poisson-gamma and zero-inflated regression models of motor vehicle crashes: balancing statistical fit and theory. Accid. Anal. Prev. 37 1 , 35–46. doi:10.1016/j.aap.2004.02.004

38. Iyinam, A.F., Iyinam, S., Ergun, M., 1997. Analysis of Relationship Between HighwaySafety and Road Geometric Design Elements : Turkish Case. Technical University of Istanbul.

39. Jamroz, K., 2011. Method of risk management in highway engineering. Gdansk University of Technology, Gdansk.

40. Jamroz, K., Kustra, W., 2011. The risk atlas of Poland ' s national roads 2008-2010. Foundation for Development of Civil Engineering, Gdansk.

41. Jurewicz, C., Steinmetz, L., 2012. Crash performance of safety barriers on high - speed roads. J. Australas. Coll. Road Saf. 23 3 .

42. Kiec, M., 2009. The impact of the accessibility of the road on conditions and traffic safety - PhD thesis. Cracow University of Technology.

43. Kustra, W., 2016. Modelling selected road safety measures on long road sections - thesis.

44. Kustra, W., Budzynski, M., Jamroz, K., Zukowska, J., 2015. Modelling of traffic safety indicators on Polish national road network, in: ESREL 2015 25th European Safety and Reliability Conference. Zurich, p. 7.

45. Lao, Y., Wu, Y.-J., Corey, J., Wang, Y., 2011a. Modeling animal-vehicle collisions using diagonal inflated bivariate Poisson regression. Accid. Anal. Prev. 43 1 , 220–7. doi:10.1016/j.aap.2010.08.013

46. Lao, Y., Wu, Y.-J., Corey, J., Wang, Y., 2011b. Modeling animal-vehicle collisions using diagonal inflated bivariate Poisson regression. Accid. Anal. Prev. 43 1 , 220–7. doi:10.1016/j.aap.2010.08.013

47. Lee, C., Hellinga, B., Saccomanno, F., 2006. Evaluation of variable speed limits to improve traffic safety. Transp. Res. Part C Emerg. Technol. 14 3 , 213–228. doi:10.1016/J.TRC.2006.06.002

48. Lee, J., Mannering, F., 2002. Impact of roadside features on the frequency and severity of run-off-roadway accidents: an empirical analysis. Accid. Anal. Prev. 34 2 , 149–61.

49. Li, R., Shang, P., 2014. Incident duration modeling using flexible parametric hazard-based models. Comput. Intell. Neurosci. 2014, 723427. doi:10.1155/2014/723427

50. Litman, T., 2010. Transportation Elasticities, Transportation. Victoria Transport Policy Institute, Victoria.

51. Lord, D., 2006. Modeling motor vehicle crashes using Poisson-gamma models: examining the effects of low sample mean values and small sample size on the estimation of the fixed dispersion parameter. Accid. Anal. Prev. 38 4 , 751–66. doi:10.1016/j.aap.2006.02.001

52. Lord, D., Geedipally, S.R., 2012. Examining the Crash Variances Estimated by the Poisson-Gamma and Conway-Maxwell-Poisson Models. Transp. Res. Rec. J. Transp. Res. Board 2241 979 , 56–67.

53. Lord, D., Park, B., 2012. Negative Binomial Regression Models and Estimation Methods, in: Probability Density and Likelihood Functions. Texas A&M University, Korea Transport Institute, pp. 1–15.

54. Lord, D., Park, P.Y.-J., 2008. Investigating the effects of the fixed and varying dispersion parameters of Poisson-gamma models on empirical Bayes estimates. Accid. Anal. Prev. 40 4 , 1441–57. doi:10.1016/j.aap.2008.03.014

55. Ma, J., Kockelman, K.M., Damien, P., 2008a. A multivariate Poisson-lognormal regression model for prediction of crash counts by severity, using Bayesian methods. Accid. Anal. Prev. 40 3 , 964–75. doi:10.1016/j.aap.2007.11.002

56. Ma, J., Kockelman, K.M., Damien, P., 2008b. A multivariate Poisson-lognormal regression model for prediction of crash counts by severity, using Bayesian methods. Accid. Anal. Prev. 40 3 , 964–75. doi:10.1016/j.aap.2007.11.002

57. Mannering, F., Venkataraman, S., Woodrow, B., 1996. Statistical analysis of accident rural freeways. Accid. Anal. Prev. 28 3 , 391–401.

58. Martinelli, F., La Torre, F., Vadi, P., 2009. Calibration of the Highway Safety Manual's Accident Prediction Model for Italian Secondary Road Network. Transp. Res. Rec. J. Transp. Res. Board 2103, 1–9. doi:10.3141/2103-01

59. Peer, E., Rosenbloom, T., 2013. When two motivations race: The effects of time-saving bias and sensation-seeking on

driving speed choices. Accid. Anal. Prev. 50, 1135–1139. doi:10.1016/J.AAP.2012.09.002

60. Ptak-Chmielewska, A., 2013. Generalised linear models. Warsaw School of Economic, Warsaw.

61. Rakha, H., Arafeh, M., Abdel-Salam, A.G., Guo, F., Flintsch, A.M., 2010. Linear regression crash prediction models: issues and proposed solutions, Virginia Tech Transportation Institute.

62. Reurings, M., Jannsen, T., Eenink, R., Elvik, R., Cardoso, J., Stefan, C., 2005. Accident Prediction Models and Road Safety Impact Assessment a state of the art, Ripcord. Ripcord - Iserest.

63. Ryb, G.E., Dischinger, P.C., Kleinberger, M., McGwin, G., Griffin, R.L., 2013. Aortic injuries in newer vehicles. Accid. Anal. Prev. 59, 253–259. doi:10.1016/J.AAP.2013.06.007

64. Schafer, J., 2006. Penn State Department of Statistics [WWW Document]. Dep. Stat. Eberly Coll. Sci. URL sites. stat.psu.edu

65. Scott-Parker, B., Watson, B., King, M., Hyde, M., 2012. Young, Inexperienced, and on the Road. Transp. Res. Rec. J. Transp. Res. Board. doi:10.3141/2318-12

66. Son, H. "Daniel," Kweon, Y.-J., Park, B. "Brian," 2011. Development of crash prediction models with individual vehicular data. Transp. Res. Part C Emerg. Technol. 19 6 , 1353–1363. doi:10.1016/j.trc.2011.03.002

67. Technical Committee 18, 2004. Study on Risk Management for Roads. PIARC.

68. The National Police Headquarters, 2015. SEWIK - Accident data base.

69. Vaziri, M., 2010. A comparative appraisal of roadway accident for Asia-Pacific countries. Int. J. Eng. Trans. A Basics 23 2 , 111–126.

70. Wood, G.R., 2005. Confidence and prediction intervals for generalised linear accident models. Accid. Anal. Prev. 37 2 , 267–73. doi:10.1016/j.aap.2004.10.005

71. Xie, K., Wang, X., Huang, H., Chen, X., 2013. Corridor-level signalized intersection safety analysis in Shanghai, China using Bayesian hierarchical models. Accid. Anal. Prev. 50, 25–33. doi:10.1016/J.AAP.2012.10.003

72. Yannis, G., Papadimitriou, E., Chaziris, A., Broughton, J., 2014. Modeling road accident injury under-reporting in Europe. Eur. Transp. Res. Rev. 6 4 , 425–438. doi:10.1007/s12544-014-0142-4

73. Ye, Z., Zhang, Y., Lord, D., 2013a. Goodness-of-fit testing for accident models with low means. Accid. Anal. Prev. 61, 78–86. doi:10.1016/j.aap.2012.11.007

74. Ye, Z., Zhang, Y., Lord, D., 2013b. Goodness-of-fit testing for accident models with low means. Accid. Anal. Prev. 61, 78–86. doi:10.1016/j.aap.2012.11.007

75. Zhang, W., Huang, Y.-H., Roetting, M., Wang, Y., Wei, H., 2006. Driver's views and behaviors about safety in China—What do they NOT know about driving? Accid. Anal. Prev. 38 1, 22–27. doi:10.1016/J.AAP.2005.06.015

CONTACT WITH THE AUTHORS

Wojciech Kustra
e-mail: Wojciech.kustra@pg.edu.pl

Gdańsk University of Technology
Faculty od Civil and Environmental Engineering
Narutowicza 11, 80-233 Gdansk
Poland

sciendo

POLISH MARITIME RESEARCH 2 (102) 2019 Vol. 26; pp. 104-114
10.2478/pomr-2019-0030

ROBUST MODEL PREDICTIVE CONTROL FOR AUTONOMOUS UNDERWATER VEHICLE – MANIPULATOR SYSTEM WITH FUZZY COMPENSATOR

Hossein Nejatbakhsh Esfahani
Gdansk University of Technology, Poland

ABSTRACT

This paper proposes an improved Model Predictive Control (MPC) approach including a fuzzy compensator in order to track desired trajectories of autonomous Underwater Vehicle Manipulator Systems (UVMS). The tracking performance can be affected by robot dynamical model uncertainties and applied external disturbances. Nevertheless, the MPC as a known proficient nonlinear control approach should be improved by the uncertainty estimator and disturbance compensator particularly in high nonlinear circumstances such as underwater environment in which operation of the UVMS is extremely impressed by added nonlinear terms to its model. In this research, a new methodology is proposed to promote robustness virtue of MPC that is done by designing a fuzzy compensator based on the uncertainty and disturbance estimation in order to reduce or even omit undesired effects of these perturbations. The proposed control design is compared with conventional MPC control approach to confirm the superiority of the proposed approach in terms of robustness against uncertainties, guaranteed stability and precision.

Keywords: UVMS, Model Predictive Control, Fuzzy Compensator

INTRODUCTION

Nowadays, engaging the underwater autonomous mobile platforms has been adopted by various operators and industries in order to explore underwater environment, accomplish inspections of undersea structures using non-destructive tests, detect damage revealed inside of the nuclear reactor containment and kinds of other works which are limited by the rigorous circumstances of an unknown environment. The two main parts of an autonomous system are navigation and control which recently striking researches have been presented in [15,16,17] applied to the marine navigation area such as optimized path planning and collision avoidance strategies. Regarding the control part of an underwater autonomous platform, due to the high nonlinear terms of the Underwater Vehicle-Manipulator System (UVMS) dynamics, some robust control strategies were used or contributed by the researchers as high-performance control approaches against all the uncertainties and external disturbances. The hydro-static and hydro-dynamic uncertainties discovered during underwater manipulator movement are comprised of the added mass, added Coriolis, buoyancy force, drag force and frictional forces. As a common robust approach, the Sliding Mode Controller (SMC) has been chiefly applied for controlling the robotic systems under uncertainties and nonlinear parameters [1, 2]. Nevertheless, beside of the robustness attribute in SMC, the actuator flaws and finally decreasing of the control performance, particularly

for trajectory tracking goals, has been brought about by the chattering phenomenon. As literature reviews concerning SMC application for underwater robotic systems, an optimal SMC has been designed in [3] which the critical coefficients of sliding surface have been estimated using wavelet theory in order to acquire most suitable coefficients and gains for producing the optimal input torques. In [4] a perfect robust method as a Time Delay Control (TDC) algorithm is applied for controlling the UVMS autonomously. In this work, TDC in conjunction with the Terminal Sliding Mode (TSM) was considered to promote the robustness feature and tracking accuracy. However, some of the most important parameters in the TDC control law were not adjusted adaptively and this automatic gain tuning was regarded just for SMC by the fuzzy rules. Another contribution regarding SMC improvement has been done in [5] which is dedicated to the chattering reduction issue. In this case, a new reaching mode including an exponential function was designed in order to mitigate chattering frequencies. Concerning some researches addressed to the MPC approaches, an obstacle avoidance application using MPC associated with Fuzzy logic and the model predictive control of a floating manipulator is contributed in [13] and [14] respectively. An effective method for nonlinear MPC was considered for a 6 D.O.F manipulator in [6]. In this work, the model has first been linearized and decoupled by feedback and then an MPC algorithm has been implemented. A robust multi-loop control scheme including an Integral Sliding Mode (ISM) loop and MPC loop has been presented in [7] which the ISM role is rejection of uncertain terms due to unknown dynamics. Due to the problem of planning a trajectory for robots starting in an initial state and reaching the final state, research concerning the application of MPC for reference-tracking problems has been done in [8]. In [9] a novel combination of MPC and SMC with motivation of constraint satisfaction and robustness property has been presented. In this research, the proposed control algorithm is designed based on the MPC concepts. The staple achievement of this work is increasing the robustness attribute of MPC using fuzzy rules for omission of perturbation effects upon the UVMS.

Indeed, a novel perturbation compensating algorithm is proposed to fulfill the more accurate path tracking in the presence of environmental disturbances which finally lead to a robust MPC. The capability of the novel Robust Model Predictive Fuzzy (RMPF) algorithm is first analyzed. Then, the proposed RMPC algorithm is adopted to solve the UVMS tracking problem, and its performance is compared with a conventional MPC controller.

Nevertheless, the proposed control is a combination of MPC and uncertainty estimation and fuzzy compensator as the constraint satisfaction, optimal force/torque and robustness property are provided. Also, due to the high nonlinearities, uncertainties exerted to the UVMS and applied severe external disturbance, the compensating strategy or other robust control approach must be adopted to overcome the problems raised by this issue. However, for many nonlinear applications in the robotics area, the model predictive control approach has been used as an optimal and model-based control strategy but should be enhanced in terms of the robustness factor to be more usable regarding mobile robots particularly when one uses them in more uncertain and disturbance conditions. Indeed, the motivation is to inherit the ability to explicitly deal with state and input constraints from MPC and the good perturbation effects reduction from fuzzy compensator. In the rest of this paper, the UVMS dynamical model with 4 degrees of freedom (DOF) is described and all the added forces and parameters for circle moving of the mobile spherical platform and coupled planar manipulator are shown in the next section. The third section is dedicated to explaining model predictive control approach. Then proposed robust MPC control law based on the fuzzy compensator and uncertainties estimator are presented in section IV. In section V, the computer simulation results and their comparison are shown to confirm high performance of the proposed control. Finally, the conclusion of this work is provided in section VI.

UDERWATER MANIPULATOR DYNAMICS

In a UVMS, an underwater manipulator is mounted on the vehicle. Fig. 1 illustrates a 2 DOF underwater manipulator mounted on the spherical vehicle. The coupled effect between the manipulator and the vehicle is considered. The spherical vehicle is similar to the Omni-directional Intelligent Navigator (ODIN) underwater robot [18].

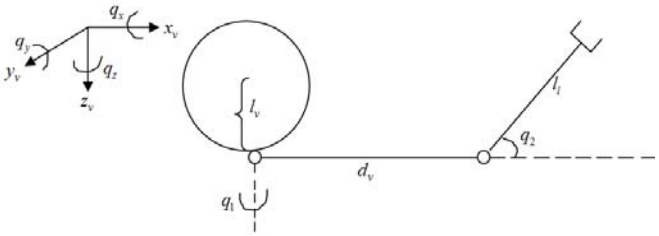

Fig.1. Underwater Vehicle-Manipulator System

The motion of ODIN consists of 3 linear motions and 3 revolute motions. Three linear motions are along the x, y and z axes that are named surge, sway and heave respectively. Also, three revolute motions are on x, y and z axes that are named roll, pitch and yaw, respectively. The Denaviat-Hratenburg (D-H) parameters for UVMS with considering only revolute motions are shown in Table. 1.

Tab.1. D-H Parameters of UVMS

Joint	a	α	d	θ
1	0	-90	0	q_x
2	0	+90	0	q_y
3	0	0	l_v	q_z
4	d_v	+90	0	q_1
5	l_l	-90	0	q_2

where
a, α, d, θ are link length, link twist, link offset and joint angle, respectively.

Fig. 2 illustrates an underwater vehicle-manipulator system 5 DOF with only revolute motions.

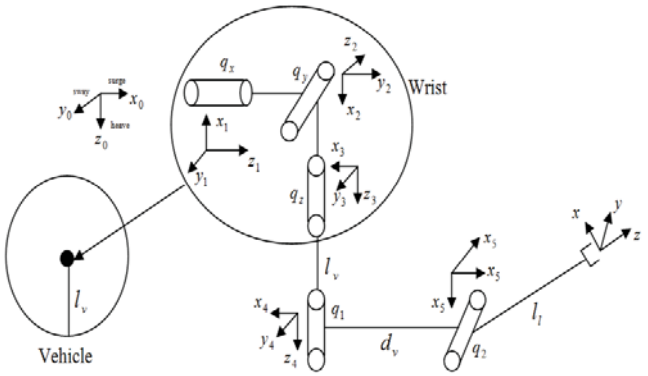

Fig. 2. UVMS with only revolute motions

KINETIC ENERGY

Added mass of an underwater vehicle-manipulator system is included in the system dynamics in the form of kinetic energy. Neglecting the kinetic energy of the manipulator due to added mass, the total kinetic energy of the UVMS can be written as

$$T = T_{RB} + T_A \tag{1}$$

Kinetic energy of the UVMS due to a rigid body is expressed as

$$T_{RB} = \frac{1}{2}m_d\dot{x}_{c_1}^2 + \frac{1}{2}m_l\dot{x}_{c_2}^2 + \frac{1}{2}I_1\dot{q}_1^2 + \frac{1}{2}I_2\dot{q}_2^2 + \frac{1}{2}I_z\dot{q}_z^2 + \frac{1}{2}I_y\dot{q}_y^2 + \frac{1}{2}I_x\dot{q}_x^2 + \frac{1}{2}m_v(\dot{x}_v^2 + \dot{y}_v^2 + \dot{z}_v^2) \tag{2}$$

In the above equation, x_{c1} and x_{c2} are mass centers of the first link (d_v) and the second link (l_l) of manipulator, respectively. Also $\dot{x}_v$, $\dot{y}_v$ and $\dot{z}_v$ are the linear velocities of the spherical vehicle along the x, y and z axes, respectively. I_1, I_2 are the moment of inertia of the manipulator. Also, I_x, I_y and I_z are the moments of inertia of spherical vehicle that is expressed as (3) [18].

$$I_x = I_y = I_z = \frac{8}{15}\pi\rho l_v^5 \tag{3}$$

where is ρ the water density and l_v is the radius of spherical vehicle. Kinetic energy of the spherical vehicle due to added mass is

$$T_A = \frac{1}{2}v_v^T M_{Av} v_v \,,\; v_v = \left[\dot{x}_v, \dot{y}_v, \dot{z}_v, \dot{q}_z, \dot{q}_y, \dot{q}_x\right]^T \tag{4}$$

when M_{Av} the inertia matrix of the spherical vehicle is expressed as the following [18].

$$M_{Av} = diag(\tfrac{2}{3}\pi\rho l_v^3, \tfrac{2}{3}\pi\rho l_v^3, \tfrac{2}{3}\pi\rho l_v^3, 0,0,0) \tag{5}$$

LAGRANGE FORMULATION

The UVMS is considered as an 8 DOF dynamic system. The Lagrange equation of motion in the matrix form is

$$\frac{d}{dt}\left(\frac{\partial T}{\partial \dot{q}}\right) - \left(\frac{\partial T}{\partial q}\right) = Q = [F_1, F_2, F_3, \tau_4, \tau_5, \tau_6, \tau_7, \tau_8]^T \tag{6}$$

where T is the total kinematic energy of the system and it is obtained from equation (1). Also, q is the vector of generalized positions and $\dot{q}$ is the vector of generalized velocities. The vector of generalized positions is

$$q = \left[x_v, y_v, z_v, q_z, q_y, q_x, q_1, q_2\right]^T \tag{7}$$

$Q_{n\times 1}$ in the equation (6) is the vector of generalized forces and torques applied to the UVMS. Substituting the above expression in equation (6), one obtains the dynamic equations of motion which include rigid body and added mass as follows

$$Q = M(q)\ddot{q} + C(q,\dot{q})\dot{q} \tag{8}$$

where,
$M_{n\times n}(q)$ is total inertia matrix including rigid body inertia matrix and added inertia matrix.
$C_{n\times n}(q,\dot{q})$ is total Coriolis and centripetal matrix including rigid body and hydrodynamic Coriolis and centripetal matrix.

DRAG FORCE

Drag force in UVMS is divided in two parts. The first part includes drag force applied on link_1 and link_2 of the manipulator that are derived from following equations

$$D_1 = \frac{\rho}{2}c_d dia_1 \int_0^{d_v} v_1^2 dx_1 \;,\quad D_2 = \frac{\rho}{2}c_d dia_2 \int_0^{l_l} v_2^2 dx_2 \tag{9}$$

where dia_1, dia_2 and c_d are the diameter of link_1, the diameter of link_2 and the drag coefficient, respectively. Also, v_1, v_2 are translational velocities of links. The second part is the drag force applied on the spherical vehicle that is [18]

$$D_v = diag(d_t|\dot{x}_v|, d_t|\dot{y}_v|, d_t|\dot{z}_v|, d_1|\dot{q}_z| + d_2, d_1|\dot{q}_y| + d_2, d_1|\dot{q}_x| + d_2)\left[\dot{x}_v, \dot{y}_v, \dot{z}_v, \dot{q}_z, \dot{q}_y, \dot{q}_x\right]^T \tag{10}$$

where d_t, d_1 and d_2 are translational quadratic damping factor, angular quadratic damping factor and angular linear damping factor respectively. Therefore, the total drag force applied on the UVMS is expressed as

$$D(q,\dot{q}) = [D_v \quad D_1 \quad D_2]^T \tag{11}$$

GRAVITATIONAL AND BUOYANT FORCES

Buoyancy force is equal to the weight of the fluid displaced by link/body and acts through the center of buoyancy of the link/vehicle. Also, buoyant force is in the opposite direction of gravitational force.

$$F_U(q) = G(q) - B(q) = mg - \rho g v \tag{12}$$

where v is the volume of the link/vehicle. Therefore, this force has affected the heave motion of vehicle and link_2. By calculating the force ($F_U(q)$) in all motion directions, the potential energy (U) is calculated. Therefore, the matrix $h(q)$ is expressed as

$$h(q) = -\frac{d}{dt}\left(\frac{\partial u}{\partial \dot{q}}\right) - \left(\frac{\partial u}{\partial q}\right) = \left(\frac{\partial u}{\partial q}\right) \tag{13}$$

$$h(q) = [h_1, h_2, h_3, h_4, h_5, h_6, h_7, h_8]^T \tag{14}$$

In the recent vector, all the components are zero except h_3, h_4.

$$h_3 = gm_v - g\rho v_v \tag{15}$$

$$h_8 = -0.5 l_l m_l g cos(q_2 + q_y) + 0.5 g cos(q_2 + q_y)\rho v_l l_l \tag{16}$$

where v_v, v_l are volume of the spherical vehicle and the cylindrical link, respectively.

FINAL DYNAMIC EQUATION OF UVMS

Using equations (8), (12), (14) one can write the final form of the dynamic motion equations of the UVMS as

$$Q = M(q)\ddot{q} + C(q,\dot{q})\dot{q} + D(q,\dot{q}) + h(q) \tag{17}$$

MODEL PREDICTIVE CONTROL

The objective of the nonlinear MPC is to accomplish a control law $\tau(t)$ in order to track the desired output path q_d at the next time $(t + t_h)$ via the minimization of Cost Function (CF).

$$CF = f(e_q(t + t_h), X, \tau) \tag{18}$$

Where $e_q(t + t_h)$ is a predicted error, $q(t + t_h)$ is a t_h-step ahead prediction of the output and $t_h > 0$ is a prediction horizon. The Taylor series expansion is derived by Lie derivatives [11] for extracting a prediction model for robotic underwater manipulator as follows:

$$q(t + t_h) = q(t) + t_h\dot{q}(t) + \frac{t_h^2}{2!}\ddot{q}(t) \tag{19}$$

The state-space model of underwater robotic manipulator is expressed as follows:

$$Q(t) = \begin{bmatrix} q(t) \\ \dot{q}(t) \\ \ddot{q}(t) \end{bmatrix} = \begin{bmatrix} X_1 \\ X_2 \\ -M^{-1}(X_1)(C(X_1,X_2)X_2 + h(X_1) + D(X_1,X_2)) \end{bmatrix} + \begin{bmatrix} 0 \\ 0 \\ M^{-1}(X_1)\tau(t) \end{bmatrix} \tag{20}$$

Then, the prediction model (19) is rewritten as

$$q(t + t_h) = T(t_h)Q(t) \tag{21}$$

where,

$$T(t_h) = \left[I_{nn} \quad t_h * I_{nn} \quad \left(\frac{t_h^2}{2!}\right) * I_{nn}\right]$$

Based on the same approach, the predicted desired trajectory q_d is shown as

$$q_d(t + t_h) = T(t_h)Q_d(t) \tag{22}$$

where,

$$Q_d(t) = [q_d \quad \dot{q}_d \quad \ddot{q}_d]^T$$

Now, the predicted error can be calculated by

$$e_q(t + t_h) = q(t + t_h) - q_d(t + t_h) = T(t_h)(Q(t) - Q_d(t)) \tag{23}$$

The cost function based on the tracking error is presented upon the future horizon:

$$CF = \frac{1}{2}\int_0^{t_d}\left(q(t+t_h) - q_d(t+t_h)\right)^T \left(q(t+t_h) - q_d(t+t_h)\right) dt_h \quad (24)$$

The control effort can be achieved by tuning t_d. By the prediction model of error (23), the *CF* can be rewritten as

$$\begin{aligned} CF &= \frac{1}{2}\int_0^{t_d} e_q(t+t_h)^T e_q(t+t_h)\ dt_h \\ &= \frac{1}{2}\int_0^{t_d}(T(t_h)(Q(t) - Q_d(t)))^T (T(t_h)(Q(t) - Q_d(t)))\ dt_h \\ &= \frac{1}{2}\left(Q(t) - Q_d(t)\right)^T R(Q(t) - Q_d(t)) \end{aligned} \quad (25)$$

where,

$$R = \int_0^{t_d} T(t_h)^T T(t_h)\ dt_h = \begin{bmatrix} t_d * I_{nn} & \left(\frac{t_d^2}{2}\right) * I_{nn} & \left(\frac{t_d^3}{6}\right) * I_{nn} \\ \left(\frac{t_d^2}{2}\right) * I_{nn} & \left(\frac{t_d^3}{3}\right) * I_{nn} & \left(\frac{t_d^4}{8}\right) * I_{nn} \\ \left(\frac{t_d^3}{6}\right) * I_{nn} & \left(\frac{t_d^4}{8}\right) * I_{nn} & \left(\frac{t_d^5}{20}\right) * I_{nn} \end{bmatrix} = \begin{bmatrix} R_1 & R_2 \\ R_2^T & R_3 \end{bmatrix}$$

The required condition, in order to minimize *CF*, is

$$\frac{\partial\,(CF)}{\partial \tau} = 0 \quad (26)$$

The above mentioned condition can be rewritten by the (20) and (25) as

$$\begin{aligned} &\left(\frac{\partial\left(M^{-1}(X_1)\tau(t)\right)}{\partial\,\tau(t)}\right)^T [R_2^T \quad R_3](N(t) - Q_d(t)) \\ &+\left(\frac{\partial\left(M^{-1}(X_1)\tau(t)\right)}{\partial\,\tau(t)}\right)^T R_3 M^{-1}(X_1)\,\tau(t) = 0 \end{aligned} \quad (27)$$

Hence, the optimal control is

$$\tau(t) = -\hat{M}(X_1)\{[R_3^{-1}R_2 \quad I_{nn}](N(t) - Q_d(t))\} \quad (28)$$

where,

$$N(t) = \begin{bmatrix} q(t) \\ \dot{q}(t) \\ -M^{-1}(X_1)(C(X_1, X_2)X_2 + h(X_1) + D(X_1, X_2)) \end{bmatrix}$$

$$[R_3^{-1}R_2 \quad I_{nn}] = \left[\frac{10}{(3t_d^2)} * I_{nn} \quad \frac{5}{(2t_d)} * I_{nn} \quad I_{nn}\right]$$

Finally, the control law (28) of MPC is rewritten as

$$\tau_{MPC}(t) = -M(X_1)\begin{Bmatrix} K_1(q - q_d) + \\ K_2(\dot{q} - \dot{q}_d) \\ -M^{-1}(X_1)(C(X_1, X_2)X_2 \\ +h(X_1) \\ +D(X_1, X_2)) - \ddot{q}_d \end{Bmatrix} - \delta_{est}(t) \quad (29)$$

where,

$$k_1 = \frac{10}{(3t_d^2)} * I_{nn} \quad (30)$$

$$k_2 = \frac{5}{(2t_d)} * I_{nn} \quad (31)$$

$\delta_{est}(t)$ is the estimation of uncertainties which the approach calculation can be found in the next section.

ROBUST MPC

PERTURBATION ESTIMATOR

The stability analysis of the proposed control approach is carried out by the Lyapunov's second method [12] by which the stability of this highly uncertain robotic system is guaranteed. Due to the underwater circumstances, the matrices of *M, C* and h are affected by added mass, added Coriolis and buoyancy effects respectively. The changing of these matrices can be expressed by ΔM, ΔC, Δh as uncertainties. In addition to these uncertainties, drag force *D* , and external disturbance U_d are also considered and the entire perturbation effect δ is written as

$$\delta = -\{\Delta M\ddot{q} + \Delta C\dot{q} + \Delta h(q) + D(q, \dot{q}) + U_d\} \quad (32)$$

Based on the Lie derivatives and UVMS dynamical model, without considering the perturbation, one can write

$$\begin{aligned} \dot{q} &= L_f h_1(x) = X_2 \\ \ddot{q} &= L_f^2 h_1(x) + L_{g_2} L_f h_1(x)\tau \\ &= -\widehat{M}^{-1}(q)\left(\hat{C}(q, \dot{q})\dot{q} + \hat{h}(q) + \hat{D}(q, \dot{q})\right) + \widehat{M}^{-1}(q)\tau \end{aligned} \quad (33)$$

Substituting the MPC control law (29) in the dynamical model (33) and with considering the δ in (32), dynamical equation of the tracking error can be extracted as

$$\ddot{e}_q(t) + k_2\dot{e}_q + k_1 e_q = M^{-1}e_\delta(t) \quad (34)$$

where, $e_\delta(t) = \delta - \delta_{est}$.

The state-space of the above dynamical equation concerning tracking error is expressed as

$$\dot{\tilde{e}} = \alpha\tilde{e} + \beta M^{-1} e_\delta \tag{35}$$

with $\tilde{e} = \begin{bmatrix} e_q \\ \dot{e}_q \end{bmatrix}$, $\alpha = \begin{bmatrix} 0_{nn} & I_{nn} \\ -k_1 & -k_2 \end{bmatrix}$, $\beta = \begin{bmatrix} 0_{nn} \\ I_{nn} \end{bmatrix}$

One can express the following Lyapunov equation if one declares the matrix α as Hurwitz. With determining the positive definite matrix ψ the equation is written as

$$\alpha^T\psi + \psi\alpha = -\varphi \tag{36}$$

The Lyapunov function is defined as

$$V = \tilde{e}^T\psi\tilde{e} + e_\delta^T\xi e_\delta \tag{37}$$

where, the matrix ξ is considered as a positive definite symmetric.

The time derivative of equation (37) is expressed in regards with (35) and (36) as

$$\dot{V} = -\tilde{e}^T\varphi\tilde{e} + 2e_\delta^T\{(M^{-1})^T\beta^T\psi\tilde{e} + \xi\dot{e}_\delta\} \tag{38}$$

If one determines $\dot{e}_\delta$ as

$$\dot{e}_\delta = -\xi^{-1}(M^{-1})^T\beta^T\psi\tilde{e} \tag{39}$$

Regarding uncertainty variations, because these are not considered, one can assume $\dot{\delta}(t) = 0$. The estimation of uncertainties can be written as dynamical equation based on (39) as

$$\dot{\delta}_{est} = \xi^{-1}(M^{-1})^T\beta^T\psi\tilde{e} \tag{40}$$

The globally stability is guaranteed by satisfying the $\dot{V} \le 0$ which this satisfaction can be proven by substituting (38) in (39) and finally the derivative of Lyapunov is expressed as

$$\dot{V} = -\tilde{e}^T\varphi\tilde{e} \le 0 \tag{41}$$

Since matrix φ is assumed as a positive definite symmetric matrix, the condition $\tilde{e}^T\varphi\tilde{e} > 0$ is true for all vectors $\tilde{e} \neq 0$. Therefore, $\dot{V} \le 0$ and this assure that $\tilde{e}$ and e_δ and are bounded based on the propriety of boundedness. By LaSalle's invariance theorem, the origin is also asymptotically stable. The global asymptotic stability of the estimated closed loop system with uncertainties is guaranteed.

FUZZY COMPENSATOR

If one considers $\tilde{e} = g_1(e,\dot{e})$ and $\rho = g_2(e,\dot{e})$ it can be written as $\rho + \tilde{e} = g_3(e,\dot{e})$ and the equation (40) can be changed to

$$\begin{aligned} \delta_{est} &= \int \xi^{-1}(M^{-1})^T\beta^T\psi\, g_3(e,\dot{e}) - \int \rho\xi^{-1}(M^{-1})^T\beta^T\psi + \varepsilon_1 \\ \delta_{est} &= \hat{L}_1(e,\dot{e}) + \hat{L}_2(e,\dot{e}) + \varepsilon_1,\ \hat{k} = \hat{L}_1 + \hat{L}_2 \end{aligned} \tag{42}$$

$$\rho\delta_{est} = \rho\hat{k}(e,\dot{e}) + \rho\varepsilon_1 \tag{43}$$

The output of fuzzy compensator is defined as follows

$$u_{fuzzy} = \rho(x)\delta_{est} + \varepsilon \tag{44}$$

where $\rho(x)$, is output of fuzzy compensator after defuzzification computed by the Center of Gravity (COG) approach as follow

$$z = \frac{\sum_{i=1}^{n} c_i \mu_{A_i}(x)\mu_{B_i}(y)}{\sum_{i=1}^{n} \mu_{A_i}(x)\mu_{B_i}(y)} \tag{45}$$

Regarding compensator architecture, a two-input single-output Mamdani's inference fuzzy engine is adopted. $\rho(x)$ is determined by inference on input linguistic variables $e(\mathrm{t})$ and $\dot{e}(t)$. Also, fuzzy inference engine is implemented using 49 rules of Table 2 in which the following symbols have been used:

NB: Negative Big; NM: Negative Medium; NS: Negative Small; ZE: Zero; PS: Positive Small; PM: Positive Medium; PB: Positive Big.

Fuzzy implication is modeled by Mamdani's minimum operator, the conjunction operator is Min, the t-norm from compositional rule is Min and for the aggregation of the rules the Max operator is used.

For the fuzzy compensator, the error signal and its derivative are adopted as input signals which fuzzification stage is conducted by the membership function shown in Fig. 3.

Tab. 2. Fuzzy Inference Rules

$\dot{e}/e$	NB	NM	NS	ZE	PS	PM	PB
NB	NB	NB	NB	NB	NM	NS	PS
NM	NB	NM	NM	NM	NS	ZE	PS
NS	NB	NM	NS	NS	ZE	PS	PM
ZE	NM	NM	NS	ZE	PS	PM	PM
PS	NS	NS	ZE	PS	PS	PM	PB
PM	NS	ZE	PS	PM	PM	PM	NB
PB	ZE	PS	PM	PB	PB	PB	ZE

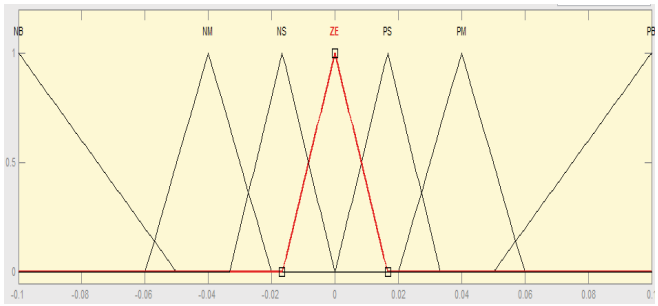

a) input membership function (e, ė)

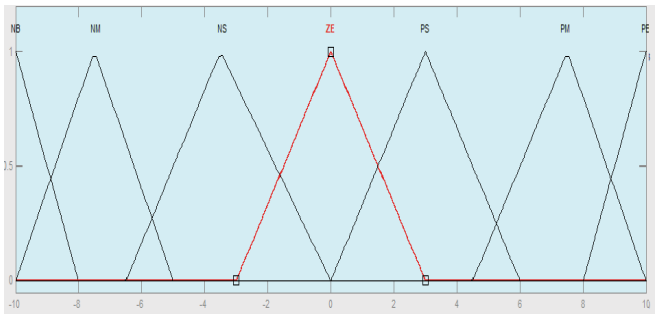

b) output membership function ρ
Fig. 3. Input-Output Membership Functions

Concerning promoted control law, the proposed Robust Model Predictive Fuzzy (RMPF) control law is considered as

$$U_{RMPF}(t) = U_{MPC}(t) - U_{fuzzy}(t) + U_d \tag{46}$$

The proposed control system of UVMS is shown in Fig. 4.

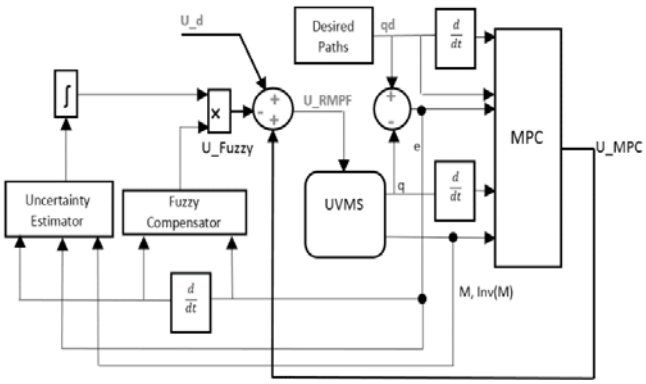

Fig. 4. Proposed Control RMPF

COMPUTER SIMULATIONS

In this section, in order to argue the mathematical model of the proposed controller, the simulations of proposed design RMPF and also MPC are done. The desired trajectories which must be tracked in the time interval of 20 seconds by 4 degree of freedom UVMS are chosen as.

A circle trajectory for mobile platform using X (surge motion) and Z (heave motion) axis and also with a pitch motion. Initial conditions are considered zero.

$$X = \sin\left(\frac{\pi}{5}t\right)$$
$$Z = \cos\left(\frac{\pi}{5}t\right)$$
$$q_{Pitch} = \pi(1 - e^{-\frac{t}{2}})$$

For a 1 degree of freedom movement for a coupled manipulator the initial condition is considered zero.

$$q_{Link} = \pi(1 - e^{-\frac{t}{2}})$$

Fig. 5 illustrates a four degree of freedom underwater vehicle-manipulator system with the following vector of positions:

$$q = [X, Z, q_{Pitch}, q_{Link}]^T$$

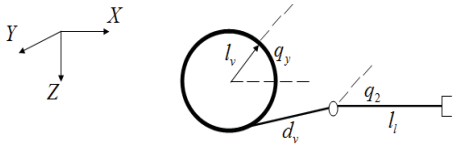

Fig. 5. UVMS with 4 Degree of Freedom

Also, external disturbances are shown in Fig. 6 and variable mass of manipulator is expressed as

$$m_{Link}(t) = m_0 + 10\cos(0.5t)$$

Table. 3 gives the parameters of underwater vehicle-manipulator system that was used in computer simulations.

Table. 3. Parameters of UVMS

Added Mass Force Coefficient	$E_1 = 2kg$, $E_2 = 2kg$ $E_3 = 1kg$, $E_4 = 1kg$
Drag Force Coefficient	$F_1 = 5kg$, $F_2 = 5kg$ $F_3 = 1kg$, $F_4 = 1kg$
Mass of Spherical Vehicle m_v	100 (kg)
Mass of Link m_l	20 (kg)
Radius of Spherical Vehicle l_v	1 (m)
Length of Link l_l	1 (m)

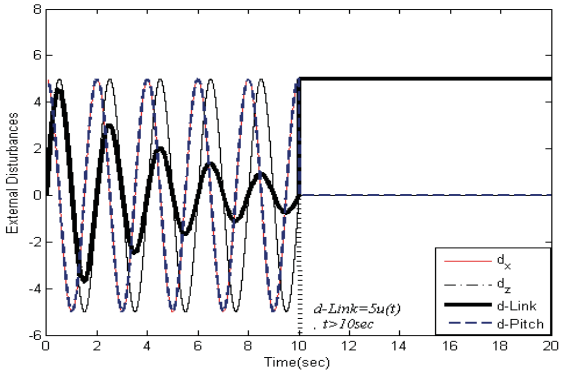

Fig. 6. External Disturbances

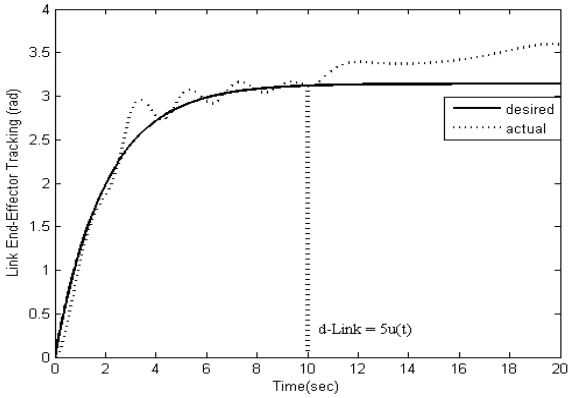

A1-Trajectory tracking

Also, concerning adjustable coefficient of MPC, the value of τ_r is given by 1. The simulation results of MPC are shown in Fig. 7 and with sustaining of the same perturbation conditions, the simulated results of the proposed controller are shown in Fig. 8.

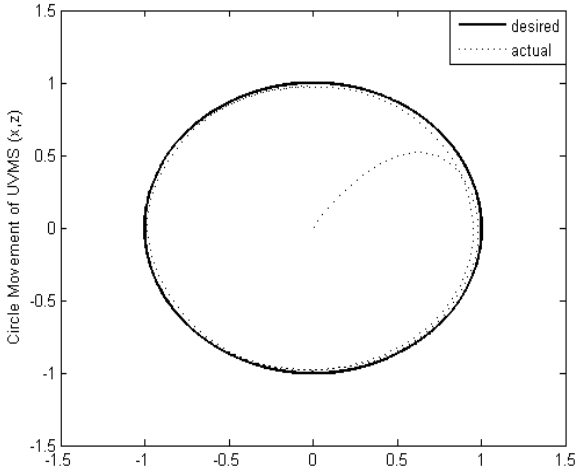

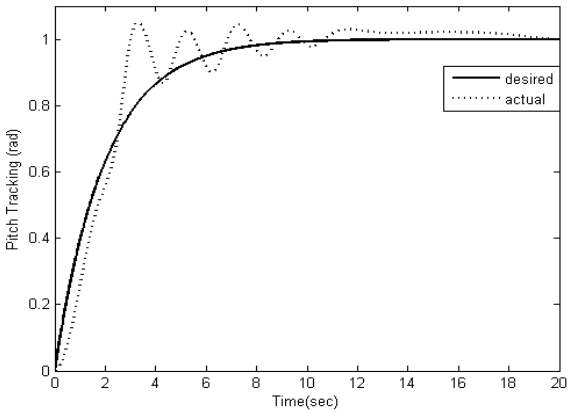

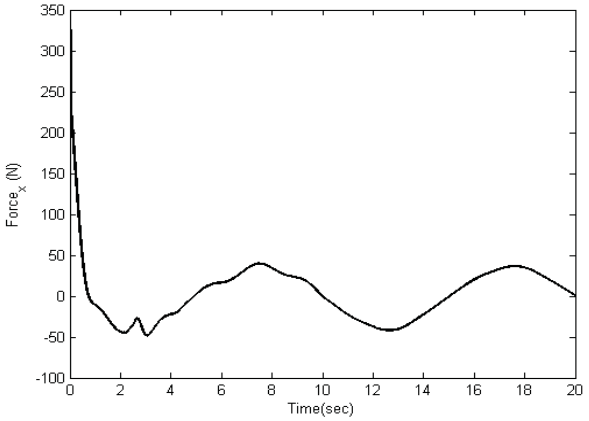

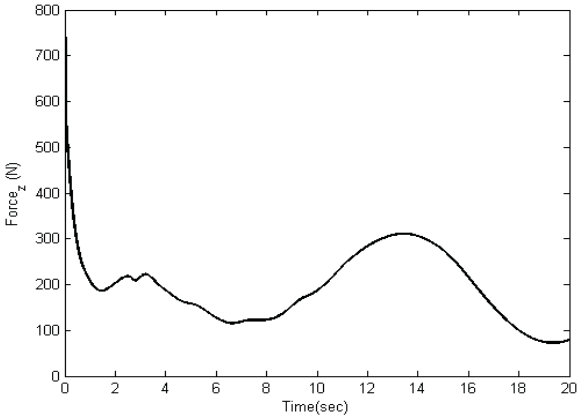

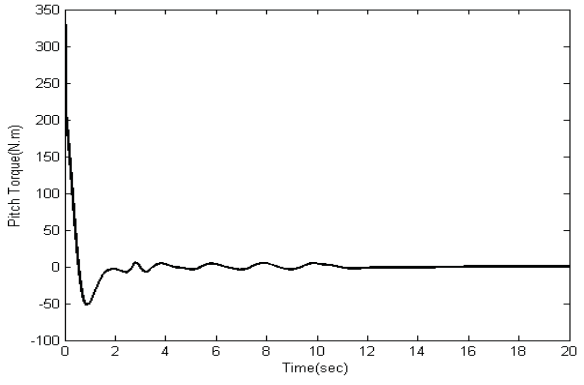

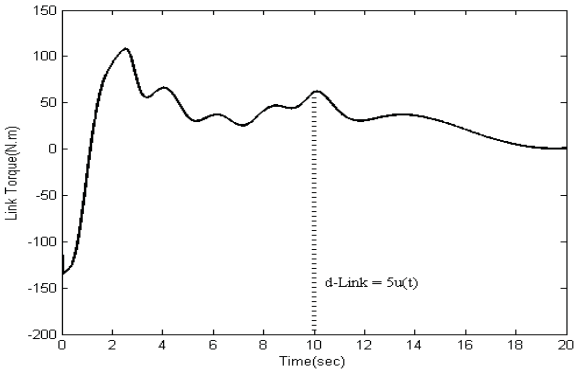

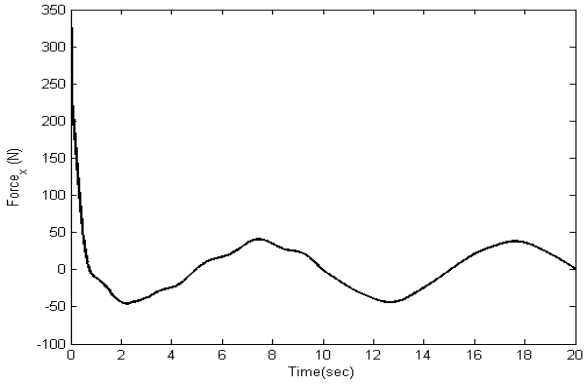

B1-Input control signals
Fig. 7. MPC approach

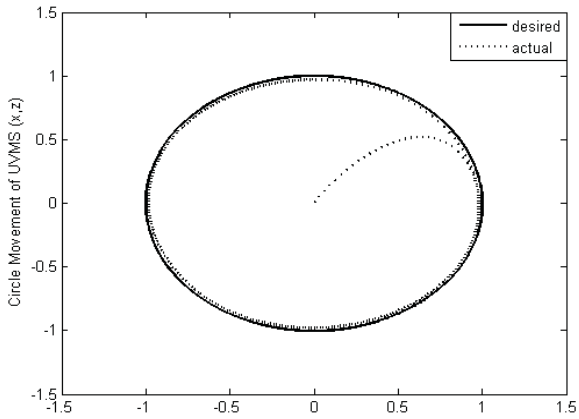

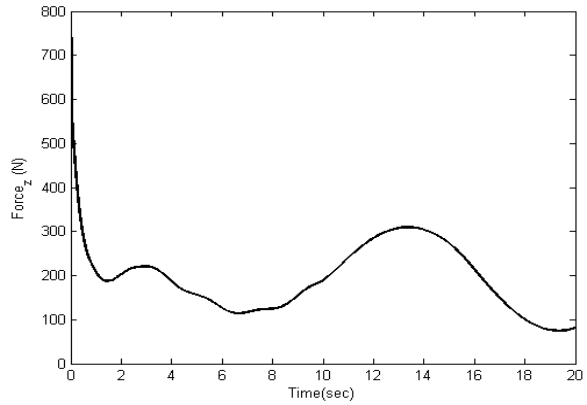

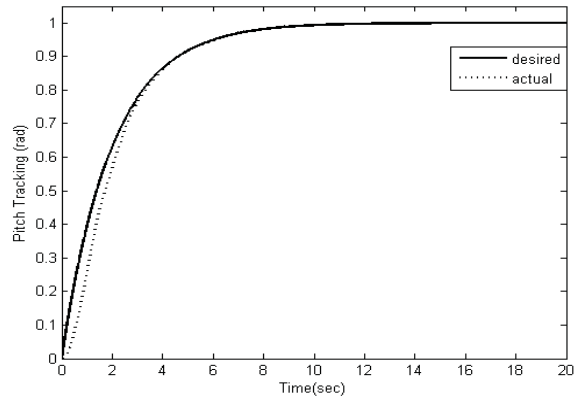

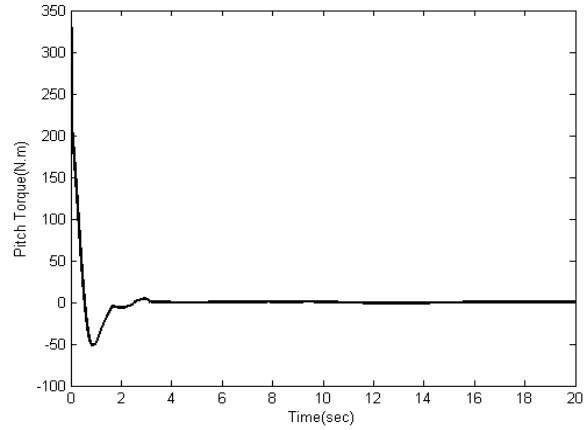

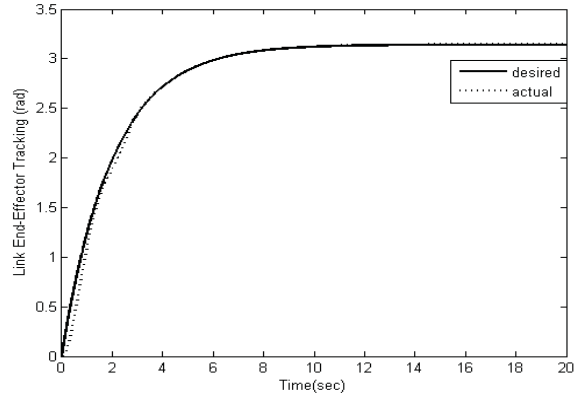

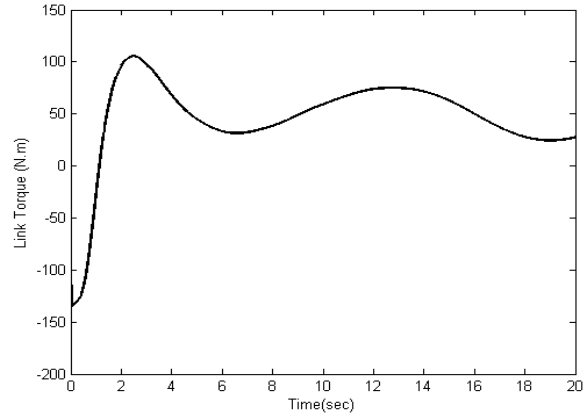

A2-Trajectory tracking

B2-Input control signals

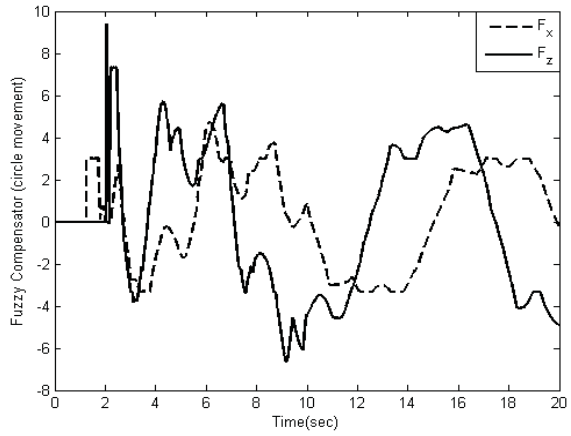

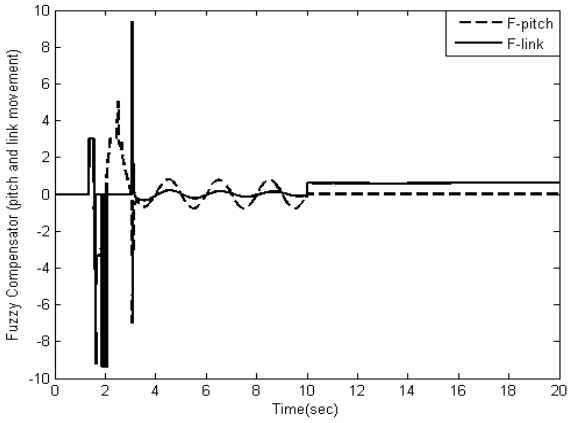

C-Output of fuzzy compensator
Fig. 8. Proposed control approach RMPF

The proficient performance of the proposed controller is obviously observed by a comparative appraisal. Indeed, when the applied external disturbance considered for coupled manipulator is switched over to the other kind of disturbance signal shown in Fig. 6, the MPC is not capable to follow the rest of the desired link path shown in Fig. 7-A1. For a similar condition, in terms of switching over of applied external disturbance of coupled link while the proposed controller RMPF is operated, the tracking duty is literally provided by this controller and there is no divergence shown in Fig. 8-A2 because of good operation of the fuzzy compensator. Also, concerning the pitch motion of UVMS, the control response for the proposed controller is much more applicable than MPC. The RMPF response is critically damped and all the under damping symptoms observed in MPC response are removed.

CONCLUSION

Water depths are one of the environments in which operation of the robotic systems such as Autonomous UVMS, Remotely Operated Vehicle (ROV), and fixed underwater manipulators is intensively influenced by the special forces and finally high nonlinear terms and uncertainties are unfolded by the rewritten dynamical equations. Commonly, robustness property of designed controllers for the mentioned underwater systems is achieved by applying the robust strategies such as SMC. However, SMC in conjunction with the chattering effects on the input control signals is particularly visible in the presence of severe external disturbances. In this research, because of gathering the robustness property and MPC attributes simultaneously, MPC based approach with two main subsystems including perturbation estimator and fuzzy compensator is chosen as the proposed method. The computer simulations are done with high accuracy in tracking and are obviously observed in comparison with conventional MPC.

REFERENCES

1. Islam S., Liu J.: *Robust Sliding Mode Control for Robot Manipulators.* IEEE Transactions on Industrial Electronics, vol. 58(6), pp. 2444-2453, 2011.

2. *F. Piltan and B. Sulaiman.: Review of Sliding Mode Control of Robotic Manipulator. World Sciences Journal, vol. 18(12), pp. 1855-1869, 2012.*

3. Esfahani H. N., Azimirad V., Eslami A., Asadi S.: *An optimal sliding mode control based on immune-wavelet algorithm for underwater robotic manipulator.* Proceedings of the 21st Iranian Conference on Electrical Engineering (ICEE). Mashhad, Iran, 2013. DOI: 10.1109/IranianCEE.2013.6599587.

4. Esfahani H. N., Azimirad V., Danesh M.: *A time delay controller included terminal sliding mode and fuzzy gain tuning for underwater vehicle-manipulator systems.* Ocean Engineering, vol. 107, pp. 97-107, 2015.

5. Esfahani H. N., Azimirad V., Zakeri M.: *Sliding Mode-PID Fuzzy controller with a new reaching mode for underwater robotic manipulators.* Latin American Applied Research, vol. 44(3), pp. 253–258, 2014.

6. Vivas A., Mosquera V.: *Predictive functional control of a PUMA robot.* Proceedings of the Conference on Automatic Control and System Engineering (ACSE 05), CICC. Cairo, Egypt, 2005.

7. Incremona G. P., Ferrara A., Magni L.: *Hierarchical Model Predictive/Sliding Mode Control of Nonlinear Constrained Uncertain Systems.* Proceedings of the 5th IFAC Conference on Nonlinear Model Predictive Control (NMPC). Seville, Spain, 2015. DOI: 10.1016/j.ifacol.2015.11.268.

8. Ghazaei Ardakani M., Olofsson B., Robertsson A., Johansson R.: Real-Time Trajectory Generation using Model Predictive Control. Proceedings of the IEEE International Conference on Automation Science and

Engineering (CASE). Gothenburg, Sweden. pp. 942 – 948, 2015. DOI: 10.1109/CoASE.2015.7294220.

9. Wang Y., Chen W., Tomizuka M., Alsuwaidan B. N.: *Model predictive sliding mode control: for constraint satisfaction and robustness.* ASME 2013 Dynamic Systems and Control Conference, Palo Alto, California, USA. vol. 3, ISBN 978-0-7918-5614-7, 2013.

10. Fossen. T. I.: *Marine Control Systems: Guidance, Navigation and Control of Ships, Rigs and Underwater Vehicle.* Marine Cybernetics AS, Norway. pp. 570-579, ISBN 82-92356-00-2, 2002.

11. Krid. M, Benamar. F, and Lenain. R.: *A new explicit dynamic path tracking controller using Generalized Predictive Control.* International Journal of Control, Automation and Systems, Springer, vol. 15, Issue 1, pp. 303-314, 2017.

12. Spong M.W., Hutchinson S., Vidyasagar M.: *Robot Dynamics and Control.* 2nd ed. John Wiley & Sons, Inc.; Hoboken, NJ, USA: 2004.

13. Jasour A. M., Farrokhi M.: *Path Tracking and Obstacle Avoidance for Redundant Robotic Arms Using Fuzzy NMPC.* Proceedings of the American Control Conference, pp. 1353-1358. St. Louis, MO, USA, 2009. DOI: 10.1109/ACC.2009.5160408.

14. Rubus. T, Seweryn. K, and Sasiadek. J. Z.: *Application of predictive control for manipulator mounted on a satellite.* Archives of Control Sciences, vol. 28(LXIV), pp. 105–118, 2018.

15. Lisowski. J.: *Analysis of Methods of Determining the Safe Ship Trajectory.* TRANSNAV-INTERNATIONAL JOURNAL ON MARINE NAVIGATION AND SAFETY OF SEA TRANSPORTATION, Vol. 10(2), pp. 223-228, JUN 2016.

16. Lisowski. J.: *Optimization-supported decision-making in the marine mechatronics systems.* mechanics and material II. Book series: solid state phenomena, Vol. 210, pp. 215-222, 2014.

17. Tomera. M.: *Ant colony optimization algorithm applied to ship steering control.* KNOWLEDGE-BASED AND INTELLIGENT INFORMATION & ENGINEERING SYSTEMS 18TH ANNUAL CONFERENCE, KES-2014 Book Series: Procedia Computer Science, Vol. 35, pp. 83-92, 2014.

18. Sun, Y. C., Cheah, C. C.: *Adaptive set point control for autonomous underwater vehicles.* In: Proceedings of IEEE Robotics Decision and Control Conference, Hawaii USA, 2, pp. 1262–1267,2003.

CONTACT WITH THE AUTHOR

Hossein Nejatbakhsh Esfahani
e-mail: nejatbakhsh.application@yahoo.com

Gdansk University of Technology
ul. G. Narutowicza 11/12 , 80-233 Gdansk
Poland

sciendo

POLISH MARITIME RESEARCH 2 (102) 2019 Vol. 26; pp. 115-125
10.2478/pomr-2019-0031

ON SOME PROBLEMS IN DETERMINING TENSILE PARAMETERS OF CONCRETE MODEL FROM SIZE EFFECT TESTS

Ireneusz Marzec
Jerzy Bobiński
Gdansk University of Technology, Poland

ABSTRACT

The paper presents results of numerical simulations of size effect phenomenon in concrete specimens. The behaviour of in-plane geometrically similar notched and unnotched beams under three-point bending is investigated. In total 18 beams are analysed. Concrete beams of four different sizes and five different notch to depth ratios are simulated. Two methods are applied to describe cracks. First, an elasto-plastic constitutive law with a Rankine criterion and an associated flow rule is defined. In order to obtain mesh independent results, an integral non-local theory is used as a regularisation method in the softening regime. Alternatively, cracks are described in a discrete way within Extended Finite Element Method (XFEM). Two softening relationships in the softening regime are studied: a bilinear and an exponential curve. Obtained numerical results are compared with experimental outcomes recently reported in literature. Calculated maximum forces (nominal strengths) are quantitatively verified against experimental values, but the force – displacement curves are also examined. It is shown that both approaches give results consistent with experiments. Moreover, both softening curves with different initial fracture energies can produce similar force-displacement curves.

Keywords: Concrete, Size effect, Fracture energy, elasto-plasticity, XFEM

INTRODUCTION

Concrete is one of the most popular materials used in civil engineering to erect buildings, bridges and other structures on land and various port facilities like breakwaters or quays. Its tensile strength is several times smaller than compressive one, therefore it is usually applied with steel reinforcing bars. These bars are responsible to carry (mostly) tensile stresses, while the concrete itself sustains compressive stresses, and the tensile strength of concrete is neglected. The situation is different in plain or weekly reinforced massive concrete structures in civil or coastal engineering, like foundations, dams etc. The tensile strength of concrete cannot be neglected and the proper estimation of the concrete's properties in tension is of great importance.

One of the salient phenomenon observed in concrete structures is the presence of size effect. The strength (and other properties) of material depends on the size of a specimen examined; small elements have a greater nominal strength than bigger ones. It is caused by the existence of the so-called fracture process zone (FPZ), which size is not negligible comparing to the size of the specimen. Deformations localise inside these zones; at the beginning as a set of diffused micro-cracks and later a discrete macro-crack. The observed size effect results are placed between plastic limit theory and linear elastic fracture mechanics solutions. Therefore, the proper theoretical capture of the size effect phenomenon is crucial

when experimental results from tests performed on small specimens are to be extrapolated into bigger ones.

Within continuum mechanics, cracks can be described as a smeared (continuous), discrete (discontinuous) or by coupling these two approaches (Mazars et al. [20], Marzec et al. [18], Unger et al. [26], Bobiński and Tejchman [5]). The first (smeared) approach defines a crack as region (band) with a certain width, while in the second formulation it is presented as a line (surface) with zero thickness and assumed displacement jump across. When using classical constitutive laws with strain softening, a mesh dependency is observed. In order to obtain mesh independent results and to restore the well-posedness of the boundary value problem, a regularisation method is needed. This enrichment introduces a characteristic length of the microstructure into the macroscopic material description. It can be done via a non-local theory, gradient terms or using viscosity in dynamic problems (Brinkgreve [6], Glema et al. [10], Marzec et al. [19], Wang et al. [27], Winnicki et al. [29]). More sophisticated formulations couple continuous and discontinuous descriptions (Simone et al. [22, 23]). Non-locality can be also introduced via fractional differential operators (Beda [3], Błaszczyk [4], Lazopoulos i Lazopoulos [17], Sumelka [24], Sumelka et al. [25]).

Despite a huge amount of performed experiments on concrete specimens, there is still no consensus in describing the fracture process in concrete. Due to several factors influencing the results and a small number of specimens tested in a single experimental programme, it is very hard to properly compare the obtained results and to form general conclusions. Therefore, some experimental campaigns were executed recently to overcome these limitations. Hoover et al. [15] examined in plane geometrically scaled unnotched and notched concrete beams under three-point bending. Four different beam sizes and five different notch to depth ratios were analysed. In total 18 different geometries were defined and more than one hundred specimens were tested. Çağlar and Şener [7] examined geometrically identical beams (80 specimens), but cast in a horizontal position. A slightly smaller number of beams (34 specimens) was tested by Grégoire et al. [12]. They analysed beams of four different sizes and three different notch to depth ratios (unnotched and notched).

Different constitutive laws were used later to reproduce obtained experimental results. Hoover and Bažant [16] used the crack band and a bilinear softening law. They stated that an exponential softening curve was not able to give realistic results. Grégoire et al. [12] applied the isotropic damage constitutive law coupled with the integral non-local theory and an exponential curve defined in softening. A similar model was used in numerical simulations presented by Havlásek et al. [13]. In addition, they studied standard and distance based averaging methods in non-locality.

In the paper, numerical simulations of size effect in plain concrete beams under bending are presented. Two alternative crack descriptions are used: a smeared one via an elasto-plastic with a Rankine criterion enriched by a non-local theory in the softening regime and a discrete one within XFEM. The influence of defined softening curve and assumed value of the initial fracture energy in both approaches on the obtained results is investigated. Such vast analysis with two different crack descriptions and two different softening curves has not been performed yet. In addition, the deficiencies of the initial fracture energy are pointed out. Numerical results are compared with experimental outcomes.

The paper is organised as follows. The constitutive models are described in Section 2. The problem data are given in Section 3. Obtained results and discussion are presented in Section 4. Conclusions and final remarks are listed in Section 5.

CONSTITUTIVE LAWS

ELASTO-PLASTICITY

As a first option, a smeared description of cracks in concrete is used. An elasto-plastic constitutive law with the classical Rankine criterion is proposed. The yield criterion in 2D is postulated as

$$f = \max\{\sigma_1, \sigma_2\} - \sigma_t(\kappa_C) \tag{1}$$

where:
σ_1, σ_2 – the principal stresses,
σ_t – the tensile yield stress,
κ_C – the softening state variable.

The tensile yield stress σ_t is defined in Sec. 2.3 and the state variable κ_C is equal to the maximum principal plastic strain. Plastic strains are calculated assuming an associated flow rule.

When defining strain softening with the standard constitutive laws, classical finite element calculations fail. Obtained result are mesh dependent and a regularisation method is required to restore the well posedness of the boundary value problem. Here, an integral non-local theory is applied. Non-local rates of state variables $\mathrm{d}\kappa_C$ are evaluated as (after Brinkgreve [6])

$$\mathrm{d}\bar{\kappa}_C(\boldsymbol{x}) = (1-m)\mathrm{d}\kappa_C(\boldsymbol{x}) + m\mathrm{d}\hat{\kappa}_C(\boldsymbol{x}) \tag{2}$$

where:
$\boldsymbol{x}$ – point under consideration,
m – non-locality parameter,
$\mathrm{d}\hat{\kappa}_C$ – rate of averaged state variable.

The non-locality parameter m should be greater than 1 to effectively apply the non-local theory with elasto-plasticity (so called over-non-local formulation). The rate of averaged state variable is calculated as:

$$\mathrm{d}\hat{\kappa}_C(\boldsymbol{x}) = \frac{\int_V \omega(\|\boldsymbol{x}-\boldsymbol{\xi}\|)\mathrm{d}\kappa_C(\boldsymbol{\xi})\mathrm{d}\boldsymbol{\xi}}{\int_V \omega(\|\boldsymbol{x}-\boldsymbol{\xi}\|)\mathrm{d}\boldsymbol{\xi}} \tag{3}$$

where:
V – volume of the integration domain,
$\boldsymbol{\xi}$ – surrounding point coordinates,
ω – the weighting function.

The weighting function reflects the influence of the surrounding points on the material's behaviour in the considered point $\boldsymbol{x}$. Here a Gauss distribution is applied:

$$\omega(r) = \frac{1}{l\sqrt{\pi}}\exp\left(-\left(\frac{r}{l}\right)^2\right) \tag{4}$$

where:
r – the distance between points,
l – the characteristic length.

The characteristic length is the link with the micro-structure of the material. The characteristic length l (but also the non-locality parameter m, the definition of the weight function ω and the formulation of the constitutive law) influences the width of the localisation zone, which in general depends on concrete mesostructure. The averaging in Eqn. (4) is restricted only to a small neighbourhood around a point considered (the influence of points at the distance of $r=3l$ is only of 0.01%). Therefore, although the weight function ω defined in Eqn (4) has unbounded support, only points at the distance no larger than $r=3l$ from the integration domain V. For points $\boldsymbol{x}$ lying close to the boundary, only points lying within a circle with a radius $r=3l$ and belonging to the specimen are taken into account (see Fig. 1a). In both cases, the denominator in Eqn (3) normalises the averaging operation; the uniform local field remains unchanged after applying the Eqn (3). Near notches so called "shading effect" is taken into account (Fig. 1b).

EXTENDED FINITE ELEMENT METHOD

As an alternative approach, cracks can be described as displacement jumps within continuum. In the paper eXtended Finite Element Method (XFEM) is utilised. It is based on a local partition of the unity (PUM) concept by (Melenk and Babuška [21]). It enables adding 'ad hoc' extra terms to a standard FE displacement field interpolation to capture displacement jumps across a crack. As a consequence, cracks can be placed through elements; they do not have to follow elements' edges.

In the paper the formulation (with minor improvements and modifications) proposed by Wells and Sluys [28] for cohesive cracks is adopted. The only major change is the application of the so-called shifted-basis enrichment proposed by Zi and Belytschko [30]. Theoretically, this improvement is equivalent to the classical model, but it simplifies the implementation (only two types of finite elements exist and total nodal displacements are equal to the standard ones).

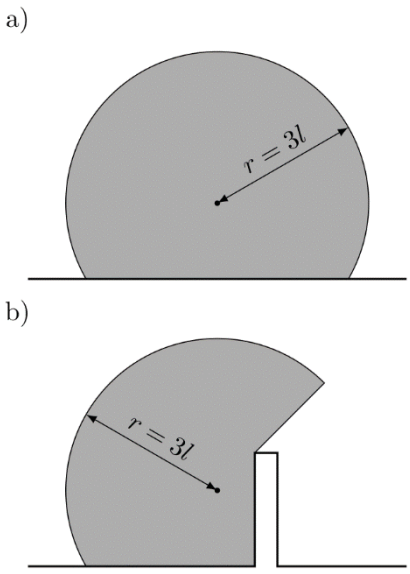

Fig. 1. Averaging domain (grey area) for a point near boundary (a) and close to a notch (b)

Two constitutive relationships have to be declared to describe the behaviour of the material. Outside a crack in a solid (bulk) body a linear elasticity law is assumed. Along the crack a constitutive law between displacement jumps $[[\boldsymbol{u}]]$ and tractions $\boldsymbol{t}$ is postulated. The following loading function is assumed:

$$f([[u_n]],\kappa_D) = [[u_n]] - \kappa_D \tag{5}$$

where:
$[[u_n]]$ – normal component of [[u]],
κ_D – the softening state variable.

The state variable κ_D is calculated as a maximum crack opening $[[u_n]]$ attained during the load history. In active loading (growth of the crack opening) the normal traction t_n is equal to the yield traction t_y defined as:

$$t_y = D_f \sigma_t \tag{6}$$

where:
D_f – correction term,
σ_t – the yield stress defined in Sec. 2.3.

The correction term D_f improves the performance of the model in tension-compression transition cases. It is defined as:

$$D_f = 1 - \exp\left(-\kappa_D \frac{d_f f_t}{G_F}\right) \tag{7}$$

where:
d_f – the drop factor (Cox [8]),

f_t – the tensile strength,
G_F – the total fracture energy.

In unloading/reloading a return to the origin (damage formulation) is assumed:

$$t_n = \frac{t_y}{\kappa_D}[[u_n]] \tag{8}$$

In compression a penalty stiffness is taken. It is calculated as:

$$T_n = \frac{d_f f_t^2}{G_F} \tag{9}$$

In tangential direction, a linear dependence between shear tractions t_s and tangential displacement jump $[[u_s]]$ is assumed:

$$t_s = T_s \frac{t_y}{f_t}[[u_s]] \tag{10}$$

where:
T_s – the initial shear stiffness.

SOFTENING CURVES

In both smeared and discrete crack descriptions two softening curves are used in the numerical simulations. In the present section, symbol κ should be taken either as the state variable κ_C or as the state variable κ_D. First, a bilinear relationship is taken (Fig. 2a):

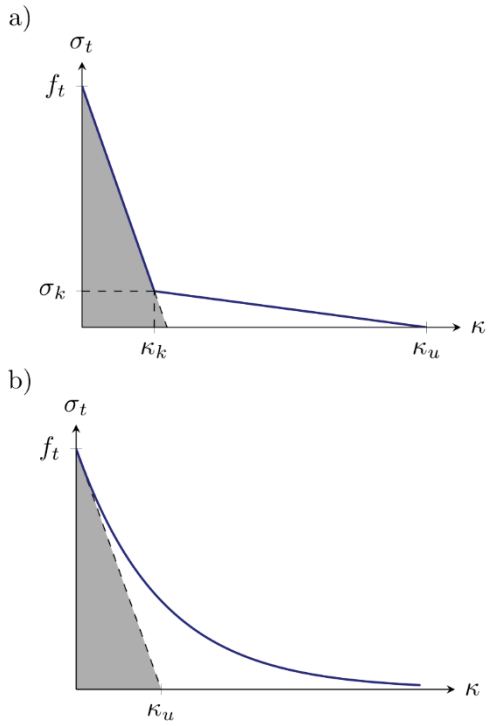

Fig. 2. Bilinear (a) and exponential (b) softening curves (grey area – initial fracture energy)

$$\sigma_y(\kappa) = \begin{cases} f_t + (\sigma_k - f_t)\dfrac{\kappa}{\kappa_k} & \kappa < \kappa_k \\ \sigma_k \dfrac{\kappa_u - \kappa}{\kappa_u - \kappa_k} & \kappa_k \le \kappa < \kappa_u \\ 0 & \kappa \ge \kappa_u \end{cases} \tag{11}$$

where:
σ_k – the yield stress at the kink point,
κ_k – the state variable at the kink point,
κ_u – the state variable at zero stress.

Alternatively, an exponential definition is used (Fig. 2b):

$$\sigma_y(\kappa) = f_t \exp\left(-\frac{\kappa}{\kappa_u}\right) \tag{12}$$

where:
κ_u – controls the slope of the curve.

More advanced exponential relationship was proposed by Hordijk ([14]) based on experimental outcomes.

In eXtended Finite Element Method, state variables κ_k (only for bilinear softening) and κ_u can be directly related to the initial fracture energy G_f and the total fracture energy G_F. The initial fracture energy G_f (Bažant [1]) is the area under the initial tangent line from the peak at the stress – displacement curve (grey regions in Fig. 2), while the total fracture energy G_F is the area under the whole curve. In bilinear softening these parameters can be derived as:

$$\kappa_k = \frac{2G_f}{f_t^2}(f_t - \sigma_k) \tag{13}$$

and:

$$\kappa_u = \frac{2}{\sigma_k}\left(G_F + G_f\left(\frac{\sigma_k}{f_t} - 1\right)\right) \tag{14}$$

while in exponential softening:

$$\kappa_u = \frac{G_F}{f_t} \tag{15}$$

PROBLEM

In the paper the experiment performed by Hoover et al. [15] is numerically simulated. They examined 128 unnotched and notched plain concrete beams under three-point bending. Figure 3 presents the geometry of a beam. Four different beam sizes were tested with height (depth) D taken as 500,

215, 93 and 40 mm, labelled here as a huge, large, medium and small specimen, respectively. The length to depth ratio was kept constant and it was equal to 2.4 for all beams and the span length L was defined as 2.176D. Five different notch to depth ratios α_0 were assumed: 0.0 (no notch), 0.025, 0.075, 0.15 and 0.30. In total 18 different geometries were defined (small and medium beams with the ratio α_0=0.025 were not cast). The thickness of all beams was B=40 mm and the width of the notch was equal to 1.5 mm for all specimens.

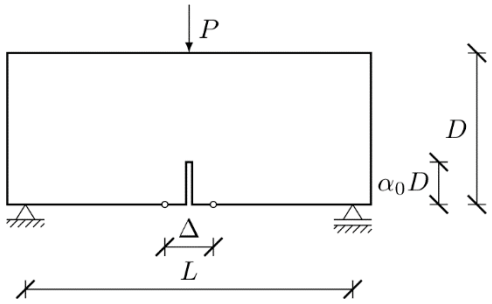

Fig. 3. Boundary conditions and geometry of a beam

A load was imposed in the middle of the top edge of the specimen. Steel plates were placed at supports and under the load. A hard (rigid) contact was assumed between concrete and steel plates at the supports and under the load. All tests were executed under crack mouth opening displacement control by increasing the distance between two chosen points at the bottom edge symmetrically with the respect to vertical axis of symmetry. The initial distance between these two points depended on the beam size D and the ratio α_0 (it was between 12.7 and 162 mm).

FE-CALCULATIONS

INPUT DATA

Numerical simulations are performed in Abaqus Standard programme. The total elongation of the gauge is set to Δ=0.3 mm and an indirect displacement method is used. At least 250 increments are required to complete a simulation. Plane stress conditions are assumed with 3-node constant strain triangular finite elements. In elasto-plasticity an approximated method is used in calculations of averaged quantities. In an integration point the influence of the neighbour points is determined with values from the previous iteration. The refined FE mesh along the vertical axis of symmetry is defined in all specimens with the maximum element size not greater than 1 mm for calculations with elasto-plasticity and 2 mm for XFEM simulations. The total number of finite elements varies between 6967 and 55251 and between 4981 and 11660 in calculations with smeared and discrete cracks, respectively. A denser FE-mesh for calculations with elasto-plasticity ensures the effective application of the non-local theory ever for small values of the characteristic lengths and obtaining mesh independent results. Some comparative simulations with XFEM have shown that identical results have been received using coarser and denser meshes. An exemplary FE-mesh used in XFEM calculations in the region around the notch for the medium beam and the notch to depth ratio α_0=0.15 is shown in Fig. 4.

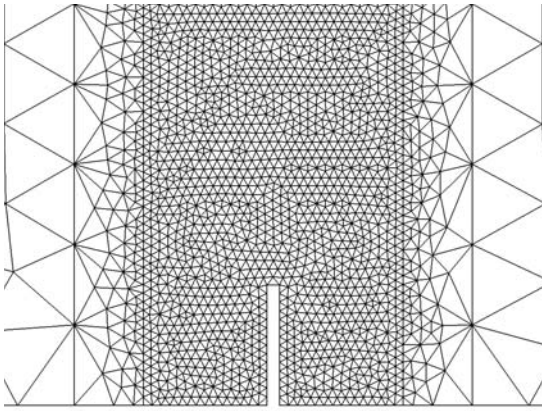

Fig. 4. Exemplary FE mesh around the notch

In the simulations the Young's modulus is assumed as E=41.25 GPa and the Poisson's ratio is ν=0.172 (taken from experiments by Hoover et al. [15]). The total fracture energy is set to G_F=70 N/m (after Hoover and Bažant [16]). In bilinear softening the yield stress at the kink point is always defined as σ_k=0.15f_t. In XFEM the drop factor is equal to d_f=10^4 and the shear stiffness is T_s=0.0 N/m^3. Material for steel plates is taken as a linear elastic with the Young's modulus E_s=200 GPa and the Poisson's ratio ν_s=0.3.

RESULT AND ERROR MEASURES

The experimental nominal (ligament) strength $\sigma_N^{\exp}$ is calculated as:

$$\sigma_N^{\exp} = \frac{3}{2}\frac{2.176P_u^{\exp}}{B^{\exp}D^{\exp}} \tag{16}$$

where:
$P_u^{\exp}$ – the experimental max. force,
$B^{\exp}$ – the experimental thickness,
$D^{\exp}$ – the experimental height.

The numerical nominal strength σ_N^{FEM} is defined as:

$$\sigma_N^{FEM} = C_f\frac{3}{2}\frac{2.176P_u^{FEM}}{BD} \tag{17}$$

where:
P_u^{FEM} – the numerical max. force,
C_f – the correction factor.

The correction factor takes into account deviations of real dimensions with the respect to nominal ones. It is defined as:

$$C_f = \frac{2}{3}\frac{\sigma_N^{\exp} BD}{2.176 P_u^{\exp}} \tag{18}$$

In order to rate a simulation quality, the following relative error Err_0 is introduced:

$$Err_0 = \frac{\sigma_N^{FEM} - \sigma_N^{\exp}}{\sigma_N^{\exp}} \tag{19}$$

The whole set is evaluated using errors Err_1 and Err_2:

$$Err_1 = \sum_{i=1}^{N} \frac{Err_0}{N} \text{ and } Err_2 = \sum_{i=1}^{N} \frac{|Err_0|}{N} \tag{20}$$

where:
N – the number of beams (N=18).

In statistics, the errors Err_1 and Err_2 are called the mean percentage error (MPE) and the mean absolute percentage error (MAPE), respectively. The presence of the negative error values allows for distinguish between underestimated and overestimated numerical results.

RESULTS WITH XFEM

First, simulations with bilinear softening curve are executed. In order to find the values of the tensile strength f_t and the initial fracture energy G_f, seed calculations are performed. The tensile strength f_t changes between 3.6 MPa and 5.6 MPa with an increment 0.4 MPa. The initial fracture energy G_f varies between 30 N/m and 54 N/m with an increment 2 N/m. Obtained error Err_1 and Err_2 isolines are depicted at Fig. 5. It can be seen that for both measures the best f_t and G_f pairs form an inclined line (or region), but they do not indicate a single optimum point. Please note, however, that not only peak values, but also agreement between whole numerical and experimental curves has to be taken into account. Finally, the tensile strength is set to f_t=5.0 MPa and the initial fracture energy is taken as G_f=48 N/m. With these values the following errors are obtained: Err_1=0.67% and Err_2=2.69%. Figure 6a presents a comparison between nominal strength obtained in the experiment and FE-calculations. Generally, a very good agreement can be observed. The largest deviation (the error Err_0=10.7%) is for the small beam (D=40 mm) and the notch to depth ratio α_0=0.3. Whole force – displacement curves are presented in Fig. 7. It can be seen that numerical results fit nicely into experimental ranges (grey regions). This fact confirms the proper assumption of the total fracture energy G_F=70 N/m.

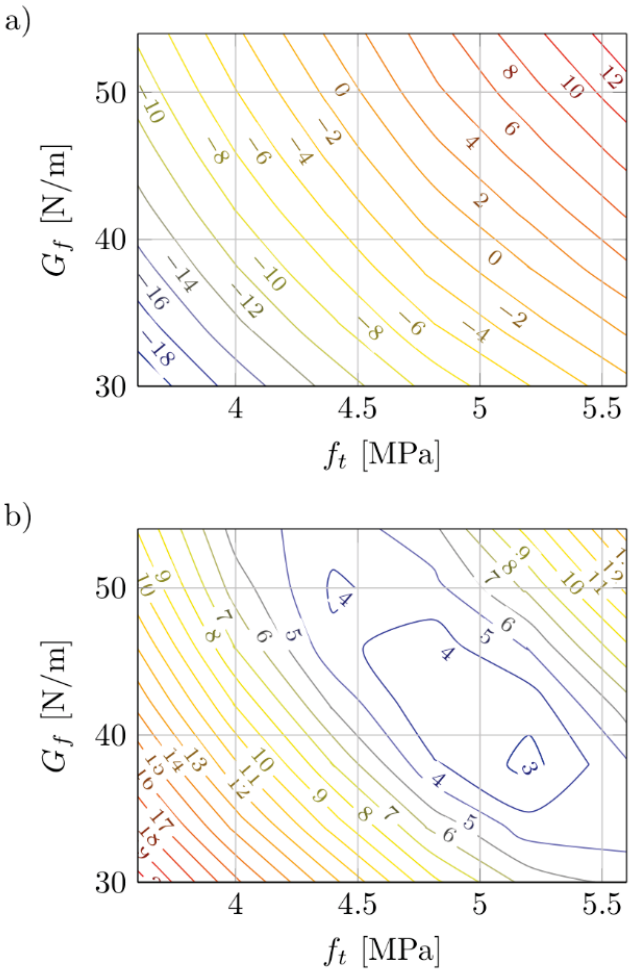

Fig. 5. Error contour maps for seed calculations with XFEM: Err_1 (a) and Err_2 b) (in percentages)

The performance of the exponential softening curve with the following parameters: f_t=4.8 MPa and G_f=35 N/m is studied also (values based on some initial calculations). In the case of the exponential softening, there is no possibility to control independently both: initial G_f and total G_F fracture energies. The initial fracture energy G_f is always equal to 50% of the total fracture energy G_F. FE-calculations with above parameters produce the following errors: Err_1=0.20% and Err_2=3.65%, comparable to values obtained with the bilinear softening. Here the worst specimen is the huge beam (D=500 mm) and the notch to depth ratio α_0=0.3; it gives the error Err_0=8.9%. Comparison between experimental and numerical nominal strength is done in Fig. 6b. Again, a good agreement is achieved (here some differences occur also for unnotched beams).

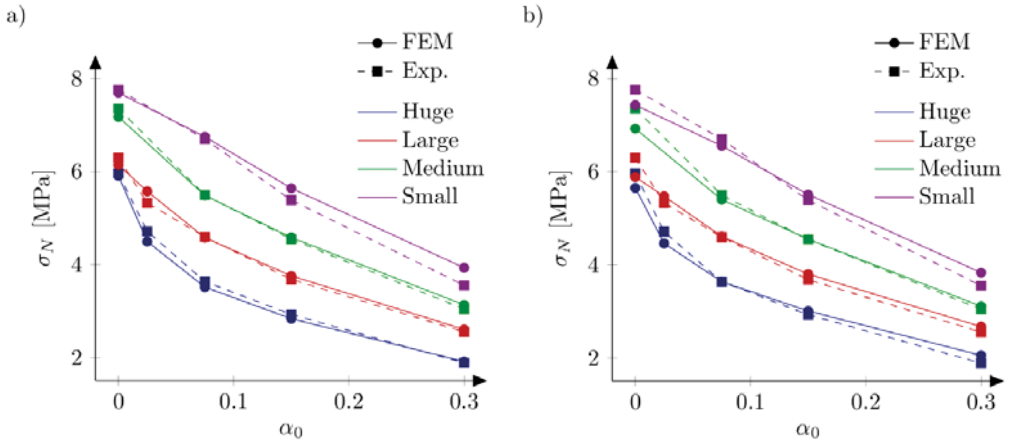

Fig. 6. Nominal (XFEM calculations) and experimental strengths with the bilinear softening curve, f_t=5.0 MPa and G_f=48 N/m (a) and the exponential softening, f_t=4.8 MPa and G_f=35 N/m (b)

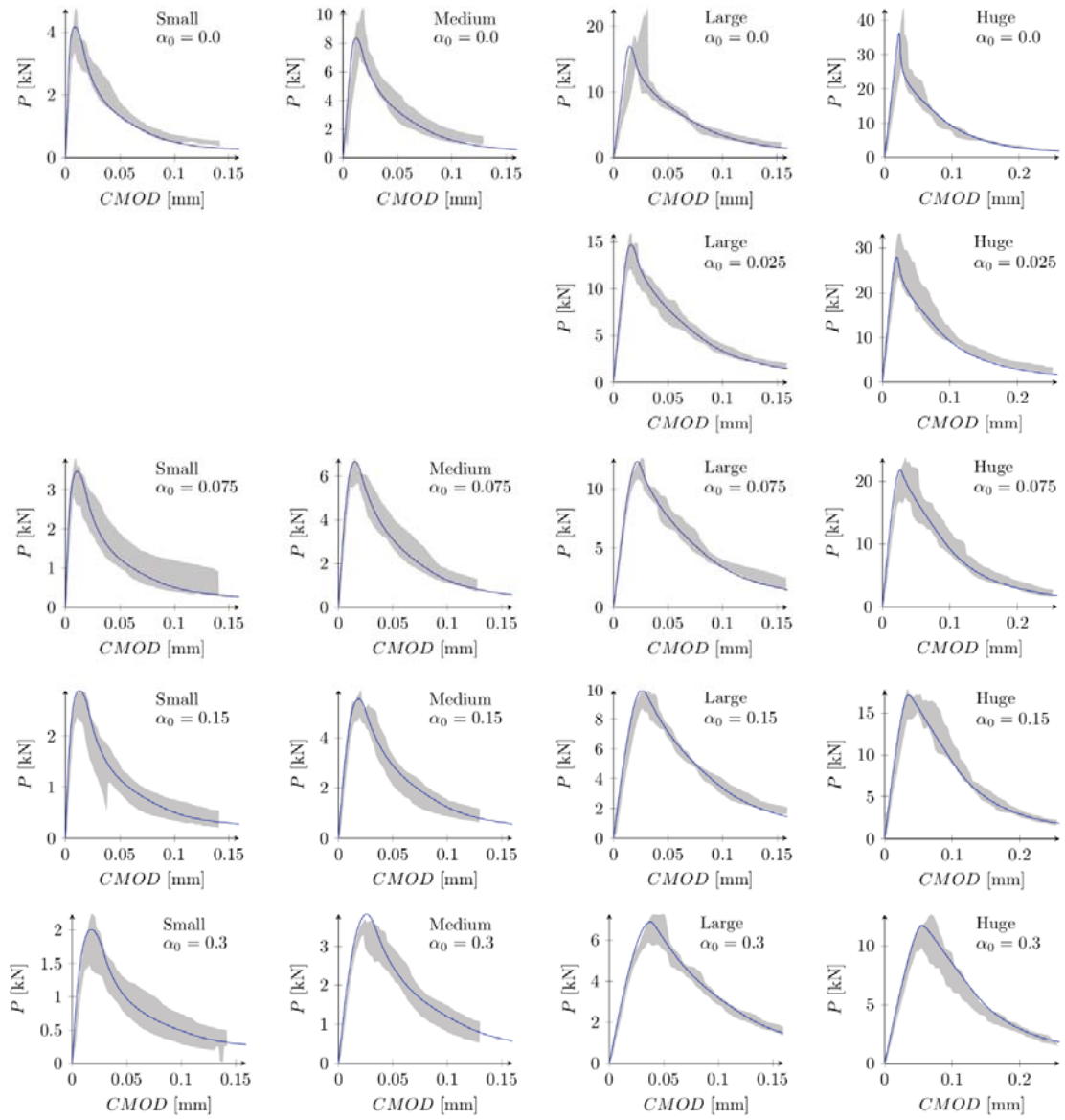

Fig. 7. Experimental and numerical (XFEM calculations) force – crack mouth opening displacement (CMOD) curves for bilinear softening, f_t=5.0 MPa and G_f=48 N/m

RESULTS WITH ELASTO-PLASTICITY

Next the numerical simulations are repeated with the elasto-plastic constitutive law with a Rankine criterion. Two characteristic lengths are assumed: l=5 mm and l=2 mm. The values of κ_u (for both softening curve definitions) are chosen in such a way to obtain the identical force-displacement curves with XFEM and elasto-plastic model with any of two characteristic lengths analysed. In calculations with the bilinear softening the ultimate value of the state variable is taken as κ_u=4.05·10^{-3} and κ_u=10.13·10^{-3} for the characteristic length l=5 mm and l=2 mm, respectively (to obtain initial fracture energy G_f=48 N/m). The tensile strength is f_t=5.0 MPa (as in XFEM calculations). Simulations give the following errors: Err_1=Err_2=9.76% for the characteristic length l=5 mm and Err_1=Err_2=6.80% for the characteristic length l=2 mm. Comparison between numerical and experimental nominal strengths is made in Fig. 8. In general, both parameter sets overestimate experimental outcomes. The worst specimen returns errors Err_0=28.1% and Err_0=19.2% (the small beam with α_0=0.3). Fortunately, the overestimation reduces with decreasing the characteristic length. It suggests the smaller values should be assumed in simulations.

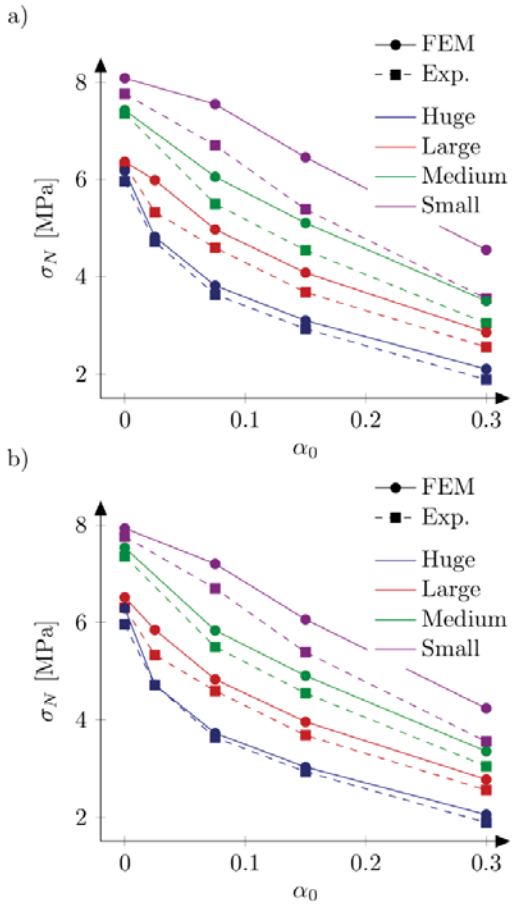

Fig. 8. Nominal (elasto-plasticity calculations) and experimental strengths with the bilinear softening curve, f_t=5.0 MPa, G_f=48 N/m and the characteristic length l=5 mm (a) and l=2 mm (b)

Slightly better results are obtained from simulations with the exponential softening law. Here the ultimate value of the softening parameter is assumed as κ_u=0.758·10^{-3} and κ_u=1.894·10^{-3} for the characteristic length l=5 mm and l=2 mm, respectively (to obtain initial fracture energy G_f=35 N/m). The tensile strength is f_t=4.8 MPa (as in XFEM calculations). The following errors are returned: Err_1=4.91% and Err_2=6.82% for the characteristic length l=5 mm and Err_1=2.43% and Err_2=4.16% for the characteristic length l=2 mm. Again, in general too high peak loads are obtained in calculations, although last errors Err_2 is already comparable with error values produced in XFEM simulations. Figure 9 presents a comparison between numerical and experimental nominal strengths, while force – CMOD curves are shown in Fig. 10. Despite the overestimation of peak loads, numerical curves fit into experimental limits.

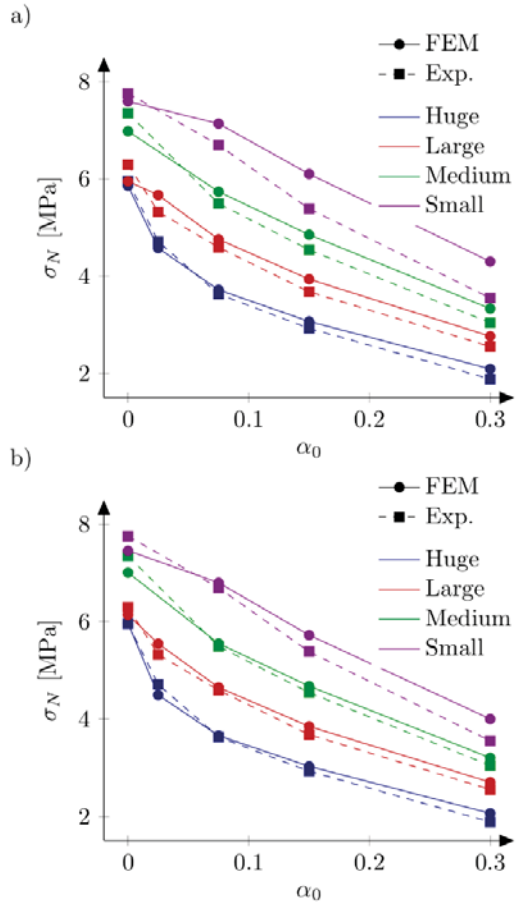

Fig. 9. Nominal (elasto-plasticity calculations) and experimental strengths with the exponential softening curve, f_t=4.8 MPa, G_f=35 N/m and the characteristic length l=5 mm (a) and l=2 mm (b)

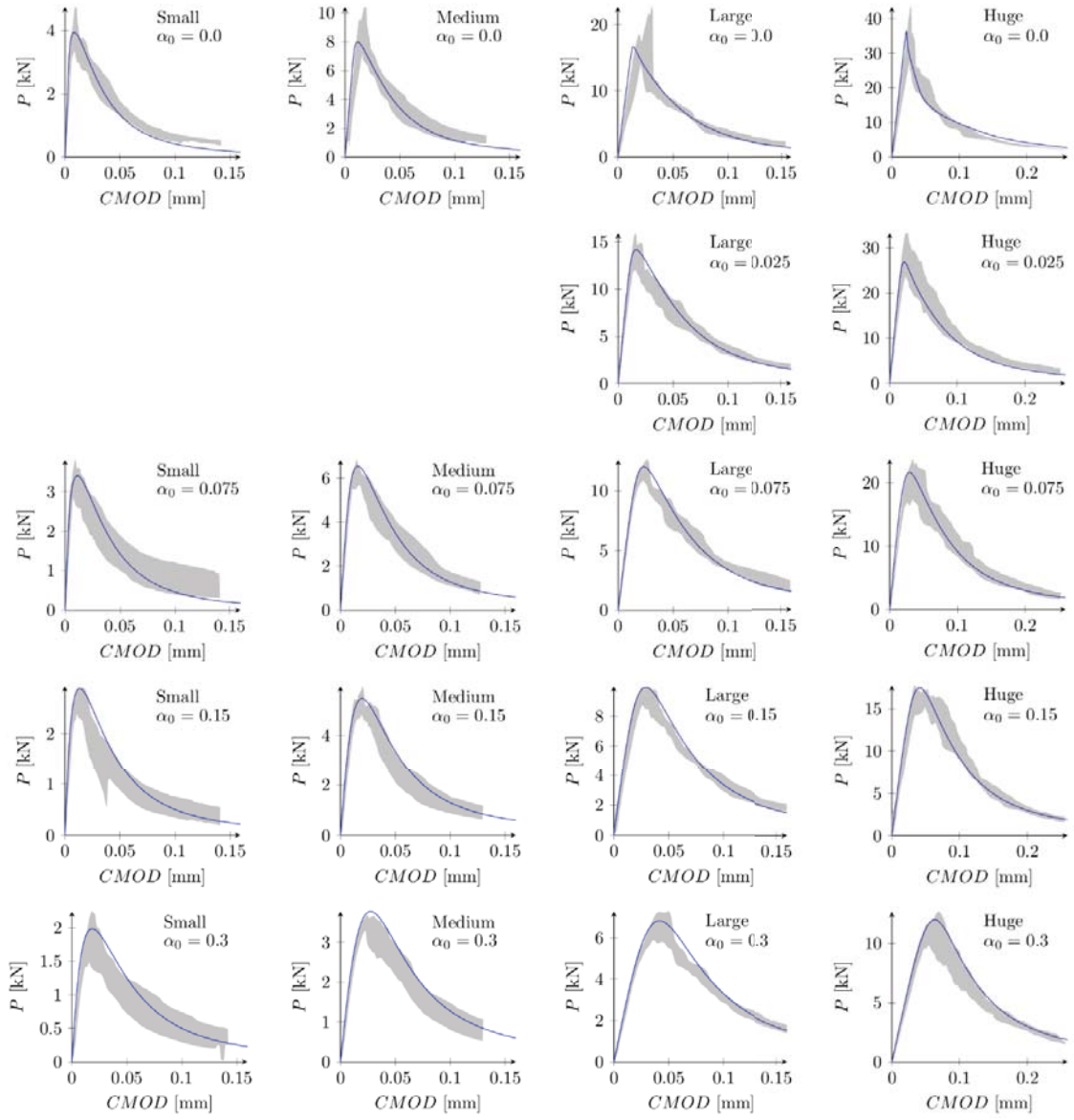

Fig. 10. Experimental and numerical (elasto-plasticity calculations) force – crack mouth opening displacement (CMOD) curves for exponential softening, f_t=4.8 MPa and G_f=35 N/m

CONCLUSIONS

In the paper the size effect phenomenon in plane concrete beams under bending has been investigated. The numerical calculations using smeared and discrete methods describing cracks in concrete have been executed. Obtained results have been compared with experimental outcomes. Both approaches gave results consistent with experiments, although smaller errors have been attained with XFEM. In elasto-plasticity, simulations with smaller values of the characteristic length have returned better results (smaller errors have been obtained). Both softening curves have produced comparable results, assuming different initial fracture energies. This observation points some problems in unique identification of the initial fracture energy, when different curve definitions in softening are used. When assuming a curved softening relationship (e.g. exponential one) purely geometrical definition of the initial fracture energy is not sufficient and the curvature of the curve in the domain after the peak should be taken into account.

The ongoing research is focused on improving the agreement of numerical results obtained with elasto-plastic constitutive law with experimental curves. More advanced, anisotropic averaging schemes in non-locality proposed by Giry et al. [9] and Grassl et al. [11] are investigated. The consequences of decreasing the fracture energy in the boundary layer (Bažant et al. [2]) are also examined.

ACKNOWLEDGEMENTS

Calculations were carried out at the Academic Computer Centre in Gdańsk.

BIBLIOGRAPHY

1. Bažant Z.P.: *Concrete fracture modelling: testing and practice*. Engineering Fracture Mechanics 2002; 69:165-206.

2. Bažant Z.P., Le J.-L., Hoover C.G.: *Nonlocal boundary layer (NBL) model: overcoming boundary condition problems in strength statistics and fracture analysis of quasibrittle materials*. Proceedings of the 7th International Conference on Fracture Mechanics of Concrete and Concrete Structures 2010; 135–143.

3. Beda P.B.: *Dynamical Systems Approach of Internal Length in Fractional Calculus*. Engineering Transactions 2017, 65:209-215.

4. Błaszczyk T.: *Analytical and numerical solution of the fractional Euler–Bernoulli beam equation*. Journal of Mechanics of Materials and Structures 2017; 12:23:34.

5. Bobiński J., Tejchman J.. *A coupled constitutive model for fracture in plain concrete based on continuum theory with non-local softening and eXtended Finite Element Method*. Finite Elements in Analysis and Design 2016; 114:1-21.

6. Brinkgreve R.B.J.: *Geomaterial models and numerical analysis of softening*. PhD Thesis, TU Delft 1994.

7. Çağlar Y., Şener S.: Size effect tests of different notch depth specimens with support rotation measurements. Engineering Fracture Mechanics 2016; 157:43–55.

8. Cox J.V.: *An extended finite element method with analytical enrichment for cohesive crack modelling*. International Journal for Numerical Methods in Engineering 2009; 78:48-83.

9. Giry C., Dufour F., Mazars J.: *Stress-based nonlocal damage model*. International Journal of Solids and Structures 2011; 48:3431–3443.

10. Glema A., Łodygowski T., Perzyna P.: *Interaction of deformation waves and localization phenomena in inelastic solids*. Computer Methods in Applied Mechanics and Engineering 2000; 183:123-140.

11. Grassl P., Xenos D., Jirásek M., Horák M.: *Evaluation of nonlocal approaches for modelling fracture near nonconvex boundaries*. International Journal of Solids and Structures 2014; 51:3239–3251.

12. Grégoire D., Rojas-Solano L., Pijaudier-Cabot G.: *Failure and size effect for notched and unnotched concrete beams*. International Journal for Numerical and Analytical Methods in Geomechanics 2013; 37:1434–1452.

13. Havlásek P., Grassl P., Jirásek M.: *Analysis of size effect on strength of quasi-brittle materials using integral-type nonlocal models*. Engineering Fracture Mechanics 2016; 157:72–85.

14. Hordijk D.A.: *Local approach to fatigue of concrete*. PhD Thesis, TU Delft 1991.

15. Hoover C.G., Bažant Z.P., Vorel J., Wendner R., Hubler M.H.: *Comprehensive concrete fracture tests: Description and results*. Engineering Fracture Mechanics 2013; 114:92–103.

16. Hoover C.G., Bažant Z.P.: *Cohesive crack, size effect, crack band and work-of-fracture models compared to comprehensive concrete fracture tests*. International Journal of Fracture 2014; 187:133–143.

17. Lazopoulos K.A., Lazopoulos A.K.: *Fractional vector calculus and fluid mechanics*. Journal of the Mechanical Behavior of Materials 2017; 26:43-54.

18. Marzec I., Skarżyński Ł., Bobiński J., Tejchman J.: *Modelling reinforced concrete beams under mixed shear-tension failure with different continuous FE approaches*. Computers and Concrete 2013; 12:585-612.

19. Marzec I., Tejchman J., Winnicki A.: *Computational simulations of concrete behaviour under dynamic conditions using elasto-visco-plastic model with non-local softening*. Computers and Concrete 2015; 15(4):515-545.

20. Mazars J., Hamon F., Grange S.: *A new 3d damage model for concrete under monotonic, cyclic and dynamic load*. Materials and Structures 2015; 48:3779–3793.

21. Melenk J.M., Babuška I.: *The partition of unity finite element method: basic theory and applications*. Computer Methods in Applied Mechanics and Engineering 1996; 139:289-314.

22. Simone A., Wells G.N., Sluys L.J.: *From continuous to discontinuous failure in a gradient-enhanced continuum damage model*. Computer Methods in Applied Mechanics and Engineering 2003; 192:4581-4607.

23. Simone A., Sluys L.J.: *The use of displacement discontinuities in a rate-dependent medium*. Computer Methods in Applied Mechanics and Engineering 2004; 193:3015-3033.

24. Sumelka W.: *Non-local Kirchhoff–Love plates in terms of fractional calculus*. Archives of Civil and Mechanical Engineering 2015; 15:231-242.

25. Sumelka W., Błaszczyk T., Liebold C.: Fractional Euler–Bernoulli beams: Theory, numerical study and experimental validation. European Journal of Mechanics - A/Solids 2015; 54:243-251.

26. Unger J.F., Eckardt S., Könke C.: *Modelling of cohesive crack growth in concrete structures with the extended finite element method*. Computer Methods in Applied Mechanics and Engineering 2007; 196:4087–4100.

27. Wang W.M., Sluys L.J., de Borst R.: *Viscoplasticity for instabilities due to strain softening and strain-rate softening*. International Journal for Numerical Methods in Engineering 1997; 40:3839-3864.

28. Wells G.N., Sluys L.J.: *A new method for modelling cohesive cracks using finite elements*. International Journal for Numerical Methods in Engineering 2001; 50:2667-2682.

29. Winnicki A., Pearce C.J., Bićanić N.: *Viscoplastic Hoffman consistency model for concrete*. Computers & Structures 2001; 79:7-19.

30. Zi G., Belytschko T.: *New crack-tip elements for XFEM and applications to cohesive cracks*. International Journal for Numerical Methods in Engineering 2003; 57:2221-2240.

CONTACT WITH THE AUTHORS

Ireneusz Marzec
e-mail: irek@pg.edu.pl

Gdansk University of Technology
Narutowicza 11/12, 80-233 Gdańsk
Poland

Jerzy Bobiński
e-mail: bobin@pg.edu.pl

Gdansk University of Technology
Narutowicza 11/12, 80-233 Gdańsk
Poland

sciendo

POLISH MARITIME RESEARCH 2 (102) 2019 Vol. 26; pp. 126-133
10.2478/pomr-2019-0032

APPLICATION OF REVERSE ENGINEERING TECHNOLOGY IN PART DESIGN FOR SHIPBUILDING INDUSTRY

Mariusz Deja[1]
Michał Dobrzyński[1]
Marcin Rymkiewicz[2]
[1] Gdansk University of Technology, Faculty of Mechanical Engineering, Department of Manufacturing and Production Engineering, Poland
[2] „Scan 3D", Gdynia, Poland

ABSTRACT

In the shipbuilding industry, it is difficult to create CAD models of existing or prototype parts, especially with many freeform surfaces. The paper presents the creation of the CAD 3D model of a shipbuilding component with the application of the reverse engineering technology. Based on the data obtained from the digitization process, the component is reconstructed in point cloud processing programs and the CAD model is created. Finally, the accuracy of the digital model is estimated.

Keywords: reverse engineering, laser scanning, freeform surface, measurement techniques

INTRODUCTION

Minimising the time needed for preparing a new project, with the resulting reduction of production costs, is of special importance in both implementing new innovative watercraft structures and retrofitting the existing ones. Reverse engineering (RE) is one of the methods used to support these activities, in particular for controlling the quality of elements used in shipbuilding, redesigning prototype structures, retrofitting existing constructions, etc. The main measurement methods used for shape data acquisition in the marine industry are: conventional manual measuring instruments, mechanical devices, scanning lasers, and photogrammeters [10].

Reverse engineering, in combination with laser scanning technologies and post-processing, is extremely useful in redesigning, testing, and updating the structure of watercraft components. Measuring and modelling of such a component with the aid of conventional measurement methods is very difficult, as it refers, as a rule, to a product with geometrically complex freeform shapes. In this case, the use of scanned data in the form of clouds of points allows the seagoing watercraft designer to create a precise CAD 3D model, which can then be used for assessing the quality of manufacturing, as well as for

CAE system-based redesigning, engineering and simulation tests, etc. This way, the laser scanning technology supports the ship control process and provides a method of data acquisition which may turn out profitable for the shipbuilding industry due to its time and cost saving nature. According to the ASE report on the National Shipbuilding Research Programme (NSRP), 3D laser scanning during ship data acquisition and postprocessing can decrease the cost by 37% and time by 39%, compared to traditional methods making use of traditional/manual measuring instruments [13].

The reverse engineering technology is also used for supporting engineering calculations [23, 25], and to obtain more accurate results in highly precise machining [26]. Its use also makes it possible to increase the accuracy of geodetic and astronomical measurements performed using radio telescopes [24] and to investigate and assess the architectonic heritage [22].

The following chapters of the article present: the literature review on the use of reverse engineering, especially in the shipbuilding industry, and the methodology of CAD 3D model creation with the use of the reverse engineering technology for a given ship component. Then, based on the data obtained from the digitisation process, the component is reconstructed in computer programmes for point cloud processing and the CAD model is created. The final stage of the analysis is the accuracy assessment of the digitised model.

LITERATURE REVIEW

The use of modern CAD/CAM systems and special measuring instruments for creating CAD 3D models of existing objects plays a key role in reverse engineering [19, 20], especially in the case of large-size elements [1] in the shipbuilding industry [14, 16] and aeronautics [7]. This is of special importance for a model of the part created in the absence of digital data related with the reconstructed object or when the part is to be retrofitted. The problem which consisted in applying reverse engineering techniques to retrofit the existing watercraft, or in the absence of basic technical data, such as construction plans, the data on the hull and machines installed on the deck, and/or working drawings of components, was studied by Tasseti at al. [17].

As far as object reconstruction is concerned, its requirements depend on the planned application, i.e. whether it is part replication, reconstruction, measurement, and/or modification related with change of the structure of the analysed model. Part modification can be easily performed following the approach presented in [19], which assumes reconstructing the design concept from the already existing objects. The obtained 3D models are based on geometric features (feature-based) and comprise the geometry description which provides opportunities for easy introduction of constructional changes to new innovative applications. A similar approach proposed in [4, 5] is additionally combined with virtual machining, which makes it possible to recognise technological features (feature recognition). In [11], the authors propose the reverse engineering-based approach to support regeneration of worn out parts. The CAD/CAM system generates tool paths for a device which will execute the virtual repair process, for instance for a robot welding a joint to fill the damaged area of the regenerated part with a given volume of welding material. Then, this part is machined on a five-axis CNC milling machine to a required dimension.

The use of modern measurement techniques in combination with additive techniques makes it possible to produce a wide variety of parts needed, for instance, to repair damaged devices on ships or offshore steel structures [6, 18], or in the automotive industry [15]. A structurally advanced group of products with complex geometry and higher-quality surface requirements are high-pressure stage blades in gas turbines used in ship propulsion systems or in Tesla turbines. The geometry of these blades is very complex, with additional elements such as holes and passages intended to deliver the cooling medium under the blade surface. The blades are tested both experimentally on real prototype objects, and with the aid of numerical methods [8].

Manufacturing of hull elements is one of key processes in shipbuilding. However, this process is still performed at low degree of automation. From 30% to 70% of typical ship hulls comprise parts with freeform surfaces shaped by experienced workers. The hull part measurement system is a component of the production automation system which allows the production assistance programme to generate proper data for part shaping [9]. In [14], large hull parts were scanned, after which the measured data were compared with the required geometry to check whether the required shape was achieved and to select heating line parameters for possible shape correction in further operations. The experiments were performed on real ship hull parts, and the obtained results demonstrated a possibility for automating the production process on the shipyard's heating line.

The complex object modelling methodology which utilizes photogrammetric and laser methods to generate a high-density cloud of points was presented by Menna and Troisi [12]. The structures analysed by them were small screw propellers, and the obtained results demonstrated the applicability of a hybrid approach which integrates the two considered technologies. The use of digital photogrammetric techniques for modelling 3D objects is essential in designing marine screw propellers and complex hull geometries [3].

In [16], using a 12-metre long yacht as an example, a methodology was presented for determining the symmetry plane of an object based on the cloud of points obtained from laser scanning or other measurement techniques. Precise finding of the vertical symmetry plane of the examined yacht provided opportunities for correct assessment of its future behaviour during the navigation. A possibility to increase the accuracy of measurements of prototype ship models built in decreased scale was presented in [2], where fast and compact terrestrial laser scanners (TLS) were used for this purpose. In that case the measurement accuracy was of special importance, as all measurement errors would be multiplied on the full-scale object.

OBJECT OF EXAMINATION AND MEASUREMENT METHODS

The object of examination was the housing of the main propulsion propeller shaft for a newly designed vessel. The initial product was a prototype element made using a conventional lamination technology with additional machining of selected structural elements. It had overall dimensions φ290 × 425 mm and numerous freeform surfaces which ensured correct functioning of the entire unit during yacht navigation in marine conditions (Fig. 1).

Fig. 1. View of prototype product

The measurements were performed using a 7-axis articulated measuring arm SMART Arm 7 2.5 produced by Nikon Smart Solutions, with the measuring range of 2,5 m, volumetric accuracy of ± 0,043 mm, and point repeatability of 0,030 mm (uncertainty within the entire operating range of the arm, values given for 2 sigma). The arm was made of light and durable materials: carbon fibre, aluminium, and titanium.

The measuring arm was equipped with a MMDx Nikon Metrology laser scanner, with laser beam width of 100 mm. The maximum number of really scanned points per second was 80 000. The Model Maker laser head was equipped with the Enhanced Scanning Performance (ESP3) technology, which adapted the laser power to the type of surface of the scanned object, for instance its structure and quality of finishing, among other features. Basic parameters of the laser head are given in Table 1.

Tab. 1. Parameters of MMDx 100 laser head

Accuracy (1σ)	10 µm
Stripe width (Y)	100 mm
Measuring range (Z)	100 mm
Stand-off	100 mm
Min. point resolution	65 µm
Max. data rate	150 Hz
Laser power	Class 2, 660 nm

The data generated by the 3D laser scanner were analysed using the Geomagic software, mainly Design X and Wrap [21]. After analysing and processing, the obtained clouds of points and triangle meshes made a basis for generating a parametric CAD model of the real prototype object. Then, using the processed scan of the element as a basis, a CAD 3D model was created in the Autodesk Inventor software. The final verification of this model was performed using the Geomagic Control X software.

RESULTS OF TESTS

The process of object surface digitisation was performed with the laser beam of 100 mm in width, as shown in Fig. 2a. The raw data obtained in the above way have the form of a cloud of points shown in Fig. 2b. Then, the point-defined object was converted to a so-called polygon model by imposing a surface of triangles onto the cloud of points (Fig. 3a).

Noteworthy are the defects which appear during model surface mapping (Fig. 3b). They result from two main causes: collection of insufficient number of data points in some object surface areas, and surface and/or geometry imperfections of the real prototype object resulting from insufficient precision of its manufacturing.

a)

b)

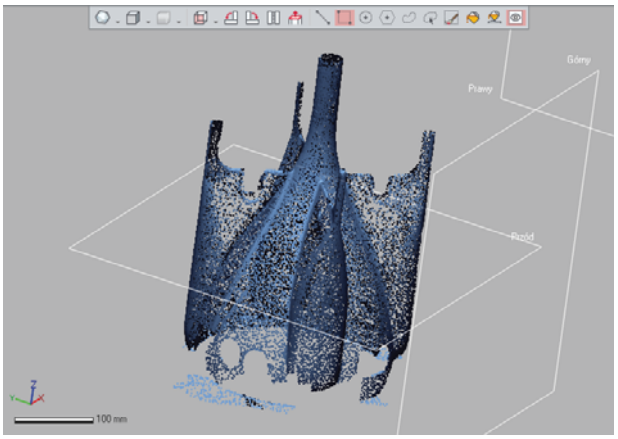

Fig. 2. Product surface digitisation with the aid of measuring arm SMART Arm 7 equipped with laser head MMDx 100 (a) and cloud of points obtained from the measurement (b)

a)

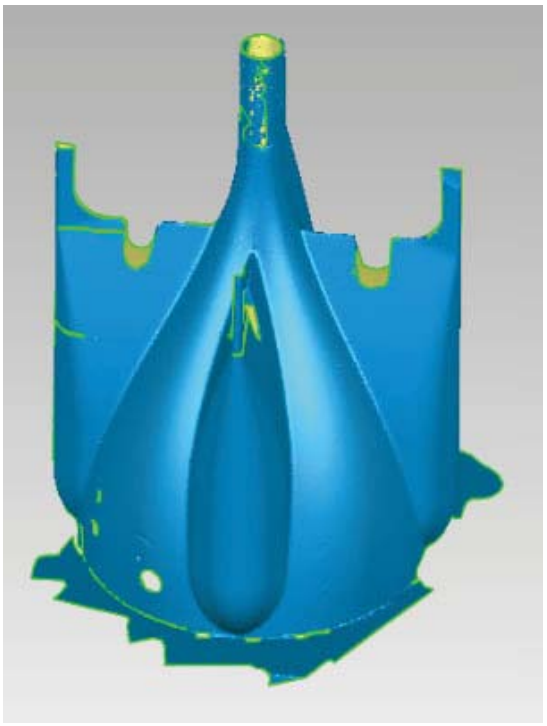

b)

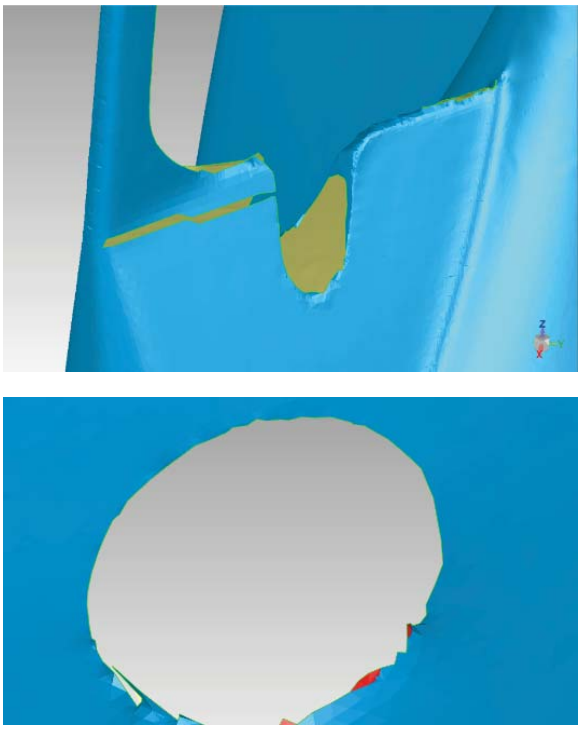

Fig. 3. Polygon model of the object (a), examples of surface defects (b)

In was therefore necessary to reconstruct the model mesh by filling small holes, smoothing and cleaning the mesh, removing model discontinuities and double walls, etc. This task was performed using mathematical algorithms directly implemented in Geomagic software. Moreover, some free-standing triangles which represented noise in the mesh (red areas) were removed (Fig. 3b).

Larger defects which came into existence as a result of the digitisation process and had the form of holes and surface discontinuities were removed using various programming functions, (Fig. 4). For instance, the function "bridge" was applied to increase the accuracy of adaptation of the filling to the surrounding mesh by dividing each discontinuous element into smaller parts. All this made it possible to reconstruct more precisely the areas in which the data from scanning were incomplete or missing.

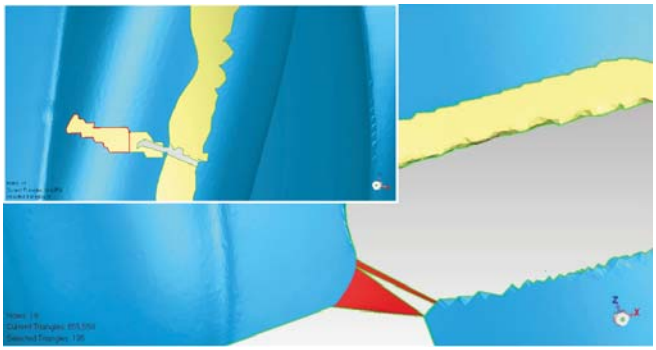

Fig. 4. Object imperfections identified after digitisation as surface discontinuities in the CAD model

The final refinement of the model was performed using the pre-installed functions "Relaxpolygons" which made it possible to smooth the model locally and improve the mesh. This was done by setting three main parameters: smoothing level, force, and required curvature, in selected areas of the model. The final view of the digitised model of the examined part is shown in Fig. 5a, and the corresponding *.stl view prepared in Inventor software in Fig. 5b.

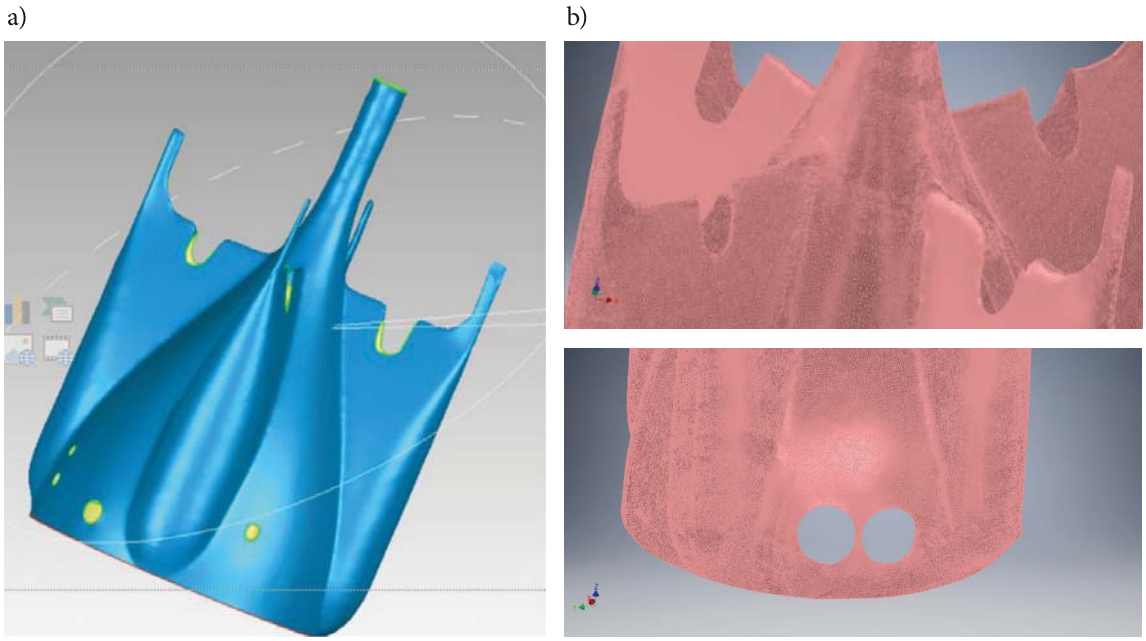

*Fig. 5. View of object model after correcting measures (a), and *.stl model prepared in Autodesk Inventor software (b)*

The obtained triangle mesh was used in the redesign process, which was performed under the assumptions of preserving the initial prototype geometry, especially the freeform surfaces, and meeting the symmetry condition by the product to be designed. Hybrid modelling functions were used for this purpose, such as the functions of rotation about axis, extrusion, and linking of solids, for instance. The accuracy of the created model was assumed at the level of about +/- 1,5 mm. Fig. 6a shows the final CAD 3D model (yellow) along with the applied *.stl mesh, while Fig. 6b presents selected views of the model.

The accuracy of the created CAD 3D model of the examined part was assessed using Geomagic Control X, an advanced software package used for controlling the quality of products based on point clouds recorded by scanning devices. In the examined case, the scanned 3D object was compared with the created CAD 3D model and the resulting deviations were analysed.

The CAD 3D model control was done after importing the following files:

- Reference data – the symmetrical CAD 3D model of the product, created in Autodesk Inventor software based on the modified *.stl file prepared in Geomagic software.
- Control data – the *.stl file being the input data for editing the point cloud in Geomagic software.

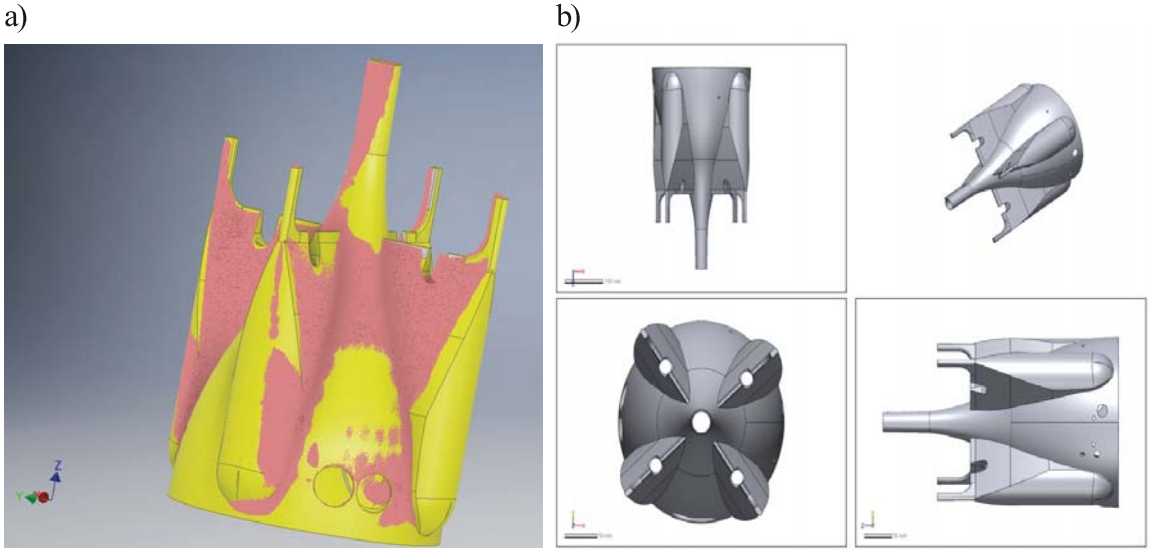

*Fig. 6. CAD 3D model of the object after redesigning and *.stl mesh (a), selected views (b)*

Based on the measurement report, the maximum deviation of the measured data from the CAD model was 7,66 mm (Fig. 7a). The average deviation over the entire model was

0,59 mm, with standard deviation SD= 1,75 mm. Large maximum deviation values are not acceptable taking into consideration the function of the product. The observed errors mainly result from the applied production technology which did not ensure preservation of the basic structural condition, i.e. geometrical symmetry of the product. This deficiency is clearly visible in the view of the propeller shaft guide sleeve (Fig. 7b).

a) b)

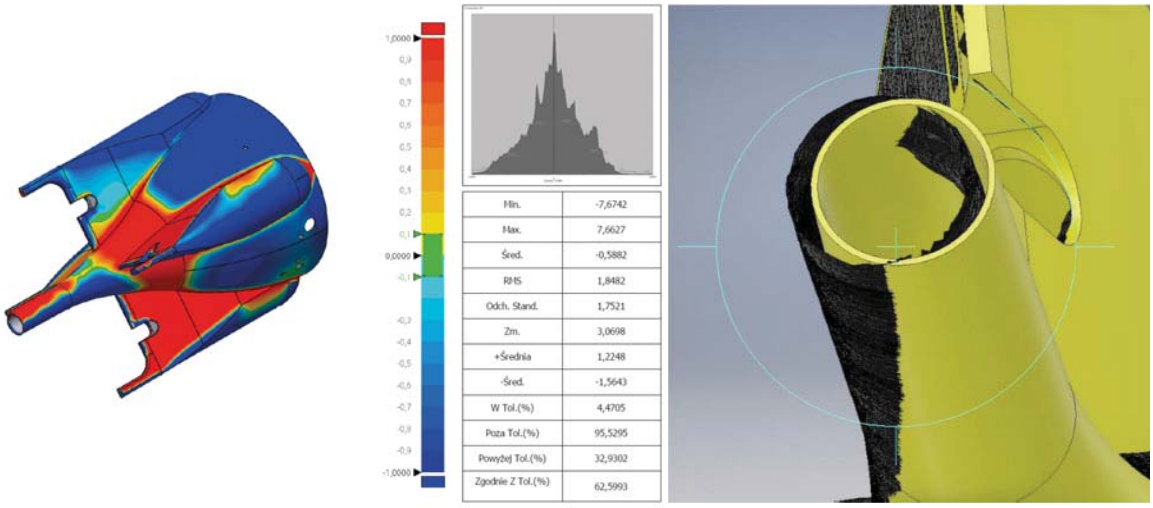

Fig. 7. Measuring report (a) and view of guide sleeve (b)

CONCLUSIONS

In traditional approach to the design process, creating a product is always preceded by the description of its structure, which makes it possible to assess its geometrical features, dimensional relations and their tolerances. Engineering drawings are usually used for this purpose. However, at present, the construction description has more and more frequently the form of a virtual CAD 3D model, obtained as a result of digital mapping of real objects (reverse engineering). This is of special importance in designing for the shipbuilding industry, where the geometry of a new target product is based on its initial prototypes and corresponding free surfaces. In this situation, the processes of digitisation and processing of clouds of points obtained from scanning, with further creation of CAD 3D models, become essential. The article analysed all steps of the CAD 3D model creation procedure, and the results of this analysis allowed formulating the following conclusions:

- Digitisation performed with the aid of an articulated measuring arm equipped with laser head provides an opportunity for wide-range measurements with volumetric accuracy of ± 0,043 mm and point repeatability of 0,030 mm.
- Due to faults and discontinuities of the object, the process of point cloud processing after digitisation is crucial for the entire task and requires special software.
- The accuracy of a CAD 3D model obtained in the redesign process can be assessed by comparing with data from measurements. In the analysed case, the average deviation over the entire model was 0,59 mm, with standard deviation SD= 1,75 mm.
- The maximal deviation reached nearly 7,66 mm, which was associated with the lack of symmetry of the prototype product caused by the applied production technology. Therefore, it is advisable to apply an alternative production process to ensure that the product will meet constructional requirements.

BIBLIOGRAPHY

1. 3D Measurement Solutions for Every Industry. https://www.faro.com/metrology-3d-documentation-solutions-from-faro/3d-measurement-solutions-for-every-industry , dostęp: 29.11.2018.
2. ABBAS, Mohd Azwan, et al. Improvements to the accuracy of prototype ship models measurement method using terrestrial laser scanner. Measurement, 2017, 100: 301-310.
3. ACKERMANN, S., et al. Digital photogrammetry for high precision 3D measurements in shipbuilding field. In: 6th CIRP International Conference on ICME-Intelligent Computation in Manufacturing Engineering. 2008.
4. ANWER, Nabil; MATHIEU, Luc. From reverse engineering to shape engineering in mechanical design. CIRP Annals, 2016, 65.1: 165-168.
5. BUONAMICI, Francesco, et al. Reverse engineering of mechanical parts: A template-based approach. Journal of Computational Design and Engineering, 2018, 5.2: 145-159.

6. DEJA, Mariusz, et al. Application of Rapid Prototyping Technology in the Manufacturing of Turbine Blade with Small Diameter Holes. Polish Maritime Research, 2018, 25.s1: 119-123.

7. GÓMEZ, A., et al. Manufacturing of custom-made parts for assembly of large aircraft components. Procedia engineering, 2015, 132: 1006-1013.

8. KACZYŃSKI, Piotr, et al. Leakage flow reduction in different configuration of labyrinth seal on a turbine blade tip. In: Journal of Physics: Conference Series. IOP Publishing, 2018. p. 012012.

9. KO, Kwang Hee, et al. Development of software for computing forming information using a component based approach. International Journal of Naval Architecture and Ocean Engineering, 2009, 1.2: 78-88.

10. KOELMAN, Herbert J. Application of a photogrammetry-based system to measure and re-engineer ship hulls and ship parts: An industrial practices-based report. Computer-Aided Design, 2010, 42.8: 731-743.

11. LI, Lingling, et al. An integrated approach of reverse engineering aided remanufacturing process for worn components. Robotics and Computer-Integrated Manufacturing, 2017, 48: 39-50.

12. MENNA, F.; TROISI, S. Low cost reverse engineering techniques for 3D modelling of propellers. International Archives of Photogrammetry, Remote Sensing and Spatial Information Sciences, 2010, 38. Part 5: 452-457.

13. NSRP ASE Ship Check Data Capture Follow-on Project (NSRP ASE 05-01) Final Report (FY06), 2007.

14. PARK, Jung Seo; SHIN, Jong Gye; KO, Kwang Hee. Geometric assessment for fabrication of large hull pieces in shipbuilding. Computer-Aided Design, 2007, 39.10: 870-881.

15. PAULIC, Matej, et al. Reverse engineering of parts with optical scanning and additive manufacturing. Procedia Engineering, 2014, 69: 795-803.

16. ROCA-PARDIÑAS, Javier, et al. Assessing planar asymmetries in shipbuilding from point clouds. Measurement, 2017, 100: 252-261.

17. TASSETTI, N.; MARTELLI, Michele; BUGLIONI, Gabriele. Reverse engineering techniques for trawler hull 3D modelling and energy efficiency evaluation. In: Proc of NAV 2015 18th International Conference on Ships and Shipping Research. 2015. p. 24-26.

18. Using Artec 3D scanning technology to keep naval ships in perfect condition. https://www.artec3d.com/news/3d-scanning-reverse-engineering-for-navy , dostęp: 29.11.2018

19. WANG, Jun, et al. A framework for 3D model reconstruction in reverse engineering. Computers & Industrial Engineering, 2012, 63.4: 1189-1200.

20. ZHANG, Yu. Research into the engineering application of reverse engineering technology. Journal of Materials Processing Technology, 2003, 139.1-3: 472-475.

21. Geomagic Design X: https://www.3dsystems.com/software/geomagic-design-x [accessed on January 22, 2019].

22. COSTA-JOVER, Agustí, et al. Using the terrestrial laser scanner and simple methodologies for geometrically assessing complex masonry vaults. Journal of Cultural Heritage, 2018, https://doi.org/10.1016/j.culher.2018.10.003.

23. GUARATO, Alexandre Zuquete, et al. Conversion of 3D scanned point cloud into a voxel-based representation for crankshaft mass balancing. The International Journal of Advanced Manufacturing Technology, 2018, 95.1-4: 1315-1324.

24. HOLST, Christoph, et al. Terrestrial Laser Scanner Two-Face Measurements for Analyzing the Elevation-Dependent Deformation of the Onsala Space Observatory 20-m Radio Telescope's Main Reflector in a Bundle Adjustment. Sensors, 2017, 17.8: 1833.

25. ŠTALMACH, Ondrej, et al. Conversion of data from the laser scanner to the Ansys Workbench. In: MATEC Web of Conferences. EDP Sciences, 2019. p. 02003.

26. ZHANG, Hongyao; LI, Lun; ZHAO, Jibin. Robot automation grinding process for nuclear reactor coolant pump based on reverse engineering. The International Journal of Advanced Manufacturing Technology, 2019, 1-13.

CONTACT WITH THE AUTHORS

Mariusz Deja
e-mail: mdeja@pg.edu.pl

Gdańsk University of Technology
Faculty of Mechanical Engineering
Department of Manufacturing
and Production Engineering
G. Narutowicza 11/12, 80-233 Gdańsk
Poland

Michał Dobrzyński
e-mail: michal.dobrzynski@pg.edu.pl

Gdańsk University of Technology
Faculty of Mechanical Engineering
Department of Manufacturing
and Production Engineering
G. Narutowicza 11/12, 80-233 Gdańsk
Poland

Marcin Rymkiewicz
e-mail: marcinrymkiewicz@gmail.com

Scan 3D
J. Sobieskiego 13, 81-198 Gdynia
Poland

sciendo

POLISH MARITIME RESEARCH 2 (102) 2019 Vol. 26; pp. 134-141
10.2478/pomr-2019-0033

NEW CONCEPT OF HYBRID PROPULSION WITH HYDROSTATIC GEAR FOR INLAND WATER TRANSPORT

Daniel Piątek
Gdansk University of Technology, Poland

ABSTRACT

The article presents the development of author's concept of a diesel/hydraulic propulsion system for inland watercraft. Due to specific nature of vessel navigation on rivers, classical propulsion systems with shaft lines can be effectively replaced by systems with hydraulic power transmission. A solution is also presented of a hybrid design with extra electric port having the form of a pumping system driven from a battery of accumulators. Strong and weak points of the proposed solution are discussed and its energy efficiency is assessed.

Keywords: inland water transport; propulsion system; hybrid propulsion; hydrostatic gear; energy efficiency

PROPULSION SYSTEM AND MANOEUVRABILITY OF INLAND VESSEL

The power source on a typical inland vessel (Fig. 1a) is a diesel engine which drives a fixed pitch propeller. In early solutions, for instance the pusher tug Nosorozec built in the 1960s, it was a medium-speed engine (nominal speed: 500–750 rpm), while in more recent vessels, such as the pusher tug Bizon built in 1990s, high-speed engines were used (nominal speed: 1500–1800 rpm). The power transmission system consists of a single-stage reverse reduction gear with gear transmission ratio of up to 5.

Fig. 1. Visualisation of inland vessel propulsion system (own elaboration)
a) System with shaft line and mechanical gear *b) System with hydrostatic gear*

In the solution proposed by the author, the power transmission system comprises a so-called hydrostatic gear consisting of a pump, a hydraulic motor, and connecting hoses. The pump converts the mechanical energy of the internal combustion engine into the energy of the flowing liquid, which, in turn, is converted in the hydraulic motor into the mechanical energy needed for driving the screw propeller. To increase the energy efficiency of the proposed solution, the parameters of its operation are to be optimised. Increasing the operating pressure will lead to better power concentration, with the resulting smaller overall dimensions, mass, and inertia of the main system elements.

The energy efficiency can also be increased by changing rotational speed of the pump and hydraulic motor. The same pump driven by an internal combustion engine intended for use in the automotive industry (nominal speed 3000–4000 rpm) will generate twice as large a liquid flow, which will allow afurther decrease of the overall dimensions. Compared to typical engines intended for use on inland vessels, the automotive engines are characterised by lower cost of purchase, which is, however, accompanied with higher specific fuel consumption.

Proper selection of geometric parameters of the hydraulic motor makes it possible to decrease the rotational speed of the propeller, and thus improve its efficiency. It is noteworthy, however, that this will lead to the increase of propeller diameter, which is considered unfavourable taking into account rather small depth of rivers in Poland. Compared to a typical mechanical gear, the hydrostatic gear provides opportunities for reaching almost unlimited transmission ratio. Additionally, hydraulic power transmission eliminates a mechanical gear from the power transmission system, which minimises the risk of system failures resulting from propeller's contact with the river bed.

Within the low-speed engines, it is a group of satellite motors which reveal favourable parameters. Moreover, these motors can be supplied with water-based liquids, which is of certain importance for environment protection [1], [2], [3]. Frequently changing conditions of river navigation require numerous start-ups and low-temperature operation of the propulsion system [4], [5], [6].

The use of hydraulic gear makes it possible to shorten the motor compartment and easily distribute all propulsion system components, which is a great advantage when referring to inland watercraft.

Figure 2 shows the inland vessel propulsion and control structures which were selected for analysing mainly with respect to vessel manoeuvrability. This feature is very important for tourist vessels, which can be navigated by a low-experienced crew. It is noteworthy, however, that manoeuvrability improvement will be associated with the increase of system cost, and the final selection can only be made after proper financial analyses.

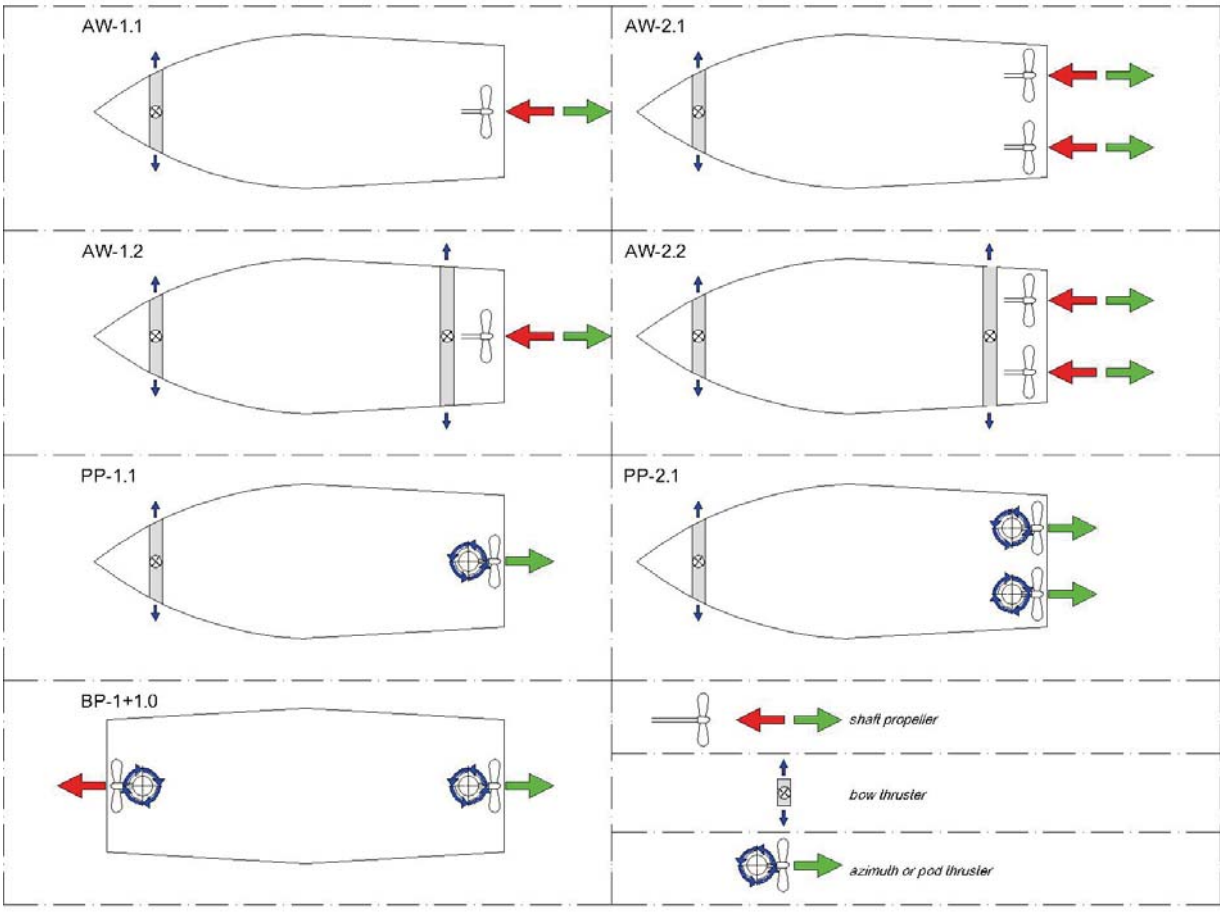

Fig. 2. Analysed structures of inland vessel control – description in the text (own elaboration)

The structure AW-1.1 is an adaptation of a system with classic shaft line in which the shaft line has been replaced with hydraulic gear. The direction of vessel motion is changed using a single-plate rudder (not shown in the figure), which results in poor manoeuvrability, especially at low speeds. The manoeuvrability can be improved by using a bow thruster with hydrostatic drive. The presented structure makes it possible to simplify the hydraulic system, to minimise its mass, and to maximise its energy efficiency. It is also easy for installation.

The structure AW-2.1 is almost identical with the previous one, with the use of two propellers instead one being the only difference. On a classic vessel, this will correspond with the use of two internal combustion engines. This modification increases the system construction cost, at the same time improving the safety of its operation and making it possible to obtain a torque by generating thrust forces in opposite directions (forward and backward).

The structures AW-1.2 and AW-2.2 result directly from the corresponding earlier systems, with the only difference consisting in the presence of an additional stern thruster. These structures allow the watercraft to be controlled easily and independently in longitudinal and transverse directions. A problem to be solved in this case is thruster location in the stern section of the hull. **The use of an additional stern thruster in the group of vessels selected for adaptation provides a reference manoeuvrability pattern.**

In the structure PP-1.1, the propeller and the single-plate rudder are replaced with a propeller/control device being an azimuth or nacelle propeller. This device increases the overall cost and requires interference into vessel's hull structure, but provides opportunities for smooth thrust generation within the 360° range, thus improving vessel's manoeuvrability.

The use of two rotatable thrusters (PP-2.1) which can rotate independently of each other provides good manoeuvring characteristics. Moreover, with the crew experienced in watercraft navigation, it makes it unnecessary to use a bow thruster.

The last structure BP-1+1.0 represents the vessel equipped with two rotatable thrusters (at bow and stern). This system allows the vessel to move in an arbitrary direction with respect to its axis. In this case, the bow thruster is exposed to the contact with the river bed or infrastructure, which can lead to its damage. However, the thruster can be protected against these unexpected contacts by proper design of bow hull section or the use of a catamaran type system.

The system of symmetric hull with two rotatable thrusters, at bow and stern, is an optimal solution for houseboat type watercraft from the point of view of its manoeuvrability.

For classic existing vessels, the form A seems to be most profitable, due to the smallest scope of the required adaptability work and the resulting low investment costs, which in this case mainly include the cost of hydraulic system purchase and installation.

DEVELOPING THE CONCEPT OF DIESEL/HYDRAULIC SYSTEM

There are ship design solutions in which extended hydrostatic systems are used for driving and supplying technological systems. A good example of such a solution is the fishing vessel KR-10 [7]. The propulsion system of this vessel comprises a traction motor which has been individually adapted for marine conditions. The above adaptation mainly consisted in adding a cooling system making use of salt water. The motor drives a variable-pitch propeller via a reduction gear and shaft line. This solution has rarely been used on small vessels. From the operational point of view, it makes it possible to change smoothly the thrust, regardless of motor revolutions, when operating the fishing trawl. The system of technological devices installed on the vessel, with trawl winch motors as main receivers, is powered from a constant delivery pump suspended on the main gearbox (PTO output – power take-off port). To reduce the cost of electrical installation, a decision was made to resign from ~220 V voltage and to use 24 V instead, together with hydraulic supply of larger receivers, such as fire pumps for instance.

Fig. 3. KR-10 fishing vessel: propulsion system with hydraulic drive of technological devices [7]

In years 2003–2006, the European Project Incowatrans was carried out which aimed at constructing a ferry for inland transport over Polish waterways on the route E-70 (Berlin-Kaliningrad). These waterways are characterised by low technical parameters (transit depth, length of locks, etc.) For these reasons, the constructed ferry consists of two

low-draught modules playing the role of hotel section and pusher tug, the latter driven by two diesel/hydraulic/electric units.

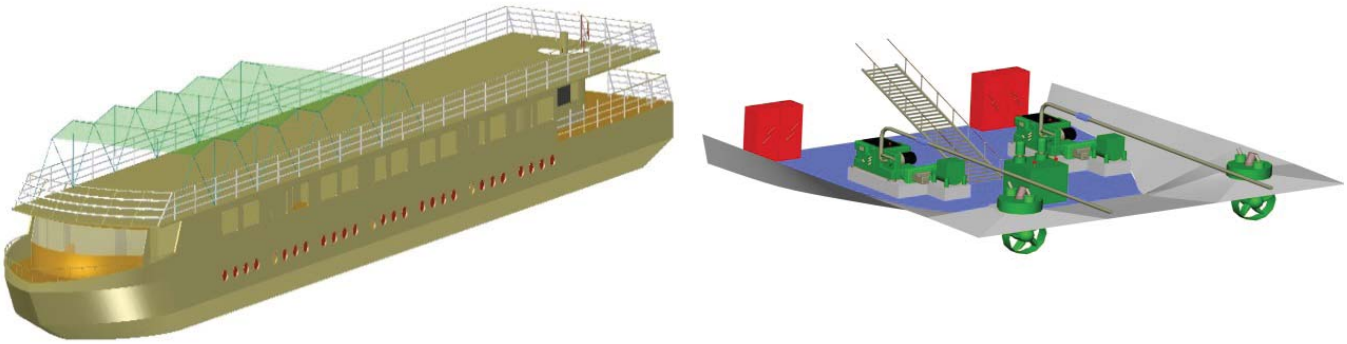

Fig. 4. Inland passenger ship Eureka – diesel/hydraulic drive, with rotatable hydraulic thrusters [8]

Each of two adapted internal combustion engines, which come from the automotive market, drives, via the main gearbox, a variable-delivery hydraulic pump and an electric generator. The hydraulic energy is used for driving two azimuth propellers with gearboxes in *L*-arrangement, which provides the vessel with good propulsion and manoeuvrability control, while the electric power is mainly consumed by passengers and crew. Depending on current needs, for instance upstream or downstream navigation, the contribution of particular types of energy in the internal combustion engine load can be changed smoothly.

each circuit powered with an individual pump. The main drive is powered with a variable-delivery multi-piston axial pump working in closed circuit at working pressure p = 32 MPa.

The screw propeller is also driven with a typical multi-piston axial hydraulic system. This solution makes it possible to minimise the total mass of the used hydraulic components and to change smoothly propeller revolutions at constant rotational speed of the internal combustion engine. In the field of hydraulic drives, the applied components enable reaching the highest possible efficiency of the system at a relatively low investment cost.

The past experience gained by the author has made the basis for identifying the development trends in hydraulic power transmission systems on small vessels. These trends are collated in Fig. 6, with special focus on inland vessels. The bottom row indicates the solutions which are most desirable at the highest technological level:

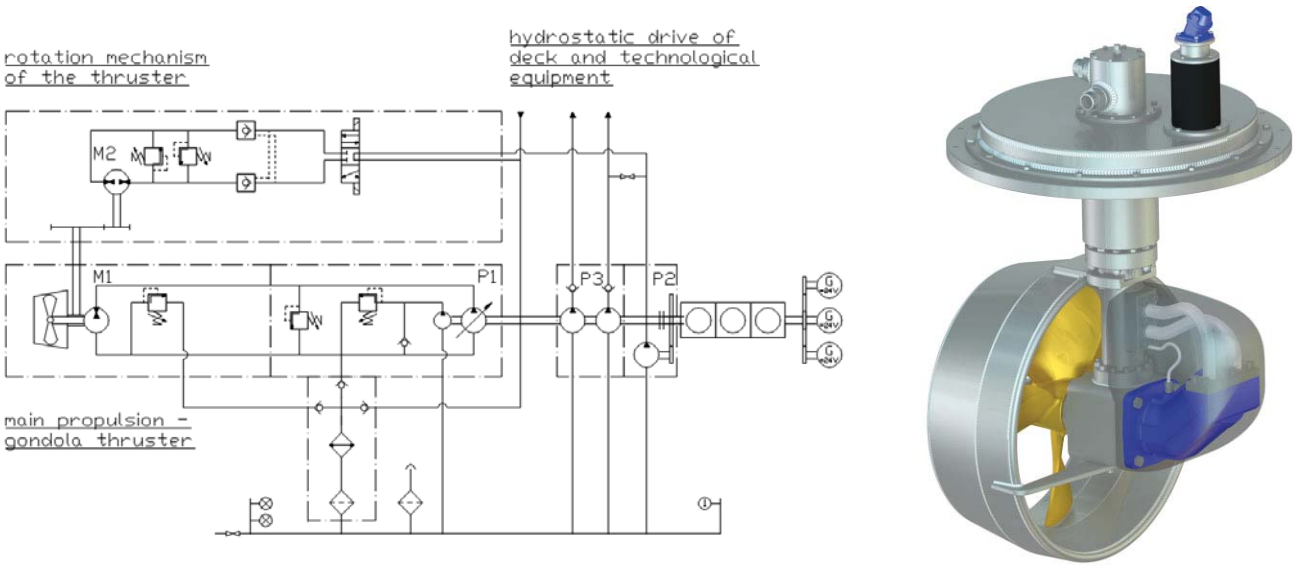

Fig. 5. Diesel-hydraulic propulsion of the vessel with hydraulic nacelle propeller [10], [11]

The essential component of the vessel propulsion system is a hydraulic nacelle propeller (Fig. 5). The hydraulic system is rather complex and consists of 3 functional circuits: main drive, propeller rotation drive, and drive for auxiliary devices,

- Diesel engine with rotational speed of 2800–3000 rpm, coming from the automotive industry and adapted for marine conditions and biogas feeding (due to easy CNG, LPG adaptation);
- Hybrid (diesel/electric) propulsion with hydraulic power transmission. The electric propulsion is used for navigation

in eco mode, with internal combustion engine switched off, and is powered from a battery of accumulators. The main high-pressure hydraulic propulsion, with nominal pressure of about 32 MPa, is generated by variable-delivery pumps in closed circuit;

- Nacelle propeller-based propulsion, with hydraulic motor(s) placed in a nacelle, performs the propulsion and control tasks.

for the vessel. However, including the eco pump to the system, and in particular recovery of energy needed for charging accumulators, makes the system structure more complex. Therefore, it is proposed to use the generator 10 suspended on the internal combustion engine.

The modular nature of the described solution results from the modularity of hydraulics with respect to the creation of multi-flow pumps, as a result of which a number of receivers

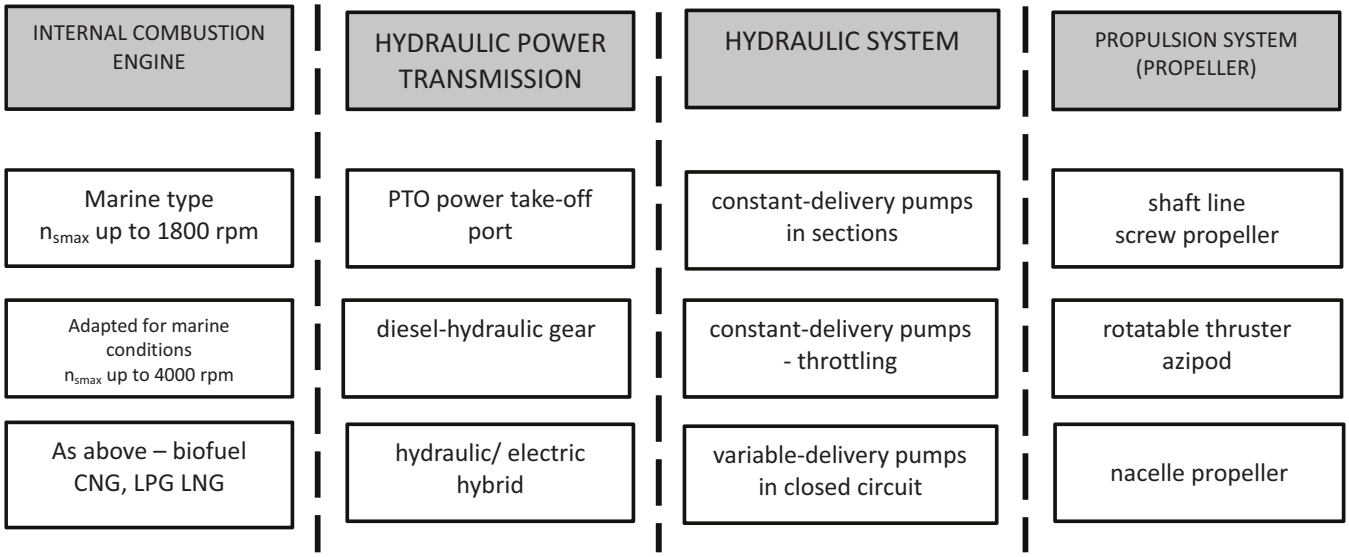

Fig. 6. Development in hydraulic power transmission systems on inland vessels [own elaboration]

We should be aware that due to a wide spectrum of vessels and investment cost criteria, the technically optimal solutions are not necessarily used on low-budget vessels.

MODULAR HYBRID DIESEL/ HYDRAULIC PROPULSION SYSTEM WITH ELECTRIC PORT

Fig. 7 shows concepts of hybrid diesel/electric propulsion systems with fully hydraulic power transmission. Concepts a) and b) in open circuit are intended for use on low-budget vessels with smaller power demand, such as the abovementioned houseboats, while version c) presents a system with variable-delivery pumps working in closed circuit, which is intended for use on inland vessels with highest power demand, for instance the abovementioned 250-kW IV-class pusher tugs.

During regular navigation, in all systems the internal combustion engine 1 drives the main pump 2, while when navigating in eco mode, with internal combustion engine switched off, in the zone of silence for instance, the propulsion role is taken over by the electric motor 8 which drives the eco pump 7 through valve blocks 11. Based on author's experience, the power of the eco pump has been selected as equal to 30% of nominal power of the main pump. Selection of fully hydraulic power transmission, even in eco mode, is motivated by a wish to use a hydraulic nacelle propeller 6 as the optimal propeller can be driven from one propulsion unit, without use of any mechanical gear (Fig. 5, for instance).

The proposed solution has all advantages of a hydraulic system. However, an issue which cannot be omitted is its competitiveness with rapidly developing systems with electric power transmission. Based on the performed analyses [9], electric systems do not have such serious advantages in marine applications as it is commonly believed. For a 300-kW vessel equipped with azimuth propellers, the hydraulic system is lighter by about 40 % than its electric equivalent, due to better power concentration. This is a very important parameter, as it affects the load capacity of a small vessel sailing on inland waters. The other parameter used in comparison is the investment cost, which has also turned out more profitable for hydraulic power transmission (77/100 ratio). This is mainly caused by the fact that a hydraulic system is constructed from typical components with certificates already issued by classification societies, while the electric transmission components can be licensed for operation in water environment only after making certain payments. Moreover, the main components of the electric transmission system and its control elements are frequently manufactured individually or in small series to custom order.

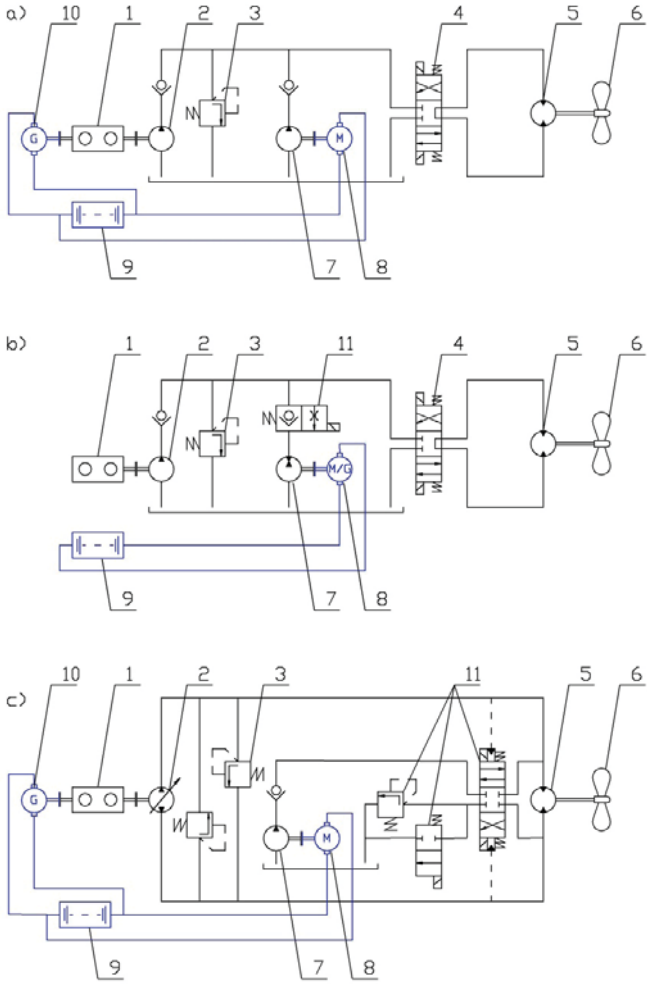

Fig. 7: Concept of diesel/electric system with hydraulic power transmission [own elaboration]:
a) – open hydraulic circuit, charging accumulators from mechanical system;
b) – open hydraulic circuit, charging accumulators from hydraulic system;
c) – closed hydraulic circuit (accumulators charged from mechanical system);
1 – internal combustion engine, 2 –main drive hydraulic pump, 3 – safety valve, 4 – divider controlling the direction of propeller revolutions (only open circuit); 5 – hydraulic propeller propulsion motor; 6 – propeller, 7 – eco pump with electric drive, 8 – motor driving the eco pump, 9 – battery of accumulators, 10 – electric generator with mechanical drive, 11 – eco pump switching unit (flushing function in closed circuit)

A basic criterion in the system performance evaluation is energy efficiency, i.e. losses generated during energy transmission. The author prefers determining the power flow direction in a system which is consistent with the increasing power demand from the receiver's side [12]. In this approach, the starting point is the power demand from the receivers, after which the system losses are to be assessed and complemented, and the final delivered power results from the total system demand. The above approach is consistent with the course of the design process.

The applied hydraulic transmission, which consists in double energy conversion (from mechanical to hydraulic energy in the pump and again to mechanical energy in the hydraulic motor), undoubtedly worsens the energy efficiency. Therefore, it is necessary to assess the range of this worsening and decide whether it is acceptable, i.e. whether the energy efficiency decrease is sufficiently small to be compensated by the remaining advantages of the hydraulic power transmission.

Tables 1 and 2 collate the efficiency values of the propulsion system components shown in Fig. 1. They were assessed for the nominal point of system operation, based on the results of flue tests of propulsion systems with hydraulic power transmission (power of 40 and 90 kW). Due to the multidisciplinary nature of the issue, use was made of data presented in producers' catalogues and publications [13].

Tab. 1. Efficiency of components of the conventional system with shaft line

Name	Symbol	Value [-]
SCREW PROPELLER		
total efficiency of propeller	η_S	0, 45
SHAFT LINE		
efficiency of shaft line	η_W	0, 96
INTERNAL COMBUSTION ENGINE		
engine efficiency	η_D	0, 35
PROPULSION SYSTEM with shaft line		
total efficiency	η	0, 151

Tab. 2: Efficiency of components of the system with hydraulic power transmission

Name	Symbol	Value [-]
SCREW PROPELLER		
total efficiency of propeller	η_S	0, 45
HYDROSTATIC GEAR		
efficiency of hydraulic power transmission	η_H	0, 80
INTERNAL COMBUSTION ENGINE		
engine efficiency	η_D	0, 35
PROPUSION SYSTEM with hydraulic power transmission		
total efficiency	η	0, 126

When analysing the obtained results, we can see that the total efficiency of the propulsion systems on a small vessel is very low and does not exceed 20%. This rather surprising result is mainly caused by low efficiency of main system components (Fig. 8). Peculiar navigation conditions make that the propeller efficiency oscillates around 45%. The total efficiency of the internal combustion engine has been determined from individual tests performed by the author.

The shaft line efficiency takes into account losses in bearings and in the reduction gear, which in marine version has, as a rule, viscous clutches (gear loss of about 3–4%). The efficiency of the hydrostatic gear depends on the control structure and efficiency of individual components. For the analysed case, the efficiency of the multi-piston components was assumed as follows: pump ηP=0,90, hydraulic motor η_M=0,92, and hoses η_C=0,97.

The energy balances of the two analysed systems are given in Fig. 9. The efficiency difference between the shaft line and hydraulic power transmission is high and amounts to 16%.

However, low efficiency of the remaining components makes that the total efficiency difference is much smaller and only equals 2,5%.

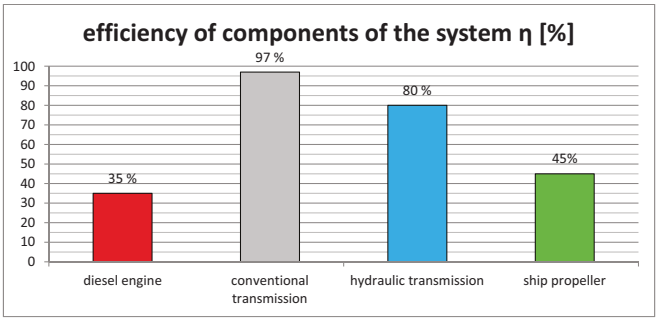

Fig. 8: Efficiency of main components of the propulsion system [own elaboration]

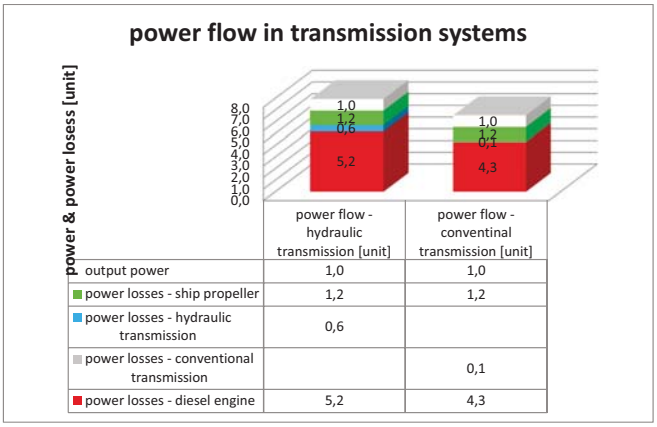

	power flow - hydraulic transmission [unit]	power flow - conventinal transmission [unit]
output power	1,0	1,0
power losses - ship propeller	1,2	1,2
power losses - hydraulic transmission	0,6	
power losses - conventional transmission		0,1
power losses - diesel engine	5,2	4,3

Fig. 9: Power loss distribution in systems with mechanical and hydraulic power transmission [own elaboration]

SUMMARY AND CONCLUSIONS

The article presents the results of studies upon possible use of hydraulic systems for driving vessels. The analysed systems can be used on fishing vessels and/or dredgers, for instance, where the demand for hydraulic energy is natural.

In inland navigation, the analysis of current condition of waterways in Poland and their development prospects resulting from government plans has made a basis for selecting a wide spectrum of vessels, starting from low-budget houseboats up to commercial pusher tugs, on which the use of hydraulic power transmission is clearly advantageous, as compared to the conventional shaft line system. These advantages include:

- full resignation from a rigid shaft line, which in conventional solutions determines the distribution of propulsion system components and occupies a place which otherwise would be used for extra cargo;
- arbitrary distribution of devices in the engine compartment inside the hull;
- smaller space required for propulsion devices inside the vessel – the engine compartment can be shortened;
- very good manoeuvring characteristics of the vessel when hydraulic nacelle propellers are used;
- full resignation from reduction gears, which are most sensitive propulsion system components in conventional solutions;
- one large internal combustion engine can be replaced by a number of smaller engines, with higher speed, to drive directly hydraulic pumps;
- a larger number of independent energy sources, with a possibility of their distribution in separate compartments, increases the reliability of the propulsion system and, consequently, the safety of navigation;
- the engine compartment does have to be high, which provides a possibility for more effective use of valuable space on an inland vessel by situating the engine compartment in the least attractive section of the hull;
- lower hull vibrations caused by the work of engines driving propellers, with the resulting lower total noise level and higher comfort of navigation.

The above advantages are believed to fully compensate lower energy efficiency of systems with hydraulic power transmission.

The systems with hydraulic power transmission have high power concentration and can be based on typical components and subsystems. As a consequence, they usually have smaller mass and lower purchase price, compared to the presently developed electric propulsion systems.

The proposed concept makes it possible to adapt propulsion systems with hydraulic power transmission to legal regulations, which consist in introducing zones where the navigation of vessels with internal combustion engines is forbidden.

The research activities which are in progress now aim at:

- developing a concept of hybrid propulsion with hydraulic power transmission and preparing a real 40-kW system for field tests;
- working out a series and building a prototype of a hydraulic low-power nacelle propeller.

BIBLIOGRAPHY

1. Śliwiński, P.: Flow of liquid in flat gaps of the satellite motor working mechanism. Polish Maritime Research, Vol. 21, iss. S1 (82) (2014), s.50-57, DOI:10.2478/pomr-2014-001;

2. Śliwiński, P.: The influence of water and mineral oil on mechanical losses in the displacement pump for offshore and marine applications. Polish Maritime Research. Vol. 25, iss. S1 (97) (2018), s.178-188, DOI: 10.2478/pmr-2018-0040;

3. Śliwiński, P.: The influence of water and mineral oil on volumetric losses in a hydraulic motor. Polish Maritime Research Special Issue 2017 S1 (93) 2017 Vol. 24; s. 213-223 10.1515/pomr-2017-0041;

4. Jasiński R.: Problems of the starting and operating of hydraulic components and systems in low ambient temperature (Part III). Methods of determining parameters for correct start-ups of hydraulic components and systems in low ambient temperatures. Polish Maritime Research, Vol. 16, 4/2009;

5. Jasiński R.: Influence of design of hydraulic components on their operation in low ambient temperatures. Key Engineering Materials: Fundamentals of Machine Design, Vol. 490, 2012;

6. Jasiński R.: Problems of the starting and operating of hydraulic components and systems in low ambient temperature (Part V). Methods ensuring correct start-up of hydraulic components of ship›s onboard devices in low ambient temperatures. Polish Maritime Research, Vol. 24, Pages: 47-56, 4/2017;

7. Dymarski C.: Prolusion and control of a fishing vessel (in Polish). IX Seminar on Propulsion and control'2003, Fairs of Producers, Cooperants and Sellers of Propulsion Units and Control Systems (in Polish), Katowice 2003.

8. Dymarski C., Skorek G.: A design concept of main propulsion system with hydrostatic transmission gear for Island waterways ship. Polish Maritime Research, z. 2/2006.

9. Dymarski Cz., Rolbiecki R.: Comparative analysis of selected design variants of propulsion system for an inland waterways ship. Polish Maritime Research, 1(47)-2006.

10. Dymarski, Cz., Piątek, D.: Diesel/hydraulic propulsion system on a small fishing vessel (in Polish). Hydraulika i Pneumatyka. - 2012, nr 1, str. 19 -22;

11. Dymarski, Cz., Zagórski, M.: Azimuth POD propeller with hydraulic drive for a small vessel (in Polish). In: Tests, construction, production and operation of hydraulic systems (in Polish). Collective work edited by red. A. Klich, A. Kozieł, E. Palczak. Gliwice: KOMAG Institute of Mining Technology, 2011, S. 53 – 63;

12. Paszota, Z.: Energy losses in hydrostatic drive (…). Lambert Publications, 2016. ISBN - 978-36-596399-6-8;

13. Kulczyk, J., Winter, J.: Inland water transport (in Polish). Wroclaw 2003, electronic version: http://www.dbc.wroc.pl/Content/1322/srodladowy_transport_wodny.pdf;

CONTACT WITH THE AUTHOR

Daniel Piątek
e-mail: freitag@pg.edu.pl

Gdansk University of Technology
Faculty of Ocean Engineering and Ship Technology
Narutowicza 11/12, 80-233 Gdańsk
Poland

sciendo

POLISH MARITIME RESEARCH 2 (102) 2019 Vol. 26; pp. 142-154
10.2478/pomr-2019-0034

SELECTED PROBLEMS OF EXPERIMENTAL TESTING MARINE STERN TUBE BEARINGS

Agnieszka Barszczewska
Ewa Piątkowska
Wojciech Litwin
Gdańsk University of Technology, Poland

ABSTRACT

This paper presents typical methods for conducting experimental tests on main shaft slide bearings. There are described their possible testing capabilities , advantages , drawbacks and limitations. Various testing methods were analyzed to find a solution able of providing a wide range of possible investigations at possibly acceptable limitations.

Keywords: marine bearings, polymer journal bearings, tribology, real scale test,

INTRODUCTION

Marine main shaft bearings, especially heavy loaded stern tube bearings constitute crucial subsystems in any ship propulsion system. Safety at sea depends on their durability and reliability [1]. From the very beginning of application of mechanical propulsion to ships, i.e. since over 150 years they have sometimes produced serious problems [2]. A failure of one of them may lead to catastrophic consequences resulting from breakdown of ship propulsion system. [3]. In the case of finding a defect in bearings docking the ship is necessary for disassembling the shaft line and carrying out repair or exchanging failed components.

The technological development which has occurred for the last decades made it possible to improve step by step shaft line subsystems. Novel bearing materials and seals as well as environment friendly lubricants have been worked out [4].

For many years in scientific and research centres worldwide have been carried out experimental investigations on bearings for ship main shafts, water turbines or pumps. Sometimes it turns out that obtained results appear incredible. This often results from imperfectness and limitations of test stands or simply due to selection of an inappropriate test method.

During testing the slide bearings many very different parameters are measured. The resistance to motion determined in the form of friction coefficients is one of the crucial indices reflecting working conditions and energy losses in bearing, which lead to heat generation in friction zone. Measurements of bearing bush temperature are ones of those made most often. During testing the bearings which work in the regime of liquid friction hydrodynamic pressure in lubrication clearance as well as shaft axis orbits, i.e. its trajectories, are measured.

One of the main problems during carrying out experimental tests on slide bearings is the question of scale – that is how big in size a bearing subjected to testing should be to get credible results. The testing of bearings in real scale,i.e. that in which they work in a real object, would be most desired. This is often practically not possible because of a huge cost of such tests. For this reason an object to be tested is extended to a possible largest size in order to allow to install measuring instruments without exceeding assigned funds and taking into account capability of a laboratory infrastructure being at one's disposal.

PROBLEM

A test stand for slide bearings, if it has to be a source of credible measurements, should be similar as to its construction to a machine in which a given solution will be implemented. Hence in some countries the experimental objects (water power plants) have been developed for testing various novel solutions. It is a well known fact that bearings producers implementing some new solutions conclude agreements with ship owners to introduce new, experimentally not tested technologies into real objects. In case of an untimely failure they have to cover repair costs. However in practice it is very costly. Therefore various test stands are built. The most costly ones make it possible to test full scale bearings and their driving power exceeds 500 kW [5][6].

There are built usually test stands for testing the bearings for shafts of a diameter below 100 mm. It is very rare case that the stands are of a design which reflects features of a given application. This results from the fact that e.g. a stand for testing ship propeller shaft system consisted of a propeller shaft and two bearings, though very expensive, has limited possibilities for conducting measurements. Hence in most cases there are built stands intended for testing a single bearing bush only.

REVIEW OF TYPICAL SOLUTIONS

A stand built in 2010 at Gdansk University of Technology for testing propeller shaft water-lubricated bearings makes it possible to test them in a system which has been earlier applied on a small fishing ship

(Fig. 1). It is consisted of the forward bearing housing (5) and stern tube aft bearing housing (3) of different lengths (that results from rules of classification institutions), the bearing bush coupling (9) which connects the bushes into a common unit together with propeller shaft tube and propeller shaft itself. Like in real conditions the shaft (1) is loaded by propeller weight represented here by the steel discs (10).

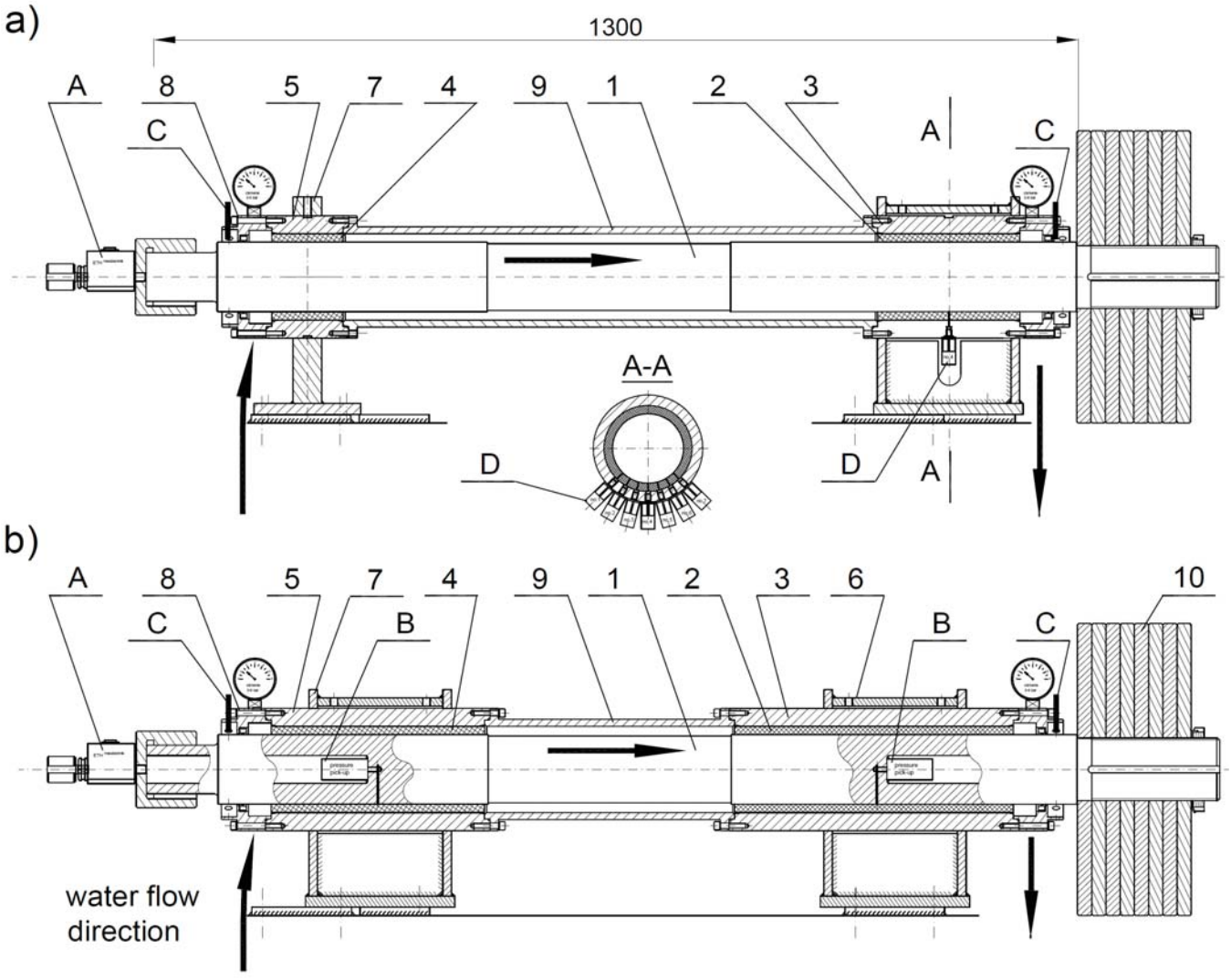

Fig. 1. Stand for testing propeller shaft unit - shown in two variants, 1 – main shaft, 2 – stern tube aft bearing, 3 – stern tube aft bearing housing, 4 – forward bearing, 5 – forward bearing housing, 6 – aft bearing support, 7 – forward bearing support, 8 – cover with seal, 9 – bearing bush coupling, 10 – loading steel discs – representing propeller weight

The described configuration of the test stand which corresponds to a real application, has some significant drawbacks and limitations. It can be stated that like on a real ship there certainly occurs a misalignment of both bearings against the shaft [7]. For identifying it a special measurement instrumentation should be used. Possible range of testing is also limited. Practically, it is not possible to measure resistance to motion in each of the bearings. The torque meter (A) allows to measure friction torque and calculate total friction coefficient for both bearings. In practice the quantity is not useful because of differences in radial load in both bearings as the forward bearing housing (5) is low loaded and the stern tube aft bearing housing (3) transfers most of radial load and in consequence it constitutes the weakest link of the propeller shaft bearing system. It fails most often in spite of that classification societies require to select a minimum length of bushes equal to two up to four diameters (depending on a used material) in order to reduce mean pressure to occur in the bearing.

During the testing of the propeller shaft unit pressure values in lubricating film of stern tube bearing were additionally recorded by means of the pressure sensors placed in the bush, (D), as well as in the shaft, (B). They allowed to confirm hydrodynamic phenomena occurring in the bearing [8][9]. And, measurements of shaft axis trajectories were also conducted by using the contactless distance sensors (C).

During the tests it turned out that to apply greater radial loads in the form of hung weight is difficult. Therefore the shaft loading system was tested with the use of an additional pneumatic actuator. As results from the literature sources the so designed testing system is used very rarely. In most cases only single bearings are tested. The most frequently used solution is supporting the shaft by means of two rolling bearings between which a tested slide bearing loaded by radial force is installed (Fig. 2) [10][11][12][13][14][15]. In some solutions the rolling bearings are installed close to each other and the tested bush is fixed on a pin protruding outside [16][11][17][18][19].

Such solution is commonly applied due to many advantages, as it is first of all a simple construction and provides a wide range of possible testing. There is good access to the tested bearing and measuring instruments can be installed on the tested bush. In such case, values of resistance to motion are usually recorded – by measuring friction torque, pressure in lubricating film – by sensors installed in bearing bush, shaft centre orbits – by using contactless sensors, as well as temperature in bushes.

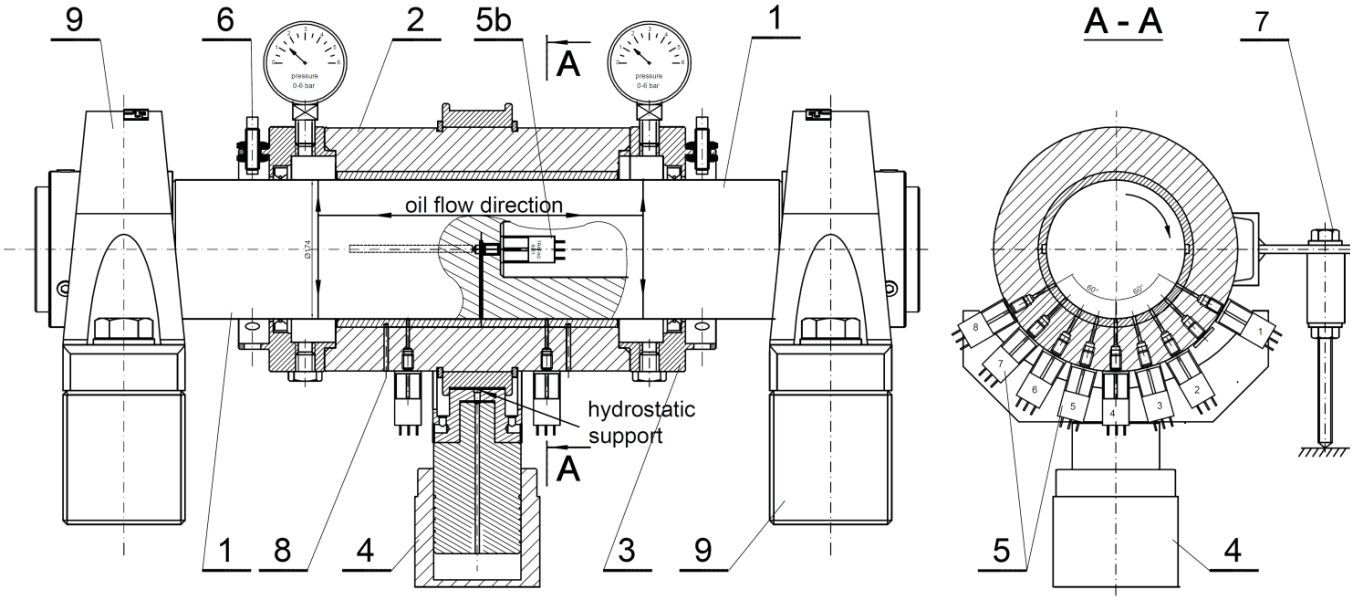

Fig. 2. Single bearing test stand (SBTS) developed in Gdansk University of Technolgy ; 1- main shaft, 2- tested bushing unit, 3- covers with seals, 4 - load exertion system – hydraulic jack , 5- pressure sensors, 5b- pressure sensor in the shaft, 6- distance sensors, 7- friction force sensor, 8 - temperature sensors installed in the bushing sliding layer; 9 – supporting shaft roller bearings

MEASUREMENT PROBLEMS

Unfortunately, any of the methods used for testing slide bearings has some limitations and drawbacks. Hence, a specific type of test stand should be selected for given purposes.

MEASUREMENTS OF RESISTANCE TO MOTION

Resistance-to-motion measurements make it possible to draw Stribeck curve which describes friction coefficient in function of rotational or sliding speed. On a typical diagram, zones of boundary, mixed and fluid friction can be identified. In case of experimental investigations friction torque is usually measured and on its basis friction coefficient is calculated. As much as such measurements can be performed enough precisely when a bearing operates in the boundary friction zone, i.e. when resistance to motion is rather large, a problem arises with its small values which appear e.g. in testing the bearings lubricated with liquids of a low viscosity. Friction

coefficient may then reach a value of about 0.001 and this is the case when measurement accuracy should be particularly considered. First of all, hardly ever resistance to motion of a single bearing can be successfully measured, hence total resistance covering also drag in sealing is usually measured (Fig. 1 and 2); additionally, the lubricant supply pipes to the bearing unit and possible additional instruments cause the conducting of a precise measurement difficult.

However it seems that for practical reasons it is not not necessary to reach an ideal precision. Practicioners are usually interested in information about when a given bearing passes to work in the desired regime of fluid friction as well as how big margin of hydrodynamic capacity is left. Therefore even the Stribeck curve diagram loaded with a certain inaccuracy is deemed useful. Worth adding, that it is often difficult to perform precise measurements in the phase of transition from the mixed to fluid friction. Usually, the test stand driving system has some limitations and in such transition phase to keep a constantly low rotational speed is difficult. This is necessary if the researchers want to obtain a possibly accurate diagram of Stribeck curve precisely showing the instance of transition from mixed to fluid friction (Fig. 3). For this reason during the investigations carried out at Gdansk University of Technology a special two-gear drive unit intended for keeping a selected constant speed within the whole range of speed from 0 up to 11 rps was applied (Fig. 3).

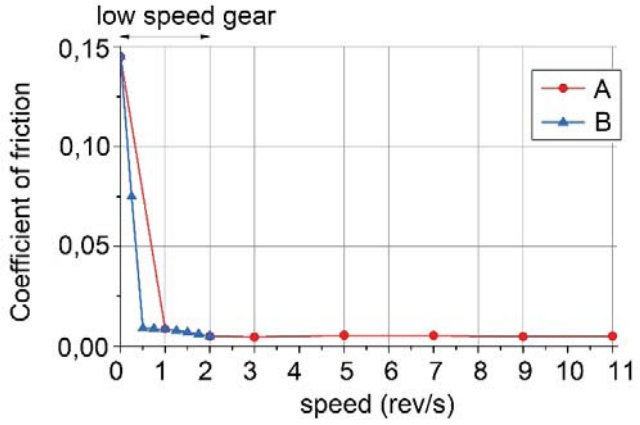

Fig. 3. Friction coefficient values calculated on the basis of resistance to motion measured at the SBTS stand for water-lubricated bearings with polymer bush; A- characteristics for typical measurement points, B- for thickened spacing of measurements points at two-gear drive system operation – with indicated the thickened spacing area of measurements in the phase of transition from mixed friction to fluid friction

It's worth paying attention to the fact that the experimentally obtained friction coefficient characteristics differ from the theoretical ones. According to these authors' opinion it results a.o. from the fact that the diagram presents the deformed bearing friction characteristics, usually enlarged by drag in sealing system and lubricant supply pipes, etc.

Making an attempt to describe problems of measuring the resistance to motion, the question should not be omitted of exerting radial load onto a tested bearing and its impact on friction torque recorded during testing. The commonly applied method of exerting load onto bearing bush by means of rolls introduces another significant measurment error which is difficult to assess, and has a special effect on very low values of resistance to motion during the fluid friction working phase. Therefore it seems necessary to apply a contactless load exertion system based on electromagnetic field (passive or active magnetic bearing) or hydrostatic lubricating film. Such method is applied a. o. to the SBTS stands of Gdansk University of Technology (Fig. 2), and other ones as well [20].

MEASUREMENT OF PRESSURE IN LUBRICATION CLEARANCE

Pressure measurement in lubrication clearance makes it possible to test experimentally a bearing in respect of hydrodynamic and hydrostatic phenomena which occur in lubrication clearance. In practice two measurement methods are used, however both of them have some limitations. Sensors for measuring fast-varying pressure can be installed either in the bush (that is rather often applied) or in the rotating shaft (Fig. 2). In both the cases it's worth paying attention to the fact that recorded pressure values are measured in a very thin lubricating film even a few micrometers thick only. When a measurement hole in wall of the bush or shaft is of 1mm diameter only, even then it must have a negative effect on measurement accuracy as it causes a perturbation in lubricant flow. Another problem results from constructional limitations as only in a very rare case it is possible to place pressure sensor close to very surface of shaft or bush. Usually, the sensor is connected through a fine hole therefore never it can be sure that the system is not airlocked and the possible left air does not dump pressure signal under pressure. Moreover, if the hole is made in the shaft then the centrifugal force will act on the liquid column in its interior and this fact should be taken into account in processing results of measurements.

The measurements carried out by pressure sensors placed in the bush allow to monitor pressure changes in lubricating film. This is a typical phenomenon for every bearing working in the fluid friction regime. As results from that, the fluid friction process is a very complex phenomenon as a load-carrying lubricating film occurs in response to an externally exerted load. For this reason the shaft axis circles – round a repeatable trajectory, called usually orbit, within the bush. On its size an instatntaneous thickness of lubricating film, hence also dynamic pressure changes in the film, depend. However, such approach is rather limited by that the sensors , in view of their size, cannot be placed close to each other, that would be especially desired in the area of a rapid drop of pressure when cavitation appears. For this reason the research authors usually present the diagrams of mean pressure in lubricating film, based on measurements conducted by using a few sensors placed in the bush (Fig. 4).

In contrast, a sensor placed in the shaft can record pressure distribution run with a given frequency and thus it is possible to make a precise measurement during one full rotation of the shaft. However, the problem consists in that the recorded values of pressure in lubricating film are instantaneous.

If the shaft centre orbit is little and amounts to a few or a dozen or so micrometers only then pressure pulses are small and the involvrd measurement error is acceptable. However, the installation of a sensor in the shaft provides a unique advantage – it is possible to conduct pressure field measurements by shifting step by step the bush over the sensor along an appropriately elongated shaft. Such method was applied during testing the bearing of modified geometry in which both hydrostatic and hydrodynamic phenomena occurred simultaneously (Fig. 5).

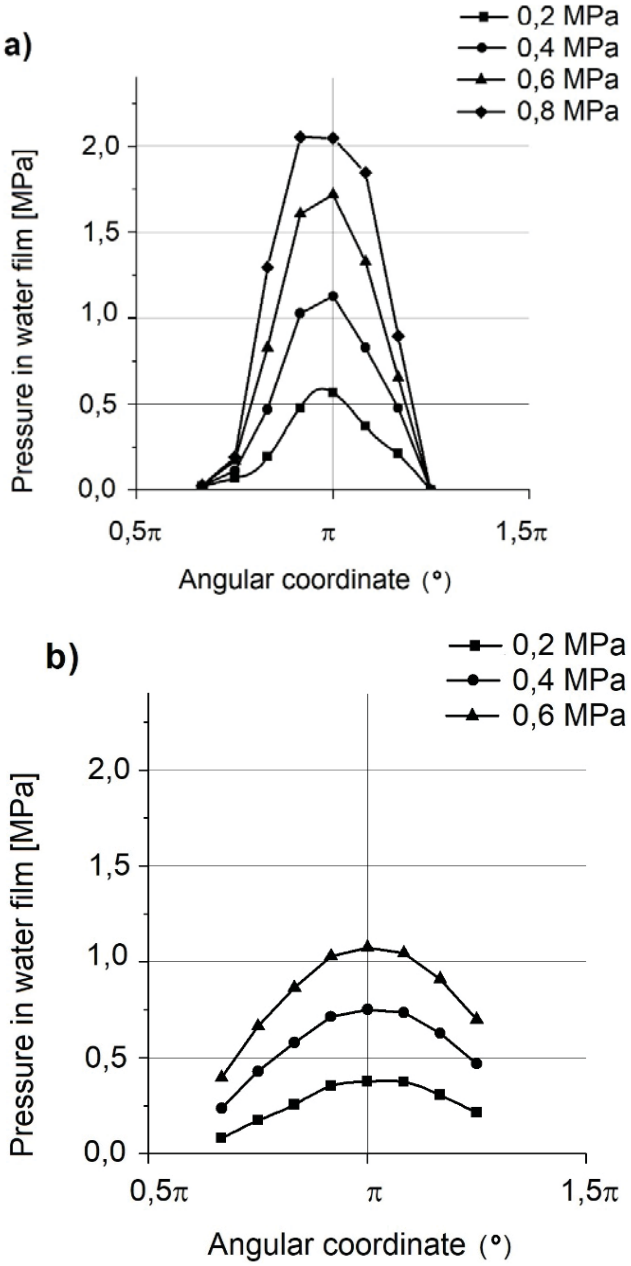

Fig 4. Hydrodynamic pressure distribution in the water-lubricated bearings for different mean pressure values ranging from 0,2 to 0,8 MPa; a) the stiff bush made of PTFE , b) the elastic rubber bush – NBR

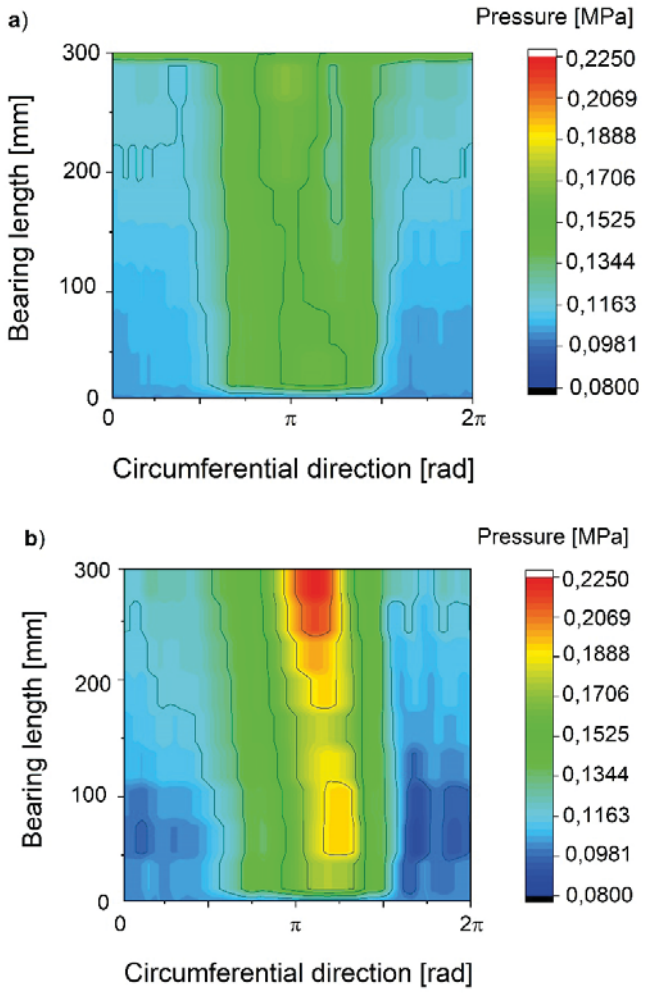

Fig. 5. Hydrostatic pressure distribution (a), and both hydrostatic and hydrodynamic pressure distribution (b) in lubricating film, the measurements conducted by using the pressure sensor installed in the shaft

MEASUREMENTS OF SHAFT AXIS TRAJECTORY

For many years contactless eddy current sensors have been used in rotary machinery diagnostics. They make it possible to perform contactless measurements of a distanace between the housing and rotating shaft with a very high accuracy. If a pair of sensors making measurements along two axes, usually vertical and horizontal, are installed, then to draw a shaft orbit is possible. (Fig. 6). Results of such operation are a very valuable source of information on bearing features. If extreme positions of the shaft journal in the bush are experimentally determined, which is usually made at still standing machine and in consequence a contact between the shaft journal and the bush is reached, then it will be possible to localize position of the so called circle of clearance (Fig. 6A). The trajectory located within clearance circle allows to assess a real instantaneous thickness of lubricating film. In the below presented case (Fig. 6A) in the mineral oil lubricated bearing with white metal bush the film thickness amounts to about 10 μm, whereas the orbit size reaches about 50μm. In such

case it is hard to speak about any margin of its hydrodynamic load-carrying capacity.

For the water-lubricated bearings with polymer bushes there is possible to draw a real contact zone between shaft and bush (clearance circle), that allows to identify errors in bush geometry (Fig. 6B). Such errors usually result from bush machining, assemblage of bushing and material expansion resulting from water absorption by polymer. The deformed sliding pair geometry, elastic bush deformation and low viscosity of the lubricant (water) cause that to assess thickness of very thin lubricating films is not possible. Therefore justified doubts may be raised as to the working conditions of the bearing. In such case the remaining measurements – of resistance to motion and pressure field – become helpful.

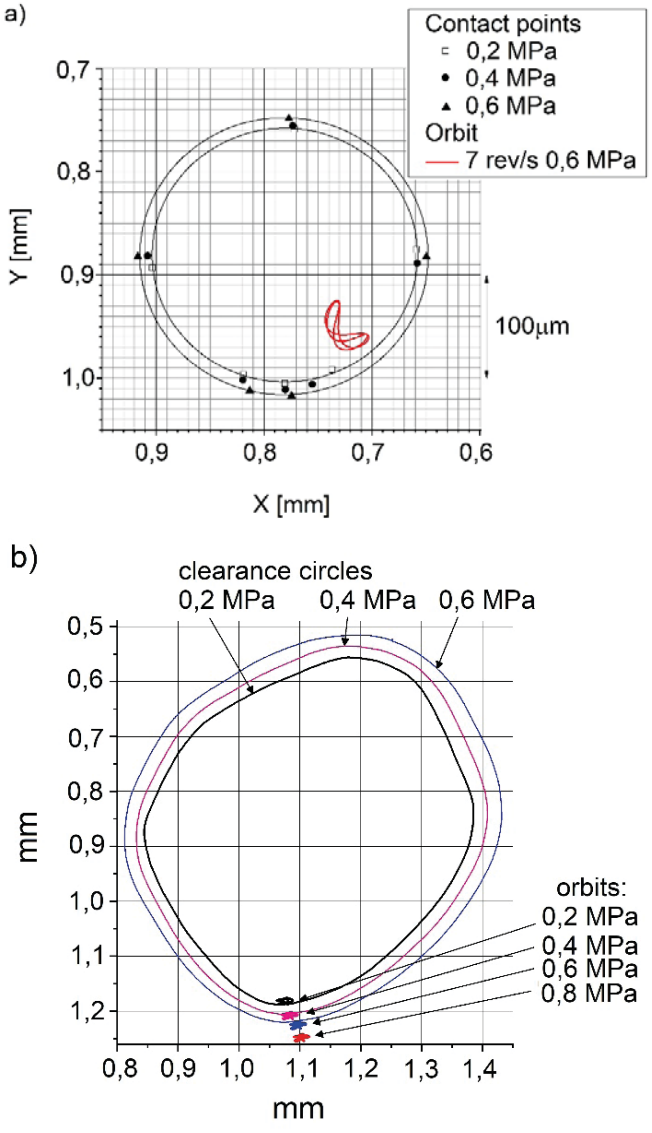

Fig. 6. Shaft centre orbits and experimentally recorded clearance circles; A – oil-lubricated bearing, clearance circles verified by contact points; B – water-lubricated bearing – shaft centre orbits and deformed real clearance circles

MEASUREMENTS OF TEMPERATURE IN POLYMER BUSHES

Temperature is one of the crucial diagnostic parameters of bearing performance. If in bearing operation an excessive increase of pressure happens it may demonstrate that a failure approaches. The most frequent cause of overheating the bearing with polymer bush results from its insufficient cooling by lubricant supplied to friction zone. This may occur e.g. as a result of gradual clogging up the filter. What's worse, together with temperature rise the bearing clearance drops due to thermal expansion and consequently flow drag increases. For this reason the temperature rise process usually develops very violently. Character of wear of polymer bushes may be different from that of bushes with white metal slide layer [21][22]. In extreme cases the bush melting or its jamming on the shaft may happen [23][24], which leads to rapid stopping the machine (Fig.7).

Fig. 7. The bush melt in laboratory conditions, shaft diameter: 100 mm, bush material: elastomer

Formerly, to observe changes in bearing operational conditions, temperature of the oil flowing out from the bearing unit has been measured. In view of a low sensitivity to reactions occurring inside the bearing and their fastness, such measurement was supplemented with the measurement of bush temperature in an area of hydrodynamic lubicating film where temperature is high [25][26].

A direct measurement of temperature in lubricating film is practically impossible because of a high elasiticity of polymer bushes and a possible failure of a sensor or shaft sliding inside the bush. Hence, temeperature in polymer bushes is measured by using sensors placed no more than a few milimeters under sliding surface [27][28].

In many research centres a thermocouple is the most often used up to now sensor for measuring temperature in lubricating film as well as on sliding surfaces [6][29][6] [30][31][32]. An unquestionable merit of a thermocouple compared with a resistance gauge [33] is its rather small size – its diameter can be as small as 0,1 mm, a low time of response to rapid temperature changes, assembling easiness and low purchase cost. Unfortunately, the application of

thermocouples for measuring the temperature in bearing with polymer bush has important limitations.

As it is known, the measurement of lubricating film temperature in a bearing with metal sliding surface where thermocouple and sliding surface are faced to each other [34][35] is loaded by a rather small error. Flowing oil heat of permeats to the sensor through the measuring tip but is also transferred to the remaining part of the sensor through the sourrounding bush material which becomes heated relatively fast due to its high thermal conductivity.

According to S. B. Glavatskih investigations, if the thermocouple is placed a few milimeters under babit sliding layer and the hole where the thermocouple has been placed is flooded by flowing warm oil, then indications of the thermocouples will be close to those obtained from the thermocouples facing with sliding surface. However it turns out that, if the PTFE material is used for sliding layer, indications of the thermocouples are much lower than a real oil temperature [36]. The difference results from a low value of heat conductivity of PTFE sliding layer which effectively isolates the neighbourhood of the measuring sensor from heat source.

An additional limitation in applying the thermocouples to temperature measurement in polymer bushes is that the thermocouples placed in steel housing carry off heat from the measuring tip to the environment through their cases. It is deemed that to eliminate completely this effect the thermocouple should be immersed in the medium up to the depth ten times greater than its diameter; it means that a thermocouple of 1 mm diameter would be immersed 10 mm deep [37]. In the case of measuring temperature in lubricating film or in polymer bush of a high heat transfer resistance to make such measurement is not possible. In the case of bearings with metal sliding layer the effect of heat carrying-off from measurement point through thermocouple is negligibly small because of rather similar values of heat conductivity coefficients of bearing material and thermocouple. Unfortunately, in case of temperature measurements in polymer bush the heat carrying-off effect additionally reduces thermocouple indications in view of a much greater heat conductivity of thermocouple steel case compared with that of polymer material.

Irrespective of a kind and location of temperature sensor, the error of temperature measurements in polymer surfaces, which results from polymer insulating properties, will be always greater than in the case of temperature measurements in metal surfaces.

The tests performed with a bearing of 100 mm diameter, fitted with elastomer bush showed that the bearing which operates under 0,2 MPa pressure and a lack of flow of lubricant, suffered a failure at 30°C flowing water temperature (measured before and behind the bearing) and 27°C temperature measured 3 mm deep below sliding surface. The bearing producer informs that 60°C temperature is the ultimate one for the bearing working in wet conditions. The test results presented in Fig. 7 clearly show that this temperature was exceeded and consequently the error of its measurement was high.

In order to recognize the problem of heat transfer through polymer bush, an examination of temperature distribution in the bush was performed in its steady state (Fig. 8). To this end, 4 thermocouples were radially placed and 4 ones – along bush axis (Fig. 8), at different distances from bush sliding surface (namely : 3, 6, 9 mm and in the water). During temperature measurements, when temperature of water inside the bush was kept constant, it was observed that indications of all radially placed thermocouples were lower by 15°C than those of thermocouples placed along the bush axis.

Moreover, the indications of the thermocouple radially located 3 mm deep below sliding surface (i.e. like in the tests during which a failure in polymer bush happened) were by 20°C lower than the temperature of water (100°C). The estimated amount of heat transferred through bush walls was abt. 50 W.

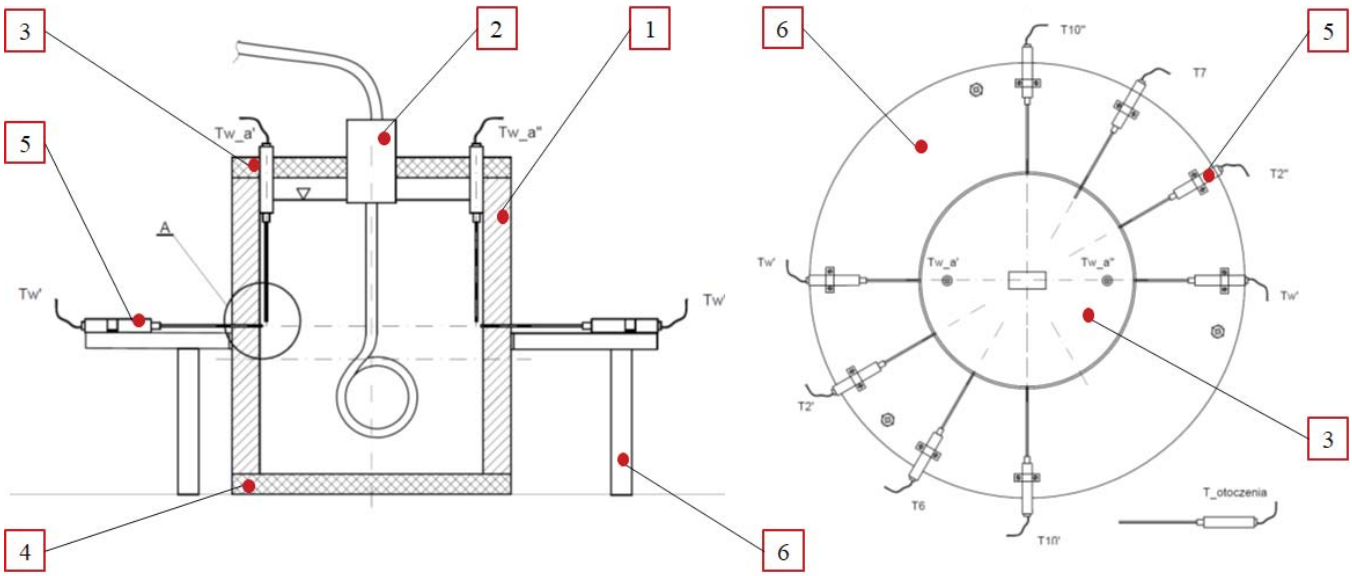

Fig. 8. Test stand for examining heat exchange through bush wall; 1 – tested bush, 2 – electric heater of 300 W power, 3 – cover (PMMA), 4 – bottom (PMMA), 5 – thermocouples K Ø1 mm, 6 – sensor support

As results from the performed investigations, temperature measurements in polymer bushes will be always loaded by a large error, especially when thermocouples fitted with steel case are used. The error can be lowered by:

- application of thermocouples of a smaller diameter (lower heat losses),
- application of thermocouples with uncovered measuring tips (exposed junction) and remaining parts covered with insulation of a low heat conductivity.

TESTS OF BEARINGS LUBRICATED WITH CONTAMINATED LIQUIDS

In practice, many different additives are applied to improve properties of lubricants. Experimental tests showed that certain nanoparticles (metal oxides, metals, sulphides, rare chemical compounds, carbon, nanocomposites etc) are capable of improving tribological properties of oil-lubricated sliding pairs [38].

Apart from the desired additives which positively affect plastic-metal sliding pair, some undesired additives can be present in the form of contaminations – solid particles, usually. They appear during operation or standstill of machines and the following ones may be numbered among them: e.g. wear products from machine elements co-working in sliding as well as particles which fell by chance into lubricant or also those coming from outside, such as pulver, dust or sand. The contaminations, causing an increase in sliding pair friction, negatively affect performance and life of machines. The solid particles which fell into the system cause an excessive and premature wear and in consequence service standstills necessary to repair or replace failed elements.

Sliding pairs are the places where a greater operational durability is required for co-working elements of machines and devices, such as e.g. shaft journal and bush. Both the elements are to be mutually well-matched. The shaft external layer is to have a proper chemical content, hardness and roughness because post machining traces are always left on its surface – they are called surface topography (usually visible in the form of circumferential grooves) ; a possible influence of constructor on it is rather limited.

The considerations of the effects of contaminations in the form of solid particles on wear of shaft journal and bearing bush were presented in detail in the publication [39] where conclusions were drawn from the so far made experiments concerning the relation between size and occurence frequency of solid particles and lubricating film thickness and their common effect onto wear process [40][41].

The first research work concerning effects of contaminations on machine performance, probably done in 1927, proved that presence of solid contaminations resulted in an increase of friction. Several researchers showed that for determining degree of wear the ratio between size of contamination particles and minimum thickness of lubricating film is of a great importance. If the ratio is greater than 1, the wear is high, and it takes its largest value when the ratio is equal to 1. Another tests concerned concentration of contaminations – the higher the concentration the greater friction and wear. In the subsequent work, effects of shape and hardness of solid contaminations on bearing performance were considered; it was concluded that the ratio between shaft hardness and bush hardness taking value from 3 to 4 leads to the largest wear. Effects of roughness in contaminated bearings were also examined – surfaces of a initially high roughness (if only the contamination particles are small) cause a low wear. Also, the bush surface wearing-in effect was observed when the particles are very small and motion speeds – very high. An explanation was also obtained as to the role of motion velocity of the particles and their sedimentation on bearing surface. During further research a relationship dealing with bearing surface hardness was established. As a result, limits for the ratio between hardness of journal, bush and contamination particles, leading to a minimum wear, were suggested. Also, the effect of solid contaminations on seizing temperature was considered with taking into account different features of solid particles.

Results of the so far performed investigations may be helpful in the selecting of proper materials for shafts, bearings, size of particles to be tested, as well as working parameters. To this end, various test stands were developed for carrying out experiments on appropriateness of application of filters for measuring contamination level and matching oil film thickness in sliding pair [39], as a result, experimental strategies were proposed for testing the role of various additives in limiting degree of bearing wear and temperature rise and in forming minimum oil layer thickness in a lubricating contact. The effect of surface texture on operational characteristics and life of journal bearings working in a contaminated lubrication system was also investigated [42]; to this end, experimental tests were performed on smooth and textural surfaces of bearings operating under different loads and with different speeds; for the tests lubrication circumference was so modified as to allow for controlling injection of a contaminated mixture (oil / Al oxide pulver) into the main oil flux. In the subject – matter literature can be found research results focused on size and hardness of solid particles, lubricating film thickness as well as crack propagation [43]. The removing from oil (filtering-off) the contamination particles greater than minimum thickness of hydrodynamic layer was suggested. The solid particles getting in between shaft journal and bearing bush are " hammered " into a more soft material of the bush and act as a cutting tool impairing shaft journal surface and leading this way to its failure.

The subsequent wear tests were performed with the use of the tribotesters such as: the "cylinder on disc" [44][45] [46], "pin on disc" [47][48], "block on ring" [49] and " ball on disc" [50]. During the tests the following quantities were measured a. o.: the friction coefficient at different sliding speeds, lubricating film thickness, radial wear of material, loss of journal mass, surface morphology of used elements as well as a change in surface roughness. All the tests were carried out for different working parameters.

The considerations and experimental tests concerning the effect of solid particles on friction and wear in oil lubricated

machinery have been rather comprehensively described in the literature, however, only a relatively scarce scope of information on application of such lubricant as water, can be found there.

In some simple intight solutions where a working liquid such as sea or river water serves as lubricating medium, wear process is greatly affected by amount and kind of particles. For instance, the Baltic Sea has been thoroughly examined as to the concentration and size of solid particles present in its waters [51]; also water salinity, temperature and turbidity were measured in different seasons [52], mineral and geochemical variability of surface sediments was reported [53], also there were determined transport paths of sediment materials in the form of kaolinite and chlorite coming from estuaries of rivers of southern and eastern drainage basins of the Baltic Sea and from the North Sea through Danish straits, which lead towards deposit basins of the Baltic Sea [54], as well as effects of various factors on concentration and spatial distribution of the sediments brought by rivers to the sea [55].

Water contaminations in the form of sand greatly impacts tribological features of friction pairs (stainless steel – plastic) of ship shaft line stern tube bearings. For examining the phenomenon the pin- on- disc tribotesters were used [56] [57][58].

During the measurements different particle sizes were taken into consideration at varying working parameters. The tests were conducted for the particles size ranging from 53 to 106 μm and their concentration of 0%, 1%, 2%, 4% and 6% ratio in 3 l water container, under different loads of 8 N, 17,5 N, 26 N, 36,5 N and 46 N as well as sliding speed values of 0,393 m/s, 0,767 m/s, 1,158 m/s and 1,557 m/s. From the experimental tests were drawn the conclusions that the friction coefficient and mass loss are decreasing along with sliding speed and load increasing, while they are decreasing along with contamination level increasing.

A more intensive wear of shaft journal and bearing bush operating in unfavourable working conditions such as contaminated liquids is determined by the following factors : sliding speed, quantity of exerted load, contamination concentration as well as different size of sand grains [58]. The tests showed that along with increasing the parameters also friction coefficient increases due to the damaging effect of surface roughness and sand grains onto water film.

The above presented methods may serve as a basis for the suitable selecting optimal (most favourable) working parameters for sliding pairs of ship shaft lines at unfavourable operational conditions in order to assure this way safe and reliable performance of their water-lubricated bearings.

As results from an analysis of literature sources, none determined method exist for testing the bearings lubricated with liquids containing solid particles. Most of the published investigations was carried out with the use of tribotesters that may produce measurement results not representing real objects.

In the Laboratory of Marine Machinery and Systems, Gdansk University of Technology, there was developed a test stand which make it possible to test slide bearings lubricated with water containing contaminations in the form of solid particles (sand), undesired in real working conditions. For such tests a way of inserting contaminations to the bearing, of mixing the liquid, as well as a quantity (weight/volume) and size of particles are of a great importance. The particles may be inserted directly to the bearing or the contaminated liquid can be only churned up and this way not all the particles will come in between bearing bush and shaft journal. An unquestionable effect on wear process of elements under friction is associated with quantity of exerted load and sliding speed as well. The recently made tests (to be published soon) have showed that the water containing particles inserted directly to the bearing intensifies the wear process in the bush and journal. The tests with the same sliding pairs but immersed in the mixture of the same concentration showed that the wear process was much slower, which undoubtedly is associated with another way of water inserting.

DISCUSSION

It's worth paying attention to the fact that in many articles are published results of tribological tests recorded by means of tribotesters, i.e. with the use of the test stands intended for testing resistance to motion and wear process on small specimens [59] [60] [61] [62] [63] [64] [65] [66] [67] [68]. However in this case contact geometry is different from that typical for slide bearing, e.g. the pin- on- disc contact. Such tests usually allow to perform only a comparative analysis of tested sliding pairs. In some cases such tests may be also aimed at identification of dynamic features of a bearing [69].

The tests carried out on greater stands, where real objects are tested, are undoubtedly more expensive but they allow – in spite of the described limitations – to bring working conditions closer to those occurring in real applications.

Technological development allows to create more and more perfect testing stand solutions. A very interesting concept close – for many reasons – to an ideal is the stand for testing a single bearing, in which, instead of supporting roll bearings, active magnetic bearings are used [70], [71], [72]. Owing to that, it is possible to fluently exert a load coming from the two-sided support and, additionally, to set a skew position which usually has a destructive effect on slide bearing and practically always happens in spite of the measures to reduce it to a minimum regardless the costs.

The question of similarity between a real system and test stand has been already discussed many times. It's worth adding that there is another reason why a stand differs from a real system. This is the question of heat exhange with the environment. On a ship, in water pump or water turbine the surrounding environment, i.e. water has usually a lower temperature than that in which laboratory tests are carried out. Moreover, different are also heat exchange conditions. Therefore it is worth directing attention to this fact when conducting the research focused on thermal questions, e. g. overheating the bearings in limited lubrication conditions. Only in some cases a tested object was immersed in water,

that obviously to a great extent complicated construction of the test stand, making carrying out the tests more difficult and providing considerable difficulties in installation design process and functioning of measurement instruments [73].

CONCLUSIONS

The development of modern sliding materials, more and more restrictive requirements for objects designed for purposes of shipbuilding, off-shore engineering or power industry result in that the qustion of a proper selection and design of bearing systems is more and more often discerned. New legal limitations associated with environmental protection, which force limitations in applying mineral oils, result in that novel lubricants based on water or vegetable oils are experimentally searched for. However, responsibility of producers of such lubricants is high because to predict consequences of a failure in bearing system may be difficult. For this reason the demand on performing experimental tests increases to a great extent.

It's worth adding that, since names of products should not be referred to in scientific publications, the producers more and more willingly agree to make their materials available for testing and more and more willingly give approval to use them for comparative tests and publish their results. It makes it possible to objectively compare properties of various materials. Owing to that, the producers have opportunity of getting knowledge on merits and drawbacks of their products, that undoubtedly encourages for developing their products. It's worth additing, that complex experimental tests on tribological properties allow to determine to which objects given specific solutions are applicable the most, and where they should not be used at all. For instance the tests carried out in the past proved that the materials most suitable for main shaft bearings did not perform well when applied to rudder bearings or water turbine guide apparatuses.

ACKNOWLEDGEMENTS

This work was a part of the research grant No. 2016/23/B/ST8/03104 entitled "Research on water lubricated sliding couples in improper lubrication conditions" financed by the Polish National Science Centre.

BIBLIOGRAPHY

1. R. Orndorff :*Water lubricated rubber bearings, history and new developments*, Nav Eng J, 1985, pp. 39–52,.
2. H. Hirani and M. Verma: *Tribological study of elastomeric bearings for marine propeller shaft system*, Tribol. Int., vol. 42, 2009, No. 2, pp. 378–390.
3. W. Litwin and C. Dymarski: *Experimental research on water-lubricated marine stern tube bearings in conditions of improper lubrication and cooling causing rapid bush wear*, Tribol. Int., vol. 95, 2016, pp. 449–455,.
4. W. Litwin : *Properties comparison of rubber and three layer PTFE-NBR-bronze water lubricated bearings with lubricating grooves along entire bush circumference based on experimental tests*, Tribol. Int., vol. 90, 2015, pp. 404–411.
5. B. J. Blair: *Getting the most from your bearings*. World Pumps, vol. 2016,No. 7–8, pp. 36–40,.
6. M. Wodtke and M. Wasilczuk: *Evaluation of apparent Young's modulus of the composite polymer layers used as sliding surfaces in hydrodynamic thrust bearings*, Tribol. Int., vol. 97, 2016, pp. 244–252.
7. W. Litwin, A. Olszewski, and M. Wodtke: *Influence of Shaft Misalignment on Water Lubricated Turbine Sliding Bearings with Various Bush Modules of Elasticity.* Key Eng. Mater., vol. 490, 2011, pp. 128–134,
8. W. Litwin: *Water lubricated marine stern tube bearings – Attempt at estimating hydrodynamic capacity*," in Proceedings of the ASME/STLE International Joint Tribology Conference 2009*,* IJTC2009, 2010.
9. W. Litwin: *Influence of local bush wear on water lubricated sliding bearing load carrying capacity*. Tribol. Int., vol. 103, 2016.
10. Q. Hongling, Z. Xincong, X. Chuntao, W. Hao, and L. Zhenglin: *Tribological Performance of a Polymer Blend of NBR Used for Stern Bearings*, 2012, pp. 133–139,.
11. Y. Wang, X. Shi, and L. Zhang,: *Experimental and numerical study on water-lubricated rubber bearings*, Ind. Lubr. Tribol. Exp., vol. 2, 2014, no. 51175275, pp. 282–288,.
12. M. Del Din and E. Kassfeldt: *Wear characteristics with mixed lubrication conditions in a full scale journal bearing*, Wear, vol. 232, 1999, no. 2, pp. 192–198,
13. D. L. Cabrera, N. H. Woolley, D. R. Allanson, and Y. D Tridimas: *Film pressure distribution in water-lubricated rubber journal bearings*, Proc. Inst. Mech. Eng. Part J J. Eng. Tribol., vol. 219, 2005, no. 2, pp. 125–132,
14. Y. Zhimin *et al.*: *Study on tribological and vibration performance of a new UHMWPE/graphite/NBR water lubricated bearing material*, Wear, vol. 332–333, 2015, pp. 872–878.
15. R. Colsher, I. Anwar, J. Dunfee, and M. Kandl: *Development of Water Lubricated Bearing for Steam Turbine Application*, J. Lubr. Technol., vol. 105, 1983, no. 3, p. 318.

16. G. Gao, Z. Yin, D. Jiang, and X. Zhang: *Numerical analysis of plain journal bearing under hydrodynamic lubrication by water*, Tribol. Int., vol. 75, 2014, pp. 31–38.

17. A.-F. Cristea, J. Bouyer, M. Fillon, and M. D. Pascovici; Transient Pressure and Temperature Field Measurements of a Lightly Loaded Circumferential Groove Journal Bearing, Tribol. Trans., vol. 54, 2011, no. 5, pp. 806–823.

18. R. Gawarkiewicz and M. Wasilczuk: *Wear measurements of self-lubricating bearing materials in small oscillatory movement*, Wear, vol. 263, 2007, no. 1–6 SPEC. ISS., pp. 458–462.

19. A. Olszewski, M. Wodtke, and P. Hryniewicz: *Experimental Investigation of Prototype Water-Lubricated Compliant Foil Bearings*, Key Eng. Mater., vol. 490, 2011, pp. 97–105.

20. M. Wodtke, A. Schubert, M. Fillon, M. Wasilczuk, and P. Pajaczkowski: *Large hydrodynamic thrust bearing: Comparison of the calculations and measurements*, Proc. Inst. Mech. Eng. Part J J. Eng. Tribol., vol. 228, 2014, no. 9, pp. 974–983.

21. M. Mehdizadeh and F. Khodabakhshi: *An investigation into failure analysis of interfering part of a steam turbine journal bearing*, Case Stud. Eng. Fail. Anal., vol. 2, 2014, no. 2, pp. 61–68,.

22. W. Wieleba: *The Mechanism of Tribological Wear of Thermoplastic Materials*, Arch. Civ. Mech. Eng., Vol. VII, 2007, No. 4.

23. J. Takabi and M. M. Khonsari: *On the thermally-induced seizure in bearings: A review*, Tribol. Int., vol. 91, 2015, pp. 118–130.

24. Q. Wang : *Seizure failure of journal-bearing conformal contacts*, *Wear,* vol. 210, 1997, no. 1–2, pp. 8–16.

25. D. Garner, A. L.-P. of the 13th, and undefined 1984, *Temperature measurements in fluid film bearings*, *oaktrust.library.tamu.edu*.

26. P. De Choudhury and E. W. Barth: *A Comparison of Film Temperatures and Oil Discharge Temperature for a Tilting-Pad Journal Bearing*, J. Tribol., vol. 103, 1981, no. 1, p. 115.

27. S. Strzelecki, Z. S.- Tribologia, and undefined 2011, *Operating temperatures of the bearing system of grinder spindle*, *t.tribologia.eu*.

28. D. G. Lee and S. S. Kim*: Failure analysis of asbestos-phenolic composite journal bearing*, Compos. Struct., vol. 65, 2004, no. 1, pp. 37–46.

29. S. B. Glavatskih and M. Fillon: *TEHD Analysis of Thrust Bearings With PTFE-Faced Pads*, J. Tribol., vol. 128, 2006, no. 1, p. 49.

30. O. Nosko, T. Nagamine, A. L. Nosko, A. M. Romashko, H. Mori, and Y. Sato: *Measurement of temperature at sliding polymer surface by grindable thermocouples*, Tribol. Int., vol. 88, 2015, pp. 100–106.

31. M. Hoić, M. Hrgetić, and J. Deur: *Design of a pin-on-disc-type CNC tribometer including an automotive dry clutch application*, Mechatronics, vol. 40, 2016, pp. 220–232.

32. E. Ciulli, P. Forte, M. Libraschi, and M. Nuti : *Set-up of a novel test plant for high power turbomachinery tilting pad journal bearings*, Tribol. Int., vol. 127, no. November 2017, pp. 276–287, 2018.

33. P. Śliwiński : *The Influence of Water and Mineral Oil On Mechanical Losses in the Displacement Pump for Offshore and Marine Applications*: Polish Marit. Res., vol. 25, 2018, no. s1, pp. 178–188.

34. A. Dadouche, M. Fillon, and J. . Bligoud: *Experiments on thermal effects in a hydrodynamic thrust bearing*, *Tribol. Int.*, vol. 33, 2000, no. 3–4, pp. 167–174.

35. B. Remy, B. Bou-Saïd, and T. Lamquin : *Fluid inertia and energy dissipation in turbocharger thrust bearings*, *Tribol. Int.*, vol. 95, 2016, pp. 139–146.

36. S. B. Glavatskih: *A method of temperature monitoring in fluid film bearings*, Tribol. Int., vol. 37, 2004, no. 2, pp. 143–148.

37. T. W. Kerlin and M. Johnson: *Practical Thermocouple Thermometry (2nd Edition)*. ISA, 2012.

38. W. Dai, B. Kheireddin, H. Gao, and H. Liang : Roles of nanoparticles in oil lubrication, Tribol. Int., vol. 102, 2016, pp. 88–98.

39. J. Duchowski : *Examination of journal bearing filtration requirements*, Lubr. Eng., vol. 09, 1998, pp. 1–9.

40. J. Duchowski, H. International, and J. Duchowski: *Filtration requirements for journal bearings exposed to different contaminant levels,* Lubr. Eng., vol. 06, 2002, no. July, pp. 34–39.

41. D. Hargreaves and S. C. Sharma: *Effects of solid contaminants on journal bearing performance*, Proceedings of the 2nd World Tribology Congress*, 3-7 September 2001*. pp. 237–240.

42. A. Dadouche and M. J. Conlon: *Operational performance of textured journal bearings lubricated with a contaminated fluid*, Tribol. Int., vol. 93, 2016, pp. 377–389.

43. M. M. Khonsari and E. R. Booser: *Effect of contamination on the performance of hydrodynamic bearings*, Proc. Inst. Mech. Eng. Part J J. Eng. Tribol., vol. 220, 2006, no. 5, pp. 419–428.

44. A. Akchurin, R. Bosman, P. M. Lugt, and M. van Drogen: *Analysis of Wear Particles Formed in Boundary-Lubricated Sliding Contacts*, Tribol. Lett., vol. 63, 2016, no. 2, pp. 1–14.

45. A. Akchurin, R. Bosman, and P. M. Lugt: *Generation of wear particles and running-in in mixed lubricated sliding contacts,* Tribol. Int., vol. 110, 2017, no. February, pp. 201–208.

46. A. Akchurin, R. Bosman, and P. M. Lugt: *A Stress-Criterion-Based Model for the Prediction of the Size of Wear Particles in Boundary Lubricated Contacts*, Tribol. Lett., vol. 64, 2016, no. 3, pp. 1–12.

47. G. Pintaude: *Characteristics of Abrasive Particles and Their Implications on Wear*, New Tribol. Ways, no. April 2011.

48. C. Q. Yuan, Z. Peng, X. C. Zhou, and X. P. Yan : *The characterization of wear transitions in sliding wear process contaminated with silica and iron powder*, Tribol. Int., vol. 38, 2005, no. 2, pp. 129–143.

49. L. Peña-Parás *et al.*: *Effects of substrate surface roughness and nano/micro particle additive size on friction and wear in lubricated sliding,* Tribol. Int., vol. 119, 2018, no. February 2017, pp. 88–98.

50. S. M. Park, G. H. Kim, and Y. Z. Lee: *Investigation of the wear behaviour of polyacetal bushings by the inflow of contaminants*, *Wear*, vol. 271, 2011, no. 9–10, pp. 2193–2197.

51. E. Szymczak and D. Burska *: Charakterystyka rozkładu wielkości cząstek in situ w strefie rozpływu wód Wisły (Zatoka Gdańska) (in Polish).* ?? pp. 1–2, 2014.

52. M. Damrat, A. Zaborska, and M. Zajaczkowski: *Sedimentation from suspension and sediment accumulation rate in the River Vistula prodelta, Gulf of Gdańsk (Baltic Sea), Oceanologia*, vol. 55, 2013, no. 4, pp. 937–950.

53. I. Geologiczny and I. Geologii ?? : *Litologia i skład mineralny osadów z dna Basenu Gdańskiego (in Polish),* ?? vol. 313, 1980, no. 2.

54. T. Leipe and B. Sea : *The kaolinite/chlorite clay mineral ratio in surface sediments of the southern Baltic Sea as an indicator for long distance transport of fine-grained material*, Baltica, vol. 16, 2003, pp. 31–36.

55. A. Ya and T. Yu : Revealing the influence of various factors on concentration and spatial distribution of suspended matter based on remote sensing data, *Proc. SPIE*, vol. 9638, 2015, pp. 1–12.

56. Y. Solomonov: *Experimental investigation of tribological characteristics of water-lubricated bearings materials on a pin-on-disk test rig,* Yuriy Solomonov Master of Philosophy Thesis, The University of Adelaide School of Mechanical Engineering April 2014.

57. C. L. Dong, C. Q. Yuan, X. Q. Bai, Y. Yang, and X. P. Yan: *Study on wear behaviours for NBR/stainless steel under sand water-lubricated conditions*, Wear, vol. 332–333, 2015, pp. 1012–1020.

58. C. Yuan, Z. Guo, W. Tao, C. Dong, and X. Bai: *Effects of different grain sized sands on wear behaviours of NBR/casting copper alloys*, Wear, vol. 384–385, 2017, pp. 185–191.

59. C. P. Gao *et al.*: *Tribological behaviors of epoxy composites under water lubrication conditions*, Tribol. Int., vol. 95, 2016, pp. 333–341.

60. S. Thörmann, M. Markiewicz, and O. von Estorff: *On the stick-slip behaviour of water-lubricated rubber sealings*, J. Sound Vib., vol. 399, 2017, pp. 151–168.

61. B. S. Mann and V. Arya : *An experimental model for mixed friction during running-in*, Wear, vol. 253, 2002, no. 5–6, pp. 541–549.

62. L. Deleanu and C. Georgescu: *Water lubrication of PTFE composites*, Ind. Lubr. Tribol., vol. 67, 2015, no. 1, pp. 1–8.

63. S. Chen *et al.*: *Tribological properties of polyimide-modified UHMWPE for bushing materials of seawater lubricated sliding bearings*, Tribol. Int., vol. 115, 2017, no. 126, pp. 470–476.

64. A. Ismailov, M. Järveläinen, and E. Levänen: *Problematics of friction in a high-speed rubber-wheel wear test system: A case study of irregularly rough steel in water lubricated contact*, Wear, vol. 408–409, 2018, no. December 2017, pp. 65–71.

65. C. Dong, L. Shi, L. Li, X. Bai, C. Yuan, and Y. Tian : *Stick-slip behaviours of water lubrication polymer materials under low speed conditions*, Tribol. Int., vol. 106, 2017, no. October 2016, pp. 55–61.

66. S. Meicke and R. Paasch : *Seawater lubricated polymer journal bearings for use in wave energy converters*, Renew. Energy, vol. 39, 2012, no. 1, pp. 463–470.

67. S. Jiang, Z. Guo, C. Yuan, A. Liu, and X. Bai : *Study on the tribological properties of modified polyurethane material*

for water-lubricated stern bearing, J. Appl. Polym. Sci., vol. 135, 2018, no. 22, pp. 1–13.

68. J. Bouyer and M. Fillon : *Experimental measurement of the friction torque on hydrodynamic plain journal bearings during start-up*, *Tribol. Int*., vol. 44, 2011, no. 7–8, pp. 772–781.

69. Ł. Breńkacz and G. Żywica :*The experimental identification of the dynamic coefficients for two hydrodynamic journal bearings*, *SIRM 2017,* Schwingungen rotierenden Maschinen, vol. 24, 2017, no. 96, pp. 157–164.

70. T. Dimond, R. D. Rockwell, P. N. Sheth, and P. E. Allaire: *A New Fluid Film Bearing Test Rig for Oil and Water Bearings*, Struct. Dyn. Parts A B*, Vol. 5*, 2008, pp. 1101–1110.

71. N. Wang and Q. Meng : *Research on wireless nondestructive monitoring method for film pressure of water-lubricated bearing*, Ind. Lubr. Tribol., vol. 67, 2015, no. 4, pp. 349–358.

72. N. Wang, Q. Meng, P. Wang, T. Geng, and X. Yuan: *Experimental Research on Film Pressure Distribution of Water-Lubricated Rubber Bearing With Multiaxial Grooves*, J. Fluids Eng., vol. 135, 2013, no. 8, p. 84501.

73. S. Yamajo and F. Kikkawa: *Development and Application of PTFE Compound Bearings*, Dyn. Position. Conf., 2004.

CONTACT WITH THE AUTHORS

Agnieszka Barszczewska
e-mail: agnbarsz@pg.edu.pl

Gdańsk University of Technology
ul. Narutowicza 11/12, 80-233 Gdańsk
Poland

Ewa Piątkowska
e-mail: ewapiatk@pg.edu.pl

Gdańsk University of Technology
ul. Narutowicza 11/12, 80-233 Gdańsk
Poland

Wojciech Litwin
e-mail: wlitwin@pg.edu.pl

Gdańsk University of Technology
ul. Narutowicza 11/12, 80-233 Gdańsk
Poland

sciendo

POLISH MARITIME RESEARCH 2 (102) 2019 Vol. 26; pp. 155-162
10.2478/pomr-2019-0035

VEHICLE-DECK FIRES ABOARD ROPAX SHIPS: A COMPARISON BETWEEN NUMERICAL MODELLING AND EXPERIMENTAL RESULTS

Ahmed Salem[1, 2]

[1] King Abdulaziz University, Jeddah, Saudi Arabia

[2] Alexandria University, Alexandria, Egypt

ABSTRACT

According to an official study conducted by the IMO Correspondence Group on Casualty Analysis concerning the fire incidents that occurred on the vehicle-decks of RoPax ships, covering the period from 1994 to 2011, it has been shown that a very serious incident has occurred every other year since 2002, resulting in six constructive total losses. The results of this review shed the light on the need to investigate the application of fire models to simulate fire scenarios that may occur on the vehicle-decks aboard RoPax ships. This will be very useful for the RoPax designers who are willing to introduce new technologies or deviate from the current prescriptive regulations of fire safety design in order to reduce the risk of such catastrophic accidents. The aim of this paper is to present the results of a comparison between the predictions of three different fire models and the experimental results of a model-scale fire test that represents a fire scenario on a vehicle-deck aboard a RoPax ship. A statistical analysis technique was used to illustrate the ability of each fire model to predict five outputs of concern. The main conclusion of this comparison is that there is always an optimal fire model that can predict one or more of the five outputs of concern with results in good agreement with the measured values.

Keywords: Vehicle-deck fires; RoPax ships; zone models; field models; model-scale fire tests

INTRODUCTION

Fires aboard RoPax ships are gaining increased interest, and cause the development of new rules & regulations as well as new methods to reduce the risk of fires on board such vessels which is of great importance. Statistical analyses of the records of previous ship accidents covering the periods from 1996 to 2005 (Karlsson and Ulfvarson 2008) and from 2000 to 2012 (Eleftheria et al. 2016) showed that fire is the second frequent type of accident that resulted in the total loss of RoPax ships. Moreover, Wikman et al. (2017), in a very recent study commissioned by the European Maritime Safety Agency, EMSA, reported that around 30% of the fires that occurred aboard RoPax ships during the period from 2002 to 2015 were originated on the vehicle-deck and that about 90% of these accidents are caused by the cargo being transported. Furthermore, considering the number of fatalities that occurred, Karlsson and Ulfvarson (2008) and Eleftheria et al. (2016) have illustrated that RoPax ships were the leaders among all other ship types that have been analysed.

DNV GL is one of the leading classification societies that reported the growing safety concern of fire incidents on vehicle-decks of RoPax ships, Vehicle carriers and general Ro-Ro cargo vessels (DNV 2005), (DNV GL 2016). In their older report (DNV 2005), 25 fires on vehicle-decks (7 of them occurred aboard RoPax ships) between 1990 and 2003 have been identified. In their recent report (DNV GL 2016), 35 fires on vehicle-decks (18 of them occurred aboard RoPax ships) between 2005 and 2016 have been identified. The difference between the findings of the two reports has been clarified by a larger fleet, better accident reporting and most importantly by the more recent fires that have occurred aboard RoPax ships. Figure 1 shows a photograph of one of

the most recent fire accidents that occurred on the vehicle-deck of the Italian-flagged RoPax ferry "Norman Atlantic" in December 2014.

Fig. 1. Smoke plumes from the Italian-flagged RoPax ship "Norman Atlantic" that caught fire in the Adriatic Sea on December 2014 (Taylor 2015)

Vehicle-decks can be classified into three types: closed vehicle-decks, open vehicle-decks (opening on sides and at one or both ends) and weather vehicle-decks (no overhead deck). DNV GL (2016) reported that fires resulted in many of the recorded total losses of RoPax ships were originated on open vehicle-decks. The report has clarified this by the fact that open vehicle-decks are well-ventilated and the overhead steel decks reflect heat and accumulate fire effluents. It is worth mentioning here that the fire accident aboard Norman Atlantic has originated at one of her open vehicle-decks, where the temperature was estimated to be more than 1000°C (Croccolo 2015). Moreover, DNV GL (2016) also reported that some of the major fire accidents that occurred aboard RoPax ships were due to fires originated on closed vehicle-deck spaces.

Several literature works have estimated the frequency of occurrence of fire accidents on vehicle-decks of RoPax ships. Table 1 shows a list of the available source literature, the covered periods and the estimated frequencies. These estimates highlight once more the recent increase in the number of vehicle-deck fires aboard RoPax ships and an urge of the interested-parties (especially in the research arena) to gather their efforts to improve the current situation. Improving the fire safety design and utilising the state-of-the-art technology in novel designs could be one way to improve the vehicle-deck fires issue aboard RoPax ships.

Tab. 1. List of the estimated frequencies of fire accidents on vehicle-decks of RoPax ships found in the literature

Source Literature	Period Covered	Estimated Frequency (per ship-year)
(DNV Technica 1996)	1978–1994	8.00E–04
(DNV 2005)	1990–2003	5.83E–04
(Konovessis and Vassalos 2008)	1994–2004	1.02E–03
(DNV GL 2016)	2005–2016	2.00E–03
(Wikman et al. 2017)	2002–2015	5.79E–03

The fire safety design of all types of ships, including RoPax ships, is governed by Chapter II-2 of the SOLAS convention. In its revised copy, in force, since July 01, 2002, SOLAS Chapter II-2 has a new regulation (Regulation 17) that sets out a methodology for approving novel (alternative) designs that deviate from the prescriptive regulations. This methodology allows the use of fire and evacuation simulation models as consequence analysis tools to carry out the approval process. Numerous literature works have tested and used some of these models within a comparative analysis methodology in several studies concerning the fire safety design of both passenger and RoPax ships (Salem 2007; Salem 2010; Salem and Leheta 2011; Salem 2013; Salem et al. 2013; Salem et al. 2016; Salem 2016; Azzi 2010; Azzi and Vassalos 2010; Azzi et al. 2011; Themelis and Spyrou 2012). The results of these studies have shown the capability of the tested consequence analysis tools in assessing the level of fire safety of the ship compartment under consideration. It should be noted here that there is a lack of published research on the utilisation of fire simulation programs in simulating vehicle-deck fires aboard RoPax ships. This, of course, highlights the significance of examining the performance of these programs in simulating this important type of fires.

In general, there are two types of fire simulation models: zone models and field (CFD) models. On one hand, zone models divide the compartment of fire origin into a limited number of control volumes (zones). The widespread type is the two-zone model, where the fire compartment is divided into an upper hot layer (zone) and a lower cold layer. The prime merit of this type is the fact that the computational time for the solution is in the order of seconds, while its main drawback is the generality and uncertainty of its results (Averill 1998). On the other hand, field (CFD) models divide the fire compartment into several tens of thousands of control volumes or zones, hence present a more accurate scientific approach. The most significant limitations of field models are cost and time. Salem (2007) identified the existence of 56 zone models and 26 field models. The most widespread zone models in use in many practical applications are CFAST (Peacock et al. 2016) and BRANZFIRE (Wade 2004), while the most popular and well-founded field model is the Fire Dynamics Simulator, FDS (McGrattan et al. 2017).

The performance of a fire model is always examined by direct comparison of model outputs with experimental data. These data are usually obtained from either large-scale or model-scale fire tests. A literature survey was conducted to search for published experimental data of either large-scale or model-scale vehicle-deck fire tests. A limited number of such data were found. SP Technical Research Institute of Sweden (formerly known as SP Swedish National Testing and Research Institute) is an active firm in the area of fire testing. The firm has conducted and published several large-scale and model-scale RoPax vehicle-deck fire tests (see e.g., Arvidson 1997; Larsson et al. 2002; Arvidson 2009; Arvidson 2014).

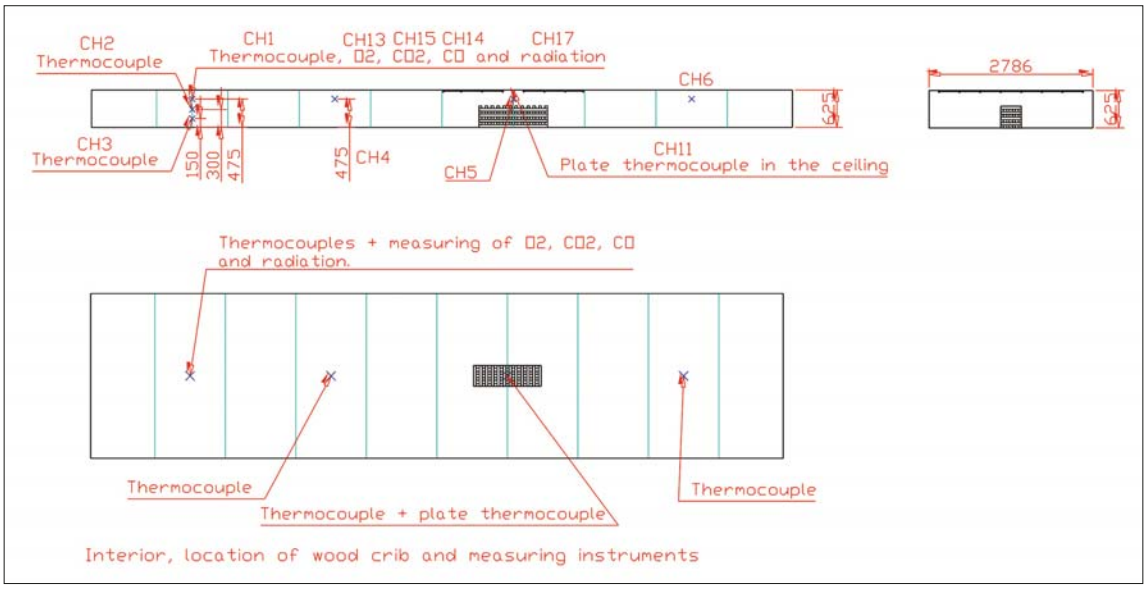

Fig. 2. Schematic drawing of the scale model (Larsson et al. 2002)

AIM AND OBJECTIVE

The aim of the work outlined in this paper is to present the results of a comparison between two fire models of the zone type (CFAST and BEANZFIRE) and one fire model of the field type (FDS) with the experimental results of one of the model-scale fire tests on vehicle-deck aboard a RoPax ship, which was carried out by the SP Swedish National Testing and Research Institute (Larsson et al. 2002). Keeping in mind the fact that no zone fire model is best suited for all applications (Walton 1995) and the fact that field models are more precise than zone models, the main objective of this study is to demonstrate the ability of each of the three fire models to predict the environment inside a vehicle-deck space onboard a RoPax ship in the event of a fire outbreak.

SUMMARY OF THE EXPERIMENTAL TEST SETUP

The SP Technical Research Institute of Sweden conducted a series of model-scale fire tests with the aim to investigate the effect of different ventilation conditions on fire development in a vehicle-deck onboard a RoPax ship. A complete description of the fire tests can be found in (Larsson et al. 2002). In this section, only a brief description of the experimental test setup is presented.

Larsson et al. (2002) explained that the model used in the model-scale fire tests was built on a small scale of 1:8. The model has a rectangular cross-section of 11.425 m in length, 2.786 m in width and 0.625 m in depth (see Figure 2). This would correspond to a full-scale vehicle-deck of approximately 91×22×5 min size. The model was equipped with a stairwell, ventilation shaft, large door openings, drainage scuppers, and a ventilation fan. The walls, ceiling, and floor of the model were constructed of 12 mm nominally thick Promatect–H boards (a fire-resistant material) with thermal properties as shown in Table 2.

Tab. 2. Thermal properties of the Promatect-H board material

Material	Density (kg/m^3)	Thermal Conductivity (W/m K)	Specific Heat (kJ/kg K)
Promatect-H Boards	870	0.190	1.130

Moreover, Larsson et al. (2002) clarified that the experiment has used the wood crib as a source of fire; and the peak value of the heat release rate (HRR) was measured in a free burning test and found to be around 400 kW, which is an equivalent to a burning truck with a fire output of approximately 70 MW in full-scale. By varying the model parameters, Larsson et al. were able to perform 18 tests. Among these tests, the author of this study has chosen "Test # 04" to conduct the comparison between the three fire models and the experimental results (the test number used here corresponds to the test number mentioned in (Larsson et al. 2002)). In Test # 04, the ventilation shaft and the drainage scuppers were left open to maintain a natural ventilation condition. During the test, the fire was self-extinguished due

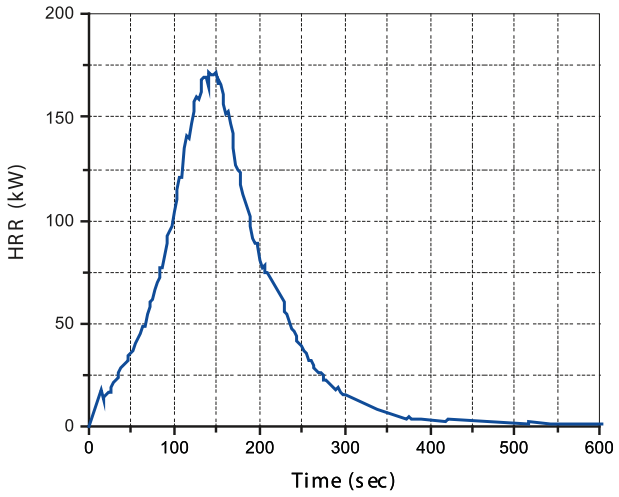

Fig. 3. Measured HRR-time history of Test # 04

to a low oxygen concentration in the hot gas layer formed near the model ceiling. This condition occurred immediately after the hot gas layer reached the floor level of the model, where oxygen concentration within the layer was measured and found to be between 13 and 17 percent. Figure 3 shows the measured HRR-time history for Test # 04.

NUMERICAL MODELLING OF THE SELECTED MODEL-SCALE FIRE TEST

Two zone fire models, namely *CFAST 7.2.0* (Peacock et al. 2016) and *BRANZFIRE 2012.01* (Wade 2004) and one CFD fire model, namely *FDS 6.5.3* (McGrattan et al. 2017), have been selected to simulate the fire scenario representing the selected model-scale fire test, Test # 04. For this purpose, the input file for each fire model was carefully prepared using the data provided from the experimental setup. Table 3 summarizes these input data. The hot layer temperature, the smoke layer height, and the concentrations of oxygen, carbon monoxide & carbon dioxide were the output of interest which were decided to be predicted by each of the three fire models and compared with the experimental results.

Tab. 3. Summary of the input parameters

Input Parameter	Value
Compartment Dimensions (L×W×H)	11.425×2.786×0.625 m
Boundary Surface Material	12 mm thick Promatect-H Boards (for specs see Table 2)
Fire Source	Actual HRR from the experimental result was used in the simulation (see Figure 3)
Vents	Ventilation shaft was simulated by assuming a horizontal opening at the ceiling (Area = 0.02 m^2)
Ambient Conditions	Interior Temp. = 20°C Exterior Temp. = 15°C Relative Humidity = 65%

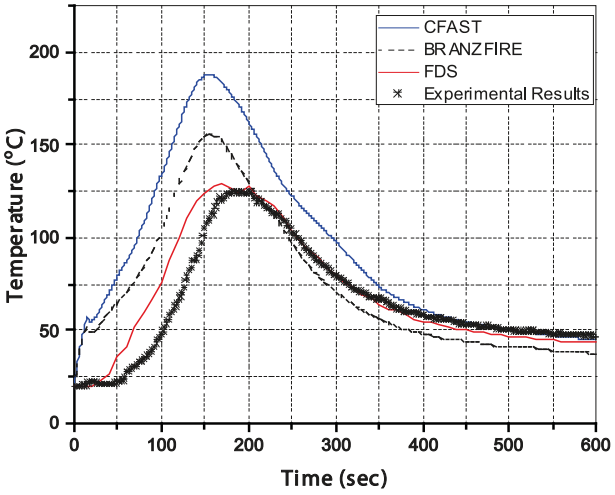

Fig. 4. Predicted and measured hot layer temperatures

Figures 4 through 8 show the results of the comparison between the values of the 5 outputs of interest, which were predicted by the two zone fire models and the field model, and those measured by the experimental model test (Test # 04).

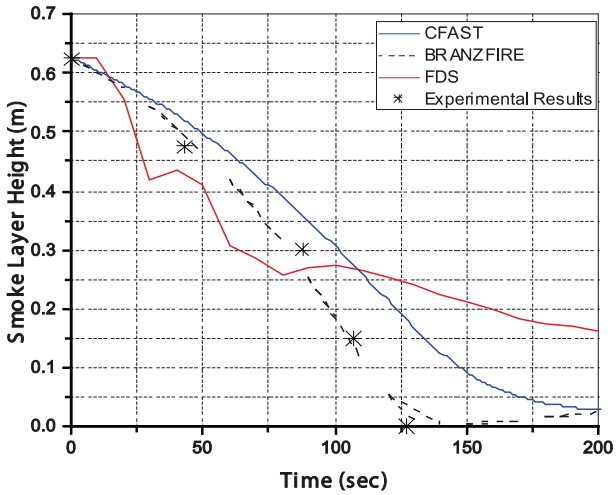

Fig. 5. Predicted and measured smoke layer heights

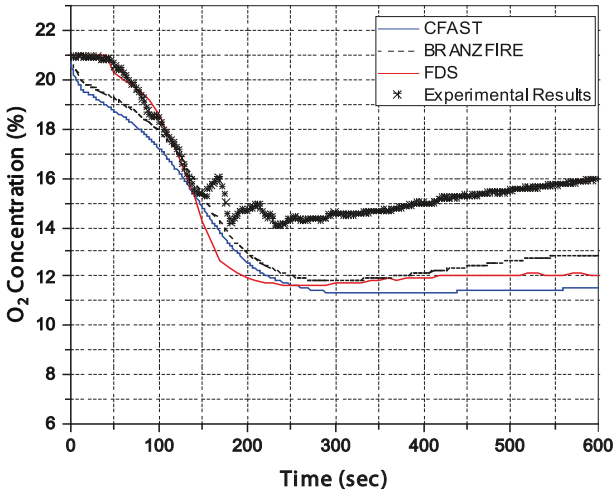

Fig. 6. Predicted and measured oxygen concentration

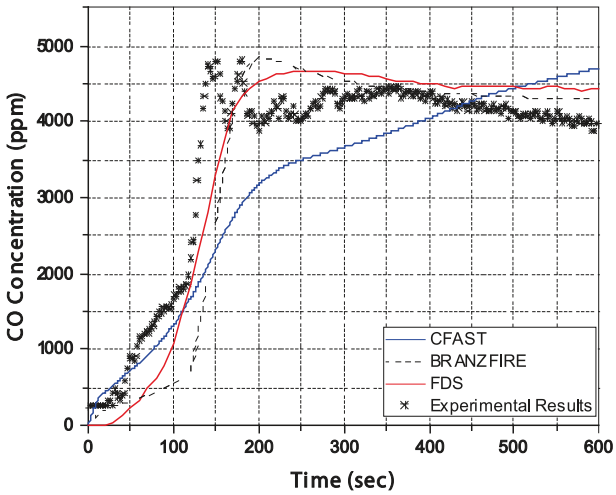

Fig. 7. Predicted and measured carbon monoxide concentration

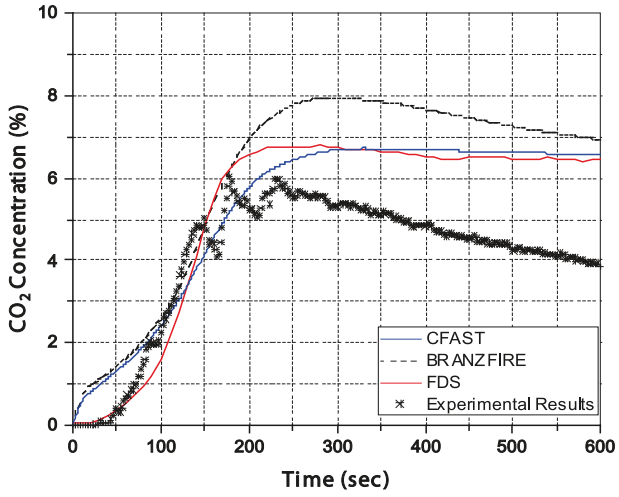

Fig. 8. Predicted and measured carbon dioxide concentration

To evaluate the predictive power of the three fire models, the author decided to use an approach introduced by Kobayashi and Salam (2000) and called mean squared deviation (*MSD*). In their work, Kobayashi and Salam (2000) highlighted the usefulness of their approach in quantifying the deviation of model outputs from measurements and its ability in locating possible cause(s) of the deviation. A brief description of the *MSD* approach is presented below.

The difference between the predicted values from simulation (x_i) and the measured values from the experiment (y_i) for (n) measurements is calculated with the *MSD* as:

$$MSD = \frac{1}{n}\sum_{i=1}^{n}(x_i - y_i)^2 \quad (1)$$

The *MSD* can be divided into three components, namely:

$$MSD = SB + SDSD + LCS \quad (2)$$

where, *SB* is the squared bias, given as;

$$SB = (\bar{x} - \bar{y})^2 \quad (3)$$

where, $\bar{x}$ and $\bar{y}$ are the mean of x_i and $y_i (i = 1, 2 \ldots n)$, respectively.

SDSD is the squared difference between predicted and measured standard deviations given as;

$$SDSD = (SD_s - SD_m)^2 \quad (4)$$

where, SD_s and SD_m are the standard deviations of the simulation and the measurement, respectively. The value of *SDSD* measures the difference of the magnitude of fluctuation between measured and predicted values.

LCS is the lack of positive correlation weighted by the standard deviations of simulation and measurement given as:

$$LCS = 2\,SD_s + SD_m\,(1 - r) \quad (5)$$

where: r is the correlation coefficient between the simulation and the measurement. *LCS* measures the pattern of fluctuation between predicted and measured values.

According to Kobayashi and Salam (2000), when comparing the simulation to the measurement, the lower the value of the *MSD*, the closer the simulation is to the measurement. Moreover, a smaller value of *SB* shows good agreement between the predicted and measured means. A smaller value of *SDSD* indicates the ability of the model to simulate the magnitude of fluctuation between the (n) measurements, while a smaller value of *LCS* shows the ability of the model to simulate the variation pattern of the (n) measurements.

Figures 9 through 13 show the results of the comparison of the *MSD* and its three components (*SB*, *SDSD* & *LCS*) for the predicted values of the 5 outputs of interest, which predicted by the three fire models.

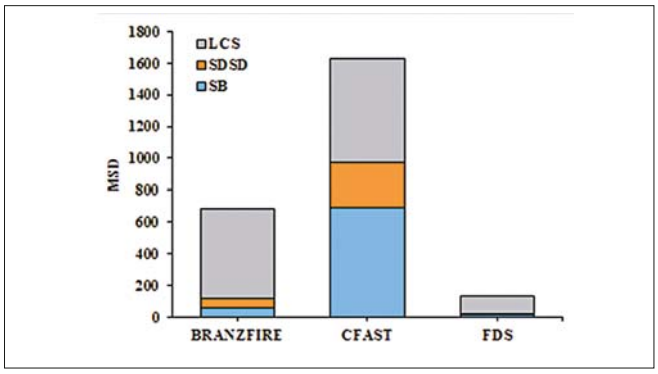

Fig. 9. Comparison of the MSD and its components for the three fire models for hot layer temperature predictions

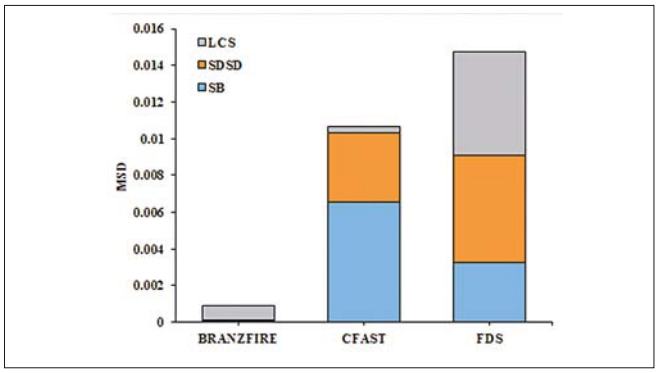

Fig. 10. Comparison of the MSD and its components for the three fire models for smoke layer height predictions

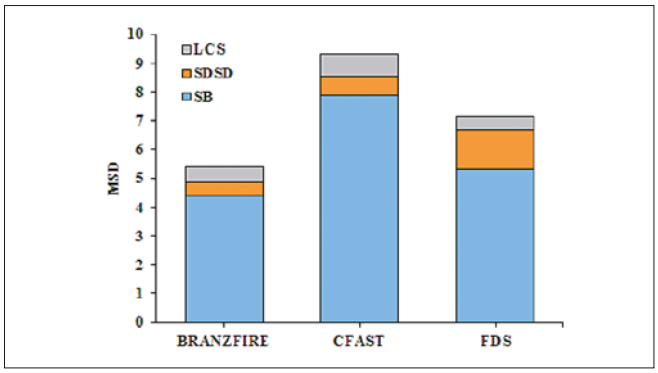

Fig. 11. Comparison of the MSD and its components for the three fire models for oxygen concentration predictions

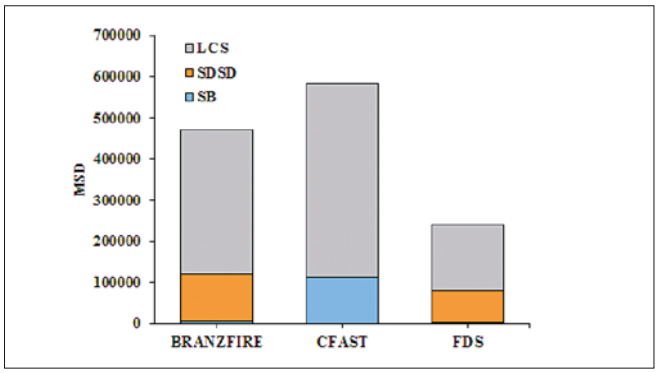

Fig. 12. Comparison of the MSD and its components for the three fire models for carbon monoxide concentration predictions

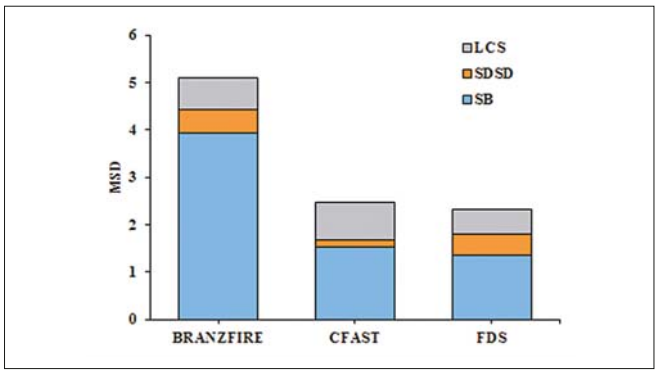

Fig. 13. Comparison of the MSD and its components for the three fire models for carbon dioxide concentration predictions

ANALYSIS OF THE RESULTS

Figures 4 through 13 show the results of the comparison between the three fire models and the model-scale fire test of the five outputs of concern. It is apparent from these results that:

1) **With regard to the "Hot Layer Temperature"**, and considering Figures 4 & 9, not surprisingly, *FDS* is the model with the best prediction (being it has the least *MSD*). In addition, the *CFD* model (*FDS*) was able to obtain the same profile as the experimental results (being it has the least *SDSD* and *LCS*). It should be noted that *FDS* fairly over-predicted the hot layer temperature during the fire growth period and there was a slight shift in the peak value. Among the two zone fire models, *BRANZFIRE* is the model that obtained reasonably good results of hot layer temperature. In spite of being initially highly over-predicted the hot layer temperature, *CFAST* was able to show very precise predictions in the last 200 seconds of simulation.
2) **Regarding the "Smoke Layer Height"**, and taking into account Figures 5 & 10, *BRANZFIRE* is the model with the best prediction. *CFAST* came in second with a reasonably good prediction of the smoke layer height. It should be noted that, in *CFD* models such as *FDS*, there are generally no distinct zones, but rather a continuous temperature profile. However, there are methods that can be utilised to estimate the height of the smoke layer from a continuous vertical temperature profile, and *FDS* uses one of these methods (Coyle and Novozhilov 2007). From the results of this comparison, it is clear that *FDS* over-predicted the smoke layer height until the time of approximately 90 sec with a maximum error of approximately 11 percent and under-predicted it for the remainder of the simulation time with a maximum error of approximately 75 percent. The higher values of both *SDSD* and *LCS* indicate that *FDS* failed to simulate the magnitude of oscillation and the variation pattern of the experimentally measured values of smoke layer height.
3) **With regard to the "Oxygen Concentration"**, and considering Figures 6 & 11, *BRANZFIRE* was the model with the best-predicted O_2 concentration results. Despite coming in second, *FDS* managed to obtain very precise predictions of O_2 concentration during the first 150 sec, in which the model began to show over-predicted results, as did the other two zone fire models.
4) **Regarding the "Carbon Monoxide Concentration"**, and taking into account Figures 7 & 12, *FDS* is the model with the least *SB*, *SDSD* and *LCS*, i.e., *FDS* is the model with the best prediction of CO concentration. Though *BRANZFIRE* came in the second place, *CFAST* was able to display the lowest *SDSD* value compared to the other two fire models. This means that *CFAST* was the model that was able to simulate the magnitude of oscillation between experimental results.
5) **With regard to the "Carbon Dioxide Concentration"**, and considering Figures 8 & 13, *FDS* is the model that shows the best prediction of CO_2 concentration. The results of *CFAST* are very close to the results of *FDS*. *BRANZFIRE* has shown over-predicted results with greater bias than the bias shown in the results obtained by both *FDS* and *CFAST*. The three fire models over-predicted the CO_2 concentration during the decay period of the fire.

Table 4 shows the recommended fire model to use when predicting each of the five outputs of concern in similar Vehicle Deck fire scenarios.

Tab. 4. The best fire model to use in similar Vehicle Deck Fire Scenarios

Output Parameter	Recommended Fire Model
Hot Layer Temperature	FDS
Smoke Layer Height	BRANZFIRE
Oxygen Concentration	BRANZFIRE
Carbon Monoxide Concentration	FDS
Carbon Dioxide Concentration	FDS/CFAST

CONCLUDING REMARKS

A comparison was performed between the predictions of three different fire models, namely, *CFAST*, *BRANZFIRE* and *FDS*, and the experimental results of a model-scale fire test representing a fire scenario on a vehicle-deck aboard a RoPax ship. The results have been analyzed using a statistical analysis technique. The most important conclusion of this

comparison is that there is no fire model that can predict each of the five outputs of concern. In addition, there is always an optimal fire model that can predict one or more of the five outputs of concern with results that are in good agreement with the measured values. While both zone fire programs (*BRANZFIRE* and *CFAST*) are based on the same assumptions and limitations, their outputs are different. The *BRANZFIRE* developer, Colleen Wade, commented on this issue by saying that the differences in outputs between *BRANZFIRE* and *CFAST* may be due to the differences in many of the algorithms used to build the program. Attention should be paid to some of the outputs of concern when using the results of zone models due to the prior knowledge of the deficiency in their predictions. For example, the results of the comparison show that *CFAST* always significantly over-predicts the temperature of the hot layer. Similarly, it is well known that *BRANZFIRE* uses a conservative model to predict the carbon monoxide concentration that causes the program to over-predict it.

ACKNOWLEDGEMENTS

This work was funded by the Deanship of Scientific Research (DSR), King Abdulaziz University, Jeddah, under Grant No. 980-124-D1438. The author, therefore, acknowledges with thanks to DSR technical and financial support.

REFERENCES

1. Arvidson M, Axelsson J, Simonson M, Tuovinen H. 2006. *Fire safety approach on the DESSO ROPAX*. SP Rapport 2006:01.

2. Arvidson M. 1997. *Large scale Ro-Ro vehicle deck fire test. Nordtest project 1299-96. Brandforsk project 421-941*. SP Swedish National Testing and Research Institute. Fire Technology. SP Report; 1997:15.

3. Arvidson M. 2009. *Large-scale ro-ro deck fire suppression tests*. SP-Report. 2009:29.

4. Arvidson M. 2014. *Large-scale water spray and water mist fire suppression system tests for the protection of Ro–Ro cargo decks on ships*. Fire Technology. 50(3):589–610.

5. Averill JD. 1998. *Performance-based codes: Economics documentation, and design [dissertation]*. [Worcester (MA)]: Worcester Polytechnic Institute.

6. Azzi C, Pennycott A, Mermiris G, Vassalos D. 2011. *Evacuation simulation of shipboard fire scenarios. Paper presented at: FEMTC 2011*. Fire and Evacuation Modelling Technical Conference; Maryland (USA).

7. Azzi C, Vassalos D. 2010. *Performance-Based design for fire safety on board passenger ships. Paper presented at PRADS 2010*. 11th International Symposium on Design of Ships and Other Floating Structures; Rio de Janeiro (Brazil).

8. Azzi C. 2010. *Design for fire safety onboard passenger ships [dissertation]*. [Glasgow]: Glasgow and Strathclyde Universities.

9. Coyle P, Novozhilov, V. 2007. *Further validation of fire dynamics simulator using smoke management studies*. International Journal on Engineering Performance-Based Fire Codes, 9(1):7-30.

10. Croccolo F. 2015. *Fires on board RoPax ferries-Lessons learned. Presentation at 40th Annual Interferry Conference*. Copenhagen, Denmark. October 3-7, 2015.

11. DNV GL. 2016. *Fires on Ro-Ro decks*. Paper no. 2016-P012.

12. DNV Technica. 1996. *Safety Assessment of Passenger Ro-Ro Vessels*. Main Report (Document Number: REP-T09-003), Joint North-West European Project. 28:1996.

13. DNV. 2005. *Fires on Ro-Ro decks*. Paper no. 2005-P018.

14. Eleftheria E, Apostolos P, Markos V. 2016. *Statistical analysis of ship accidents and review of safety level*. Safety science. 85:282–292.

15. Karlsson U, Ulfvarson A. 2008. *Chain Breakers—A Survey of Fatal ship accidents with the event-chain method*. Marine Technology. 45(3):182–190.

16. Kobayashi K, Salam MU. 2000. *Comparing simulated and measured values using mean squared deviation and its components*. Agronomy Journal. 92(2): 345–352.

17. Konovessis D, Vassalos D. 2008. *Risk evaluation for RoPax vessels. Proceedings of the Institution of Mechanical Engineers*, Part M: Journal of Engineering for the Maritime Environment. 222(1):13–26.

18. Larsson I, Ingason H, Arvidson M. 2002. *Model-scale fire tests on a vehicle deck onboard a ship*. SP Swedish National Testing and Research Institute, SP Fire Technology. SP Report 2002:05.

19. McGrattan K, Hostikka S, McDermott R, Floyd J, Weinschenk C, Overholt K. 2017. *Fire Dynamics Simulator, User's Guide*. NIST Special Publication. 1019(6):1–296.

20. Peacock RD, Reneke PA, Forney GP. 2016. *CFAST–Consolidated Fire And Smoke Transport (Version 7) Volume 2: User's Guide*. Technical Note, National Institute of Standards and Technology (NIST), Gaithersburg, Maryland. 1889(2):1–85.

21. Salem AM, Dabess EM, Banawan AA, Leheta HW. 2013. *The use of consequence analysis tools in fire-safety design*

of Nile-floating hotels. In: Soares CG, Pena FL, editors. *Developments in maritime transportation and exploitation of sea resources*. Proceedings of the 15th International Congress of the International Maritime Association of the Mediterranean (IMAM); 14–17 October 2013; A Coruña (Spain).

22. Salem AM, Dabess EM, Banawan AA, Leheta HW. 2016. *Fire safety design of Nile-floating hotels*. Ships Offshore Struct. 11(5):482–500.

23. Salem AM, Leheta HW. 2011. *Sensitivity analysis of a fire model used in fire consequence calculations*. In: Rizzuto E, Soares CG, editors. *Sustainable Maritime Transportation and Exploitation of Sea Resources*. Proceedings of the 14th International Congress of the International Maritime Association of the Mediterranean (IMAM); 13–16 September 2011; Genova (Italy).

24. Salem AM. 2007. *Risk-based design for fire safety of RoRo/ Passenger ships [dissertation]*. [Glasgow]: Glasgow and Strathclyde Universities.

25. Salem AM. 2010. *Fire engineering tools used in consequence analysis*. Ships Offshore Struct. 5(2):155–187.

26. Salem AM. 2013. *Parametric analysis of a cabin fire using a zone fire model*. Alexandria Eng J. 52(4):627–636.

27. Salem AM. 2016. *Use of Monte Carlo Simulation to assess uncertainties in fire consequence calculation*. Ocean Engineering, 117:411–430.

28. Taylor A [Internet]. 2015. *The deadly fire aboard the ferry Norman Atlantic*; [cited 13 May 2017], http://www.theatlantic.com/photo/2015/01/the-deadly-fire-aboard-the- ferry-norman-atlantic/100882/.

29. Themelis N, Spyrou KJ. 2012. *Probabilistic fire safety assessment of passenger ships*. J Ship Rese. 56(4):252–275.

30. Wade CA. 2004. *A User's Guide to BRANZFIRE. Building Research Association of New Zealand (BRANZ)*, Wellington, New Zealand.

31. Wikman J, Evegren F, Rahm M, Leroux J, Breuillard A, Kjellberg M, Gustin L, Efraimsson F. 2017. *Study investigating cost effective measures for reducing the risk from fires on ro-ro passenger ships (FIRESAFE)*. European Maritime Safety Agency, EMSA.

CONTACT WITH THE AUTHORS

Ahmed Salem
e-mail: amsalem@kau.edu.sa

King Abdulaziz University
Al-Morjan District
21581 Jeddah
Saudi Arabia

Alexandria University
Al-Hadara Al-Baharia
21517 Alexandria
Egypt

sciendo

POLISH MARITIME RESEARCH 2 (102) 2019 Vol. 26; pp. 163-172
10.2478/pomr-2019-0036

NUMERICAL PREDICTION OF PROPELLER-HULL INTERACTION CHARACTERISTICS USING RANS METHOD

Tran Ngoc Tu
Do Duc Luu
Nguyen Thi Hai Ha
Nguyen Thi Thu Quynh
Nguyen Minh Vu
Vietnam Maritime University, Hai Phong City, Vietnam

ABSTRACT

The paper presents the results of computational evaluation of the hull-propeller interaction coefficients, also referred to propulsive coefficients, based on the unsteady RANS flow model. To obtain the propulsive coefficients, the ship resistance, the open-water characteristics of the propeller, and the flow past the hull with working propeller were computed. For numerical evaluation of propeller open-water characteristics, the rotating reference frame approach was used, while for self-propulsion simulation, the rigid body motion method was applied. The rotating propeller was modelled with the sliding mesh technique. The dynamic sinkage and trim of the vessel were considered. The free surface effects were included by employing the volume of fluid method (VOF) for multi-phase flows. The self-propulsion point was obtained by performing two runs at constant speed with different revolutions. The well-known Japan Bulk Carrier (JBC) test cases were used to verify and validate the accuracy of the case studies. The solver used in the study was the commercial package Star-CCM+ from SIEMENS.

Keywords: Propeller, interaction, hull, wake fraction, thrust deduction, relative rotative efficiency, RANS equations

INTRODUCTION

In assessing the performance of the propeller working behind the ship hull plays an important role in the design process and it is still one of the most demanding challenges in computational ship hydrodynamics. The interaction between the propeller and the ship comprises wake fraction, thrust deduction, and relative rotative efficiency. Correct design of the ship propulsion system depends on the accuracy in determining those components.

Nowadays, scale model tests still provide the most accurate data for hull-propeller interaction. However, these tests are both time-consuming and cost–intensive with respect to both model manufacturing and the experiment itself. Thus, this method is impractical generally for hydrodynamics optimization studies, especially those involving hull-propeller interaction.

Computational Fluid Dynamics (CFD) has made a remarkable progress in the past few decades in the field of ship hydrodynamics. With the development of computational resources, CFD methods have been widely applied in practical ship designing and performance predictions. They provide relatively accurate results, and are relatively fast and inexpensive, compared to the experimental data. Moreover, they provide the visualization of flow quantities, i.e. pressure and velocity, the latter in the form of contour maps, vector maps, and streamlines, which may often allow the designers to develop or improve their design. The group of CFD methods used to solve hydrodynamics problems includes: potential flow theory (panel code), Reynold Averaged Navier-Stokes (RANS) equations, and Large Eddy Simulation (LES). At the moment, the most popular approach is the RANS method, as it provides a sufficient accuracy for engineering purposes at reasonable computational time [1]. Thus, this paper uses the RANS method for evaluating the hull-propeller interaction coefficients.

Some useful results using the RANS method for simulation of propeller-hull interaction have been already achieved. Villa

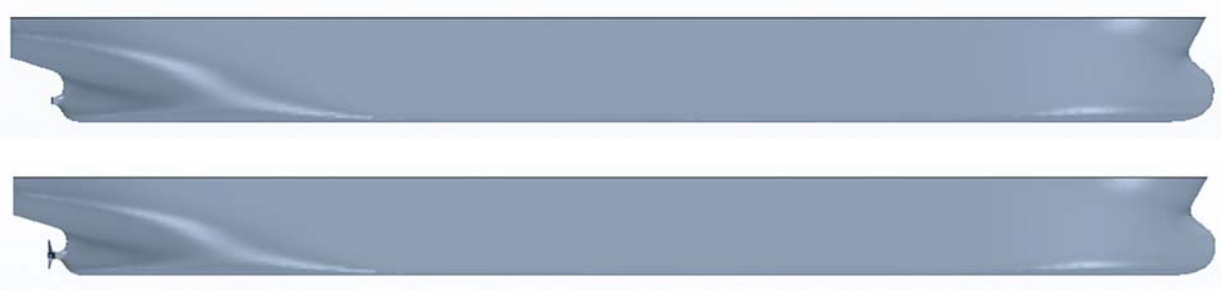

Fig. 1. JBC geometry for simulations of case study "ship resistance" (top) and case study "self-propulsion" in calm water (bottom)

et al. [2], Pacuraru et al. [3] and Win et al. [4] used this method in combination with the actuator disk method, instead of the actual propeller, to perform the self-propulsion simulation. That approach allowed the authors to avoid complexities associated with moving meshes and to achieve, as a result, shorter run times. However, the applied method could not provide the detailed flow field around the propeller. Bugalski et al. [5] used the RANS method together with the rigid body motion method (actual rotating propeller) to simulate the self-propulsion. The dynamic sinkage and trim of the vessel were not considered. That approach helped to avoid the uncertainties caused by the dynamic fluid body interaction (DFBI) model used to simulate the ship's behaviour with the hull free to move in the pitch and heave directions, and thus to accelerate the simulation convergence. Bekhit [6] used the RANS method to study self-propulsion of the Japan Bulk Carrier (JBC) ship model using the body force propeller method and the fully discretized propeller model. The results of that study have shown that the propeller model provides efficient and reliable results, and that the flow characteristics and blade pressure distributions can be fully visualized. However, it takes a significant computational time, and both modelling and computations themselves are more complex in comparison with the body force propeller method. Seo et al. [7] and Gokce et al. [8] used the RANS method to simulate ship resistance, and propeller open-water and self-propulsion characteristics in order to evaluate the hull-propeller interaction coefficients. Seo et al. focused on flexible meshing techniques, while the base of choice for computational domain, time step, y+ value, and mesh convergence was not considered, although these are the key issues determining the numerical accuracy. In the study by Gokce et al., the discrepancy between computed and experimental results of open-water propeller performance was especially sound at higher advance coefficients.

The abovementioned literature has played an important role for further researches using the RANS method to assess the performance of a propeller working behind the ship hull. In the research reported in this paper, the ship resistance, the propeller open-water characteristics, and the thrust/torque characteristics behind the ship hull were computed to obtain the coefficients of hull-propeller interaction. For this purpose, the RANS method with Star-CCM+ solver was used. The ship resistance was computed for the hull free to sink and trim. In the computations of propeller open-water characteristics, the rotating reference frame was used. This approach, consisting in considering additional terms in the momentum equation, is fully suitable for open-water analyses and its results are fully equivalent to the case of actual propeller rotation, while the computational time is reduced and the convergence is faster, as physical motion of the computational mesh can be avoided [9]. For the self-propulsion simulation, the rigid body motion method was applied. The rotating propeller was modelled with the sliding mesh technique. The dynamic sinkage and trim of the vessel were considered. The base of choice for computational domain, time step, y+ value, and mesh convergence was considered in this study. The case study used to verify and validate the computational model was the well-known JBC ship model; the geometry of which and the experimental data for validation are available on the website of the Workshop on CFD in Ship Hydrodynamics, Tokyo 2015 [10], [11].

NUMERICAL SIMULATION

GEOMETRY AND CONDITIONS

Ship and propeller geometry

The JBC is a hypothetical modern bulk carrier designed and tested experimentally to provide data for both exploration of flow physics and CFD validation. The data of ship resistance, propeller open water characteristics, and self-propulsion characteristics in model scale ($\lambda = 40$) are available in [10], [11].

The JBC hull and propeller geometry are shown in Fig.1. and Fig. 2, while its dimensions and geometrical properties are listed in Table 1 and Table 2.

Fig. 2. JBC propeller geometry for case study "propeller open-water simulation"

Tab. 1. Main particulars of JBC [10]

Descriptions		Full scale	Model
Scale factor	λ	–	40
Length between perpendiculars	L_{PP} (m)	280.00	7.00
Length of waterline	L_{WL} (m)	285.00	7.125
Breadth	B (m)	45.00	1.125
Draft	T (m)	16.5	0.4125
Volume	∇ (m^3)	17837	2.7870
Wetted surface	S (m^2)	19556	12.222
Longitudinal Centre of Buoyancy From Midship	LCB (%L_{PP}), fwd+	2.5475	
Propeller centre, long. location (from FP)	x/L_{PP}	0.985714	
Propeller centre, vert. location (bellow WL)	$-z/L_{PP}$	−0.0404214	
Propeller rotation direction (view from stern)	–		

Tab. 2. Propeller principal particulars [10]

Descriptions		Unit	Value
Diameter	D	m	0.203
Blade area ratio	A_E/A_0	–	0.5
Hub ratio	D_h/D	–	0.18
Number of blades	Z	–	5
Pitch ratio	$P_{0.7}/D$		0.75
Direction of rotation	–	–	Right-handed

Test case conditions

For the case studies (1) "ship resistance" and (3) "self-propulsion", the computations were performed for the design draft T = 0.4125 m, corresponding to the hull displacement volume ∇ = 2.7870 m^3, and for Froude number Fr = 0.142 and Reynolds number Re = $7.46.10^6$.

The settings used in the ship resistance simulation correspond to case 1.1a according to [11], i.e.:

- Calm water condition;
- Without rudder and Energy Saving Device (ESD), without propeller;
- The vessel is free to trim and sink.

The settings used in the self-propulsion simulation correspond to case 1.5a according to [11] i.e.:

- Calm water condition;
- Without rudder and ESD, with propeller;
- The vessel is free to trim and sink.

The case study (2) "propeller open water simulation" was carried out for the same conditions as the experiment labelled as 'case 1.5a' according to [11]. A number of simulations were carried out for different advance coefficients J which varied from 0.4 to 0.8 (to reflect the typical propeller operation range) with the step equal to 0.1. The propeller revolutions were kept constant and equal to n=20 rps, and J was changed by changing the advance velocity.

The water parameters for all three case studies corresponded to the values recorded in the experiment: water density ρ = 998.2 kg/m^3, water kinematic viscosity ν = $1.1070x10^{-6}$ m^2/s) [11].

COMPUTATIONAL SETUP

COMPUTATIONAL DOMAIN AND BOUNDARY CONDITIONS

The commercial package Star-CCM+ from SIEMENS was used for the computations.

For case (1) "ship resistance", one half of the hull was considered due to flow symmetry, while in case (3) "self-propulsion", the entire ship hull with propeller was analysed.

Based on the recommendations given by ITTC [12] and sample settings provided in the software documentation [13], the dimensions of the computational domain built around the ship hull for case (1) were as follows: the inlet boundary was located at a distance of 1.5Lpp from FP, the outlet boundary at 2.5Lpp behind AP, and the bottom and top boundaries at 2.5Lpp and 1.25Lpp from the free surface, respectively. The lateral boundary was located 2.5Lpp from the hull symmetry plane.

For case (2) "propeller open water simulation", the computational domain was cylindrical and characterized by the following dimensions, expressed as multiples of propeller diameter D: the inlet was located 3D from the midpoint of the chord of the root section, while the outlet ant the outer boundaries were located 4D from the propeller plane and the propeller axis, respectively. It should be noted that the locations of boundaries were selected based on the applications reported in studies [14] and recommendations given by ITTC [15].

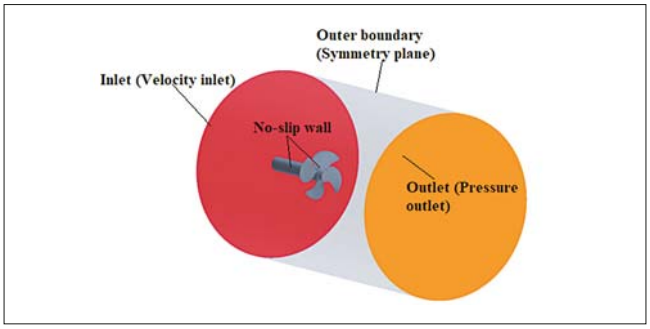

Fig. 3. Computational domain and boundary conditions in propeller open water simulation

For the self-propulsion simulation, the computational domain was divided into two regions: the stationary region surrounding the whole modelled system, and the rotating sub-region having the form of a cylinder surrounding the propeller (see Fig. 8).

Regarding the boundary conditions – for cases (1) and (3), the prescribed velocity conditions were used at inlet, top

and bottom. The no-slip wall condition was applied on hull and propeller surfaces. At outlet, the hydrostatic pressure was specified. The slip wall condition was used on the side walls. The free surface was located at z = 0. The ship stern (aft perpendicular) was located at x = 0. For case (2), the velocity condition was used at inlet and the pressure condition at outlet. The symmetry plane condition was used at outer boundary. The no-slip wall condition was used on propeller, hub and shaft surfaces (Fig. 3).

Mesh generation

The mesh used for all three case studies was the hexahedral mesh.

For case study (1), to avoid using fine mesh resolution where unnecessary, local volume refinement was applied at bow and stern. To capture the exact flow behaviour near the walls, prism layers were used. Moreover, to resolve the flow around the hull near the free surface, a finer mesh was created in the free surface region. The average Y+ value on the submerged part of the hull was 50 (Fig. 4). The mesh generated for case study (1) is shown in Fig. 5.

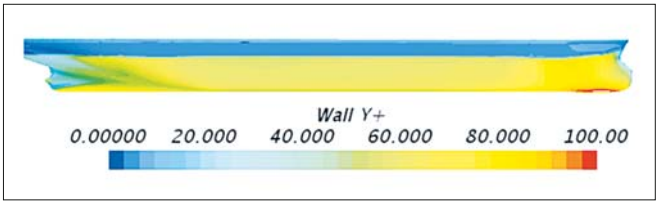

Fig. 4. Y+ value on hull surface

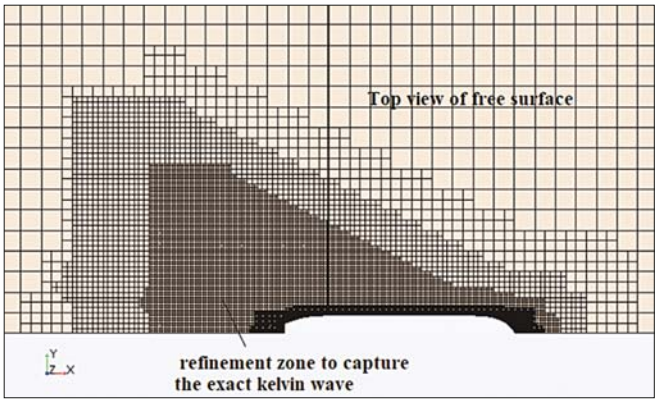

Fig. 5. Mesh structure for ship resistance simulation

For case study (2), to avoid using fine mesh resolution where unnecessary, i.e. at large distance from the propeller, local refinement was applied around the propeller. Moreover, the regions of leading edge, trailing edge and tip of propeller blades were further refined due large curvature of the blade surface in these regions [5]. To resolve the boundary layer, the prism layer was used. In mesh generation, the dimensionless normal distance y^+ of the first cell layer adjacent to the wall was kept well below 5 to resolve the near wall boundary layer. Such a range corresponds to the viscous sublayer in the model scale simulation [16]. The mesh generated for this case is shown in Fig. 7.

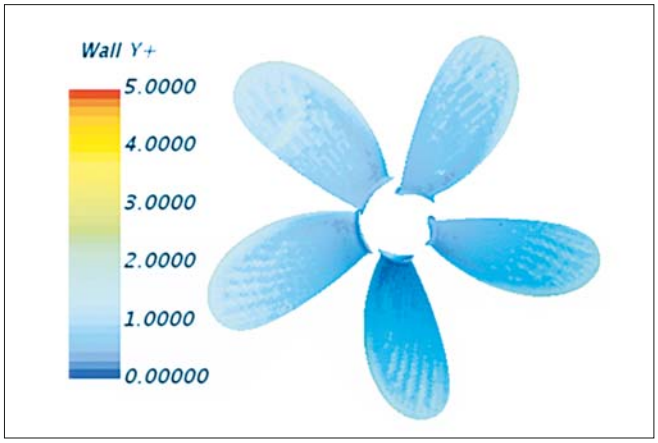

Fig. 6. Y+ value on propeller blades

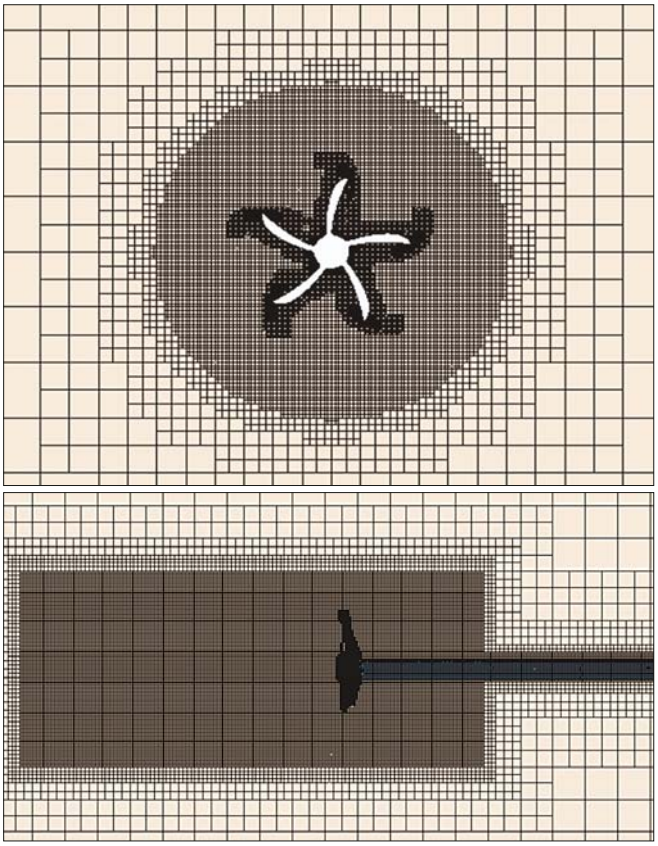

Fig. 7. Mesh structure for open water simulation

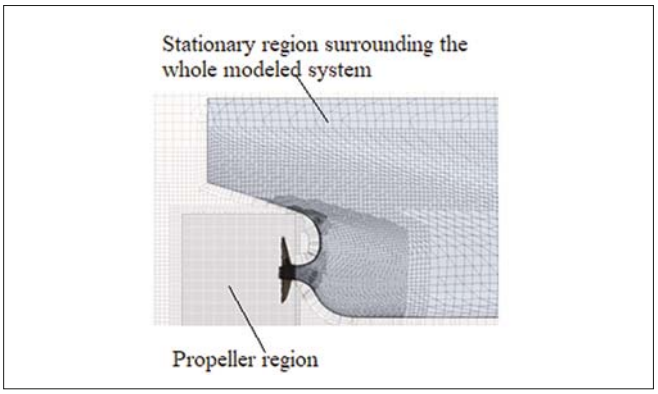

Fig. 8. Mesh structure for self-propulsion simulation

For case study (3), the mesh setup for the ship and propeller regions was the same as for cases (1) and (2). The refined mesh was used near the stern region surrounding the propeller to capture properly the wake field. The sliding mesh technique was used for the rotating propeller.

Physical model

The computation was carried out using the Reynolds Averaged Navier-Stokes (RANS) equations. The turbulence model used in all three case studies was SST K-omega [12].

- For the propeller open-water analysis, the propeller inflow was uniform, so the steady RANS equations with the rotating reference frame were used. This approach is fully equivalent to the case of actual propeller rotation, while the computational time is reduced and the convergence is faster, as physical motion of the computational mesh is avoided [9].
- For ship resistance computations, the 6-DOF motion and the VOF multiphase model were employed to handle running trim, sinkage, and the free surface wave flow around the hull. The hull motion was captured during the computation by using the DFBI Equilibrium option, i.e. the dynamic fluid-body interaction motion solver optimized for fast heading towards the steady state solution (Y-axis rotation and Z-direction motion was allowed for the hull). Wave damping in the region beginning about 0.5L away from the hull was applied to reduce the resistance force fluctuation due to wave reflections within the domain.
- In the case of propeller working behind the ship, the rigid body motion method was applied. The propeller rotation was introduced by the DFBI Superposed Rotation model (it superimposes an additional fixed body rotation onto the DFBI motion, thus making it possible to model a propeller attached to the ship [13]).

Choice of time step

One of the key issues determining the numerical accuracy is choosing the time step size. For resistance computations, the time step is the function of ship's length and speed, according to the ITTC equation [12]:

$$\Delta t = 0.005 \sim 0.01 L/\mathrm{V} \tag{1}$$

where V and L are the ship's speed and length, respectively.

For the self-propulsion simulation, according to the ITTC recommendation [15], the time step was selected such that the propeller rotation angle was one degree per time step.

RESULTS AND DISCUSSION

MESH DEPENDENCY STUDY

One of key issues determining the numerical accuracy is mesh dependency. Due to finite size of the finite-volume cells, some discretization errors appear, being the difference between the solution of the difference equations and the exact (continuum) solution of the differential equations. It is important to know the magnitude of these discretization errors and to ensure that the used mesh is fine enough to reduce the error to an acceptable level [17]. In the present case, the mesh sensitivity study has been conducted using three meshes with non-integer mesh refinement ratio $r_G = \sqrt{2}$ (the value recommended by ITTC [18]) so that the coarse, medium, and fine mesh corresponded to the cell number of 0.696, 1.315 and 2.845 million cells, respectively, for the ship resistance study, and to 0.852, 1.568 and 3.7 million cells for the propeller open-water simulation at advance coefficient J = 0.5.

Mesh refinement was done by reducing the cell size in all directions outside the prism layer. The idea here was to keep the same y+ values at near-wall cells for all three cases.

The mesh sensitivity study was performed by comparing the quantities recorded in the experiment (EFD), denoted as D and treated as reference values, with the corresponding S values obtained from CFD:

$$E\%D = \frac{(D-S)}{D}.100\% \tag{2}$$

Changes between the simulations performed for two different meshes, i.e. fine-medium ε_{12} and medium-coarse ε_{23}, are defined as follows:

Tab. 3. Ship resistance at Fr=0.142 for different meshes

Parameter		EFD (D) [11]	V&V Study			ε_{32} %	ε_{12} %
			Mesh#3	Mesh#2	Mesh#1		
$C_T x10^3$	Value	4.289	4.392	4.370	4.350	–0.50	–0.46
	E%D	/	–2.401	–1.889	–1.421	/	/
$C_F x10^3$	Value	/	3.112	3.150	3.161	1.21	0.35
	E%D	/	/	/	/	/	/
$C_P x10^3$	Value	/	1.280	1.220	1.189	–4.92	–2.61
	E%D	/	/	/	/	/	/

$$\varepsilon_{12} = (S_1 - S_2)/ S_1; \varepsilon_{23} = (S_2 - S_3)/ S_2 \quad (3)$$

The results of the mesh dependency study for ship resistance and propeller open-water simulations are illustrated in 0 and 0, respectively. In the present case, a tendency to converge in both case studies was observed for the considered meshes, i.e. the resulting resistance coefficient and the propeller characteristics changed monotonically with mesh density (the solution change between meshes 1 and 2 (ε_{12}) was smaller than that between meshes 2 and 3 (ε_{23}), and the solution changes between meshes 1 and 2 (ε_{12}), were very small for all case studies). Besides, the comparison has shown quite good agreement between simulation (CFD) and experimental values (EFD), especially for the fine mesh (the errors of CT for fine meshes were less than 1.5% for ship resistance and propeller open water predictions), so the fine mesh was used in further studies of propeller open-water and self-propulsion simulations.

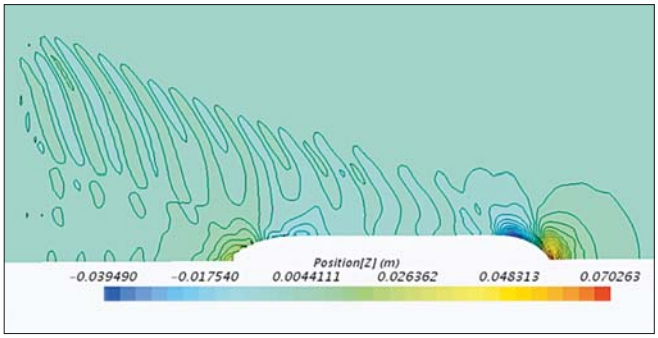

Fig. 9. Wave elevation contour plot [Mesh 1]

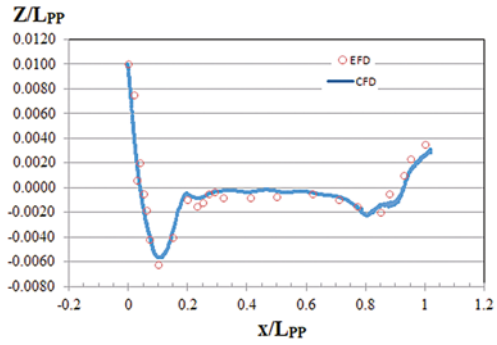

Fig. 10. Comparison of wave profile

The wave pattern for fine mesh is presented in Fig.9. The wave profiles along the hull surface are compared in Fig.10. The wave obtained from CFD shows good agreement with the experimental data.

Results of open-water propeller simulation

The comparison between the calculated and measured values of the open-water propeller characteristics shown in Table 5 shows that good agreement has been achieved.

Results of self-propulsion simulations

The self-propulsion simulations were performed using the fine mesh for both the hull and the propeller. Unlike in the resistance computations, here both sides of the hull were modelled directly. The total number of mesh elements was 6.8 million cells (4.2 million cells for the stationary region

Tab. 4. Results of mesh independency study at advance coefficient J=0.5

Parameter		EFD (D) [11]	V&V Study			ε_{32} %	ε_{12} %
			Mesh#3	Mesh#2	Mesh#1		
K_T	Value	0.1798	0.181	0.1805	0.1803	–0.28	–0.11
	E%D	/	–0.67	–0.39	–0.28	/	/
K_Q	Value	0.2479	0.2413	0.243	0.2445	0.70	0.61
	E%D	/	2.66	1.98	1.37	/	/
η_0	Value	0.5771	0.597	0.591	0.587	–0.98	–0.73
	E%D	/	–3.43	–2.43	–1.68	/	/

Tab. 5. Open-water simulation results vs. experimental data

J	K_T			$10K_Q$			η_0		
	EFD [11]	CFD	E%D [%]	EFD [11]	CFD	E%	EFD [11]	CFD	E%D [%]
0.4	0.2214	0.227	–2.47	0.2871	0.281	2.12	0.4909	0.5143	–4.8
0.5	0.1798	0.1803	–0.28	0.2479	0.2445	1.37	0.5771	0.5868	–1.7
0.6	0.1349	0.1358	–0.66	0.2027	0.203	–0.15	0.6354	0.6388	–0.5
0.7	0.0867	0.0905	–4.20	0.1509	0.154	–2.05	0.64	0.6547	–2.3
0.8	0.0353	0.0371	–4.85	0.0921	0.0905	1.74	0.4879	0.5220	–7.0

surrounding the whole modelled system, and 2.6 million cells for the rotating sub-region surrounding the propeller). The hull was free to trim and sink. Propeller rotation was introduced by using the DFBI Superposed rotation model.

The self-propulsion computations were performed at ship self-propulsion point, where the rate of propeller revolutions *n* was adjusted to obtain force equilibrium (thrust/drag balance). In practice, it is difficult to obtain this condition in one run, and a common practice is to carry out at least two constant-speed runs with different revolutions, hence the discrepancy between the total self-propulsion resistance RT(SP) and the thrust of the propeller working behind the ship T equals zero. The model simulations considered the applied towing force (Skin Friction Correction, SFC [19], which takes into account the difference in skin friction coefficients between the model and the full scale ship):

$$T = R_{T(SP)} - SFC \tag{4}$$

where SFC = 18.2 N, (the value computed from experimental data [11]).

The computed results of ship's thrust and resistance versus propeller revolutions are shown in Table 6 and in Fig. 111 for the velocity of 1.179 m/s. The self-propulsion point was searched using linear interpolation, and the obtained rotational speed 2 was n = 7.88 *rps* (see Fig. 11).

Tab. 6. Calculated results of two rps cases

n [rps]	$R_{T(SP)}$ – SFC [N]	T [N]	$10K_{Q(SP)}$
7.7	22.4	21.9	0.283
7.9	23.47	23.52	0.289

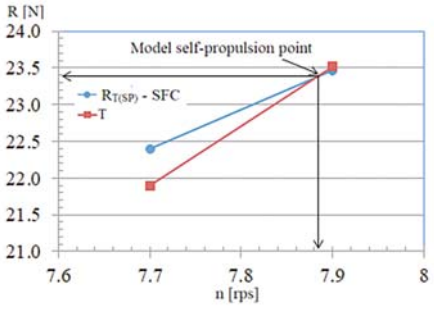

Fig. 11. Model self-propulsion point

Based on the computed self-propulsion point, the propulsive coefficients were determined as follow:

The thrust deduction t is given by the following formula [19]:

$$t = \frac{T + SFC - R_T}{T} \tag{5}$$

where R_T is the total ship resistance without propeller working behind the ship.

The effective wake fraction w_T and the relative rotative efficiency η_R were obtained using thrust identity with the open water propeller results (see Fig. 14) from Fig.12. The wake fraction is given by the following formula [20]:

$$w_T = 1 - \frac{J_0}{J_{SP}} \tag{6}$$

while the relative rotative efficiency is given by [20]:

$$\eta_R = \frac{K_{Q0}}{K_{Q(SP)}} \tag{7}$$

where J_0 and K_{Q0} are the advance and torque coefficients, respectively, obtained from the open-water propeller characteristics – Fig. 12, while J_{SP} and $K_{Q(SP)}$ are the advance and torque coefficients obtained from the self-propulsion simulation.

Table 7 compares the self-propulsion parameters obtained from the computation with the experimental data taken from [11]. Good agreement between these two data is observed.

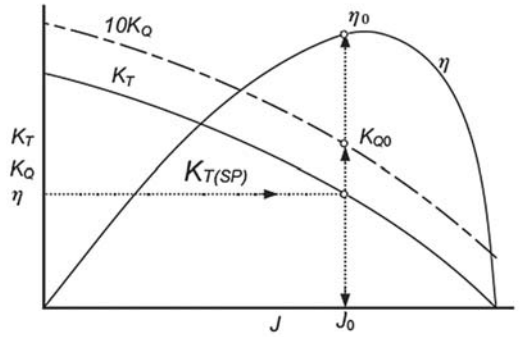

Fig. 12. Open-water curve and thrust identity [20]

Tab. 7. Comparing computed propeller-hull interaction results with experimental data

Parameter	EFD (D)	CFD (S)	E%D
$R_{T(SP)}$ [N]	40.79	41.60	–1.99
$R_{P(SP)}$ [N]	–	14.72	–
$R_{F(SP)}$ [N]	–	26.88	–
R_T [N]	36.36	36.88	–1.43
R_P [N]	–	10.08	–
R_F [N]	–	26.8	–
n [rps]	7.8	7.88	–1.03
T [N]	22.56	23.4	–3.72
$K_{T(SP)}$	0.217	0.222	–2.45
$K_{Q(SP)}$	0.0279	0.0288	–3.23
K_{Q0}	0.0283	0.0293	–3.53
SFC	18.2	18.2	0.00
J_0	0.408	0.405	0.74
J_{SP}	0.745	0.737	1.02
t	0.109	0.113	–4.47
w	0.452	0.451	0.34
η_R	1.014	1.017	–0.298

The distributions of the flow quantities: velocity and pressure, in the stern region and over the propeller's blade surface are shown in Fig. 13, Fig. 14 and Fig. 16.

As can be seen, the wake behind the ship strongly influences the propeller, and the propeller also influences the ship flow.

The influence of the propeller on the ship flow can be clearly observed in the pressure field. The propeller accelerates the flow ahead of it, thus reducing the pressure on the aft part of the hull (Fig. 13 and Fig. 14) and increasing the pressure resistance. The value of pressure resistance in the self-propelled condition is 1.46 times as large as that of the hull without propeller (see Table 7).

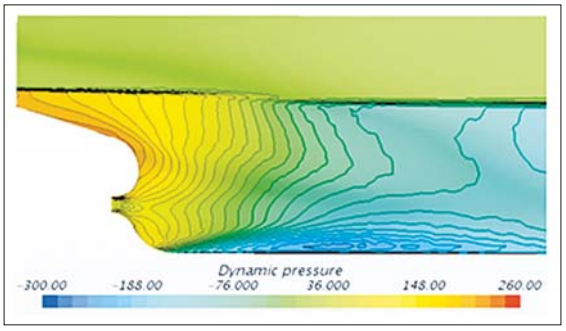

Fig. 13. Dynamic pressure contours on hull surface in ship resistance case

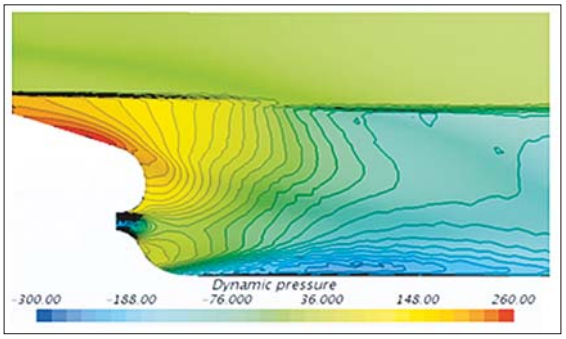

Fig. 14. Dynamic pressure contours on hull surface in self-propulsion case

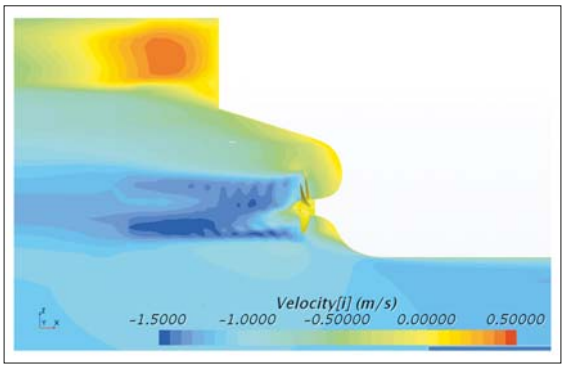

Fig. 15. Axial velocity field in symmetry plane

Due to the hull shape curvature in the aft part and the boundary layer development effects, the wake structure and its influence on the propeller are non-uniform, which can be clearly observed in the axial velocity field behind the propeller (Fig. 15). The asymmetric velocity distribution is expected to occur as the effect of different pressure distributions on individual propeller blades, both on their suction and pressure sides (Fig. 16).

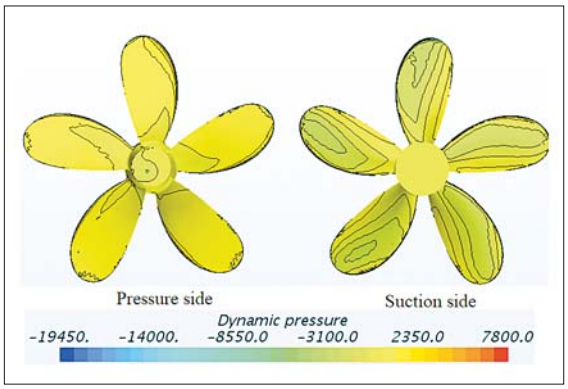

Fig. 16. Dynamic pressure contours on propeller blade surfaces in self-propulsion case

The computed axial velocity distributions are compared in Fig. 17 and Fig. 18 with the measured values for the case without and with propeller, respectively.

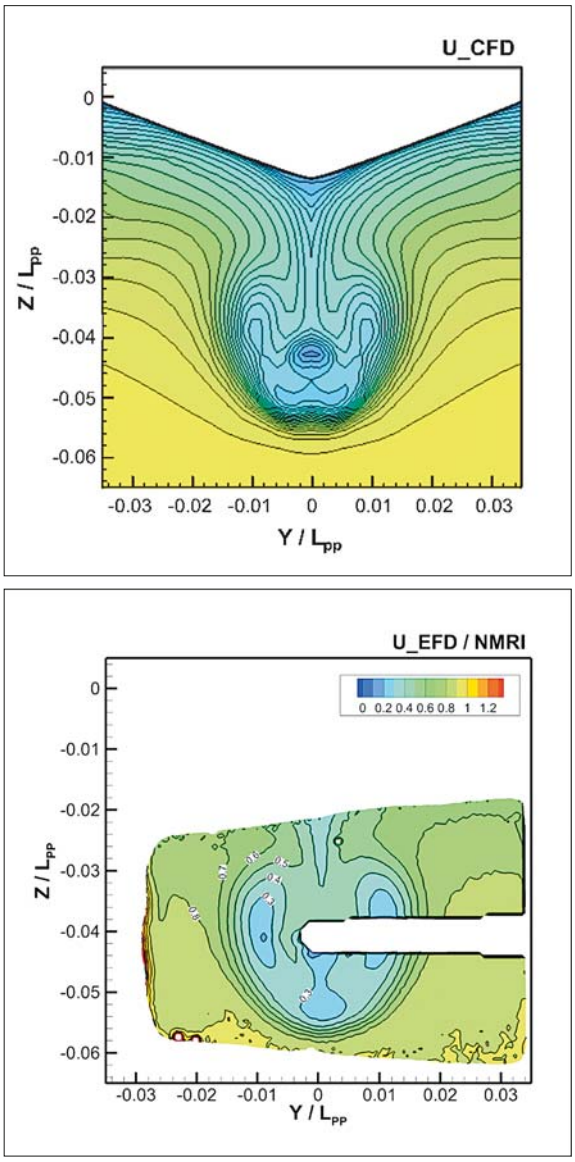

Fig. 17. Comparing computed axial velocity distributions in propeller's plane with EFD [21] in ship resistance condition

Comparing the axial velocity distributions in Fig. 17 reveals that the computed wake is in a reasonable agreement with the measured one.

In Fig. 18, the results of wake distribution demonstrate velocity acceleration and asymmetric flow configuration inside the propeller region due to propeller rotation.

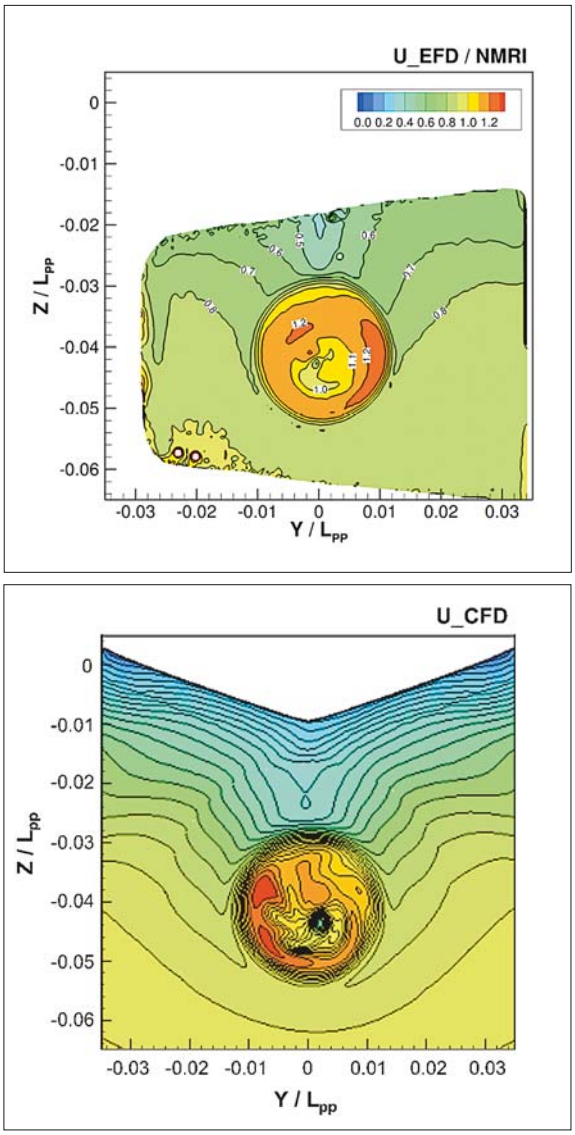

Fig. 18. Comparing computed axial velocity distributions in AP section with EFD [21] in self-propulsion condition

CONCLUSIONS

In the present study, the Unsteady RANS method has been applied to predict the coefficients of hull-propeller interaction for the JBC ship model. To obtain these coefficients, three case studies were analysed: ship resistance, propeller open-water, and self-propulsion simulations. In the resistance computations and in the self-propulsion simulation, the hull was free to trim and sink. In numerical computations of propeller open water characteristics, the rotating reference frame was used. For the propeller working behind the ship, the rigid body motion method was applied by using the sliding mesh technique.

The factors affecting the numerical accuracy of the obtained results, such as computational domain, time step, y+ value, mesh generation technique, and mesh dependency, were considered in this study.

The results of computations of individual components representing the interaction between the propeller and the ship hull, including thrust deduction (t), wake fraction (w_T), and relative rotative efficiency (η_R) showed good agreement with the experimental data. The error between computed and measured results was within 0.298 to 4.47%.

ACKNOWLEDGMENT

The authors are grateful to the Vietnam Maritime University for providing necessary research facilities during current research work.

REFERENCES

1. Tu, T.N., et al., *Numerical Study on the Influence of Trim On Ship Resistance In Trim Optimization Process*. Naval Engineers Journal, 2018. 130(4): p. 133–142.
2. Villa, D., S. Gaggero, and S. Brizzolara. *Ship Self Propulsion with different CFD methods: from actuator disk to viscous inviscid unsteady coupled solvers. in The10th International Conference on Hydrodynamics*. 2012.
3. Pacuraru, F., A. Lungu, and O. Marcu. *Self-Propulsion Simulation of a Tanker Hull. in AIP Conference Proceedings*. 2011. AIP.
4. Win, Y.N., et al., *Computation of propeller-hull interaction using simple body-force distribution model around Series 60 CB= 0.6*. Journal of the Japan Society of Naval Architects and Ocean Engineers, 2013. 18: p. 17–27.
5. Bugalski, T. and P. Hoffmann. *Numerical simulation of the self-propulsion model tests. in Second International Symposium on Marine Propulsors smp*. 2011.
6. Bekhit, A. *Numerical simulation of the ship self-propulsion prediction using body force method and fully discretized propeller model. in IOP Conference Series: Materials Science and Engineering*. 2018. IOP Publishing.
7. Seo, J.H., et al., *Flexible CFD meshing strategy for prediction of ship resistance and propulsion performance.* International Journal of Naval Architecture and Ocean Engineering, 2010. 2(3): p. 139–145.
8. Gokce, M.K., O.K. Kinaci, and A.D. Alkan, *Self-propulsion estimations for a bulk carrier.* Ships and Offshore Structures, 2018: p. 1–8.
9. Tran Ngoc Tu, N.M.C., *Comparison Of Different Approaches*

For Calculation Of Propeller Open Water Characteristic Using RANSE Method. Naval Engineers Journal, 2018. Volume 130, Number 1, 1 March 2018, pp. 105–111(7).

10. http://www.t2015.nmri.go.jp/jbc_gc.html.

11. http://www.t2015.nmri.go.jp/Instructions_JBC/instruction_JBC.html.

12. *ITTC 2011b Recommended procedures and guidelines 7.5-03-02-03*.

13. *CD-ADAPCO. User Guide STAR-CCM+, Version 13.02. 2018*.

14. Baltazar, J.M., D.R. Rijpkema, and J. Falcao De Campos. *Numerical studies for verification and validation of open-water propeller RANS computations. in Proceedings of the 6th International Conference on Computational Methods in Marine Engineering (Rome, Italy)*. 2015.

15. https://www.ittc.info/media/8169/75-03-03-01.pdf.

16. Chen, Z., *CFD investigation in scale effects on propellers with different blade area ratio*. 2015.

17. Wilcox, D.C., *Turbulence modeling for CFD*. Vol. 2. 1998: DCW industries La Canada, CA.

18. *ITTC-Quality Manual 7.5-03-01-01, 2008.*

19. https://ittc.info/media/1587/75-02-03-011.pdf.

20. Molland, A.F., S.R. Turnock, and D.A. Hudson, *Ship resistance and propulsion*. 2017: Cambridge university press.

21. http://www.t2015.nmri.go.jp/Presentations/Day1-AM2-JBC-TestData1-Hirata.pdf.

CONTACT WITH THE AUTHORS

Tran Ngoc Tu
e-mail: tutn.dt@vimaru.edu.vn

Vietnam Maritime University
Lay Tray, 1800 Hai Phong
Vietnam

sciendo

POLISH MARITIME RESEARCH 2 (102) 2019 Vol. 26; pp. 173-182
10.2478/pomr-2019-0037

THE INFLUENCE OF WATER AND MINERAL OIL ON VOLUMETRIC LOSSES IN THE DISPLACEMENT PUMP FOR OFFSHORE AND MARINE APPLICATIONS

Paweł Śliwiński
Gdańsk University of Technology, Poland

ABSTRACT

In this paper, volumetric losses in a positive displacement pump supplied with water and mineral oil are described and compared. The experimental tests were conducted using a prototype of a satellite pump (with a non-circular tooth working mechanism). In this paper, the sources of volumetric losses in this pump are characterized. On this basis, a mathematical model of these losses has been presented. The results of the calculation of volumetric losses according to the model are compared with the results of the experiment. Experimental studies have shown that the volumetric losses in the water pump are even 3.2 times greater than the volumetric losses in the oil pump. It has been demonstrated that the mathematical model describing the volumetric losses both in the water pump and in the oil pump is quite good. It has been found that the results from the loaded pump simulation (at Δp=25MPa and ant n=1500rpm) differ from the results of the experiment by no more than 5% both for oil and water.

Keywords: volumetric losses, satellite pump, water, oil

INTRODUCTION

A pump is the most important element in a hydraulic system [3-10,17,18,20,22]. Its purpose is to convert mechanical energy into hydraulic energy. The energy carrier in hydraulic systems is a liquid. The type of liquid is determined by the requirements for the system. The liquid commonly used in hydraulic systems is mineral oil. However, in some industrial sectors, the requirement is a non-flammable (mining, steel mills, etc.) or non-toxic (food industry) liquid. In such a case, non-flammable synthetic liquids, water or water-based liquids (i.e. HFA-E emulsion) are used instead of mineral oil [21,32]. Water is a liquid which is non-flammable, non-toxic and certainly suitable for energy transfer in hydraulic systems. In comparison to mineral oil, water has a very low viscosity and low lubricating properties [15]. These parameters have a significant impact on the size of mechanical, volumetric and pressure losses in hydraulic machines [22]. These losses have an impact on the energy conversion efficiency in these machines and have an impact on the noise [16,19,21,29,30,31,34]. Furthermore, the design parameters of hydraulic components have an influence on energy conversion efficiency [13,14,20,29,32].

Generally, each hydraulic device is dedicated to a specific type of working liquid. For example, a positive displacement pump dedicated to oil systems should not be used in systems where the working medium is water.

There is a growing trend in the world towards research and development of components and hydraulic systems supplied with water [2,3,13,14,21,32].

Studies of hydraulic systems, where water is the working medium, are especially important in marine technology. In offshore technology and marine applications, hydraulic power circuits are used frequently and water is generally available as a working liquid [2]. Thus, in order to eliminate the pollution of the environment and marine waters, it seems reasonable and justified to eliminate oil systems and replace them with water systems. To this end, it is necessary to develop and test innovative components for hydraulic water systems [20-25]. Thus, it was reasonable to develop a new positive displacement water pump called the satellite pump and mark it with the

PSM symbol. The pump contains an innovative operating mechanism consisting of non-circular gears [20,22-26]. The construction of this pump is described in the next section. The PSM pump can be used in a small portable power pack supplying various onboard devices on ships, rescue devices or hydraulic hand tools.

The development of the PSM pump enabled an investigation of the influence of the working liquid type (that is water and oil) on the energy losses that occur in this pump. This article is limited to the description of volumetric losses.

The impact of the type of liquid on volumetric losses in positive displacement pumps has not yet been analyzed by other researchers. In the literature, the volumetric losses in displacement machines have been describe in general, without specifying the type of clearances [1,19].

The first information about the impact of water and oil on volumetric losses in displacement machine are given in [25,28]. The biggest influence on the volumetric losses in hydraulic displacement machines has a leakage in the clearances of working mechanism [20,26,34]. It has been proved that in a displacement machine working mechanism clearances, not-fully developed turbulent flow takes place. This is particularly well visible in the case of using low viscosity liquid as a working medium [26]. Besides, in a displacement machine, there are other sources of volumetric losses, in addition to the clearances. The sources of these losses are described later in this article.

Therefore, the influence of the type of liquid on volumetric losses in a positive displacement pump is a new issue. It is cognitive and it represents an important scientific problem. Consequently, the following objectives have been defined for this article:

- indication and description of the sources of volumetric losses in a satellite pump;
- definition of the mathematical model of volumetric losses in pump working with mineral oil and with water;
- comparison of volumetric losses in a pump supplied with mineral oil and water;
- comparison of results of experimental research with the mathematical model.

SATELLITE PUMP

The experimental research on the influence of the type of liquid on volumetric losses was carried out using a prototype of a positive displacement pump that was developed by the author. For experimental tests, a prototype of a satellite pump was selected and marked with the symbol PSM-0,75 (Fig. 1). The design of this pump is presented in Fig. 2. The working mechanism of the satellite pump is a specific gear mechanism in which the rotor rotates around the shaft axis and the revolving motion is done by satellites which are in gear with the stator and the rotor (Fig. 3).

Fig.1. General view of PSM-0,75 pump [27]

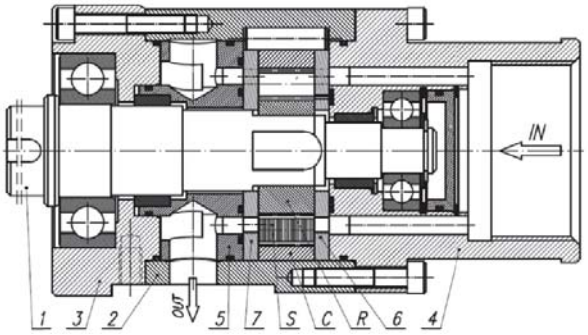

Fig.2. Axial cross section of PSM-0,75 pump [25,27]: C – curvature, S – satellite, R – rotor, 1 – shaft, 2 – casing, 3 – front casing, 4 – rear casing (suction manifold), 5 – pressure manifold, 6 and 7 – compensation (commutation) plates

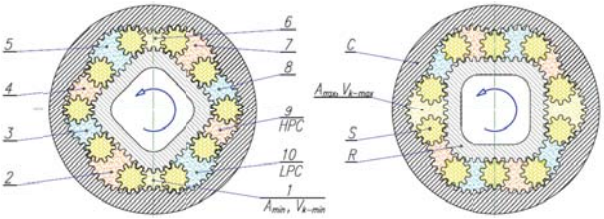

Fig.3. The working mechanism of a satellite pump [20,22-28]: C – curvature, R – rotor, S – satellite, 1÷10 – working chambers, LPC – low pressure working chamber, HPC – high pressure working chamber, $V_{k\text{-}min}$ – working chamber with minimum area A_{min} (dead chamber), $V_{k\text{-}max}$ – working chamber with maximum area Amax

The toothed unit, shown in Fig. 3, is the satellite working mechanism of the pump. It consists of a toothed rotor R (4 humps), toothed curvature C (6 humps) and ten wheels S (satellite).

The principle of operation of the satellite mechanism is that when the rotor rotates, the volume of the space between the satellites changes. This space forms the working chamber. When its volume increases, the filling cycle takes place. Conversely, when its volume decreases, the emptying cycle occurs. Twenty-four cycles correspond to one shaft revolution. The chambers in the satellite mechanism are closed by commutation plates (Fig. 2 – elements 6 and 7, Fig. 4), which also play the role of compensation plates. Thus, the satellite pump has the ability to compensate axial clearances of the rotor and the satellites [20,22-28].

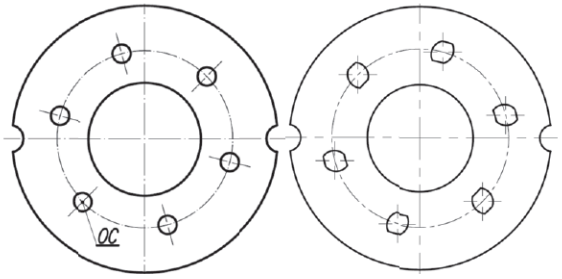

Fig.4. High pressure commutation plate (left) and suction commutation plate (right) [20,22-28]

Experimental studies of the pump PSM-0,75/15 were carried out using the following liquids:

- the Total Azolla 46 oil (parameters in temp. 43°C: kinematic viscosity ν=40cSt, density ρ=873kg/m^3, dynamic viscosity μ=35mPas);
- tap water (parameters in temp. 27°C: ν=0,85cSt, ρ=996kg/m^3).

The tested pump was characterized by the following parameters:

- theoretical displacement qt=18,63 cm^3/rev.;
- teeth module m=0,75mm;
- height of working mechanism H=15mm.

In hydraulic systems, a fixed displacement pump driven by an electric motor with a frequency converter is being used increasingly. This solution is also possible on ships. Thus, the desired pump capacity is achieved by changing its rotational speed. Therefore, it was necessary to conduct experimental tests of the pump in a wide range of rotational speeds.

TEST STAND

The PSM pump was tested on the test stand with power recuperation. The diagram of the measurement system of this test stand is shown in Fig. 5. The test stand enables testing of the pump in a wide range of rotational speed (from 30 to 1500 rpm).

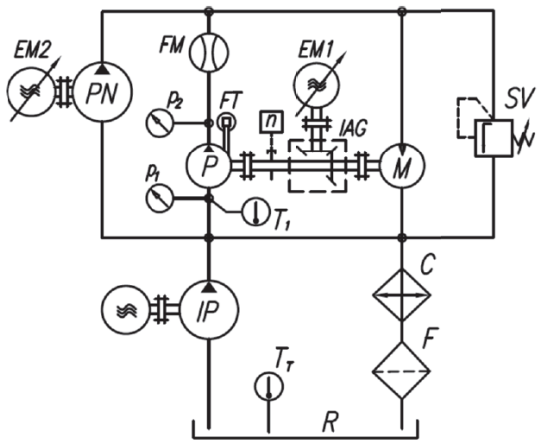

Fig.5. The diagram of the measurement system of the test stand [27]: P – tested pump, M – hydraulic motor, PN – pump for fill the leaks in P and M, IP – impeller pump (pre-supply pomp), SV – safety valve, C – cooler, F – filter, R – reservoir, IAG – intersecting axis gear, EM1 and EM2 – electric motors with frequency converters, other designations – description in the text below

During the test of the pump the following parameters were measured:

- pressure p_1 in suction port (strain gauge pressure transducer, range –1÷+3 bar, accuracy 0,3%);
- the pressure p_2 in pumping port (strain gauge pressure transducers, range 0÷25 bars and 0÷250 bars, accuracy 0,3%);
- the pump delivery Q (mass flow meter FM, range 0÷33 l/min, class 0,1);
- the torque M (strain gauge force transducer FT mounted on the arm 0,5m (arm attached to the pump body), range 0÷100N, class 0,1);
- the rotational speed of shaft n [rpm] (inductive sensor, the accuracy of measurement ±1rpm);
- the temperature T_1 of liquid in the suction port of the pump (RTD temperature sensor, class A, max. measurement error 0,5°C). The temperature of liquid was stabilized (for oil T_1=43±2 °C, for water T_1=27±2 °C).

PRESSURE DROP IN INTERNAL CHANNELS

The volumetric losses depend on the pressure increase Δp_i in the working chambers of the pump. This pressure is difficult to measure. On the other hand, it is easy to measure the pressure increase Δp in the pump ports. The relationship between Δp and Δp_i is as follows:

$$\Delta p_i = \Delta p - \Delta p_{ich} \quad (1)$$

where Δp_{ich} is the pressure drop in internal channels of the pump. The methodology of measuring Δp_{ich} is described in [23].

The internal channels have a complicated geometry. The non-fully developed turbulent flow takes place in these channels. Therefore, to describe Dpich, it is proposed to adopt the following simplified relationship [23]:

$$\Delta p_{ich} = C_t \cdot \rho \cdot Q^2 + C_l \cdot \mu \cdot Q \quad (2)$$

where C_l and C_t are coefficients that are mainly dependent on the geometrical dimensions of the internal channel. The values of these coefficients are calculated from experimental data.

SOURCES OF VOLUMETRIC LOSSES

The volumetric losses Q_{vl} in a displacement pump are calculated on the base of experimental data using the following formula:

$$Q_{vl} = q \cdot n - Q \quad (3)$$

where:

Q – effective flow of pump;

q– theoretical pump displacement;
n – pump input shaft speed.

In a satellite pump the sources of volumetric losses are:

a. the liquid flow rate in flat clearances in satellite mechanism (Fig. 6);
b. the liquid flow rate in the spaces between the teeth of the working mechanism (tip clearances Tc and backlashes G) (Fig. 7);
c. the liquid flow rate in clearances in commutation unit (short clearances) in satellite mechanism (Fig. 8);
d. the liquid flow rate caused by the cyclic elastic deformation of the working chambers, mainly due to the cyclic deformation of the stator as the element with the smallest stiffness;
e. the liquid flow rate depending on its compressibility;
f. external leakage.

In the satellite pump, the leakage Q_{Lfg} is drained to the shaft chamber (Fig. 6).

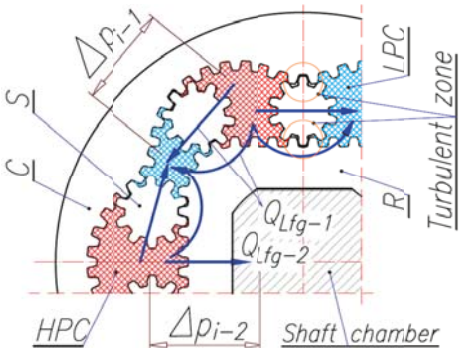

Fig.6. Flows of liquid in flat clearances [25,26,28]

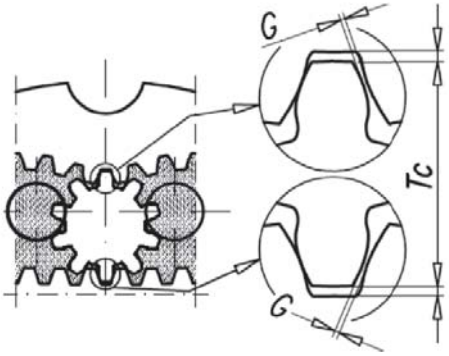

Fig.7. Tip clearance T_c and backlash G [22,27,28]

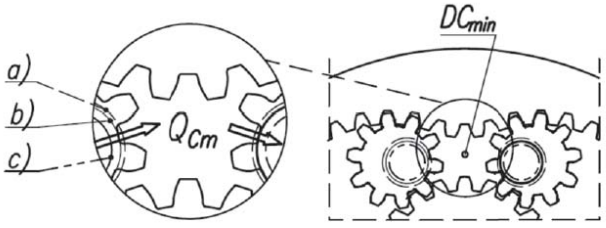

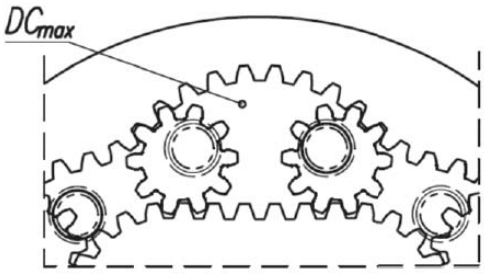

Fig.8. Flow QC in clearances of commutation unit [24]: DC_{min} – minimum volume of chamber, DC_{max} – maximum volume of chamber; a), b) and c) negative overlap, zero overlap and positive overlap, respectively

KNOWN MODELS OF VOLUMETRIC LOSSES IN A PUMP

A number of mathematical formulas have been developed over the past 50 years to characterize the flow loss in hydraulic positive displacement machine, that is in pump and hydraulic motor. For example, in last years, models of volumetric losses in a hydraulic motor were described in [1,4,11,19,25,28]. Some of them can be adopted to describe the volumetric losses in a pump if the pump is the same type like the motor (for example axial piston pump and axial piston motor). It is possible because the physical phenomena in the same type hydraulic motor and pump is similar. For example, this mathematical model is [11,4]:

$$Q_{vl} = C_\mu \cdot \frac{\Delta p}{\mu} + C_\nu \cdot n + C_V \cdot \left(\frac{\Delta p}{\rho}\right)^{0,5} + C_P \cdot \frac{\rho n^3}{\Delta p} + C_\beta \cdot n \cdot \Delta p + Q_{Lo} \quad (4)$$

where:

C_μ, C_ν, C_V, C_P, C_β – coefficients;
n – speed of pump;
C_{Lo} – constant flow loss.

Another method of describing the volumetric losses in any type of pumps is [33]:

$$Q_{vl} = (C_1 + C_5 \cdot n + C_4 \cdot n \cdot q) \cdot \Delta p + \left(C_2 + C_3 \cdot n^{3/2}\right) \cdot \Delta p^2 \quad (5)$$

where C_1, C_2, C_3, C_4 and C_5 are coefficients.

A similar mathematical model, taking into account the influence of liquid viscosity μ, is proposed in [5]:

$$Q_{vl} = \sum_{i=0}^{p} \sum_{j=0}^{q} \sum_{k=0}^{r} \sum_{l=0}^{s} \left(C_{ijkl} \cdot q^i \cdot n^j \cdot \Delta p^k \cdot \mu^l\right) \quad (6)$$

where C_{ijkl} is the coefficient.

Another way of describing the volumetric losses in a pump with constant displacement is proposed in [19]:

$$Q_{vl} = k_1 \cdot q \cdot n \cdot \left(\frac{\Delta p_i}{p_n}\right)^{a_{pv}} \cdot \left(\frac{\nu}{\nu_n}\right)^{a_{vv}} \quad (7)$$

where:

k_1, k_9, a_{pv}, a_{vv}, a_{nv} – coefficients;
p_n – nominal pressure in the hydraulic circuit;
ν_n – related kinematic viscosity (ν_n = 35cSt).

The inconvenience of these models for pumps is that they describe the volumetric losses in general, without specifying the type of gaps and other sources of these losses. In addition, the authors of these mathematical formulas do not write about whether they are suitable for the description of the volumetric losses in a pump working with low viscosity liquid like water.

NEW MODEL OF VOLUMETRIC LOSSES IN SATELLITE PUMP

The mathematical model describing the volumetric losses in hydraulic motor supplied with different liquids was presented in [25,28]. This model is dedicated to satellite motor and was designed taking into account the sources of volumetric losses into this motor. Due to the fact, that the construction of a satellite pump is based on the design of the satellite motor, the sources of volumetric losses in the pump are the same as in the motor. Therefore, it is sensible to adopt the model of volumetric losses in a satellite motor to describe the volumetric losses in a satellite pump. Thus, the volumetric losses in a satellite pump can be described with the equation [25,28] (Fig. 9):

$$Q_{vl} = Q_{Lfg} + Q_C + \Delta Q_{vl} + Q_{ex} \tag{8}$$

where:

Q_{Lfg} – the flow rate in flat clearances of the working mechanism;

Q_C – the flow rate in clearances of the commutation unit (short clearances);

ΔQ_{vl} – the increasing of flow rate;

Q_{ex} – external leakage.

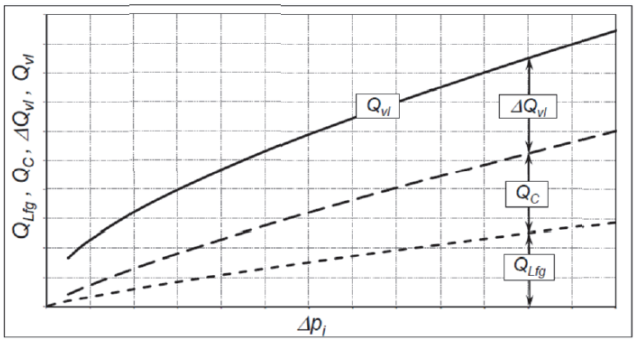

Fig.9. Characteristic of components of volumetric losses in pump

FLOW RATE Q_{LFG} IN FLAT CLEARANCES

The methodology of measuring the flow rate Q_{Lfg} in flat clearances is described in [25,26]. The flow rate Q_{Lfg} can be described by the equation [25,26]:

$$Q_{Lfg} = \left(\frac{1}{\nu}\right)^{\left(\frac{\beta}{2-\beta}\right)} \cdot \left(\frac{1}{K \cdot \rho}\right)^{\left(\frac{1}{2-\beta}\right)} \cdot A_1 \cdot m \cdot \left(\frac{2 \cdot h^3}{A_2 \cdot m}\right)^{\left(\frac{1}{2-\beta}\right)} \cdot \Delta p_i^{\left(\frac{1}{2-\beta}\right)} \tag{9}$$

where:

β – the degree of laminarity of the flow [25,26];
ν – kinematic viscosity of liquid;
ρ – density of liquid;
m – teeth module;
A_1, A_2, K – coefficients;
h – equivalent axial clearances of rotor and satellites

The equivalent axial clearances are described as [25,26]:

$$h = \frac{h_R + h_S}{2} - (D_C \cdot H + D_k) \cdot \Delta p_i \tag{10}$$

where:

h_R and h_S – respectively: axial clearance of rotor and satellites;

H – height of working mechanism (equal to height of curvature);

D_k – the coefficient depends on stiffness of axial clearance compensation unit;

D_C – the coefficient depends on stiffness of stator.

The degree of laminarity of the flow β for oil is [25,26]:

$$\beta_O = \frac{2 \cdot ln\left(E \cdot X^F\right) + ln\left(\frac{K_W}{K_O} \cdot \frac{\rho_W}{\rho_O}\right)}{ln\left(E \cdot X^F\right) + ln\left(\frac{\nu_O}{\nu_W}\right)} \tag{11}$$

where:

$$X = \frac{1}{2} \cdot \frac{m}{h^3} \cdot K_W \cdot {\nu_W}^2 \cdot \rho_W \cdot A_2 \tag{12}$$

and the "o" and "w" indices refer to oil and water respectively.

The degree of laminarity of the flow β for water is [25,26]:

$$\beta_W = 2 - \frac{2 - \beta_O}{1 + F \cdot (2 - \beta_O)} \tag{13}$$

The coefficient F is calculated from the following equation:

$$E \cdot (\Delta p_i)^F = \frac{Q_{Lfg,W}}{Q_{Lfg,O}} \tag{14}$$

where:

$Q_{Lfg,W}$ and $Q_{Lfg,O}$ – obtained from experimental data;
E – the constant.

The characteristics of $\beta = f(\Delta p_i)$ for oil and for water are shown in Fig. 10. For simplicity, it can be accepted that for both liquids in the whole range of Δp_i the β is constant.

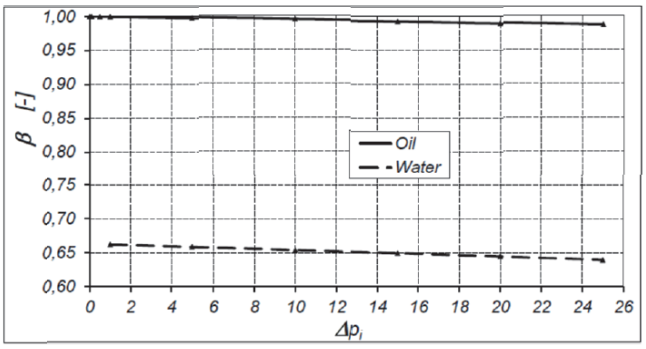

Fig.10. Degree of laminarity of the flow β in flat clearances of the pump for oil and water [25]

The values of coefficients β, A_1, A_2, K, D_k and D_C are calculated from experimental data and the methodology is shown in [25,26].

FLOW RATE Q_C IN COMMUTATION UNIT CLEARANCES

The methodology of measuring the flow rate Q_C in commutation unit clearances (Fig. 7) is described in [24,25]. The Q_C is described as [24,25]:

$$Q_C = C_1 \cdot (D_o \cdot h_s)^{C_2} \cdot \left(\frac{1}{\rho \cdot \nu^{C_3}}\right)^{\gamma} \cdot \Delta p_i{}^{\gamma} \quad (15)$$

where:

D_o – the diameter of the outflow hole in commutation plate;

C_1, C_2, C_3 and γ – coefficients.

The values of coefficients C_1, C_2, C_3 and γ are calculated from experimental data and the methodology is shown in [24,25].

COMPONENT DQ_{VL}

After determination of Q_{Lfg} and Q_C the component ΔQ_{vl} can be calculated from equation (7) (from the experiment data) as:

$$\Delta Q_{vl} = Q_{vl} - \left(Q_{Lfg} + Q_C + Q_{ex}\right) \quad (16)$$

According to [25,28] the component ΔQ_{vl} is defined as:

$$\Delta Q_{vl} = \Delta Q_{fc} + \Delta Q_{dch} + \Delta Q_b + \Delta Q_{id} \quad (17)$$

where:

ΔQ_{fc} – the flow rate depends on the compressibility of the liquid;

ΔQ_{dch} – the flow rate caused by the elastic deformation of working chambers;

ΔQ_b – the flow rate depends on the backlash size;

ΔQ_{id} – the flow rate depending on: the inertia of satellites, the inertia of the liquid in the working chambers.

The components ΔQ_{fc}, ΔQ_{dch}, ΔQ_{vb} and ΔQ_{id} are precisely described in [25].

The component ΔQ_{vl} can be also written in a general form as:

$$\Delta Q_{vl} = \Delta q \cdot n \quad (18)$$

where Δq is the increase in displacement [cm³/rev].

INCREASE IN DISPLACEMENT Δq

It follows from equations (3), (15) and (17) that:

$$\Delta q = q - \frac{Q + Q_{Lfg} + Q_C + Q_{ex}}{n} \quad (19)$$

In [25,28] it has been shown that Δq can be described by the formula:

$$\Delta q = \left(C \cdot \Delta p_i + \frac{C_{id}}{n^{0,5}}\right) \cdot m^2 \cdot H \quad (20)$$

where C and C_{id} are coefficients. The values of these coefficients are calculated from the experiment.

EXTERNAL LEAKAGE

The source of external leakage Q_{ex} is the lack of tightness in pump ports. In normal pump operation conditions, Q_{ex} cannot occur and then Q_{ex}=0.

MODEL OF VOLUMETRIC LOSSES

The volumetric losses Q_{vl} in the pump, expressed by the formula (8), in a developed form are as follows [25]:

$$Q_{vl} = \left(\frac{1}{\nu}\right)^{\left(\frac{\beta}{2-\beta}\right)} \cdot \left(\frac{1}{K \cdot \rho}\right)^{\left(\frac{1}{2-\beta}\right)} \cdot A_1 \cdot m \cdot \left(\frac{2 \cdot h^3}{A_2 \cdot m}\right)^{\left(\frac{1}{2-\beta}\right)} \cdot \Delta p_i{}^{\left(\frac{1}{2-\beta}\right)} + B_1 \cdot (D_o \cdot h_s)^{B_2} \cdot \left(\frac{1}{\rho_O \cdot \nu_O{}^{B_4}}\right)^{B_3} \cdot \Delta p_i{}^{B_3} + \left(C \cdot \Delta p_i + \frac{C_{id}}{n^{0,5}}\right) \cdot m^2 \cdot H \cdot n \quad (21)$$

RESULTS OF EXPERIMENT

The test of the pumps prototype was conducted in a wide range of rotational speed n in order to show the pumps performance and possibility to work with an electric drive equipped with a frequency converter.

The experimentally determined characteristics Q_{vl} (divided into components $Q_{Lfg} + Q_C$ and ΔQ_{vl}) as a function of pressure increase Δp_i in the working chambers are shown in Fig. 11 and in Fig. 12.

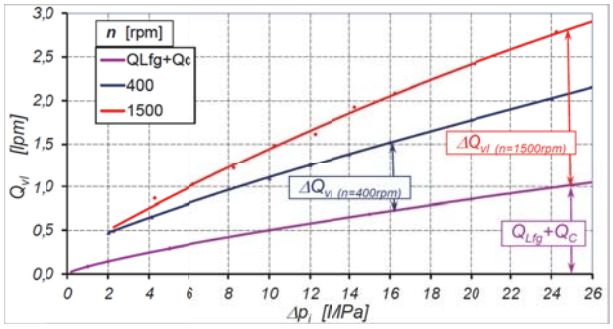

Fig.11. Characteristics of $Q_{vl}=f(\Delta p_i)$. Working medium: oil

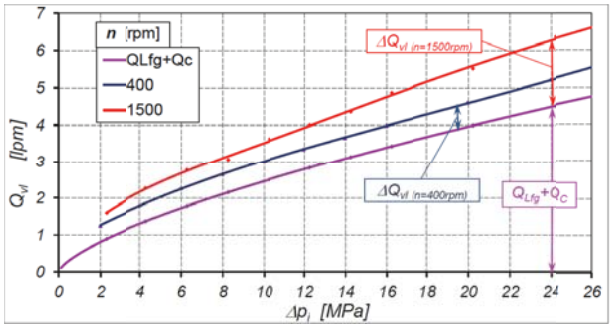

Fig.12. Characteristics of $Q_{vl}=f(\Delta p_i)$. Working medium water

The characteristics of Δq vs Δp_i designated according to (19) from experimental data are shown in Fig. 13 and in Fig. 14.

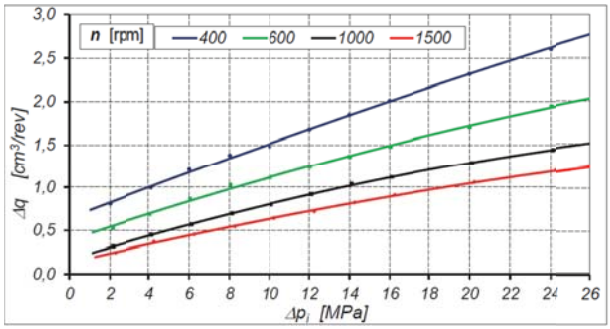

Fig.13. Experimental characteristics of $\Delta q=f(\Delta p_i)$. Working medium: oil

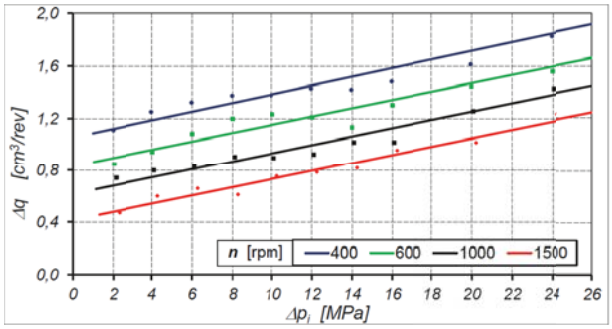

Fig.14. Experimental characteristics of $\Delta q=f(\Delta p_i)$. Working medium: water

The values of all mathematical model coefficients are calculated from experimental data and given in Tab. 1.

Tab.1. Values of coefficients in volumetric losses model for pump PSM-0,75 [24,25,26]

	A_1	A_2	β	K_O
	[-]	[-]	[-]	$\left[\frac{m}{MPa \cdot s}\right]$
Oil	0,145	0,17	0,99	1,141
Water	0,145	0,17	0,65	1,0
	C_1	C_2	C_3	C_{id}
	[-]	[-]	[-]	$\left[\frac{1}{(obr \cdot min)^{0,5}}\right]$
Oil	0,154	1,26	0,684	1,18
Water	2,5	1,05	0,183	2,37
	C_1	C_t	γ	C
	[-]	[-]	[-]	$\left[\frac{1}{MPa \cdot obr}\right]$
Oil	$0{,}583 \cdot 10^{-5}$	$0{,}282 \cdot 10^{-7}$	0,76	$5{,}12 \cdot 10^{-3}$
Water	$0{,}343 \cdot 10^{-3}$	$0{,}146 \cdot 10^{-7}$	0,55	$3{,}56 \cdot 10^{-3}$

RESULTS OF CALCULATIONS

Based on the formula (20) the characteristics of $\Delta q=f(\Delta p_i)$ are plotted in Fig. 15 and in Fig. 16.

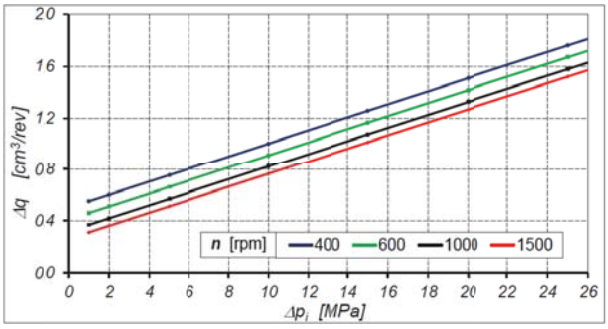

Fig.15. Characteristics of $\Delta q=f(\Delta p_i)$ – the result of calculation according to formula (20). Working medium: oil

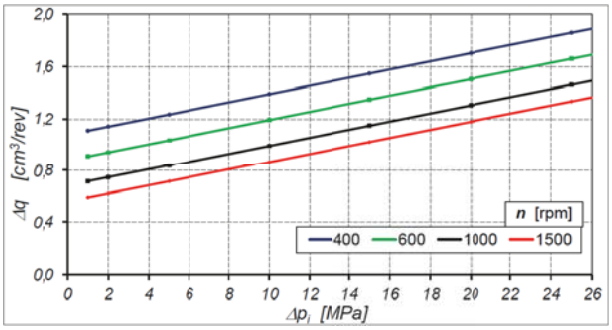

Fig.16. Characteristics of $\Delta q=f(\Delta p_i)$ – the result of calculation according to formula (20). Working medium: water

The characteristics of $Q_{vl}=f(\Delta p_i)$, plotted according to the formula (20), are shown in Fig. 17 and in Fig. 18.

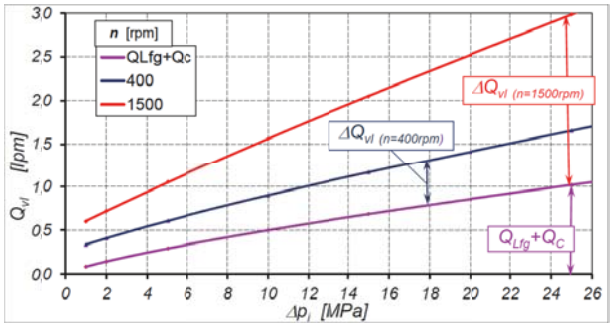

Fig.17. Characteristics of $Q_{vl}=f(\Delta p_i)$ – the result of calculation according to formula (21). Working medium: oil

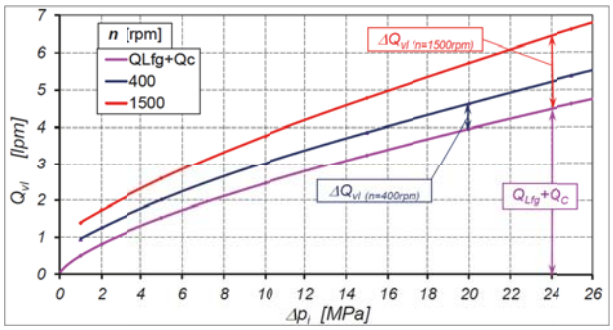

Fig.18. Characteristics of $Q_{vl}=f(\Delta p_i)$ – result of calculation according to formula (21). Working medium: water

DISCUSSION

The research results prove that the volumetric losses in the pump pumping water are at most three times greater than the volumetric losses in the pump pumping oil (Fig. 19). The greatest difference is observed in the pump working at low speed. Furthermore, for n=const., the ratio of $\frac{Q_{vl-w}}{Q_{vl-o}}$ is variable and decreases with increasing Δp. The smallest value of $\frac{Q_{vl-w}}{Q_{vl-o}}$ is observed for the biggest values of n.

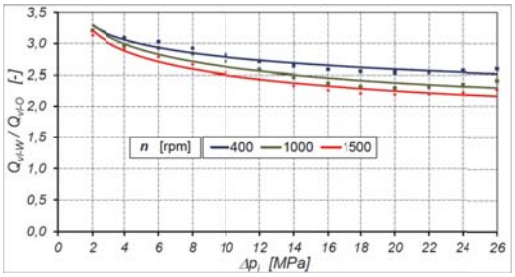

Fig.19. Characteristics of $\frac{Q_{vl-w}}{Q_{vl-o}} = f(\Delta p_i)$

The values of volumetric losses (both for oil and water) in the pump, calculated according to the formula 21), differ from the values determined experimentally. These differences are defined as:

$$\delta Q_{vl} = \frac{Q_{vl} - Q_{vl(calc)}}{Q_{vl}} \cdot 100\% \quad (22)$$

The characteristics of $\delta Q_{vl}=f(\Delta p_i)$ for oil and for water are shown in Fig. 20 and Fig. 21 respectively.

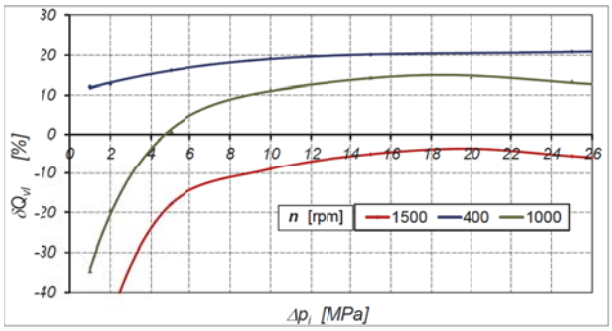

Fig.20. Characteristics of $\delta Q_{vl}=f(\Delta p_i)$. Working medium: oil

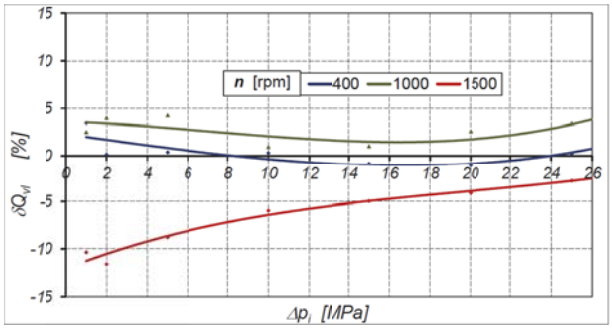

Fig.21. Characteristics of $\delta Q_{vl}=f(\Delta p_i)$. Working medium: water

It turns out that the greatest impact on the accuracy of calculation of the volumetric losses has the accuracy of calculation of the change of pump displacement Δq. The Δq calculated according to (20) gives the biggest mistake in the range of small values of rotational speed n (the biggest differences are observed for n < 600 rpm – Fig. 13 ÷ Fig. 16).

SUMMARY

The article presents the results of experimental research on volumetric losses in the newest satellite pump, for which the working medium was water and mineral oil. The experimental studies have shown that the type of liquid has an impact on the values of losses. The volumetric losses are bigger in a water pump than in an oil pump – especially at low loads Δp and low speeds n.

Experimental tests have also shown that the PSM pump can operate at a low rotational speed. It is recommended that the minimum speed is 400 rpm. At lower speed, there is too much leakage in relation to the pump capacity, which results

in a significant decrease in the pump's volume efficiency. Therefore, the experiment was done at a minimum rotational speed of 400 rpm.

Experimental studies have shown that the greatest source of volumetric losses in the pump is leakages in the working mechanism.

The mathematical model of volumetric losses in satellite motor has been adopted and developed for satellite pump. This model is based on an analysis of the sources of leakages in the pump. The coefficients in the mathematical model were calculated on the basis of the experimental data. This mathematical model quite accurately describes the volumetric losses in a satellite pump working with both mineral oil or water. For a pump speed of 1500 rpm (typical for pumps) and operating pressure above 8 MPa, the differences between simulation results and test results do not exceed 10%. Therefore, the volumetric losses in the pump supplied with various liquids can be assessed by comparison of the model coefficients.

The mathematical model presented in this article, is a component of a model of overall efficiency of the pump.

REFERENCES

1. Balawender A.: Physical and mathematical model of losses in hydraulic motors. Developments in mechanical engineering, Gdansk University of Technology Publishers. Gdansk 2005, Poland

2. Dymarski C., Dymarski P.: Developing Methodology for Model Tests of Floating Platforms in Low-Depth Towing Tank. Archives of Civil and Mechanical Engineering, No 1/2016, DOI: dx.doi.org/10.1016/j.acme.2015.07.003.

3. Guzowski A., Sobczyk A.: Reconstruction of hydrostatic drive and control system dedicated for small mobile platform. American Society of Mechanical Engineers, 2014 doi: dx.doi.org/10.1115/FPNI2014-7862.

4. Hall S., Steward B.: Comparison of steady state flow loss models for axial piston pumps. 53rd, Fluid power; 2014 IFPE Technical Conference; Where all the Solutions Come Together and Connections are Made; 2014. Las Vegas, USA.

5. Ivantysyn J., Ivantysynova M., Hydrostatic pumps and motors, principals, designs, performance, modelling, analysis, control and testing. New Delhi, 2000. Akademia Books International.

6. Jasinski R.: Influence of design of hydraulic components on their operation in low ambient temperatures. Key Engineering Materials, Vol. 490, 2012. DOI:10.4028/www.scientific.net/KEM.490.106.

7. Jasinski R.: Problems of the starting and operating of hydraulic components and systems in low ambient temperature. Part IV. Modelling the heating process and determining the serviceability of hydraulic components during the starting-up in low ambient temperature. Polish Maritime Research, No 3 (95) 2017. DOI: 10.1515/pomr-2017-0089.

8. Jasinski R.: Problems of the starting and operating of hydraulic components and systems in low ambient temperature. Part I. Polish Maritime Research, No 4/2008. DOI: doi.org/10.2478/v10012-007-0095-9.

9. Jasinski R.: Problems of the starting and operating of hydraulic components and systems in low ambient temperature. Part II. Polish Maritime Research, No 1/2009. DOI: doi.org/10.2478/v10012-008-0012-x.

10. Jasinski R.: Problems of the starting and operating of hydraulic components and systems in low ambient temperature. Part III. Methods of determining parameters for correct start-ups of hydraulic components and systems in low ambient temperatures. Polish Maritime Research, No 4/2009. DOI: doi.org/10.2478/v10012-008-0052-2.

11. Jeong H-S.: A novel performance model given by the physical dimensions of hydraulic axial piston motors: model derivation. Journal of mechanical science and technology, Vol. 21, No 1/2007. DOI: doi.org/10.1007/BF03161714.

12. Kollek W., Osinski P., Warzynska U.: The influence of gear micro pump body asymmetry on stress distribution. Polish Maritime Research, No 1/2017. DOI: doi.org/10.1515/pomr-2017-0007.

13. Litwin W., Dymarski C.: Experimental research on water lubricated marine stern tube bearings in conditions of improper lubrication and cooling causing rapid bush wear. Tribology International Vol. 95 (2016). DOI: 10.1016/j.triboint.2015.12.005.

14. Litwin W., Olszewski A.: Water-Lubricated Sintered Bronze. Journal Bearings - Theoretical and Experimental Research. Tribology Transactions, vol. 57, No. 1/2014. DOI: 10.1080/10402004.2013.856980.

15. Lubinski J., Sliwinski P.: Multi parameter sliding test result evaluation for the selection of material pair for wear resistant components of a hydraulic motor dedicated for use with environmentally friendly working fluids. Solid State Phenomena, No 225/2015. DOI: doi.org/10.4028/www.scientific.net/SSP.225.115.

16. Maczyszyn A.: Investigation method and mathematical model of pressure losses in hydraulic rotary motor. Polish Maritime Research, No. 97/2018 Vol. 25. DOI: 10.2478/pomr-2018-0011.

17. Osinski P., Chruscielski G.: Strength calculations of an element compensating circumferential backlash in the external gear pump. Journal of Theoretical and Applied Mechanics. Vol. 54, No. 1/2016. DOI: 10.15632/jtam-pl.54.1.251.

18. Osinski P., Deptula A., Partyka M.: Discrete optimization of a gear pump after tooth root undercutting by means of multi-valued logic trees. Archives of Civil and Mechanical Engineering, No 4/2013, DOI: 10.1016/j.acme.2013.05.001.

19. Paszota Z.: Energy losses in hydrostatic drive. LABERT Academic Publishing, 2016.

20. Patrosz P.: Deformation in the axial clearance compensation node in the satellite pump unit. Hydraulika i Pneumatyka 1/2014, Poland.

21. Pobedza J., Sobczyk A.: Properties of high pressure water hydraulic components with modern coatings. Advanced Materials Research. Trans Tech Publications Ltd, 849/2014. DOI: 10.4028/www.scientific.net/AMR.849.100.

22. Sliwinski P.: New satellite pumps. Key Engineering Materials, No 490/2012. DOI: doi.org/10.4028/www.scientific.net/KEM.490.195.

23. Sliwinski P.: Pressure losses and power balance in the unloaded satellite pump. Hydraulika a Pneumatika, No 1-2/2013.

24. Sliwinski P.: Influence of water and mineral oil on the leaks in satellite motor commutation unit clearances. Polish Maritime Research. Vol. 24, 3 (95) 2017. DOI: 10.1515/pomr-2017-0090.

25. Sliwinski P.: Satellite displacement machines. Basis of design and analysis of power loss. Gdansk University of Technology Publishers, 2016.

26. Sliwinski P.: The flow of liquid in flat gaps of satellite motors working mechanism. Polish Maritime Research, No 2/2014. DOI: 10.2478/pomr-2014-0019.

27. Sliwinski P.: The influence of water and mineral oil on mechanical losses in the displacement pump for offshore and marine applications. Polish Maritime Research. Vol. 25, Special Issue S1 (97) (2018). DOI: 10.2478/pmr-2018-0040.

28. Sliwinski P.: The influence of water and mineral oil on volumetric losses in a hydraulic motor. Polish Maritime Research. Vol. 24. Special Issue S1 (93) (2017). DOI: 10.1515/pomr-2017-0041.

29. Stosiak M., Kollek W., Osiński P., Cichon P., Wilczynski A.: Problems relating to high-pressure gear micro pumps. Archives of Civil and Mechanical Engineering, No 1/2014. DOI: 10.1016/j.acme.2013.03.005.

30. Stosiak M.: The impact of hydraulic systems on the human being and the environment. Journal of Theoretical and Applied Mechanics, Vol. 53 No 2/2015. DOI: 10.15632/jtam-pl.53.2.409 .

31. Stosiak M.: The modeling of hydraulic distributor slide–sleeve interaction. Archives of Civil and Mechanical Engineering, No 2/2012. DOI: 10.1016/j.acme.2012.04.002.

32. Walczak P., Sobczyk A.: Simulation of water hydraulic control system of francis turbine. American Society of Mechanical Engineers, 2014. DOI: dx.doi.org/10.1115/FPNI2014-7814.

33. Zarotti G., Nevegna N.: Pump efficiencies - approximation and modeling. Fluids quarterly, No 14/1983.

34. Zloto T., Nagorka A.: An efficient FEM for pressure analysis of oil film in a piston pump. Applied Mathematics and Mechanics, vol.30, No 1/2009. DOI: 10.1007/s10483-009-0106-z.

CONTACT WITH THE AUTHOR

Paweł Śliwiński
e-mail: pawel.sliwinski@pg.edu.pl

Gdańsk University of Technology
Narutowicza 11/12
80-233 Gdansk
Poland

sciendo

POLISH MARITIME RESEARCH 2 (102) 2019 Vol. 26; pp. 183-197
10.2478/pomr-2019-0038

DESIGN OF JACK-UP PLATFORM FOR 6 MW WIND TURBINE: PARAMETRIC ANALYSIS BASED DIMENSIONING OF PLATFORM LEGS

Paweł Dymarski
Gdańsk University of Technology, Poland

ABSTRACT

The article presents the results of the research conducted within the framework of the project entitled WIND-TU-PLA (ERA-NET, MARTEC II), the general aim of which was to design and analyse supporting structures for wind turbines intended for operation on the South Baltic area. The research part described in the article aimed at developing a preliminary design for a jack-up platform which can operate on water areas with depth of 40 m. The main task was to determine optimal dimensions of platform legs and the radius of their spacing. Two jack-up platform concepts differing by spacing radius and hull dimensions were designed with the intention to be used as a supporting structure for a 6-MW offshore wind turbine. For each concept, the parametric analysis was performed to determine optimal dimensions of platform legs (diameter Dleg and plating thickness tleg). Relevant calculations were performed to assess the movements of the platform with parameters given in Table 1 in conditions simulating the action of the most violent storm in recent 50 years. The obtained results, having the form of amplitudes of selected physical quantities, are shown in comprehensive charts in Fig. 6 and 7. Based on the critical stress values (corresponding to the yield stress), the area was defined in which the impact strength conditions are satisfied (Fig. 14).
Then, the fatigue strength analysis was performed for two selected critical leg nodes (Fig. 12). Its results were used for defining the acceptable area with respect to structure's fatigue (Fig. 14). Geometric parameters were determined which meet the adopted criteria, Table 6. The decisive criterion turned out to be the fatigue strength criterion, while the yield point criterion appeared to be an inactive constraint.

Keywords: support structure, jack-up platform, offshore wind turbine, fatigue, sea loads, parametric study, Morison equation

INTRODUCTION

The history of offshore wind energy utilisation began in 1991, when the first offshore wind farm (Vindeby) was installed in Denmark. Until the end of 2017, the total power output of offshore wind power plants amounted to nearly 19GW [1]. The leading countries in this area are: UK (6836MW), Germany (5355MW), PR China (2788MW), Denmark (1271), Netherlands (1118), and Belgium (877). The contribution of other countries is insignificant.

So far in Poland (year 2018), no offshore wind farms have been built, but significant investors, such as PGE, PKN Orlen, and Polenergia, include building offshore farms in the Polish Exclusive Economic Zone in their development plans. Here, the investment leader is Polenergia, which was the first to obtain the environmental decision for the offshore farm Central Baltic III in July 2016, and then, in April 2017, for the next farm Central Baltic II. The expected total power output of these two farms is 1200MW [2].

At present, offshore wind farms are being built on solid support structures. However, prototypes of floating power plants have also been tested, and in October 2017, a mini floating farm was built which consisted of 5 spar-type platforms – project Hywind [3].

A natural tendency is to build supporting structures which can be installed at increasing depths. Therefore, it is floating structures which attract growing interest of researches and designers. Already, there are designs, and even demonstrators, of semi-submersible platforms [4, 5]. Moreover, the Tension Leg Platform structures have been designed and tested [6, 7, 8]. Numerical analyses have been performed for spar-type platforms [9, 10, 11]

This article presents the results of the research conducted within the framework of the project entitled WIND-TU-PLA, the general aim of which was to design and analyse supporting structures for wind turbines intended for operation on the South Baltic area. The research part described in the article aimed at developing a preliminary design for a jack-up platform which can operate on water areas with depth of about 40 m. The main task was to determine optimal dimensions of platform legs and the radius of their spacing. An assumption was made that the platform rests on three legs. The main criterion was the fatigue strength of the structure on welds. The calculations were performed based on nominal stresses.

Fatigue analyses of supporting structures which utilise plating model-based FEM calculations can be found in [12, 13, 14], while the use of the beam model for analysing the jack-up platform is described in [15].

The jack-up platform belongs to the family of platforms resting on solid base. The platform consists of the deck (platform), a number of legs with feet at their lower ends, and auxiliary devices used for lowering/lifting of legs during installation or change of working area. The concept of the jack-up platform intended to be analysed in this project assumes that the module used for leg lowering/lifting is interchangeable, which makes the production and installation costs of a single platform significantly lower.

The jack-up platform has its own displacement, which allows it to be towed to the destination place. The platform should have positive stability during transportation (when its legs are lifted up).

The advantage of platforms resting on solid structures is their very limited response (movements) to environmental excitations (wind, waves). As a rule, the amplitude of motion of such a platform does not exceed 1 m, even in storm conditions.

Since the platform is supported on three or more legs of very similar length and in similar support conditions, it can be basically assumed that the platform only moves in the horizontal plane, while possible deck rotations about horizontal *Oy*- and *Ox*-axes are very small, and vertical movements are completely negligible.

During the operation, the platform hull (pontoon) stays always over water surface and hydromechanical excitations generated by waves and currents act only on the platform legs. A relatively high position of the platform deck is also favourable with respect to bending moments carried by the turbine tower and the platform as a result of aerodynamic forces acting on the wind turbine.

It was assumed in the project that the jack-up platform can be used on water areas with depth from 30 to 50 m. At greater depths, it seems more profitable economically to use floating platforms, while at smaller depths traditional solutions, such as monopile, jacket, tripod, etc, function sufficiently well [16, 17].

Tripile-type platforms have already been installed at similar depths (up to 50m) (Fig. 1). The advantage of the triple-type platform is its relatively simple structure (platform elements are permanently fixed to each other). However, proper preparation of the foundation is required in this case, and the platform elements can only be installed using special (large) vessel. Moreover, a platform of this type does not have own displacement, nor hydromechanical stability during transportation.

Fig.1. Tripile-type platforms – project BARD offshore 1 – Germany. Approximate depth of water area 40m [www.windpoweroffshore.com,www.hadel.net]

The main problems which had to be solved when designing the preliminary prototype of the jack-up platform included determining the amplitude of motion of the hull and the nacelle, and assessing the internal forces carried by the main structural components (legs, tower, hull) as functions of dimensions of basic platform components. The performed parametric analysis made the basis for determining boundaries of the acceptable area with respect to structural loads. Moreover, parameters were determined which best fulfilled a given target function (stress minimisation, or structure mass minimisation for the assumed acceptable stresses, for instance).

CALCULATION MODEL FOR PARAMETRIC ANALYSIS

For the purpose of the parametric analysis, a simplified model with two degrees of freedom (DOFs) was developed. The first DOF was the linear (horizontal) motion of platform hull, while the second DOF was the linear (horizontal) motion of nacelle with turbine.

The platform hull rests on three legs anchored to the seabed. Each leg ends with a foot of larger diameter, the underside of which has the shape of an inverted cone or pyramid, Fig. 2. The legs are permanently fixed to the hull. The nacelle and the hull are connected together by the tower (single tube) permanently fixed to the hull. It is assumed that the tower column can freely rotate at the nacelle side, due to small moment of inertia of the nacelle with turbine (bending moment equal to zero).

It was assumed at the preliminary stage that the stiffness of the hull is much larger than that of the legs and tower (the hull does not deform). Due to this large hull stiffness and due to the fact that the hull is supported on three legs, the hull rotation about the horizontal axis which is perpendicular to

the wave propagation direction *Oy* does not exist. That means that the rotations of leg ends are blocked at points of their connection with the hull. Similarly, the rotation of the tower at the point of its connection with the hull is also blocked. Another simplifying assumption which was adopted is that the ground under the platform is so flexible that it does not block the leg rotation. Consequently, an articulated joint was assumed at lower end of each leg (which is a conservative approach). The structural scheme of the platform is shown in Fig. 3.

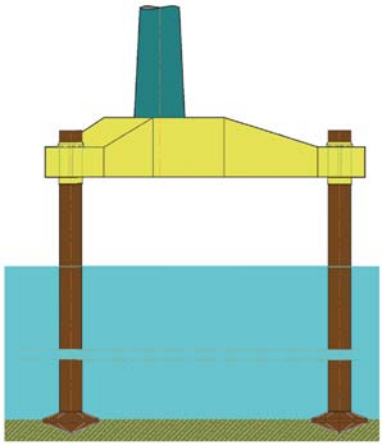

Fig. 2. Scheme of jack-up platform foundation

The stiffness of a single leg with respect to horizontal hull motion is:

$$k_{1leg}=\frac{3\,EI_{leg}}{l_{leg}^3}\ , \tag{1}$$

Then, the stiffness of the joint between hull and nacelle with respect to relative horizontal hull/nacelle motion is:

$$k_{tower}=\frac{3\,EI_{tower}}{l_{tower}^3}\ , \tag{2}$$

where:

E is the modulus of elasticity of steel,

I_{leg}, I_{tower} are the moments of inertia of the cross sections of a single leg and the tower, respectively,

l_{leg}, l_{tower} are the length of the legs and the height of the tower (measured from pontoon deck to turbine axis), respectively, see Table 2.

The above formulas were used for creating the structural stiffness matrix in the simplified model.

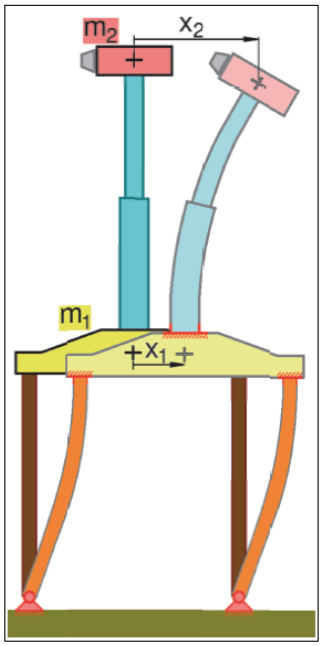

Fig. 3 Structural strength scheme of jack-up platform with tower. Determining degrees of freedom.

STIFFNESS MATRIX. EQUATION OF PLATFORM MOTION

Stiffness matrix

The forces acting on the hull and nacelle as a result of dislocation of main structure nodes are given by the formula [18, 19]:

$$\begin{bmatrix}F_1^{stiff}\\F_2^{stiff}\end{bmatrix}=-\begin{bmatrix}k_{1,1} & k_{1,2}\\k_{2,1} & k_{2,2}\end{bmatrix}\begin{bmatrix}x_1\\x_2\end{bmatrix}, \tag{3}$$

where:

F_1^{stiff}, F_2^{stiff} are the generalised forces resulting from dislocation of relevant structure nodes (1 or 2); $k_{i,j}$ are the stiffness matrix elements which define the force acting at the i-th node due to (elementary) dislocation of the j-th node, and x_1, x_2 are the node dislocations.

Elements of stiffness matrix:

$k_{1,1}$ - describes the force acting at node 1 as a result of elementary node dislocation with respect to the immovable remaining nodes and supports:

$$k_{1,1}=n_{leg}k_{1leg}+k_{tower}\ , \tag{4}$$

where:

n_{leg} is the number of platform legs.

$k_{1,2}$, $k_{2,1}$ – describe the force acting at node 1 as a result of elementary dislocation of node 2, and the force acting at node 2 as a result of elementary dislocation of node 1:

$$k_{1,2}=k_{2,1}=-k_{tower} \tag{5}$$

$k_{2,2}$ – describes the force acting at node 2 as a result of elementary dislocation of this node:

$$k_{2,2}=k_{tower} \tag{6}$$

The structural model of the platform is linear, but the external excitations acting on the platform and the turbine have the form of aero- and hydrodynamic forces described by the expanded Morison equation [20,7]. The force acting on the *i*-th fragment of the structure (leg segment, for instance) is given by the formula:

$$F_{x,i}=\frac{1}{2}C_{D,x}\rho A_{p,x}|u-\dot{x}|(u-\dot{x})+\rho V_b(1+C_{A,x})\frac{\partial u}{\partial t}-\rho V_b C_{A,x}\ddot{x} \quad , \tag{7}$$

where
$C_{D,x}$ is the drag coefficient in the *x* direction,
ρ is the fluid density,
$A_{p,x}$ is the projection of the segment area onto the *x* direction,
u is the fluid velocity component in the *x* direction,
V_b is the volume of the segment (fragment of structure),
$C_{A,x}$ is the added water mass coefficient in the *x* direction,
$\dot{x}$, $\ddot{x}$ are the segment velocity and acceleration in the *x* direction, respectively.

The main force acting on the nacelle is the turbine thrust force [21], which should be additionally complemented by the aerodynamic drag force acting on the upper part of the tower:

$$F_2=\frac{1}{2}C_T\rho_{air}A_T|u_{w,2}-\dot{x}_2|(u_{w,2}-\dot{x}_2) +\frac{1}{2}C_{D,tower}\rho_{air}A_{p,tower}|u_{w,2}-\dot{x}_2|(u_{w,2}-\dot{x}_2) \quad , \tag{8}$$

where C_T is the turbine thrust coefficient, $C_{D,tower}$ is the tower drag coefficient, ρ_{air} is the air density, A_T is the turbine circle area, $A_{p,tower}$ is the tower projection onto the *x* direction, $\dot{x}_2$ is the velocity of node 2 (nacelle), and $u_{w,2}$ is the wind velocity at the nacelle height.

The forces acting on the platform hull (pontoon) can be described as:

$$F_1=F_{1,hydro}(t)+\frac{1}{2}C_{D,hull}\rho_{air}A_{p,hull}|u_{w,1}-\dot{x}_1|(u_{w,1}-\dot{x}_1) \quad . \tag{9}$$

The first term on the right-hand side of Equation 9 represents the hydrodynamic forces (this issue will be discussed further in the article), while the second term represents the aerodynamic thrust force acting on the hull. $C_{D,\mathrm{hull}}$ is the hull (pontoon) drag coefficient, $A_{p,hull}$ is the projection of the hull surface area onto the *x* direction, $\dot{x}_1$ is the velocity of node 1 (hull), and $u_{w,1}$ is the wind velocity at the hull height.

The forces acting directly on the platform (hull) are relatively small. The main external excitation being the source of platform motion is the excitation acting on platform legs. The elementary force acting on the leg segment of length δ*z* is [20]:

$$\delta F_{sect}=\frac{1}{2}C_D\rho A_{p,sect}|u-\dot{x}_{sect}|(u-\dot{x}_{sect}) +\rho V_{b,sect}(1+C_A)\frac{\partial u}{\partial t}-\rho V_{b,sect}C_A\ddot{x}_{sect} \quad , \tag{10}$$

where: C_D, C_A are the drag coefficient and the added mass coefficient of legs (see table 2), ρ is the water density, $A_{p,sect}$ is the projection of the surface area of the structure segment onto the x direction, $V_{b,sect}$ is the (submerged) volume of the structure segment, *u* is the water velocity, and , $\dot{x}_{sect}$, $\ddot{x}_{sect}$ are the velocity and acceleration of the structure segment, respectively.

Let us consider the platform leg as a beam resting on two supports: seabed at the bottom (simple support), and platform at the top (blocked rotation). If the force F_{sect} acts on the leg segment, then the leg acts on the platform with the force equal to the reactive force at the support [22]:

$$\delta F_{1,hydro}=\delta F_{sec}\left[1-\frac{a^2}{2l_{leg}^3}(3l_{leg}-a)\right], \tag{11}$$

where $a = z_{hull} - z_{sect}$ is the distance between the segment of concern and the point of leg-hull fixing.

Finally, the total hydromechanical force passed from the legs to the platform is:

$$F_{1,hydro}(t)=\sum_{i_{leg}}\int_{-d}^{0}q(z,t)\left[1-\frac{(z_{hull}-z)^2}{2l_{leg}^3}(3l_{leg}-(z_{hull}-z))\right]dz \tag{12}$$

The continuous load *q(z)* acting on platform legs can be determined from Equation 13:

$$q(z,t)=\frac{1}{2}C_D\rho D_{leg}|u-\dot{x}|(u-\dot{x}) +\rho\frac{\pi D_{leg}^2}{4}(1+C_A)\frac{\partial u}{\partial t}-\rho\frac{\pi D_{leg}^2}{4}C_A\ddot{x} \tag{13}$$

The water velocity *u=u(x,z,t)* is calculated based on the theory of waves (the Airy model, or the second-order Stokes model [18, 19, 20, 23, 24]). The position *x=x(z,t)* of a given leg section and its derivatives (velocity and acceleration) are given by the hull position x_1 and the modal function of leg deflection, which can be approximately defined (based on support conditions) as:

$$x(z,t)=x_1(t)\psi(z)$$

where

$$\psi(z)=\sin\left[\frac{\pi(z-z_{base})}{2l_{leg}}\right] \tag{14}$$

The last term in Equation 13 represents the force acting on the legs during the accelerated motion, and is related with the presence of the added mass. The acceleration of a selected leg section can be determined via double differentiation of Equation 14

$$\ddot{x}(z,t)=\ddot{x}_1\psi(z) \tag{15}$$

If we define the last term in Equation 9 as $q_{am}(z,t)$, i.e.:

$$q_{am}(z,t)=-\rho\frac{\pi D_{leg}^2}{4}C_A\ddot{x} \tag{16}$$

then the force passed to the platform can be obtained from Equation 8 as:

$$F_{1,am}(t)=-m_a\ddot{x}_1 \tag{17}$$

where the added mass m_a is calculated from formula:

$$m_a=\rho\frac{\pi D_{leg}^2}{4}C_A\sum_{i_{leg}}\int_{-d}^{0}\psi(z)\left[1-\frac{(z_{hull}-z)^2}{2l_{leg}^3}\left(3l_{leg}-(z_{hull}-z)\right)\right]dz, \tag{18}$$

or:

$$m_a=n_{leg}\rho\frac{\pi D_{leg}^2}{4}d\cdot C_A f_{1,am},$$

where:

$$f_{1,am}=\frac{1}{d}\int_{-d}^{0}\psi(z)\left[1-\frac{(z_{hull}-z)^2}{2l_{leg}^3}\left(3l_{leg}-(z_{hull}-z)\right)\right]dz \tag{19}$$

The coefficient $f_{1,am}$ represents part of the added mass which contributes to the increase of the force of inertia at a given node of the structure (here: platform hull) as a result of the motion of this node. The above coefficient ranges from 0 to 1. The diagram of its changes as a function of relative leg draught d/l_{leg} for boundary conditions as in the discussed issue is shown in Fig. 4

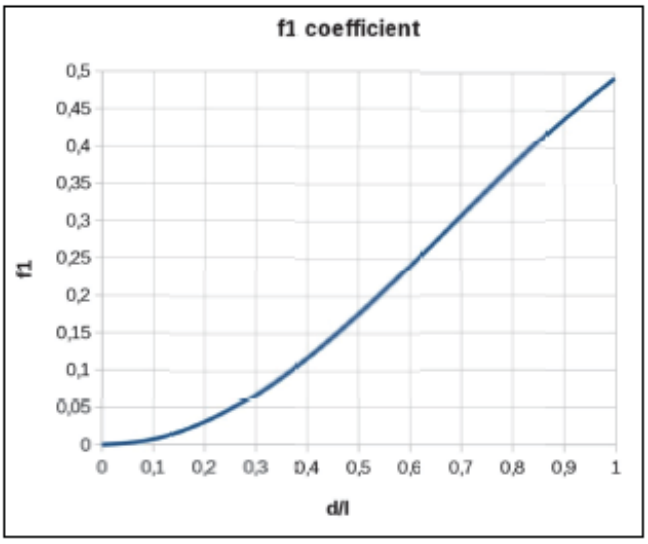

Fig. 4. Coefficient f_1 describing the contribution of leg related added water mass to platform hull inertia as function of relative leg draught d/l_{leg}

Equation of platform motion

The equation of motion of the platform as an object with two degrees of freedom has the following form:

$$\begin{bmatrix}m_1 & 0\\ 0 & m_2\end{bmatrix}\begin{bmatrix}\ddot{x}_1\\ \ddot{x}_2\end{bmatrix}+\begin{bmatrix}k_{1,1} & k_{1,2}\\ k_{2,1} & k_{2,2}\end{bmatrix}\begin{bmatrix}x_1\\ x_2\end{bmatrix}=\begin{bmatrix}F_1(x_1,\dot{x}_1,\ddot{x}_1,u)\\ F_2(x_2,\dot{x}_2,\ddot{x}_2,u_{w,2})\end{bmatrix} \tag{20}$$

where m_1, m_2 are the masses of relevant nodes of the structure (hull, nacelle, see Fig. 3) with part of the mass of the elements connecting these nodes (legs, tower).

Although this equation does not include explicitly a damping term, damping is present in the right-hand side of the excitation vector $[F_1\ F_2]^T$. Due to nonlinear nature of damping, it cannot be explicitly "extracted".

DESCRIPTION OF SELECTED HYDRO-METEOROLOGICAL CONDITIONS

It was assumed in the model that the platform can be subjected to the action of wind, waves and sea currents. The effect of sea currents on platform dynamics is relatively small, and usually has the form of intensified damping of platform motion. It was assumed in the calculations that for the wind velocity $u_{w,2}$=25m/s, which is the value similar to those recorded in violent storms, the surface water velocity is $u_{curr}(0)$=0.45 m/s. It was also assumed that the vertical velocity distribution profile below sea surface is exponential (Equation 21) [18]. This distribution profile was confirmed in measurements performed at the Maritime Institute in Gdansk [23].

$$u_{curr}(z)=\left(1+\frac{z}{d}\right)^{1/7}\cdot u_{curr}(0) \tag{21}$$

The analysis was performed using weather conditions corresponding to the most violent storm in recent 50 years. The following wave conditions were assumed as a result of statistical data processing at the Maritime Institute in Gdansk [23]:

Significant wave height: H_s=9.01m, peak period: T_p=11.3s, peak shape coefficient: γ=4.14.

The waves were modelled using the JONSWAP spectrum [24].

The method to determine the velocity and acceleration of fluid particles based on the assumed wave spectrum can be found in [24, 16, 23].

The analyses were performed for the 50-years' storm with time duration of 3600 seconds. Prior to that, the analysis of results had been performed for three variants of waves in such a storm, which differed by random parameters. Then, one variant was selected in which the highest wave was recorded, along with the highest amplitude of structural response.

For the above wave parameters, the obtained significant amplitude of the horizontal water velocity component is $u_{A,1/3,z=0}$ =2.8 m/s at surface and $u_{A,1/3,z=-40m}$ =1.3 m/s near the seabed. Taking additionally into account the range of leg diameter changes (Table 1), we arrive at the range of the Keulegan-Carpenter number K_C=4-11. The maximal (and also dominating) value of the added water mass coefficient

within this range of K_C is: C_A=1.0 [25, 23]. The assumed drag coefficient is C_D=1.0, which is the smallest value in the above range of K_C (conservative approach).

The calculations were performed for the following wind velocities at turbine axis height:
$u_{w,2}$=25m/s, $u_{w,2}$=11.4m/s and $u_{w,2}$=0m/s

The velocity $u_{w,2}$=25m/s is the velocity of turbine shut-down, while $u_{w,2}$=11.4m/s is the velocity of maximal turbine thrust, and $u_{w,2}$=0m/s represents the zero (average) thrust. This last velocity corresponds to minimal real thrust and the resulting minimal aerodynamic damping, which is why this state can generate relatively high amplitudes.

The results obtained for $u_{w,2}$=25m/s are less favourable than those for $u_{w,2}$=11.4m/s, as the turbine thrust is significantly smaller [27, 28], with the resulting smaller damping of the motion generated by aerodynamic forces. The least favourable conditions are for $u_{w,2}$=0m/s. However, it was decided that the absence of wind combined with the presence of maximal waves is a highly unlikely variant. For statistical reasons, this case cannot be the subject of the fatigue analysis making use of Weibull distribution.

The results presented further in the article refer to the case $u_{w,2}$=25m/s.

DESCRIPTION OF SELECTED MODEL PARAMETERS AND DETERMINING THEIR RANGES

The main model parameters are those describing the geometry of platform legs: diameter D_{leg} and plating thickness t_{leg}.

The next parameter whose effect on the dynamics of the structure was analysed was the leg spacing radius r_{leg}, i.e. the distance of legs from central platform axis.

The first two parameters are decisive for leg strength characteristics: stiffness EI_{leg} and bending coefficient $W_{leg}=2I_{leg}/D_{leg}$,

The third parameter affects the mass of the hull (length of platform "arms") and the distribution of axial forces in legs, due to the action of the moment generated by the turbine thrust force.

The matrix of parameters for which the calculations were performed is given in Table 1:

Tab.1. Matrix of parameters of jack-up platform

	r_{leg} = 20 m			r_{leg} = 25 m		
	D_{leg}=2.8 m	D_{leg}=3.2 m	D_{leg}=3.6 m	D_{leg}=2.8 m	D_{leg}=3.2 m	D_{leg}=3.6 m
t_{leg}=50 mm	x	x	x	x	x	x
t_{leg}=60 mm	x	x	x	x	x	x
t_{leg}=70 mm	x	x	x	x	x	x

The remaining geometric/mass parameters are collated in Table 2. The hull masses M_{hull} have been approximately determined based on a preliminary draft of the structure, which was used for assessing the hull plating surface area. The assumed average thickness of plating was t_p=20mm.

Tab.2. Main quantities assumed in calculations

Mass of hull "alone" (for r_{leg}=20 m and r_{leg}=25 m)	M_{hull}=520 t, 600 t
Mass of nacelle with turbine	$m_{nacelle}$=480 t
Length of legs, to platform bottom	l_{leg0}=52 m
Length of legs assumed in calculations (including hull height)	l_{leg}=54 m
Height of tower (from deck to turbine axis)	h_{tower}=75 m
Height of turbine axis	h_{turb}=95 m
Tower diameter in lower part (to half length)	$D_{1,tower}$=6.25 m
Tower plating thickness in lower part	$t_{1,tower}$=35 mm
Tower diameter in upper part (to half length)	$D_{2,tower}$=5.5 m
Tower plating thickness in upper part	$t_{2,tower}$=25 mm
Added mass coefficient of legs	C_A=1.0
Drag coefficient of legs	C_D=1.0
Drag coefficient of tower	$C_{D,tower}$=0.8

The turbine data were selected based on the manufacturer's data [26]. However, since the manufacturer does not make all data available (aerodynamic coefficients, for instance), some of the assumed values, turbine thrust coefficient CT, for instance, were taken from the description of the reference turbine of the US National Renewable Energy Laboratory – NREL 5MW [27]. Also, the 6MW DOWEC turbine has similar coefficients [28].

Tab.3. Turbine data for jack-up platform. The data of turbines SENVION and NREL included for comparison.

Type	Senvion 6.2M	NREL 5 MW	**Value assumed for simulations**
Turbine power	6.15MW	5 MW	**6 MW**
Rated wind speed	14.0 m/s	11.4 m/s	**11.4 m/s**
Max working speed of wind	30 m/s	25 m/s	**25 m/s**
Diameter of rotor	126 m	126 m	**126 m**
RPM range	7.7 – 12.1 rpm	6.9 – 12.1 rpm	-
Mass of nacelle+rotor	480 tonnes	350 tonnes	**480 tonnes**
Height of rotor axis	85 m – 117 m	90 m	**95 m**
Thrust coefficient C_T (11.4 m/s, 25 m/s)	N/A	0.73, 0.074	**0.73, 0.074**

RESULTS OF PARAMETRIC ANALYSIS

The results of the parametric analysis are presented in the form of time-histories of the following quantities: position x and acceleration $\ddot{x}$ of nacelle and hull, longitudinal stresses in platform legs $\sigma_{n,leg}$ and in tower plating $\sigma_{n,tower}$, and maximal bending moments in platform legs M_{leg} and in tower M_{tower}.

The diagrams of position, acceleration, stresses and bending moments for the selected set of parameters are shown in Fig. 5 a-d. These diagrams, together with those obtained from calculations for other sets of parameters, have made the basis for preparing bar graphs of extreme values as functions of leg diameter D_{leg} and plating thickness t_{leg} (see Fig. 6-7).

These bar graphs can be used for determining the range of acceptable solutions and selecting a point, or area, which is optimal with respect to the assumed criteria.

Additionally, the diagrams in Figs. 8-9 present the mass of the structure (without nacelle and turbine) as a function of parameters.

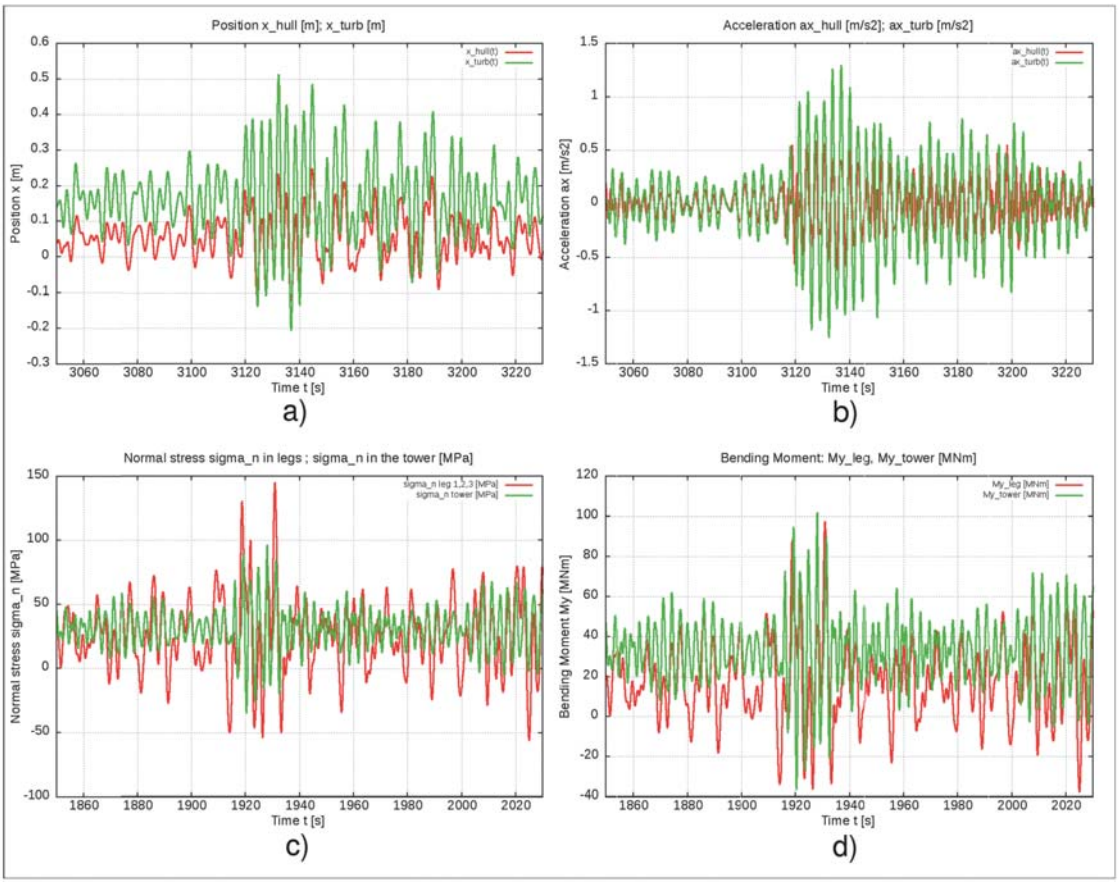

Fig. 5. Platform variant: r_{leg} = 25 m, D_{leg}=3.6 m, t_{leg}=70 mm. Sea conditions: H_s=9.0 m, T_p=11.3 s, γ=4.14, wind speed U_w=25 m/s. Time-histories of: a) longitudinal oscillations of hull and nacelle: $x_{hull} = x_{hull}(t)$, $x_{turb} = x_{turb}(t)$; b) longitudinal accelerations (along x-axis) of hull and nacelle: $a_{x,hull} = a_{x,hull}(t)$, $a_{x,turb} = a_{x,turb}(t)$; c) normal stresses in hull legs $\sigma_{n,leg}$ and in tower plating $\sigma_{n,tower}$; d) maximal bending moments in hull legs $M_{y,leg}$ and in tower plating $M_{y,tower}$.

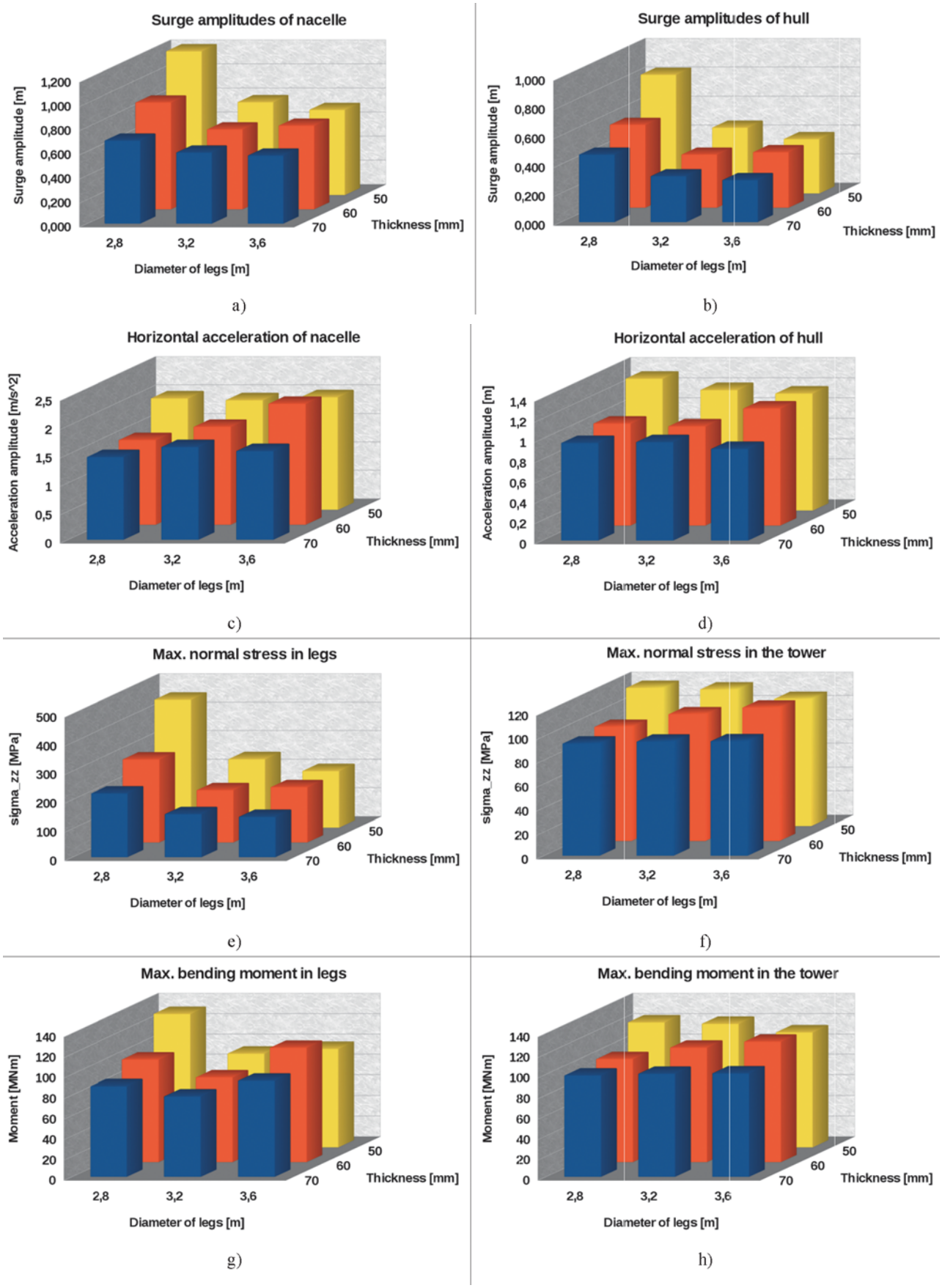

Fig. 6. Jack-up platform, r_{leg}=20m: a-d) Amplitudes of movements and accelerations of nacelle and hull; e), f) maximal stresses in hull legs and in tower plating, g), h) internal forces in hull legs and in tower plating.

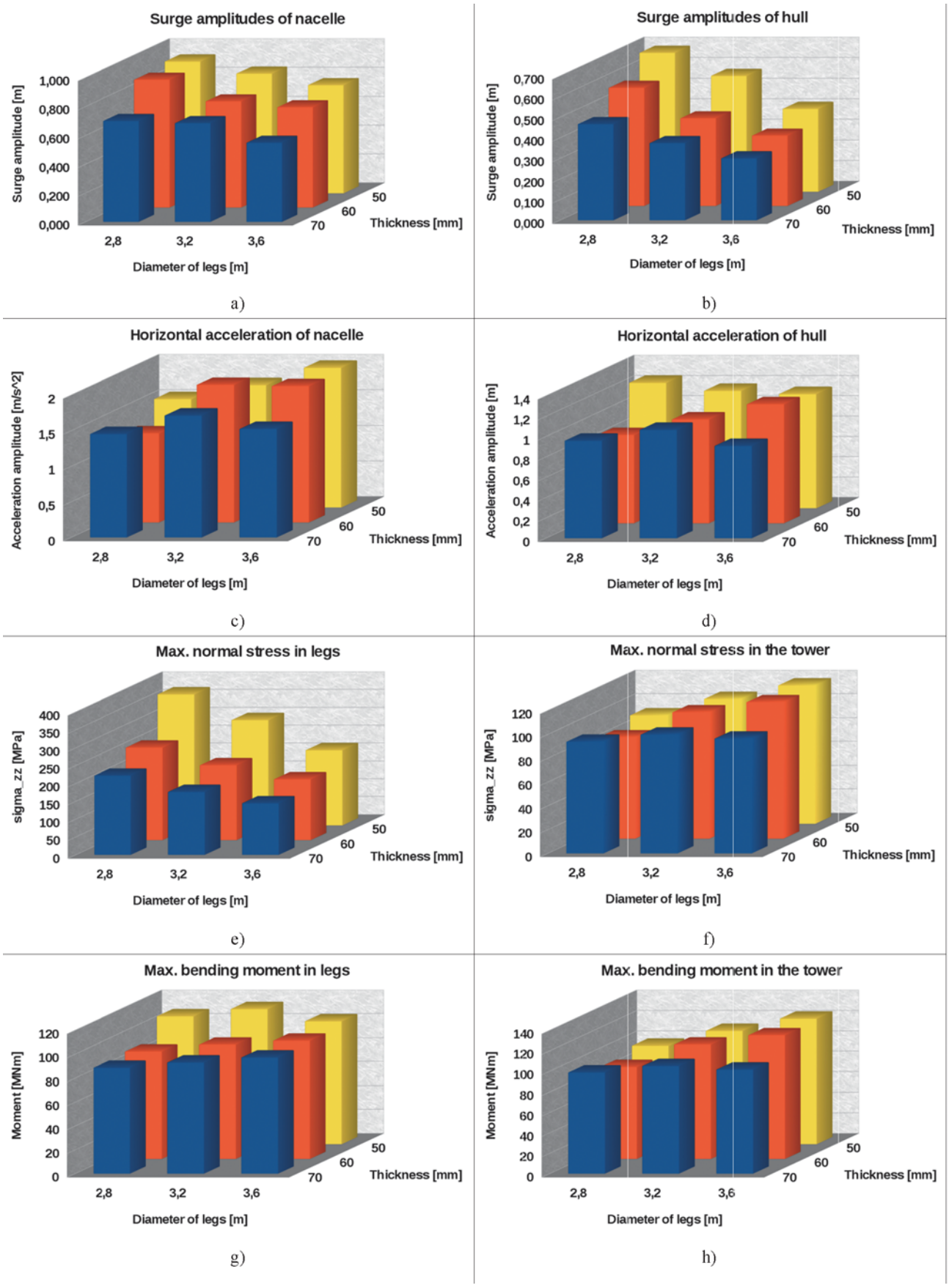

Fig. 7 Jack-up platform, r_{leg}=25m: a-d) Amplitudes of movements and accelerations of nacelle and hull as functions of parameters D_{leg} and t_{leg} ; e), f) maximal stresses in hull legs and in tower plating, g), h) internal forces in hull legs and in tower plating.

Additionally, Table 4 collates the masses of the structure as a function of parameters. The mass of steel is a decisive factor for the price of the structure, it also affects the price of its transportation and installation. This way, it is a factor which limits, for economic reasons, the area of applicable solutions.

The mass of the structure increases with the increase of leg diameter and plating thickness. On the other hand, the stresses in platform legs decrease with the increase of leg diameter and/or plating thickness. The mass and stress bar graphs are shown in Fig. 8 and Fig. 9. They reveal that the optimal solution should be searched on the line of acceptable stresses. Determining the acceptable values at selected nodes will be discussed in detail in the next Chapter.

Table 4. Mass matrix of jack-up platform structure as function of parameters. The presented values include the masses of hull, legs, and tower, but exclude the masses of nacelle and turbine.

	r_{leg} = 20 m			r_{leg} = 25 m		
	D_{leg}=2.8 m	D_{leg}=3.2 m	D_{leg}=3.6 m	D_{leg}=2.8 m	D_{leg}=3.2 m	D_{leg}=3.6 m
t_{leg}=50 mm	*1465 t*	*1553 t*	*1641 t*	*1545 t*	*1633 t*	*1721 t*
t_{leg}=60 mm	*1588 t*	*1694 t*	*1800 t*	*1668 t*	*1774 t*	*1880 t*
t_{leg}=70 mm	*1712 t*	*1835 t*	*1959 t*	*1792 t*	*1915 t*	*2039 t*

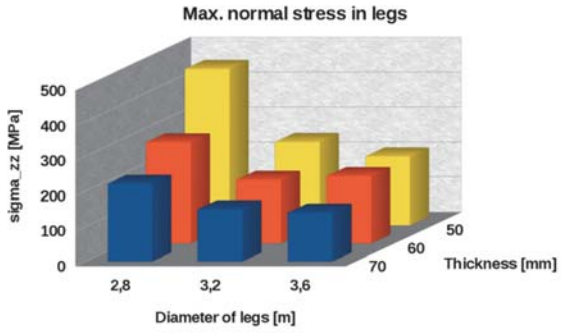

a)

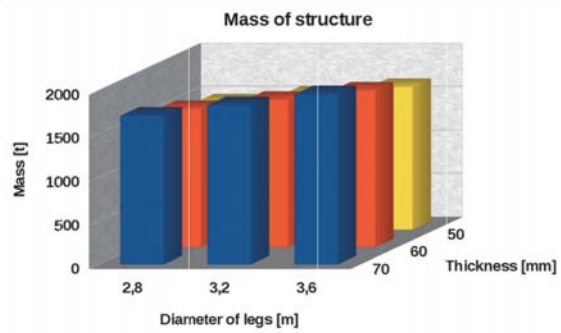

b)

Fig. 8. Bar graphs of maximal stresses in legs (a) and platform mass (b) as functions of parameters D_{leg} and t_{leg} for platform leg spacing radius r_{leg} = 20 m.

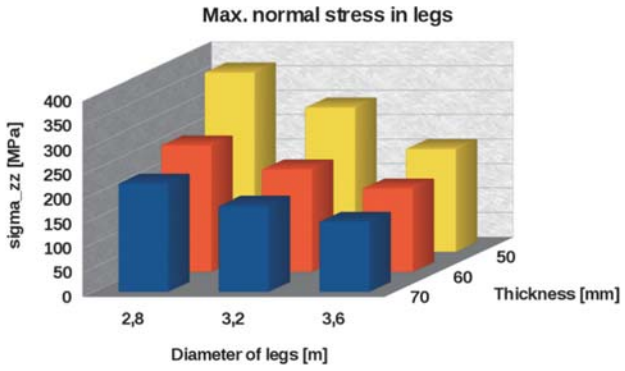

a)

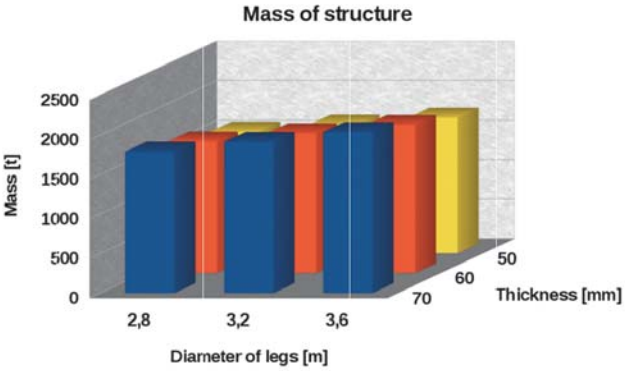

b)

Fig. 9. Bar graphs of maximal stresses in legs (a) and platform mass (b) as functions of parameters D_{leg} and t_{leg} for platform leg spacing radius r_{leg} = 25 m.

CRITERION RESULTING FROM FATIGUE STRENGTH OF THE STRUCTURE

A basic criterion which should be taken into account when analysing the jack-up platform structure is fatigue strength. A simplified fatigue analysis was performed based on two-parameter Weibull distribution.

The main parameter describing the material effort is the largest stress range $\Delta\sigma_0$ recorded during n_0 cycles [29]

The range of normal stresses $\Delta\sigma_n$ was determined from the stress time-history shown in Fig. 10. The diagram presents stresses in platform legs, in the area close to leg fixing to the hull.

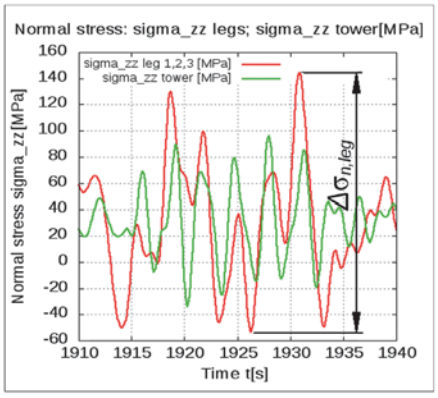

Fig. 10 Time-histories of stresses in legs $\sigma_{n,leg}$ (red), and in tower $\sigma_{n,tower}$ (green). Definition of maximal stress range $\Delta\sigma_{n,leg}$

The above definition of maximal stress range $\Delta\sigma_n$ was used to analyse the stress time-histories for the above matrix of cases. The results of this analysis are shown as bar graphs in Fig. 11.

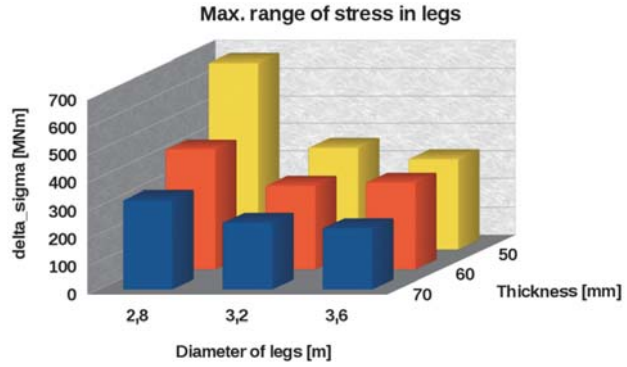

a)

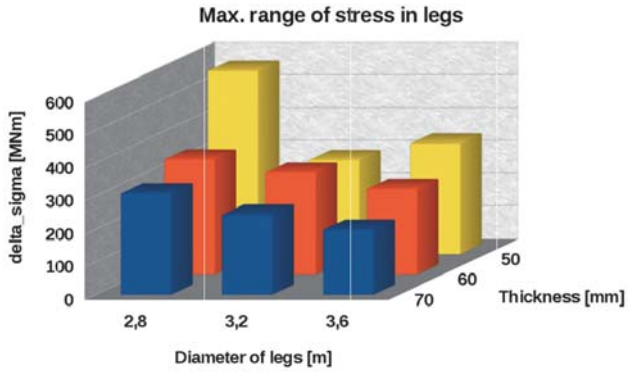

b)

Fig. 11 Maximal stress range $\Delta\sigma_{n,leg}$ for platform with leg spacing diameter: a) r_{leg} = 20 m, b) r_{leg} = 25 m

DETERMINING ACCEPTABLE STRESS RANGE

Before determining the acceptable stress range $\Delta\sigma_{all}$, the structure node (weld) should be selected which is most vulnerable with respect to fatigue strength.

Bearing in mind that the planned analysis is of preliminary nature and precise geometry in the areas of leg fixing to the hull and foots is not known yet, nodes were selected in leg (tube) parts situated beyond these areas.

Two nodes were selected, (see Fig. 12):

1. Node 1 was situated in the area of maximal bending moment appearance, i.e. in the leg part close to the hull and above water surface.

2. Node 2 was situated in the submerged part of the leg, in the area of maximal bending moment appearance, close to water surface.

An additional assumption was made that a transverse weld is situated in each of these areas, and the stress comes mainly from leg bending due to horizontal movements of the platform.

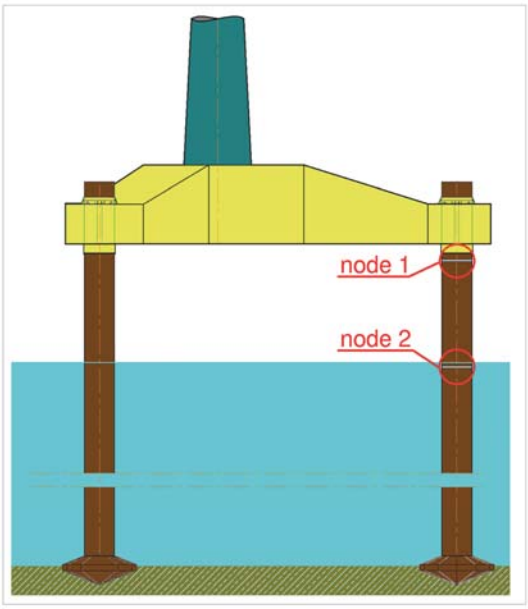

Fig. 12. Positions of structure nodes at which fatigue strength was analysed

FATIGUE STRENGTH ANALYSIS AT NODE 1

According to the relevant regulations [29] (Table A-9 and Table A-5), the C-type S-N curve was applied to the transverse weld shown in Fig. 12 as node 1. The assumed shape parameter of the adopted Weibull distribution was h=1.0.

The number of cycles expected during the platform lifetime, t_{life}=20 years, was determined as equal to 1.0·108, assuming that the duration of one cycle is T=6.3 s (as the average wave period).

For the C-type S-N curve and the shape coefficient h=1.0, the acceptable stress range for a structural element situated in air is $\Delta\sigma_{all}$ = 377.2 MPa ([29] Table 5-2).

The above stress range is given for the reference thickness, which is equal to t_{ref}=16 mm for pipe joints and 25 mm for remaining joints ([29], Par. 2.4.)

Correction of acceptable stresses due to wall thickness

When the plating/element thickness is greater than t_{ref}, the acceptable stress range is equal to ([29], Par. 5.2):

$$\Delta\sigma_{all,t} = \Delta\sigma_{all,tref}\left(\frac{t_{ref}}{t}\right)^k \quad (22)$$

The exponent k given in Table 2-3 [29] for pipe joints is k=0.25.

The acceptable stress ranges, calculated as a function of thickness t, are equal to:

$\Delta\sigma_{all,50mm}$ = 283.7 MPa; $\Delta\sigma_{all,60mm}$ = 271.1 MPa; $\Delta\sigma_{all,70mm}$ = 260.8 MPa

Design Fatigue Factor DFF

Design fatigue factors are used to decrease the likelihood of appearance of fatigue damage. The *DFF* value depends on the importance (function) of the structural element, as well as

on the accessibility (and frequency) of inspections of a given structure fragment, along with possible future repairs. [29]

If the consequences of structural damage are assessed as small and the structure meets the requirements of ALS [Accidental Limit States], then the following *DFF* values apply (depending on inspection accessibility) [30]:

Tab.5. Design fatigue factors, DFF, in relation to structure area [30]

DFF	*Structural element*
1	Internal structure, accessible and not welded directly to the submerged part.
1	External structure, accessible for regular inspection and repair in dry and clean conditions.
2	Internal structure, accessible and welded directly to the submerged part.
2	External structure not accessible for inspection and repair in dry and clean conditions.
3	Non-accessible areas, areas not planned to be accessible for inspection and repair during operation.

Although the platform leg parts situated above water surface are easily accessible for inspection, a pessimistic variant was assumed that no structure repairs are planned during 20 years of platform operation. Consequently, the assumed DFF value based on Table 5 is *DFF*=3.

After 20 years, a general overhaul of the structure (with possible repairs of elements) is planned to receive approval for its further operation.

The utilisation factor, read from [29], Table 5-8 for *DFF*=3 and t_{life}=20 years, is η=0.33. The considered node is in the air, above water surface.

The utilisation factor η=0.33 and the assumed Weibull distribution shape parameter *h*=1 were used for determining the acceptable stress reduction coefficient, C_r=0.748 ([29], Table 5-5)

The final reduced acceptable stress was calculated from formula:

$$\Delta\sigma_{all,t,\eta} = C_r \cdot \Delta\sigma_{all,t} \tag{23}$$

Hence:

$\Delta\sigma_{all,50mm,0.33}$ = 0.748·283.7 MPa = 212.2MPa
$\Delta\sigma_{all,60mm,0.33}$ = 0.748·271.1 MPa = 202.8 MPa
$\Delta\sigma_{all,70mm,0.33}$ = 0.748·260.8 MPa = 195.1 MPa

The nominal stress ranges obtained from the platform dynamics calculations are shown in Fig 11.

These ranges should be properly increased if the stress concentration resulting from connecting elements with different plating thickness takes place at the analysed node ([29], Par. 3.3). Moreover, the stress concentration increases when the connected leg segments are not coaxial and/or with deviations from roundness.

The stress concentration coefficient for the pipe joint of two elements with the same plating thickness is given by formula [29]:

$$SCF = 1 + \frac{3(\delta_m - \delta_0)}{t} e^{-\alpha} \tag{24}$$

where:

δ_m – maximal plating eccentricity, see Fig. 13.

δ_0 – characteristic eccentricity for S-N data for butt welds. For pipe joints δ_0=0.05t.

L – weld face width

$\alpha = \frac{0.91L}{\sqrt{Dt}}$, where D is the diameter of the connected elements (here $D=D_{leg}$)

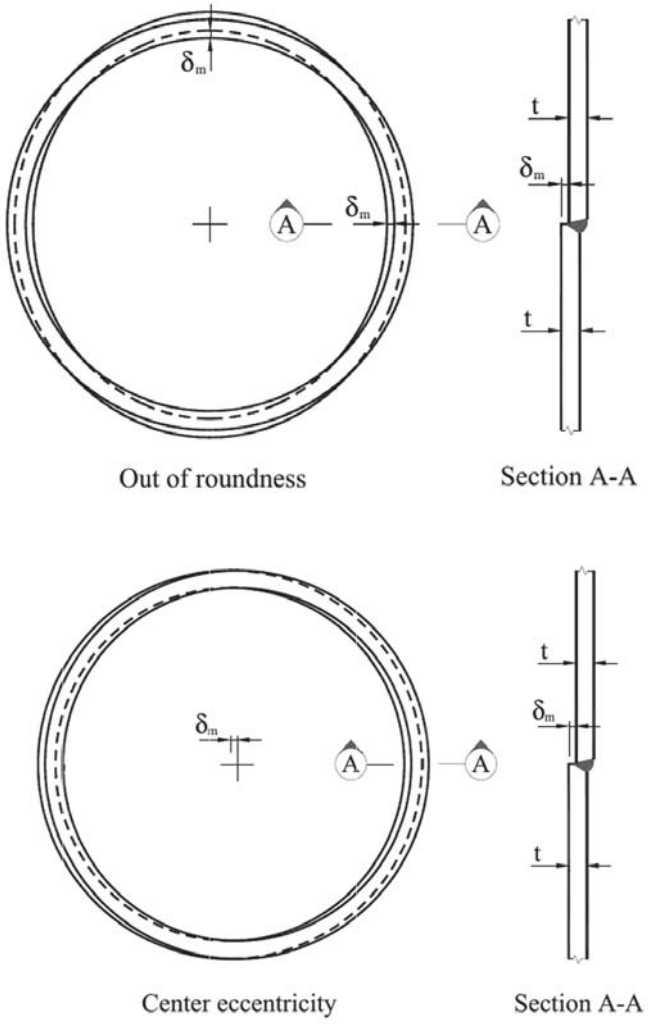

Fig. 13 Sketch presenting a procedure to determine geometric imperfection δ_m on butt weld of two pipe elements, according to DNV GL [29]

Here, an assumption was made that $\delta_m \le \delta_0$ (welds will be ground), hence *SCF*=1, which means that the stress concentration in the weld area does not exceed the value recorded in samples used to obtain the S-N data.

Table 6 collates the leg stress ranges $\Delta\sigma_o$ obtained from platform motion calculations. Additionally, the acceptable

stress ranges $\Delta\sigma_{all}$ corresponding to the thickness of the used plating are included.

Tab.6. Maximal stress ranges in jack-up platform legs as functions of leg plating thickness t_{leg} and leg diameter D_{leg}. Comparing with acceptable stress ranges for given thickness. Node 1.

	r_{leg} = 20 m			r_{leg} = 25 m			
	D_{leg}=2.8 m	D_{leg}=3.2 m	D_{leg}=3.6 m	D_{leg}=2.8 m	D_{leg}=3.2 m	D_{leg}=3.6 m	$\Delta\sigma_{all,t0.33}$
t_{leg}=50 mm	672.4 MPa	365.9 MPa	324.5 MPa	558.5 MPa	286.4 MPa	336.9 MPa	212.2 MPa
t_{leg}=60 mm	431.3 MPa	299.7 MPa	310.7 MPa	349.9 MPa	309.7 MPa	259.9 MPa	202.8 MPa
t_{leg}=70 mm	321.5 MPa	242.3 MPa	222.0 MPa	308.2 MPa	243.9 MPa	198.6 MPa	195.1 MPa

Only the solution for the platform with leg spacing radius r_{leg} = 25 m, leg diameter D_{leg}=3.6 m, and plating thickness t=70 mm meets about all requirements concerning the fatigue stress of the structure, as $\Delta\sigma_o \approx \Delta\sigma_{all,70mm,0.33}$. A sketch of the area of acceptable solutions due to constraints resulting from impact and fatigue strength requirements is shown in Fig. 14. The diagram reveals that acceptable solutions should be searched within sets of parameters where the plating thickness tleg is larger than 70 mm and/or the leg diameter D_{leg} is larger than or equal to 3.6m. Acceptable solutions can also be found in the area with smaller plating thickness than t_{leg}=70 mm, but in those cases the leg diameter D_{leg} should be increased. Similarly, acceptable solutions can be found for leg diameters D_{leg} smaller than 3.6 m, but in those cases the increase of the plating thickness is very large and may reach values which would pose a challenge for present technologies.

Since the decisive factor in platform leg dimensioning is fatigue strength, a decision was made for the structure to be made mainly of normal-strength steel. Consequently, the assumed acceptable stress due to impact strength was 235 MPa.

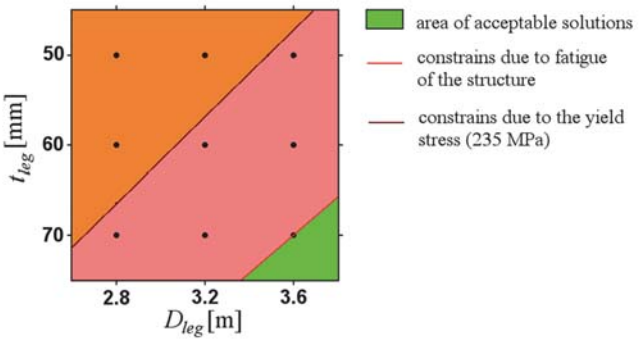

Fig. 14. Area of acceptable solutions with constraints for the structure with leg spacing radius rleg = 25 m. Node 1.

FATIGUE STRESS ANALYSIS AT NODE 2.

The basic differences between nodes 1 and 2 are:

- node 2 is situated lower (closer to the seabed), therefore the bending stresses will be smaller (as they are proportional to the distance from the seabed);
- node 2 is submerged (cathode protection is assumed), therefore the acceptable stresses for submerged nodes will be smaller.

The height of node 1 above seabed was H_{node1} = 52 m, while the height of node 2 is H_{node2} = 40 m. The plating thickness at node 2 is the same as that at node 1.

The stress range can be re-calculated for node 2 (for acceptable variant: t_{leg}=70 mm, D_{leg}=3.6 m, r_{leg}=25 m) as:

$$\Delta\sigma_{node2} = \Delta\sigma_{node1}\frac{H_{node2}}{H_{node1}} \tag{25}$$

The resulting value of the stress range for node 2 is $\Delta\sigma_{node2}$=152.8 MPa

The fatigue analysis for node 2 was performed for the same assumptions as for node 1. The only difference was that the structure fragment with node 2 is submerged in seawater and the cathode protection is applied.

The results of the fatigue analysis performed using a simplified method for node 2 are as follows:

The acceptable maximal stress range for components in seawater with cathode protection and for 1·108 cycles is $\Delta\sigma_{all}$=336.7 MPa, [29], Table 5-3.

The coefficient k given in Table 2-3 [29] for pipe joints is k=0.25. After substituting it to Equation 22, the obtained stress range is $\Delta\sigma_{\sigma all,70mm}$ = 232.8 MPa.

Node 2 is the area which is not accessible for inspection and not planned to be accessible for inspection and repair during structure's operation, therefore *DFF*=3. The utilisation factor read from [29], Table 5-8, for t_{life}=20 years is η=0.33.

The considered node is submerged in seawater and has cathode protection. Therefore, the acceptable stress reduction coefficient is C_r=0.785 ([29], Table 5-7).

The final value of the acceptable stress range for node 2 is: $\Delta\sigma_{all,70mm,0.33}$ = 0.785·232.8 MPa = 182.7 MPa.

Since the stress concentration coefficient for this weld is *SCF*=1, the stress range at node 2 meets the condition: $\Delta\sigma_{node2} \leq \Delta\sigma_{all,70mm,0.33}$

SUMMARY, CONCLUSIONS AND COMMENTS

Within the framework of the presented research, two jack-up platform concepts differing by leg spacing radius and hull dimensions were designed with the intention to be used as a supporting structure for a 6-MW offshore wind turbine.

For each concept, the parametric analysis was performed to determine optimal dimensions of platform legs: diameter D_{leg} and plating thickness t_{leg}. The platform motion was calculated for conditions characteristic for most violent storm in recent 50 years on the South Baltic area, for the platform parameters given in Table 1.

The obtained results, having the form of amplitudes of selected physical quantities, are shown in comprehensive charts in Fig. 6 and 7. Based on the critical stress values (corresponding to the yield stress), the area was defined in which the impact strength conditions are satisfied (Fig. 14).

The fatigue strength analysis was performed for two selected critical leg nodes. Its results were used for defining the acceptable area with respect to structure's fatigue (Fig. 14). Geometric parameters were determined which meet the adopted criteria, Table 6.

The decisive criterion turned out to be the fatigue strength criterion, while the yield point criterion appeared to be an inactive constraint.

In practice, the only solution which meets the fatigue strength criterion (along with the impact strength criterion) is the solution with the following set of parameters:
r_{leg}=25.0 m, D_{leg}=3.6m, t_{leg}=70mm.

Extrapolating the obtained results, we can conclude that the above criteria will also be met by platforms with leg diameter D_{leg} greater than 3.6m, and platforms with plating thickness t_{leg} greater than 70mm. However, the mass of legs in those solutions will be larger. Decreasing the leg diameter is also possible, but it would require proper increase in plating thickness. Similarly, reducing the leg plating thickness is possible, at simultaneous increase of leg diameter (Fig. 14).

It is noteworthy that the presented method is applicable for preliminary selection of basic dimensions of the platform, especially leg dimensions. The analyses described in the article were simplified, as they referred to the parametric design stage, when no complete geometric model of the structure is available. Major simplifications assumed in the analyses were constant values of wind speed and turbine thrust coefficient C_T. These simplifications originated from the fact that for the assumed conditions, the dominating loads were hydrodynamic forces generated by waves.

Further research and design steps will include analysing the operation of the turbine-tower-supporting structure system in various weather conditions. It will also take into account loads generated by wind (to meet the requirements formulated in the relevant Standard [31]).

ACKNOWLEDGEENT

This research was supported by the Polish National Centre for Research and Development (NCBR) under the project "WIND-TU-PLA" ERA-NET MARTEC II (Agreement No. MARTECII/1/2014)

REFERENCES

1. GWEC. (2018). Global Wind Statistics 2017. Global Wind Energy Council, 14 February 2018.

2. http://www.polenergia.pl/pol/pl/strona/farmy-morskie (12/12/2018)

3. https://www.equinor.com/en/what-we-do/hywind-where-the-wind-takes-us.html (12/12/2018)

4. Fukushima Floating Offshore Wind Farm Demonstration Project (Fukushima FORWARD). Source: http://www.fukushima-forward.jp/pdf/pamphlet3.pdf (13/12/2018)

5. Fulton G.R., Malcolm D.J., Elwany H., Stewart W., Moroz E., Dempster H.: Semi-Submersible Platform and Anchor Foundation Systems for Wind Turbine Support. National Renewable Energy Laboratory (U.S.), Subcontract Report NREL/SR-500-40282, December 2007

6. Bachynski E.E., Moan T. (2012). Design considerations for tension leg platform wind turbines. Marine Structures 29 (2012) 89–114.

7. Żywicki J., Dymarski P., Ciba E., Dymarski C. (2017). Design of Structure of Tension Leg Platform for 6 MW Offshore Wind Turbine Based on Fem Analysis. Polish Maritime Research 24(s1), 230-241. https://doi.org/10.1515/pomr-2017-0043

8. Dymarski C., Dymarski P., Żywicki J. (2017). Technology Concept of TLP Platform Towing and Installation in Waters with Depth of 60 m. Polish Maritime Research 24(s1), 59-66. https://doi.org/10.1515/pomr-2017-0022

9. Karimirad M., Moan T. (2012). Feasibility of the Application of a Spar-type Wind Turbine at a Moderate Water Depth. DeepWind, 19-20 January 2012, Trondheim, Norway. Energy Procedia 24(2012) 340-350

10. Duan F., Hu Z., Niedzwecki J.M. (2016). Model test investigation of a spar floating wind turbine. Marine Structures 49 (2016) 76-96

11. Dymarski P. Ciba E. (2017). Design of a cell-spar platform for a 6 MW wind turbine. Parametric analysis of the mooring system. Twenty First International Conference on Hydrodynamics in Ship Design and Operation - HYDRONAV, Gdańsk, 28-29 June 2017

12. Yeter B., Garbatov Y., Soares C.G. (2014). Fatigue damage analysis of a fixed offshore wind turbine supporting structure. Developments in Maritime Transportation and Exploitation of Sea Resources, Taylor & Francis Group, London

13. Velarde J., Bachynski E.E. (2017). Design and fatigue analysis of monopile foundations to support the DTU 10 MW offshore wind turbine. 14th Deep Sea Offshore Wind R&D Conference, EERA DeepWind'2017, 18-20 January 2017, Trondheim, Norway. Energy Procedia 137 (2017) 3–13

14. Bogdaniuk M. (2017). Estimation of the fatigue life of the hull of TLP [in Polish]. Technical Report. Polish Register

of Shipping, Gdańsk 2017

15. Rozmarynowski B., Mikulski T. (2018). Selected problems of sensitivity and reliability of a jack-up platform. Polish Maritime Research 25(1(97)), 77-84. https://doi.org/10.2478/pomr-2018-0009

16. Dymarski C., Dymarski P., Żywicki J. (2015). DESIGN AND STRENGTH CALCULATIONS OF THE TRIPOD SUPPORT STRUCTURE FOR OFFSHORE POWER PLANT. Polish Maritime Research 22(1(85)), 36-46. https://doi.org/10.1515/pomr-2015-0006

17. Kahsin M., Łuczak M. (2015). Numerical Model Quality Assessment of Offshore Wind Turbine Supporting Structure Based on Experimental Data. Structural Health Monitoring 2015: System Reliability for Verification and Implementation: Proceedings of the 10th International Workshop on Structural Health Monitoring. Vol. 1/ ed. Fu-Kuo Chang, Fotis Kopsaftopoulos 439 North Duke Street · Lancaster, PA 17602-4967, U.S.A. : DEStech Publications, Inc., 2015, 2817-2824

18. Wilson J.F.: Dynamics of Offshore Structures (2nd Edition). John Wiley & Sons, Inc., Hoboken, New Jersey, 2003

19. Chandrasekaran S.: Dynamic Analysis and Design of Offshore Structures (Ocean Engineering & Oceanography). Springer, New Delhi, 2015

20. Sarpkaya T. Wave Forces on Offshore Structures. Cambridge University Press, New York, 2010

21. Offshore Standards DNV-OS-J103 (2013). Design of Floating Wind Turbine Structures. Det Norske Veritas, June 2013

22. Niezgodziński M.E., Niezgodziński T.: Strength formulas, diagrams, and tables [in Polish]. WNT, Warszawa 2013.

23. Dymarski P., Ciba E., Marcinkowski T. (2016). Effective method for determining environmental loads on supporting structures for offshore wind turbines. Polish Maritime Research 23(1(89)), 52-60. https://doi.org/10.1515/pomr-2016-0008

24. Recommended Practice DNV-RP-C205 (2010). Environmental Conditions and Environmental Loads. Det Norske Veritas, October 2010

25. Sarpkaya T. (1986). In-line and transverse forces on smooth and rough cylinders in oscillatory flow at high Reynolds numbers, Monterey, California. Naval Postgraduate School

26. Product Portfolio Overview. The Senvion 6.XM series.

27. Jonkman J., Butterfield S., Musial W., Scott G. (2009). Definition of a 5-MW Reference Wind Turbine for Offshore System Development. National Renewable Energy Laboratory, Technical Report NREL/TP-500-38060 February 2009

28. Kooijman H.J.T., Lindenburg C., Winkelaar D., van der Hooft E.L. (2003). DOWEC 6 MW PRE-DESIGN. Aero-elastic modelling of the DOWEC 6 MW pre-design in PHATAS. Report DOWEC-F1W2-HJK-01-046/9 (public version). September 2003

29. Recommended Practice DNVGL-RP-C203 (2016). Fatigue design of offshore steel structures. DNV GL, April 2016

30. Offshore Standards DNVGL-OS-C101 (2016). Design of offshore steel structures, general - LRFD method. April 2016

31. EUROPEAN STANDARD IEC 61400-3 (2009). Wind turbines - Part 3: Design requirements for offshore wind turbines (IEC 61400-3:2009)

CONTACT WITH THE AUTHOR

Paweł Dymarski
e-mail: pawdymar@pg.edu.pl

Gdańsk University of Technology
Faculty of Ocean Engineering and Ship Technology
Narutowicza 11/12
80-233 Gdansk
Poland

sciendo

POLISH MARITIME RESEARCH 2 (102) 2019 Vol. 26; pp. 198-211
10.2478/pomr-2019-0039

THE PREDICTION OF HULL GESTURE AND FLOW AROUND SHIP BASED ON TAYLOR EXPANSION BOUNDARY ELEMENT METHOD

Jiaye Gong
College of Shipbuilding Engineering, Harbin Engineering University, Harbin, China
Yunbo Li
College of Ocean Science and Engineering of SMU, Shanghai Maritime University, Shanghai, China

ABSTRACT

Based on the potential flow theory and traditional boundary element method (BEM), Taylor expansion boundary element method (TEBEM) is introduced in this paper for the prediction of the flow field around ship, as a result, hull gesture and pressure distribution on hull surface are obtained. By this method, dipole strength of every field point is expanded in Taylor expansion, so that approximately continuous hull and free surface boundary condition could be achieved. To close the new equation system, the boundary condition of tangent velocity in every control point is introduced. With the simultaneous solving of hull boundary condition and free surface condition, the disturbance velocity potential could be obtained. The present method is used to predict the flow field and hull gesture of Wigley parabolic hull, Series 60 and KVLCC2 models. To validate the numerical model for full form ship, the wave profile, the computed hull gesture and hull surface pressure of KVLCC2 model are compared with experimental results.

Keywords: TEBEM, potential flow, flow field, hull gesture, surface pressure

INTRODUCTION

In ship hydrodynamics, prediction of flow around ship and hull gesture in calm water is a fundamental problem, and a high degree of numerical calculation precision and efficiency is required for ship design [24]. Based on the viscous flow theory, there has been used some commercial software to predict accurately the resistance of ship hull, but a large number of numerical iterations in a big spatial computational domain is necessary, which is time-consuming and limiting its application for practical design and hull form optimization [25, 26], especially in case of a large-scale model. For some problems less affected by fluid viscosity, such as the wave profile and ship hull gesture [17], the potential flow theory is still an effective method to solve the problems.

For potential flow methods, Dawson's method [3] is still a very effective and popular method for the prediction of wave-making resistance, because both pressure distribution on hull surface and the near-field flow can be predicted by this method. But, for the limitation of the streamline mesh and difference, the original Dawson's method is not accurate enough. Rapid method [15, 16] is proposed to solve the fully non-linear wave-making problem. By numerical iteration of the free surface, wave profile and pressure distribution along hull surface could be obtained, and the result is precise and close to the experimental result. By large amount of experiments and regression analysis, the numerical prediction method is improved for wave-making resistance of ships with transom-stern [4, 5]. The empirical formula obtained from experiments is used to predict the ventilation length and depth behind transom-stern, and the result is in good agreement with the experimental result. The Dawson's method is improved and the numerical method is optimized [21]. The improved method is used to predict the wave-making resistance of fixed ship hull. Based on the boundary element method (BEM), panels are arranged on the bottom to predict the wave-making resistance of a catamaran at a finite water depth [22]. The wave-making resistance of a pentamaran is

predicted at infinite depth of water by using the BEM and the linearized free surface condition with second order terms [19], and the Froude number up to 0.8. Linear wave-making theory is applied to determine the bow bulbs and hull form for full body ship with the minimum total resistance [25, 26].

In nowadays marine industry, full form ships still play a main role in passenger and freight service, such as commercial bulk carriers and container ships with block coefficient larger than 0.6 and 0.8 , respectively. In recent years, with the Energy Efficiency Design Index (EEDI) introduced by IMO, the demand for improved cargo capacity, fuel efficiency, low emissions and optimized operation is more and more important during the process of ship design and optimization [9, 12], and it also influences the design and the selection of operational profile with emphasis on low speed service. Consequently, most of the research about hull form optimization of full body ship is carried out for bulk carriers, container ships and oil tankers with low design speed [11, 18]. Compared with a high-speed slim ship, the prediction of flow field and hull gesture is more complex for ships with full hull form with low speed [14], because the surface curvature of full form ship is relatively larger in stem and stern areas, and the numerical solution is usually not stable in the areas as oscillation of the wave profile usually occurs. Therefore, it is meaningful to improve the numerical method to predict efficiently and stably the flow field and hull gesture of ships with large block coefficient and low speed.

In 2012, by expanding dipole potential in Taylor expansion, the 2-D TEBEM was proposed [6]. This way the precision of the tangential velocity could be improved in the non-smooth boundary. If the first-order derivative is kept, it is called the first-order TEBEM. If the second-order derivative is kept, it is called the second-order TEBEM. By combining the first-order TEBEM and the second-order TEBEM, the TEBEM method is applied to solve 3-D hydrodynamic characteristics of ship with forward speed [1], and the calculated result is in good agreement with the experimental one.

In this paper, the TEBEM is combined with linear wave-making theory to predict the wave-making resistance and hull gesture. The expansion of dipole potential will lead to a non-closed equation system, whereas the derivation of a complementary equation is completed. The convergence of the method is tested, and its application to different hull forms is analyzed. By numerical simulation of different hull forms, the numerical results of wave making resistance, hull gesture, wave profile and hull surface pressure are compared with the experimental result to validate the accuracy of this method.

METHODS

The TEBEM is firstly introduced into the numerical simulation of flow and hull gesture. Because of the expansion of dipole strength in Taylor expansion, the derivation of the new boundary condition is discussed in this section.

BASIC EQUATION

The coordinate system is fixed to ship hull, and its origin is in an undisturbed free surface amidships. The x-axis and y-axis extend to stern and starboard respectively. A ship is advancing at a constant speed U along the positive direction of x-axis.

It is assumed that the fluid is ideal, the flow around the ship is constant, and the water depth is infinite. Φ is defined as the total velocity potential which satisfies Laplace equation:

$$\nabla^2 \Phi = 0 \tag{1}$$

The total velocity potential Φ is divided into the double-body flow velocity potential ϕ and the perturbed velocity potential φ, where φ represents the interaction between ship hull and the free surface:

$$\Phi = \phi + \varphi \tag{2}$$

$$\zeta = \xi + \eta \tag{3}$$

where ζ, ξ and η are the wave profile corresponding to total velocity potential Φ, double-body flow velocity potential ϕ and perturbed velocity potential φ.

The double-body flow velocity potential ϕ is subdivided into the velocity potential of incoming flow potential and velocity potential $\overline{\varphi}$, which represents the perturbation by the double-body:

$$\phi = Ux + \overline{\varphi} \tag{4}$$

Because the velocity potential of incoming flow is included in the double-body flow potential, the perturbed velocity potential φ is assumed much lower than double-body velocity potential ϕ. The corresponding wave profile follows the similar assumption:

$$\varphi << \phi \quad \eta << \xi \tag{5}$$

HULL SURFACE BOUNDARY CONDITION

The normal velocity components of both the double-body potential ϕ and the perturbed potential φ are zero on the hull surface:

$$\nabla \overline{\varphi} \cdot \boldsymbol{n} = -\boldsymbol{U} \cdot \boldsymbol{n} \tag{6}$$

$$\nabla \varphi = 0 \tag{7}$$

Where $\boldsymbol{n}$ is specified as the normal vector of the hull surface.

FREE SURFACE CONDITION

The total velocity potential Φ satisfies both the kinematic condition and dynamic condition on the free surface:

$$\Phi_x\zeta_x+\Phi_y\zeta_y-\Phi_z=0 \qquad z=\zeta \tag{8}$$

$$g\zeta+\frac{1}{2}(\nabla\Phi\cdot\nabla\Phi-U^2)=0 \qquad z=\zeta \tag{9}$$

We eliminate the ζ from simultaneous Eqs. (8) and (9) to obtain the free surface condition

$$\nabla\Phi\nabla\left[\frac{1}{2}(\nabla\Phi\nabla\Phi)\right]+g\Phi_z=0 \quad z=\zeta \tag{10}$$

We insert Eqs. (1) to Eqs. (10) to get the total velocity potential Φ expanded in Taylor expansion about $z=\xi$ and $z=0$ respectively. The nonlinear term of φ is neglected to obtain linearized free surface condition:

$$\frac{1}{2}\phi\,(\phi_x^2+\phi_y^2)_x+\frac{1}{2}\phi_y(\phi_x^2+\phi_y^2)_y+\phi_x(\phi_x\varphi_x+\phi_y\varphi_y)_x+\phi_y(\phi_x\varphi_x+\phi_y\varphi_y)_y$$
$$+\frac{1}{2}\varphi_x(\phi_x^2+\phi_y^2)_x+\frac{1}{2}\varphi_y(\phi_x^2+\phi_y^2)_y+g\varphi_z=0 \qquad z=0 \tag{11}$$

Because $\varphi<<\phi$, it is assumed that:

$$\varphi_x+\varphi_y=\varphi_l \tag{12}$$

where the subscript l represents the derivation along streamline of double-body flow ϕ.

The free surface condition is obtained as follows:

$$2\phi_l\phi_{ll}\varphi_l+\phi_l^2\varphi_{ll}+g\varphi_z=-\phi_l{}^2\phi_{ll} \quad z=0 \tag{13}$$

The radiation condition is also satisfied on the free surface. Based on the investigation by Nakos [13], the truncation error of the upstream free surface will significantly affect the simulation result. So, to make the radiation condition satisfied, an upstream finite difference scheme [3, 21] is applied to make sure that the flow propagates downstream, and the boundary conditions $\varphi_x=U$ and $\varphi_y=0$ are used in the upstream panels far from the ship by means of virtual panels.

APPLICATION OF THE TEBEM

Laplace equation is transformed to integral form:

$$4\pi\bar{\varphi}=-\iint_{S_B}\frac{\partial}{\partial n}(\frac{1}{r})\bar{\varphi}dS+\iint_{S_B}(\frac{1}{r})(\frac{\partial\bar{\varphi}}{\partial n})dS \tag{14}$$

The double-body velocity potential in i-th panel of hull surface is specified as $\bar{\varphi}(i)$. Eqs. (14) is discretized and expressed as:

$$4\pi\bar{\varphi}(i)=-\sum_{j=1}^{N_B}\iint_{S_B}\frac{\partial}{\partial n_j}(\frac{1}{r_{ij}})\bar{\varphi}(j)dS_j+\sum_{j=1}^{N_B}\iint_{S_B}(\frac{1}{r_{ij}})(\frac{\partial\bar{\varphi}(j)}{\partial n_j})dS_j \tag{15}$$

where r_{ij} is the distance between i-th field point and j-th source point.

In the right side of Eqs. (15), the first term is the dipole model, and the second term is the source model. (x',y',z') is specified as the local co-ordinate system of source panel. The dipole density $\bar{\varphi}(j)$ of j-th panel is expanded in Taylor expansion in the local co-ordinate system, and the first order of $\bar{\varphi}(j)$ is kept:

$$\bar{\varphi}(j)=\bar{\varphi}(j_0)+\frac{\partial\bar{\varphi}(j_0)}{\partial x'}x'+\frac{\partial\bar{\varphi}(j_0)}{\partial y'}y' \tag{16}$$

where j_0 represents the origin of j-th panel.

After inserting Eqs. (16) to Eqs. (15), the discretized Eqs. (15) can be expressed as:

$$4\pi\bar{\varphi}(i)+\sum_{j=1}^{N_B}\iint_{S_B}\frac{\partial}{\partial n_j}(\frac{1}{r_{ij}})\bar{\varphi}(j)dS+\sum_{j=1}^{N_B}\iint_{S_B}\frac{\partial}{\partial n_j}(\frac{1}{r_{ij}})\bar{\varphi}_{x'}(j)x'dS_j$$
$$+\sum_{j=1}^{N_B}\iint_{S_B}\frac{\partial}{\partial n_j}(\frac{1}{r_{ij}})\bar{\varphi}_{y'}(j)y'dS_j$$
$$=-\sum_{j=1}^{N_B}\iint_{S_B}(\frac{1}{r_{ij}})(\boldsymbol{U}\cdot\boldsymbol{n}_j)dS_j \tag{17}$$

where $i=1,2...,N_b$

In Eqs. (17), the double-body flow velocity potential and its tangential derivatives are the unknown numbers to be determined. For 3-D problem, if the hull surface is discretized into N panels, there are $3N$ unknown numbers to be found. Hence, we should introduce $2N$ equations to complete the equation system.

We specify (x,y,z) as the co-ordinate system of i-th field panel, introduce the tangential derivation of Eqs. (17) along the x-axis and y-axis, and the complete equation system is obtained:

$$4\pi(\bar{\varphi})_i+\sum_{j=1}^{N_b}D_{ij}(\bar{\varphi})_j+\sum_{j=1}^{N_b}(D^{x'})_{ij}(\bar{\varphi}_{x'})_j+\sum_{j=1}^{N_b}(D^{y'})_{ij}(\bar{\varphi}_{y'})_j=-\sum_{j=1}^{N_b}S_{ij}(\boldsymbol{U}\cdot\boldsymbol{n}_j) \tag{18}$$

$$4\pi(\bar{\varphi}_x)_i+\sum_{j=1}^{N_b}(D_x)_{ij}(\bar{\varphi})_j+\sum_{j=1}^{N_b}(D_x^{x'})_{ij}(\bar{\varphi}_{x'})_j+\sum_{j=1}^{N_b}(D_x^{y'})_{ij}(\bar{\varphi}_{y'})_j=-\sum_{j=1}^{N_b}(S_x)_{ij}(\boldsymbol{U}\cdot\boldsymbol{n}_j) \tag{19}$$

$$4\pi(\bar{\varphi}_y)_i+\sum_{j=1}^{N_b}(D_y)_{ij}(\bar{\varphi})_j+\sum_{j=1}^{N_b}(D_y^{x'})_{ij}(\bar{\varphi}_{x'})_j+\sum_{j=1}^{N_b}(D_y^{y'})_{ij}(\bar{\varphi}_{y'})_j=-\sum_{j=1}^{N_b}(S_y)_{ij}(\boldsymbol{U}\cdot\boldsymbol{n}_j) \tag{20}$$

where

$$D_{ij}=\iint_{Sb_j}\frac{\partial}{\partial n_j}\left(\frac{1}{r_{ij}}\right)ds_j \quad (D^{x'})_{ij}=\iint_{Sb_j}x'\frac{\partial}{\partial n_j}\left(\frac{1}{r_{ij}}\right)ds_j \quad (D^{y'})_{ij}=\iint_{Sb_j}y'\frac{\partial}{\partial n_{ij}}\left(\frac{1}{r_{ij}}\right)ds_j \quad S_{ij}=\iint_{Sb_j}\frac{1}{r_{ij}}ds_j$$

$$(D_x)_{ij}=\iint_{Sb_j}\frac{\partial}{\partial x}\left(\frac{1}{r_{ij}}\right)ds_j \quad (D_x^{x'})_{ij}=\iint_{Sb_j}x'\frac{\partial}{\partial x}\left(\frac{1}{r_{ij}}\right)ds_j \quad (D_x^{y'})_{ij}=\iint_{Sb_j}y'\frac{\partial}{\partial x}\left(\frac{1}{r_{ij}}\right)ds_j \quad (S_x)_{ij}=\iint_{Sb_j}\frac{\partial}{\partial x}\left(\frac{1}{r_{ij}}\right)ds_j$$

$$(D_y)_{ij}=\iint_{Sb_j}\frac{\partial}{\partial y}\left(\frac{1}{r_{ij}}\right)ds_j \quad (D_y^{x'})_{ij}=\iint_{Sb_j}x'\frac{\partial}{\partial y}\left(\frac{1}{r_{ij}}\right)ds_j \quad (D_y^{y'})_{ij}=\iint_{Sb_j}y'\frac{\partial}{\partial y}\left(\frac{1}{r_{ij}}\right)ds_j \quad (S_y)_{ij}=\iint_{Sb_j}\frac{\partial}{\partial y}\left(\frac{1}{r_{ij}}\right)ds_j$$

Consequently, the amount of the equations is equal to the amount of the unknown numbers. The double-body flow velocity potential $\overline{\varphi}$ and its derivatives $\overline{\varphi}_{x'}$ and $\overline{\varphi}_{y'}$ are obtained by solving the linear system from Eqs. (18) to (20).

The integration procedure of the coefficients in Eqs. (18) to (20) is similar to the Hess-Smith approach [2], which is estimated in the local coordinate system of the panel S_j. The centre of local coordinate system is the geometric centre of the panel S_j. If we take D_{ij}, $(D_x)_{ij}$ and $(D_y)_{ij}$ for example, the integration can be expressed as

$$D_{ij}=\sum_{k=1}^{N}(\arctan\frac{m_{k,k+1}c_k-h_k}{z'_i\,r_k}-\arctan\frac{m_{k,k+1}c_{k+1}-h_{k+1}}{z'_i\,r_{k+1}}) \tag{21}$$

$$(D_x)_{ij}=-2z'_i\sum_{k=1}^{N}\frac{(y'_{k+1}-y'_k)(r_k+r_{k+1})}{r_k r_{k+1}\left[(r_k+r_{k+1})^2-l_{k,k+1}^2\right]} \tag{22}$$

$$(D_y)_{ij}=2z'_i\sum_{k=1}^{N}\frac{(x'_{k+1}-x'_k)(r_k+r_{k+1})}{r_k r_{k+1}\left[(r_k+r_{k+1})^2-l_{k,k+1}^2\right]} \tag{23}$$

$$c_k=(x'_k-x'_i)^2+z'^2_i \qquad h_k=(x'_k-x'_i)(y'_k-y'_i) \tag{24}$$

$$m_{k,k+1}=\frac{y'_{k+1}-y'_k}{x'_{k+1}-x'_k} \qquad r_k=\sqrt{c_k+(y'_k-y'_i)^2} \tag{25}$$

where (x'_i,y'_i,z'_i) is the position of field point, (x'_j,y'_j,z'_j) is the position of source point, and (x'_k,y'_k,z'_k) is the k-th corner point of the panel j. $N=3$ for a triangular panel on the hull surface, and $N=4$ for a four-nodes panel on the free surface. $l_{k,k+1}$ is the distance between k-th corner point and $(k+1)$-th corner point. In the local coordinate system (x',y',z'), the normal vector is assumed to point to the inside of the hull on the hull surface panel and upward on the free surface panel. When $i=j$, the integration in Eq. (21) is analytically performed giving $D_{ij}=2\pi$. More details about the integration of the coefficients can be found in [2, 7].

The same method is used to expand the perturbed velocity potential φ, and the hull surface boundary condition is similar to that of Eqs. (18), (19) and (20):

$$4\pi(\varphi)_i+\sum_{j=1}^{N_b+N_f}D_{ij}(\varphi)_j+\sum_{j=1}^{N_b+N_f}(D^{x'})_{ij}(\varphi_{x'})_j+\sum_{j=1}^{N_b+N_f}(D^{y'})_{ij}(\varphi_{y'})_j=0 \tag{26}$$

$$4\pi(\varphi_x)_i+\sum_{j=1}^{N_b}(D_x)_{ij}(\varphi)_j+\sum_{j=1}^{N_b}(D_x^{x'})_{ij}(\varphi_{x'})_j+\sum_{j=1}^{N_b}(D_x^{y'})_{ij}(\varphi_{y'})_j=0 \tag{27}$$

$$4\pi(\varphi_y)_i+\sum_{j=1}^{N_b}(D_y)_{ij}(\varphi)_j+\sum_{j=1}^{N_b}(D_y^{x'})_{ij}(\varphi_{x'})_j+\sum_{j=1}^{N_b}(D_y^{y'})_{ij}(\varphi_{y'})_j=0 \tag{28}$$

where $i=1,2,...,N_b$.

On the free surface, the boundary condition is:

$$4\pi(\varphi)_i+\sum_{j=1}^{N_b+N_f}D_{ij}(\varphi)_j+\sum_{j=1}^{N_b+N_f}(D^{x'})_{ij}(\varphi_{x'})_j+\sum_{j=1}^{N_b+N_f}(D^{y'})_{ij}(\varphi_{y'})_j=\sum_{j=1}^{N_f}S_{ij}(\varphi_{z'})_j \tag{29}$$

$$4\pi(\varphi_x)_i+\sum_{j=1}^{N_b+N_f}(D_x)_{ij}(\varphi)_j+\sum_{j=1}^{N_b+N_f}(D_x^{x'})_{ij}(\varphi_{x'})+\sum_{j=1}^{N_b+N_f}(D_x^{y'})_{ij}(\varphi_{y'})_j=\sum_{j=1}^{N_f}(S_x)_{ij}(\varphi_{z'})_j \tag{30}$$

$$4\pi(\varphi_y)_i+\sum_{j=1}^{N_b+N_f}(D_y)_{ij}(\varphi)_j+\sum_{j=1}^{N_b+N_f}(D_y^{x'})_{ij}(\varphi_{x'})_j+\sum_{j=1}^{N_b+N_f}(D_y^{y'})_{ij}(\varphi_{y'})_j=\sum_{j=1}^{N_f}(S_y)_{ij}(\varphi_{z'})_j \tag{31}$$

where $i=1,2,...,N_f$.

From Eqs. (29) to (31), the extra unknown number $\varphi_{z'}$ should be eliminated to complete the equation system. Hence, we transform the free surface condition as follows:

$$\varphi_{z'}=-\frac{1}{g}\phi_l^2\phi_{ll}-\frac{2}{g}\phi_{ll}\varphi_l-\frac{1}{g}\phi_l^2\varphi_{ll} \tag{32}$$

In the right side of Eqs. (32), the value of the first term is known, and the other two terms are unknown terms to be solved. We insert Eqs. (32) to Eqs. (29), (30) and (31). Before combining the terms with the same unknown number, the variables should be transformed into the same co-ordinate system by using the transition matrix:

$$\begin{bmatrix}(\varphi_x)_j\\(\varphi_y)_j\end{bmatrix}=\begin{bmatrix}a_1 & b_1\\a_2 & b_2\end{bmatrix}\begin{bmatrix}(\varphi_{x'})_j\\(\varphi_{y'})_j\end{bmatrix} \tag{33}$$

Through transformation of co-ordinates, φ_l and φ_{ll} in panel j can be expressed as:

$$(\varphi_l)_j = (\varphi_x)_j (l_x)_j + (\varphi_y)_m (l_y)_j$$
$$= [(a_1)_j (\varphi_{x'})_j + (b_1)_j (\varphi_{y'})_j](l_x)_j + [(a_2)_j (\varphi_{x'})_j + (b_2)_j (\varphi_{y'})_j](l_y)_j \quad (34)$$

$$(\varphi_{ll})_j = (l_x)_j \frac{\partial}{\partial x}[(\varphi_x)_j (l_x)_j + (\varphi_y)_j (l_y)_j] + (l_y)_j \frac{\partial}{\partial y}[(\varphi_x)_j (l_x)_j + (\varphi_y)_j (l_y)_j] \quad (35)$$
$$= (\varphi_{xx})_j (l_x^2)_j + 2(\varphi_{xy})_j (l_x l_y)_j + (\varphi_{yy})_j (l_y^2)_j$$

The second order derivatives φ_{xx}, φ_{xy} and φ_{yy} in Eqs. (35) can be expressed as:

$$\begin{cases} (\varphi_{xx})_j = [(\varphi_x)_L]_j [L_x]_j + [(\varphi_x)_H]_j [H_x]_j \\ (\varphi_{xy})_j = [(\varphi_x)_L]_j [L_y]_j + [(\varphi_x)_H]_j [H_y]_j \\ (\varphi_{yy})_j = [(\varphi_y)_L]_j [L_y]_j + [(\varphi_y)_H]_j [H_y]_j \end{cases} \quad (36)$$

where L and H is specified as the difference operator in the longitudinal direction and lateral direction, which is given in [21].

By inserting Eqs. (33) and (36) into Eqs. (35), φ_{ll} can be expressed by $\varphi_{x'}$ and $\varphi_{y'}$. Consequently, $\varphi_{z'}$ can also be expressed by $\varphi_{x'}$ and $\varphi_{y'}$. on inserting $\varphi_{z'}$ into Eqs. (29), (30) and (31), and combining the like terms. The perturbed velocity potential φ and its tangential derivatives $\varphi_{x'}$ and $\varphi_{y'}$ can be obtained by solving the simultaneous equation system consisted of Eqs. (26) to (31).

WAVE PROFILE, WAVE-MAKING RESISTANCE AND HULL GESTURE

When the velocity potential ϕ, φ and their tangential derivatives $\phi_{x'}$, $\phi_{y'}$, $\varphi_{x'}$, $\varphi_{y'}$ are obtained, we transform the velocity in control points to global coordinate system by using transformation matrix:

$$\begin{bmatrix} \phi_x \\ \phi_y \\ \phi_z \end{bmatrix} = [\boldsymbol{T}] \begin{bmatrix} \phi_{x'} \\ \phi_{y'} \\ 0 \end{bmatrix} \quad (37)$$

where T is the transformation matrix.

The velocity vector in control point of hull surface:

$$\boldsymbol{V} = \nabla\overline{\varphi} + \nabla\varphi - (\boldsymbol{U}\cdot\boldsymbol{n})\boldsymbol{n} \quad (38)$$

The velocity vector in control point of free surface:

$$V_x = U + \varphi_x - \frac{1}{4\pi}\sum_{j=1}^{N_b}(D_x)_{ij}(\overline{\varphi})_j - \frac{1}{4\pi}\sum_{j=1}^{N_b}(D_x^{x'})_{ij}(\overline{\varphi}_{x'})_j - \frac{1}{4\pi}\sum_{j=1}^{N_b}(D_x^{y'})_{ij}(\overline{\varphi}_{y'})_j - \frac{1}{4\pi}\sum_{j=1}^{N_b}(S_x)_{ij}(\boldsymbol{U}\cdot\boldsymbol{n}_j)$$
$$V_y = \varphi_y - \frac{1}{4\pi}\sum_{j=1}^{N_b}(D_y)_{ij}(\overline{\varphi})_j - \frac{1}{4\pi}\sum_{j=1}^{N_b}(D_y^{x'})_{ij}(\overline{\varphi}_{x'})_j - \frac{1}{4\pi}\sum_{j=1}^{N_b}(D_y^{y'})_{ij}(\overline{\varphi}_{y'})_j - \frac{1}{4\pi}\sum_{j=1}^{N_b}(S_y)_{ij}(\boldsymbol{U}\cdot\boldsymbol{n}_j) \quad (39)$$

The pressure coefficient of hull surface, coefficient of wave-making resistance and wave profile can be obtained by:

$$C_p = 1 - (\frac{\nabla\Phi}{U})^2 \quad (40)$$

$$C_w = \sum_{i=1}^{N_b} C_{p_i} n_{x_i} S_i \Big/ \sum_{i=1}^{N_b} S_i \quad (41)$$

$$C_{Fz} = \sum_{i=1}^{N_B} C_{p_i} n_{zi} S_i \Big/ \sum_{i=1}^{N_b} S_i \quad (42)$$

$$C_{Ny} = \sum_{i=1}^{N_B} C_{p_i} \left[(z_i - z_g) n_{xi} - (x_i - x_g) n_{zi} \right] S_i \Big/ \sum_{i=1}^{N_b} x_i S_i \quad (43)$$

$$\zeta = \frac{1}{2g}(|\boldsymbol{U}|^2 - |\boldsymbol{V}_i|^2) \quad (44)$$

where S_i is the wetted area of hull surface, x_i, z_i are the coordinates of i-th control point, x_g, z_g are the coordinates of ship gravity centre, n_{xi}, n_{zi} are the normal vectors of *i*-th panel.

The problem discussed in this paper is steady, but the hull gesture (i.e. its floating position against calm water line) will be obtained by iteration method. To this end, a time step Δt is used to calculate the change of trim and sinkage in the next step. After calculating the lifting force and trim moment, the hull position of the next step is obtained, and the hull surface under free surface will be re-meshed. The most part of the mesh can be used again, only the part near the waterline should be re-meshed:

$$S_{t+\Delta t} = S_t + \frac{F_z}{m}\Delta t \qquad T_{t+\Delta t} = T_t + \frac{N_y}{m}\Delta t \quad (45)$$

where m is the mass of ship, S_t and T_t are sinkage and trim in time step t, respectively. After performing iterations until the convergence condition ($F_z < \varepsilon, N_y < \varepsilon$) is satisfied, the wave-making resistance, hull sinkage and trim, and wave profile are obtained.

RESULTS AND DISCUSSION

In this section, the Wigley hull is used to test the convergence and difference schemes of the current method. Then, S60 and KVLCC2 models with the block coefficient of 0.6 and 0.8 , respectively, are simulated to validate the current method.

3.1 WIGLEY HULL

Wigley hull model is taken as an example, and different numerical methods and mesh schemes are used to discuss the convergence of the TEBEM and the effect of different parameters on the result. The Wigley hull model is define by the analytical formula as follows:

$$y = \frac{B}{2}(1-(\frac{x}{L/2})^2)(1-(\frac{z}{D})^2)$$

where L, B and D are the waterline length, breadth and depth of Wigley hull , respectively, and the main ship dimension ratios are $B/L = 0.1$, $D/L = 0.063$, and $C_b = 0.444$.

The mesh generation is similar to that given in [21], but, in this paper, every rectangular panel of hull surface is divided into two triangular panels. Ship hull is divided into 70 sections longitudinally and 5 sections vertically, so there are 70×12 panels on a half of the hull surface, which is shown in Fig. 1. Free surface panel mesh varies with the Froude number, and every wavelength is divided into 20 sections in the longitudinal direction. The length of panels before stem and behind stern are enlarged in a ratio of 1.06, and , similarly, their breadth values. The length of the panels before stem, behind stern and their breadth are kept greater than $1L$, $1.5L$ and $1L$, respectively. The free surface is discretized into the mesh of 30×84 when F_n is 0.25. Fig. 2 shows the free surface panel arrangement at F_n=0.25.

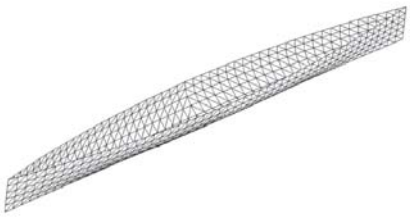

Fig. 1. Panel arrangement of Wigley hull model.

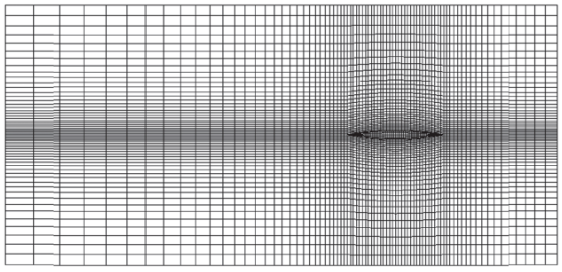

Fig. 2. Free surface panel arrangement at F_n=0.25.

The current numerical method is applied to calculate the hull gesture, wave profile and wave-making resistance of Wigley model, The convergence and difference schemes are discussed.

The two-point, three-point and four-point difference operators are used for calculation to discuss the effect of various difference operations on the results. In Fig. 3, the wave-making resistance with free sinkage and trim obtained from three kinds of difference operators are compared with the experimental results carried out by Ship Research Institute [8]. It shows that the four-point difference operator will lead to oscillation of the result at some Froude numbers. The result obtained from the three-point difference operator is accurate in a wide range of Froude numbers. Consequently, the three-point operator is used as the most stable difference scheme for the TEBEM method at a wide range of Froude numbers.

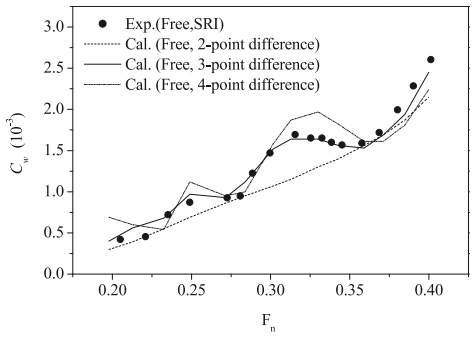

Fig. 3. Wave-making resistance of Wigley hull by using various difference operators (Free).

The convergence of the TEBEM is also tested. The hull surface is discretized into the mesh of 50×8, 70×10 and 90×12 respectively. The wave-making resistance, sinkage and trim calculated with different mesh schemes are compared in Fig. 4, Fig. 5 and Fig. 6, It shows that the results for wave-making resistance obtained from the mesh of 50×8 and 70×10 are almost the same with each other, and calculations of trim and sinkage converge faster than wave-making resistance. Hence, for the TEBEM method, discretizing the hull surface into triangular grids may be efficient enough for numerical simulation. Compared with source panel, the dipole is more sensitive to the gap between two panels, when the four points of panel is projected to the same plane, but with the use of the triangular grid this problem can solved for dipole.

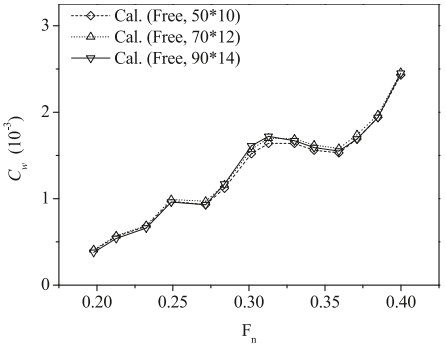

Fig. 4. Calculated wave-making resistance by using different mesh schemes (Free).

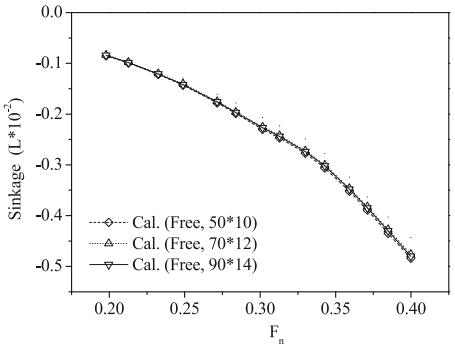

Fig. 5. Calculated sinkage by using different mesh schemes (Free).

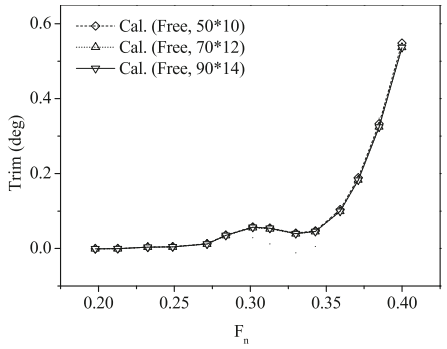

Fig. 6. Calculated trim by using different mesh schemes (Free).

3.2 SERIES 60 MODEL

The main characteristic particulars of Series 60 are as follows: $C_b = 0.6$, $B/L = 0.133$ and $D/L = 0.054$. Hull surface is discretized into 74×20 mesh. On the free surface, 30 panels per wavelength are kept in the direction of x-axis, and the width of the first panel near the ship is $0.018L$. The enlarging rates in the ship longitudinal and lateral direction are the same, equal to 1.06. The free surface is discretized into 136×30 mesh when Froude number is 0.316. Fig. 7 shows the panel arrangement of Series 60 model.

(a)

(b)

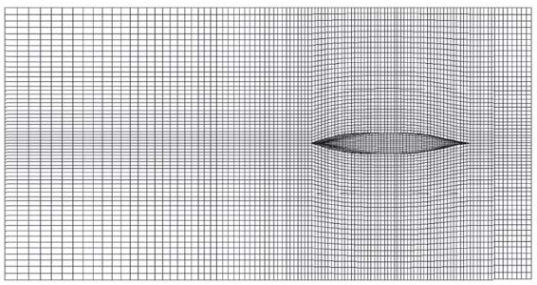

Fig. 7. Panel arrangement of Series 60 model : (a) Panel arrangement of hull surface, (b) Panel arrangement of free surface.

The fixed model without sinkage and trim is calculated first, and the calculated wave-making resistance and wave profile are compared with the experimental result. Fig. 8 shows the comparison of the calculated wave-making resistance with the results of the experiment carried out by Ishikawajima-Harima Heavy Industries Co., Ltd. and University of Tokyo [8], respectively.

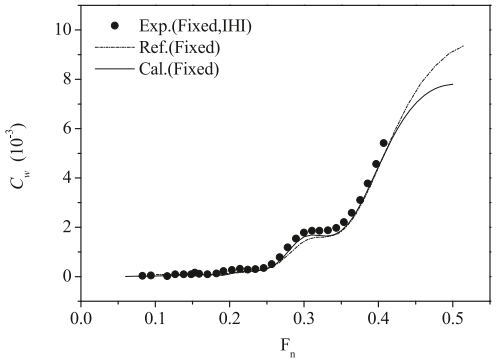

Fig. 8. Wave-making resistance of Series 60 model (Fixed)

In Fig. 9, the calculated wave profile of Series 60 model with fixed sinkage and trim is compared with the experimental result and the result presented in [21] achieved by using the improved Dawson's method; the experiment was carried out by Ship Research Institute [8]. The calculated result is in a good agreement with the experimental result at different Froude numbers. It shows that the accuracy of the wave profile along ship is improved, and almost all the difference appears in the first crest of the wave profile, but the difference is relatively smaller for different Froude numbers..

(a)

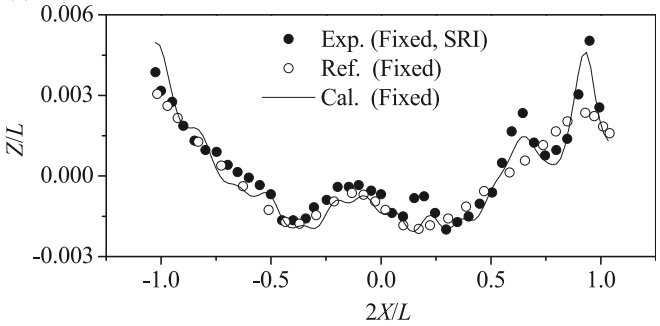

(b)

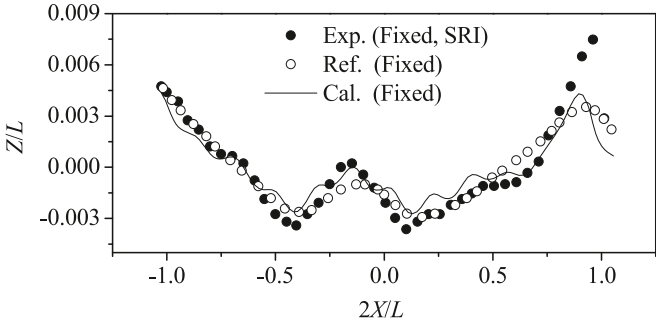

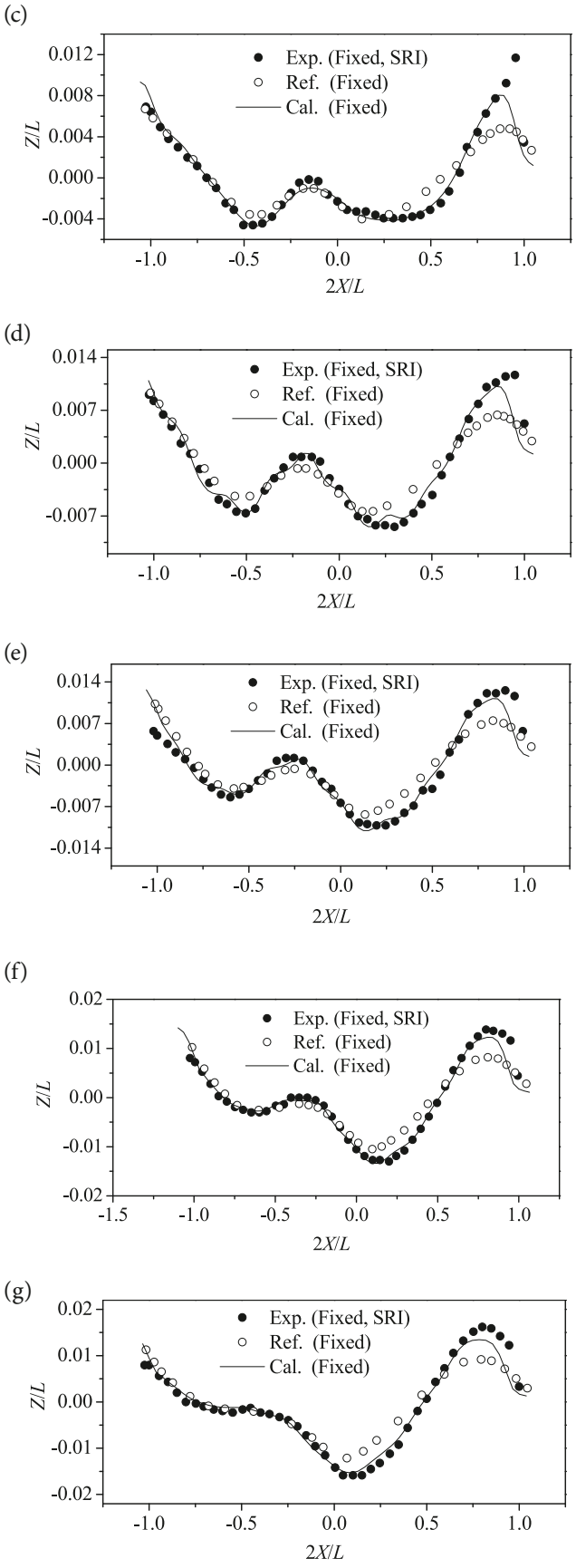

Fig. 9. Wave profile of Series 60 model at different F_n (Fixed). (a) wave profile at F_n=0.18 (b) wave profile at F_n=0.22, (c) wave profile at F_n=0.25, (d) wave profile at F_n=0.28, (e) wave profile at F_n=0.30, (f) wave profile at F_n=0.32, (g) wave profile at F_n=0.34.

To test the propagation and dissipation of waves, the calculated and experimental wave profiles in different longitudinally placed cross-sections are compared with each other (F_n=0.316). The experiment was carried out by Iowa Institute of Hydraulic Research [23]. Fig. 10 shows that only at the cross-section y=0.2067L a little phase difference appears.

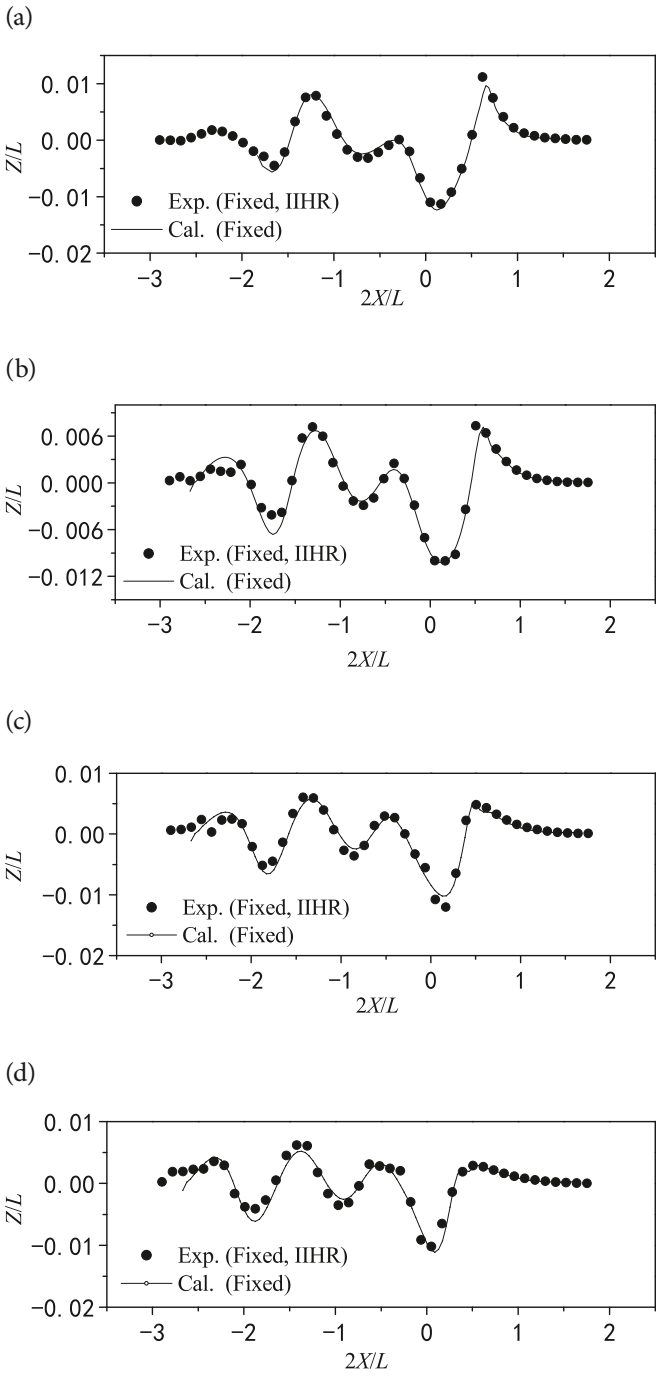

(e)

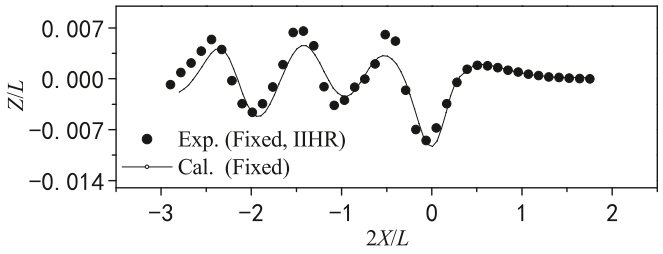

Fig. 10. Wave profile of Series 60 model in different longitudinally placed cross-sections at $F_n = 0.316$ *(Fixed). (a) wave profile at* $y = 0.1083L$*, (b) wave profile at* $y = 0.1411L$*, (c) wave profile at* $y = 0.1739L$*, (d) wave profile at* $y = 0.2067L$*.*

Numerical simulation of Series 60 model with free sinkage and trim was also carried out. The calculated wave-making resistance and hull sinkage and trim are compared with the experimental result in Fig. 11, 12 and 13. All the experiment was carried out by Iowa Institute of Hydraulic Research [23].

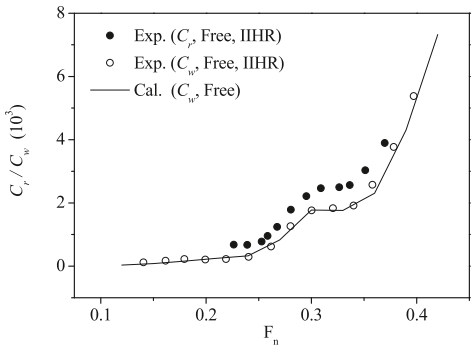

Fig. 11. Wave-making resistance of Series 60 model (Free).

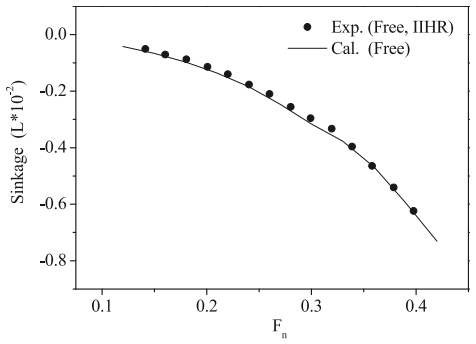

Fig. 12. Sinkage of Series 60 model (Free).

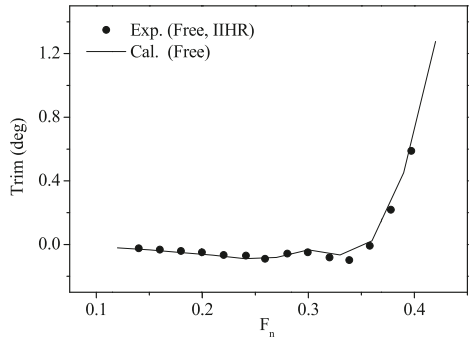

Fig. 13. Trim of Series 60 model (Free).

Fig. 14 shows the wave pattern of Series 60 model at different Froude numbers.

(a)

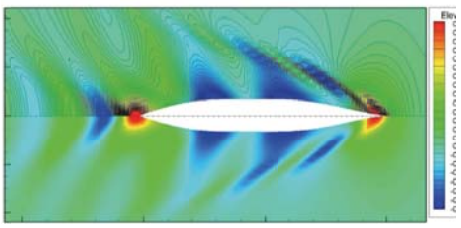

(b)

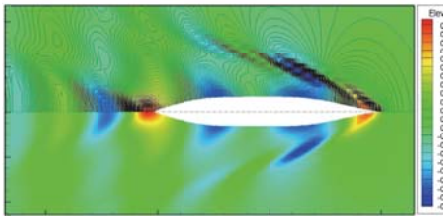

(c)

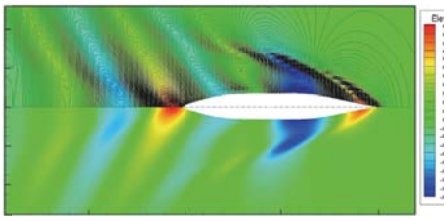

(d)

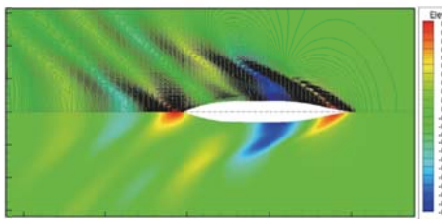

(e)

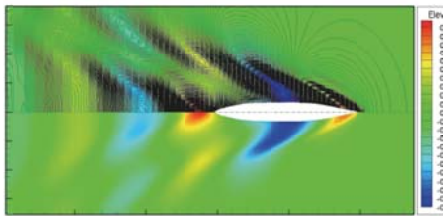

Fig. 14. Wave pattern of Series 60 model at different F_n *(Free). (a) wave pattern at* F_n=0.22*, (b) wave pattern at* F_n=0.26*, (c) wave pattern at* F_n=0.30*, (d) wave pattern at* F_n=0.34*, (e) wave pattern at* F_n=0.38*.*

KVLCC2 MODEL

KVLCC2 models are taken as examples to validate application of the numerical method based on the TEBEM

for full form ship. Compared with the series 60 models, the simulation of flow around a full form ship, such as KVLCC2 one, is relatively more complicated. In the reference [14] about the prediction of flow around full form ship, the domain of free surface behind the stern is neglected to avoid the oscillation of wave-making. In this section, both the free and fixed KVLCC2 model was calculated. To compare with the experimental and CFD results, when simulating the fixed and free model, the simplified rudder which is of the same size as that used in the Gothenburg Workshop 2010 [10], is included. The main characteristic particulars of KVLCC2 model are as follows: block coefficient $C_b = 0.8$, $B/L = 0.178$ and $D/L = 0.064$.

The fixed KVLCC2 model with and without rudder is calculated at Fn=0.142 first to test the accuracy of wave profile. Because a part of the ship hull is parallel body and its block coefficient is very large, a triangular mesh is applied to make the hull surface smoother. Fig. 15 shows the panel arrangement on hull surface and free surface.

(a)

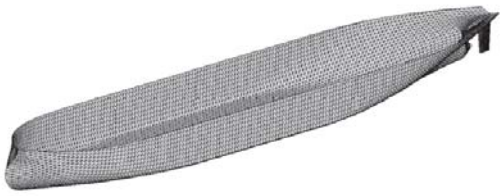

(b)

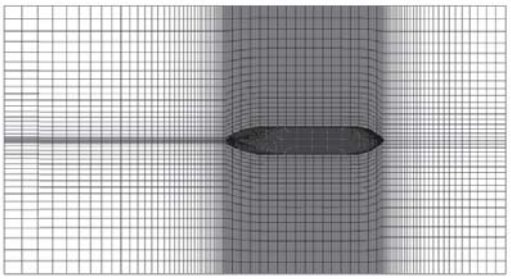

Fig. 15. Panel arrangement of KVLCC2 model with rudder. (a) Panel arrangement on hull surface, (b) Panel arrangement on free surface at F_n=0.142.

The mesh generation is the same as for Wigley hull, the domain size is $3.5L \times 1.0L$, where the length before stem is $1.0L$, the length behind stern is $1.5L$, and the width of the domain is $1.0L$ [14], and the free surface is divided into 25×297 panels at $Fn = 0.142$. Because KVLCC2 model is a full form ship, three sets of hull surface mesh schemes are used to test the calculation convergence.

Based on Fig. 16, Fig. 17 and Fig. 18, the result shows that the 4596 cell mesh is fine enough for calculating hull gesture and wave profile as the relative difference of the sinkage and trim results calculated with the use of 4596 panels and 7578 panels is lower than 1%. For the numerical simulation of full form ship by the TEBEM it is enough to divide half of the hull surface into 4596 panels, but compared with series 60 form, a greater number of cells is necessary for full form ship, especially for the area of stem and stern. Based on Fig. 16, we can also make sure ourselves that for the full form ship, the radiation condition suggested by Nakos [13] is well satisfied on the free surface before the bow, and the wave elevation goes to zero when, $2X/L \to 2$.

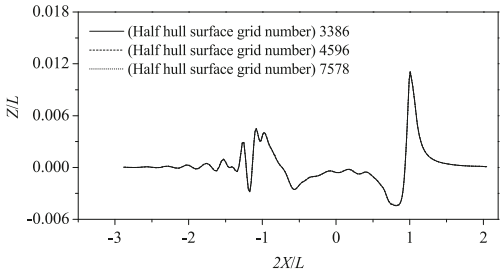

Fig. 16. Computed wave profile along the hull by using different hull surface meshes at F_n=0.15 *(Free model).*

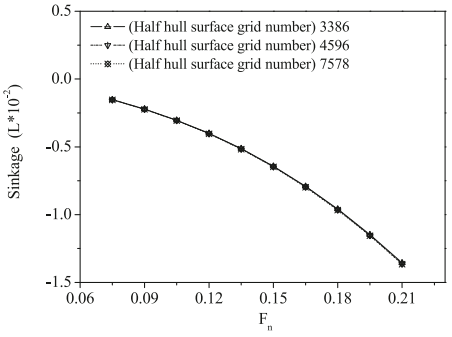

Fig. 17. Computed sinkage by using different mesh schemes (Free model)

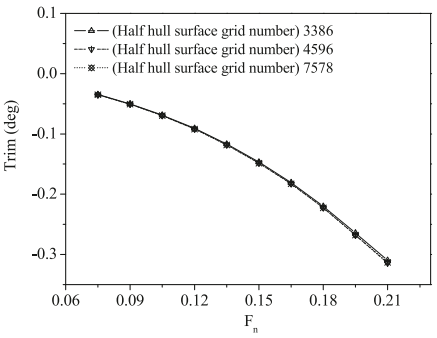

Fig. 18. Computed trim by using different mesh schemes (Free model)

In Fig. 19, the calculated wave profiles of the fixed model at different cross-sections are compared with the experimental results and CFD results; all the data come from the report of Gothenburg Workshop 2010 [14]. Fig. 19 (a) shows that the computed wave profile for the model without rudder is in a good agreement with the experimental results, and the first peak and hollow values differ by 4.5% and 9.1%, respectively, from their experimental results. The computed pressure coefficient of the hull surface is shown in Fig. 20(a), and the Fig. 20(b) presents the comparison between the computed results and CFD ones [10]. Fig. 21shows the contour of wave elevation.

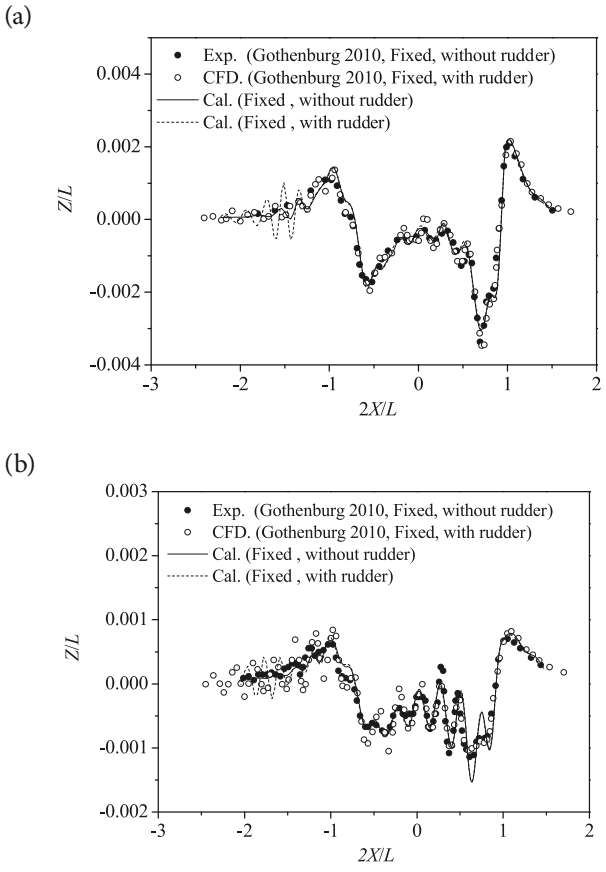

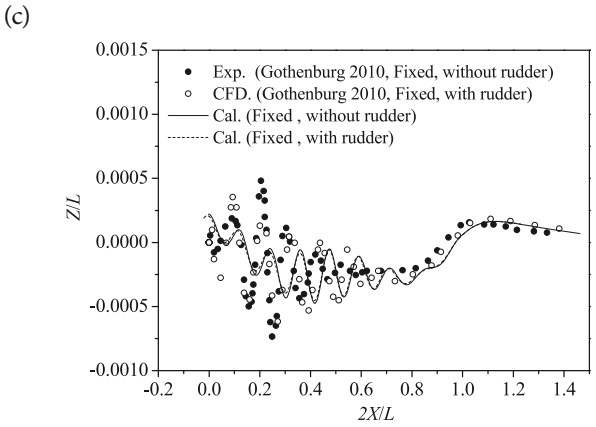

Fig. 19. Wave profile of KVLCC2 model in different longitudinally situated cross-sections at F_n=0.142 (Fixed). (a) wave profile at y=0.096L , (b) wave profile at y=0.158L (c) wave profile at y=0.299L .

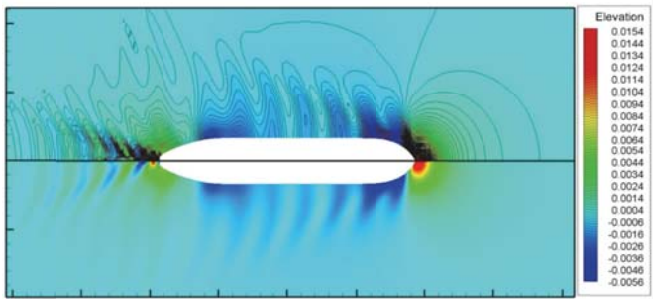

Fig. 21. Wave pattern for KVLCC2 model at F_n=0.142 (Fixed, without rudder).

In Fig. 19(b), some oscillations of the wave-making appear behind stern for both the computed and CFD result, which reflects the effect of rudder on wave pattern. From Fig. 19(c) it also results that the wave profile computed by the TEBEM method damps faster than in case of experimental and CFD

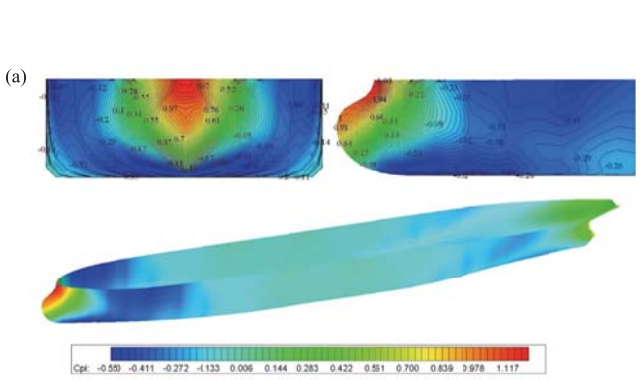

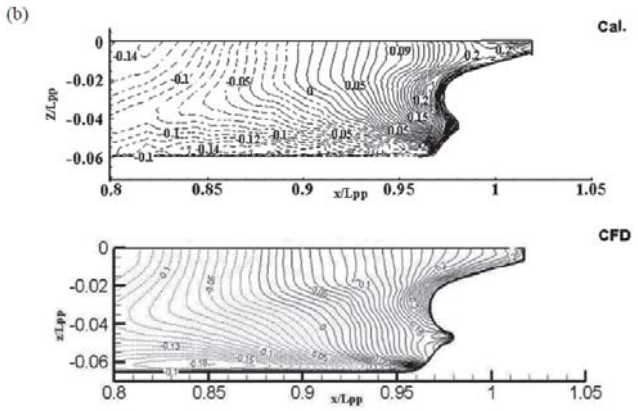

Fig. 20. Pressure coefficient field on KVLCC2 hull surface at F_n=0.142 (Fixed, without rudder), (a) computed result, (b) comparison with CFD result [10].

results, when a considered field point is distant far away from the hull surface, and both the results obtained from CFD and TEBEM calculations show a phase difference compared with the experimental result. The comparison given in Fig. 20(b) shows that the tendency of the pressure gradient lines obtained by means of the current method is similar to that of the CFD result. But the negative pressure area calculated by using the current method is larger than that by CFD, it is probably because the viscous effect is neglected, and the streamline separation by an adverse pressure gradient in this area may also affect the pressure distribution. Fig. 21 shows that, though the wave profile in different sections is in a good agreement with the experimental result, some short waves, especially the break waves generated by the bow with large curvature, are not covered by the current methods,

The KVLCC2 model with free trim and sinkage is simulated at different Froude numbers, and the results are compared with the experimental and CFD results taken from the report of Gothenburg Workshop 2010 [14], which is shown in Fig. 22 and 23. To keep the computed model the same as that used for the experiment, the rudder is included in the free model. Fig. 24 shows the wave pattern of free KVLCC2 model with rudder for three different Froude numbers.

Fig. 22. Sinkage of KVLCC2 model (Free, with rudder).

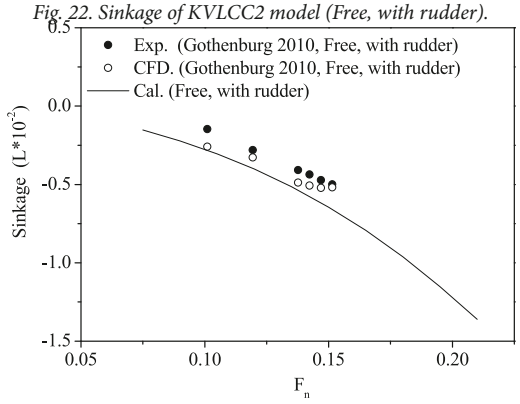

Fig. 23. Trim of KVLCC2 model (Free, with rudder).

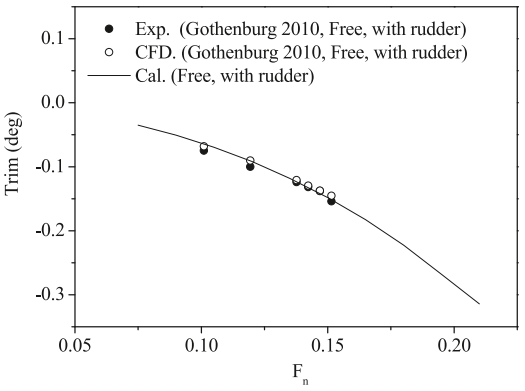

(a)
(b)
(c)

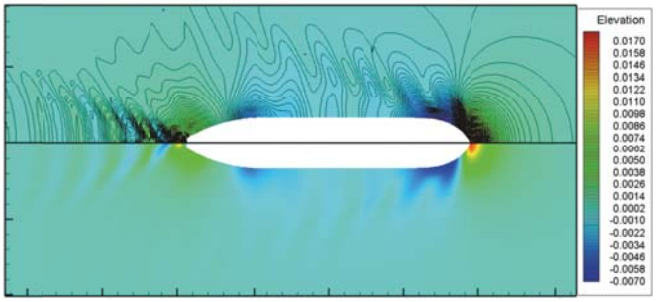

Fig. 24. Wave pattern for KVLCC2 model (Free, with rudder), (a) F_n=0.15 (b) F_n=0.15 (c) F_n=0.21.

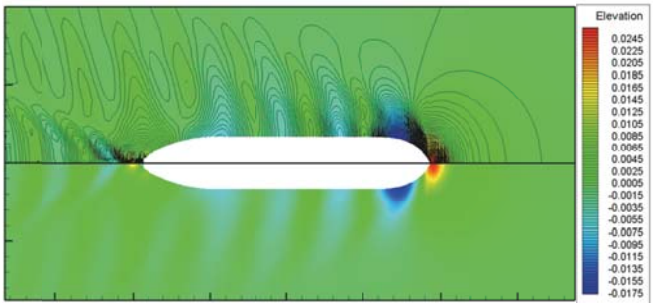

Based on the simulation of KVLCC2 model with free trim

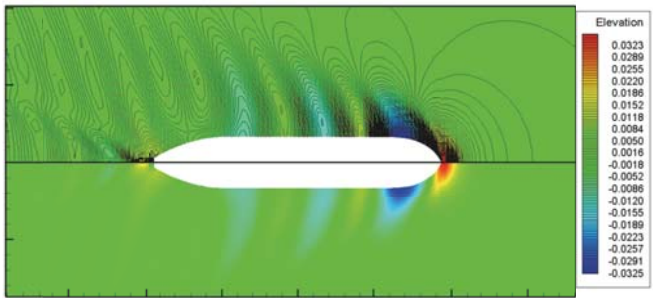

and sinkage, Fig. 22 and Fig. 23 shows that the computed trim of full form ship is in a good agreement with the experimental result, and the sinkage is larger than that from both the experimental and CFD results. The wave contour of Fig. 24 shows that the wave for full form ship computed by using the current method is stable at different Froude numbers without excluding the free surface mesh behind the transom stern, and the wave generated by both the bulbous bow and transom stern can be successfully determined without oscillation, which is very important for hull form optimization, because a comparison of the wave profiles is a traditional method to judge the resistance performance.

CONCLUSIONS

The TEBEM combined with the simplified free surface condition is presented in this paper for the prediction of the wave-making resistance, hull gesture and wave profile of

different hull forms, and the calculated results for different hull forms are compared with the experimental results. The following conclusions are drawn from this paper:

When the TEBEM is applied the boundary condition of tangential velocity is exerted at every control point and calculated directly. The computed results show that the TEBEM method is efficient in predicting the wave-making resistance, hull gesture and wave pattern for different hull forms, and accurate wave profile and hull response can be obtained even for a full form ship with large block coefficient.

The calculations based on different schemes of hull surface discretization proved that the calculation with the use of the current method converges well, whereas the mesh scheme has a little effect on the computed results.

Because the TEBEM leads to the three times greater amount of the known numbers than the traditional method, the computing time for the TEBEM is relatively greater than in case of the traditional method.

For the full form ship, some short waves are not contained in the computed wave pattern, and the negative pressure area of hull surface is relatively larger than that resulting from the CFD calculations, which leads to that the sinkage computed by using the current method is a little larger. This is perhaps limited by the non-viscosity and the linear free surface condition, therefore in the future work the TEBEM method will be applied to a nonlinear method.

BIBLIOGRAPHY

1. Chen J.K., Duan W.Y., Zhao B.B., Ma Q.W. : *Time domain hybrid TEBEM for 3D hydrodynamics of ship with large flare at forward speed.* The 32nd International Workshop on Water Waves and Floating Bodies, Dalian, China, , 2017, pp. 23-26.

2. Dai, Y. : *Potential flow theory of ship motions in waves*. National Defense Industry Publication, Beijing, , 2008. 11-33.

3. Dawson C.W.: A practical computer method for solving ship-wave problems. *In: Proceedings of Second International Conference on Numerical Ship Hydrodynamics*, pp. 30-38.

4. Doctors L.J., 2006. *A numerical study of the resistance of transom-stern monohulls.* In: Fifth International Conference on High-Performance Marine Vehicles, 1977, pp. 1-14.

5. Doctors L.J., Macfarlane G.J., Young R. : *A study of transom-stern ventilation*. In: International Shipbuilding Progress, 54, 2007, pp. 145-163.

6. Duan W.Y. : *Taylor expansion boundary element method for floating body hydrodynamics*. In: 27th International Workshop on Water Waves and Floating Bodies, 2012. Copenhagen, Danmark.

7. Duan W.Y., Chen, J.K., Zhao, B.B. : *Second-order Taylor expansion boundary element method for the second-order wave radiation problem*. Applied Ocean Research, 52, 2015, pp. 12-26.

8. IHI, SRI, U. of Tokyo and Yokohama N.U. : *Cooperative experiments on Wigley parabolic models in Japan*, 1983.

9. Guha A., Falzaranoa J. : *Application of multi-objective genetic algorithm in ship hull optimization*. Ocean System Engineering, Vol. 5, No. 2 (2015) , pp. 91-107.

10. Larsson L., Stern F., Visonneau M.: *A workshop on numerical ship hydrodynamics*. Gothenburg, Sweden, 2010.

11. Lu Y., Chang X., Hu A.K.: *A hydrodynamic optimization design methodology for a ship bulbous bow under multiple operating conditions*. Engineering Applications of Computational Fluid Mechanics, Vol. 10, 2016, No. 1, pp. 330–345.

12. Minchev A., Schmidt M., Schnack S. : *Contemporary bulk carrier design to meet IMO EEDI requirements*. Third International Symposium on Marine Propulsors, Launceston, Tasmania, 2013.

13. Nakos, D. E.: *Ship wave patterns and motions by a three dimensional Rankine panel method*. Massachusetts Institute of Technology, 1990.

14. Peng H., Ni S., Qiu W.: *Wave pattern and resistance prediction for ships of full form*. Ocean Engineering, 87, 2014 , pp. 162-173.

15. Raven H.C. :. *Nonlinear ship wave calculations using the rapid method*. In: Sixth International Conference on Numerical Ship Hydrodynamics, Iowa City, 1994

16. Raven H.C.: *A solution method for the nonlinear ship wave resistance problem*. A Dissertation for the Degree of Doctor., Delft University of Technology, 1996.

17. Sherbaz S.: *Ship Trim Optimization for Reducing Resistance by CFD Simulations*. A Dissertation for the Degree of Doctor, Harbin Engineering University, 2014.

18. Sun J.L., Tu H.W., Chen Y.N., Xie D., Zhou J.J.: *A study on trim optimization for a container ship based on effects due to resistance. Journal of Ship Research*, Vol. 60, 2016, No. 1, pp. 30–47

19. Tarafder M.S., Alia M.T., Nizamb M.S. : *Numerical prediction of wave-making resistance of pentamaran in unbounded water using a surface panel method.* Procedia Engineering, 56, 2013, pp. 287-296.

20. Takeshi H., Hino T., Hinatsu M., Tsukada Y., Fujisawa J.: *ITTC Cooperative Experiments on a Series 60 Model at Ship Research Institute-Flow Measurements and Resistance Test* , 1987

21. Tarafder M.S., Suzuki K. : *Numerical calculation of free-surface potential flow around a ship using the modified Rankine source panel method*. Ocean Engineering, 35, 2008, pp. 536-544.

22. Tarafder M.S., Suzuki K.: *Wave-making resistance of a catamaran hull in shallow water using a potential-based panel method*. Journal of Ship Research, 52(1), 2008, pp. 16-29.

23. Toda Y., Stern F., Longo J. : *Mean-flow measurements in the boundary layer and wake and wave field of a Series 60 CB=0.6 ship model for Froude Numbers 0.16 and 0.316*. IIHR Report, No. 352, 1991.

24. Zhang B.J. *The optimization of the hull form with the minimum wave making resistance based on Rankine source method*. Journal of hydrodynamics, 21(2) , 2009, pp. 277-284.

25. Zhang B.J., Miao A.: *The design of a hull form with the minimum total resistance.* Journal of Marine Science and Technology, 23(5) , 2015, pp. 591-597

26. Zhang B.J., Miao A. : *Research on design method of the full form ship with minimum thrust deduction factor*, China Ocean Eng., 29(2), 2015, pp. 301-310

CONTACT WITH THE AUTHORS

Yunbo Li
e-mail: yunboz@163.com

College of Ocean Science and Engineering of SMU,
Shanghai Maritime University
Shanghai
CHINA